LBL-2299
c.1

INORGANIC MATERIALS RESEARCH DIVISION
Annual Report 1973

For Reference

Not to be taken from this room

Lawrence Berkeley Laboratory
University of California Berkeley

LBL-2299
c.1

IMRD

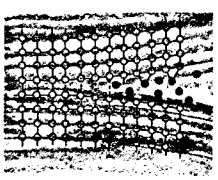

Metallurgical Engineering

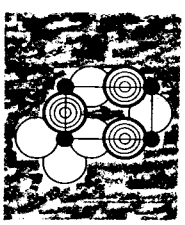

Chemistry

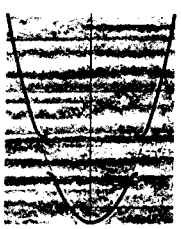

Solid-State Physics

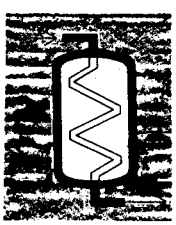

Chemical Engineering

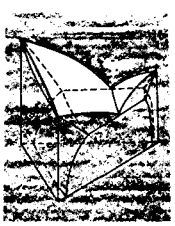

Ceramic Engineering

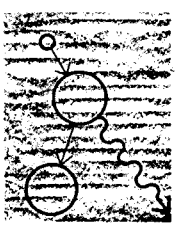

Nuclear Engineering

DISCLAIMER

This document was prepared as an account of work sponsored by the United States Government. While this document is believed to contain correct information, neither the United States Government nor any agency thereof, nor the Regents of the University of California, nor any of their employees, makes any warranty, express or implied, or assumes any legal responsibility for the accuracy, completeness, or usefulness of any information, apparatus, product, or process disclosed, or represents that its use would not infringe privately owned rights. Reference herein to any specific commercial product, process, or service by its trade name, trademark, manufacturer, or otherwise, does not necessarily constitute or imply its endorsement, recommendation, or favoring by the United States Government or any agency thereof, or the Regents of the University of California. The views and opinions of authors expressed herein do not necessarily state or reflect those of the United States Government or any agency thereof or the Regents of the University of California.

LBL-2299
UC-2 General, Miscellaneous,
and Progress Reports
TID-4500-R61

INORGANIC MATERIALS RESEARCH DIVISION ANNUAL REPORT, 1973

April 1974

Lawrence Berkeley Laboratory
University of California
Berkeley, California

Work done under
U.S. Atomic Energy Commission
Contract No. W-7405-eng-48

Printed in the United States of America
Available from
National Technical Information Service
U.S. Department of Commerce
5285 Port Royal Road
Springfield, Virginia 22151
Price: Printed Copy $7.60; Microfiche $1.45

INORGANIC MATERIALS RESEARCH DIVISION ANNUAL REPORT, 1973*

Contents

GENERAL INTRODUCTION xi

I. CHEMISTRY

A. Inorganic Chemistry

William L. Jolly, Principal Investigator

1. Estimation of Atomic Charges by an Electronegativity Equalization Procedure Calibrated with Core Binding Energies 3
2. Reactions of the Heptasulfur Imide Anion 3
3. The Reaction of Hydrogen with Copper (I) in Liquid Ammonia-Amide Solutions 4
4. The Reaction of Potassium Germyl with Boron Trimethyl 4
5. Research Plans for Calendar Year 1974 5
6. 1973 Publications and Reports 5

Robert E. Connick, Principal Investigator

1. Oxygen-17 NMR Studies of the Rate of Water Exchange from Partially Complexed Nickel Ion 7
2. The Exchange Lifetime of Water Molecules in the Second Coordination Sphere of Chromic Ion 7
3. Computer Simulation of Solvent Exchange with the First Coordination Sphere of Metal Ions 7
4. Research Plans for Calendar Year 1974 7
5. 1973 Publications and Reports 8

Neil Bartlett, Principal Investigator

1. Noble-Gas Chemistry 9
2. Use of O_2^+ Salts in the Generation of Novel Cations and Radicals 11
3. High Oxidation States of the Heavy Elements 12
4. Research Plans for Calendar Year 1974 12
5. 1973 Publications and Reports 13

B. Solid State Chemistry and Physics

Norman E. Phillips, Principal Investigator

1. Heat Capacity of the Kondo-Superconductor $(La,Ce)Al_2$ 15
2. Heat Capacity of the Singlet-Ground-State Systems $PrCu_2$, $TmCu_5$ and $HoCu_5$ 16
3. The Heat Capacity of Terbium Ethyl Sulphate 16
4. The Low-Temperature Heat Capacity of Natrolite 17
5. Magnetic Field Dependence of the Low-Temperature Heat Capacity of Neodymium 17
6. Research Plans for Calendar Year 1974 17
7. 1973 Publications and Reports 18

George Jura, Principal Investigator

1. Heat Capacities of Metals Under High Pressure 19
2. Optical Studies of Solids Under High Pressure 19
3. Heat Capacity of Bismuth at High Pressure 21
4. Research Plans for Calendar Year 1974 22

Gabor A. Somorjai, Principal Investigator

1. Low Energy Electron Diffraction (LEED) Studies of Surfaces 23
2. Auger Electron Spectroscopy of Surfaces 24
3. Catalysis by Single Crystal Surfaces 25
4. Molecular Beam Scattering from Surfaces 26
5. Solar Cell Research 27
6. Research Plans for Calendar Year 1974 28
7. 1973 Publications and Reports 29

Lee F. Donaghey, Principal Investigator

1. Chemical Vapor Deposition 30
2. Chemical Transport 32
3. Crystallization 33
4. Sputter Deposition 33
5. Solid-State Electrochemistry 33
6. Research Plans for Calendar Year 1974 34
7. 1973 Publications and Reports 35

C. Electrochemistry
Charles W. Tobias, Principal Investigator
1. Fundamental Studies of Ionic Mass Transport 36
2. Electrolysis at High Current Densities 37
3. Electrochemistry in Nonaqueous Solvents 40
4. Research Plans for Calendar Year 1974 40
5. 1973 Publications and Reports 40
Rolf H. Muller, Principal Investigator
1. Optical Studies of Interfacial Phenomena 42
2. Hydrogen Economy 45
3. Research Plans for Calendar Year 1974 45
4. 1973 Publications and Reports 46
John Newman, Principal Investigator
1. Current Distribution on a Rotating Sphere Below the Limiting Current 47
2. The Short-Time Response of a Disk Electrode 47
3. Measurement of the Transient Response of a Disk Electrode 48
4. Transient Convective Diffusion to a Disk Electrode 49
5. Rotating Ring-Disk Electrodes 49
6. Mass Transfer to a Plane Below a Rotating Disk 50
7. Mass Transfer to a Rotating Disk Electrode in the Region of Transition to Turbulent Flow 50
8. Mass Transfer in Porous Electrodes 50
9. Steady State Current Distribution on a Rotating Disk Below the Limiting Current for a Redox Reaction 51
10. The Removal of Lead Ions from very Dilute Solutions Using a Porous Flow-Through Electrode 51
11. Admittance Coupling on a Ring-Disk Electrode 53
12. Research Plans for Calendar Year 1974 53
13. 1973 Publications and Reports 53
D. Physical Chemistry
Leo Brewer, Principal Investigator
1. Thermodynamic Properties of Third and Fourth Group Transition Metals with Platinum Group Metals 55
2. Application of the Regular Solution Theory to Metallic Solutions 55
3. Thermodynamic Evaluation and Compilation of Metal Alloy Systems 55
4. The Matrix Spectra of Ca with O, O_2, and N_2O 55
5. Research Plans for Calendar Year 1974 55
6. 1973 Publications and Reports 56
Charles B. Harris, Principal Investigator
1. Excited Triplet States in Molecules and Molecular Crystals 57
2. Optical Detection of Coherence in Molecular Excited Localized and Delocalized Band States 57
3. Exciton-Trap Interactions in the Coherent and Incoherent Limits 58
4. The Decay of Localized States into Delocalized Band States 59
5. The Theory of Optically Detected Spin Coherence in Excited Triplet States 59
6. The Theory of Optically Detected Spin Coherence in Non-Stationary States 59
7. Optically Detected Carr-Purcell Trains and Coherent Averaging Theory . . . 59
8. Optically Detected Spin Locking and Its Applications to Kinetic Phenomena 60
9. Optically Detected Adiabatic Demagnetization in Excited Triplet States in Zero-Field and the Application to Kinetic Phenomena 60
10. Optically Detected Rotary Echo Trains in Excited Triplet States 60
11. Picosecond Spectroscopy: Coherence in Vibrational Relaxation 60
12. Energy and Electron Transfer in Photosynthetic Bacterial Systems 61
13. Research Plans for Calendar Year 1974 61
14. 1973 Publications and Reports 62

Alexander Pines, Principal Investigator
1. Nuclear Magnetic Double Resonance Spectrometer 63
2. Magnetic Shielding in Single Crystals 64
3. Dynamics of Nuclear Magnetic Double Resonance 67
4. Long-Lived Nuclear Spin Transients in Solids 68
5. Spin Thermodynamics in Time-Dependent Fields 69
6. Research Plans for Calendar Year 1974 70
7. 1973 Publications and Reports 71

Ronald R. Herm, Principal Investigator
1. Crossed Beams Chemistry: Alkaline Earth Atom Reactions 72
2. Photodissociation of NaBr, NaI, and KI Vapors and Collisional Quenching of $Na^*(3^2P)$, $K^*(4^2P)$, and $K^*(5^2P)$ by Foreign Gases 73
3. Energy Dependence of Sensitized Fluorescence: $Hg^* + Tl \rightarrow Hg + Tl^*$ 74
4. Collision Dynamics Involving Metal Atoms 76
5. Research Plans for Calendar Year 1974 76
6. 1973 Publications and Reports 76

Harold S. Johnston, Principal Investigator
1. Experimental Studies 78
2. Theoretical Studies 80
3. Research Plans for Calendar Year 1974 83
4. 1973 Publications and Reports 83

Bruce H. Mahan, Principal Investigator
1. Dynamics of the O^+-H_2 Reaction: Reactive Scattering at Relative Energies above 15 eV 85
2. Analytical Treatment of the Sequential Impulse Model for Chemical Reaction 86
3. Dynamics of the C^+-H_2 Reaction 86
4. Large Angle Inelastic Scattering of Na^+ by D_2 87
5. Dynamics of the N^+-H_2 Reaction at Low Energies 88
6. Research Plans for Calendar Year 1974 88
7. 1973 Publications and Reports 88

William H. Miller, Principal Investigator
1. Improved Classical Path Approximation for the Boltzmann Density Matrix 90
2. Potential Curves and Inelastic Cross Sections for Low-Energy Collisions of O^+ and He 90
3. Partial Averaging in Classical S-Matrix Theory: Vibrational Excitation of H_2 by He 91
4. Penning and Associative Ionization of Triplet Metastable Helium Atoms . . 92
5. Research Plans for Calendar Year 1974 93
6. 1973 Publications and Reports 93

Rollie J. Myers, Principal Investigator
1. Molecular Field Effects in Electron Paramagnetic Resonance Spectroscopy 95
2. Electron Spin Relaxation for $Cu(NH_3)_6^{2+}$ in Liquid Ammonia 95
3. Electron Spin Relaxation for $Ni(H_2O)_6^{2+}$ in Solution 96
4. Electron-Electron Double Resonance for Two Radicals in Solution 97
5. Electron Paramagnetic Resonance Spectra of Radical Anions in Liquid Ammonia 98
6. Research Plans for Calendar Year 1974 98
7. 1973 Publication 98

Kenneth S. Pitzer, Principal Investigator
1. Solutions of Electrolytes 99
2. Nuclear Spin Species Effects in the Heat Capacity of CH_4 99
3. Anomalous Internal Motions in Molecules 99
4. Research Plans for Calendar Year 1974 100
5. 1973 Publications and Reports 100

E. Nuclear Science
Donald R. Olander, Principal Investigator
1. Isotope Exchange of Water Vapor on Pyrolytic Graphite 102
2. The Oxidation of Ammonia by O_2 on Polycrystalline Platinum by Modulated Molecular Beam Mass Spectrometry 102
3. The Thermal Accommodation Coefficients of Helium and Xenon on UO_2 and Stainless Steel 102
4. Diffusion of Lanthanum in Molten Uranium 103
5. Oxygen Redistribution in Ceramic Nuclear Fuels 103
6. The Conservation Equations Governing Porosity and Actinide Redistribution in Mixed Oxide Fuels 104
7. The Kinetics of Actinide Redistribution by Vapor Migration in Mixed Oxide Fuels (I). By Cracks 104
8. The Kinetics of Actinide Redistribution by Vapor Migration in Mixed Oxide Fuels (II). By Pores 105
9. The Shape of the Doppler-Broadened Spectral Lines Produced by Light-Atom Bombardment of Metals 105
10. Research Plans for Calendar Year 1974 105
11. 1973 Publications and Reports 105

II. METALLURGY
A. Crystal Imperfections
Jack Washburn, Principal Investigator
1. Transmission Electron Microscope Investigation of the Growth of Copper Precipitate Colonies in Silicon 109
2. Determination of Loop Type in As^+ Implanted Silicon 109
3. Memory Switching Effects in As-Te-I Chalcogenide Glass 109
4. Computer Simulation of Frank Loop Contrast in Field Ion Images 110
5. On the Annealing of Stacking Fault Tetrahedra and Frank Dislocation Loops in Silver 110
6. On the Nature of the Long-Term Degradation of "Cadmium Sulfide" Solar Cells 111
7. Electron Microscope Studies of Microerosion in MgO Single Crystals 111
8. Research Plans for Calendar Year 1974 111
9. 1973 Publications and Reports 112
B. Theoretical Metallurgy
John W. Morris, Jr., Principal Investigator
Introduction 113
1. Thermodynamics 113
2. Correlation of Microstructure to Processing 116
3. Correlation of Mechanical Properties to Microstructure 117
4. Alloy Design 130
5. Research Plans for Calendar Year 1974 137
6. 1973 Publications and Reports 137
C. Microstructure, Properties and Alloy Design
Gareth Thomas, Principal Investigator
Synopses of Research Programs on Structure, Properties, and Design of Materials 139
1. Design of Experimental Strong, Tough, Economical Structural Steels 139
2. The Stress-Induced Martensite-Austenite Interface in Fe-15Ni-15Cr Single Crystals 146
3. On Structural Interpretation of Short Range Order 147
4. Lattice Imaging of Ordered Alloys 147
5. The Metastable Phase Ni_2Mo and the Initial Stages of Ordering in Ni-Mo Alloys 148
6. Loss of Coherency in Spinodally Decomposed Cu-Ni-Fe Alloys 149
7. Research in Progress 149
8. Research Plans for Calendar Year 1974 151
D. High Voltage Electron Microscopy
Gareth Thomas, Principal Investigator
1. Current Research Programs 152
2. Research Plans for Calendar Year 1974 158
3. 1973 Publications and Reports 158

E. Alloy Design
Victor F. Zackay and Earl R. Parker, Principal Investigators
Introduction 160
1. Design of Interstitial-Free Cryogenic Alloys 160
2. Influence of Microstructure on Fatigue Crack Propagation in a Cryogenic Alloy 162
3. Microstructural Variables and Fracture Toughness of High Strength C-Mo and C-Mo-Ni Steels 163
4. Influence of Heat Treatment on the Fatigue Crack Growth Rates in a Secondary Hardening Steel 165
5. Structure and Elevated Temperature Properties of Non-Carbon-Containing Ferritic Alloys Strengthened by a Laves Phase 167
6. Investigation of Bainitic Hardenability in Steels by the use of a Rapid Magnetometric Technique 169
7. An Isothermal Study of Bainitic and Martensitic Transformations in Some Low Alloy Steels 171
8. Research Plans for Calendar Year 1974 173
9. 1973 Publications and Reports 173

F. High Field Superconductivity
Milton R. Pickus, Principal Investigator
Introduction 175
1. Present Status of IMRD Powder Rolled Superconducting Tape 175
2. Research Plans for Calendar Year 1974 176
3. 1973 Publications and Reports 177

G. Powder Metallurgy
Milton R. Pickus, Principal Investigator
Introduction 178
1. Summary of Activities in 1973 178
2. Research Plans for Calendar Year 1974 178
3. 1973 Publications 179

H. Advanced Materials
Robert H. Bragg, Principal Investigator
1. K-Emission Spectra of Glassy Carbon-Advanced Materials 180
2. Void Structure of Glassy Carbon 181
3. Charge Transport in Glassy Carbon 181
4. Electronic Properties of Unidirectionally Solidified Eutectics 182
5. Small-Angle Scattering by Pyrolytic Graphite 182
6. Other Work in Progress 182
7. Research Plans for Calendar Year 1974 183
8. 1973 Publications and Reports 183

III. CERAMIC SCIENCE

A. High Temperature Reactions
Alan W. Searcy, Principal Investigator
1. The Variation with Temperature of the Congruent Vaporization Composition of Gallium Sesquisulfide (Ga_2S_3) 187
2. Kinetics of Dissociative Vaporization Reactions 188
3. Thermodynamics of Decomposition of Strontium Sulfate and Barium Sulfate. 188
4. Magnetic Moment of the Se_2 Molecule 189
5. The Kinetics of Decomposition of Barium Carbonate 190
6. Research Plans for Calendar Year 1974 190
7. 1973 Publications and Reports 191

B. Microstructure and Mechanical Behavior of Ceramic Materials: Glass- and Ceramic-Metal Systems
Joseph A. Pask, Principal Investigator
1. Diffusion and Phase Relationship Studies in the Silica-Alumina System 192
2. Permeation of Silicates in Magnesia and Forsterite Compacts. 193
3. Phase Distribution in Solid-Liquid-Vapor Systems 193
4. Thermodynamics of Wetting 194
5. Thermodynamics of Solid State Sintering 194
6. Kinetics of Intermediate and Final Stages of Solid State Sintering 194
7. Kinetics and Thermodynamics of Liquid Phase Sintering 195
8. Polycrystalline Spinel from Powders Prepared by Freeze Drying Technique . . 196
9. Effect of Fabrication on Polycrystalline MgO Microstructure 196

10. Impact Fracture of Brittle Transparent Materials 197
11. Creep of Lithium Fluoride Single Crystals at Elevated Temperatures 197
12. Time-Dependence of Mechanical Behavior of MgO Single Crystals 198
13. Interfacial Reactions and Wetting Behavior of Glass-Iron Systems 199
14. Effect of Composition on Glass-Metal Interfact Reactions and Adherence . . 199
15. Metal-Glass Interfaces 199
16. Research Plans for Calendar Year 1974 200
17. 1973 Publications and Reports 200

C. Relation of Microstructure to Properties in Ceramics
Richard M. Fulrath, Principal Investigator
Introduction 202
1. Relation of Processing Parameters to the Properties of Lithium Ferrite 202
2. A liquid Phase Densification Technique for the Lead Zirconate Titanate System 204
3. Liquid Phase Sintering in Selected Systems 206
4. Solid State Sintering Studies 208
5. Permeation of Helium in Polycrystalline Al_2O_3 211
6. Research Plans for Calendar Year 1974 211
7. 1973 Publications and Reports 212

IV. SOLID STATE PHYSICS

A. Theoretical Solid State Physics
Marvin L. Cohen, Principal Investigator
Introduction 215
1. Semiconductors and Insulators. 215
2. Amorphous Materials 215
3. New Theoretical Methods for Solid State Studies 216
4. Crystal Structure 216
5. Metals, Superconductivity and X-Ray Scattering 217
6. Research Plans for Calendar Year 1974 217
7. 1973 Publications and Reports 217

B. Far Infrared Properties of Solids
Paul L. Richards, Principal Investigator
1. Far Infrared Photoconductivity of Ultrapure Germanium 220
2. Balloon-Based Measurements of the Cosmic Background Radiation 220
3. Surface Magnetic Resonance in MnF_2 222
4. Far Infrared Nonlinear Spectroscopy in $LiNbO_3$ 223
5. Instrumentation for Fourier Spectroscopy 224
6. Far Infrared Spectra of Mn^{3+} in Al_2O_3 224
7. Superconducting Tunnel Junction Bolometers 225
8. Research Plans for Calendar Year 1974 225
9. 1973 Publications and Reports 226

C. Superconductivity
Gene I. Rochlin, Principal Investigator
1. Pair-Quasiparticle Interference Current in Superconducting Tunnel Devices 227
2. Tunnel Junctions with Fluorocarbon Barriers 227
3. Metal Oxide Tunnel Barriers 228
4. Research Plans for Calendar Year 1974 228
5. 1973 Publications and Reports 228

John Clarke, Principal Investigator
1. 1/f Noise in Diffusive Systems 230
2. 1/f Noise in Critical Systems 231
3. Relaxation of Quasiparticle Branch Imbalance in Superconductors 231
4. Electron Focusing in Bismuth: A New Method of Measuring the Diameter of a Fermi Surface 232
5. Determination of BCS Parameter N(O)V in "Normal" Metals 233
6. Superconducting Tunnel Junction Bolometers 234
7. Stable Sensitive Superconducting Devices 234
8. Research Plans for Calendar Year 1974 234
9. 1973 Publications and Reports 235

D. Experimental Solid State Physics and Quantum Electronics
Y. Ron Shen, Principal Investigator
1. Tunable Far Infrared Generation by Optical Mixing 237
2. Optical-Field Induced Ordering in the Isotropic Phase of a Nematic Liquid Crystal 238
3. Experimental Study of Transient Self-Focusing 239
4. Luminescence at High Exciton Densities in CdSe 239
5. Dispersion of Nonlinear Optical Susceptibilities $\chi^{(2)}(2\omega)$ of III-V Semiconductors 240
6. Resonant Raman Scattering in Cu_2O 240
7. Absorption, Photoluminescence, and Resonant Raman Scattering in BiI_3--The Nonexistence of Bielectrons in BiI_3 241
8. Resonant Raman Scattering in Crystalline Se 242
9. Wavelength-Modulation Spectroscopy of Solids 242
10. Rayleigh-Wing Scattering in a Liquid Crystalline Material 243
11. Theoretical Problems 243
12. Research Plans for Calendar Year 1974 244
13. 1973 Publications and Reports 244

APPENDICES
IMRD STAFF FOR 1973 249
VISITING SCIENTISTS 255
DEGREES AWARDED IN 1973 256

*Preceding Annual Reports: LBL-425, LBL-1400.

GENERAL INTRODUCTION

Leo Brewer, Division Head
Victor F. Zackay, Associate Head
Rolf H. Muller, Assistant to Division Head

1973 has been a year with an increase in productivity for the division with 24 Ph.D., 4 Doctor of Engineering and 16 Master of Science degrees being awarded to our students. Journal articles and book chapters published numbered 190, including 14 articles based on work supported by other agencies such as DOT, NSF, EPA, and NASA. Support from these other agencies continues to be a significant fraction of our total this year amounting to approximately 15% of the total budget for the division. Postdoctorals and sabbatical visitors were at an all-time high of 52 for 1973, while our graduate student population remains at about 180 - the same level as in the previous 5 or 6 years.

Principal Investigators in the Inorganic Materials Research Division continue to be involved in the University Campus Administration.

Professor Joseph Pask is an Assistant Dean of the College of Engineering, Professor Rollie Myers is Assistant Dean of the College of Chemistry, and Professor Alan Searcy was Acting Chairman of the Materials Science and Engineering Department from January to June.

Awards and honors were received by a number of the division's investigators in 1973:

Professor Neil Bartlett--Elected Fellow of the Royal Society.

Professor Harold Johnston--1974 American Chemical Society Award

Professor Bruce Mahan--Miller Research Fellowship

Professor J. W. Morris, Jr.,--Robert Lansing Hardy Gold Medal by the Metallurgical Society of AIME.

Professor Earl Parker--Gave the first ASM Western Lecture at the 1973 Western Metal and Tool Exposition and Conference.

Professor Gareth Thomas--Was keynote speaker at the Third International Conference on High Voltage Electron Microscopy, Oxford University, England, August 26-30, 1973.

Several investigators were on sabbatical leave during 1973:

Professor Charles Harris--Fall Quarter in Berkeley.

Professor John Newman--Fall Quarter at the University of Wisconsin.

Professor Joseph Pask--Winter Quarter - extended visits to several laboratories and attended an International Conference on Sintering in Yugoslavia.

Professor Yuen-Ron Shen--University of Paris at Orsay (February through July).

Professor Charles Tobias--Winter and Spring Quarters in Berkeley.

Professor Victor Zackay--Fall Quarter in Berkeley.

The Seventh Annual IMRD Program Review meeting was held on February 1 and 2, 1973. In addition to representatives from the U.S. Atomic Energy Commission Division of Physical Research, and from other laboratories, universities and industrial organizations, the formal reviewers were:

Professor C. S. Barrett, University of Denver.

Professor Emeritus J. Chipman, Massachusetts Institute of Technology.

Professor N. Nachtrieb, The University of Chicago.

Dr. E. Rudy, Oregon Graduate Center for Research.

Professor O. Sherby, Stanford University.

Professor J. Shyne, Stanford University.

Professor W. Smeltzer, McMaster University.

Professor W. Weltner, University of Florida.

I. Chemistry

A. INORGANIC CHEMISTRY

William L. Jolly, Principal Investigator

1. ESTIMATION OF ATOMIC CHARGES BY AN ELECTRONEGATIVITY EQUALIZATION PROCEDURE CALIBRATED WITH CORE BINDING ENERGIES*

William L. Jolly and Winfield B. Perry

The favorite and most practical method for quantitatively describing electron distribution in a molecule is the assignment of partial charges to the atoms. A wide variety of theoretical and empirical methods have been used for evaluating atomic charges, and most of these have served advantageously in the correlation of atomic charge related properties. There is need for a simple method for calculating atomic charges which not only has theoretical justification but also can be related to an experimental measurement that depends fairly directly on atomic charges. We believe that such a method is now possible in the form of the technique of electronegativity equalization calibrated with X-ray photoelectron spectroscopic core binding energies.

The concept of atomic electronegativity equalization has been developed into the concept of the equalization of the electronegativities of bonding orbitals. We define orbital electronegativity as a quantity proportional to the derivative of the energy of an atom with respect to the charge in a particular atomic orbital. It is assumed that the orbital charge may have either an integral or nonintegral value and that the energy may be expressed as quadratic function of the orbital charge. According to the assumptions of the method, the energy is minimized when the orbital electronegativities of each bond are equal.

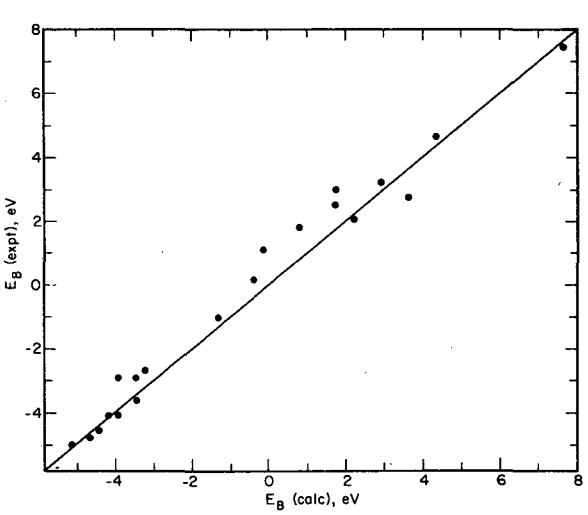

Fig. 1. Plot of E_B(calcd) for nitrogen 1s electrons. (XBL 732-5824)

The calculation involves four empirical parameters (only two of which are needed for most molecules), which have been evaluated by application of the potential model equation for calculating core binding energies to 126 experimental 1s binding energies for 66 gaseous compounds. The method yields standard deviations in the binding energies of carbon, nitrogen, oxygen, and fluorine of ±0.69, ±0.53, ±0.74, and ±0.36 eV, respectively. To illustrate the power of the method in correlating core binding energies, we show in Fig. 1 a plot of experimental E_B's vs calculated E_B's for gaseous nitrogen compounds.

*Abstracted from J. Amer. Chem. Soc. 95, 5442 (1973).

2. REACTIONS OF THE HEPTASULFUR IMIDE ANION*

Marshall H. Mendelsohn and William L Jolly

Various N-substituted derivatives of heptasulfur imide have been prepared by reaction of the imide with strong Lewis acids and with strongly electrophilic reagents. A much wider range of derivatives is potentially available from reactions of the deprotonated imide, S_7N^-. Olsen et al. were the first to report the use of S_7N^- in the synthesis of alkyl derivatives. They concluded, partly because they were unable to deprotonate S_7NH quantitatively, that the treatment of S_7NH with bases causes an irreversible ring-cleavage reaction in addition to deprotonation. They also suggested that the S_7N^- ion is in equilibrium with an open chain isomer. In this paper, we describe a method for the quantitative deprotonation of S_7NH, present data which help clarify the nature of the ring-cleavage and isomerization, and report the synthesis of several new organo derivatives of S_7NH.

Heptasulfur imide can be completely deprotonated by treatment of its solution in tetrahydrofuran with powdered KOH at -62°C for 15 min; the resulting solution of $K^+S_7N^-$

reacts with CH_3I to give an essentially quantitative yield of the N-methyl derivative of heptasulfur imide. Extended treatment of a $K^+S_7N^-$ solution with KOH causes irreversible decomposition. In solution, the S_7N^- ion undergoes spontaneous isomerization, probably to an open chain form; at temperatures above about -40°C, the rate of isomerization is sufficient to permit equilibrium between the two forms to be readily achieved. The compounds benzyl heptasulfurimidoformate, ethyl heptasulfurimidoformate, and heptasulfurimidotrimethylsilane are formed by the action of the ring form of S_7N^- on the corresponding chloro compounds.

*Abstracted from J. Inorg. Nucl. Chem. 35, 95 (1973).

3. THE REACTION OF HYDROGEN WITH COPPER (I) IN LIQUID AMMONIA-AMIDE SOLUTIONS*

Kenneth A. Strom and William L. Jolly

Only a few reactions of molecular hydrogen have been studied in liquid ammonia. The amide-catalyzed para-ortho conversion and isotope exchange reactions have been found to be first order in amide concentration and first order in hydrogen concentration. The reaction

$$e^-_{am} + NH_3 \rightleftharpoons NH_2^- + 1/2H_2$$

has been found to be reversible. Hydrogenation of trans 1,2-diphenylethylene and diphenylacetylene in the presence of potassium amide and a reduced iron oxide catalyst has been reported.

We now wish to report the reaction of hydrogen with copper(I) amide complex [probably $Cu(NH_2)_2^-$] in the presence of excess potassium amide or cesium amide to form thermally unstable orange-red solids with the approximate compositions $K_2Cu_3H_5 \cdot xNH_3$ and $CsCuH_2 \cdot xNH_3$. The compounds have been characterized by elemental analysis, X-ray powder diffractometry, and, in the case of the potassium compound, Raman spectroscopy and magnetic measurements.

The preparation of the ternary hydrides can be represented by the equations

$$5H_2 + 2K^+ + 3Cu(NH_2)_2^- \rightarrow K_2Cu_3H_5 + 5NH_3 + NH_2^-$$

and

$$2H_2 + Cs^+ + Cu(NH_2)_2^- \rightarrow CsCuH_2 + 2NH_3.$$

The mechanism probably involves either the intermediate formation of hydride ion from the reaction of hydrogen with amide, or a concerted reaction involving a Cu^+-H_2-NH_2^- complex. Examples of both types of mechanism are known.

*Abstracted from J. Inorg. Nucl. Chem. 35, 3445 (1973).

4. THE REACTION OF POTASSIUM GERMYL WITH BORON TRIMETHYL*

Esther R. de Staricco, Chris Riddle, and William L. Jolly

Potassium germyltrihydroborate, $KGeH_3BH_3$, was prepared and characterized in this laboratory. Two other germylborates, $LiGePh_3BPh_3$ and $LiGeEt_3BPh_3$, are known, and there is evidence that similar species, $KGeH_3BX_3$, are the initial products of reaction between potassium germyl, $KGeH_3$, and several BX_3 compounds (X = I, Cl, OMe). In this note we describe the reaction between $KGeH_3$ and boron trimethyl to form the adduct $KGeH_3BMe_3$.

The potassium germyl solutions reacted with boron trimethyl at 0°C to produce clear colorless solutions which became straw-colored after several hours. Generally a trace of germane, equivalent to ca 1% of the germanium, was the only volatile product. When more than an equimolar amount of BMe_3 was used, the excess BMe_3 was recovered. Hydrolysis of the final reaction mixture gave hydrogen, germane, and digermane. The data taken as a whole are consistent with the initial formation of the germyltrimethylborate ion:

$$GeH_3^- + BMe_3 \rightarrow GeH_3BMe_3^- .$$

In a mater of minutes, this species undergoes disproportionation:

$$2GeH_3BMe_3^- \rightarrow HBMe_3^- + Ge_2H_5BMe_3^- .$$

The latter reaction is analogous to the disproportionation of GeH_3BH_3:[1]

$$2GeH_3BH_3^- \xrightarrow{B_2H_6} BH_4^- + Ge_2H_5BH_3^- .$$

*Abstracted from J. Inorg. Nucl. Chem. 35, 297 (1973).

1. D. S. Rustad and W. L. Jolly, Inorg. Chem. 7, 213 (1968).

5. RESEARCH PLANS FOR CALENDAR YEAR 1974

William L. Jolly

a. X-Ray Photoelectron Spectroscopy

The following projects are nearing completion, and the results should be published in 1974: (a) a study of static relaxation in germane and the estimation of relaxation energy differences from Auger and core binding energies of germanium compounds, (b) determination of the electron distribution in methoxy(methyl)carbenepentacarbonylchromium(0) by X-ray photoelectron spectroscopy, (c) the correlation of core electron binding energies with charge distributions for compounds of carbon, silicon, and germanium, (d) a study of core electron binding energies of thiazyl fluoride and other sulfur compounds, (e) a study of charge distribution in a variety of nickel coordination compounds, (f) a study of the valence MO levels in some volatile compounds of silicon and germanium, and (g) an extension of the electronegativity equalization method for estimating atomic charges to compounds containing any elements from the periodic table.

We plan to study a variety of oxyfluoride compounds such as POF_3, SO_2F_2, SOF_2, etc., to determine the importance of hyperconjugation or "no-bond" resonance in such compounds. We have begun, and will continue, a study of the series of compounds PMe_3, PMe_3BH_3, PMe_3CH_2, PMe_3NH, and PMe_3O. It will be of interest to determine whether it is necessary to include phosphorus d orbitals in the bonding to account for the charge distributions in these molecules.

We shall continue to work on the problem of studying high-temperature vapor species. It is hoped that a new spectrometer, incorporating the capability of studying such species, will be built in a year or so.

b. Boron Hydride Chemistry

We are completing a study of the quenching flow reactor in the synthesis of BH_3OH^- and $OONO^-$; the results should be published in 1974. We plan to investigate the possible application of BH_3OH^- as a stereospecific or selective reducing agent in organic and inorganic synthesis. The reduction of octyl halides (to octane) and substituted cyclohexanones (to the corresponding alcohols) will be studied.

c. Germanium Chemistry

We plan to study the kinetics and mechanism of the decomposition of aqueous solutions of GeH_3CO_2K and GeH_3CO_2H. It will be of interest to compare the data for the decarbonylation and decarboxylation reactions with data for the corresponding reactions of the carbon analogs, CH_3CO_2K and CH_3CO_2H. Preliminary work indicates that the decomposition reaction in basic solution is first order in $GeH_3CO_2^-$ and that in strongly basic solution the decarboxylation reaction is accompanied by a side reaction involving the formation of H_2.

We plan to complete a study of the preparation and characterization of organic esters of GeH_3CO_2H. These studies should give insight to the fundamental differences between the chemistries of the Group IV elements.

d. Liquid Ammonia Chemistry

Having recently completed a study of the kinetics of the hydrolysis of BH_4^- in aqueous solutions, we plan to investigate the corresponding ammonolysis reaction in liquid ammonia. Even the stoichiometry of the $NH_4^+ + BH_4^-$ reaction in liquid ammonia is unknown; useful synthetic as well as mechanistic information should be obtained. The work will require measurements on high-pressure ammonia solutions at room temperature and above.

6. 1973 PUBLICATIONS AND REPORTS

William L. Jolly and Associates

Journals and books

1. M. H. Mendelsohn and W. L. Jolly, Reactions of the Heptasulfur Imide Anion, J. Inorg. Nucl. Chem. 35, 95 (1973)(LBL-820).

2. E. Staricco, C. Riddle, and W. L. Jolly, The Reaction of Potassium Germyl with Boron Trimethyl, J. Inorg. Nucl. Chem. 35, 297 (1973)(LBL-826).

*3. W. L. Jolly, Sodium and Potassium Products and Production, in Encyclopaedia Britannica, 1973 ed.

*4. W. L. Jolly, Hydrogen and Its Compounds, in Encyclopaedia Britannica, 1973 ed.

5. K. A. Strom and W. L. Jolly, The Reaction of Hydrogen with Copper(I) in Liquid Ammonia-Amide Solutions, J. Inorg. Nucl. Chem. 35, 3445 (1973)(LBL-1439).

*6. W. L. Jolly, book review: "Preparative Methods in Solid State Chemistry," P. Hagenmuller, ed., Synth. Inorg. and Metalorg. Chem. 3, 319 (1973).

7. W. L. Jolly and W. B. Perry, Estimation of Atomic Charges by an Electronegativity Equalization Procedure Calibrated with Core Binding Energies, J. Am. Chem. Soc. 95, 5442 (1973)(LBL-1492).

Papers presented

1. X-Ray Photoelectron Spectroscopy, three ACS local section talks in Kingsport, Oak Ridge, and Nashville, Tenn., March 5-7, 1973.

2. W. L. Jolly, "A Comparison of the Chemistries of Carbon and Germanium" and X-Ray Photoelectron Spectroscopy," two talks presented at Indiana University, Bloomington, Indiana, March 8-9, 1973.

3. W. L. Jolly, Applications of X-Ray Photoelectron Spectroscopy in Inorganic Chemistry, du Pont Experimental Station, Wilmington, Delaware, June 11, 1973.

4. W. L. Jolly, X-Ray Photoelectron Spectroscopy and the Estimation of Atomic Charges, Arizona State University, Tempe, Arizona, Sept. 21, 1973.

5. W. L. Jolly, "Atomic Charges and X-Ray Photoelectron Spectroscopy" and "Thermodynamic Aspects of X-Ray Photoelectron Spectroscopy," du Pont Lectureship, Georgia Institute of Technology, Atlanta, Georgia, Nov. 29-30, 1973.

LBL reports

1. O. Pont, X-Ray Photoelectron Spectroscopy of Some Nickel and Iron Compounds (M.S. thesis), LBL-1829, June 1973.

2. W. L. Jolly, The Application of X-Ray Photoelectron Spectroscopy to Inorganic Chemistry, submitted to Coordination Chemistry Reviews (LBL-1878, July 1973).

3. L. O. Pont, A. R. Siedle, M. S. Lazarus, and W. L. Jolly, X-Ray Photoelectron Spectroscopy of Some Nickel Compounds, Inorg. Chem., in press (LBL-1897, Aug. 1973).

4. J. W. Reed, H. H. Ho, and W. L. Jolly, Chemical Synthesis with a Quenched Flow Reactor. Hydroxytrihydroborate and Peroxynitrite, submitted to J. Am. Chem. Soc. as a Communication (LBL-2206, Aug. 1973).

5. W. B. Perry and W. L. Jolly, Static Relaxation in Germane and the Estimation of Relaxation Energy Differences from Auger and Core Binding Energies of Germanium Compounds, submitted to Chem. Phys. Letters (LBL-2216, Aug. 1973).

6. W. B. Perry, T. F. Schaaf, W. L. Jolly, L. J. Todd, and D. L. Cronin, Determination of the Electron Distribution in a Transition Metal Carbene Complex by X-Ray Photoelectron Spectroscopy, submitted as Note to Inorg. Chem. (LBL-2237, Sept. 1973).

7. W. B. Perry and W. L. Jolly, The Correlation of Core Electron Binding Energies with Charge Distributions for Compounds of Carbon, Silicon and Germanium, submitted to Inorg. Chem. (LBL-2238, Sept. 1973).

8. K. A. Strom and W. L. Jolly, The Synthesis and Characterization of Methyl 2-Germaacetate and Ethyl 2-Germaacetate, submitted J. Organometallic Chemistry (LBL-2223, Sept. 1973).

9. W. L. Jolly, M. S. Lazarus, and O. Glemser, Core Electron Binding Energies of Thiazyl Fluoride and other Sulfur Compounds, submitted to Zeitschrift für anorganische und allegemeine Chemie (LBL-2503, Nov. 1973).

---

*Work not supported by A.E.C.

Robert E. Connick, Principal Investigator

1. OXYGEN-17 NMR STUDIES OF THE RATE OF WATER EXCHANGE FROM PARTIALLY COMPLEXED NICKEL ION

Thomas V. Rowland

Nickel ion, when complexed by tridentate iminodiacetate ion (IDA) has three coordination positions occupied by waters, with two of the waters equivalent. Observation of the broadening of the oxygen-17 nuclear magnetic resonance of the bulk water shows that the rates of exchange of the two waters differ measurably, i.e., ca. fivefold. A least-squares fit of the data will be made to determine the rate and NMR parameters with as high accuracy as possible. The previously observed line broadening near 0°C has been found to be due to unexpected pH changes in the solutions. An investigation using the nickel bisiminodiacetate complex, where all six coordination positions are complexed by IDA, has been started to determine whether there is appreciable water exchange at the positions normally occupied by the carboxylate arms of the IDA. The preliminary results indicate very little exchange with water.

2. THE EXCHANGE LIFETIME OF WATER MOLECULES IN THE SECOND COORDINATION SPHERE OF CHROMIC ION

William L. Earl

NMR studies of the exchange lifetimes of solvent molecules in paramagnetic solutions normally measure the lifetime of solvent in the first coordination sphere. It is also of interest to know about the dynamic behavior of solvent molecules beyond the first sphere. Olson, Kanazawa, and Taube [J. Chem. Phys. 51, 289 (1969)] have used the transverse relaxation times of ^{17}O in solutions of Cr(III) and V(II) to set a limit on the lifetime of water molecules in the second sphere. The present work will measure the lifetime of water molecules in the second coordination sphere of Cr(III) using a combination of the transverse and longitudinal relaxation times. Our preliminary measurements indicate that the lifetime of water molecules in the second sphere of Cr(III) is 3×10^{-10} sec. In order to refine this measurement we are employing nonlinear least-squares fits of the absorption spectra and the power saturation curves. We are also attempting to measure the longitudinal relaxation times by another method, i.e., pulsed NMR techniques.

3. COMPUTER SIMULATION OF SOLVENT EXCHANGE WITH THE FIRST COORDINATION SPHERE OF METAL IONS

Robert E. Connick

The computer calculations initiated last year on the modeling of the exchange of a bulk solvent molecule with a solvent molecule in the first coordination sphere of a metal ion have been continued and extended. Currently we are working in two dimensions with an 18-step potential well designed to correspond approximately to a charge-dipole attraction. Results at low activation energies indicate no unique geometry for the activated complex but rather many different geometries. At high activation energies the computer time necessary for finding even a single event becomes prohibitive. Therefore we are attempting to hold the "exchanging" particle in a ring at about the distance it would occupy in the activated complex, while the system equilibrates. The "exchanging" particle is then released and followed forward and backward in time to see if it does in fact exchange. The work is being done in collaboration with Dr. Berni Alder of the Lawrence Livermore Laboratory.

4. RESEARCH PLANS FOR CALENDAR YEAR 1974

Robert E. Connick

The work on rates of water exchange of nickel complexed by iminodiacetate ion and exchange from the second coordination sphere of chromic ion will be completed. Further studies of water exchange rates will be undertaken on one or more of the following problems: The water exchange of cupric ion and the dynamic Jahn-Teller effect; the very fast water exchange of ions such as Sc^{3+}, Ca^{2+}, Zn^{2+}, UO_2^{2+}, Th^{4+}, etc.; the effect of ligands on water exchange rates of other partially complexed metal ion species; the effect of complexing on second coordination sphere rates of exchange. The work on computer modeling of exchange reactions will be extended to three dimensions, and the effect on the rate of exchange of potential depth, potential

shape, and radius ratio will be determined. The nature of the configuration of the activated complex will be investigated. The applicability of the computer results to actual exchange reactions in solution will be looked at carefully.

5. 1973 PUBLICATIONS AND REPORTS

Robert E. Connick and Associates

Journal

1. Edward E. Genser and Robert E. Connick, Exchange of Iodide Ion with Triiodide Ion Studied by Nuclear Magnetic Resonance, J. Chem. Phys. 58, 990 (1973)(LBL-869).

Neil Bartlett, Principal Investigator

1. NOBLE-GAS CHEMISTRY

a. Krypton Chemistry

Douglas E. McKee and Neil Bartlett

The high cost of the cyclotron time for KrF_2 synthesis led, early this year, to a suspension of the program of KrF_2 chemistry started last year. However, the extraordinary oxidizing power of KrF^+ first utilized by us in the synthesis of the novel $XeOF_5^+$ species has been exploited further by others. The projected synthesis of BrF_6^+ utilizing cationic krypton fluoride species, mentioned in our research plans for 1973, has been achieved by R. J. Gillespie and his co-workers (Inorg. Chem., in press).

b. Argon Fixation

Kevin Leary and Neil Bartlett

The matter of AuF_6 synthesis (see gold fluorides) has assumed priority in our attack on the argon fixation problem.

c. Xenon Chemistry

Christopher J. Adams, Boris Žemva, Aachim W. Roland, and Neil Bartlett

(i) Crystallographic Studies (in collaboration with D. H. Templeton, A. Zalkin, B. G. DeBoer, F. J. Hollander, and D. L. Ward of the Nuclear Chemistry Division): Single-crystal studies of the salts $XeF^+AsF_6^-$, $Xe_2F_3^+AsF_6^-$, and $XeF_5^+AsF_6$ have been completed. The essential features of the structures are shown in Fig. 1. The geometry of the $XeF^+AsF_6^-$ unit is remarkably like that of $XeF^+RuF_6^-$, although the packing of these units in the crystal is different for each case. As in the case of $XeF^+RuF_6^-$ discussed in an earlier report (1971) the major canonical form, in the resonance hybrid description of $XeFAsF_6$, must be $XeF^+AsF_6^-$. The comparison of $XeF^+AsF_6^-$ and $XeF^+RuF_6^-$ is of particular interest because of the widely held view that the bonding within the MF_6^- transition metal species is fundamentally different from that in non-transition element species. It is evident from these structures that not only are the two anions very similar in size and shape (they are distorted in their interaction with the cation) but their interactions with the XeF^+ species are similar. Evidently the nature of the F ligand in RuF_6^- is very like that in AsF_6^-. This suggests essentially the same bonding model for each anionic species.

The $Xe_2F_3^+$ ion is a F^- bridged Xe(II) relative of the $Xe_2F_{11}^+$ ion which was reported last year. The shape and dimensions of the $Xe_2F_3^+$ are consistent with $(F\text{-}Xe)^+F^-(Xe\text{-}F)^+$ as the major canonical form. The XeF_5^+ species seen in $XeF_5^+AsF_6^-$ is not significantly different from XeF_5^+ in other salts which we have studied, but the packing of

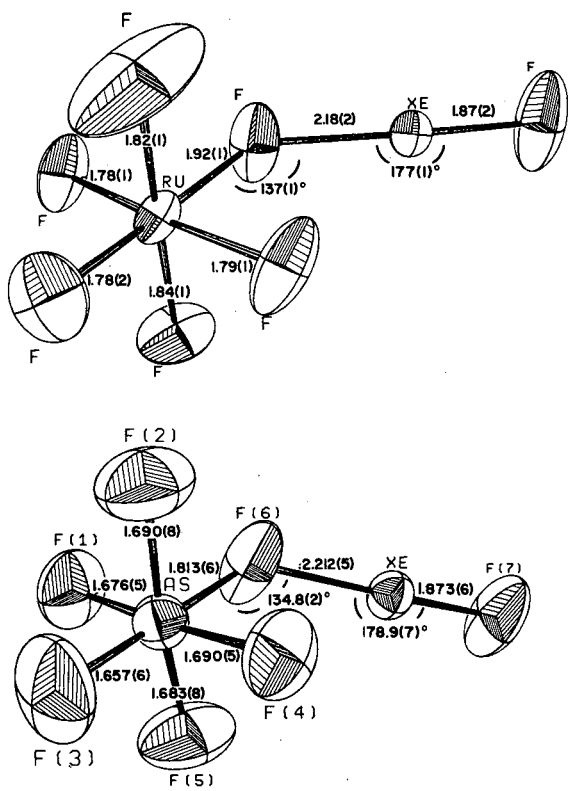

Fig. 1(a). The structural units of $[XeF][AsF_6]$ and $[XeF][RuF_6]$. (XBL 7311-6807)

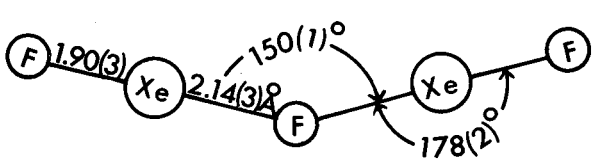

Fig. 1(b). The structural unit of $[Xe_2F_3^+]$. (XBL 738-1120)

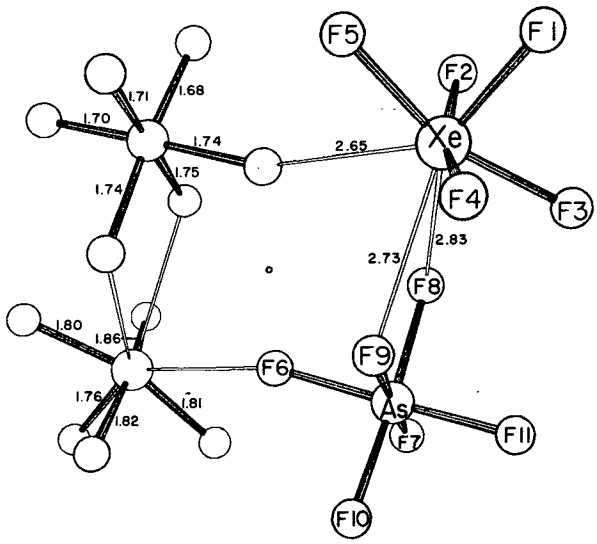

Fig. 1(c). The structural unit in $[XeF_5][AsF_6]$. (XBL 724-665)

the ions differs from that of $XeF_5^+ MF_6^-$ (M = Os, Ir, Pt, Ru, Rh). Curiously, $XeF_5^+ AuF_6^-$ (C. J. Adams) is isostructural with $XeF_5^+AsF_6^-$, and the $(XeF_5MF_6)_2$ structural unit for these compounds is almost identical with the rings seen in the $(XeF_5^+)_2PdF_6^{2-}$ structure reported last year.

(ii) A Raman Study of XeF_6 and Its Complexes (C. J. Adams): The X-ray crystallographic data reported here and earlier have been utilized in assigning the Raman spectra of complexes of XeF_6 with Lewis acids (BF_3, PdF_4, PF_5, AsF_5, RuF_5, PtF_5, and AuF_5) which contain XeF_5^+ or $Xe_2F_{11}^+$ cations.

A full vibrational analysis has been made for the square-pyramidal XeF_5^+ cation. The axial Xe-F stretching fundamental and force constant are anomalously low in comparison with IF_5 (see table), but are well in line with values for other xenon fluorides.

The $Xe_2F_{11}^+$ cation, defined crystallographically in the salt $Xe_2F_{11}^+AuF_6^-$ and reported last year, behaves as two XeF_5^+ species joined by a bridging fluoride ion. The stretching force constant of the bridging Xe-F bond is ca. 0.8 mdyne $Å^{-1}$.

The Raman fingerprints obtained for XeF_5^+ and $Xe_2F_{11}^+$ in this work, and derived for $(XeF_5^+F^-)_x$ (x = 4,6) and molecular XeF_6 from earlier studies of solid and gaseous xenon hexafluoride[5] have been used to investigate the structure of xenon hexafluoride in ionizing and non-ionizing solvents. In HF, xenon hexafluoride, which in concentrated solution is present as $[XeF_5^+F^-]_x$, progressively ionizes on dilution to give $Xe_2F_{11}^+$ and XeF_5^+. On the other hand, in WF_6, $[XeF_5^+F^-]_x$ is in equilibrium with molecular XeF_6. The Spectra of the latter indicate that it is an essentially octahedral molecule which is perturbed by a second-order Jahn-Teller effect.

1. A. G. Robiette, R. H. Bradley and P. N. Brier, Chem. Commun. 1567 (1971).
2. N. Bartlett, M. Gennis, D. D. Gibler, B. K. Morrell, and A. Zalkin, Inorg. Chem. 12, 1717 (1973)
3. K. O. Christe, E. C. Curtis, C. J. Schack, and D. Pilipovich, Inorg. Chem. 11, 1679 (1972).
4. K. Leary, D. H. Templeton, A. Zalkin, and N. Bartlett, Inorg. Chem. 12, 1726 (1973).
5. E. L. Gasner and H. H. Claasen, Inorg. Chem. 6, 1937 (1967); H. H. Claasen, G. L. Goodman, and H. Kim, J. Chem. Phys. 56, 5042 (1973).

	IF_5(g)	XeF_5^+ (in $XeF_5^+RuF_6^-$)
M-F_{ax} (R), Å	1.844(25)[1]	1.793(8)[2]
M-F_{eq} (r), Å	1.869(5)	1.845(9)
< F_{ax}-M-F_{bas} (β), Å	81.9(1)	79.0(17)
f_R, mdyne $Å^{-1}$	4.82[3]	4.25±0.2
f_r, mdyne $Å^{-1}$	3.82	3.95±0.2

(iii) Xenon Difluoride Complexes of PdF_4 and PtF_5 and A Novel Synthesis of Xenon Tetrafluoride (B. Zemva): At 140-150° liquid xenon difluoride oxidizes paramagnetic palladium trifluoride (black) to yield yellow diamagnetic Pd(IV) complexes:

$$(2X+1)XeF_2 + 2PdF_3 \rightarrow 2(XeF_2)_x \cdot PdF_4 + Xe \quad (1)$$

Removal of xenon difluoride under vacuum at 0°C yields sequentially the compounds $4XeF_2 \cdot PdF_4$; $3XeF_2 \cdot PdF_4$, $2XeF_2 \cdot PdF_4$, and finally $XeF_2 \cdot PdF_4$ which is stable with respect to dissociation at 0°. Infrared and Raman spectra of this compound indicate that it is the salt $(XeF^+)_x(PdF_5^-)_x$ the anion of which may be a tetramer like the $(RhF_5)_4$ described last year. This 1:1 compound loses XeF_2 under vacuum at 160° and falls to the compound $XeF_2 \cdot 2PdF_4$. The X-ray powder photographs and vibrational spectra of this compound are almost identical with those of $XePt_2F_{10}$ reported[1] by Jha and Bartlett in 1963. The vibrational evidence suggests that these compounds are the salts $(XeF^+)_x(Pd_2F_9^-)_x$. (It is possible that the anion is a $Pd_8F_{36}^{4-}$ F-bridged cage species.)

Efforts to remove XeF_2 from $XeF_2 \cdot 2PdF_4$ to yield PdF_4 resulted in reduction of the Pd(IV) to PdF_3 and simultaneous oxidation of the xenon difluoride to xenon tetrafluoride. The latter was uncontaminated by XeF_2, the change being cleanly:

$$XeF_2 \cdot 2PdF_4 \rightarrow XeF_4 + 2PdF_3 \quad (2)$$

The sum of Eqs. (1) and (2) amounts to the effective conversion of two moles of XeF_2 to one mole of XeF_4 and one mole of Xe (a pseudo-disproportionation) by the agency of two moles of palladium trifluoride.

A similar study of the $XeF_2 + PtF_4$ system showed that liquid xenon difluoride at ~ 130° oxidized PtF_4 to Pt(V) and yielded the known complexes $Xe_2F_3^+ PtF_6^-$ and $XeF^+PtF_6^-$.

$$5XeF_2 + 2PtF_4 \rightarrow 2Xe_2F_3^+ PtF_6^- + Xe .$$

The $Xe_2F_3^+PtF_6^-$ salt went to $XeF^+PtF_6^-$ under vacuum at 70°. At 140° the $XeF^+PtF_6^-$ salt decomposed to yield $XeF_2 \cdot 2PtF_4$ (which proved to be identical with the material prepared by Jha and Bartlett[1]), and the only xenon fluoride evolved was XeF_4. The decomposition was:

$$2XeF^+PtF_6^- \rightarrow XeF_4 + XeF_2 \cdot 2PtF_4$$

Hitherto XeF_4 has been difficult to prepare in high purity and all syntheses have involved fluorinations in bombs. These reactions provide a convenient route to high-quality material via the difluoride. The latter can be made in pyrex vessels and is relatively safe to handle.

---

1. N. Bartlett and N. K. Jha, in Noble Gas Compounds, edited by H. H. Hyman (University of Chicago Press, Chicago, 1963), p. 23.

(iv) Xenon Compounds Involving SF_5 groups (A. W. Roland): An improved synthesis of SF_5Br was developed to make available macroscopic quantities of high-purity material for the attempted generation of $Xe(SF_5)_2$ and related compounds. Unfortunately all attempts to use SF_5Br, as a route to these compounds, failed. Surprisingly the high-purity compound proved to be relatively inert to cold pure water and unreactive towards mercury--observations which are contrary to those previously reported for this compound. A full vibrational analysis has been made of the compound.

2. USE OF O_2^+ SALTS IN THE GENERATION OF NOVEL CATIONS AND RADICALS

T. J. Richardson and Neil Bartlett

The recent development in these laboratories[1] of convenient high-yield syntheses of high-purity dioxygenyl salts has made these powerfully oxidizing reagents readily available.

We have long sought to oxidize organic aromatic systems with the powerfully oxidizing hexafluorides and although aromatic cation species have been indicated as reaction intermediates, the great lability of the transition metal hexafluorides and their anions has always led to carbon-carbon bond cleavage as a consequence of fluorination reactions involving the hexafluorospecies. The kinetic stability of species such as AsF_6^- and SbF_6^- avoids this difficulty. Hence the salts $O_2^+AsF_6^-$ and $O_2^+SbF_6^-$ offered excellent prospects for the synthesis of $C_6F_6^+$ by the generalized reaction:

$$C_6F_6 + O_2^+A^- \rightarrow C_6F_6^+A^- + O_2 .$$

(The electron affinity of O_2^+ is 12.2 eV, whereas the ionization potential of C_6F_6 is 10 eV.)

This conversion has been realized for the AsF_6^-, SbF_6^-, and $Sb_2F_{11}^-$ cases. The salts are yellow or yellow-orange and are paramagnetic. Their synthesis is carried out in liquid tungsten hexafluoride which serves as diluent for the C_6F_6 and heat sink (the reactions are moderately exothermic and the salts are thermally unstable). The best-characterized salt is $C_6F_6^+AsF_6^-$. It is a yellow-orange paramagnetic solid, m.p. 69.1 (with decomp.). E.p.r. spectra of the solid show a very intense broad signal centered at g = 2.006. This is in agreement with a value given for a $C_6F_6^+$ species detected previously in SbF_5 solution. The salt interacts with NO(I = 9.5 eV) in accord with the equation

$$NO + C_6F_6^+AsF_6 \rightarrow NO^+AsF_6^- + C_6F_6 .$$

Single crystals of the compound have been grown from liquid hydrogen fluoride, and Weissenberg photographs show them to be rhombohedral, space group $R3^-$, the hexagonal unit cell having the dimensions

$$a=10.55\ (1),\ C=7.66\ (1),\ V=738Å^3,\ \rho=2.53\ g\ cm^{-3},\ z=3.$$

The symmetry indicates either that the $C_6F_6^+$ possesses a threefold axis or that the ion placement is somewhat disordered. The cation should exhibit a Jahn-Teller distortion.

A study of the chemical properties of this interesting ion will be undertaken.

---

1. D. E. McKee and N. Bartlett, Dioxygenyl Salts $O_2^+SbF_6^-$ and $O_2^+Sb_2F_{11}^-$ and Their Convenient Laboratory Syntheses, Inorg. Chem. 12, 2738 (1973).

3. HIGH OXIDATION STATES OF THE HEAVY ELEMENTS

Kevin Leary, Boris Žemva, Thomas C. Parsons, and Neil Bartlett

(i) Gold Chemistry (Kevin Leary): attempts to obtain macroscopic quantities of AuF_5 by the more conventional procedures of high-pressure synthesis, or acid displacement from AuF_6^- salts, have been fruitless.

The observed chemistry demonstrates the powerful oxidizing nature of non-anionic Au(V). Thus destruction of the O_2^+ salt, $O_2^+ AuF_6^-$, in iodine pentafluoride proceeds according to the equation

$$3IF_5 + 4O_2AuF_6 \xrightarrow{25°} 4O_2 + 3IF_6^+ AuF_6^- + AuF_3.$$

Clearly, free AuF_5 is capable of oxidizing IF_5 to IF_7 at room temperature. This oxidizing capability rivals that of KrF_2.

The range of known AuF_6^- salts has been expanded to include $KAuF_6$ and $NOAuF_6$. The latter is isomorphous with $O_2^+AuF_6^-$, but the unit cell is slightly larger (a finding in harmony with earlier results, which indicate that NO^+ is approximately 2Å^3 more voluminous than O_2^+). A magnetic study of $O_2^+AuF_6^-$ indicates Curie-Weiss behavior with $\theta = -3.0°$ and $\mu_{eff} = 1.66$ B.M. A Mössbauer study of several AuF_6^- salts has been published.[1] Experiments involving the electrolysis of AuF_6^- salts as a source of AuF_6 are planned.

---

1. G. Kaindl, K. Leary, and N. Bartlett, Mössbauer Study of Quinquevalent Gold Compounds, J. Chem. Phys., 59, 5050 (1973).

(ii) Neptunium and Related Chemistry (B. Žemva, in collaboration with Thomas C. Parsons): Efforts to prepare $NpOF_5$ by direct fluorination and oxyfluorination of NpO_2 have suggested novel species (indicated by infrared spectroscopy) but have not so far given acceptable evidence for the oxide pentafluoride. Low-temperature synthesis may be essential for species such as $NpOF_5$ and the new work will take this approach.

4. RESEARCH PLANS FOR CALENDAR YEAR 1974

Neil Bartlett

Noble-Gas and Related Chemistry. The spontaneous fixation of krypton (by AuF_6 or some other agency) continues to be a major concern as does the synthesis of an ArF^+ salt.

The $XeOF_5^+$ species has still not been properly characterized structurally. Solution ^{19}F NMR studies and crystallographic studies are planned. Attempts will also be made to isolate the parent base $XeOF_6$.

Electrochemical and other approaches will be explored as a route to AuF_6, which is

considered to be the most promising oxidative species for argon fixation and ArF^+ preservation.

The exploitation of XeF_2 in oxide systems (including water) as a powerful oxidative reagent for the generation of novel oxide and oxyhalide species remains to be properly explored. Species such as IrO_4, OsO_2F_4 and $OBrF_5$ will be sought.

Charge Annhilation Syntheses. The exploitation of O_2, XeF^+ and KrF^+ salts as powerful oxidizers offers the prospect of high-oxidation-state species previously unobtainable by purely chemical means. The O_2^+ cation is particularly attractive (as has been demonstrated this year with $C_6F_6^+$ synthesis) in the generation of species which are themselves chemically unsaturated. Both O_2^+ and KrF^+ offer the prospect of charge annhilation syntheses of the type $O_2^+(KrF^+) + A^- \rightarrow O_2(Kr + 1/2\ F_2) + A$. In this fashion we can hope to generate species A at low temperature. Thus even species of low thermodynamic stability such as $SbF_6\cdot$ radical, $NpOF_5$, or NpF_7 molecules can hopefully be generated and preserved.

5. 1973 PUBLICATIONS AND REPORTS

Neil Bartlett and Associates

Journals and books

1. D. E. McKee, C. J. Adams, A. Zalkin, and N. Bartlett, Cations KrF^+, $XeOF_3^+$, and $XeOF_5^+$ and Oxidizing Properties of KrF^+; J. Chem. Soc. Chem. Commun. 26 (1973) (LBL-1163).

2. K. Leary, A. Zalkin, and N. Bartlett, Crystal Structure of $[Xe_2F_{11}]^+$ $[AuF_6]^-$, J. Chem. Soc. Chem. Commun. 131 (1973) (LBL-1189).

3. D. E. McKee, A. Zalkin, and N. Bartlett, Crystal Structure of $[XeF_3^+][Sb_2F_{11}^-]$, Inorg. Chem. 12, 1713 (1973)(LBL-1160).

4. N. Bartlett, M. Gennis, D. D. Gibler, B. K. Morrell, and A. Zalkin, Crystal Structures of $[XeF^+]$ $[RuF_6^-]$ and $[XeF_5^+]$ $[RuF_6^-]$, Inorg. Chem. 12, 1717 (1973) (LBL-850).

5. D. E. McKee, C. J. Adams, and N. Bartlett, Preparation and Raman Spectra of Salts $[XeF_3^+]$ $[SbF_6^-]$, $[XeF_3^+]$ $[Sb_2F_{11}^-]$, $[XeOF_3^+]$ $[SbF_6^-]$, and $[XeOF_3^+]$ $[Sb_2F_{11}^-]$; Inorg. Chem. 12, 1722 (1973) (LBL-1423).

6. K. Leary, D. H. Templeton, A. Zalkin, and N. Bartlett, Crystal Structure of $[XeF_5^+]_2[PdF_6^{2-}]$, Inorg. Chem. 12, 1726 (1973)(LBL-1171).

7. N. Bartlett and F. O. Sladkey, The Chemistry of Krypton, Xenon and Radon, in Comprehensive Inorganic Chemistry, Vol. 1, 213 (1973)(UCRL-19658).

8. D. E. McKee and N. Bartlett, Dioxygenyl Salts $O_2^+SbF_6^-$ and $O_2^+Sb_2F_{11}^-$ and Their Convenient Laboratory Syntheses, Inorg. Chem. 12, 2738 (1973)(LBL-1494).

9. B. K. Morrell, A. Zalkin, A. Tressaud, and N. Bartlett, Crystal Structure of Rhodium Pentafluoride, Inorg. Chem. 12, 2640 (1973)(LBL-1154).

10. G. Kaindl, K. Leary, and N. Bartlett, Mössbauer Study of Quinquevalent Gold Compounds, J. Chem. Phys. 59, 5050 (1973) (LBL-1841).

Invited lectures

1. N. Bartlett, "Concerning the Bonding in Noble-Gas Compounds," The Departmental Colloquium, Purdue University, Feb. 17, 1973.

2. N. Bartlett, "Bonding in Noble-Gas and Related Compounds," Joint Inorganic-Organic Seminar, U.C.L.A., March 1, 1973.

3. N. Bartlett, Twentieth Gilbert Newton Lewis Memorial Lecture, "Structure and Bonding in Noble-Gas Compounds," U. C. Berkeley, Oct. 23, 1973.

4. N. Bartlett, "Chemistry of the Noble Gases," Noble Gases Symposium, Las Vegas, Sept. 24-28, 1973.

Papers presented

1. C. J. Adams and N. Bartlett, "Tautomersion in Xenon Hexafluoride--A Raman Study of XeF_6 and Its Complexes," presented at The Fluorine Symposium, Salt Lake City, Utah, July 13, 1973 and at The Dalton Symposium of The Chemical Society, University of East Anglia, Sept. 24-27, 1973 (LBL-1859 Abs.).

The following papers were presented at The Seventh International Symposium on Fluorine Chemistry, Santa Cruz, California, July 15-20, 1973.

2. T. Richardson,* D. E. McKee, and N. Bartlett, "Approaches to Novel Cations and Radicals."

3. K. Leary* and N. Bartlett, "AuF_5 Complexes".

4. N. Bartlett*, B. Žemva, and A. Tressaud, "Concerning the Crystal Structures of Platinum Metal Tetrafluorides (Ru, Rh, Pd, Ir, and Pt) and their $(MF_4 + y^-)_x$ Derivatives."

*Speaker.

LBL reports

1. K. Leary, A. Zalkin, and N. Bartlett, The Crystal Structure of $Xe_2F_{11}^+AuF_6^-$ and the Raman Spectrum of $Xe_2F_{11}^+$, LBL-1426, Jan. 1973.

2. N. Bartlett, B. G. DeBoer, F. J. Hollander, F. O. Sladky, D. H. Templeton, and A. Zalkin, Crystal Structures of $[Xe_2F_3^+][AsF_6^-]$ and $[XeF_5^+][AsF_6^-]$, LBL-1170, Sept. 1973.

3. N. Bartlett, Krypton, LBL-1862, July 1973.

4. Donald D. Gibler (Ph.D. thesis), Perfluoro Cations of the Non-Metallic Elements, LBL-1157, April 1973.

5. Douglas Edward McKee (Ph.D. thesis), Preparative and Structural Studies Involving Noble-Gas and Related Compounds, LBL-1814, May 1973.

6. Christopher J. Adams, The Raman Spectra of Solid Xenon Tetrafluoride and Its Adduct with Xenon Difluoride, LBL-1888, Aug. 1973.

B. SOLID STATE CHEMISTRY AND PHYSICS

Norman E. Phillips, Principal Investigator

1. HEAT CAPACITY OF THE KONDO-SUPERCONDUCTOR (La,Ce)Al_2*

Samuel D. Bader and Norman E. Phillips

It has been known for some time that magnetic impurities have a dramatic effect on properties of the superconducting state, and recently it has been recognized that the type of behavior should depend on the nature of the magnetic impurity. If there is a Kondo effect associated with the impurity the breaking of the Cooper pairs should be temperature dependent. In that case "reentrant" behavior--the existence of upper and lower critical temperatures--has been predicted. The system (La,Ce)Al_2 has been identified as belonging to this category--some evidence for a Kondo effect in the normal state has been reported and reentrant behavior observed.[1] Calorimetric measurements on this system were undertaken in this laboratory to (1) verify the normal-state Kondo effect, (2) study the transition at the lower critical temperature, T_{c1}, and (3) study the development of spin compensation in the superconducting state.

Measurements were made on three alloys: 0.906 at.% $CeAl_2$ in $LaAl_2$, for which superconductivity is completely suppressed; a 0.64 at.% sample, for which reentrant behavior has been observed; and a 0.193 at.% sample which shows only a single transition. Measurements on pure $LaAl_2$ were also made. The normal-state data for all samples could be represented by the sum of electronic and lattice contributions that were independent of concentration, and a magnetic contribution that was proportional to concentration. In low magnetic fields (necessary to suppress superconductivity in all except the 0.906 at.% sample) the magnetic heat capacity is very similar to that observed[2] in CuFe and CuCr, as shown in Fig. 1. This fact and the proportionality to concentration confirm the identification of these alloys as Kondo systems.

The slight anomaly at T_{c1} in zero magnetic field for the 0.64 at.% sample is also apparent in Fig. 1. The size of this anomaly is reasonably consistent with the existence of bulk superconductivity, estimates of the Landau-Ginsberg parameter, and measurements[3] of the upper critical field. At T_{c2} (as determined magnetically) no structure in the zero-field heat capacity is observed. A certain amount of broadening of the transition is of course expected (and observed at T_{c1}) but the data suggest that

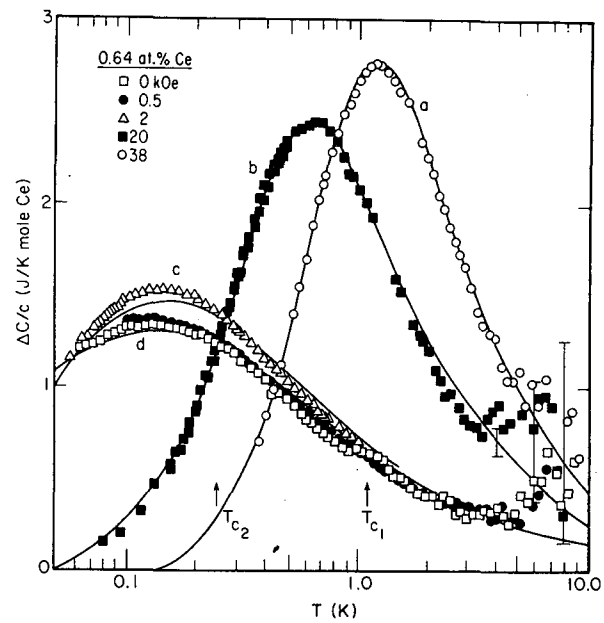

Fig. 1. The heat capacity of 0.64 at.% $CeAl_2$ in $LaAl_2$. Curve d represents zero-field experimental data and also theoretical data for other Kondo systems (see Ref. 2). (XBL 7311-6628)

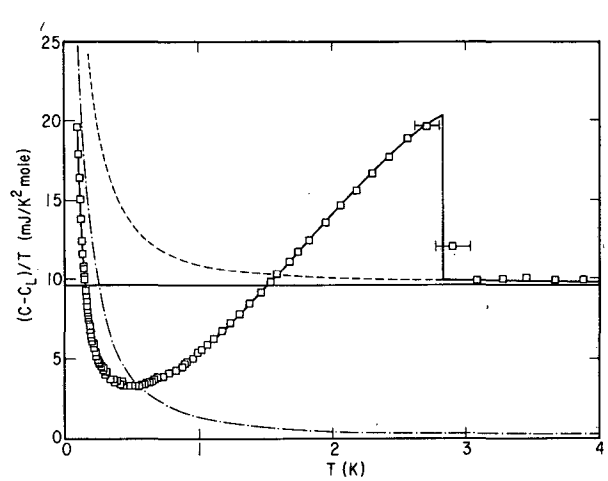

Fig. 2. The heat capacity of 0.193 at.% $CeAl_2$ in $LaAl_2$. The dot-dash and dash curves represent the normal-state magnetic and total normal-state heat capacities. (XBL 7311-6624)

the transition is probably of higher order than second. Additional measurements on a more highly homogenized sample are planned to clarify this point.

The zero-field data for the 0.193 at.% sample is compared with the normal-state magnetic heat capacity in Fig. 2. It is clear that the magnetic ordering in the superconducting state is substantially depressed relative to that in the normal state. Qualitatively this can be understood as reflecting a competition between two types of order--Cooper pairs, and spin compensation in the Kondo sense.

---

*This work done in collaboration with M. Brian Maple.

1. For references to theoretical and earlier experimental work see M. Brian Maple, in Magnetism, Vol. V, edited by Harry Suhl (Academic Press, New York and London, 1973).
2. B. B. Triplett and N. E. Phillips, Phys. Rev. Letters 27, 1001 (1971).
3. G. Riblet and K. Winzer, Solid State Comm. 11, 175 (1972); K. Winzer, Z. Physik 265, 139 (1973).

2. HEAT CAPACITY OF THE SINGLET-GROUND-STATE SYSTEMS $PrCu_2$, $TmCu_5$, AND $HoCu_5$

Gary P. Schwartz, Marilyn Wun, and Norman E. Phillips

Heat capacity and magnetic susceptibility data on $PrCu_2$ have been interpreted as showing cooperative nuclear ordering via the hyperfine interaction in a singlet-ground-state system.[1] Earlier measurements in this laboratory[2] showed some differences in behavior that cast doubt on that interpretation. To test the possibility that deviations from stoichiometry or inhomogeneity of the sample contributed to the differences, a second sample was prepared and measured. The results were similar to those obtained with the first sample. The heat capacity of $LaCu_2$ was also measured to provide an estimate of the lattice heat capacity. As shown in Fig. 1, the 6°K anomaly in the heat capacity is much sharper on the high-temperature side than a Schottky anomaly. Furthermore, the measurements on $LaCu_2$ suggest that the anomalous contribution to the heat capacity extends to above 20°K. For both these reasons it appears that the electronic transitions are more complicated than was originally assumed.

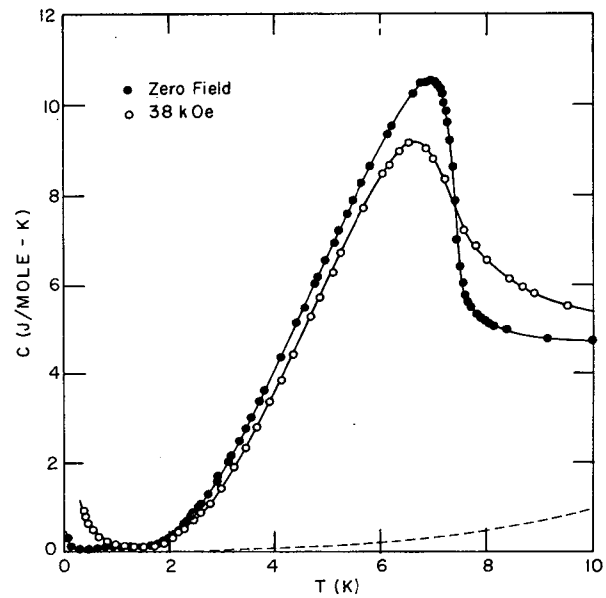

Fig. 1. The heat capacity of $PrCu_2$. The dashed curve represents the lattice heat capacity. (XBL 741-5467)

Heat capacity measurements on $TmCu_5$ and $HoCu_5$ have also been made. In both cases hyperfine and electronic contributions are approximately separable. Analysis of these data is in progress.

---

1. K. Andres, E. Bucher, J. P. Maita, and A. S. Cooper, Phys. Rev. Letters 28, 1652 (1972).
2. IMRD Annual Report for 1973, LBL-1400, April 1973, p. 19.

3. THE HEAT CAPACITY OF TERBIUM ETHYL SULPHATE*

Marilyn Wun and Norman E. Phillips

Terbium ethyl sulphate is a singlet-ground-state system in which an anomaly in the magnetic susceptibility occurs near 0.2°K.[1] As shown in Fig. 1, the heat capacity indicates a cooperative transition at 0.24°K. This temperature is of the order of magnitude of the expected dipole-dipole interaction, suggesting that this is the driving force for moment formation rather than the more usual exchange interaction.

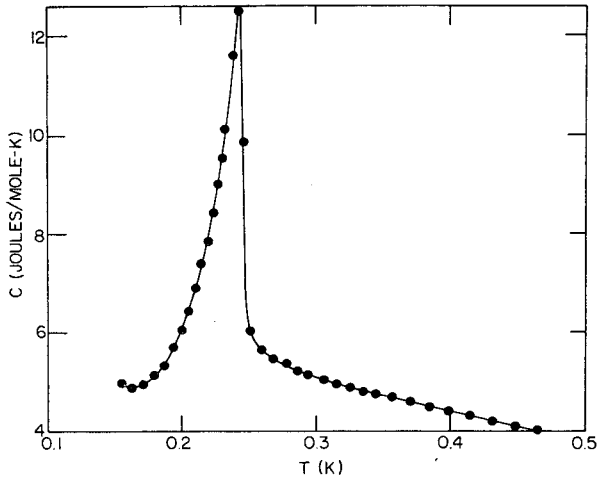

Fig. 1. The heat capacity of terbium ethyl sulphate. (XBL 741-5466)

*This work done in collaboration with T. E. Katila.

1. T. E. Katila, private communication.

4. THE LOW-TEMPERATURE HEAT CAPACITY OF NATROLITE

Samuel D. Bader, Gerald D. Fong, and Norman E. Phillips

It has been suggested that the anomalous low-temperature heat capacity of amorphous dielectrics may be associated with voids, in which case similar anomalies might be observed in zeolites.[1] To test this possibility, the heat capacity of Indian Natrolite, which is obtainable as natural large single crystals, was measured. The sample studied did exhibit an anomalously large heat capacity, but measurements in magnetic fields showed that it was largely, if not entirely, magnetic in origin. Any linear term in the heat capacity of this sample is an order of magnitude smaller than those observed in several amorphous materials.

1. C. Kittel, private communication.

5. MAGNETIC FIELD DEPENDENCE OF THE LOW-TEMPERATURE HEAT CAPACITY OF NEODYMIUM

William E. Fogle and Norman E. Phillips

The heat capacity of β-cerium showed a large, weakly field-dependent, temperature-proportional term that dominated the heat capacity to temperatures of the order of 0.1°K, below which it was masked by the hyperfine heat capacity of impurities. To see whether similar heat capacities might be found in other rare earth metals, we have measured the heat capacity of a neodymium sample enriched to 99.8% in even-even isotopes. Results obtained in several magnetic fields are shown in Fig. 1. The hyperfine heat capacity becomes increasingly important below 0.2°K, but it is clear that there is a large linear term. In magnitude, the linear term is similar to that observed in cerium, but its field dependence is much greater. The data obtained so far do not extend to high enough fields to estimate a high-field limit, but it appears that that limit is of the order of magnitude of typical transition-metal electronic heat capacities, suggesting that most of the zero-field linear term is magnetic in origin.

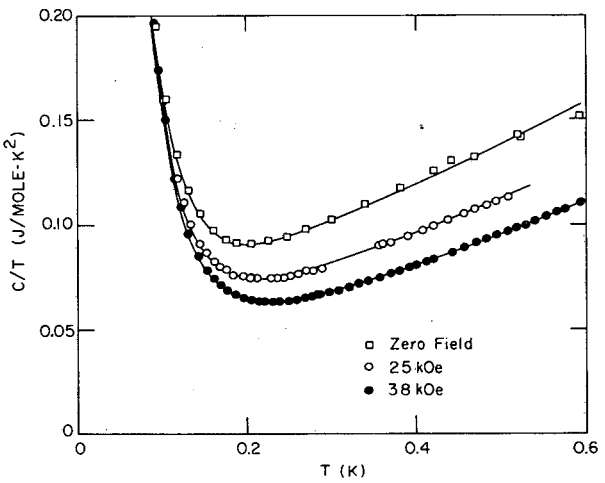

Fig. 1. The heat capacity of neodymium. (XBL 741-5465)

6. RESEARCH PLANS FOR CALENDAR YEAR 1974

Norman E. Phillips

Calorimetric investigations on dilute magnetic alloys will be continued. The actual choice of systems is still not settled, but possibilities include further measurements on the $(LaCe)Al_2$ system; on the

(LaGd)Al_2 system, which is also superconducting but appears to involve a different kind of spin ordering; and on rare earths in noble metals. The latter class of materials is of interest from several points of view, including the possible identification of alloys with low Kapitza resistance to ^{3}He. Some of these measurements will be made by Mr. W. E. Fogle, and will probably make use of techniques for higher magnetic fields and lower temperatures that he is developing.

A new student, Mr. Brent Krusor, has taken up the measurements on liquid ^{4}He and is continuing the design of modifications to the apparatus that will permit measurements to lower temperatures.

Drs. E. W. Hornung and G. Brodale will continue to develop apparatus for measurements in the mK region. It is planned to redesign the dilution refrigerator and add a demagnetization stage.

7. 1973 PUBLICATIONS AND REPORTS

Norman E. Phillips and Associates

Journals

1. W. R. Gardner, J. K. Hoffer, and N. E. Phillips, Thermodynamic Properties of ^{4}He. The hcp Phase at Low Densities. Phys. Rev. A 7, 1029 (1973)(LBL-1123).

2. N. E. Phillips, T. L. Thorp, and B. B. Triplett, Implications of New Data on the Heat Capacity of Tungsten, for the Powdered Cerium Magnesium Nitrate Temperature Scale. Phys. Letters 43A, 285 (1973) (LBL-1453).

3. D. B. McWhan, J. P. Remeika, S. D. Bader, B. B. Triplett and N. E. Phillips, Heat Capacity of Metallic V_2O_3 at High Pressure, Phys. Rev. B 7, 3079 (1973)(LBL-1467).

4. S. D. Bader, N. E. Phillips, and D. B. McWhan, Heat Capacity and Resistivity of Metallic SmS at High Pressure, Phys. Rev. B 7, 4686 (1973)(LBL-1194).

*5. O. Avenel, M. P. Berglund, R. G. Gylling, N. E. Phillips, A. Vetleseter, and M. Vuorio, Improved Thermal Contact at Ultralow Temperatures between ^{3}He and Metals Containing Magnetic Impurities, Phys. Rev. Letters 31, 76 (1973).

6. B. B. Triplett, N. E. Phillips, T. L. Thorp, D. A. Shirley, and W. D. Brewer, Critical Field for Superconductivity and Low-Temperature Normal-State Heat Capacity of Tungsten, J. Low Temp. Phys. 12, 499 (1973)(LBL-1497).

*Supported by the National Science Foundation.

George Jura, Principal Investigator

1. HEAT CAPACITIES OF METALS UNDER HIGH PRESSURE

George Jura and Tang-hua Chen

A real test for the pulse method for the determination of the heat capacity under pressure are the metals, aluminum and copper; and they are equally difficult. The reason for the difficulty lies in their low specific resistance. Aluminum is chosen over copper because there is some idea as to the variation of the heat capacity of aluminum as a function of pressure. The variation is estimated from the change in Debye temperature as a function of resistance. The Debye was determined from the variation in resistivity as a function of temperature. Some credence can be placed in these values, since they connect well with the heat capacity data obtained from shock experiments.

Ten different currents were used at each pressure. The heat capacities were determined at 5-kbar intervals from 30 to 100 kbars.

The heat capacity decreased between 4% and 5% in this pressure interval, in good agreement with the data obtained from the resistivity data.

2. OPTICAL STUDIES OF SOLIDS UNDER HIGH PRESSURE

Raymond F. Glienna

Crystalline 1,2,4,5 tetrachloro benzene (TCB) has been used as a model in calculations of one-dimensional electronic energy processes.[1] The crystal structure of TCB is monoclinic ($P2_1/a$) with lattice constants a_0=9.725Å, b_0=10.602Å, c_0=3.850Å, β=103.28° with a bimolecular unit cell.[2] The molecular arrangement within the crystal is similar to that of naphthalene, with the molecules lying in two sets of parallel planes. The perpendicular distance between parallel planes can be taken as a "nearest neighbor" distance R disregarding a small angular factor. At low temperature (150°K) there is a phase transition to a triclinic polymorph with only about a 5% change in the lattice constants and even less change in α and γ.

It was thought that the effects of hydrostatic or uniaxial compression on a crystal of TCB would shed light on the form of interaction among neighboring TCB molecules. The a priori assumption was made by Decius[3] that the out-of-plane normal modes would interact via an induced dipole-induced dipole potential of the form $V'=a/R^3$, where a is a constant including both induced dipole moments of neighboring molecules for a given normal mode and angular factors.

An infrared absorption experiment was performed at from one atmosphere to a nominal load of about 40,000 atmospheres. Infrared light was chosen, in part, because of the

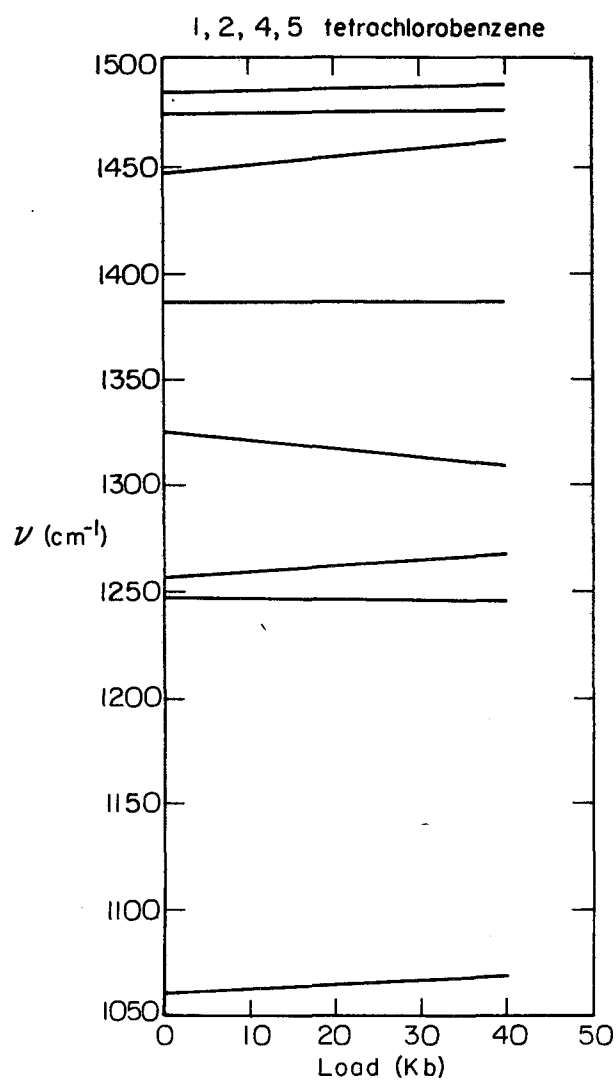

Fig. 1. 1,2,4,5 tetrachloro benzene energy level diagram. (XBL 741-5434)

simplicity of vibrational wave functions. Crystalline TCB was cleaved perpendicular to a long crystal axis into samples about 0.075 mm thick. The alignment of the sample was such that the out-of-plane normal modes would be excited by the incident light. A high-pressure Drickamer cell[4] modified for infrared measurements[5] was used in the experiments. The results for the frequency region 1000 to 1500 cm^{-1} are shown systematically in Fig. 1.

The complexity of the energy level diagram and the uncertainty of spectral assignment precluded immediate accurate determination of interaction terms for this crystal. Therefore a system having only one out-of-plane normal vibration was next investigated.

At one atmosphere pressure and room temperature, $BaCO_3$ has the aragonite structure with a vertical distance, R, between nearest neighbor carbonate ions = 3.275Å.

The infrared spectrum of a 0.075-mm-thick polycrystalline sample of Witherite ($BaCO_3$) was measured from a pressure of one atmosphere to a nominal load of 40,000 atmospheres. The results are shown in Fig. 2. The out-of-plane vibration ν_2 has a fundamental frequency which decreases from 860 cm^{-1} at one atmosphere to about 850 cm^{-1} near 40,000 atmospheres. There is much complex structure to this broad absorption band, so the corresponding absorption maximum was measured at all pressures. Both the symmetric stretch ν_1 and degenerate bend ν_4 increase in frequency from one atmosphere to 40,000 atmospheres (see Table I).

Table I.

$\Delta\nu_1/\Delta P$	2.5×10^{-4} cm^{-1}/atm
$\Delta\nu_2/\Delta P$	-1.7×10^{-4} cm^{-1}/atm
$\Delta\nu_4/\Delta P$	1.2×10^{-4} cm^{-1}/atm

The signs of these frequency shifts imply positive interaction constants for the two in-plane vibrations measured and a negative interaction term for the out-of-plane mode. These facts definitely justify Decius'[3] choice of a dipole-dipole type of interaction among nearest neighbors in $BaCO_3$. More quantitative calculations on an exact value for the transition dipole moment of carbonate ion in $BaCO_3$ and other carbonates will be made pending the acquisition of more complete compressibility data.

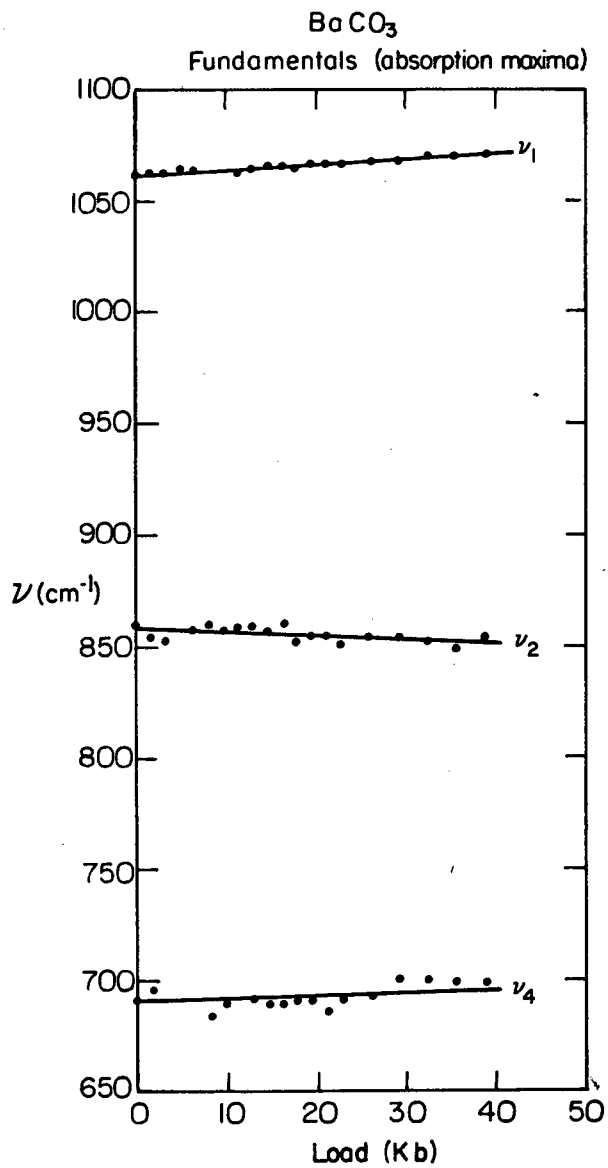

Fig. 2. $BaCO_3$ energy level diagram [fundamentals (absorption maxima)]. (XBL 741-5435)

1. M. D. Fayer and C. B. Harris, private communication.
2. Wyckoff, Structure of Crystals, Vol. 6, p. 348.
3. J. C. Decius, J. Chem. Phys. 23, 1290 (1955).
4. E. Fishman and H. G. Drickamer, Anal. Chem. 28, 804 (1956).
5. C. K. Wu, Ph.D. dissertation, University of California (1971).

3. HEAT CAPACITY OF BISMUTH AT HIGH PRESSURE

George Jura and Berardo Jurado

Very extensive measurements have been completed on the heat capacity of bismuth as a function of pressure at room temperature using the short (1-msec) constant-current pulsing technique developed in this laboratory.

There has been an improvement in the method of recording the pulses as well as on the analysis. For the data on bismuth a borrowed Fabritek 1070 minicomputer digitizer with a 9-bit resolution and a 20-μsec-per point sampling interval was used. The additive feature permitted the collection of many pulses to increase the resolution. A total of 8 pulses for each current increased the resolution to 12 bits (one part in 4096) and a total of 10 currents was taken for each pressure. Data were taken every 1.5 kbars from 0 to 100 kbars.

The data were transferred onto magnetic tape for a permanent record and subsequent analysis in the Laboratory's CDC 7600. This method of data acquisition is much superior to the one of taking oscilloscope pictures, both in the time saved as well as in the accuracy of the measurements.

The basic equation for the heat capacity that takes into consideration the heat losses due to conduction can be written in the following form:

$$C_p \int dE(t) = I^2R' \int E(t)dt - K \int [E(t)-E(0)]dt, \qquad (1)$$

where E(t) is the e.m.f. drop across the sample, R' is the thermal coefficient of the resistance, I is the current, C_p is the heat capacity at constant pressure, and K is the heat leakage constant. In the limiting case as $t \to 0$ it becomes

$$C_p = \frac{I^2R'E(0)}{(dE/dt)_0} = I^3R_oR'/(dE/dt)_o \ . \qquad (2)$$

Equation (2) can be used satisfactorily for metals like Fe for which there is a linear region beyond the first 100 μsec of the pulse where there are rise time effects, and one needs only to measure the limiting slope. For Bi the pulse is curved, thus making the determination of the initial slope difficult. The parameter that determines the amount of curvature in the traces is the time constant $t_{1/2}$ (the time at which the heat losses are one half of the total heat imput) which can be shown to be proportional to the ratio C_p/K. K depends mainly on the geometry of the system, the surface of the wire, and the thermal conductivity of the pressure medium. A great deal of the curvature in Bi is due to a lower heat capacity per unit volume with respect to Fe (smaller by a factor of 3) and the restrictions by the size of the pressure cell on the use of a wire of greater diameter which would reduce the surface to volume ratio.

The integrations needed in Eq. (1) in order to solve for C_p and K are performed numerically either directly on the data or on smoothed data through the use of polynomial fits. The results are essentially the same.

The following is a table of C_p and K values as a function of current for Bi at 50 kbars:

I (A)	$C_p(\times 10^5)$ (J/deg)	$K(\times 10^2)$ (J/deg-sec)
4.484	4.21	2.4
4.582	4.14	2.5
4.682	4.11	2.5
4.778	4.09	2.6
4.887	4.04	2.7
4.985	3.98	2.8
5.061	3.93	2.9
5.176	3.95	2.8
5.272	3.85	3.0
5.369	3.86	3.0

There is a small current dependence of C_p and K which cannot be accounted for at the present. Whenever possible the same set of currents were used.

A great deal of interest in Bi comes from the number of solid polymorphic transitions (see phase diagram, Fig. 1). There are a total of five known solid phases, four of which exist at room temperature in the 0-100 kbar interval. They can be easily detected by large discontinuities of the electrical resistance with pressure. There are also two postulated phase transitions at 45 and 65 kbars observed by P. W. Bridgman through volume changes but which have not been observed by many other investigators either in a volume change change or a discontinuity in the resistance. It was expected that C_p could show discontinuities at those pressures if those transitions were real as well as in the other well-known transitions.

The experimental results are shown in Figs. 2 and 3. First, one can observe no changes in any of the physical properties of Bi at 45 and 65 kbar. Thus within the experimental uncertainties there are no indications

of intermediate phases in the 30-90 kbar pressure region. There are huge discontinuities at all the other known phase transitions (25.4, 27, and 88 kbars).

Secondly, there are huge increases in C_p in going from phase I to phase III and from phase III to phase V. Due to the

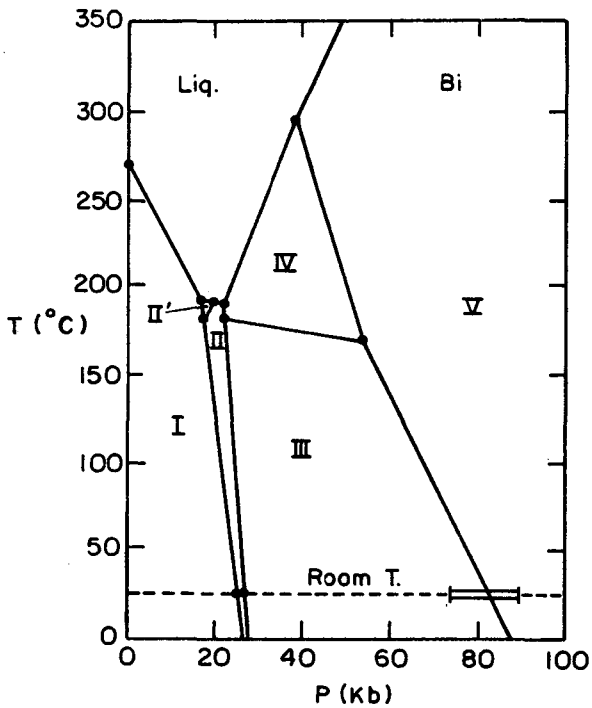

Fig. 1. Phase diagram of Bi.
(XBL 741-5436)

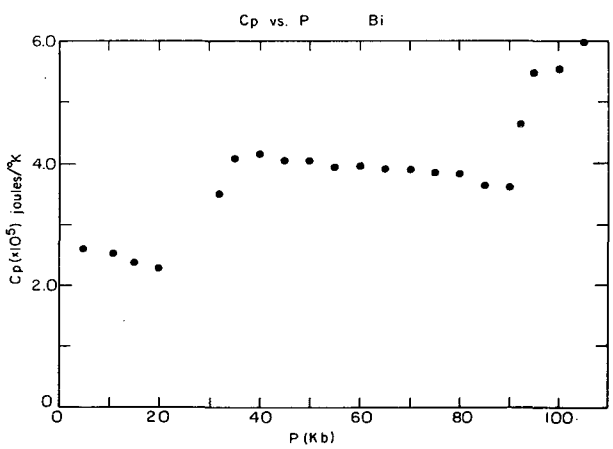

Fig. 2. C_p vs. P (Bismuth sample).
(XBL 741-5437)

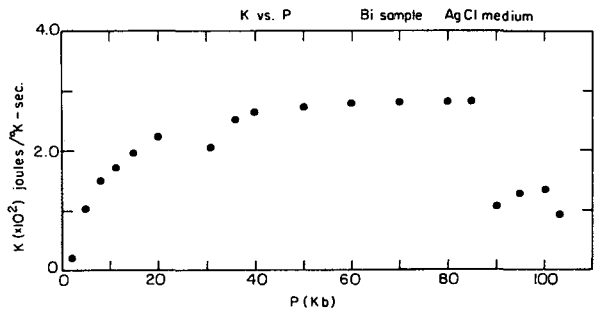

Fig. 3. K vs P (Bismuth sample)
(XBL 741-5438)

narrowness of phase III, R' measurements are difficult to make and are not available now, so there are no C_p points in that phase.

K increases to about 90 kbars where it drops abruptly. The initial increase of K can be explained entirely in terms of a better contact between the sample wire and the AgCl pressure medium as well as an increase of the thermal conductivity of the AgCl with pressure. The drop at 90 kbar is consistent with a known phase transition of AgCl at that pressure.

The reason for the very large increase in C_p, if true, are not as yet known. They could be due to some type of hidden systematic error within the experiment that has not been discovered. However, if real, they are hard to explain since with a Debye temperature of about 100°K Bi is is already at the classical limit of the lattice heat capacity in phase I. The increase could be due to an unusually large electronic contribution to the heat capacity at room temperature of an unprecedented nature.

More measurements need to be done as a function temperature as well as pressure to test the hypothesis of a large electronic heat capacity contribution.

4. RESEARCH PLANS FOR CALENDAR YEAR 1974

George Jura

We will continue in the development of a method for determining the specific heats of metals and alloys under high pressures. Also continuation and extension of high pressure optical experiments with applications to polymers and organic materials.

Gabor A. Somorjai, Principal Investigator

1. LOW ENERGY ELECTRON DIFFRACTION (LEED) STUDIES OF SURFACES

a. Low Energy Electron Diffraction and Work Function Studies of Adsorbed Organic Layers on the (100) and (111) Crystal Surfaces of Platinum

John L. Gland and Gabor A. Somorjai

The adsorption of a group of organic compounds has been studied on the platinum (100) and (111) single-crystal surfaces. Low energy electron diffraction has been used to determine surface structures. Work function change measurements have been made to determine the charge redistribution which occurs on adsorption. The molecules which have been studied are acetylene, aniline, benzene, biphenyl, n-butylbenzene, t-ubtybenzene, cyanobenzene, 1,3-cyclohexadiene, cyclohexane, cyclohexene, cyclopentane, cyclopentene, 2,6-dimethylpyridine, 3,5-dimethylpyridine, ethylene, n-hexane, isoquinoline, mesitylene, 2-methylnaphthalene, napthalene, nitrobenzene, piperidine, propylene, pyridine, pyrrole, quinoline, styrene, toluene, m-xylene. All molecules studied adsorb on both the Pt(111) and Pt(100)-(5×1) surfaces. All molecules studied act as electron donors to the metal surface. The adsorbed layers are more ordered on the hexagonally symmetric Pt(111) surface than on the square symmetric Pt(100) surface. Unsaturated molecules generally adsorb on the Pt(111) and Pt(100) surface by forming π-bonds with the metal surface.

b. Low Energy Electron Diffraction and Work Function Change Studies of Paraffins Adsorbed an Platinum Single Crystal Surfaces

Lawrence E. Firment and Gabor A. Somorjai

Low energy electron diffraction studies with simultaneous measurements of the change in the plantinum work function were made during adsorption of hydrocarbons on the Pt(111) and Pt(100) surfaces. The adsorption of the simplest hydrocarbons, the normal paraffins C_nH_{2n+2}, for n=2-7 was examined. Of these, only n-heptane produced an ordered surface structure on Pt(111), at room temperature. The work function change on adsorption was also largest for n-heptane: - 1.3 volts on Pt(111), -1.0 volts on Pt(100). The shorter paraffins caused proportionately smaller changes in work function. The paraffins C_2-C_5 were readily displaced from the surface by background gases, notably CO. These data indicate that the binding energy of these molecules to the Pt surfaces increases gradually with carbon chain length.

c. Application of Low Energy Electron Diffraction Theory to Surface Structure Analysis of Platinum and of Adsorbed Layers

Larry Kesmodel and Gabor A. Somorjai

The primary goal of low energy electron diffraction (LEED) has been the development of a surface crystallography similar to the X-ray method for bulk crystallography. The need for a workable surface crystallography is evident in the field of chemisorption where quantitative information generally requires an accurate knowledge of surface atomic geometry. The standard analysis in LEED is the measurement of the intensity of the electrons scattered elastically from the crystal surface as a function of incident beam energy at a given diffraction spot. Unfortunately, these data cannot be directly inverted to give details of surface crystal structure. Instead one must rely on comparisons between experimental results and calculations based on models of the crystal structure and the diffraction process. In recent years the quantum-mechanical scattering theory relevant to LEED has been developed to sufficient accuracy to give good agreement between theory and experiment for a number of clean metal surfaces. Moreover, within the past year several chemisorbed overlayer systems have been successfully analyzed by various researchers and bonding lengths have been determined.

We are using a multiple-scattering theory of LEED to investigate the surface structure of clean platinum surfaces and adsorbed gas overlayers. The theoretical work centers on development of fast and accurate perturbation methods for computing the scattering intensities, since conventional "exact" methods are prohibitively long, especially when applied to complex overlayer systems.

d. Development of Rapid Measurement of LEED Intensity Data for Surface Crystallography

Thomas Kaminska, Larry L. Kesmodel and Gabor A. Somorjai

Work has continued on the development of improved photographic and scanning techniques to produce intensity vs. electron energy curves

of low-energy electrons diffracted from clean and gas-covered crystal surfaces. Spots produced on a phosphor screen by diffracted electrons are photographed as a function of energy with an aerial Tri-X film, SO-265. The film is machine-processed in duPont XPD to achieve an ASA speed rating of about 8000. The film density is determined with a computer-controlled stepping scanner which puts the density data on magnetic tape for further processing. Computer programs are being developed to integrate and plot the density data in I vs. eV curves for comparison with theoretical calculations. The technique will allow rapid analysis of complex crystal surfaces such as those that are reconstructed or adsorbed gas overlayers.

e. Low Energy Electron Diffraction Studies of Vanadium Crystal Surfaces

Clifford Megerle, Frederick J. Szalkowski, and Gabor A. Somorjai

The intensities of LEED beams diffracted from single-crystal surfaces depend on the mean vibrational amplitudes of the atoms from which the incident electrons are scattered. Intensity vs. temperature curves for the (00) diffraction beams were obtained for the clean V(100), the V(100)·c(2×2)S, and the V(100)-(1×1)S surfaces. These data were obtained at several incident beam energies, and extrapolation to 0 eV incident beam energy permitted the calculation of a surface mean-square vibrational amplitude, and a surface Debye temperature, for each surface studied.

Both LEED and AES studies were carried out on the (100) face of vanadium metal. It was found that the essentially clean metal surface displays a (1×1) diffraction pattern indicating a surface structure identical with the corresponding plane in the bulk, but that sulfur segregates to the surface upon heating and transforms the surface into a c(2×2) structure. Room temperature gas adsorption studies on the V(100)-(1×1) surface indicate that oxygen diffuses into the lattice and produces a disordered structure while carbon monoxide adsorbs upon the surface in a (1×1) array. Oxygen adsorption on the V(100)-c(2×2) surface produced a complex structure in which no oxygen was observed within the probed surface layer. This structure has been interpreted in terms of additional sulfur segregating to the solid-gas interface under the influence of the altered surface conditions (i.e., oxygen adsorption) with the subsequent desorption of the oxygen as this occurs.

f. Low Energy Electron Diffraction Studies from Iron Single Crystal Surfaces

Clifford A. Megerle and Gabor A. Somorjai

A series of LEED Auger studies were carried out on iron single-crystal samples in order to develop a treatment to facilitate the preparation of a clean iron surface. It was discovered that sulfur was the most tenaciously held contaminant, and that heating an Fe(100) sample in flowing hydrogen at atmospheric pressure resulted in the removal of all of the sulfur from the crystal. During these studies, the following sulfur structures were observed; Fe(100)(disordered)S, Fe(100)c(2×2)S, Fe(100)($\sqrt{5}\times\sqrt{5}$)R 26.5° S, and Fe(111)(disordered)S.

2. AUGER ELECTRON SPECTROSCOPY OF SURFACES

a. Auger Electron Spectroscopy Investigation of Chemical Shifts in the Vanadium Compounds and the Oxidation of Vanadiums

Frederick J. Szalkowski and Gabor A. Somorjai

Characteristic Loss measurements were performed on vanadium metal and V_2O_3 for the primary beam energy range of 100 to 700 eV. Mechanisms which are consistent with all of the observations reported on vanadium to date have been proposed for the observed peaks. The somewhat unexpected and interesting phenomenon that a multiple interband transition loss may occur with a probability greater than that of a single interband transition loss is pointed out and is instrumental in explaining the observed data.

AES chemical shift studies were carried out on V_2O_4, V_2O_3, VO, VN, VC, V_2S_3, and VSi_2. The shifts of the totally inner shell $L_3M_{2,3}M_{2,3}$ transition and the single valence band $L_3M_{2,3}V$ transition were measured relative to their energies in metallic vanadium. The $L_3M_{2,3}M_{2,3}$ transition displayed a systematic shift which could be associated with the successive transfer of the 4s and 3d valence band electrons to the anion, and the observed shifts were correlated with the Philips-Van Vechten ionicity scale. Correlation of the chemical shift data and the O/V peak intensity ratio for the known vanadium oxides enables one to unambiguously determine the chemical composition of the compound formed by oxidizing vanadium metal under different temperature and pressure conditions. In addition to the "normal" vanadium oxides, the production of the V_3O_5 Magneli phase was observed during this set of experiments. The $M_{2,3}VV$ double valence

band transition was also observed and its behavior upon oxidation indicates that at least one 4s electron is involved in this transition as opposed to the case of the $L_3M_{2,3}V$ transition which appears to overwhelmingly involve the 3d valence band.

b. Auger Electron Spectroscopy Studies of the Surface Composition of Binary Alloys as a Function of Bulk Composition and Temperature (Surface Phase Diagrams)

Steven Overbury and Gabor A. Somorjai

The surface composition of binary systems that obey regular solution theory may be very different from the bulk composition as predicted by surface thermodynamics. In addition the surface composition is also temperature dependent. Since the nature of surface chemical reactions depend on the surface composition, it is of importance to determine the composition as a function of temperature and bulk composition (surface phase diagrams) by Auger electron spectroscopy. The Au-Ag system is being studied. The concentration gradient between the surface and the bulk is determined along with the effect of segregated impurities or adsorbed gases at the surface on the surface composition. These studies will be extended to complex binary alloy systems (Au-Hf, Au-Zr, and Au-Ta) where the surface composition may again be different from that in the bulk. The formation of surface compounds with unique physical-chemical properties is likely.

3. CATALYSIS BY SINGLE CRYSTAL SURFACES

a. The Influence of Step Density on the Reactivity and Chemisorption of n-heptane on a Series of Low and High Miller Index Platinum Crystals and Polycrystalline Platinum

Kenneth Baron, Donald W. Blakely, and Gabor A. Somorjai

The reactions of n-heptane, in the presence of hydrogen, on platinum in the form of single crystals (high and low Miller index) and polycrystalline foil, has been studied using the techniques of Auger electron spectroscopy, quadrupole mass spectrometry, and low energy electron diffraction (LEED). The specific activities for the dehydrocyclization reaction to form toluene, the hydrogenolysis reaction to form saturated hydrocarbons, and the isomerization reactions to form methylhexanes and dimethylpentanes have been obtained. The atomic surface structures detectable after these reactions by LEED have been tabulated. The hydrogenolysis and isomerization reactions are favored on the single crystals with high step density, which form disordered carbonaceous layers. The dehydrocyclization reaction is most extensive on the stepped surface, which is most favorable to the formation of a $(\sqrt{3} \times \sqrt{3})$-R30^0 carbonaceous ordered structure. The chemisorption and reactivity of n-heptane on these surfaces has been compared with the data of other workers.

b. Studies of the Chemisorptive and Catalytic Activities of Iridium, Platinum, and Gold Single-Crystal Surfaces Using Low Energy Electron Diffraction, Auger Electron Spectroscopy, and Mass Spectrometry

Michael Chesters and Gabor A. Somorjai

Iridium, platinum, and gold possess similar bulk and surface crystal structures but display varying catalytic activity with particular contrast between platinum and the relatively inactive gold. Studies have been initiated on both the low-index and the high-index (stepped) surfaces of these metals to identify the relative importance of crystal surface structure and electronic structure in catalysis.

Preliminary LEED results show that the stepped gold surface AuS[6(111)×(100)] is stable in vacuum up to 800°C while its activity in chemisorption of naphthalene, monitored by Auger electron spectroscopy, is some two orders of magnitude lower than the corresponding platinum surface.

c. Studies of the Isomerization of Neo-Pentane and the Dehydrogenation of Cyclohexane on Stepped Platinum Crystal Surfaces

Donald W. Blakely and Gabor A. Somorjai

The reaction rates of these two important catalytic reactions are being measured on various stepped platinum surfaces, using a mass-spectrometer detector at a total pressure of 10^{-5}-10^{-4} Torr. The surface structure sensitivity of these reactions is explored. The active 6(111)×(100) stepped surface is studied by Auger spectroscopy and LEED to explore the structural and compositional factors controlling the reproducibility of its catalytic activity.

d. The Hydrogenolysis of Cyclopropane on Platinum Stepped Single Crystals at Atmospheric Pressure *

Daniel R. Kahn, Eugene E. Petersen and Gabor A. Somorjai

A review of the current literature in surface chemistry and heterogeneous catalysis has revealed that there is a gap between chemisorption and surface reaction studies performed in ultrahigh vacuum (10^{-4} to 10^{-9} Torr) on single-crystal surfaces and those carried out at 1 atmosphere on highly dispersed supported catalysts. Although the low-pressure work is of fundamental importance to catalysis, a direct correspondence between these studies and more conventional catalytic experiments is obscured by a number of factors, not the least of which is the enormous difference in total pressure--some 10^7 to 10^{12} orders of magnitude. Hence there is a need to measure the activity of single-crystal surfaces at high and low pressure. Furthermore, it has been shown that single-crystal surfaces would serve as ideal models for highly dispersed supported metal catalysts.

An apparatus was therefore constructed to study catalytic reactions on one or more platinum single crystals in situ both at 1 atm total pressure and in ultrahigh vacuum. The main feature of the design is a novel movable bellows-cup mechanism by which the catalyst can be encased in a small volume for the high-pressure experiments. A gas chromatographic sampling technique is employed to monitor the formation of products in the high-pressure system.

Using this apparatus, the cyclopropane hydrogenolysis has been investigated at 1 atm pressure on a platinum stepped single crystal (Pt(S)-[6(111)×(100)] having a total surface area of 0.76 cm^2. Initial specific reaction rates were reproducible to about 10%, and to within a factor of 2 were identical to published values for this reaction on highly dispersed supported platinum catalysts. The activation energy for the unpoisoned catalyst was found to be 12.2 kcal/mol, while that for the partially deactivated catalyst was 10.5 kcal/mol. The order of the reaction with respect to cyclopropane was determined to be 0.8±0.2. The conditions of hydrogen pretreatment were found to be important factors in determining the initial shape of the reaction rate curve.

This work has shown that it is possible to measure rates of reaction on a single platinum crystal having a surface area of 1 cm^2 at atmospheric pressure using a thermal conductivity detector of a gas chromatograph. Studies of this type appear to be well suited to discover the relationship between the morphology of the catalyst surface and its heterogeneous catalytic activity.

*Partially funded by the U. S. Army.

4. MOLECULAR BEAM SCATTERING FROM SURFACES†

a. The H_2-D_2 Exchange Reaction on Stepped and (111) Surfaces of Platinum Crystals

Steven L. Bernasek and Gabor A. Somorjai

The H_2-D_2 isotope exchange reaction was studied on the Pt(997) and Pt(111) single-crystal surfaces. It was found that the exchange takes place readily on the high-index surface but not at all on the (111) surface under the same conditions. Detailed investigations of the kinetics of the exchange reaction on the (997) surface have indicated a two-branch mechanism. One branch appears to be surface-diffusion-controlled with subsequent dissociation of the hydrogenic molecule at surface steps, while the other branch is direct step-aided dissociation.

b. Energy Accommodation of Gases on Scattering from Clean and Gas-Covered Platinum Surfaces

Steven L. Bernasek and Gabor A. Somorjai

The angular distributions of several monatomic and diatomic gases scattered from clean and CO-covered Pt(111) single-crystal surfaces have been studied. From the clean surface, the scattering distributions are specularly directed, while from the CO-covered surface the distribution is cosine. The efficient energy transfer indicated by the scattering distributions from the CO-covered surface is attributed to low-frequency bending modes of the CO molecules on the surface. The increased surface residence time resulting from this efficient energy transfer could be responsible for higher sticking probabilities and increased reaction rates for adsorption-limited reactions.

c. Molecular Beam-Surface Energy Exchange Studies

Stephen B. Brumbach and Gabor A. Somorjai

An apparatus has been assembled to study the energy exchange between particles in a

molecular beam and a solid surface. The purpose of these experiments is to study the translational energy accommodation between an incident atom or molecule at a particular temperature and a solid surface at some different temperature, and also to study the kinetic energy of the products of chemical reactions formed on the solid surface.

In order to measure the translational kinetic energy of the particles scattered from the surface, a variable-speed chopper is placed between the surface and a quadrupole mass spectrometer detector. The phase lag in the resulting ac signal contains information about the time of flight, and hence velocity, of the scattered particles.

†Partially funded by NSF.

5. SOLAR CELL RESEARCH‡

Wigbert J. Siekhaus and Gabor A. Somorjai

Photovoltaic conversion of sunlight into electricity in solar cells is feasible but presently uneconomical. Efficient and stable solar cells are manufactured today from high-purity silicon single crystals sliced into thin (0.3 mm) rectangular wafers of approximately 10 cm^2 area (~ 2×10^{-2} watt average output). Five thousand of these cells must be interconnected to provide 1 kW. Our research is aimed at developing a polycrystalline silicon solar cell with suitable electrical properties that will make photovoltaic energy conversion economical. 1) We are studying the various methods to deposit their layers of solar cell material with sufficient crystallinity over a large area (m^2). The catalysis of condensation and recrystallization of silicon doped with suitable impurities is investigated to produce the thin silicon layers at low temperatures. 2) Electron spectroscopy, low energy electron diffraction and electron microscopy are utilized to investigate the surface and grain boundary structure of the thin films and their effect on the electrical properties. We have dedicated to this solar cell research: an ultrahigh vacuum system equipped with LEED, a high-resolution electron spectrometer, an ion sputtering gun, and a device to break materials under ultrahigh vacuum conditions; a high-vacuum system with three electron-beam gun evaporators modified for silicon deposition work; and electronic instrumentation to measure electrical properties of solar cell films produced in the laboratory. The following experiments are planned or being performed in the laboratory.

a. Identification of Impurities Segregated on Grain Boundaries and Their Effect on Electronic Surface States

Wigbert J. Siekhaus and Gabor A. Somorjai

The review by Mönch[1] and more recent work by Rowe and Ibach[2] show clearly that the large concentration of surface states which are traps and recombination centers for photoelectrons can be filled or decreased by orders of magnitude by exposure to various adsorbates. Polycrystalline samples of electronic and metallurgical grade silicon (either before or after they have been diffused to form pn junctions) will be broken along grain boundaries under ultrahigh vacuum conditions. Impurities on the grain boundaries will be identified (qualitatively and quantitatively) using Auger electron spectroscopy. Single-crystal silicon samples with low-Miller-index surfaces will be exposed under ultrahigh vacuum conditions to various adsorbed impurities. The effect of impurities on surface states will be studied using high resolution electron loss spectroscopy and phtoelectron spectroscopy. Development work on a monochromatic He-light source (20 and 40 eV) has begun in cooperation with the nuclear chemistry group.

/

1. Winfried Mönch, On the Physics of Clean Silicon Surfaces, XIII Advances in Solid State Physics, Pergamon Press, March 1973.
2. J. E. Rowe and H. Ibach, Surface-State Transitions of Silicon in Electron Energy Loss Spectra, Phys. Rev. Letters, 9 July 1973, Vol. 31, No. 2.

b. Deposition and Characterization of Silicon Films for Solar Cell Use

Chin-An Chang, Tom Kaminski and Wigbert J. Siekhaus

Production of Si polycrystalline thin films can be achieved using techniques such as chemical vapor deposition (CVD), evaporation, sputtering, etc. The CVD method will be the main technique used in this laboratory for the near future. For the epitaxial growth of Si films using the CVD technique, silane gas, SiH_4, has been widely used. SiH_4 decomposes on a heated substrate at ~ 1100°C and silicon is deposited. The substrate temperature necessary for the thermal decomposition of silane can be significantly lowered by a codeposition of silane with another gas, diborane, B_2H_6. The lowest temperatures of decomposition that were achieved were 300-600°C.[1] The Si thin films produced this way, however, have very low

photovoltaic efficiencies because of their polycrystalline structure. To improve the film qualities, we plan to combine CVD with the ultrathin alloy-zone-crystallization (UTAZC) technique.[2] In the UTAZC technique an extremely thin alloy layer is deposited on the substrate prior to sublimation or evaporation of Si. The grain size of the Si film thus deposited was found to increase to 300 μ, compared with the usual 5-μ size achieved at a substrate temperature of 1100°C. The combined use of the CVD and UTAZC techniques could therefore produce single crystal-like Si films at lower substrate temperatures. This would allow the use of Al as the substrate material for a good electrical contact with the Si films deposited.

Systematic studies will be carried out to find the best catalyst for lower temperature CVD of silane, and the best alloy film for the UTAZC purpose. Also, cheaper starting material such as $SiCl_4$ will be tested for CVD of Si. The Si films produced will be characterized by electrical measurements (resistivity, photoconductivity, carrier mobility and lifetime) by their grain structure and surface properties. Pichaud and Drechsler[3] have shown increased surface self-diffusion and surface recrystallization of tungsten under the influence of adsorbed nickel. If such a surface alloy can be maintained during deposition of silicon, large grain silicon films can be formed at a temperature low compared with the conventional recrystallization temperature; i.e., the adsorbed species acts as a crystallization catalyst.

In the planned experiment the surface recrystallization temperature will be measured as a function of the adsorbed element. Elements will be chosen that have low bulk solubility in silicon. LEED will be used to define the recrystallization temperature.

d. Measurement of Solar Cell and Semiconductor Electrical Characteristics

Tom Kaminska and Wigbert J. Siekhaus

Facilities for measuring semiconductor and solar cell electrical parameters are being established to compliment crystallization catalysis and polycrystalline solar cell studies being conducted by the group. The measurements will serve a dual purpose: they will allow quality determination of materials produced and a detailed study of polycrystalline solar cell operation.

Van der Pauw methods[4] will be used to determine sample bulk resistivity and carrier concentrations and a photoconductivity measurement similar to that of Stevenson and Keyes[5] will determine minority carrier lifetime. The cells will be successively anodized and etched, and electrical measurements made at each step to generate a depth profile of carrier concentration and lifetimes. This will be compared with a doping concentration profile determined by ion sputtering and Auger analysis.

Surface lifetimes, surface state density, and surface state energy levels, and their variation with adsorbed gases and impurities will be studied using conductivity and temperature[6] methods in conjunction with ultraviolet photoelectron spectroscopy to determine how electronic surface states at grain boundaries affect polycrystalline solar cell resistance. With this information in hand we should be able to increase polycrystalline solar cell power output.

‡ Supported by NSF-RANN.

1. L. H. Hall and K. M. Koliwad, J. Electrochem. Soc. 120, 1438 (1973); F. C. Eversteyn and B. H. Put, ibid. 120, 106 (1973); and references therein.
2. J. D. Filby and S. Nielsen, J. Electrochem. Soc. 112, 957 (1965).
3. M. Pichaud, M. Drechsler, Surface Self-diffusion of Tungsten under the Influence of Adsorbed Nickel, Surface Sci. 36(3), 813-16 (1973).
4. L. J. Van der Pauw, A Method of Measuring Specific Resistivity and Hall Effect of Discs of Arbitrary Shape, Phillips Res. Repts. 13, No. 1, 1 (1958).
5. D. T. Stevenson and R. J. Keyes, Measurement of Carrier Lifetime in Germanium and Silicon, J. Appl. Phys. 26, 190 (1955).
6. P. M. Brown and P. V. Gray, Density of SiO_2-Si Interface States, Appl. Phys. Letters 8, 31 (1966).

6. RESEARCH PLANS FOR CALENDAR YEAR 1974

Gabor A. Somorjai

Low energy electron diffraction studies of molecular crystals surfaces are initiated. The surface structures of ice, naphtalene and phenantrene that are grown epitaxially on metal surfaces at low temperatures (~100°K) will be studied. Surface studies of high molecular weight, low vapor pressure organic solids (polymers) will be carried out.

Catalysis studies on alloy surfaces are initiated to investigate the reactivity of hydrocarbons as a function of alloy surface compositions. Gold and platinum alloys,

gold-iridium and gold-hafnium alloys are being used. The purpose of these investigations is to develop an alloy catalyst with catalytic properties identical to that of platinum for the various hydrocarbon surface reactions. Catalysis of N_2 and NO molecule reactions on iron crystal surfaces will be investigated. The catalytic hydrogenation of carbon and the catalytic dissociation of water will be studied.

The electronic surface states of silicon and platinum will be studied by electron loss and UV photoelectron spectroscopy. The effect of gas adsorption on the surface electronic properties will be studied by these techniques.

The research on solar cells has been initiated and is outlined in detail in the previous section, 5.

7. 1973 PUBLICATIONS AND REPORTS

Gabor A. Somorjai and Associates

Journals and book chapter

1. G. A. Somorjai, Low Energy Electron Diffraction and Auger Electron Spectroscopy Studies of the Structure of Adsorbed Gases on Solid Surfaces. Surface Sci. 34, 156 (1973) (LBL-878).

2. M. R. Martin and G. A. Somorjai, Determination of the Surface Geometry for the Aluminum (110) and (111) Surfaces by Comparison of Low-Energy-Electron-Diffraction Calculations with Experiment, Phys. Rev. B 7, 3607 (1973) (LBL-1151 Rev.).

3. J. L. Gland and G. A. Somorjai, LEED and Work Function Studies of Benzene, Naphthalene and Pyridine Adsorbed on Pt(111) and Pt(100) Single Crystal Surfaces, Surface Sci. 38, 157 (1973) (LBL-1422).

4. S. L. Bernasek, W. J. Siekhaus, and G. A. Somorjai, Molecular Beam Study of Hydrogen-Deuterium Exchange on Low and High Miller Index Platinum Single Crystal Surfaces, Phys. Rev. Letters 30, 1202 (1973) (LBL-1809).

5. R. W. Joyner and G. A. Somorjai, Recent Trends in the Application of Low Energy Electron Diffraction, in Surface and Defect Properties of Solids 2, 1 (1973), The Chemical Society Publ.

6. S. Berglund and G. A. Somorjai, Auger Electron Spectroscopy Study of the Surface Composition of the Lead-Indium System, J. Chem. Phys. 59, 5537 (1973) (LBL-1867).

LBL reports

1. P. A. Bertrand and G. A. Somorjai, Estimation of Surface Free Energies of Metals, LBL-1466, Feb. 1973.

2. K. Baron, D. W. Blakely, and G. A. Somorjai, LEED Studies of the Surface Structures of Adsorbed Hydrocarbons (n-Heptane, Toluene, Benzene, Ethylene, and Cyclohexane) on Stepped (High Miller Index) Platinum Surfaces, LBL-1813, May 1973 (to be published in Surface Science).

3. John Wasilczyk, Measurement of Intensities of LEED Beams from Platinum Surfaces and from Adsorbed Overlayers (M.S. thesis), LBL-1807, June 1973.

4. J. L. Gland and G. A. Somorjai, LEED and Work Function Change Studies of the Adsorption of Substituted Aromatic Molecules on the (111) and (100) Crystal Faces of Platinum, LBL-1815, July 1973 (to be published in Surface Science).

5. G. A. Somorjai and S. B. Brumbach, The Interaction of Molecular Beams with Solid Surfaces, LBL-2212, Aug. 1973.

6. Daniel R. Kahn, The Hydrogenolysis of Cyclopropane on Platinum Stepped Single Crystals at Atmospheric Pressure (Ph.D. thesis), LBL-1891, Sept. 1973.

7. F. J. Szalkowski, Auger Electron Spectroscopy Analysis of Vanadium and Vanadium Compound Surfaces (Ph.D. thesis), LBL-888, Oct. 1973.

8. G. A. Somorjai, The Structure and Thermodynamics of Clean Surfaces--Principles, LBL-2257, Oct. 1973.

9. J. L. Gland, Low Energy Electron Diffraction and Work Function Studies of Adsorbed Organic Layers on the (100) and (111) Crystal Surface of Platinum (Ph.D. thesis), LBL-1816, Sept. 1973.

10. F. J. Szalkowski and G. A. Somorjai, Auger Electron Spectroscopy Shifts in some Vanadium Compounds, submitted to J. Chem. Phys. (North American Rockwell Science Center Report) December 1973.

11. F. J. Szalkowski, P. A. Bertrand, and G. A. Somorjai, Characteristic Energy Loss Spectra of Vanadium and of V_2O_3, submitted to Phys. Rev. (North American Rockwell Science Center Report) December 1973.

Lee F. Donaghey, Principal Investigator

1. CHEMICAL VAPOR DEPOSITION

a. Thermodynamics of Phase Equilibria for Chemical Vapor Deposition of $GaAs_{1-x}P_x$*

Saleem A. Shaikh and Lee F. Donaghey

The thermodynamics of phase equilibria in the Ga-As-P-Cl-H system was studied for reactor condition allowing the chemical vapor deposition of $GaAs_{1-x}P_x$ solid solutions from $Ga_{(\ell)}$ AsH_3, PH_3, HCl, and H_2 source chemicals. The properties of reaction equilibria and the predominant chemical species were deduced for each zone of the reactor. Analytical procedures were deduced for calculating multi-component phase equilibria in terms of reduced variables. The composition of the $GaAs_{1-x}P_x$ alloy was calculated as a function of temperature and the arsine-phosphine ratio. These calculations provide a basis for efficient III-V compound reactor design and operation. The results of experimental studies provide confirmation of the phase equilibria for alloy compositions near x = 0.4.

*Abstracted from LBL-2241.

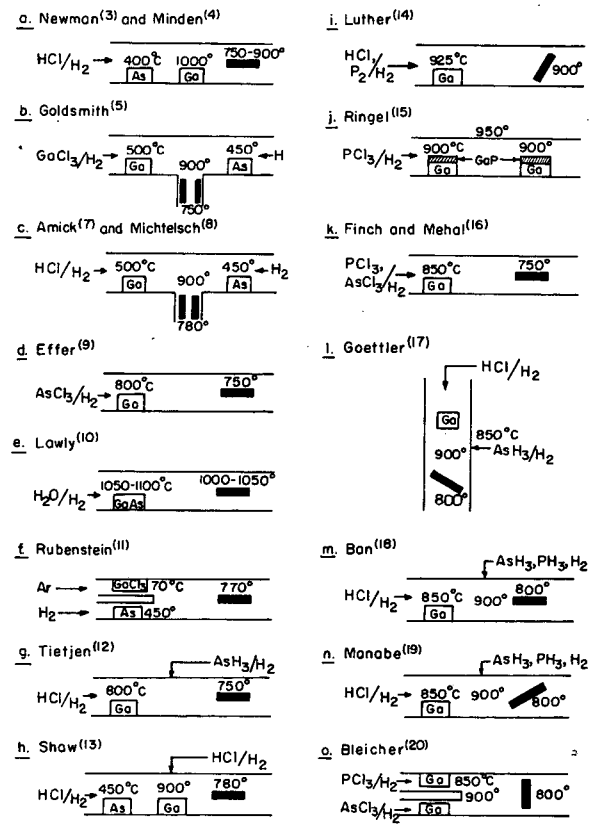

Fig. 1. Open flow reactors for the chemical vapor deposition of GaAs, GaP, and $GaAs_{1-x}P_x$ solid solutions. Refer to LBL-2518 for references. (XBL 729-6985)

b. Reactor Designs for the Chemical Vapor Deposition of Epitaxial $GaAs_{1-x}P_x$*

Saleem A. Shaikh and Lee F. Donaghey

Research and commercial reactor designs for the chemical vapor deposition of $GaAs_{1-x}P_x$ alloys were reviewed with regard to source chemicals and chemical reaction schemes. The open-flow reactors reviewed are shown schematically in Fig. 1. Reactor design criteria and limitations were deduced for open-flow reactors utilizing liquid and vapor source chemicals. Commercial reactor designs were examined for properties of reactant flow and substrate orientation. The design and operating properties of a cold-wall reactor utilizing trimethyl gallium as a source chemical is compared to hot-wall reactor properties.

*Abstracted from LBL-2518.

c. Kinetics of GaAs-GaP-HCl Reactions

Ronald H. Bissinger and Lee F. Donaghey

The kinetics of gas-solid reactions for etching and deposition are of significant importance in the processing of compound semiconductor devices. The surface morphology of sites for epitaxial growth can be optimized by controlled etching with HCl. The kinetics and morphological properties of the GaAs-HCl and GaP-HCl reactions are currently under study to characterize the mixed-diffusion-controlled and surface-reaction-controlled kinetic regimes and to allow prediction of etching rates and morphological consequences under various reaction conditions.

Two methods are presently under investigation for measurement of reaction kinetics. The first method involves thermogravimetry, at reduced pressure in order to minimize the gas phase diffusional resistance. The second method utilizes a rotating surface which, through establishing a uniform boundary layer, permits the estimation of diffusional contributions to the measured reaction rate. The goals of the program are to establish the reaction kinetics and to optimize conditions for processing substrate crystals for electro-optical device applications.

d. Chemical Vapor Deposition of Compounds in the Ti-Si-C System

Charles W. Manke and Lee F. Donaghey

The thermodynamics of alternative vapor-solid reactions are being studied to develop reaction schemes for the chemical vapor deposition of protective coatings in the Ti-Si-C system at reduced temperature. Chemical vapor deposition is appealing as a process for depositing protective coatings onto low-cost alloys. Deposition onto hardened steels has disadvantages at high temperature, however, as structural properties of the steel substrate are degraded and often the deposited layer exhibits a low impact strength. These factors point to the need for low-temperature chemical vapor depositions. This study will concentrate on phases in the Ti-Si-C system and volatile transport agents. Phases such as TiC have application as self-lubricating coatings at very low temperature.[1] A possible limitation of low-temperature reactions is slow reaction kinetics.

1. H. Gass and H. E. Hintermann, in Chemical Vapor Deposition, 4th International Conference, edited by J. M. Blocher and G. Wakefield (The Electrochemical Society, Princeton, N. J., 1973).

e. Tank-Mixing Methods for Producing Time-Varying Reactive Gas Mixtures*

Lee F. Donaghey and Saleem A. Shaikh

Tank-mixing methods are under study to provide simple means for producing controlled time-varying reactive gas mixtures for epitaxial reactors. The transient output concentrations of single and multiple mixing-tank systems with series and parallel flow were simulated for discrete changes in the input concentration, input flow rate, or tank volumes. A series arrangement of mixing tanks and the output concentration produced

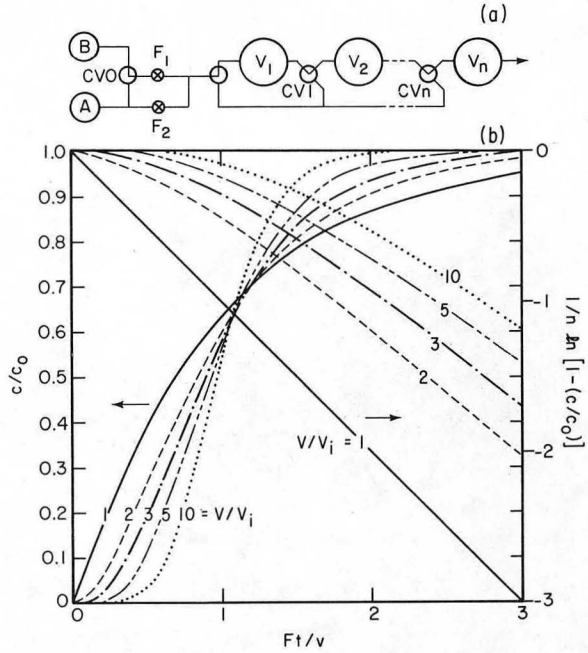

Fig. 1. Initial transient output concentration from a series of n mixing tanks with volumes $V_i = V/n$: (a) schematic of flow system, and (b) time dependence of c/c_o and $n^{-1} \ln (1 - c/c_o)$. (XBL 7311-6716)

by a step input change is shown in Fig. 1. A simple tank-mixing system is proposed for composition grading of ternary compound-alloy epitaxial layers on binary substrates. The system proposed requires changes in both gas composition and mixing tank volume.

*Abstracted from LBL-2298.

f. Characterization of III-V Compound Substrate and Epitaxial Layers by Divergent X-ray Beam Diffraction*

Lee F. Donaghey and Ronald H. Bissinger

The divergent x-ray beam diffraction method was studied for characterizing the lattice perfection in GaAs substrates and of composition variation and growth defects in epitaxial $GaAs_{1-x}P_x$ layers. Reflections from the {711}, {620}, {551}, and (400) planes predominate in pseudo-Kossel back-reflection patterns obtained from samples with (100) surface orientations, as is

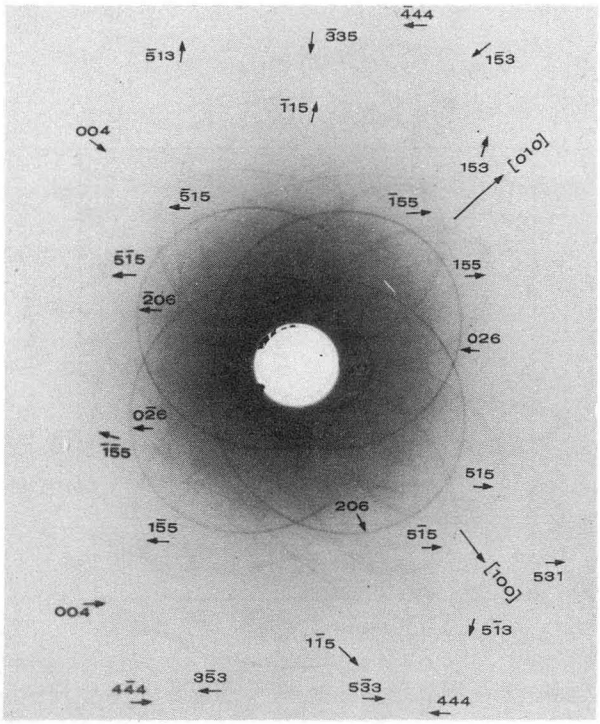

Fig. 1. Pseudo-Kossel back-reflection pattern from (100) GaAs. (XBB 737-4370)

shown in Fig. 1. The selectivity of pseudo-Kossel line displacements was assessed as a function of lattice parameter and anisotropic strain distortion. Lattice parameter variations in epitaxial layers are accurately measurable from {551}, {444}, and {422} plane reflections, while (400) line displacements can be used to measure lattice strain.

*Abstracted from LBL-1872.

2. CHEMICAL TRANSPORT

a. An Analysis of Multi-component, Chemical Transport Crystal Growth*

Rajani B. Agnihotri and Lee F. Donaghey

The chemical transport of binary compounds in closed containers is under study to assess the contribution to chemical transport crystal growth of variable transport properties under conditions of multi-component, gas phase, diffusion-controlled kinetics. The analytical approach utilized is the integration of the Stefan-Maxwell transport equations for multi-component gaseous diffusion. The diffusion flux is calculated by a self-consistent solution of diffusive transport and phase equilibria at ends of the transport path. The general analysis allows the prediction of interdiffusion contributions to the transport flux for crystal growth.

*Abstracted from LBL-2254.

b. Chemical Transport Analysis of ZnS Crystal Growth*

Rajani B. Agnihotri and Lee F. Donaghey

Crystal growth of ZnS by the closed-tube chemical transport method with iodine as a transport agent was explored by numerical simulation. An analysis of diffusion-controlled kinetics based on integration of the Stefan-Maxwell equations for multi-component diffusion was utilized to calculate the transport flux as a function of transport agent concentration and temperature gradient along the transport path. The product flux was found to increase approximately linearly with temperature gradient along the transport path for fixed initial iodine concentration, but to tend to a saturation value as the initial iodine concentration is increased for a fixed temperature gradient. The analysis provides a basis for the crystal growth of ZnS by chemical transport.

*Abstracted from LBL-2259.

c. Phase Equilibria and Transport Processes for Impurity Introduction into Compound Semiconductors

Steven R. Styer and Lee F. Donaghey

Phase equilibria between compound semiconductors and electrically active impurities are under study toward the design of processes for impurity introduction by closed and open-flow methods. Previously determined equilibria in the Zn-Ga-As system will be modeled and extended. The phase equilibria in the Cd-Ga-As system will then be predicted and confirmed by spectroscopic methods. Diffusion data will then be combined with optimal equilibrium conditions to design transport processes for the controlled introduction of electronic impurities.

3. CRYSTALLIZATION

a. Application of Velocity-Selective Freeze-Pushing to the Separation and Characterization of Particulate Matter in Air Pollution Samples†

T. Thomas Shih and Lee F. Donaghey

A new method for sampling and characterizing airborne solid particulate matter in air pollution samples was investigated. The method utilizes the phenomenon of velocity-selective freeze-pushing of particulate matter during controlled solidification of organic liquids. Selective separation of particles is achieved by differences in their interfacial physical properties relative to the organic liquid or solid. The theoretical basis of this phenomenon was explored to develop a separation factor, k*, which characterizes the effectiveness of the freeze-pushing phenomenon. The separation of particulate minerals with H_2O was explored quantitatively using the zone chromatographic separation technique. The experimental separation of graphite and hematite particles with thymol was investigated toward deducing conditions leading to optimum separation.

†Abstracted from LBL-2243.

b. Congruent Saturating Solvents for Garnet Crystal Growth

Pei Shiun Chen and Lee F. Donaghey

The PbO-BaO-B_2O_3 solvent system was studied to determine compositions allowing congruent saturation of rare-earth-substituted magnetic garnets. Because the solvents $BaO \cdot B_2O_3$ and PbO have different affinities for rare earth and iron oxides, respectively, it should be possible to determine solvent mixtures such that solutions in equilibrium with a given compound have component ratios which are the same as those in the compound itself. The problem is complicated by limited stability ranges for complex crystal structures such as the rare-earth-substituted iron garnets. Congruently saturating solvents would nevertheless allow significant increases in crystal yield from the growth solution and improve crystalline perfection through reducing interfacial instabilities caused by constitutional supercooling.

Experimental studies were conducted to explore phase equilibria in the pseudo-ternary system, $(Eu_xEr_{1-x})_3[Ga_yFe_{1-y}]_5O_{12}$-$PbO$-$BaO \cdot B_2O_3$. Liquid phase epitaxial crystallization of the garnet phase was carried out on axially rotating, gadolinium-gallium garnet substrates. Compositions of the epitaxial layers were determined by electron microprobe analysis. The study showed that the garnet phase is the stable solid over a wide range of solvent compositions, and that congruency of saturation is only weakly dependent on the ratios of oxide components of the garnet phase.

4. SPUTTER DEPOSITION

a. Reactive Sputter Deposition of TiO_x

Kenneth G. Geraghty and Lee F. Donaghey

The reactive sputter deposition of titanium oxides is under investigation utilizing rf sputtering of a titanium target in an argon plasma containing controlled, partial pressures of oxygen. TiO_x thin films with $1 \leqslant x \leqslant 2$ were deposited on quartz and glass substrates. Amorphous films were deposited at room temperature with deposition rates decreasing with oxidation of the target. Selected film properties are under study to determine the effect of sputter deposition parameters such as the O_2 partial pressure in the plasma. These studies will permit prediction of the stoichiometry and film properties as a function of reactive sputtering conditions.

b. Computer Simulation of Sputtering

Pravin Mundkur and Lee F. Donaghey

The sputter yield from single crystals is under study utilizing numerical methods. The sputtering of Cu with Ne^+ was simulated as a function of incident ion energy and direction, using interatomic potential functions derived from band structure considerations. The repulsive potential function giving agreement with experimental data was determined in the ion energy range from 0.5 to 1 keV. The sputtering mechanisms and energetics for different mechanisms will provide information toward predicting the dependence of yield on sputter conditions.

5. SOLID-STATE ELECTROCHEMISTRY

a. Oxygen Transfer Kinetics Between Ga-Ga_2O_3 Electrodes and the Solid Electrolyte Calcia-Stabilized Zirconia*

Lee F. Donaghey and Raymond Pong

The kinetics of oxygen transfer between

$Ga\text{-}Ga_2O_3$ composite electrodes and the solid electrolyte calcia-stabilized zirconia, $ZrO_2(CaO)$, were studied with the symmetric galvanic cell,

$$W/Ga\text{-}Ga_2O_3/Ca_{0.15}Zr_{0.85}O_{1.85}/Ga\text{-}Ga_2O_3/W,$$

over the temperature range from 800 to 900°C. Chronopotentiometric studies were conducted using current densities from 0.3 to 130 $\mu A/cm^2$ to obtain overpotentials for Faradaic oxidation and reduction reactions at the $Ga\text{-}Ga_2O_3/ZrO_2(CaO)$ interface (see Fig. 1). A linear dependence of the overpotential on current density was obtained, corresponding to a local electrode resistance of 3.8 ohm per cm^2 of electrode-electrolyte interface at 800°C. The data are in agreement with a solution-diffusion mechanism of oxygen transport through liquid Ga in the electrode between the $ZrO_2(CaO)$ electrolyte and Ga_2O_3 particles. The electrode kinetics for oxygen transfer with this electrode are faster than for other metal-metal oxide electrodes.

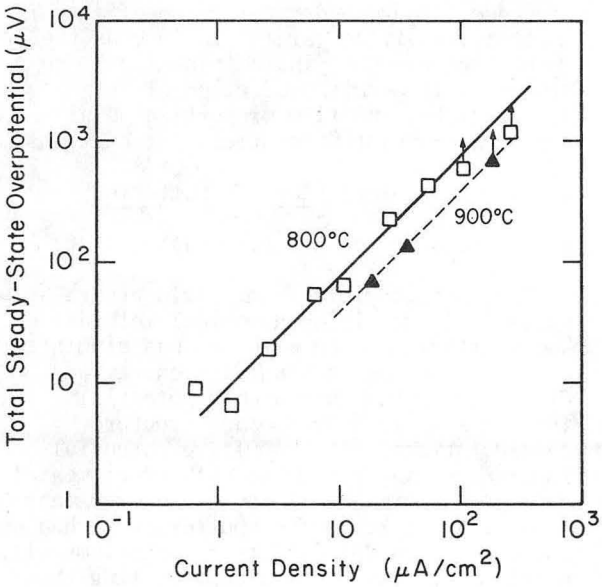

Fig. 1. Total steady-state overpotential as a function of current density for the cell $Ga\text{-}Ga_2O_3/ZrO_2(CaO)/Ga\text{-}Ga_2O_3$. (XBL 737-1573)

*Abstracted from LBL-1892.

b. Thermochemical Properties of Compound Semiconductor Alloys Solutions

Timothy J. Anderson and Lee F. Donaghey

Thermochemical properties of compound semiconductor alloys are under study by solid state galvanic cell techniques. The research shall be directed toward developing improved solution models which enable the prediction of liquid-solid phase equilibria. Currently, solution models and lattice thermodynamics are being examined to reduce apparent deficiencies and account for ionic bonding contributions. The results will be directed toward devising liquid phase epitaxial processes for electro-optical device fabrication.

c. Activities in the Ga-In-Sb System

Raymond Pong and Lee Donaghey

The thermodynamic properties of liquid compound-semiconductor alloys are under study by solid state galvanic cell techniques. Component activities of the Ga-In liquid alloys were measured with calcia-stabilized zirconia (CSZ) electrolytes. The gallium activities in the Ga-Sb system were measured with yttria-doped thoria (YDT). The experimental investigations are being extended to the Ga-In-Sb ternary.

Through refinements in solid state electrochemical cell design and the use of YDT electrolytes, accurate measurements of gallium activities in Ga-Sb liquid alloys were performed. The measurements indicate a large negative deviation from ideality that is not consistent with current solution models. Similar deviations from ideality are found in the In-Sb system. An extended quasi-chemical treatment is currently being explored, considering multipair-wise interactions in the liquid.

6. RESEARCH PLANS FOR CALENDAR YEAR 1974

Lee F. Donaghey

Studies of the chemical vapor deposition and etching kinetics of compound semiconductors will be directed toward alloy solid solutions utilizing thermogravimetry to monitor reaction rates. Alternative reaction systems for the deposition of phases in the Ti-Si-C system will be studied toward the development of low-temperature reaction processes.

Models for phase equilibria required in

the processing of compound semiconductor photovoltaic and electroluminescent devices will be explored and confirmed using high-temperature electromotive force, and optical absorption measurements. This information will be applied in the design of processes for heterostructures.

Transients during reactive sputtering deposition of titanium compounds will be studied by capacitance-voltage and optical absorption measurements. Factors affecting sputter yield of non-stoichiometric compounds produced during reactive sputtering will be studied.

7. 1973 PUBLICATIONS AND REPORTS

Lee F. Donaghey and Associates

Book contribution

1. "Introduction to Chapter 1: Fundamentals" (with McD. Robinson), in Chemical Vapor Deposition, Fourth International Conference, (The Electrochemical Society, Princeton, New Jersey, Princeton, New Jersey, 1973), pp. 3-4.

Paper presented

1. L. F. Donaghey, "Developments in Materials Coating Techniques," Am. Inst. of Chem. Engr. 74th National Meeting, New Orleans, March 15, 1973.

2. L. F. Donaghey, "Chemical Transport Analysis of CdS and MnS with Iodine," IVth International Conference on Chemical Vapor Deposition, Oct. 8, 1973.

LBL reports

1. L. F. Donaghey and R. H. Bissinger, III-V Compound Substrate and Epitaxial layer Characterization by Divergent X-ray Beam Diffraction. Accepted for publication in J. Electronic Materials (LBL-1872)(July 1973).

2. L. F. Donaghey and R. Pong, Oxygen Transfer Kinetics Between Ga-Ga_2O_3 Electrodes and the Solid Electrolyte Calcia-Stabilized Zirconia. To be published in J. Electrochemical Society (LBL-1892, Aug. 1973).

3. L. F. Donaghey and L. Wright, High Temperature Electrical Conductivity of Non-stoichiometric Gadolinium-Gallium Garnet Single Crystals. Submitted to J. Phys. Chem. Solids (LBL-2244, Oct. 1973).

4. R. B. Agnihotri and L. F. Donaghey, An Analysis of Multi-component, Chemical Transport Crystal Growth. Submitted to J. of Crystal Growth (LBL-2254, Oct. 1973).

5. R. B. Agnihotri and L. F. Donaghey, Chemical Transport Analysis of ZnS Crystal Growth. Submitted to J. of Crystal Growth (LBL-2259), Oct. 1973).

6. S. A. Shaikh and L. F. Donaghey, Thermodynamics of Phase Equilibria for Chemical Vapor Deposition of $GaAs_{1-x}P_x$. Submitted to I & EC Process Design and Development (LBL-2241, Oct. 1973).

7. T. T. Shih and L. F. Donaghey, Application of Velocity-Selective Freeze-Pushing to the Separation and Characterization of Airborne Solid Particulate Matter in Air Pollution Samples. Submitted for presentation at the March 10-13, 1974 National CIChE Meeting in Tulsa, Oklahoma, for publication in the Conference Proceedings. (LBL-2243, Dec. 1973).

8. L. F. Donaghey and S. A. Shaikh, Tank-Mixing Methods for Producing Time-Varying Reactive Gas Mixtures (LBL-2298, Nov. 19).

9. S. A. Shaikh and L. F. Donaghey, Reactor Designs for the Chemical Vapor Deposition of Epitaxial $GaAs_{1-x}P_x$. Submitted to 3rd International Conference on Reaction Engineering, August 27-29, 1974, for publication in the Conference Proceedings. (LBL-2518, Dec. 1973).

C. ELECTROCHEMISTRY

Charles W. Tobias, Principal Investigator

1. FUNDAMENTAL STUDIES OF IONIC MASS TRANSPORT

a. Distribution of Ionic Mass Transport Rates in a Flow Channel

Uziel Landau and Charles W. Tobias

Experiments to obtain current distribution and maximum mass transport rates to a segmented electrode embedded in the wall of a flow channel[1] were continued. The parameters investigated were: solution concentration and temperature (corresponding to Sc numbers of ~500-1700), rate of current and potential application, surface morphology and flow rate (up to Reynolds number of 120,000).

Since the mass transfer rates increase considerably with increasing surface roughness, especially at high flow rates, special care was taken to obtain values for transport to smooth surfaces with well-polished electrodes. In addition, many experiments were conducted with very low copper concentrations (~0.006 M), thus minimizing the amount of deposit. Figure 1 presents part of the experimental results for mass transport to a smooth electrode. The values in Fig. 1(a) agree with some of the existing correlations. Figure 1(b) shows that the Chilton-Colburn analogy for the j factor holds up to flow rates of Re=10,000. Transport rates obtained from average measurements over the entire electrode were higher than the true values obtained from local current density measurements. This effect becomes more significant at lower flow rates, where the entrance region, in which mass transport is higher, comprises a larger portion of the total electrode. The observed unsteady-state transition times were longer than those predicted by numerical solution developed by Selman.[2]

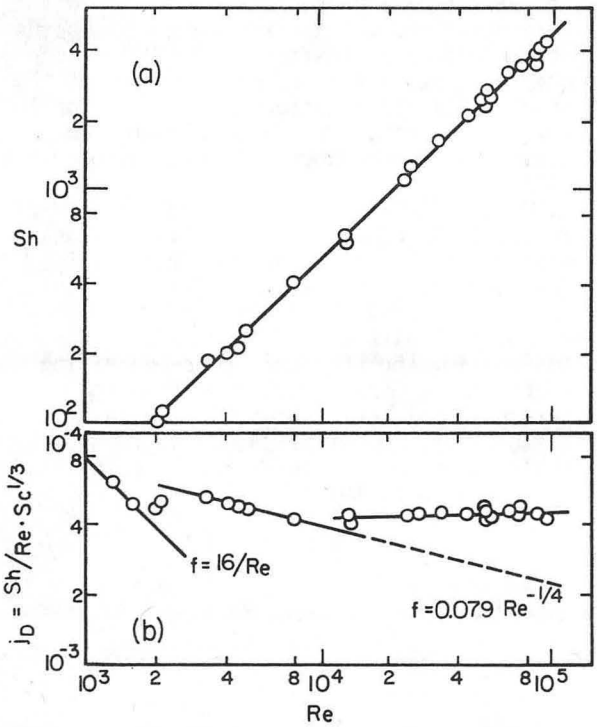

Fig. 1. Mass transport dependence on flow rate.
(a) Sh vs. Re
(b) $j_D = St \cdot Sc^{2/3}$ vs. Re. (XBL 741-5468)

1. Uziel Landau and Charles W. Tobias, Flow Circuit for Ionic Mass Transfer Studies at High Flow Rates, IMRD Annual Report for 1970, UCRL-20500, April 1971, p. 39.
2. Jan Robert Selman, Measurement and Interpretation of Limiting Currents, UCRL-20557, June 1971.

b. The Effect of Flow of Electrolyte on Surface Morphology in the Electrodeposition of Metals

Eric J. Carlson, Uziel Landau, and Charles W. Tobias

Mass transfer studies in the flow channel described previously[1] employing electrodeposition of copper revealed changes in surface characteristics indicating that investigation of the interaction of fluid mechanics and mass transfer on the morphology of the deposit would be of value.

The roughness of the deposit depends on the ratio of applied current to the maximum current allowed by convective diffusion, and migration. Depositing the same amount of copper at different fluid velocities, changes in surface morphology were evaluated by using surfanalysis and micrographic examination. Figure 1 illustrates that by increasing the flow rate while maintaining the same deposition rate a smoother surface is obtained.

Initial surface imperfections are magnified during diffusion-limited deposition.

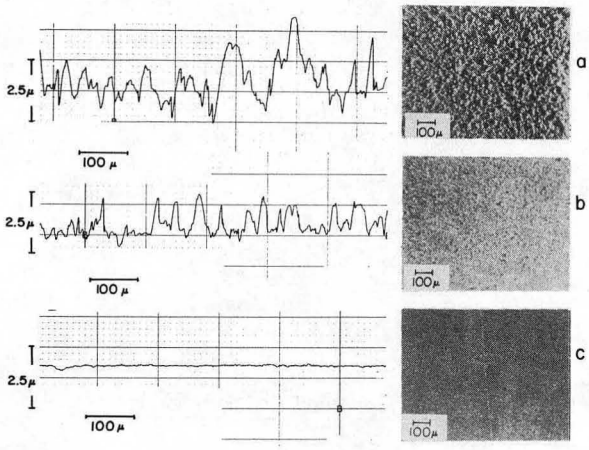

Fig. 1. Deposit roughness at constant current and different flow rates. Profile traces at left from surf-analyzer. (a) Re = 10,000, $i/i_{l.c.} \sim 0.5$. i - current density, $i_{l.c.}$ - limiting current density (note changes in magnification on different figures). Total charge passed in all three cases: 1 amperehour. (XBB 741-12)

As shown in Fig. 2, when scratches and protrusions are introduced on the surface of the substrate electrode, enhanced preferential deposition on crests is obtained. Of special interest is the wake-shaped deposit revealing the highly turbulent region following and preceding a protrusion. Preferential deposition on crests was also studied on uniformly roughened electrodes by using sand-type roughness and machined grooves.

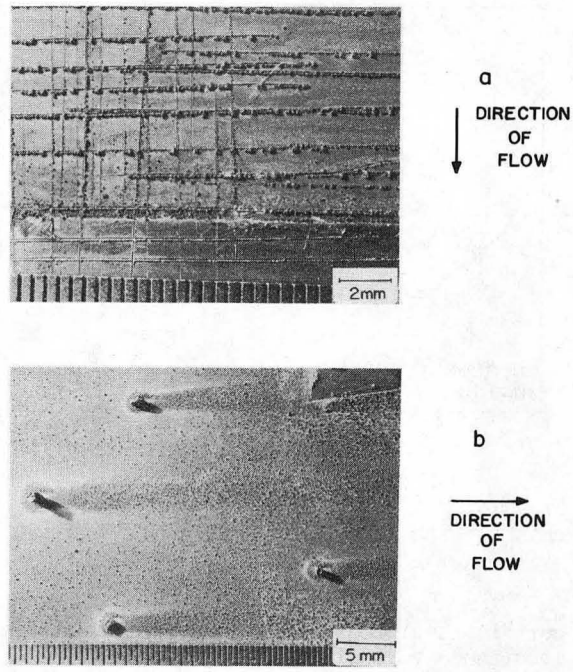

Fig. 2. Preferential deposition around protrusions at high flow rates (Re~20,000). (a) Deposition on ridges alongside grooved surface.

$\varepsilon \sim 20\ \mu$, $\delta \sim 0.4$ mm, $\varepsilon_f \sim 100\ \mu$

(b) Deposition on and around cylindrical protrusions.

$\varepsilon \sim 1$ mm, $\delta \sim 0.4$ mm .

(Scale: 2 div/mm)
ε - original protrusion height
δ - hydrodynamic boundary layer thickness
ε_f - protrusion height after deposition.
(XBB 741-11)

1. Uziel Landau and Charles W. Tobias, Flow Circuit for Ionic Mass Transfer Studies at High Flow Rates, IMRD Annual Report for 1970, UCRL-20500, April 1971, p. 39.

2. ELECTROLYSIS AT HIGH CURRENT DENSITIES

a. Mass Transfer at Closely Spaced Electrodes

Raul E. Acosta, Rolf H. Muller, and Charles W. Tobias

The study of rates of mass and momentum transfer in flow channels with very small spacings (0.05 and 0.02 cm) was brought to conclusion. In addition to the optically smooth channel reported earlier artificially roughened electrode surfaces were also investigated. Of the roughness patterns, three were of the random type, obtained by sandblasting the walls of the channel, using different abrasive grades; the fourth type of roughness was produced by "V" grooves running perpendicular to the flow direction. The value of the mass transfer coefficients measured are shown in the form of the j_D factor in Fig. 1.

As indicated earlier,[1] operation at high flow rates when using closely spaced electrodes is characterized by very large expenditures in pumping power. Hence, under

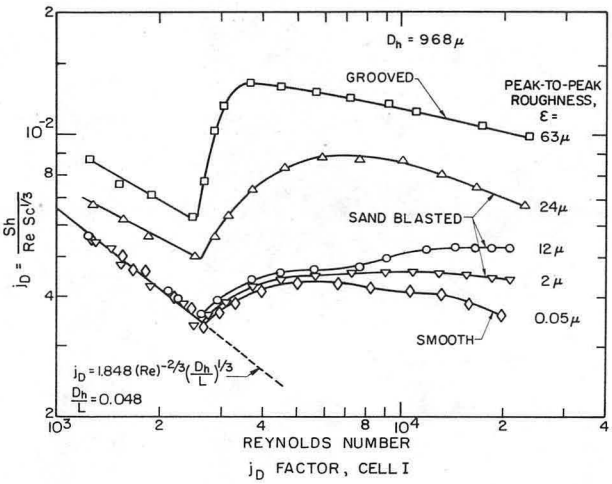

Fig. 1. Mass transfer coefficient for flow channel with D_h = 0.096 cm. (XBL 7311-6623)

certain conditions it may be of considerable importance to operate at flow rates where the ratio of the mass transfer to the friction factor coefficient, $j_D/(f/2)$, gives a maximum advantage. The value of this ratio as a function of the Reynolds number for the roughness values used is shown in Fig. 2. The decisive role played by the size and type of roughness elements is clear from this figure.

At the highest flow rate employed (74 meters/sec), with the smallest electrode separation, the equivalent mass transfer

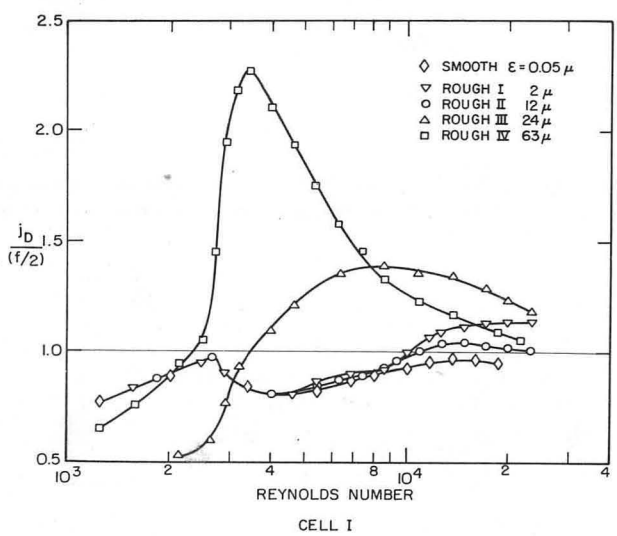

Fig. 2. Ratio of mass to momentum transfer for flow channel with D_h = 0.096 cm. (XBL 7311-6617)

boundary layer thickness was 2×10^{-5} cm. Although this allows very high charge-transfer rates with high current efficiency, the high cost of pumping of electrolyte renders applications, other than in electrochemical machining, unlikely.

---

1. Raul E. Acosta, Rolf H. Muller, and Charles W. Tobias, Electrolysis at High Current Densities: Mass Transfer at Closely Spaced Electrodes, IMRD Annual Report for 1972, LBL-1400, April 1973.

b. Periodic Phenomena in the Anodic Dissolution of Copper

John F. Cooper, Rolf H. Muller, and Charles W. Tobias

Earlier studies of anode potential oscillations during the galvanostatic dissolution of copper have been carried out under well-defined hydrodynamic conditions only up to 36 A/cm^2.[1] In order to further investigate the oscillations at higher current densities, a stagnation point flow cell has been constructed. In this system, a jet of electrolyte is allowed to impinge perpendicularly on a stationary, 0.16-cm-diameter copper disk electrode. The advantages of the system include: (1) hydrodynamic conditions may be accurately characterized; (2) the electrode surface is uniformly accessible to the electrolyte from the standpoint of mass transport; and (3) the solution flow rate just outside the diffusion boundary layer is sufficiently high to prevent excessive heating of the electrolyte at high current levels.

A different form of oscillations occurs above 70 A/cm^2, with amplitudes of about 50 volts, as shown in Fig. 1. Above 150 A/cm^2, only a few potential oscillations occur, with period lengths of about 10^{-3} sec, before continuous oxygen evolution begins and the oscillations cease. Near this upper current density limit, the potential falls from peak to trough levels within 10^{-5} sec.

The rapidity of potential decay led to considerations of possible dielectric breakdown in the thin (10^{-5} cm) cuprous oxide surface layer formed during the high-potential phase of the oscillation cycle. Cuprous oxide is known to undergo a transition from a high- to low-resistivity state upon the application of a critical field strength,[2] and similar "resistance-switching" transformations occur in a variety of metal oxides.[3] Samples for dielectric breakdown

studies were prepared by interrupting dissolution during the high-potential phase. Potential steps of 1 to 20 volts were applied to the dried, film-covered electrodes by means of point contacts of copper or graphite. The resistance between the point contact and the anode metal substrate was found to drop from 10^8 ohms to a few ohms after a potential-dependent time lag characteristic of resistance-switching transitions.[3]

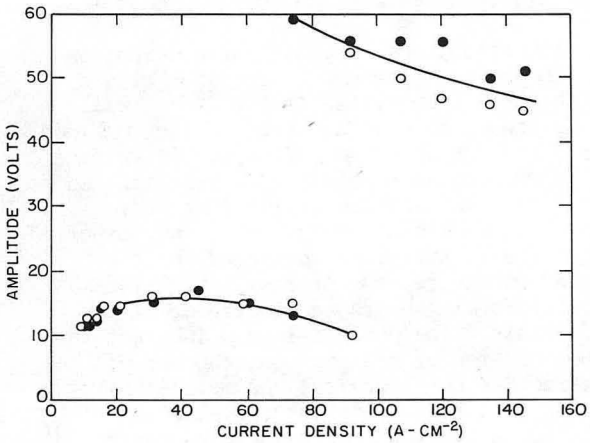

Fig. 1. Variation of oscillation amplitude with current density. Galvanostatic dissolution of 0.16-cm-diameter copper electrodes in 2 M $NaClO_3$ under conditions of stagnation point flow. Solution flow rate: (o) 93 cm/sec; (x) 193 cm/sec.
(XBL 741-5469)

1. J. Cooper, R. H. Muller, and C. W. Tobias, "Periodic Phenomena in Copper Dissolution at Constant Current," presented at 138th National Meeting of the Electrochemical Society, Atlantic City, Oct. 4-9, 1970.
2. E. L. Cook, J. Appl. Phys. 41, 551 (1970).
3. N. Klein, Adv. Elect. and Electron Phys. 26, 309 (1969).

c. Current Distribution in Electrochemical Machining

James B. Riggs, Walter T. Giba, Rolf H. Muller and Charles W. Tobias

The most serious limitation in a broader utility of electrochemical machining lies in the empirical development of tool (cathode) shape to produce the desired metal removal in the workpiece (anode). Our understanding of rate-limiting factors in high-current electrolysis that we have gained in the recent past is now being employed in developing a mathematical model to predict tool and workpiece geometries in electrochemical machining. This model is based upon a numerical solution of the Laplace equation with realistic boundary conditions to represent polarization at anode and cathode surfaces. Also, variations in the conductivity of the electrolyte due to changes in temperature and composition (including gas content) is being included in the model.

The validity of the theoretical analysis will be tested experimentally with a small technical ECM machine, obtained from surplus,[1] that has been refurnished and instrumented. Suitable test shapes will be developed for this purpose. A preliminary tool design for the experimental determination of spacial frequency transfer functions is illustrated in Fig. 1 together with the workpiece.

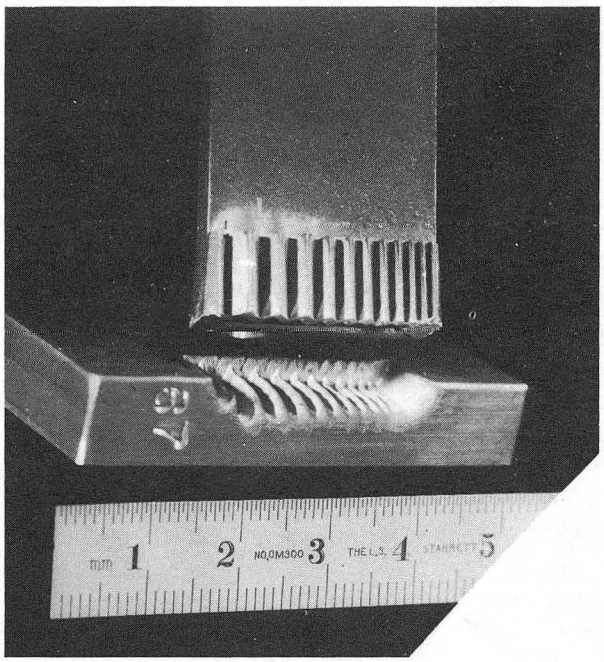

Fig. 1. Shape reproduction in electrochemical machining. Experimental tool and workpiece to quantitatively determine the reproduction of shape details.
(XBB 742-650)

1. LBL, Livermore.

3. ELECTROCHEMISTRY IN NONAQUEOUS SOLVENTS

a. Studies on the Practical Feasibility of the Electroreduction of Potassium

Oscar Chacon and Charles W. Tobias

The feasibility of depositing the alkali metals from solutions of their salts in propylene carbonate (PC) has been demonstrated in this laboratory.[1,2] This provides an attractive alternative for the primary recovery or refining of potassium metal.

Two obstacles have to be eliminated before the quantitative criteria for the practical electroreduction of potassium can be further characterized. First, potassium is not stable in vacuum-distilled PC. Experiments have shown that this instability may be explained by the reaction of potassium with propylene glycols (PG) which cannot be adequately removed from the crude solvent by distillation. A gas chromatographic method was developed to evaluate the concentration of PG in PC and a method of purification was perfected involving treatment by molecular sieve and absorption on alumina which reduces the concentration of PG below 5 ppm (limit of detection). To combat the high reactivity of potassium with moisture and oxygen, our 17 year old vacuum-dry required substantial reconditioning. A helium purifier is under construction.

---

1. Jacob Jorne and Charles W. Tobias, IMRD Annual Report for 1972, LBL-1400, April 1973.
2. Jacob Jorne (Ph.D. dissertation), Electrochemical Behavior of Alkali Metals in Propylene Carbonate, LBL-1111, Sept. 1972.

4. RESEARCH PLANS FOR CALENDAR YEAR 1974

Charles W. Tobias

a. Fundamental Studies of Ionic Mass Transport

This program is aimed at the development of quantitative methods for the prediction of mass transport rates to and from electrolyte electrode interfaces, and at the exploration of novel ways in which such transport rates may be enhanced to improve the economy of electrolysis and galvanic cell processes. Experimental techniques involve measurement of distribution of limiting currents on surfaces, direct optical observation of boundary layers by Mach Zehnder interferometry (see section under R. H. Muller), and analysis of surface topology of metal deposits using optical and scanning electron microscopy and surf-analysis (for "roughness" of extended surfaces). Primary emphasis is placed on extended planar electrodes in channel flow up to Re = 120,000. A study will be initiated of the initiation and propagation of surface imperfections in quasi-steady-state metal deposition and the nucleation and growth mechanics of bubbles in electrolytic gas evolution. These phenomena are common features of essentially all electrolytic synthesis and energy conversion processes.

b. Electrolysis at High Current Densities

Investigations aimed at the elucidation of the role of transport processes at very high current densities (> 100 A/cm^2) will be extended to consideration of the combined effects of hydrodynamic-flow, anodic surface films and cathode geometry on resulting anode geometry, and surface finish in electrochemical machining processes. A new experimental effort will be initiated for the study of the reverse process: high-rate electroforming by rapid electrodeposition of metals. The potential gain inherent in the omission of a significant number of extractive metallurgical and metal-forming steps justifies a serious reevaluation of this relatively old process technology.

c. Electrochemistry in Nonaqueous Solvents

The successful use of lithium as a reversible galvanic electrode in propylene carbonate has long been established; the solvent and some of its analogues are among the more promising organic solvent media for use in high-energy-density battery applications. Earlier work in this laboratory on the thermodynamics and kinetics of the reduction and oxidation of alkali metals in propylene carbonate provides good promise for the development of economically attractive processes for their primary recovery and refining. Investigations will be continued on solvent purification and stability with respect to the alkali metals. Emphasis will be placed on the practical recovery of potassium metal using $KAlCl_4$ solute, but the use of other anions, such as SbF_6^-, will also be explored.

5. 1973 PUBLICATIONS AND REPORTS

Charles W. Tobias and Associates

Journals

1. C. W. Tobias, New Directions in Electrochemical Engineering, J. Electrochem. Soc. 120, 65C (1973).

2. K. Kojima and C. W. Tobias, Solution-Side Transport Processes in the Electropolishing of Copper in Phosphoric Acid, J. Electrochem. Soc. 120, 1026 (1973) (LBL-1106).

3. K. Kojima and C. W. Tobias, Interpretation of Impedance Properties of the Anode Surface Film in the Electropolishing of Copper in Phosphoric Acid, J. Electrochem. Soc. 120, 1202 (1973)(LBL-1129).

Reports

1. C. W. Tobias, E. Cairns, H. J. Korp, D. G. Wilson, C. Zener, and K. H. Weil, An Evaluation of Alternative Power Sources for Low Emission Automobiles, National Academy of Sciences, April 1973.

2. F. Silvester and C. W. Tobias, Electrochemistry in Nonaqueous Solvents: Electroreduction of Calcium, LBL-2580, Dec. 1973.

Papers presented and invited lectures*

1. Charles W. Tobias, Mass Transport Processes in Electrochemical Machining, keynote address, First International Conference on Electromachining, Leicester University, Great Britain, March 26 and 27, 1973. (Extended Abstracts published by Society for Electrochemistry - E.C.M. coordinating Committee, March 1973.)

2. J. Jorne and C. W. Tobias, Electrode Kinetics of the Alkali Metals and Their Amalgams in $AlCl_3$-Propylene Carbonate Solutions (Extended Abstract No. 277), 143rd meeting, The Electrochemical Society, Chicago, Illinois, May 13-18, 1973.

3. J. Jorne and C. W. Tobias, Thermodynamic Properties of the Alkali Metals in $AlCl_3$-Propylene Carbonate Solutions (Extended Abstract No. 288), 143rd meeting of The Electrochemical Society, Chicago, Illinois, May 13-18, 1973.

4. J. Jorne and C. W. Tobias, Electroreduction of the Alkali Metals at Ambient Temperature, (Extended Abstract No. 295) 144th meeting of The Electrochemical Society, Boston, Mass., Oct. 7-11, 1973.

5. J. Jorne and C. W. Tobias, Electrochemical Behavior of the Alkali Metals in Propylene Carbonate, AICHE - C.S.Ch.E. joint meeting, Vancouver, B.C., Sept. 9-12, 1973.

6. C. W. Tobias, Electrolysis at High Current Densities-Electromachining, invited lectures given at: University of Southampton, Great Britain (March 30); Fritz Haber Institute, Berlin (April 6); University of Belgrad, Yugoslavia (April 9); Yugoslav Academy of Sciences, Zagreb (April 11); Federal Institute of Technology, Lausanne, Switzerland (April 16); Federal Institute of Technology, Zurich (April 17); Tel Aviv University, Israel (April 25); Negev Institute of Arid Zone Research (April 29); National Metallurgical Laboratory, Jamshedpur, India (Aug. 31); National Aeronautical Laboratory, Bangalore, India (Sept. 5).

7. C. W. Tobias, Research in Electrochemical Engineering at Berkeley, invited lectures given at: Croatian Chemical Society, Split, Yugoslavia, (April 14); Technion, Israel (May 2); Arya Mehr University, Iran (May 17); Indian Institute of Technology, New Delhi, (Aug. 29); Indian Institute of Science, Bangalore (Sept. 7); Indian Institute of Technology, Madras (Sept. 4); Indian Institute of Technology, Bombay (Sept. 18).

8. C. W. Tobias, Electrochemical Behavior of Alkali Metals in Propylene Carbonate, invited lectures given at: University of Berlin (April 6); Federal Institute of Technology, Zurich (April 18); National Aeronautical Laboratory, Bangalore, India (Sept. 7).

9. C. W. Tobias, Prospects for Electrochemical Energy Conversion and Storage, invited lectures given at: Institute of Petroleum Engineers, Abadan, Iran (May 16); Central Electrochemical Research Institute, Karaikudi, India (Sept. 15).

10. C. W. Tobias, Fundamentals of Electrochemical Engineering, invited lectures (five each) given at: Abadan Institute of Technology, Abadan, Iran (May 7-18); Central Electrochemical Research Institute, Karaikudi, India (Sept. 10-15).

---

*In the period Jan. 1-June 30, 1973, C. W. Tobias was on sabbatical leave. Visits to universities and governmental research laboratories were sponsored in Israel (April 19-May 4) by the Negev Institute for Arid Zone Research and in Iran (May 4-18) by the Abadan Institute of Technology. From Aug. 28-Sept. 19 C. W. Tobias served as an Exchange Scientist, sponsored jointly by the National Science Foundation and the Council for Scientific and Industrial Research of India.

Rolf H. Muller, Principal Investigator

1. OPTICAL STUDIES OF INTERFACIAL PHENOMENA

a. Interferometry of Mass Transfer Boundary Layers

Frank R. McLarnon, Rolf H. Muller, and Charles W. Tobias

Light-deflection has been shown previously to lead to serious errors in the derivation of concentration profiles from interferograms of boundary layers, unless appropriate corrections are made.[1] In order to check the computed effect of these errors experimentally, we have investigated the convectionless galvanostatic electrodeposition of Cu from a stagnant layer of 0.1 M $CuSO_4$ at 5 and 10 mA/cm^2. The theoretically expected concentration profiles under these conditions are well known.[2]

During these tests it was found that even after considering light-deflection effects, the observed interference fringes still appeared displaced normal to the electrode surface. Reflection by the slightly rounded edge of the electrode surface (unavoidable effect of polishing technique) has now been found to be the source of this displacement. The reflection also gives rise to spurious fringe shifts near the electrode/electrolyte interface that are not due to a refractive-index gradient. Figure 1 shows interferograms of the electrode/electrolyte interface with different choices of the plane of focus in the absence of refractive-index gradients. It can be seen that the position of the interface is best reproduced by the focusing as in Fig. 1D, while the focusing best suited to account for light deflection (Fig. 1B) results in significant errors. (x is the distance from the plane where light enters the cell and is measured in the direction of light propagation.) By considering light reflection from the electrode edge, we are now able to quantitatively account for both the apparent displacement of the interface and the spurious shift of

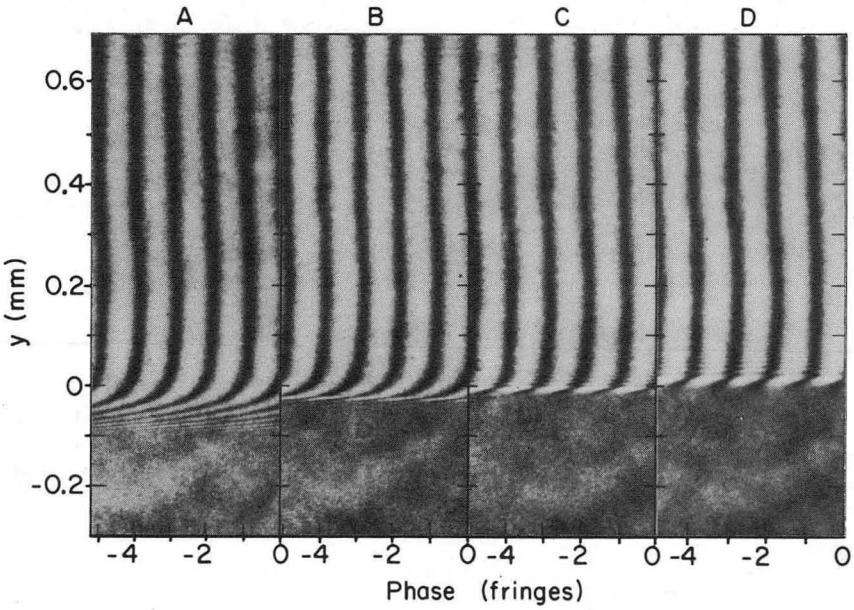

Fig. 1. Effect of light reflection on interferograms of a Cu/0.1 M $CuSO_4$ interface without a boundary layer present. Abscissa: interferogram phase, ordinate: vertical distance from true interfacial location. A: plane of focus at x = -0.5 mm, B: plane of focus at x = 0 (plane of light entrance into cell, employed in boundary layer observations), C: plane of focus at x = 0.5 mm, D: plane of focus at x = 1.0 mm. (XBB 7311-7012)

the interference fringes in the absence of concentration gradients.

If a determination of the true location of the interface by the above considerations is incorporated in the light-deflection analysis of interferograms, excellent agreement between observed and predicted interference fringes (in the absence of convection) is obtained (Fig. 2).

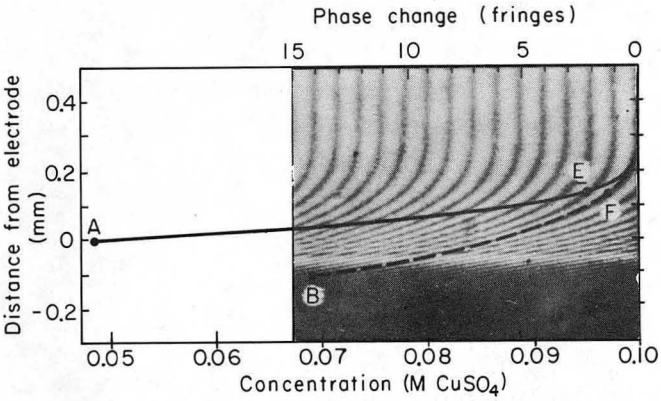

Fig. 2. Comparison of experimentally observed interferogram with interference fringe BF computed from theoretically expected[2] concentration profile AE under consideration of light deflection in the boundary layer and reflection from the electrode edge. (XBB 7311-6546)

An iterative technique, based on an analytic solution of the equation[1] describing light deflection in a refractive-index field, has been developed to calculate the concentration profile from an experimental interferogram. Compared to the previously used trial and error technique,[3] a simpler mathematical function (three instead of four free parameters) is used for the concentration profile. Thus, a better fit of experimental data and use of an automatic (rather than manual) iteration process have been made possible. The example shown in Fig. 3A demonstrates that good agreement between concentration profiles derived from interferograms with profiles expected on the basis of the Sand equation[2] is obtained for convectionless boundary layers. The similarity between convectionless and convection boundary layers, shown in Fig. 3B, suggests that the technique is also suitable for the analysis of convective transport.

The above advancements allow the application of interferometry to the study of boundary layers in large-scale electrode systems.

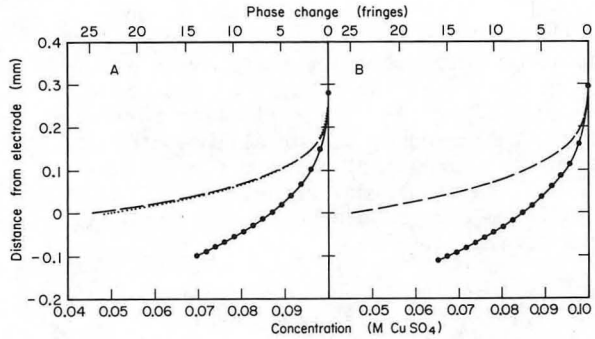

Fig. 3. Interferograms and concentration profiles in the presence and absence of convection.

I = 10 mA/cm^2, 10 sec after current switch-on.

••••Experimental interferograms

--- Concentration profiles derived from the interferograms

—— Interference fringe computed from the derived concentration profile

··· Theoretical[2] concentration profile corresponding to experimental conditions

A = Convectionless boundary layer

B = Forced convection Re=1000, 2.0 cm (1.4 hydraulic diameters) downstream from electrode leading edge.

(XBL 739-4133)

---

1. K. W. Beach, R. H. Muller, and C. W. Tobias, J. Opt. Soc. Am. 63, 559 (1973).
2. H. J. S. Sand, Phil. Mag. (6) 1, 45 (1901).
3. K. W. Beach, Ph.D. thesis, UCRL-20324, June 1971.

b. Automatic Ellipsometer

H. Jörg Mathieu* and Rolf H. Muller

Our newly built self-compensating ellipsometer that employs Faraday-cell rotators has been demonstrated to provide a combination of speed of response and resolution superior to that of any similar instrument now in use. These performance characteristics have been achieved through the use of novel Faraday solenoids, modulation with high frequency and large amplitude, and refinements in circuitry.[1] We have shown why a previously built instrument has not been able to provide the desired capabilities.[2]

Methods to quantitatively determine the dynamic response of automatic ellipsometers of different designs to variations in the optical properties of a specimen surface

have been developed and applied to our new ellipsometer. The use of rotating mirrors has been introduced for these tests in order to generate well-defined, fast optical changes in the properties of a reflecting surface. Thus, the response of our ellipsometer to step-wise changes of different magnitude, as well as sinusoidal changes of different amplitude and frequency (Fig. 1) has been characterized.[3]

Solid anodic layers formed during the dissolution of copper at moderately high current densities have been observed with the automatic ellipsometer in newly built cells for use of stagnant or flowing electrolyte. The results show that the onset of film formation occurs only after an induction period during which saturated solutions of reaction products accumulate at the interface.

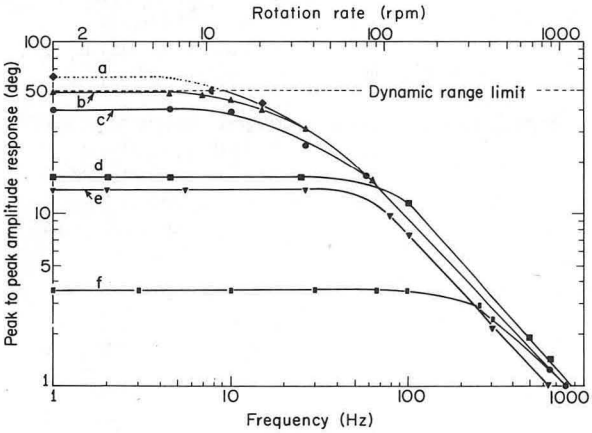

Fig. 1. Response of ellipsometer polarizer and analyzer azimuth rotation to sinusiodal signals of different amplitude and frequency due to variations in the properties of a specimen. (XBL 737-3436)

After an initial formation of a compact Cu_2O layer, 200-800 Å thick, the films become increasingly porous, particularly at higher current densities and flow velocities (Fig. 2). These observations are in agreement with independent results on the mechanism of anodic metal dissolution (See Cooper, Tobias, and Muller, p. 38).

Two additional computer programs for the interpretation of ellipsometer measurements have been prepared. One considers the effect of two layers of different optical constants and thickness, the other considers an inhomogeneous film with continuously varying optical constants, modelled by multiple films of equal thickness and monotonically changing optical properties.[4]

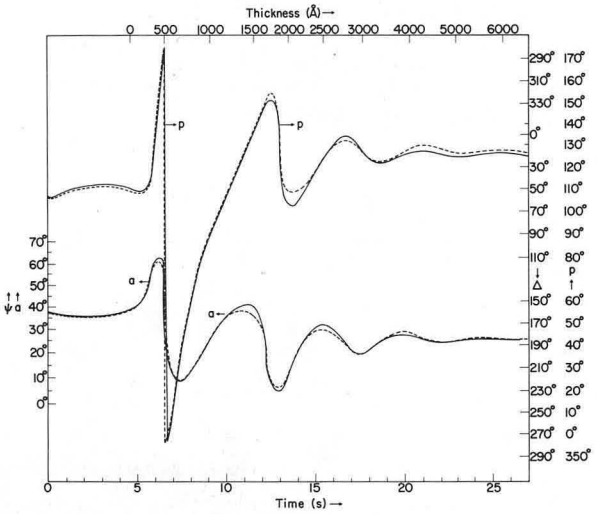

Fig. 2. Ellipsometry of surface layer in the anodic dissolution of Cu in stagnant 2 M $NaClO_3$ at 112 mA/cm^2,
—— measured analyzer and polarizer azimuths a and p.
----computation under consideration of presence of mass transport layer (150μ) and variable porosity
0-2500 Å, 0%
2500-6000 Å, 25%. (XBL 7311-4511)

---

*Supported by Deutsche Forschungsgemeinschaft.

1. Abstract of LBL-1478.
2. Abstract of LBL-1836.
3. Abstract of LBL-1857
4. Abstract of LBL-2517

c. Optical Interference in Thin Films

Charles R. Brown, Michael L. Sand, and Rolf H. Muller

The observation of interference colors is an often used tool for the study of transparent thin liquid films on metal surfaces. However, the derivation of film thickness from such observations is complicated by the phase change in reflection from the substrate surface. We have previously computed generalized series of interference colors for the precise derivation of film thicknesses and have now tested them experimentally for the widest experimentally accessible range of phase changes. Thickness profiles for tapered solid films of ZnS and cryolite on Al, Cr, and Si substrates have been derived

by two different step-height measurements, ellipsometry and interference spectroscopy. Comparison with film profiles derived from visually observed interference colors has in general shown satisfactory agreement (Fig. 1). It has also been found that colors of lower saturation than previously assumed can still be observed in practice but the distinction of different hues is not as sharp as expected.

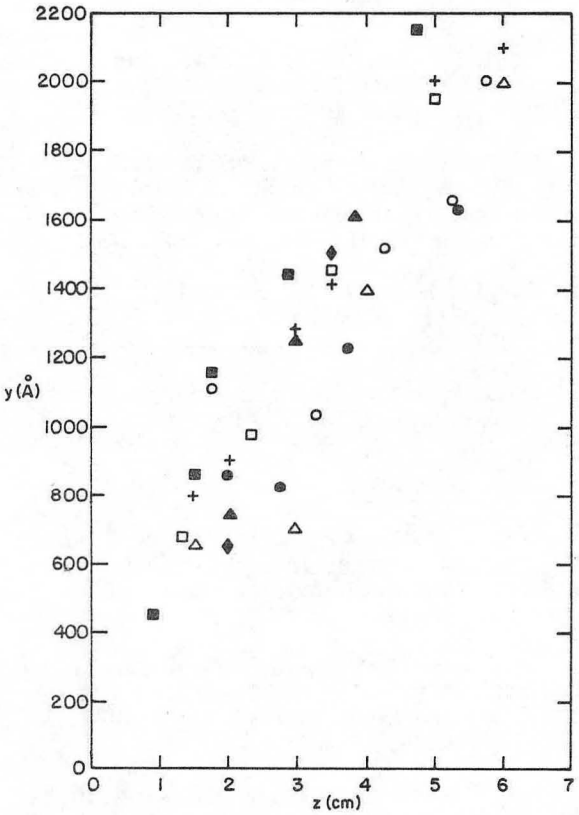

Fig. 1. Profile of ZnS film on aluminum substrate, determined by different techniques:

- ○ Interference microscope step-height
- ● Profilometer step-height
- △ Spectrophotometer, λ-scan, s-polarization
- ▲ Spectrophotometer, z-scan, s-polarization
- ◆ Spectrophotometer, z-scan, p-polarization
- + Ellipsometer
- □ Interference colors, s-polarization
- ■ Interference colors, p-polarization.

(XBL 7310-5433)

d. Laser Velocimetry

Calvin T. Chew and Rolf H. Muller

Combined forced and natural convection offers effective means to speed up mass transport at electrodes and thus significantly increase the output of electrochemical reactors, but little information is available on the flow fields existing under these conditions. Laser velocimetry is being developed to provide direct evidence of three-dimensional flow patterns existing in such boundary layers.

2. HYDROGEN ECONOMY*

Rolf H. Muller

A recent review of the prospects for a hydrogen economy has confirmed that water electrolysis is at present still the only feasible route to make hydrogen without the use of carbonaceous materials and discharge of CO_2 to the atmosphere. Undesirable features of electrolytic hydrogen production are low energy efficiency and high capital cost. New technical developments require an improved understanding of the detailed mechanism of electrolytic gas evolution.

*Abstract of LBL-2232.

3. RESEARCH PLANS FOR CALENDAR YEAR 1974

Rolf H. Muller

Convective transport in electrolysis will be systematically analyzed by interferometry. Of particular interest are the combined effect of forced and natural convection and the deliberate disturbing of boundary layers. Both of these phenomena offer promising mechanisms for substantially increasing the output of electrolytic reactors.

The dynamics of the formation of reacted surface layers (oxides and halides) on electrodes commonly encountered in primary and secondary (storage) batteries will be investigated by automatic ellipsometry. The details of these processes determine the efficiency with which battery materials are used. Electrochemically generated thin films are also critical elements in many corrosion processes.

Factors responsible for the stability of

thin liquid electrolyte films on metal surfaces will be investigated. The existance of such films is essential for the functioning of fuel-cell electrodes and appears to play an important part in many corrosion processes.

Laser velocimetry will be developed for determining the velocity distribution in mass transfer boundary layers under forced and natural convection, in order to characterize flow conditions for effective transport.

A mathematical model to predict tool and workpiece geometries in electrochemical machining will be developed. This model is to incorporate all of the understanding of high rate anodic metal dissolution that we have gained in the recent past and thus contribute to alleviating the single most serious limitation of the present practice of electrochemical machining. (See Part 2c of C. W. Tobias' section.)

An analysis of the periodic removal of solid surface layers in the high rate anodic metal dissolution will be concluded (see Part 2b of C. W. Tobias' section).

4. 1973 PUBLICATIONS AND REPORTS

Rolf H. Muller and Associates

Journals and books

1. Rolf H. Muller, editor, Optical Techniques in Electrochemistry, Vol. 9 of Advances in Electrochemistry and Electrochemical Engineering, edited by P. Delahay and C. W. Tobias (Wiley-Interscience, New York, 1973).

2. Rolf H. Muller, Principles of Ellipsometry, in above, pp. 167-226.

3. Rolf H. Muller, Double-Beam Interferometry for Electrochemical Studies, in above, pp. 281-368.

4. K. W. Beach, R. H. Muller and C. W. Tobias, Light-Deflection Effects in the Interferometry of One-dimensional Refractive-index Fields, J. Opt. Soc. Am. 63, 559-66 (1973)

LBL reports

1. H. Jorg Mathieu, Computer Programs for Ellipsometry, LBL-1470, May 1973.

2. H. J. Mathieu, D. E. McClure and R. H. Muller, Self-Compensating Ellipsometer Manual, LBL-1478, July 1973.

3. H. J. Mathieu and R. H. Muller, Faraday Solenoids for Automatic Ellipsometers, LBL-1836, Aug. 1973.

4. Rolf H. Muller, Electrochemical Aspects of the Hydrogen Economy, Symposium Summary, LBL-2232, Nov. 1973.

5. R. H. Muller and H. J. Mathieu, Performance Tests for Automatic Ellipsometers, LBL-1857, Sept 1973.

6. H. J. Mathieu, D. E. McClure, and R. H. Muller, Fast Compensating Ellipsometer, LBL-2256, December 1973.

7. F. R. McLarnon, R. H. Muller, and C. W. Tobias, Light-Deflection Errors in the Interferometry of Electrochemical Mass Transfer Boundary Layers, LBL-2240, Dec. 1973.

8. Charles R. Brown (M. S. thesis), Interferometry of Solid Thin Films, LBL-2264, Dec. 1973.

9. H. J. Mathieu, Computer Programs for Ellipsometry II, LBL-2517, Dec. 1973.

Papers presented

1. Rolf H. Muller, Periodic Phenomena During ECM, invited lecture, International Conference on Electrochemical Machining, Univ. of Leicester, England, March 26-27, 1973.

2. Rolf H. Muller, Periodic Phenomena in the Anodic Dissolution of Metals at High Rates, Bell Telephone Laboratories, Murray Hill, N. J., March 23, 1973.

3. Rolf H. Muller, Optical Studies of High-Rate Anodic Metal Dissolution, Swiss Federal Institute of Technology, Zurich, Switzerland, April 6, 1973.

4. Rolf H. Muller, Optical Techniques in Electrochemical Research, Swiss Aluminum Ltd., Research Laboratories, Neuhausen, Switzerland, April 11, 1973.

5. Rolf H. Muller, Symposium Summary on Electrochemistry, International Symposium and Workshop on the Hydrogen Economy, Cornell University, August 20-23, 1973.

6. H. J. Mathieu, Automatic Ellipsometers, IBM Research Laboratories, San Jose, Calif., March 13, 1973.

7. H. J. Mathieu, K. K. Reinhartz, and H. Rickert, The Mechanism of the Electrochemical Degradation of CdS-Cu_2S Solar Cells, 10th IEEE Photovoltaic Specialists Conference, Palo Alto, Calif., Nov. 13-15, 1973.

John Newman, Principal Investigator

1. CURRENT DISTRIBUTION ON A ROTATING SPHERE BELOW THE LIMITING CURRENT

Kemal Nişancioğlu and John Newman

The current distribution on a rotating spherical electrode is calculated at appreciable fractions of the limiting current.[1] Numerical results are given for Tafel kinetics (Fig. 1) and for high rotation speeds (Fig. 2). The current distribution depends only on the specified current level and becomes uniform when this level is set below 68% of the limiting current at high rotation speeds even if concentration polarization is present. Furthermore, since the primary distribution is uniform for the sphere, the potential distribution in the solution near the electrode surface is also expected to be uniform whenever the current distribution is uniform. These conclusions suggest the rotating sphere as a viable tool in high-rate metal deposition and dissolution studies and in potentiostatic applications.[2] In general, the results disclose a number of complementary aspects of the spherical electrode when compared with the disk electrode in electroanalytical applications.[1,2]

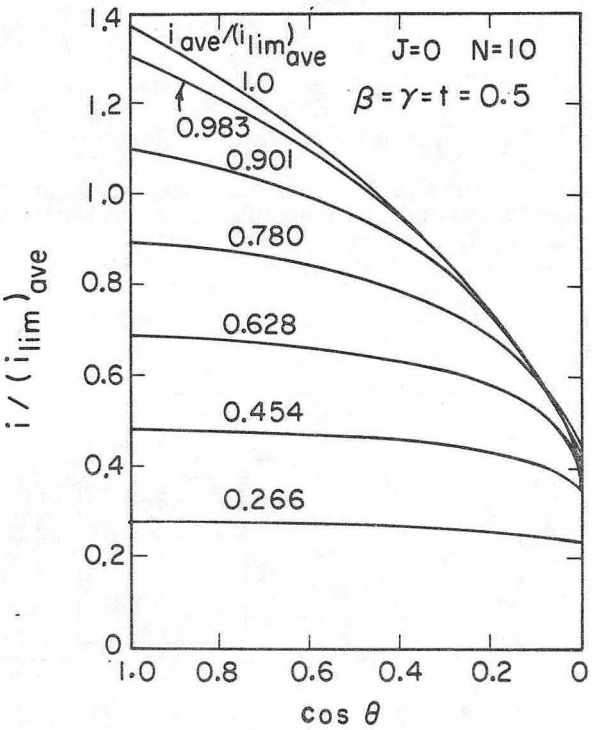

Fig. 1. Current distribution for Tafel kinetics. (XBL 735-3016)

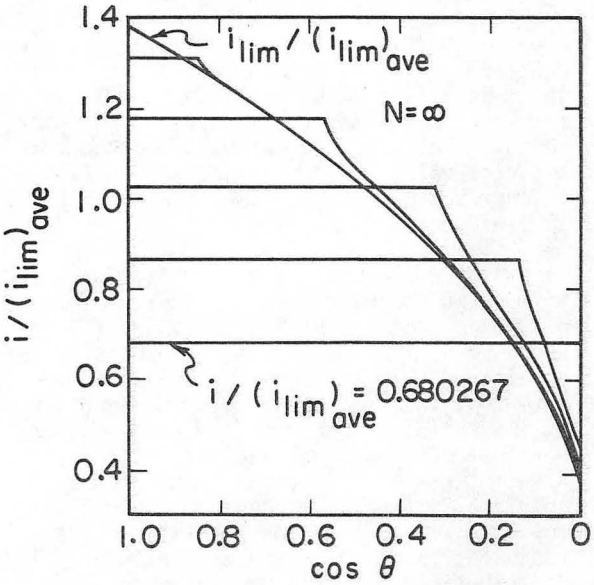

Fig. 2. Current distribution at high rotation speeds. (XBL 735-3019)

1. Kemal Nişancioğlu and John Newman, Current Distribution on a Rotating Sphere below the Limiting Current, LBL-1837; Journal of the Electrochemical Society, to be published.
2. Kemal Mustafa Nişancioğlu, Current Distribution and Mass Transfer in Rotating Electrode Systems, (Ph.D. thesis), LBL-1880, Sept. 1973.

2. THE SHORT-TIME RESPONSE OF A DISK ELECTRODE

Kemal Nişancioğlu and John Newman

A theoretical study of the transient behavior of a disk-electrode in the presence of faradaic and capacitive effects has recently been reported.[1,2] Those results are readily applicable to describe the long-time response of the disk and determine the relaxation time of the overpotential after a step change in the current or potential. However, a large number of terms need to be included in the series to express the short-time behavior adequately. Hence, an asymptotic solution valid at short times has been sought for the problem.[3]

Shortly after the cell current is switched on, the current distribution on the surface is given by the primary distribution[4,5] everywhere except at a small region near the edge of the disk. Since the primary current density is infinite at the edge, the double-layer capacity is charged more rapidly in this region than at other parts of the disk, so that the current density is reduced to a finite value. A similar situation is encountered for large values of the exchange current density.[6]

A singular-perturbation problem is formulated to treat the edge region of a disk electrode at short times and for large exchange-current densities.[3] Results are obtained for short times by expressing the potential in terms of an integral equation at the surface.[7] Results for large exchange-current densities are calculated in a more straightforward fashion by a numerical solution of Laplace's equation for the edge region. Previous series solutions for the transient response[1,2] and the secondary distribution[6] approach present results asymptotically.

---

1. K. Nişancioğlu and J. Newman, The Transient Response of a Disk Electrode, J. Electrochem. Soc. 120, 1339-1346 (1973).
2. K. Nişancioğlu and J. Newman, The Transient Response of a Disk Electrode with Controlled Potential, ibid., 120, 1356-1358 (1973).
3. K. Nişancioğlu and J. Newman, The Short-Time Response of a Disk Electrode LBL-1896, Sept. 1973.
4. J. Newman, Resistance for Flow of Current to a Disk, J. Electrochem. Soc. 113, 501-502 (1966).
5. J. Newman, Ohmic Potential Measured by Interrupter Techniques, ibid., 117, 507-508 (1970).
6. J. Newman, Current Distribution on a Rotating Disk below the Limiting Current, ibid., 113, 1235-1241 (1966).
7. Kemal Mustafa Nişancioğlu, Current Distribution and Mass Transfer in Rotating Electrode Systems (Ph.D. thesis), LBL-1880, Sept. 1973.

3. MEASUREMENT OF THE TRANSIENT RESPONSE OF A DISK ELECTRODE

Kemal Nişancioğlu and John Newman

Previous theoretical results[1,2] for the transient response of a disk electrode suggest that if the current is interrupted, the electrode potential and the potential in the solution decay, respectively, according to the time constants

$$\tau_e = \frac{r_o C}{\kappa J} \qquad (1)$$

and

$$\tau_s = \frac{1}{4.12+J} \frac{r_o C}{\kappa} , \qquad (2)$$

where r_o is the radius of the disk, C the double-layer capacity, κ conductivity of the solution, and

$$J = i_o r_o (\alpha_a + \alpha_c) F/RT\kappa$$

the dimensionless exchange-current density for linear kinetics.[2] The difference in magnitudes of these time constants may be significant if J is small and should therefore be detected with ease. The time constants can be measured separately by a double-probe reference electrode system placed in the solution near the disk electrode and connected appropriately to a dual-beam oscilloscope (see Fig. 1). The double-layer capacity can then be calculated by writing

$$\frac{1}{\tau_s} - \frac{1}{\tau_e} = \frac{4.12\kappa}{r_o C} , \qquad (3)$$

which is independent of J.

A preliminary experiment has been conducted to measure the double-layer capacity on stationary copper and mercury disk electrodes.[3] The design of the latter is

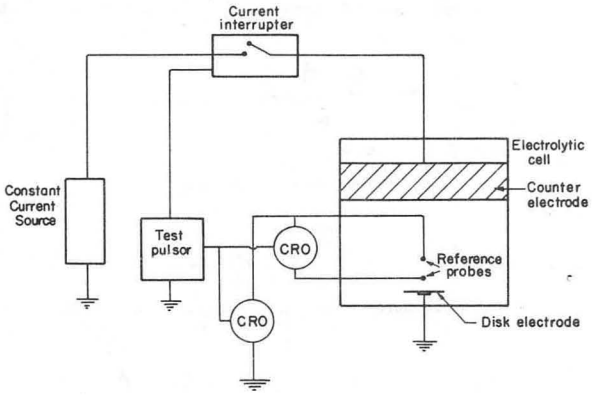

Fig. 1. Electronic circuit. (XBL 739-1885)

shown in Fig. 2. The solution used was 0.01 N KCl. Reference electrodes were calomel electrodes. The measured time constants were generally much smaller than those calculated from Eqs. 1 and 2 assuming small J values. Furthermore, the time constant from the single-probe measurement was very close to the double-probe result, indicating that impurities in the solution could not be removed adequately, and hence the value of J was probably large. Calculated capacities thus were not reproducible, but nonetheless fluctuated within the correct order of magnitude as compared to published results for mercury and copper surfaces. Possible ways of improving the method have been suggested.[3]

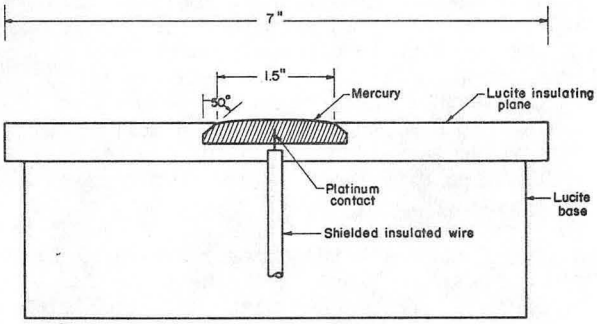

Fig. 2. Mercury-disk electrode (approximate dimensions). (XBL 739-1887)

1. J. Newman, Ohmic Potential Measured by Interrupter Techniques, J. Electrochem. Soc. 117, 507-508 (1970).
2. K. Nişancioğlu and J. Newman, The Transient Response of a Disk Electrode, ibid., 120, 1339-1346 (1973).
3. Kemal Mustafa Nişancioğlu, Current Distribution and Mass Transfer in Rotating Electrode Systems (Ph.D. thesis), LBL-1880, Sept. 1973.

4. TRANSIENT CONVECTIVE DIFFUSION TO A DISK ELECTRODE

Kemal Nişancioğlu and John Newman

Analytic solutions are obtained at large times for the transient convective diffusion equation for the disk in the absence of radial concentration gradients considering a step change in the concentration and a step change in the flux at the surface.[1] These solutions are shown to match available results for short times,[2,3] with the suggestion that the series for short times and long times can be employed interchangeably for nonsteady-state calculations.

The results are extended to investigate the effect of double-layer charging on transient mass transfer in the presence of a highly reversible electrode reaction.[4] The effect is shown to be small under the present assumptions, which state in addition to those mentioned above that the supporting electrolyte only contributes to the double-layer charge on the solution side, and possible variations in its concentration due to migration are ignored.

A method is proposed to calculate the transient behavior of a disk in the presence of radial convection as well as faradaic and non-faradaic effects at the electrode surface.[4] The formulation can be extended, if needed, to apply at moderate times by adding more terms to the regular perturbation expansions. The numerical method, even though straightforward, seems to require lengthy computations.

1. K. Nişancioğlu and J. Newman, Transient Convective Diffusion to a Disk Electrode, LBL-1881, July 1973.
2. Jan Robert Selman, Measurement and Interpretation of Limiting Currents (Ph.D. thesis) UCRL-20557, June 1971.
3. V. S. Krylov and V. N. Babak, Nonsteady-State Diffusion to the Surface of a Rotating Disc, Soviet Electrochem. 7, 626-632 (1971) [Élektrokhimiya 7, 649-654 (1971)].
4. Kemal Mustafa Nişancioğlu, Current Distribution and Mass Transfer in Rotating Electrode Systems, (Ph.D. thesis), LBL-1880, Sept. 1973.

5. ROTATING RING-DISK ELECTRODES

Pete Pierini and John Newman

Rotating ring-disk electrodes are now being used more frequently in research applications. Data have been taken for a ferro-ferri cyanide redox reaction.[1] The limiting current was computed and measured with excellent agreement. However, data were present for operating conditions below the limiting current, but no computations were attempted. We are presently making these computations utilizing methods

presented in Newman[2] for potential distribution and mass transfer which have not yet had such a test of validity. The redox kinetic expression[3] is being used and we will obtain parameters for the ferro-ferri cyanide reaction which are not presently available. Finally an explanation of anomalous limiting currents measured on the ring with the disk operating at a net zero current will be made.

---

1. W. H. Smyrl and N. Newman, Ring-Disk and Sectioned Disk Electrodes, J. Electrochem. Soc. 119, 212-219 (1972).
2. J. Newman, The Fundamental Principles of Current Distribution and Mass Transport in Electrochemical Cells, in Electroanalytical Chemistry, edited by Allen J. Bard (Marcel Dekker, New York, 1973), Vol. 6, pp. 187-352.
3. J. Newman, Electrochemical Systems (Prentice-Hall, Englewood Cliffs, N.J., 1973), 432 pp.

6. MASS TRANSFER TO A PLANE BELOW A ROTATING DISK

Robert V. Homsy and John Newman

The rate of mass transfer to a plane below a rotating disk has been measured experimentally by the electrodeposition of copper from an aqueous solution of copper sulfate and excess sulfuric acid at the limiting current. Early experiments were beset with natural convection effects caused by concentration stratification within the solution. This effect was considerably reduced by operating at lower concentration of copper sulfate (0.01 M) and the addition of glycerol (6 M) to the solution. The local mass transfer rate, which is proportional to the thickness of the copper deposit, agrees well with that predicted theoretically.[1] However, at the center of the electrode, the rate appears to be larger than expected, possibly due to lingering natural convection effects or error in the alignment of the electrode below the rotating disk.

The current distribution on the plane below the rotating disk was calculated theoretically at various fractions of the limiting current.[2] Numerical results show that the current density on the plane becomes more nonuniform as the limiting current is approached.

---

1. R. V. Homsy and J. Newman, Mass Transfer to a Plane below a Rotating Disk at High Schmidt Numbers, AIChE J. 19, 929-933 (1973).
2. R. V. Homsy and J. Newman, Current Distribution on a Plane below a Rotating Disk, LBL-1887, Aug. 1973.

7. MASS TRANSFER TO A ROTATING DISK ELECTRODE IN THE REGION OF TRANSITION TO TURBULENT FLOW

Charles Mohr and John Newman

Visual[1] and electrochemical[2] evidence has been presented suggesting that in the region of transition from laminar to turbulent flow ($1.5\times10^5 < Re < 3.5\times10^5$) on a rotating disk, the flow is characterized by a periodic vortex structure, the exact nature of which is unknown. Since mass transfer to a disk has been well described in the laminar and turbulent[3] regimes, it would seem desirable to obtain a correlation describing mass transfer in this intermediate region. An experiment is now in progress to measure this by depositing copper, at the limiting current, on a large rapidly rotating disk and examining the deposit. Preliminary results show no trace of the wavy surface predicted in Ref. 1 and although insufficient data have been gathered to formulate a correlation, the mass transfer rate in this region seems to increase smoothly to that predicted for the turbulent region at its outer edge.

---

1. N. Gregory et al., Phil. Trans. Roy. Soc. A248, 155 (1955).
2. D. T. Chin and M. Litt, Flow Instability on a Rotating Disk, J. Fluid Mech. 54, 613 (1972).
3. B. Ellison and I. Cornet, J. Elec. Chem. Soc. 118, 68 (1971).

8. MASS TRANSFER IN POROUS ELECTRODES

Peter Appel and John Newman

Experiments were conducted in an electrochemical cell packed with uniform spherical stainless steel pellets to measure mass transfer coefficients at low Reynolds numbers. A redox reaction was employed (ferri-ferro cyanide), and measurements were made at the limiting current. Results show that the low Reynolds number asymptote is that predicted by an analysis[1] employing the Graetz solution for a model picturing the bed as a collection of straight cylindrical pores. At higher Reynolds numbers, the results lie between predictions based on

the correlations of Wilson et al.[2] and Bird et al.[3]

---

1. John Newman, private communication.
2. E. J. Wilson and C. J. Geankoplis, Ind. Eng. Chem. Fundamentals 5, 9 (1966).
3. R. B. Bird, W. E. Stewart, and E. N. Lightfoot, Transport Phenomena (Wiley and Sons, New York, 1960), pp. 411 and 679.

9. STEADY STATE CURRENT DISTRIBUTION ON A ROTATING DISK BELOW THE LIMITING CURRENT FOR A REDOX REACTION

Peter Appel and John Newman

Redox reactions on a rotating disk differ from deposition reactions in that the presence of the product species at the surface enters into the kinetics and tends to drive the reaction in the opposite direction. Numerical calculations[1] made for simplified kinetic expressions show that at current densities below the limiting current, the current distribution is more nonuniform than for the corresponding case with a deposition reaction, as calculated by Newman.[2] This effect is most pronounced at low current densities.

---

1. Peter Appel, Ph.D. thesis, LBL-2280 (in progress).
2. J. Newman, J. Electrochem. Soc. 113, 1235 (1966).

10. THE REMOVAL OF LEAD IONS FROM VERY DILUTE SOLUTIONS USING A POROUS FLOW-THROUGH ELECTRODE

James Trainham and John Newman

It has been shown by Bennion and Newman[1] that a fixed porous flow-through carbon electrode device can be used to remove copper ions from dilute solutions. Also, they[1] have suggested that this method should work well for other metal systems such as: Ag, Au, Cd, Hg, and Pb.

Here a similar study for the removal of lead in excess supporting electrolyte consisting of sulfuric acid and sodium sulfate is considered. The industrial importance of the Pb-$PbSO_4$ system stems not from the economic recovery of lead as a marketable product, but from an industrial waste problem. Lead sulfate is produced as a by-product in the flue gases during roasting of lead sulfide ores, by the aqueous oxidation of galena in zinc electrolytic plant trailings, and in lead acid storage battery production. Though $PbSO_4$ is quite insoluble in most industrial waste streams, it still exists in very dilute concentrations, approximately 5 mg/liter; this concentration is high enough to be toxic to animal and plant life. The environmental Protection Agency (EPA) maximum limit on the discharge of lead into streams is approximately 0.1 mg/liter. To date the methods employed by industry to meet the EPA requirements are inadequate.

Design Problem. The design problem is to reduce a lead ion feed concentration from 1.45 mg/liter to a dilute product concentration of 0.05 mg/liter. The electrochemical reaction is: $Pb^{+2} + 2e^- \rightarrow Pb$.

When designing an electrochemical system, the ohmic potential drop is of primary importance if unwanted side reactions are to be avoided. In this case the evolution of hydrogen, $H^+ + e^- \rightarrow 1/2\ H_2$ is an unwanted side reaction: For a porous electrode with a high matrix conductivity, the potential of the matrix phase Φ_1 can be considered constant across the electrode. The ohmic potential drop in the solution phase sets the size of electrode. The standard electrode potential of lead is $U^\theta = -0.126$ V. The hydrogen electrode at pH = 0 is at a potential of 0 V. Thus, hydrogen will be evolved first before any lead is deposited, unless there is a sufficient hydrogen overpotential on the cathode material. With this restriction the maximum allowable potential drop was taken to be 0.1 V.

The electrode can now be designed using the equations in (1) and the data found in Table I. The results are given in Table II.

Economic Analysis. The cost per pound of lead recovered ($/lb) as well as the cost per thousand gallons (¢/kgal) of lead solution processed for the electrode design above is shown in Table III. The cost of lead[2] is 18¢/lb. Comparison with the results in Table III shows the process will lose 13¢ for every pound of lead recovered. Though the process is not profitable, it is an effective form of pollution abatement. At this time no data are available on other competitive processes.

Experimental. The same porous electrode cell built by Bennion[1] for the copper process was used. The cathodic reaction

was: $Pb^{2+} + 2e^- \rightarrow Pb$ and the counter electrode reaction was: $Cu \rightarrow Cu^{2+} + 2e^-$.

Unlike Bennion,[1] limiting current curves were not obtained, the experiments being plagued by hydrogen evolution. This problem should be alleviated with small modifications in the cell design. Suggestions are: (1) the heads of the cell should be made hemispherical with a gas release valve at the top of the head, and (2) lead spheres should be used in place of carbon for the matrix material.

The experiments were not a total loss, however, and gave some very encouraging results. For a feed concentration of 4.32 mg/liter 15 gallons of solution was processed. Dilute product concentrations were found to be 1.45 and 0.55 mg/liter, yielding a separation factor of 3 and 8 respectively, the separation increasing with decreased flow rate.

Table I. Design parameters.

Feed concentration, mg/liter	1.45
Product concentration, mg/liter	0.05
Allowable potential variation, V	0.1
Solution conductivity, mho/cm	0.8
Specific electrode area, cm^{-1}	25
Molecular weight of lead, g/mol	207.19
Valence of lead ions	2
Diffusion coefficient of lead ions, cm^2/sec	4.0×10^{-6}
Void fraction	0.3
Density of lead, g/cm^3	11.4
Density of solution, g/cm^3	1.28
Particle shape factor	0.86
Kinematic viscosity, cm^2/sec	0.016

Table II. Design results.

Electrode thickness, cm	60
Time to plug electrode, days	377
Superficial velocity, cm/sec	0.64
Reynolds number	1.88
Mass transfer coefficient, cm/sec	1.45×10^{-3}

Table III. Economic evaluation.

	¢/kgal	$/lb
Electrode capital cost	0.2222	0.1836
Operating labor	0.0218	0.0180
Electrical energy	0.0021	0.0018
Pumping energy	0.132	0.109
Total	0.38	0.31

1. D. N. Bennion and J. Newman, Electrochemical Removal of Copper Ions from Very Dilute Solutions, J. Appl. Electrochem. 2, 113-122 (1972).
2. N. A., "Commodity Index," Wall Street Journal, Dec. 1973.

11. ADMITTANCE COUPLING ON A RING-DISK ELECTRODE

Joseph J. Miksis, Jr. and John Newman

A theoretical analysis was made for a ring disk system exhibiting constant disk and ring potential, Φ_d and Φ_r, respectively, to determine that if

$$I_d = Y_d^d \Phi_d + Y_d^r \Phi_r \quad (1)$$

and

$$I_r = Y_r^d \Phi_d + Y_r^r \Phi_r \quad (2)$$

where I_d, I_r are the average currents on the disk and ring, respectively, Y_i^i the admittance on surface i due to potential Φ_i on surface i, Y_i^j the admittance on surface i due to potential Φ_j on surface j, then

$$Y_r^d = Y_d^r \quad (3)$$

Previous experimental results[1] indicated this coupling relationship to exist.

A computer program was made to test the validity of Eq. (3) for systems of various disk and ring radii. The current density as a function of radius was also determined.

Analysis showed that only primary current distributions need be considered for Eq. (3) to be valid.

1. C. Gabrielli et al, Étude de la Répartition du Potentiel a la Surface d'une Électrode a Disque-Anneau, J. de Chimie Physique 69, 739 (1972).

12. RESEARCH PLANS FOR CALENDAR YEAR 1974

John Newman

Mass transfer for turbulent flow between rotating concentric cylinders separated by a very thin gap will be measured using the ferri-ferro cyanide redox reaction in an attempt to improve upon existing correlations for such systems. Measurements of mass transfer rates to a rotating disk in transitional flow will be continued. A study of electro-osmosis and transport in ion-exchange membranes will be begun.

13. 1973 PUBLICATIONS AND REPORTS

John Newman and Associates

Journals and books

1. J. Newman, Electrochemical Systems (Prentice-Hall, Englewood Cliffs, N.J.), 1973.

2. J. Newman, Fundamental Principles of Current Distribution and Mass Transport in Electrochemical Cells, Electroanalytical Chem., edited by Allen J. Bard, 6, 187-352 (1973) (UCRL-20547).

3. W. Tiedemann, D. Bennion, and J. Newman, Error in Measurements of Electrode Kinetics Caused by Nonuniform Ohmic-Potential Drop to a Disk Electrode, J. Electrochem. Soc. 120, 256-268 (1973) (LBL-890).

4. T. Chapman and J. Newman, Restricted Diffusion in Binary Solutions, AIChE J. 19, 343-348 (1973) (LBL-1142).

5. K. Nişancioğlu and J. Newman, Diffusion in Aqueous Nitric Acid Solutions, AIChE J. 19, 797-802 (1973) (LBL-1428).

6. J. Newman, Analysis of Porous Electrodes with Sparingly Soluble Reactants, II. Variable Solution Properties, Convection and Complexing, J. Electrochem. Soc. 120, 906-913 (1973).

7. R. Homsy and J. Newman, Mass Transfer to a Plane below a Rotating Disk at High Schmidt Numbers, AIChE J. 19, 929 (1973) (LBL-1420).

8. C. Mohr and M. Williams, Diffusion of Gas into a Non-Newtonian Falling Film, AIChE J. 19, 1047 (1973).

9. K. Nişancioğlu and J. Newman, Transient Response of a Disk Electrode, J. Electrochem. Soc. 120, 1339-1346 (1973) (LBL-1109).

10. K. Nişancioğlu and J. Newman, Transient Response of a Disk Electrode with Controlled Potential, J. Electrochem. Soc. 120, 1356-1358 (1973) (LBL-1173).

11. J. Newman and J. E. Harrar, Potential Distribution in Axisymmetric Mercury Pool Electrolysis Cells at the Limiting Current, J. Electrochem. Soc. 120, 1041-1044 (1973) (LBL-1155).

12. J. Newman, Separation Processes Based Primarily on Action in a Field, Chemical Engineer's Handbook, 5th Edition, edited by R. H. Perry and C. H. Chilton (McGraw-Hill, New York, 1973), pp. 17-49 to 17-58.

13. C. Mohr and J. Newman, Mass Transfer in Cylindrical Couette Flow, Electrochimica Acta, 18, 761 (1973) (LBL-1141).

14. N. Vahdat and J. Newman, Corrosion of Iron Rotating Disks, J. Electrochem. Soc. 120, 1682 (1973) (LBL-896).

Papers presented

1. J. Newman, Electrochemical Reactors. Annual Review Symposium of the United States Atomic Energy Commission. Inorganic Materials Research Division, Lawrence Berkeley Laboratory, Berkeley, Feb. 1, 1973.

2. J. Newman, Electrochemical Removal of Lead from Process Streams, lecture at Globe-Union, Inc., Milwaukee, Wisconsin, Feb. 9, 1973.

3. J. Newman, Flow-through Porous Electrodes with Applications to Water-pollution Abatement, invited lecture at Texas Tech University, Lubbock, Texas, March 22, 1973.

4. J. Newman, The Transient Response of a Disk Electrode (with Kemal Nişancioğlu, Newman giving address). An invited address at the symposium on Engineering Analysis of Electrochemical Systems at the Chicago meeting of the Electrochemical Society, May 1973.

5. J. Newman, Electrochemical Concentrating and Purifying from Dilute Copper Solutions (with Robert S. Wenger and Douglas N. Bennion, the latter presenting the paper). Symposium on Engineering Analysis of Electrochemical Systems at the Chicago meeting of the Electrochemical Society, May 1973.

6. J. Newman, Mass Transfer of Minor Components in a Propagating Crack (with William H. Smyrl, who presented the paper). Symposium on Engineering Analysis of Electrochemical Systems at the Chicago meeting of the Electrochemical Society, May, 1973.

7. J. Newman, Corrosion of Rotating Iron Disks, lecture at the University of Illinois, Urbana, May 18, 1973.

8. J. Newman, Current Distribution on a Rotating Spherical Electrode Below the Limiting Current, lecture at Argonne National Laboratory, Argonne, Illinois, Oct. 12, 1973.

9. J. Newman, Removal of Metal Ions from Electrolytic Solutions Using Flow-Through Porous Electrodes, invited lecture at the Chicago Section of the Electrochemical Society, Nov. 8, 1973.

10. J. Newman, Removal of Metal Ions from Electrolytic Solutions Using Flow-Through Porous Electrodes, invited lecture before the Chemical Engineering Department, Northwestern University, Evanston, Illinois, Nov. 9, 1973.

LBL reports

1. R. Homsy and J. Newman, Current Distribution on a Plane Below a Rotating Disk, LBL-1887, Aug. 1973.

2. R. Homsy and J. Newman, An Asymptotic Solution for the Warburg Impedance of a Rotating Disk Electrode, LBL-2209, Aug. 1973.

3. K. Nişancioğlu, Current Distribution and Mass Transfer in Rotating Electrode Systems (Ph.D. thesis), LBL-1880, Sept. 1973.

4. K. Nişancioğlu and J. Newman, Current Distribution on a Rotating Sphere Below the Limiting Current, LBL-1837, June 1973.

5. K. Nişancioğlu and J. Newman, Transient Convective Diffusion to a Disk Electrode, LBL-1881, July 1973.

6. K. Nişancioğlu and J. Newman, The Short-Time Response of a Disk Electrode, LBL-1896, Sept. 1973.

Translations

1. C. Gabrielli et al., Study of the Potential Distribution on the Surface of a Ring-Disk Electrode, J. de Chimie Physique 69, 739 (1972), translated by Charles Mohr, UCRL-Trans-1498, May 1973.

D. PHYSICAL CHEMISTRY

Leo Brewer, Principal Investigator

1. THERMODYNAMIC PROPERTIES OF THIRD AND FOURTH GROUP TRANSITION METALS WITH PLATINUM GROUP METALS

John P. Stiga and Gary B. Bullard

The variation of Gibbs energy of dilution with concentration is expected to show unusual behavior for strongly interacting solutions of third and fourth group transition metals with platinum group metals at compositions corresponding to full utilization of low-energy orbitals. Some information can be obtained by determination of the constant boiling compositions of these alloy solutions. As the volatilities are very low, electron beam heating is being used to produce sufficiently high rates of vaporization. These results are being supplemented by data obtained from high-temperature-solid-electrolyte cells.

2. APPLICATION OF THE REGULAR SOLUTION THEORY TO METALLIC SOLUTIONS

John P. Stiga

A modification of the regular solution theory that uses promotion energies to obtain cohesive energies is being tested for metallic solutions that do not have strong interactions due to electron transfer. The relation of volume expansion to internal pressure difference and excess partial molal entropy of solution is also being examined.

3. THERMODYNAMIC EVALUATION AND COMPILATION OF METAL ALLOY SYSTEMS

Leo Brewer, Ralph R. Hultgren, and John Chipman

The following compilations were completed and published in 1973. (1) Ralph R. Hultgren, Pramod D. Desai, Donald T. Hawkins, Molly Gleiser, Kenneth K. Kelley, and Donald D. Wagman, Vol. 2, Selected Values of the Thermodynamic Properties of the Elements (American Society for Metals, Metals Park, Ohio, 1973) 636 pp.
(2) Ralph R. Hultgren, Pramod D. Desai, Donald T. Hawkins, Molly Gleiser, and Kenneth K. Kelley, Vol. 2, Selected Values of the Thermodynamic Properties of Binary Alloys (American Society for Metals, Metals Park, Ohio, 1973) 1435 pp.
(3) Donald T. Hawkins and Ralph R. Hultgren, Constitution of Binary Alloys in Metals Handbook, Vol. 8, Metallography, Structures, and Phase Diagrams, edited by T. Lyman, 8th ed., (American Society for Metals, Metals Park, Ohio, 1973) (supported by ASM), pp. 251-376.
(4) Leo Brewer and Shih-Ger Chang, Constitution of Ternary Alloys, ibid., pp. 377-434 (supported by ASM).

The following compilations are still in progress: (1) Compilation of thermodynamic properties of molybdenum and its compounds. (Supported by International Atomic Energy Agency.) (2) Calculation of the thermodynamic properties and phase diagrams of the alloy systems of the lanthanide and actinide elements. (3) Calculation of solubilities of intermetallic compounds in iron and prediction of behavior of all the metallic elements when dissolved in iron.

4. THE MATRIX SPECTRA OF Ca WITH O, O_2, AND N_2O[†]

Walter D. Duley

The spectra of species formed upon cocondensation of calcium vapor with O, O_2, and N_2O in rare gas matrices at liquid hydrogen temperatures have indicated an unusually complex system with a number of species. Variation of concentrations and isotopic substitutions are being used to identify the species.

[†]Supported by N.S.F.

5. RESEARCH PLANS FOR CALENDAR YEAR 1974

Leo Brewer

Work will continue on the characterization of the Gibbs energy of dilution as a function of concentration for strongly interacting transition metal alloys in an effort to improve the characterization of the Gibbs energy of transition metal alloys. Compilation activities will continue on Mo, Fe, and the lanthanides and actinides with the objective of providing thermodynamic data that will allow prediction of the metallurgical and chemical behavior of these metals. Work will continue on the characterization of the matrix spectra of CaO_x species with

possible extension to MgO_x species. It is hoped that manuscripts on the thermodynamic properties of TiO gas, the transition probability of the Swan bands of C_2, and the ground electronic state of CaO will be completed.

6. 1973 PUBLICATIONS AND REPORTS

Leo Brewer and Associates

Journals and books

1. Leo Brewer, Transition Metal Alloys--A Chemist's View, 18th Annual Conference on Magnetism and Magnetic Materials--1972, Denver, Proceedings of AIP Conference (AIP, 1973), No. 10, Pt. 1, pp. 1-16 (LBL-1424).

2. Leo Brewer and Paul R. Wengert, Transition Metal Alloys of Extraordinary Stability; An Example of Generalized Lewis-Acid-Base Interactions in Metallic Systems, Met. Trans. 4, 83-104 (1973) (LBL-807).

3. Leo Brewer and Shih-Ger Chang, Constitution of Ternary Alloys, Metals Handbook, Vol. 8, Metallography, Structure, and Phase Diagrams, edited by T. Lyman, 8th ed. (American Society for Metals, Metals Park, Ohio, 1973), pp. 377-434.

4. Donald T. Hawkins and Ralph R. Hultgren, Constitution of Binary Alloys, Metals Handbook, Vol. 8, Metallography, Structures, and Phase Diagrams, edited by T. Lyman, 8th ed. (American Society for Metals, Metals Park, Ohio, 1973), pp. 251-376.

5. Ralph R. Hultgren, Pramod D. Desai, Donald T. Hawkins, Molly Gleiser, Kenneth K. Kelley, and Donald D. Wagman, Vol. 1, Selected Values of the Thermodynamic Properties of the Elements, (American Society for Metals, Metals Park, Ohio, 1973) 636 pp.

6. Ralph R. Hultgren, Pramod D. Desai, Donald T. Hawkins, Molly Gleiser, and Kenneth K. Kelley, Vol. 2, Selected Values of the Thermodynamic Properties of Binary Alloys (American Society for Metals, Metals Park, Ohio, 1973) 1435 pp.

LBL reports

1. K. A. Gingerich, Mass Spectrometric Evidence for the Very High Stability of Gaseous ThIr and ThPt and Method of Calculating Dissociation Energies of Diatomic Intermetallic Compounds with Multiple Bonds, LBL-2203, July 1973.

2. Chin-An Chang, Empirical Calculations of the Force Constants, Dissociation Energies and Bond Lengths of Diatomic Molecules, LBL-2252 , Nov. 1973.

Papers presented

1. Leo Brewer, "Relationships between Electronic Configurations, Thermodynamic Properties and Crystal Structures of Superconducting Transition Metal Phases," Gatlinburg Conference on Superconductivity and Lattice Instability, Gatlinburg, Tenn., Sept. 10-12, 1973 (LBL-1898 Abs.).

2. Leo Brewer, Prediction of Transition Metal Phase Diagrams, presented at U.S.-Japan Seminar on "Thermodynamics and Phase Relations of Nuclear Materials" at Ames Laboratory, Iowa State University, July 9, 1973 (LBL-2234 Abs. and LBL-2234).

Charles B. Harris, Principal Investigator

1. EXCITED TRIPLET STATES IN MOLECULES AND MOLECULAR CRYSTALS

Charles B. Harris

Using new techniques recently developed in these laboratories which utilize simultaneous optical and microwave pumping (Phosphorescence-Microwave-Double-Resonance Spectroscopy), we are studying molecular properties of excited triplet states and the dynamics of excited state energy transfer (excitons) in molecular crystals. In oversimplified terms, luminescence from excited triplet states of "isolated" molecules or mobile electronic states, excitons, is monitored while a microwave field changes the orientation of the electron spin in the triplet state. This causes a change in the intensity or polarization of the emission and forms the basis for a technique capable of detecting as few as 10^4 molecules in excited states. Many features of triplet states can be studied by analyzing the microwave transitions and the triplet phosphorescence. These include electron distributions, nuclear-electron interactions, excited state orbital symmetries, molecular distortions in excited states and, finally, the rates, routes, and mechanisms of inter- and intramolecular energy transfer. In addition we are investigating relatively unexplored but very important aspects of excited states involving molecular processes that occur on a time scale of 10^{-9} to 10^{-12} seconds. These are all fundamental in nature and include such things as the primary mechanism in energy migration, radiationless relaxation phenomena, and electron transfer between molecules. A variety of mechanisms have been postulated and theoretically developed for these processes; however, because of the extraordinarily short time scale of the processes, few have been studied. Using Picosecond (10^{-12}) Laser Spectroscopy certain key aspects of the above phenomena are being experimentally investigated in our laboratory. In effect, a picosecond laser pulse is used to generate molecules in excited states and then it is used to follow spectroscopically the time development of the system under investigation. Since it is possible to obtain the complete spectra of molecules in $\sim 3\times10^{-13}$ second using picosecond techniques, the primary events and time-dependent changes associated with excited states, such as energy transfer, radiationless transitions, and the coherence associated with oscillating electric dipolar states in molecules can be systematically investigated.

2. OPTICAL DETECTION OF COHERENCE IN MOLECULAR EXCITED LOCALIZED AND DELOCALIZED BAND STATES

Charles B. Harris

Although coherent phenomena in an ensemble of two-level systems can observed by monitoring a macroscopic oscillating magnetic dipole as in conventional magnetic resonance or a macroscopic oscillating electric dipole as in superradiant emission from crystals or gases, coherent information about the time-dependent density matrix describing the ensemble cannot be generally obtained by monitoring properties associated with the population of only one of the two levels coupled to the oscillating dipole. As a result, in double resonance experiments where optical properties such as emission or absorption of light to a third level are used to measure the coherent properties of two other levels, the coherent phenomena in many cases are not directly observable via a modulation of emission or absorption of light at the oscillating dipolar frequency. Several methods have been developed that are capable of measuring any state of the coherence of an ensemble by double resonance experiments, regardless of the properties of a single level whose population is being monitored. Although the methods are applicable to any optical-optical double resonance experiment involving two electric dipole transitions, the technique has been applied in the context of optically detected magnetic resonance in molecular excited triplet states. The technique is limited only by the sensitivity of photon detection and can be used to monitor as few as 10^4 molecules. The optical detection of electron spin echoes, spin-locking, rotary echo trains, and adiabatic demagnetization in excited electronic states has been accomplished and applied to a variety of problems and phenomena associated with the solid state. These techniques have been applied to systems which provide partial information on coherent phenomena in "one-dimensional" molecular solids having, as their lowest excited states, delocalized triplet bands and localized triplet "molecular" states. Many of the experiments which have been developed utilize zero-field optically detected magnetic resonance in the excited

triplet states. A series of selected experiments and its associated theoretical interpretation demonstrating coherent migration of electronic energy at low temperatures has been carried out in the context of general considerations of transport problems.
(Partially funded by NSF)

3. EXCITON-TRAP INTERACTIONS IN THE COHERENT AND INCOHERENT LIMITS

Michael D. Fayer and Charles B. Harris

At liquid He temperature, phosphorescent emission from organic molecular crystals in general comes from low-energy traps in the lattice, although in some molecules, such as 1,2,4,5-tetrachlorobenzene and 1,4-dibromonaphthalene, exciton emission is also observed. The intensity of trap emission is highly temperature dependent in certain temperature regions. This temperature dependence is found to be explicable in terms of a theoretical framework which includes the method of energy transport in the crystal and the magnitude and sign of the intermolecular interactions which give rise to the exciton bands in the crystal.

Initially the problem was considered for an ensemble consisting of one-dimensional exciton bands and traps of only one energy. The trap intensity is given by $I_{trap}(T) = K^r_{trap}N_{trap} = K^r_{trap}N_{total}P_{trap}(T)$, where K^r_{trap} is the radiative rate constants, N_{trap} is the trap population, and N_{total} is the total excited state population of the system. Since an excitation must either be in the exciton bands or in the traps, the trap population is equal to the total population times $P_{trap}(T)$, the probability that an excitation is in a trap. The number of energy levels in a one-dimensional exciton band is equal to the number of identical molecules in the linear chain forming the exciton. These energy levels are labeled by the quantum number, k, and the energy as a function of k is given by $E(k) = 2\beta \cos ka$, where β is the nearest neighbor intermolecular interaction matrix element and a is the lattice spacing in the direction of the interactions. Using this energy relationship, the partition function z for the system can be written as

$$z = 1 + e^{-\Delta/kT} + \sum_{k=\pi/na}^{(n-1)\pi/na} 2e^{-[\Delta-2\beta(1-\cos ka)]/kT}. \quad (1)$$

The zero of energy is taken at the energy of the trap. The trap depth Δ is the difference in energy between the trap energy and the energy of the k = 0 level of the exciton band. This is the depth which is measured spectroscopically since only the k = 0 level of the origin absorbs or emits light. The first term in z is the Boltzmann factor for the trap level, the second term is for the non-degenerate k = 0 level of the band. The summation is over the remainder of the exciton states which are doubly degenerate. The trap probability $P_{trap} = 1/z$, and therefore the intensity of trap emission $I_{trap} \propto 1/z$.

If a sample of known trap concentration is prepared and the trap depth Δ is measured spectroscopically, then β can be fit to the temperature dependence of the trap emission. As depicted in Fig. 1, two cases arise depending upon the sign of β. If β is negative the exciton band spans an energy range from Δ, the k = 0 energy, to $\Delta + 4\beta$, $k=\pm\pi/a$. If β is positive the band is inverted and it spans an energy range from Δ to $\Delta-4\beta$. Thus the sign of β in addition to the magnitude of β determines the temperature dependence of the trap intensity. The above description gives excellent agreement with experiment for crystals of 1,2,4,5-tetrachlorobenzene which have one-dimensional excitons and traps of a single energy. In order for this description to work, the system must reach equilibrium within the 1 msec lifetimes of the excited states. This implies that excitations must be able

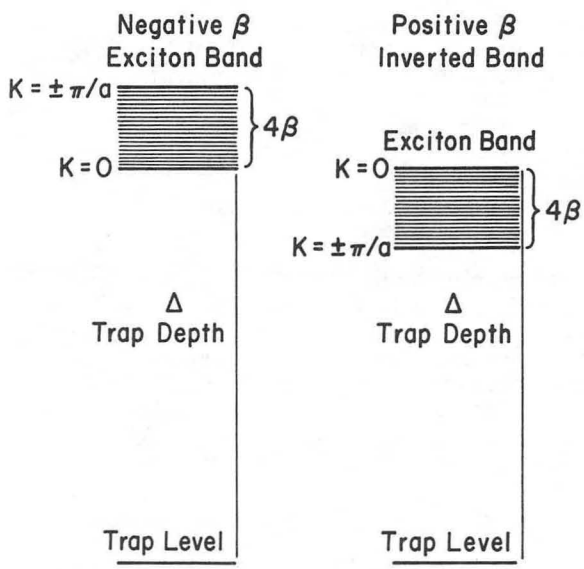

Fig. 1. Trap level and exciton band for systems containing regular and inverted exciton bands. (XBL 7210-5704)

to migrate to many trap sites in less than the lifetime. The traps in the 1,2,4,5-tetrachlorobenzene samples are of such low concentration that it is possible to distinguish between the two possible modes of exciton transport, coherent migration or random walk hopping. The coupled differential equations have been solved in the coherent limit and in the diffusion limit when the ensemble of localized trap states and delocalized band states are not in Boltzmann equilibrium. Furthermore, the full partition function has been calculated and evaluated in the temperature regime where Boltzmann statistics are applicable. The agreement between experiment and theory in this region was confirmed by a series of experiments utilizing isotopic (d) localization.
(Partially funded by NSF)

4. THE DECAY OF LOCALIZED STATES INTO DELOCALIZED BAND STATES

Michael D. Fayer and Charles B. Harris

We have developed a technique for measuring the decay of localized excited triplet states into the delocalized band states of a solid, utilizing the optical detection of electron spin coherence. Specifically, the technique employs the optical detection of electron spin locking for the measurement of kinetic phenomena in the presence of fluctuating triplet spin sublevel populations. Experimental data have been obtained which yield the temperature dependence of the phonon-assisted promotion of a localized isotopic site to an energy equal to that associated with the energies of the host exciton band. In addition, the data have been analyzed in terms of a kinetic model which relates the localized states' rate of promotion and radiationless decay into the exciton band states to explicit features of the exciton and phonon band structure and radiationless relaxation theory.
(Partially funded by NSF)

5. THE THEORY OF OPTICALLY DETECTED SPIN COHERENCE IN EXCITED TRIPLET STATES

William G. Breiland, Henry H. Brenner, and Charles B. Harris

The explicit theoretical basis for optically detected double-resonance experiments has been developed using all the available and well-known tools such as the geometrical representation of Schrödinger's equation, the generalized interaction representation, density matrices, and coherent averaging theory. This development has been applied to optically detected Fourier transform spectroscopy, optically detected spin echoes, Carr-Purcell echo trains, spin locking, and other types of experiments.

6. THE THEORY OF OPTICALLY DETECTED SPIN COHERENCE IN NON-STATIONARY STATES

William G. Breiland, Michael D. Fayer, and Charles B. Harris

The theoretical aspects of optically detected spin coherence have been developed to include the effects of feeding and decay into a two-level system. The limiting cases of slow feeding and decay have yielded expressions for optically detected free induction decay, transient nutation, spin echoes, and Fourier transform spectroscopy in an ensemble which is kinetically evolving to a new steady state under the influence of an applied coherent radiation field. The aspects of feeding and decay promise to provide an interesting way of establishing a coherent state that lasts as long as a rf or optical field is applied to the system. The possible applications of this long-term spin-coherent state are presently being investigated and being extended to include coherence in lasers in which the creation of a super-radiant state is controlled by the radiation field itself.

7. OPTICALLY DETECTED CARR-PURCELL TRAINS AND COHERENT AVERAGING THEORY

Henry C. Brenner and Charles B. Harris

The application of a series of phase-shifted (Meiboom-Gill technique) Carr-Purcell optically detected spin echoes in conjunction with coherent averaging theory developed by Waugh and co-workers has been used to partially average the effects of electron-nuclear hyperfine interactions, molecular torsions due to low-energy phonons in crystals, and nuclear spin diffusion on the electron spin T_2 relaxation time of excited triplet states in zero field.

8. OPTICALLY DETECTED SPIN LOCKING AND ITS APPLICATIONS TO KINETIC PHENOMENA

Charles B. Harris and Horst Schuch

The use of spin locking to completely remove relaxation processes (T_2) in excited triplet states has been accomplished. In effect we have been able to observe the lifetime-broadened zero-field electron spin transition, the lifetime being that associated with radiative decay or radiationless relaxation of the excited triplet state to the ground state. This allows one to use spin locking as a direct kinetic probe of phenomena (cf. Fayer and Harris) that cause a change in the Larmor frequency, $\Delta\omega$, larger than the applied spin lock field, γH_1.
(Partially funded by NSF)

9. OPTICALLY DETECTED ADIABATIC DEMAGNETIZATION IN EXCITED TRIPLET STATES IN ZERO-FIELD AND THE APPLICATION TO KINETIC PHENOMENA

Henry C. Brenner, John C. Brock, and Charles B. Harris

Using the technique of adiabatic demagnetization in the rotating frame (ADRF), electron spins in triplet excited states have been "ordered" in the local fields associated with their particular environments.

Preliminary results indicate that this ordered state can be readily obtianed, and as in the case of spin locking it is essentially lifetime limited, the lifetime being that associated with the fluctuating local field, be it the radiative decay of the excited state or other fluctuations of the local field. The results of these preliminary experiments have demonstrated the feasibility of using the ordered state as a kinetic probe of many phenomena, such as excited state energy migration, spin lattice relaxation in the excited state spectral diffusion in the excited state, optically pumped nuclear polarization, and others.
(Partially funded by NSF)

10. OPTICALLY DETECTED ROTARY ECHO TRAINS IN EXCITED TRIPLET STATES

Charles B. Harris and Ronald L. Schlupp

The rotary echo train pulse sequence has been examined as a method for observing the dynamics of phenomena correlated to electron spins in optically excited states for times longer than the electron spin relaxation time, T_2. Comprehensive experiments were performed on the $^3\pi\pi^*$ state of h_2-tetrachlorobenzene in a variety of host lattices. Although T_2 was found to increase significantly, the excited-state lifetime-limited broadening was not obtained suggesting that other methods--spin locking or adiabatic demagnetization in the rotating frame--are better for the investigation of kinetic phenomena in excited states.
(Partially funded by NSF)

11. PICOSECOND SPECTROSCOPY: COHERENCE IN VIBRATIONAL RELAXATION

Charles B. Harris, Allan M. Nishimura, and Robert M. Shelby

The technique of picosecond spectroscopy offers the possibility of investigating the coherent dynamical properties of certain systems on time scales of from a few picoseconds to tens of nanoseconds. This is made feasible through the utilization of ultra-short pulses of high-intensity coherent light from a mode-locked solid state laser to initiate a process of interest and then to spectroscopically monitor the evolution of the system in time. In this manner it has been shown in other laboratories that it is possible to record the entire spectrum of a sample and its time dependence with a single laser shot. We have constructed mode-locked ruby and Nd glass lasers, and are using single-pulse selection techniques and laser amplification to investigate the coherence associated with vibrational relaxation in molecular liquids. In the phenomenon of stimulated Raman emission, light is used to generate a frequency equal to the difference between the laser frequency and that of some molecular vibration. Because of the coherence of the emitted light, molecules are left all vibrating in phase. It has been shown in other laboratories that it is possible to detect the subsequent presence of this vibrational coherence by observing the coherent anti-Stokes Raman scattering of a delayed probe pulse of light. Using a two-photon optical analog of the conventional nuclear spin echo experiment, we are attempting to investigate the mechanisms leading to the decay of coherence in liquids. The results of these investigations should provide new knowledge of vibrational relaxation in liquids and of the dynamical structure of the liquid phase, and introduce a method which we plan to extend to the study of solids.

12. ENERGY AND ELECTRON TRANSFER IN PHOTOSYNTHETIC BACTERIAL SYSTEMS*

Robyn Goodfellow, Charles B. Harris, Allan M. Nishimura, Kenneth Sauer, and Robert M. Shelby

A mode-locked ruby laser has been used to probe absorbance changes associated with the primary processes of photosynthesis on a time scale ranging from 20 picoseconds to several nanoseconds. Preliminary results from a recent experiment designed to probe for absorbance changes at 793 nm in reaction centers from the photosynthetic bacterium Rps. spheroides indicate that there may be a bleaching of P800 at 0.5 nanosecond after excitation with 793 nm light.

---

*Collaborative with Professor Kenneth Sauer, LBL-Biodynamics.

13. RESEARCH PLANS FOR CALENDAR YEAR 1974

Charles B. Harris

a. Dynamics in Solids

The study of dynamical processes such as energy transfer in molecular crystals will be extended using the techniques of laser spectroscopy. In particular, a nitrogen-pumped tunable dye laser will be used to populate specific energies of localized and delocalized states, and the techniques developed in 1973 will be hybridized with high-resolution laser techniques to study directly additional properties of excited triplet states and exciton bands, including bimolecular exciton-exciton annihilation.

b. Phonon Interactions in Solids

The specifics of phonon interactions in molecular excited states will be investigated, utilizing the new optical detection techniques developed in this laboratory. Electron spin relaxation rates in excited triplet states will be monitored with optically detected microwave pulse techniques while the molecular crystal is subjected to controlled heat pulses.

The specifics of the phonon interaction in the molecular crystal will be mapped by varying the phonon distribution of the heat pulse. This will be accomplished by varying the voltage and the electrical pulse duration applied to the resistive element of the heater. The resistive elements are being fabricated by metal evaporation onto a quartz substrate on which the crystal is placed.

In addition, laser techniques will be employed to investigate the coherence of phonon states in solids, particularly the q=0 wavevector states.

c. Molecular Excited States on Surfaces

The recent advances in phosphorescence double resonance spectroscopy (PMDR) made in these and other laboratories have provided a great deal of new information about excited states in the bulk crystal as well as in dilute guest-host mixtures. The sensitivity of this method allows one to examine details of the excited state which have previously been inaccessible. We plan to apply these methods to investigate the nature of monolayers of organic molecules in excited states on the surface of a clean metal or semiconductor. These studies will yield information on how the metal or semiconductor affects spin-orbit coupling, lifetimes, intersystem crossing, and the geometry of the excited state of the molecule on the surface and hence give detailed information on the surface states themselves. It should also be possible to study surface energy migration and to investigate the time evolution of an ensemble of surface excited states which have been "prepared" coherently. The information thus gained would be useful in helping to understand the mechanisms of surface catalysis and to understand surface states in general.

Correlated with the experiments will be an attempt to understand the theory of surface states when the molecules deposited on the surface are within 10 Å. Naturally, the theoretical development must be guided by the experiments.

d. Picosecond Laser Technology

Additional techniques in picosecond laser technology and their application to coherent phenomena will be extended to solids if the initial experiments in liquids look promising.

e. Photosynthesis*

An attempt to understand the first three steps in photosynthesis (excitation absorption by antenna pigments, transfer of energy to the reacting center, and the formation of the supposed charge-transfer state) will be pursued, using laser and biological methods.

*Jointly with Professor Kenneth Sauer

14. 1973 PUBLICATIONS AND REPORTS

Charles B. Harris and Associates

Journals

1. W. G. Breiland and C. B. Harris, Breakdown of the Born-Oppenheimer Approximation in Radiative Transitions, Chem. Phys. Letters 18, 309 (1973) (LBL-1411).

2. C. B. Harris, Coherent Exciton Migration: An Experimental and Theoretical View, Proc. of the 6th Molecular Crystal Symposium, Germany, May 1973 (LBL-1804).

3. D. S. Tinti, G. Kothandaraman, and C. B. Harris, Determination of the Absolute Sign of the Electron Spin Dipolar and Nuclear Quadrupolar Interactions in Molecular Excited Triplet States, J. Chem. Phys. 59, 190 (1973) (LBL-1461).

4. W. G. Breiland, C. B. Harris, and A. Pines, Optically Detected Electron Spin Echoes and Free Precession in Molecular Excited States, Phys. Rev. Letters 30, 158 (1973) (LBL-1412).

5. C. B. Harris, R. L. Schlupp, and H. Schuch, Optically Detected Electron Spin Locking and Rotary Echo Trains in Molecular Excited States, Phys. Rev. Letters 30, 1019 (1973) (LBL-1412).

Invited Lectures

1. Western Spectroscopy Association, Asilomar, February 1973.

2. American Chemical Society Symposium in Chemical Physics, Dallas, Texas, April 1973.

3. Sixth Molecular Crystals Symposium, Schloss Elmau, Germany, May 1973.

4. The XIth European Congress on Molecular Spectroscopy, Tallinn, USSR, June 1973.

5. Magnetic Resonance Gordon Conference, New Hampshire, June 1973.

6. Molecular Spectroscopy Gordon Conference, New Hampshire, July 1973.

7. Jan van Guensfonds Lectures, University of Amsterdam, The Netherlands, November and December 1973.

8. American Physical Society Coherent Transients Symposium, Berkeley, California, December 1973.

LBL reports

1. M. D. Fayer and C. B. Harris, Coherent Energy Migration in Solids. I. Band-Trap Equilibria at Boltzmann and Non-Boltzmann Temperatures, LBL-1808, May 1973.

2. Rodney Michael Panos, Phosphorescence Microwave Double Resonance Studies of the Lowest Excited Triplet State of p-Dichlorobenzene (Ph.D. thesis), LBL-1822, June 1973.

3. C. B. Harris, Phosphorescence-Microwave-Double-Resonance in Exciton States of Molecular Crystals and Coherent States of Triplet Spin Ensembles, LBL-1845, June 1973.

4. C. B. Harris and M. D. Fayer, Coherent Energy Migration in Solids. II. Spin Resonance Absorption in Coherent Wave Packet States and the Effects of Phonon-Exciton Scattering, LBL-2210, Aug. 1973.

5. H. C. Brenner, J. C. Brock, and C. B. Harris, The Use of an "Ordered" Electron Spin State as a Probe in Molecular Spectroscopy: Optically Detected Adiabatic Demagnetization in Excited Triplet States in Zero Field, LBL-2293, Oct. 1973.

6. M. D. Fayer and C. B. Harris, The Decay of Localized States into Delocalized Band States. I. Theory and Preliminary Experimental Investigations Using Optically Detected Electron Spin Coherence, LBL-2550, Nov. 1973.

Alexander Pines, Principal Investigator

1. NUCLEAR MAGNETIC DOUBLE RESONANCE SPECTROMETER

Alexander Pines and Associates

A wideband nuclear magnetic double-resonance spectrometer has been constructed to permit the implementation of novel techniques for high-sensitivity detection of nuclei of low isotopic abundance. The spectrometer was fully operational early in 1973 and was used for the experiments to be described. The main application of the spectrometer to date has been the detection of ^{13}C in natural isotopic abundance (~1%); for this purpose it is of unprecedented sensitivity and large signals have been observed from small crystalline samples. The device has a fast programmable pulse unit which controls the radiofrequency modulation. This is interfaced to an on-line computer making the interchange of modulation sequences and the trial and implementation of new experiments extremely flexible. The computer also serves for on-line Fourier transformation. The magnet is a wide-bore superconducting solenoid in a LHe/LN_2 cryogenic dewar. Radiofrequency amplifiers are modified radio amateur transmitters operating at 26.7 and 106 MHz and capable of the high power output which is necessary for the solid state studies.

An important component of the spectrometer is the sample probe. This is designed for the geometry of the superconducting solenoid and is equipped with home-built variable capacitors to withstand the large (~30,000 V) radiofrequency voltages across the sample coils. A crystal goniometer controllable remotely permits precise orientation and rotation of single crystals in the magnetic field. The crystal holder is designed to transfer directly to an X-ray goniometer, allowing us to orient crystals by X-ray precession methods. Part of the probe is shown in Fig. 1, with details in the caption.

The sensitivity enhancement provided by this spectrometer takes advantage of abundant isotopic nuclear species in the sample. The abundant nuclear spins, normally ^{1}H, are polarized in the magnetic field; simultaneous irradiation with carefully selected phase and amplitude modulated radiofrequency fields at the resonance frequencies of ^{1}H

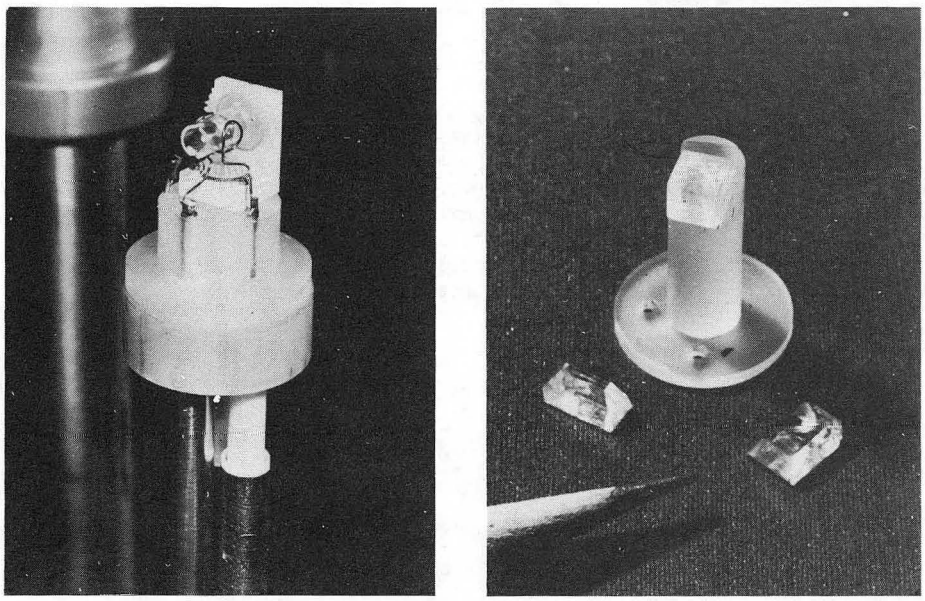

Fig. 1. Double-resonance probe head and crystal holder for X-ray goniometer. The crystals are mounted in the Kel-F cube on the end of the holder; this keys onto the gear allowing the crystal to be rotated inside the sample coils. The lower part of the probe contains the high-power tuning and matching electronics.
(XBB 742-815A)

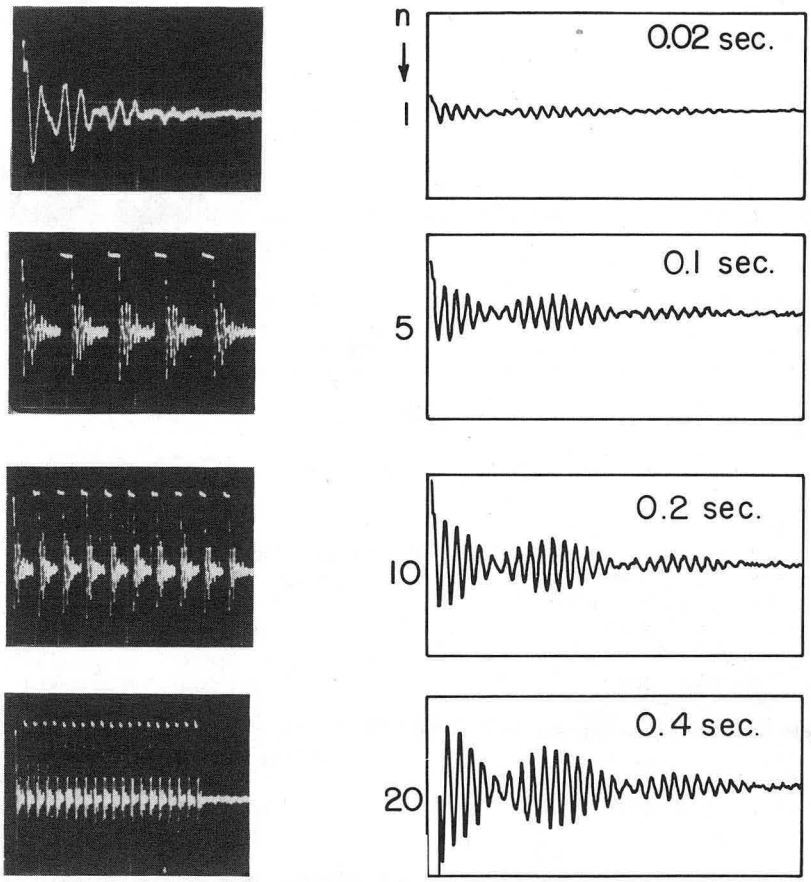

Fig. 2. Demonstration of sensitivity enhancement for rare nuclear spins. The oscilloscope photographs on the left depict the output of the ^{13}C phase detector for various numbers (n) of $^{1}H \rightarrow {}^{13}C$ cross-polarization steps in solid adamantane. The positive pulses are from rf receiver blocking during the cross-polarization, and they are followed by proton-decoupled ^{13}C free precession signals. It is these which are rapidly transferred and accumulated by the computer. The cross-polarization pulses are 5 msec long. The traces on the right show the accumulated signals and acqusition times corresponding to the number of cross-polarizations on the left. These were recorded further off resonance for display purposes.

(XBB 742-900)

and the rare nuclei under study then effects a transfer of part of the large magnetic polarization to the rare nuclei. This "cross-polarization" process can then be repeated many times and the signals from the rare spins accumulated to yield a markedly enhanced sensitivity over conventional detection techniques.

Figure 2 demonstrates this sensitivity enhancement with our spectrometer on a small polycrystalline sample of adamantane ($C_{10}H_{16}$). The two nuclear species for the double resonance are ^{1}H and ^{13}C. A strong useful ^{13}C signal is obtained in < 1 sec in this way, compared to the barely observable signals accumulated over long times by conventional approaches.

2. MAGNETIC SHIELDING IN SINGLE CRYSTALS*

Alexander Pines, James J. Chang, and Eric B. Abramson

In magnetic fields, induced electronic currents in molecules set up secondary magnetic fields at nuclei, thus influencing their nuclear magnetic resonance frequency. This phenomenon is termed magnetic shielding (or chemical shielding) and is of crucial importance in the application of nuclear

magnetism to the study of geometrical and electronic structure in molecules and solids. Since the electronic wave functions in most molecules are not isotropic, it is expected that the magnetic shielding should be dependent on the orientation of the molecules in the magnetic field. Indeed, it can be shown that the magnetic shielding should transform under rotations as a symmetric second rank tensor, $\boldsymbol{\sigma}$. Thus, six independent parameters are required to specify the magnetic shielding properties of particular nuclei in a molecule.

Most investigations of magnetic shielding have been performed in isotropic liquid solution. Since, under these conditions, molecules are reorienting rapidly on a time scale defined by the nuclear magnetic precession, only one parameter, the isotropic shielding $\bar{\sigma}$,

$$\bar{\sigma} = \frac{1}{3} \mathrm{Tr}\, \boldsymbol{\sigma} \quad , \qquad (1)$$

is extracted from such experiments; thus, to date, only severely limited insight into the nature of magnetic shielding has been available.

We have determined the full shielding tensors for ^{13}C in a number of organic single crystals. The parameters most suitable for describing the tensors are three Euler angles describing the orientation of the principal axes (1, 2, 3) of $\boldsymbol{\sigma}$ relative to fixed crystallographic or laboratory axes, and the associated three principal values σ_{ii}, i = 1-3. These values describe the magnetic shielding along the principal axes and thus provide a direct measure of the anisotropy of the magnetic shielding and of the wave function. We find in particular that the tensors are quite characteristic in magnitude and in orientation for various functional groups. Thus they should provide a powerful tool for studies of local structure, conformation, and motion in solids.

To demonstrate the information obtained, Fig. 1 shows part of the two molecules in the unit cell of one of the crystal systems studied, (D)-ammonium tartrate, formula (NH_4^+ $^-$COO-CHOH-CHOH-COO$^-$ $^+NH_4$). In isotropic liquid solution, with conventional nuclear magnetic resonance, only two lines are observed in the ^{13}C nmr spectrum, since there are clearly only two magnetically inequivalent sites (CHOH and COO$^-$) over the isotropic spatial averaging caused by molecular rotation. In the crystal, with our technique, we can distinguish eight lines in some orientations, from the eight carbon nuclei in the unit cell, as shown in Fig. 2.

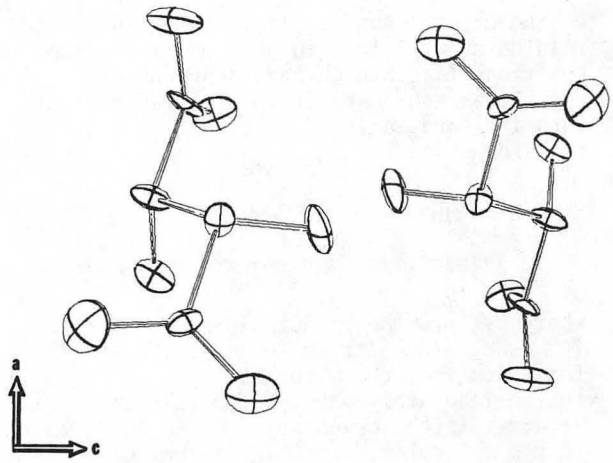

Fig. 1. Perspective view along the crystallographic b axis of two tartrate ions ($^-$OOC-CHOH-CHOH-COO$^-$) showing the carbon and oxygen atoms in the unit cell of (D)-ammonium tartrate. In general orientations, the carbon nuclei will be in magnetically inequivalent positions. (XBL 742-5592)

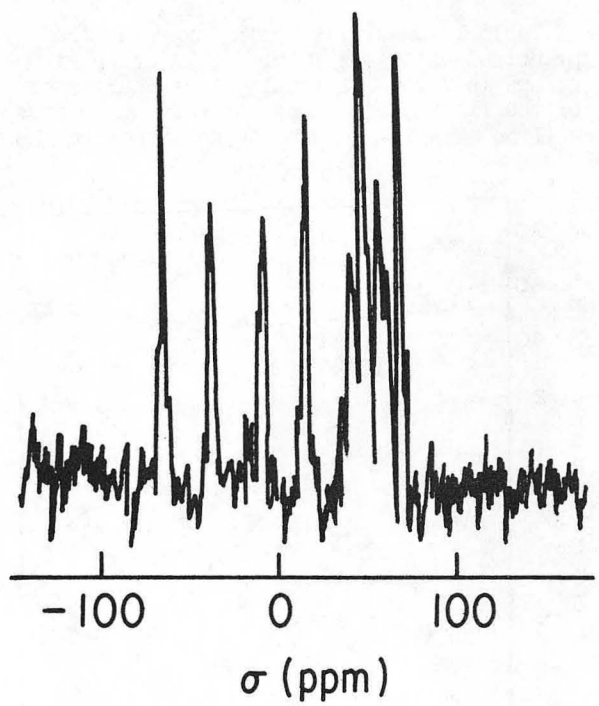

Fig. 2. Fourier transform ^{13}C nmr spectrum of single-crystal (D)-ammonium tartrate (see Fig. 1), showing separate lines for each of the carbon nuclei. The high-field lines are from the hydroxyl carbons and the low-field lines from the carboxyl carbons. The horizontal axis is in ppm relative to an external reference of liquid benzene. In isotropic solution only two lines are observed. (XBL 742-5578)

The crystal can be precisely oriented and rotated as explained in Section 1; the line positions (σ) then change as shown in Fig. 3, and the data from three independent rotations are analyzed according to the transformation

$$\sigma = \sin^2\theta \cos^2\phi \, \sigma_{11} + \sin^2\theta \sin^2\phi \, \sigma_{22} + \cos^2\theta \, \sigma_{33} , \qquad (2)$$

where σ_{ii} are the principal values of $\boldsymbol{\sigma}$ and (θ, ϕ, ψ) are Euler angles of the transformation from the principal axes (1, 2, 3) to the laboratory axes. Of particular interest is the orientation of $\boldsymbol{\sigma}$(1, 2, 3) in the molecules, since it is the local structure and symmetry which we hope to probe. This orientation can be determined using X-ray precession data on the same crystals, and Fig. 4 shows the orientation of $\boldsymbol{\sigma}$ for ^{13}C in the carboxyl (COO^-) groups. Gratifyingly, the axes are related to the local C_{2v} symmetry at the ^{13}C site. We have found this to be true in several other cases.

Table I summarizes, as an example, the principal values of $\boldsymbol{\sigma}$ for ^{13}C in carboxyl groups in several crystals. These are some of the first measurements in what we believe will be a rapidly expanding and important field.

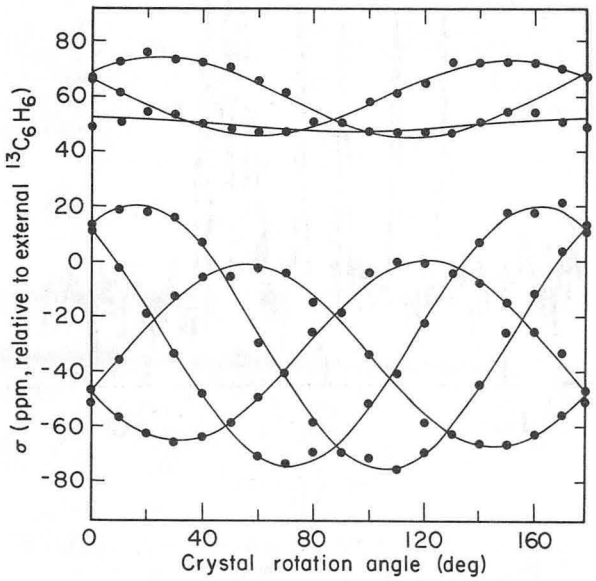

Fig. 3. Dependence of chemical shifts (line positions) of spectra such as that in Fig. 2 on crystal orientation, demonstrating the large magnetic shielding anisotropy for the carboxyl carbon (lower lines) nuclei. For this plot the crystal was rotated about a fixed axis perpendicular to the magnetic field. (XBL 741-2161)

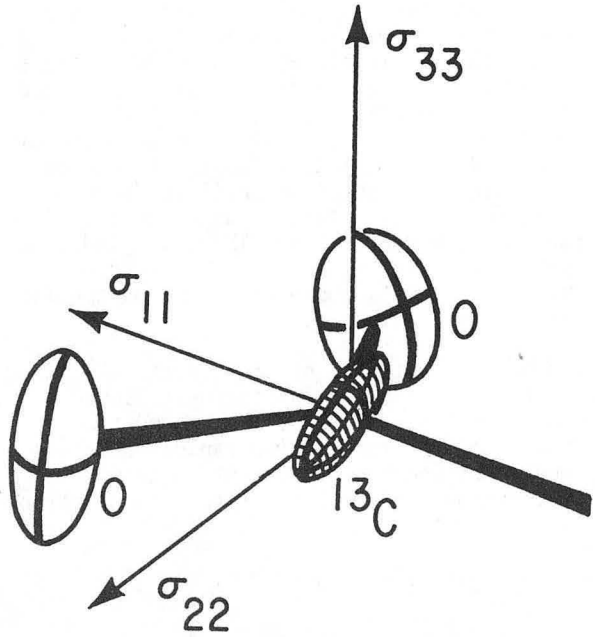

Fig. 4. Orientation of the principal axes of $\boldsymbol{\sigma}$ on the ^{13}C nucleus of the carboxyl group. The heaviest magnetic shielding occurs when the magnetic field is perpendicular to the COO^- plane and the lightest shielding when it bisects the CO bonds, thus conforming to the local symmetry. (XBL 742-5591)

Table I. Principal elements of $\boldsymbol{\sigma}$ for $^{13}COO^-$ in selected crystals in ppm (± 4) relative to external reference of $^{13}C_6H_6$.

Compound	σ_{11}	σ_{22}	σ_{33}
Glycine	-119	-55	28
Oxalic acid, anhydrous	-122	6	17
Oxalic acid, dihydrate	-124	-8	17
Ammonium oxalate	-113	-32	26
Malonic acid	-103	-47	23
Ammonium hydrogen malonate	-113	-46	26
Ammonium tartrate	-109	-60	23

*Done partially in collaboration with Robert G. Griffin, visiting IMRD from the Francis Bitter National Magnet Laboratory in Cambridge, Massachusetts.

3. DYNAMICS OF NUCLEAR MAGNETIC DOUBLE RESONANCE

Alexander Pines and Thomas W. Shattuck

An important consideration in the design and understanding of cross-polarization processes in nuclear magnetic double resonance is that of fluctuation dynamics of the magnetic dipolar coupling between the nuclear spins. To be more specific, consider the ^1H and ^{13}C nuclei in an organic crystal and imagine, as in Section 2, that we wish to transfer nuclear magnetic polarization from the ^1H to the ^{13}C spins. In order for this process to occur, energy must migrate between the nuclear spins, and it is only by fluctuating magnetic fields that this migration can be induced. Such fluctuations occur by modulation of the ^1H - ^{13}C magnetic dipolar coupling due to magnetic dipolar coupling between the ^1H spins themselves, Clearly, an understanding of this process is essential to applying it efficiently to various studies of rare nuclei. The quantity of interest is the correlation function:

$$f(\tau) = \frac{\mathrm{Tr} \sum_i b_i I_{ix} \exp(iH_d^\circ \tau) (\sum_i b_i I_{ix}) \exp(-iH_d^\circ \tau)}{\mathrm{Tr}(\sum_i b_i I_{ix})^2}, \quad (1)$$

where I_{ix} is the angular momentum operator for ^1H nuclear spin i, b_i are the coupling terms between a ^{13}C spin and the ^1H spins and H_d° is the zero-order component of the magnetic dipolar coupling between the ^1H spins.

It can be shown that for the case where

$$\| \sum_i b_i I_{ix} \| \ll \| H_d^\circ \| ,$$

i.e., the coupling between the different nuclear spins is weaker than that between like spins, that the cross-polarization time T for the migration of energy between unlike spins is related to the Fourier transform of (1):

$$T^{-1}(H_1) = \text{Const.} \times \int_0^\infty f(\tau) \cos\gamma H_1 \tau \, d\tau . \quad (2)$$

H_1 is the intensity of the rotating magnetic field on the ^{13}C spins and γ is the magnetogyric ratio. Thus, by using a series of H_1 values the experimental form of T^{-1}, the spectral density for the magnetic dipolar fluctuations, may be established. This was done by Hahn and co-workers for ^{19}F - ^{43}Ca in CaF_2 with the surprising result that T^{-1} was dependent exponentially on H_1, thus indicating that $f(\tau)$ is Lorentizian. We have found similar behavior for ^1H - ^{13}C double resonance in solids, showing that this is not an isolated phenomenon deriving from the ^{43}Ca quadrupole interactions. Figure 1 shows the dependence of T^{-1} on H_1 for adamantane, selected because of its high molecular symmetry and facile rotation, showing the exponential behavior over three orders of magnitude. This phenomenon, which indicates long-lived fluctuations, is not yet understood theoretically.

The correlation time τ_c characteristic of the loss of correlation between the spins is given by the slope of the line and is found to be ~ 140 μsec. This will be compared with values currently being calculated from the known lattice parameters of the crystal.

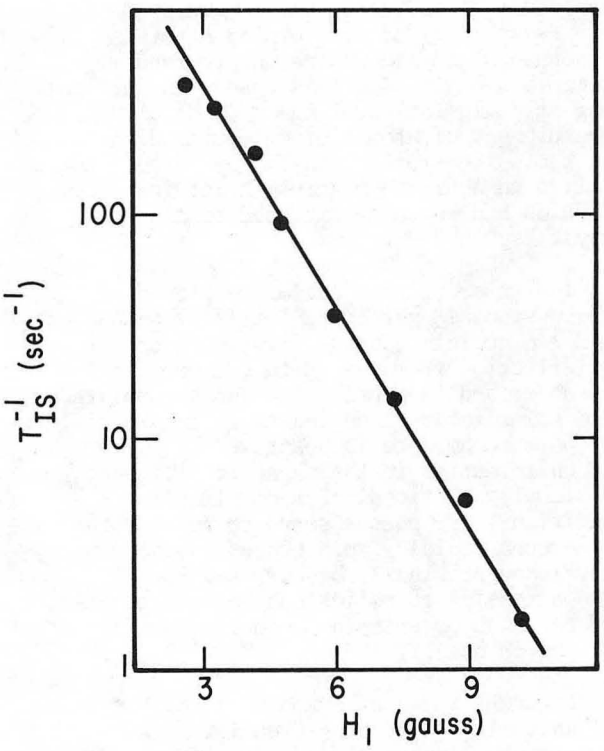

Fig. 1. Dependence of inverse cross-polarization time T_{IS}^{-1} between ^1H and ^{13}C on the strength of the rotating magnetic field. For this study, the ^1H nuclei in adamantane were polarized and then adiabatically demagnetized in the rotating frame. The ^{13}C nuclei were then polarized by turning on a resonant radiofrequency field of rotating intensity H_1. (XBL 742-5579)

This information has proved extremely useful in implementing and optimizing our new detection schemes, and has permitted the efficient acquisition of data described in other sections of this report.

4. LONG-LIVED NUCLEAR SPIN TRANSIENTS IN SOLIDS

Alexander Pines and Thomas W. Shattuck

The method of nuclear spin echoes has provided an extremely powerful tool for the direct study of diffusion in liquid-like systems. Until recently this has not been applicable to solids, since in these systems the decay of spin coherence is normally dominated by strong magnetic dipolar interactions and is thus not easily reversible. We have reported the first observation of enhanced long-lived nuclear spin echoes for dilute nuclei in solids. These experiments have allowed several novel features of high-resolution solid state nmr to emerge, e.g., the feasibility of determining natural lineshapes and linewidths due to randomly disturbed nuclei (in this case with internal magnetic dipolar coupling) and the direct measurement of atomic or molecular diffusion in the solid state. The latter extends to solids an approach reserved heretofore for liquids and recently extended to liquid crystals.

The rf modulation schemes employed in these studies, performed initially on ^1H and ^{13}C nuclei, consist firstly of cross-polarization from the ^1H to ^{13}C nuclei, as described in Section 1. The accumulated ^{13}C polarization then decays as the initially prepared coherence is destroyed by nonuniformaties in the magnetic field and residual magnetic dipolar couplings. Additional ^{13}C pulses serve to restore the coherence, yielding spin echoes in the manner developed originally by Carr and Purcell. The extension to solids can be made because of the high-power spin decoupling performed on the ^1H nuclei.

Figure 1 shows an example of the response of naturally abundant ^{13}C nuclei in a polycrystalline sample of adamantane to this type of excitation with an externally imposed magnetic field gradient. The trace shows the decay of the ^{13}C polarization, a pulse and the subsequent refocusing yielding an echo. A train of echoes with closely spaced pulses exhibits a prolonged exponential decay ($T^{+}_{2} > 200$ msec) demonstrating for the first time the high resolution attainable in solids by combining

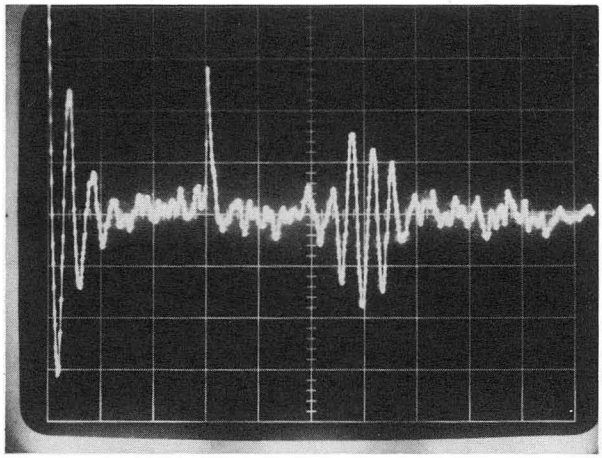

Fig. 1. Spin echo of ^{13}C in solid polycrystalline adamantane. The oscilloscope time scale is 1 msec/cm. The ^{13}C nuclei were polarized and then allowed to precess freely with the ^1H nuclei strongly irradiated at resonance to effect spin decoupling. The free precession signal decays away rapidly as shown on the left side of the photograph due to an imposed external magnetic field gradient. A subsequent pulse momentarily restores the coherence of free precession, causing a spin echo. If there is any diffusion of the molecules along the field gradient, the intensity of the echo is reduced. (XBB 738-4779)

the effective removal of static magnetic field inhomogeneity with the sensitivity and resolution enhancement.

An interesting feature of the echo decay is the exponential shape. This is in agreement with an early prediction of Kittel and Abrahams which indicates that as the distribution of nuclei progresses from periodic to random, the spectral lineshape should go from Gaussian to Lorentzian. Explicit calculations of the first few moments M_{2n} of the spectral lines:

$$M_{2n} = (i)^n \, \mathrm{Tr}[H_d^\circ \, [H_d^\circ \, \overset{n}{\cdots\cdots} [H_d^\circ, I_x]]\cdots]^2 \quad (1)$$

verify the theory for simple cases. H_d° is the zero-order component of the magnetic dipolar interaction and I_x is the nuclear spin angular momentum operator. Our work is the first experimental manifestation of this phenomenon for randomly distributed ^{13}C nuclei. This should prove useful in determining the degree to which particular nuclei are clustered or ordered in pure solids and doped materials.

Of considerable interest is the possibility, which our technique introduces, of measuring directly rapid diffusion in the solid and partially ordered systems. This is accomplished by measuring the irreversible loss of coherence with a spin echo decay envelope in pulsed magnetic field gradients of well-defined duration, magnitude, and orientation. In particular, studies are under way on anisotropic diffusion of molecules in solids, on surfaces, and in liquid crystals.

5. SPIN THERMODYNAMICS IN TIME-DEPENDENT FIELDS

Alexander Pines

The spin temperature hypothesis has provided an extremely useful tool for the understanding and development of nuclear magnetic resonance in solids. The substance of the hypothesis, as related to our interest, is that a system of nuclear spins coupled by magnetic dipolar interactions in a solid approaches, in a time T_2, a state of internal equilibrium characterized by a spin temperature. We find that when a strong time-dependent perturbation, in the form of a sequence of intense radiofrequency pulses, is applied to such a spin system, the concepts of spin thermodynamics and statistical mechanics may still be employed with respect to a time-independent average Hamiltonian in a frame of reference defined by the external perturbation. This is an extension of Redfield's hypothesis of spin temperature in the rotating frame to a more general periodic and cyclic excitation.

Figure 1 depicts one of the pulse sequences used in the present experiments, performed on the ^{19}F spins in a crystal of CaF_2. An adiabatic demagnetization in the rotating frame (ADRF) prepares the system in a state of high inverse dipolar spin temperature β_o,

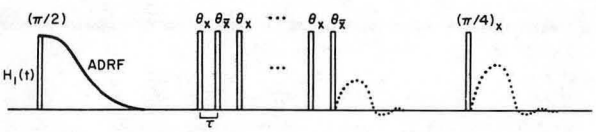

Fig. 1. Radiofrequency pulse sequence used in the experiment. θ_X denotes a pulse of nutation angle θ of phase such that H_1 is along the defined X axis in the rotating frame. The dotted lines depict schematically the type of transient signal observed.

(XBL 742-5554)

characterized by the density operator

$$\rho_o = \frac{1}{Z_o} \exp\left(-\beta_o H_d^o\right) \tag{1}$$

where $Z_o = \mathrm{Tr}\{\exp(-\beta_o H_d^o)\}$ and H_d^o is the usual truncated dipolar interaction amongst ^{19}F spins. The subsequent irradiation $H_1(t)$, consists of a series of resonant rf pulses of nutation angle θ with an alternation of phases by π every pulse. In general, the treatment of the response of the system to this excitation would be an intractable problem; however, we apply the concepts of average Hamiltonian theory, and assume that if $\tau \ll T_2$, then, in zero order, we may consider the system to behave as if under the influence of a time-independent average dipolar Hamiltonian $\bar{H}_d^o$ in an interaction picture defined by $H_1(t)$,

$$\bar{H}_d^o = \frac{1}{2\tau} \int_o^{2\tau} \tilde{H}_d^o(t)\, dt \,, \tag{2}$$

where:

$$\tilde{H}_d^o(t) = T \exp\left(\int_o^t -\frac{it'}{\hbar} H_1(t')\, dt'\right) \times H_d^o\, T \exp\left(\int_o^t \frac{it'}{\hbar} H_1(t')\, dt'\right) \tag{3}$$

and T is a time-ordering operator. We now assume that after a sufficiently long time, the system can be described in the new picture by a canonical density operator:

$$\rho_1 = \frac{1}{Z_1} \exp(-\beta_1 \bar{H}_d^o) \,. \tag{4}$$

The rf irradiation is now terminated. We can inquire into: (a) the short time behavior of the system and (b) the dipolar spin temperature of the final state. The time-dependent relative magnetization upon termination of the pulse sequence is given by

$$S_1(t) = \frac{\mathrm{Tr}\left\{\exp\left(-\frac{it}{\hbar} H_d^o\right) \rho_1 \exp\left(\frac{it}{\hbar} H_d^o\right) I_x\right\}}{\mathrm{Tr}\left\{I_x^2\right\}} \,. \tag{5}$$

Using the high-temperature approximation for ρ_1 in (4) and solving for $\bar{H}_d^o$ in the case of ideal "δ-pulses," we find:

$$S_1(t) = -\sin\theta \cos\theta\, S_d(t) \,, \tag{6}$$

where $S_d(t)$ is the normal dipolar free induction decay observed from a system in a state described by (1) after a $(\pi/4)_x$ pulse. This is exactly borne out experimentally.

To determine the long-time-behavior, we assume that during the pulse sequence the average dipolar energy $\langle H_d^o \rangle$ is conserved, and that after the irradiation, $\langle H_d^o \rangle$ is conserved. The final state of the system is described by:

$$\rho_2 = \frac{1}{Z_2} \exp(- \beta_2 \overset{o}{H_d}) \quad . \qquad (7)$$

Employing equations (1)-(4) we obtain with some simple algebra:

$$\frac{\beta_2}{\beta_o} = \frac{1}{4} (1 + 3 \cos^2\theta) \quad . \qquad (8)$$

These expressions are easily generalized to the case of non-ideal pulses.

Figure 2 depicts the nutation angle dependence of our observed signals. $S_1(t)/S_d(t)$ is the relative intensity of the transient observed on termination of the sequence, and β_2/β_o is the final relative inverse dipolar spin temperature. The agreement indicates that despite the complexity of the problem, the assumption of quasi-equilibrium during the strong time-dependent excitation is a useful one, and that quantitative predictions may be made. Thus we have demonstrated that spin thermodynamic parameters may actually be modified by the application of selected time-dependent fields. This is being applied to the development of new detection techniques for solid state magnetic resonance and to the production of large nuclear magnetic polarizations.

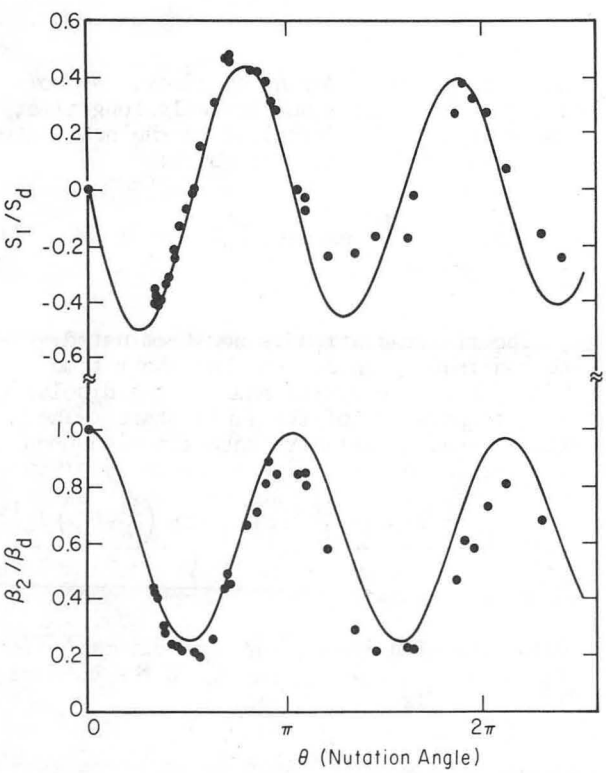

Fig. 2. Relative signal intensity for the two transients compared to the normal unperturbed dipolar free induction decay observed for ^{19}F spins in CaF_2 on application of pulse sequence in Fig. 1. S_1/S_d is the relative intensity of the first transient and β_2/β_o is the relative final inverse dipolar temperature, i.e., the relative intensity of the second transient. The solid lines are calculated theoretically.

(XBL 742-5555)

6. RESEARCH PLANS FOR CALENDAR YEAR 1974

Alexander Pines

Work will continue on magnetic shielding and structure for nuclei of low isotopic abundance. Additional functional groups and inorganic materials will be studied. This will extend to the study of ferroelectric phase transitions in the KDP crystal class by observation of ^{31}P decoupled from ^{1}H. We plan also to study fluctuations and quantum mechanical proton tunneling in hydrogen bonds, employing those same techniques, if the magnetic shielding proves sensitive to proton position. The application of magnetic shielding to the study of local electronic structure and comparisons with current molecular orbital theories of shielding will be undertaken when sufficient data are available.

As our preliminary experiments have indicated, nuclear spin transients with extremely long lifetimes can now be produced. This should allow the study of anisotropic diffusion in ordered and partially ordered systems. Such studies are being undertaken on liquid crystals and organic molecules adsorbed on solids. The diffusion will be studied along well defined pulsed magnetic field gradients. A new spectrometer and accessories are under construction for these experiments and should be completed shortly.

7. 1973 PUBLICATIONS AND REPORTS

Alexander Pines and Associates

Journals

*1. J. H. Leftin, D. Redpath, A. Pines, and E. Gil-Av, Electrochemical Synthesis of Cis-3, 4-Dicarbomethoxycyclobutene, Israel J. Chem. 11, 75 (1973).

*2. A. Pines, M. G. Gibby, and J. S. Waugh, Proton-Enhanced NMR of Dilute Spins in Solids, J. Chem. Phys. 59, 569 (1973).

*3. S. Pausak, A. Pines, and J. S. Waugh, Carbon-13 Chemical Shielding Tensors in Single Crystal Durene, J. Chem. Phys. 59, 591 (1973).

4. W. G. Breiland, C. B. Harris, and A. Pines, Optically Detected Electron Spin Echoes and Free Precession in Molecular Excited States, Phys. Rev. Letters 30, 158 (1973)(LBL-1412).

5. A. Pines and J. D. Ellett, Jr., Pulsed Spin Decoupling in Nuclear Magnetic Resonance, J. Am. Chem. Soc. 95, 4437 (1973)(LBL-1489).

6. A. Pines and T. W. Shattuck, Enhanced Inhomogeneous Nuclear Spin Echoes for Dilute Spins in Solids, Chem. Phys. Lett. 23, 614 (1973)(LBL-2235).

LBL reports

1. J. J. Chang, R. G. Griffin, and A. Pines, Chemical Shielding Tensor of ^{13}C in a Carboxyl Group, LBL-2513, Nov. 1973.

2. A. Pines and J. S. Waugh, Dipolar Spin Temperature in a Periodically Perturbed Nuclear Spin System, LBL-2515, Dec. 1973.

3. A. Pines and E. Abramson, Chemical Shielding Tensors of ^{13}C in Dimethyl Oxalate, LBL-2522, Dec. 1973.

4. T. Merrick, S. Smiriga, and A. Pines, A Simple Data Acquisition System for Proton-Enhanced Nuclear Induction Spectroscopy, LBL-2546, Dec. 1973.

5. A. Pines and T. W. Shattuck, Carbon-13 Nuclear Magnetic Polarization from Demagnetized Protons, LBL-2545, Dec. 1973.

Papers presented

1. A. Pines, "Sensitivity in Fourier Transform NMR in Solids," 14th Experimental NMR Conference, Boulder, Colorado, April 1973.

2. A. Pines, "Partially Relaxed Fourier Transform NMR Spectroscopy in Solids," ^{13}C NMR Symposium, American Chemical Society Meeting, Dallas, Texas, April 1973.

3. A. Pines, "The Advent of High Resolution NMR in Solids," Gordon Research Conference on Magnetic Resonance, Kimball Union Academy, Merriden, N. H., June 1973.

4. A. Pines, "Sensitivity in High Resolution Nuclear Magnetic Double Resonance," First Specialized Colloque Ampere, Krakow, Poland, Aug. 1973.

5. A. Pines, "Adiabatic Cross-Polarization in Nuclear Magnetic Double Resonance," Meeting of the British Radio Spectroscopy Group, Sussex, England, Sept. 1973

---

*Not supported by IMRD funds.

Ronald R. Herm, Principal Investigator

1. CROSSED BEAMS CHEMISTRY: ALKALINE EARTH ATOM REACTIONS

Ronald R. Herm, Shen-Maw Lin, and Charles A. Mims

We have now completed our exploratory crossed beams studies of the thermal energy reactions of Ba, Sr, Ca, and Mg with various halogen- and oxygen-containing molecules. Prior to our studies (and other studies initiated concurrently in other beam laboratories), there was practically no information available on the gas phase kinetics of reactions of Group IIA alkaline earth atoms despite an active interest on the part of the physical chemist in the gas phase kinetics of alkali atom reactions dating back to the classical Michael Polanyi diffusion flame studies of the 1930's. Our crossed beams studies directly provided information on the dynamical behavior (i.e., mechanism) of these reactions, and results for particular reactions have been described in previous IMRD Annual Reports and have also been published.[1]

In closing these studies, however, it seems worthwhile to summarize the contrasting reactivities which we have observed in the alkaline earth family (estimated from the strength of the alkaline earth halide or oxide product signal). This summary is shown in Table I and illustrates two points. First of all, there is often a considerable variation in the total reaction cross section (Q_R) for reaction of Ba, Sr, Ca, and Mg with a given halide or oxide reactant. Thus, we failed to observe reaction of Mg with any reagent other than the diatomic halogen molecules. For Ba, Sr, and Ca with any given reactant, we also estimate that $Q_R(Ba) > Q_R(Sr) > Q_R(Ca)$; this behavior is apparent for the PCl_3, SF_6, CCl_4, and $C_3H_7NO_2$ entries in Table I. This behavior may be contrasted with the alkali family[2] where, for a given reactant, Q_R shows only a modest decrease (typically about a factor of 2) in the Cs → Rb → K → Na → Li sequence. The second point illustrated by Table I is that, in terms of reactivity, Ba seems to behave like an alkali metal. In abstraction of a halogen atom from an alkyl halide, for example, $Q_R(-I) > Q_R(-Br) > Q_R(-Cl)$, precisely the behavior characteristic of the alkali atom reactions.

Table I. Alkaline earth atom reactions studied.[a]

	Ba	Sr	Ca	Mg
HALOGEN MOLECULES				
$M+Cl_2 \rightarrow MCl+Cl$	R	R	R	R
$M+Br_2 \rightarrow MBr+Br$	R	R	R	R
$M+ClI \rightarrow MCl+I$	R	R	R	R
$M+ICl \rightarrow MI+Cl$	R	R	R	F
$M+NCBr \rightarrow MCN+Br$	R	-	-	-
$M+BrCN \rightarrow MBr+CN$	F	-	-	-
INORGANIC HALIDES				
$M+HI \rightarrow MI+H$	R	R	R	NR
$M+HF \rightarrow MF+H$	NR	-	-	-
$M+SnCl_4 \rightarrow MCl_n+SnCl_m$	R	R	R	NR
$M+SnCl_4 \rightarrow MSnCl_3+Cl$	NR	NR	NR	NR
$M+PCl_3 \rightarrow MCl_n+PCl_m$	R	R	F	-
$M+SF_6 \rightarrow MF_n+SF_m$	R	I	NR	NR

(Table I cont.)

ORGANIC HALIDES				
$M+CH_3I \rightarrow MI+CH_3$	R	R	R	NR
$M+CH_2I_2 \rightarrow MI_2+CH_2$	R	R	R	-
$M+CF_3I \rightarrow MI(?)+CF_3$	R	-	-	-
$M+CF_3I \rightarrow MF(?)+CF_2I$	F	-	-	-
$M+CH_2Br_2 \rightarrow MBr_2(?)+CH_2$	-	-	F	-
$M+CCl_3Br \rightarrow MBr(?)+CCl_3$	-	-	NR	-
$M+CCl_3Br \rightarrow MCl(?)+CCl_2Br$	-	-	NR	-
$M+CH_2ClBr \rightarrow MBr(?)+CH_2Cl$	F	-	-	-
$M+CH_2ClBr \rightarrow MCl(?)+CH_2Br$	NR	-	-	-
$M+CCl_4 \rightarrow MCl_n+CCl_m$	R	I	NR	-
$M+CCl_3NO_2 \rightarrow MCl(?)+CCl_2NO_2$	-	-	R	-
$M+C_4H_9OH \rightarrow MOH+C_4H_9$	NR	-	-	-
OXIDES				
$M+SO_2 \rightarrow MO+SO$	R	NR	NR	-
$M+NO_2 \rightarrow MO+NO$	-	R	R	I
$M+C_3H_7NO_2 \rightarrow MO+C_3H_7NO$	R	R	NR	-
$M+C_3H_7NO_2 \rightarrow MNO_2+C_3H_7$	NR	NR	NR	-
$M+CCl_3NO_2 \rightarrow MO+CCl_3NO$	-	-	F	-

[a] I: it proved impossible to study this reaction due to experimental difficulty; NR: no product signal observed, $Q_R < \sim 1Å^2$; F: weak product signal observed, $\sim 1Å^2 < Q_R < \sim 5Å^2$; R: strong product signal observed, $Q_R > \sim 5Å^2$.

1. R. R. Herm, S.-M. Lin, and C. A. Mims, J. Chem. Phys. 57, 3099 (1972); 58, 327, 1983 (1973); J. Phys. Chem. 77, 569, 2931 (1973).
2. The alkali atom results are reviewed in: J. L. Kinsey, MTP International Review of Science, edited by J. C. Polanyi (Butterworths, London, 1972), Physical Chemistry Series One, Vol. 9, Chap. 6.

2. PHOTODISSOCIATION OF NaBr, NaI, AND KI VAPORS AND COLLISIONAL QUENCHING OF $Na^*(3^2P)$, $K^*(4^2P)$, AND $K^*(5^2P)$ BY FOREIGN GASES

Boyd L. Earl and Ronald R. Herm

Since the earliest observations by Wood, there have been many studies of the gas phase collisional quenching of the first excited ^2P configuration of alkali atoms by rare gases and simple molecules. However, only a few studies have examined the quenching of these configurations by more complex molecules, and there are very few data available on the quenching of higher energy configurations. In our own laboratory, this prompted a program of examining the quenching of $Na^*(3^2P)$, $K^*(4^2P)$, and $K^*(5^2P)$ by a variaty of molecules in order to gain further insight into the mechanism of these quenching collisions.

Experimentally, alkali halide (MX) vapor in a heated quartz cell was photodissociated at a particular ultraviolet wavelength so as to produce the alkali atom in a particular excited configuration (M^*), and the M^* resonance fluorescence emitted at a right angle to the incident ultraviolet flux was measured. Upon admission of a foreign gas at a known pressure to the cell, the cross

section (Q_q) for collisional quenching of M* was calculated from the Stern-Volmer relation and the measured foreign gas attenuation of the M* fluorescence. Table I lists values of Q_q which were measured in this work. For a given quenching gas, the entries in this table indicate that: (1) $Q_q(Na^*3^2P)$ and $Q_q(K^*4^2P)$ are of comparable magnitude and (2) $Q_q(K^*5^2P) > Q_q(K^*4^2P)$ for Class I and II molecules, the increase being particularly dramatic for Class I.

Table I. Measured Quenching Cross Sections.[a]

	$Na^*(3\ ^2P)$	$K^*(4\ ^2P)$	$K^*(5\ ^2P)$
	CLASS I		
CH_4	< 1	< 1	60
CD_4	-	-	40
C_2H_6	< 1	-	98
C_2D_6	-	-	70
CF_4	< 1	< 1	25
H_2O	3	2	84
D_2O	< 1	-	91
	CLASS II		
H_2	8	3	12
D_2	8	3	11
N_2	-	-	60
HCl	-	-	100*
DCl	-	-	100*
CO_2	68*	-	-
CH_3OH	25	24	110
CF_3Cl	100*	95*	170
CH_3CN	110*	-	-
C_2H_4	69*	51	77
C_2D_4	-	-	79
C_6H_6	110*	-	-
	CLASS III		
SO_2	150*	140	-
Br_2	230*	-	-
I_2	290*	260*	50*

[a]All cross sections are given in Å^2 and refer to a temperature of ~ 900°K. An asterisk indicates that, for this quenching system, Q_q was actually measured versus relative collision speed, g, and the Q_q value quoted refers to a collision with $g=(8kT/\pi\mu)^{1/2}$. All other values were measured for thermal speed distributions.

Collisional quenching of excited alkali atoms has often been discussed in terms of the "electron transfer model" which pictures the transfer of an electron from M* to the quenching molecule at a relatively large reactant separation given, in lowest order, by

$$R_c = e^2/(\Delta - E^*) ,$$

where E* is the excitation energy of M* and Δ is the asymptotic energy of the ion pair (i.e., the ionization potential of M minus the electron affinity of the quenching molecule). Although alternate explanations might be devised for any particular phenomenon, this model provides a language whereby the contrasting behaviors exhibited by Classes I, II, and III as well as the observed isotope effects may be rationalized. In particular, the dramatic decrease in Q_q which is observed for I_2 on proceeding from $K^*(4^2P)$ to $K^*(5\ ^2P)$ is particularly easily explained. The electron affinity of I_2 is quite large so that R_c is quite large for the $K^*(4\ ^2P)+I_2$ collision, consistent with the large Q_q value which is observed. For $K^*(5\ ^2P)+I_2$, however, $E^* > \Delta$, so that no quenching should occur in the lowest order electron transfer picture, consistent with smaller observed Q_q value.

3. ENERGY DEPENDENCE OF SENSITIZED FLUORESCENCE: $Hg^* + Tl \rightarrow Hg + Tl^*$

Ronald R. Herm and Lambert C.-H. Loh

Cario and Franck[1] first demonstrated the phenomenon of sensitized fluorescence experimentally when they observed emission from excited Tl levels upon irradiation of an Hg-Tl vapor mixture by the 2537 Å Hg resonance line. Despite many studies since then, however, the transfer of excitation from Hg* to Tl (or any other atom) is not reliably characterized quantitatively because of uncertainties regarding the presence of metastable mercury species as well as diatomic molecules (HgTl and/or Hg_2*) in the fluorescence cell. This prompted a crossed atomic beams measurement in our laboratory of the dependence on relative collision speed, g, of the cross section, $Q_{rel}(g)$, for transfer of electronic excitation from Hg* to Tl.

Experimentally, a beam of $Hg^*(^3P_0)$ and

$Hg^*(^3P_2)$ metastable states (produced in an approximate 1:5 ratio by electron bombardment excitation of an Hg beam) was crossed at a right angle by a Tl beam which had previously passed through a slotted-disk-velocity selector. Since any Tl levels which might be collisional excited have short ($\sim 10^{-7}$ - 10^{-8} sec) radiative lifetimes, they must radiate before leaving the collision zone defined by the two intersecting beams. Consequently, the cross section for collisional production of the Tl 5350 Å emission line was measured by focusing the emission originating in the beam collision zone through an interference filter which isolated the 5350 Å line and onto a photomultiplier tube. Figure 1 indicates that the 5350 Å Tl line corresponds to emission from $Tl^*(7s\ ^2S_{1/2})$ so that the 5350 Å emission observed might arise from direct collisional production of $Tl^*(7s\ ^2S_{1/2})$ or from collisional production of higher energy Tl level which relaxes to the ground state via a cascade emission process populating $Tl^*(7s\ ^2S_{1/2})$.

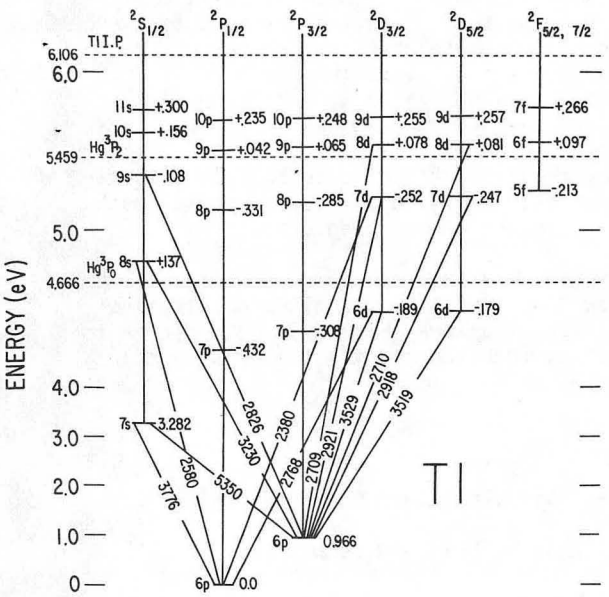

Fig. 1. Thallium energy level diagram. All energies are given in electron volts. For Tl levels below 4 eV, the energy above the ground state is indicated; for higher levels, the difference between the Tl level and nearest metastable Hg level is given. The three dashed lines indicate the $Hg^*(^3P_0)$ and $Hg^*(^3P_2)$ energies and the ionization potential of Tl. Diagonal lines indicate prominent reported mercury-sensitized emission lines of Tl (in Å). (XBL 709-6672)

Figure 2 presents the measured cross section as a function of relative collision speed. The dotted curve shown in Fig. 2, in conjunction with the energy levels in Fig. 1, illustrates that the measured cross section (at least at smaller g values) must correspond to production of a Tl^* level which is lower in energy than the parent Hg^* level. Moreover, oscillator strengths for the Tl lines indicate a very low probability of production of $Tl^*(7s\ ^2S_{1/2})$ intermediate during radiative relaxation of a ^2D or ^2F level. Thus, the cross section shown in Fig. 2 must refer to the collision process:

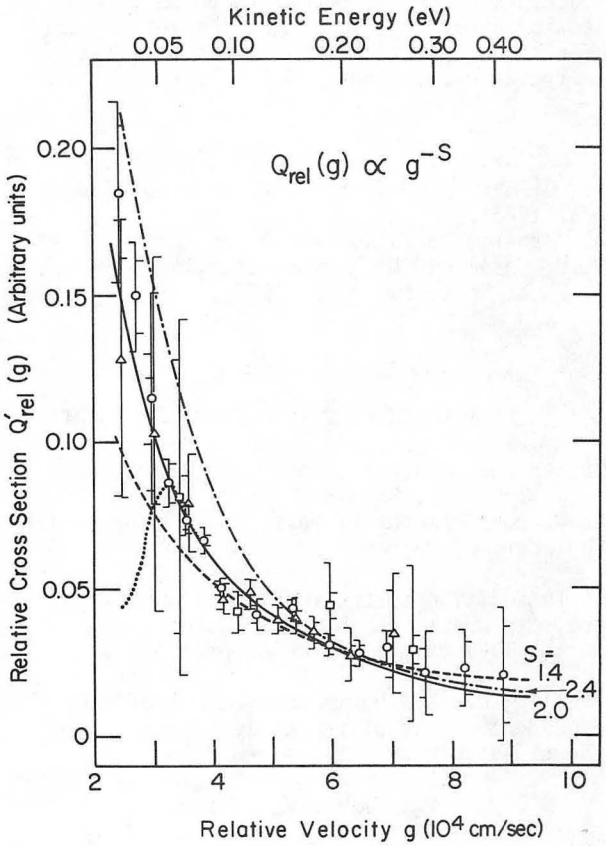

Fig. 2. Data points show measured cross section for 5350 Å Tl emission versus relative collision speed. Solid, dashed, and dot-dashed curves show fits to the data obtained by convoluting cross sections of the form g^{-s} over the experimental distribution in g. The dotted curve (which joins the solid curve at higher g) shows a similar convoluted result for a cross section which is zero below 0.042 eV [the $Tl^*(9p\ ^2P_{1/2})$-$Hg^*(^3P_2)$ energy difference] and varies as g^{-2} at higher kinetic energies. (XBL 7311-6728)

$$Hg^*(^3P_o \text{ and/or } ^3P_2) + Tl(6p^2P_{1/2}) \rightarrow Hg(^1S_o) + Tl^*(ns^2S_{1/2} \text{ and/or } mp^2P_{1/2,3/2}) , \quad (1)$$

with n=7,8, and/or 9 and m=7 and/or 8. Figure 2 indicates that $Q'_{rel}(g)$ varies approximately as g^{-2} over the range in g examined, a considerably steeper speed dependence than has been observed in previous measurements of the low-energy behavior of electronically inelastic cross sections.[2] This observed g^{-2} dependence suggests a model wherein reaction (1) may take place if the reactants manage to penetrate to an interatomic separation, R_x, under the influence of a strongly attractive force (potential energy at R_x of about - 0.5 eV).

---

1. G. Cario and J. Franck, Z. Phys. 17, 202 (1923).
2. Previous work is referenced in: M. E. Gersh and E. E. Muschlitz, Jr., J. Chem. Phys. 59, 3538 (1973).

4. COLLISION DYNAMICS INVOLVING METAL ATOMS

Richard Behrens, Jr., Andrew Freedman, Lara A. Gundel, Ronald R. Herm, Lambert C.-H. Loh, Timothy P. Parr, and Charlotte M. Sholeen

In addition to the results of specific projects described above, work continued during 1973 on the following projects.

(1) A crossed beams measurement of the dependence on relative collision speed of the cross section for the reaction

$$Hg^*(^3P_2)+MX \rightarrow HgX + M^*(^2P) ,$$

where

MX = NaBr and NaI. (LC-HL)

(2) A study of the mercurous halide electronic chemiluminescence which is observed upon irradiation of a vapor mixture of Hg and a diatomic halogen at 2537 Å. (LAG)

(3) Crossed beams studies of the reactions of Li and Na with Br_2 and other molecules, employing a combination of magnetic deflection and slotted-disk-velocity analysis to analyze the products. (CMS and LAG)

(4) Crossed beams studies of reactions involving the alkaline earth dihalides (MX_2). Thus far, these studies have demonstrated that halogen atoms are exchanged under single-collision conditions and with large reactive cross sections (1-100 Å^2) for the following collision partners: (1) BaF_2 + BCl_3 and (2) BaI_2 + Cl_2 and HCl. (RB, AF, and TPP)

5. RESEARCH PLANS FOR CALENDAR YEAR 1974

Ronald R. Herm

Since this research program is to be terminated, the thrust of our 1974 efforts will be the completion of continuing projects. In addition, however, we plan the following exploratory studies.

(1) The crossed beams apparatus which is being employed to study Li and Na reactions provides for simultaneous magnetic deflection and velocity analysis of scattered species. As such, it comprises a mass spectrometer for paramagnetic neutral species. We plan to exploit this feature of the instrument by searching for species such as Li_2X and LiX_2 (X is a halogen atom) formed as products of chemical reactions or under equilibrium conditions. Although neither type of molecule has been experimentally observed in the gas phase, both species have been predicted to exist.

(2) The crossed beams apparatus which was employed to study reactions of alkaline earth dihalides (MX_2) will be employed to study reactions of the following species: MX_2, Ca, Al, and OH.

6. 1973 PUBLICATIONS AND REPORTS

Ronald R. Herm and Associates

Journals

1. Shen-Maw Lin, Charles A. Mims, and Ronald R. Herm, Crossed Beams Chemistry: Reactions of Ba, Sr, Ca, and Mg with Cl_2 and Br_2, J. Chem. Phys. 58, 327 (1973) (LBL-1126).

2. Charles A. Mims, Shen-Maw Lin, and Ronald R. Herm, Crossed Beams Product Angular Distributions: MCl and MI from Ba, Sr, Ca, and Mg + ICl and BaCN and BaBr from Ba + BrCN, J. Chem. Phys. 58, 1983 (1973) (LBL-1134).

3. Shen-Maw Lin, Charles A. Mims, and Ronald R. Herm, Crossed-Beams Reactions of Barium, Strontium, and Calcium with Some Halides of Methane, J. Phys. Chem. 77, 569 (1973)(LBL-1175).

4. Boyd L. Earl and Ronald R. Herm, Collisional Quenching of $K^*(4p\ ^2P)$ and $K^*(5p\ ^2P)$ by H_2O, CF_4, and CH_4, Chem. Phys. Letters 22, 95 (1973)(LBL-1824).

5. Ronald R. Herm, Shen-Maw Lin, and Charles A. Mims, Crossed Beams Chemistry: Reactions of Ba, Sr, and Ca, J. Phys. Chem. 77, 2931 (1973)(LBL-1884).

LBL reports

1. Charles A. Mims, Molecular Beam Chemistry of Alkaline Earth Atoms (Ph.D. thesis), LBL-1159, May 1973.

2. Boyd L. Earl, Photochemical Studies of Alkali Halide Vapors (Ph.D. thesis), LBL-1866, Aug. 1973.

3. Boyd L. Earl and Ronald R. Herm, Photodissociation of NaBr, NaI, and KI Vapors and Collisional Quenching of $Na^*(3^2P)$, $K^*(4^2P)$, and $K^*(5^2P)$ by Foreign Gases, LBL-2500, Dec. 1973 (to be submitted to J. Chem. Phys.).

Harold S. Johnston, Principal Investigator

1. EXPERIMENTAL STUDIES

a. Visible and Ultraviolet Absorption Spectra of Oxides of Nitrogen and Oxy-acids of Nitrogen

Richard Graham and Harold S. Johnston

The object of these studies is to obtain quantitative absorption spectra at temperatures and pressures close to stratospheric conditions (1 to 100 Torr, 200-300°K) for the oxides of nitrogen and related species. Spectra have been obtained for NO_2, N_2O_5, NO_3, HNO_2, and HNO_3. The room temperature spectrum of the nitrate free radical is given as Fig. 1 and that for HNO_2 is Fig. 2.

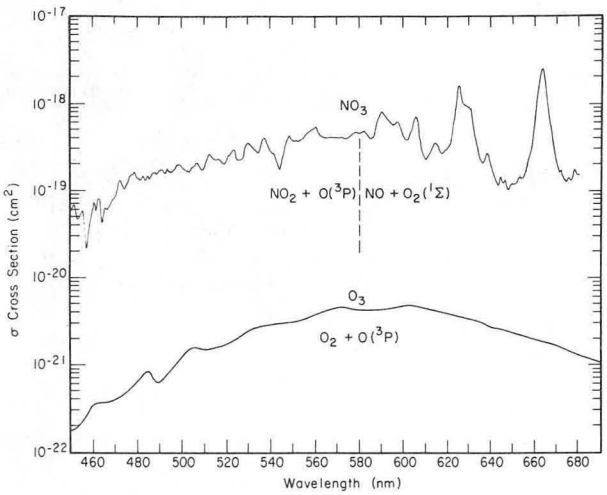

Fig. 1. Light absorption cross section for the NO_3 radical and for ozone in the visible regions of the spectrum. (XBL 738-1683)

b. Quantum Yields for the Photolysis of Nitric Acid Vapor

Shih-ger Chang and Harold S. Johnston

The oxides of nitrogen (NO and NO_2) are active in the stratosphere in the catalytic destruction of ozone. These active nitrogen oxides are partially tied up as nitric acid vapor. Nitric acid is formed from nitrogen dioxide and hydroxyl radicals:

$$HO + NO_2 \xrightarrow{M} HNO_3 \quad . \qquad (1)$$

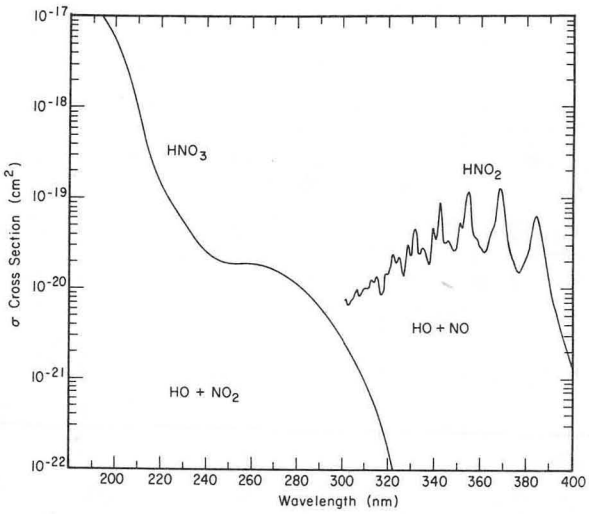

Fig. 2. Ultraviolet absorption cross sections for nitric and nitrous acid. (XBL 738-1786)

It is also destroyed by hydroxyl radicals:

$$HO + HNO_3 \rightarrow H_2O + NO_3 \quad , \qquad (2)$$

and it is destroyed by ultraviolet radiation.

In 1973 we determined the primary products of this photolysis:

$$HNO_3 + h\nu \rightarrow HO + NO_2 \qquad (3)$$

and the primary quantum yield, which is one from 200 to 310 nm.

The overall photolysis of nitric acid is a very complex reaction. Reaction (3) is typically followed by reaction (2), and then dinitrogen pentoxide is formed from the nitrate radical NO_3 and nitrogen dioxide:

$$NO_3 + NO_2 \xrightarrow{M} N_2O_5 \qquad (4)$$

Dinitrogen pentoxide (from Reaction 4) reacts with water (From Reaction 2) on the walls of the vessel to reform nitric acid

$$N_2O_5 + H_2O \xrightarrow{\text{walls}} 2HNO_3 \qquad (5)$$

The net effect of reactions 2, 3, 4, 5 is zero; there is no net chemical change. Actually, a small overall quantum yield of about 0.1 is observed because of secondary

chemical and photochemical reactions of N_2O_5 and NO_2. To obtain the primary quantum yield we add carbon monoxide as a trap for hydroxyl radicals:

$$HO + CO \rightarrow CO_2 + H \qquad (6)$$

and we add oxygen as a trap for the hydrogen atom:

$$H + O_2 + M \rightarrow HOO + M \ . \qquad (7)$$

With proper amounts of CO and O_2 the observed rate of formation of NO_2 or CO_2 gives the primary quantum yield.

When nitric acid is photolyzed in the presence of carbon monoxide and oxygen, about 40 other reactions are possible. Dr. Gary Whitten (see below) has developed a computer program for speedy, accurate solution of simultaneous kinetic equations for a large number of reactions. This program was designed for study of the complex situation in the stratosphere. It has been modified as a convenient method for analyzing complex laboratory reactions. It was used to model the 40 to 50 reactions that can be considered for the nitric acid photolysis. The build-up of the product NO_2 as observed and as calculated by this method is shown in Fig. 1. Conditions were such that most of the 50 reactions were so slow as to be negligible, but the detailed examination of the large set of reactions was a very reassuring way to handle the complex system.

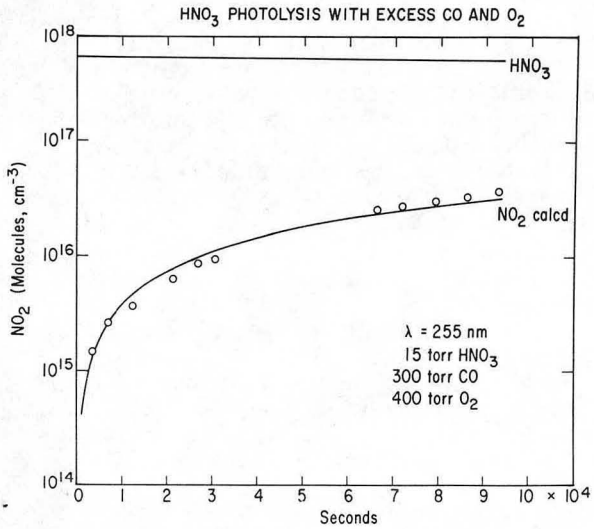

Fig. 1. Observed production of NO_2 in the photolysis of nitric acid in the presence of CO and O_2 and the calculated production of NO_2 on the basis of a 40-step mechanism.
(XBL 737-6392)

c. The Rate of Reaction of Nitrogen Dioxide and Ozone

Richard Graham and Harold S. Johnston

In the natural stratosphere by far the fastest reaction that destroys ozone is the NO_2 catalytic cycle

$$NO + O_3 \rightarrow NO_2 + O_2 \qquad (8)$$

$$\begin{array}{rl} & NO_2 + O \rightarrow NO + O_2 \\ \hline \text{net:} & O_3 + O \rightarrow O_2 + O_2 \ . \end{array} \qquad (9)$$

There is another process that is important in destroying ozone in the lowest stratosphere, the NO_3 catalytic cycle

$$NO_2 + O_3 \rightarrow NO_3 + O_2 \qquad (10)$$

$$NO_3 + h\nu \rightarrow NO + O_2 \text{ (day)} \qquad (11)$$

$$\begin{array}{rl} & NO + O_3 \rightarrow NO_2 + O_2 \\ \hline \text{net:} & 2O_3 + \text{red light} \rightarrow 3O_2 \ . \end{array} \qquad (12)$$

We have measured the rate of the $NO_2 + O_3$ reaction from 230 to 300°K; results are given by Table I. The reaction was followed by ultraviolet or visible absorption by ozone and by nitrogen dioxide. The overall thermal reaction is (10) followed by (4). The ratio of loss of NO_2 to loss of O_3 was 1.9±0.1, indicating some unknown side reaction other than (10) and (4).

Table I. Experimental conditions and rate constants for the reaction $NO_2 + O_3 \rightarrow NO_3 + O_2$.

T (°K)	No. of runs	k (10^{-17} cm^3 molecule^{-1} sec^{-1})
298.0	10	3.49
288.0	4	2.51
278.0	8	1.80
268.0	12	1.38
258.0	13	0.905
248.0	12	0.621
238.0	16	0.433
231.2	6	0.314

$k = (1.32 \pm 0.11) \times 10^{-13} \exp(-4900 \pm 40/RT)$ cm^3 molecule^{-1} sec^{-1}.

d. The Quantum Yield of Singlet Oxygen from Ozone Photolysis

Douglas Martin, John Girman, and Harold S. Johnston

When ozone absorbs visible or ultraviolet radiation, it dissociates to an oxygen molecule and an oxygen atom. The electronic state of the oxygen atom varies with wavelength:

$$O_3 + h\nu \text{ (above 320 nm)} \rightarrow O_2 + O\ (^3P)\ , \qquad (13)$$

$$O_3 + h\nu \text{ (below 300 nm)} \rightarrow O_2 + O\ (^1D)\ . \qquad (14)$$

Between 300 and 320 nm there is a mixture of $O(^3P)$ and $O(^1D)$. Singlet oxygen atoms are the key to both HO_x and NO_x chemistry in the stratosphere:

$$O(^1D) + H_2O \rightarrow 2HO\ , \qquad (15)$$

$$O(^1D) + N_2O \rightarrow 2NO\ . \qquad (16)$$

Sunlight is rapidly attenuated by ozone below 310 nm. In order to calculate the rates of reactions (15) and (16), especially in the lower stratosphere and troposphere, one must have the detailed quantum-yield curve for formation of $O(^1D)$ as a function of wavelength between 300 and 320 nm.

We have measured the quantum yield for formation of singlet oxygen atoms by the highly sensitive method of photon counting, based on the following series of reactions:

$$O_3 + h\nu \rightarrow O_2 + O(^1D)\ , \qquad (14)$$

$$O(^1D) + N_2O \rightarrow 2NO\ , \qquad (16)$$

$$NO + O_3 \rightarrow O_2 + NO_2^*\ , \qquad (12^*)$$

$$NO_2^* \rightarrow NO_2 + h\nu \text{ (red)}\ . \qquad (17)$$

Preliminary results are given in Table II.

Table II. Preliminary results for quantum yield to form $O(^1D)$ from ozone (298°K).

λ (nm)	No. of runs	Φ ($O\ ^1D$)
280	7	0.99
285	4	0.99
290	8	1.00
295	4	1.04
300	11	1.00
302	4	0.90±0.03
304	4	0.97±0.03
306	4	0.91±0.02
308	4	0.78±0.03
310	8	0.48±0.01
312	4	0.34±0.02
314	4	0.29±0.01
316	6	0.18±0.01

e. Reactivity of Hydroxyl Radicals as a Function of Vibrational Energy State

Jere Streit and Harold S. Johnston

Hydrogen atoms are produced in a microwave discharge and mixed with low-pressure ozone in a large stainless steel tank. The hydrogen atoms react with ozone to produce vibrationally excited hydroxyl radicals:

$$H + O_3 \rightarrow O_2 + HO\ (v \leqslant 9)\ .$$

These excited radicals are deactivated to lower vibrational states and they react with ozone:

$$HO(v) + O_3 \rightarrow HOO + O_2$$
$$\rightarrow H + O_2 + O_2\ .$$

The relative concentration of hydroxyl radicals is followed by visible-light emission for vibrational transitions where $\Delta v = 3$. From these data we have obtained information about the rate of deactivation of the highly vibrationally excited molecules and the rate of reaction of HO with O_3 as a function of vibrational state of HO.

2. THEORETICAL STUDIES

a. Model Calculations of Stratospheric Ozone, Including Atmospheric Motions

Gary Whitten and Harold S. Johnston

The total problem of air motions and photochemistry in the stratosphere is exceedingly complicated. However, it is not necessary to solve the total problem in order to get definite answers for certain limited questions. We have posed the following limited question: Are the pure air reactions

and air motions sufficient to account for the global ozone balance? Note the restrictions on this question: it does not ask about the distribution of ozone within the stratosphere, only the global balance; and it asks only if a set of four chemical reactions are sufficient. These reactions are:

$$O_2 + h\nu \text{ (below 242 nm)} \rightarrow O + O \,, \qquad (a)$$

$$O + O_2 + M \rightarrow O_3 + M \,, \qquad (b)$$

$$O_3 + h\nu \text{ (vis. and u.v.)} \rightarrow O_2 + O \,, \qquad (c)$$

$$O_3 + O \rightarrow O_2 + O_2 \,. \qquad (d)$$

We take the world as motions and photochemistry prepared it--with respect to temperature, air concentration, and ozone concentration. We consider sunlight above the atmosphere, and we calculate the distribution of radiation as a function of wavelength, elevation (1 km grid), longitude (15° grid), the latitude (5° grid). With this distribution of radiation we calculate the instantaneous (per second) rates of the four "pure air" reactions listed above at 43,200 volume elements over the globe, automatically including all hours of the day. Reactions (a) and (b) form ozone, reactions (c) and (b) determine the concentrations of oxygen atoms, and reaction (d) destroys ozone. We integrate these rates of formation and destruction of ozone over the entire stratosphere of the earth. The integral of the transport of ozone over the volume of the stratosphere is simply the rate of transport of ozone across the boundary of the stratosphere, and this transport has been measured by others. A typical value of global balance of ozone formation and destruction is:

ozone formation	500×10^{29} molecules sec^{-1}
transport to troposphere	6×10^{29} molecules sec^{-1}
destruction by $O + O_3$	86×10^{29} molecules sec^{-1}
unbalanced ozone production	408×10^{29} molecules sec^{-1}

If this unbalanced production of ozone continued for two weeks, the total ozone of the Earth would double. "Something else" besides pure air and atmospheric motions is responsible for 80% of the natural destruction of stratospheric ozone.

We have examined the proposal that this great discrepancy could be due to experimental error in our knowledge of the incoming solar radiation, the absorption spectrum of O_2 or O_3, or the rate constants for the chemical reactions. We have taken the National Bureau of Standards' estimate of the standard deviation of each of these five quantities, and we carried out Monte Carlo calculations that randomly deal in various magnitudes of error for each of the five quantities. Two hundred such calcalations gave a standard error of 83×10^{29} molecules sec^{-1} for the entire calculation. Thus to the 95% confidence level, "something else" besides pure air chemistry and air motions accounts for $(408\pm186)\times10^{29}$ molecules sec^{-1} of natural ozone destruction.

The "water reactions," that is, the reactions of the free radicals H, HO, and HOO were found to account for 56×10^{29} molecules sec^{-1}. This calculation used 1973 values of the rate constants for these reactions.

The oxides of nitrogen would be sufficient to account for the remaining destruction of ozone if nitric oxide, per se, is present in the stratosphere at about 4×10^{8} molecules cm^{-3}. A recent observation of NO between 17 and 35 kilometers by Ackerman and co-workers found NO to vary between 2 and 8×10^{8} molecules cm^{-3}. (Some other less extensive measurements have found NO values higher and lower than these). Thus it appears highly probable that the oxides of nitrogen in the present natural stratosphere destroy between two-thirds and three-quarters of the ozone that is produced. Thus the oxides of nitrogen appear to be a major factor in the natural ozone balance.

There are many estimates of the rate of formation of the oxides of nitrogen in the natural stratosphere, and these rates are approximately equal to the rate of injection of oxides of nitrogen into the stratosphere by 500 supersonic transports. Thus, 500 SST promise more or less to double on the global scale a very active stratospheric ingredient.

b. The Effect of Nuclear Bomb Tests (1952-62) on Stratospheric NO_x and Ozone

John Birks, Gary Whitten, and Harold S. Johnston

Foley and Ruderman[1] calculated the amount of nitric oxide that would be produced by nuclear bombs exploded in the atmosphere. This work was extended by Johnston, Whitten, and Birks,[2] by Gilmore,[3] and by Goldsmith et al.[4] The high temperature in the nuclear explosion fixes large amounts of nitric oxide from air, and the rising mushroom cloud transports much of it into the stratosphere,

if the energy of the bomb is one megaton or more. Although nitric oxide from the bombs was not measured, strontium-90, excess carbon-14, and other radioactive substances were measured in the stratosphere for many years after the termination of large-scale tests in 1962. From the observed distribution of carbon-14 in the stratosphere, one can infer the NO_x (NO, NO_2, and HNO_3) distribution (Figs. 1, 2, and 3). Most of the nuclear explosions occurred at the USSR site above the arctic circle. The average NO_x distribution over the northern hemisphere was $(2\pm1)\times10^{15}$ molecules cm^{-2}, and less than one-tenth of this in the southern hemisphere. The average natural NO_x distribution is about $(1\pm0.5)\times10^{16}$ molecules cm^{-2}. From these distributions of bomb-produced NO_x, we calculated a 5±2% reduction of ozone. Chang and co-workers[5] calculated the maximum reduction of ozone from the nuclear bombs to be 4%.

Although the quantity of ozone found in the atmosphere by the nuclear bomb tests of 1961-62 was large, the distribution was not conducive to a large reduction of ozone. At and above the dashed lines in Figs. 1, 2, and 3 the photochemical ozone replacement time is 4 months or less; at and below the heavy solid line the photochemical ozone replacement time is 10 years or longer. Relatively little NO_x from the nuclear bombs overlapped the "ozone source region." Thus the percentage reduction of ozone is at most a few percent, whereas the same quantity of NO_x spread between 20 and 30 km in the tropical stratosphere would have had a much greater impact on the ozone.

Casual inspection of the historical ozone data (Goldsmith et al.[4]) showed no large or conspicuous changes of ozone during or after the large-scale nuclear tests 1952-62. On the other hand it was only in the late 1950's or early 1960's that there were enough ozone-observing stations to give even an approximate estimate of total global or hemispheric ozone. The history of world-wide ozone before 1957-58 is largely lost for lack of data. The history of ozone during the 1960's,

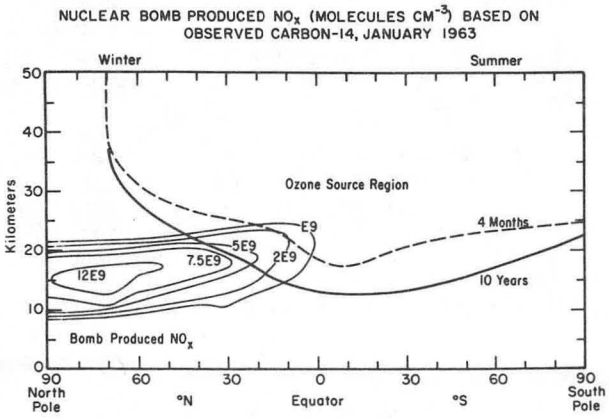

Fig. 1. Distribution of artificial NO_x ($NO + NO_2 + HNO_3$) in the stratosphere at the conclusion of large-scale atmospheric nuclear bomb tests (1952-62) on the basis of 1.0×10^{32} molecules of NO per megaton of bomb yield. The distribution is derived from observed carbon-14. The lines show the depth of penetration of ozone-producing sunlight: --- local ozone replacement time 4 months; ___ local ozone replacement time 10 years. The "ozone source region" is regarded as that where photochemical ozone replacement occurs within 4 months or at a faster rate.
(XBL 7310-5514)

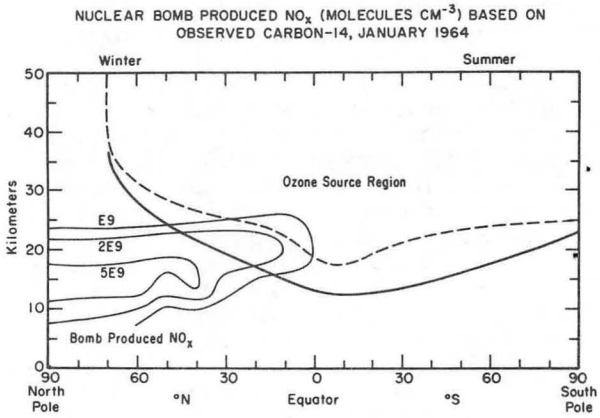

Fig. 2. One year after Fig. 1.
(XBL 7310-5513)

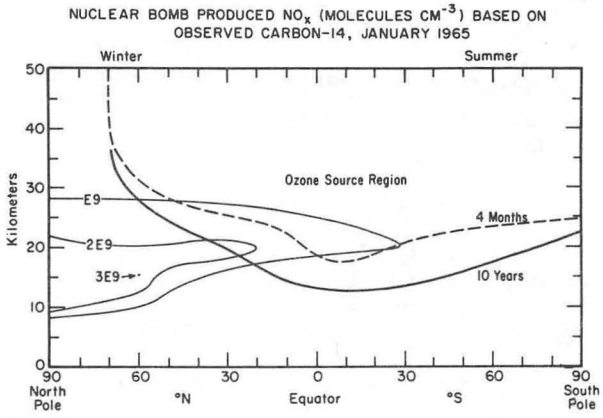

Fig. 3. Two years after Fig. 1.
(XBL 7310-5512)

however, shows a distinct, statistically significant increase in ozone. Komhyr et al.[6] analyzed the total ozone data from about a dozen selected stations for the period 1961-70, and they found a statistically significant increase of ozone at most stations, averaging about 5%. Johnston et al.[2] applied Komhyr's method to all of the stations of the world for the period 1960-70, inclusive. No significant trends were found in the southern hemisphere, but a statistically significant increase of ozone of 5±1.2% was found for the northern hemisphere for the period 1963-70, inclusive. London and Kelley[7] analyzed all data for total ozone from 1957 through 1970. They found no significant trend in the southern hemisphere. In the northern hemisphere London and Kelley report a decrease (-2.4±0.8%) over the period 1957-61 and an increase of 11±2.3% over the decade 1961-70. (The observed minimum was in 1961 although this time is uncertain by 2 or 3 years in terms of scatter of the data and the phase of the quasi-biennial cycle.)

Although the reason for the increase of ozone during the 1960's is debatable, it has been proposed (Johnston et al.[2]) that some or all of this increase may be due to the stratosphere returning to normal after the cessation of large-scale bomb tests in 1962. (All work partially supported by DOT.)

---

1. H. M. Foley and M. A. Ruderman, Stratospheric Nitric Oxide Production from Past Nuclear Explosions and Its Relevance to Projected SST Pollution, J. Geophys. Res. 78, 4441 (1973).
2. H. S. Johnston, G. Whitten, and J. Birks, The Effect of Nuclear Explosions on Stratospheric Nitric Oxide and Ozone, J. Geophys. Res. 78, 6107 (1973).
3. F. R. Gilmore, The Production of Nitrogen Oxides by Low Altitude Nuclear Explosions, preprint, Institute for Defense Analysis, July 1973.
4. P. Goldsmith, A. F. Tuck, J. S. Foot, E. L. Simmons, and R. L. Nelson, Nitrogen Oxides, Nuclear Weapons Testing, Concorde, and Stratospheric Ozone, Nature 244, 545 (1973).
5. J. S. Chang, A. C. Hindmarsh, and N. K. Matsen, Simulation of Chemical Kinetics Transport in the Stratosphere, Lawrence Livermore Report UCRL-74823 (Oct. 1973).
6. W. D. Komhyr, E. W. Barrett, G. Slocum and H. K. Weickman, Atmospheric Ozone Increase During the 1960's, Nature 232, 390-391 (1971).
7. J. London and J. Kelley, Global Trends in Atmospheric Ozone, preprint, 1973.

3. RESEARCH PLANS FOR CALENDAR YEAR 1974

Harold S. Johnston

We plan to find the quantum yield and primary photochemical products during the photolysis of the NO_3 radical

$$NO_3 + h\nu \rightarrow NO + O_2 \text{ above 578 nm,}$$

$$NO_3 + h\nu \rightarrow NO + O_2$$

$$\text{or } NO_2 + O \text{ below 578 nm .}$$

The role of the reaction, $NO_2 + O_3 \rightarrow NO_3 + O_2$, in reducing ozone depends on the products and quantum yield of the NO_3 photolysis. We plan to obtain quantum yields and primary products for the photolysis of N_2O_5 and N_2O_4. The low-temperature spectra of NO_2 and N_2O_4 should be completed next year.

The production and the photolysis of nitrous acid vapor (HNO_2) will be studied. The kinetics of the reaction $NO + NO_2 + H_2O$ will be followed, and the presumed reaction $HOO + NO_2 \rightarrow HNO_2 + O_2$ will be investigated. These reactions are of possible importance in the global ozone balance.

We hope soon to finish the study of the quantum yield of $O(^1D)$ from the photolysis of ozone.

Recently it has appeared that other man-made pollutants may have an impact on the global ozone shield. The oxides of chlorine are somewhat more active in destroying ozone than the oxides of nitrogen. The oxides of chlorine may reach the stratosphere either directly (perchlorate oxidizers from the space shuttle and other solid rocket fuels) or indirectly (chlorinated hydrocarbons and freons used at the Earth's surface). We expect to return to consideration of chlorine oxide reactions.

4. 1973 PUBLICATIONS AND REPORTS

Harold S. Johnston and Associates

Journals

1. H. S. Johnston and R. A. Graham, Gas Phase Ultraviolet Spectrum of Nitric Acid Vapor, J. Phys. Chem. 77, 62 (1973)(LBL-1179).

2. H. S. Johnston and G. Whitten, Instantaneous Photochemical Rates in the Global Stratosphere, Pure and Appl. Geophys. 106, 1468 (1973).

3. H. S. Johnston, G. Whitten, and J. Birks, The Effect of Nuclear Explosions on Stratospheric Nitric Oxide and Ozone, J. Geophys. Res. 78, 6107 (1973)(LBL-1421 Rev.).

4. A. B. Harker and H. S. Johnston, Photolysis of Nitrogen Dioxide to Produce Transient O, NO_3, and N_2O_5, J. Phys. Chem. 77, 1153 (1973)(LBL-1425).

Papers presented

1. H. S. Johnston and G. Whitten, Reactions of Ozone and Nitrogen Oxides at High Altitudes, AGARD Conference on Atmospheric Pollution by Aircraft Engines, London, England (April 1973).

2. H. S. Johnston, Photochemistry in the Stratosphere--with Applications to Supersonic Transports, National Meeting of American Chemical Society, Chicago, Ill. (Aug. 1973); LBL-2217. Submitted to Astronautica Acta.

3. H. S. Johnston and R. A. Graham, Photochemistry of NO_x and HNO_x Compounds, The Second General Scientific Assembly of the International Association of Geomagnetism and Aeronomy, Kyoto, Japan (Sept. 1973); LBL-2249.

LBL reports

1. Harold S. Johnston and Shih-Ger Chang, Photolysis of Nitric Acid Vapor, LBL-1865, July 1973. (to be published in J. Phys. Chem.)

2. D. R. Martin, Kinetics of Sulfur Dioxide Florescence (Ph.D. thesis), LBL-1199, March 1973.

Bruce H. Mahan, Principal Investigator

1. DYNAMICS OF THE O^+-H_2 REACTION: REACTIVE SCATTERING AT RELATIVE ENERGIES ABOVE 15 eV*

Keith T. Gillen, Bruce H. Mahan, and John S. Winn

We have studied the reaction $O^+(H_2,H)OH^+$ and its isotopic variants by determining the velocity vector distribution of products for initial relative energies above 15 eV. The non-reactive scattering of O^+ by the various isotopic hydrogen molecules also has been determined. Figure 1 shows that at the higher relative energies, much of the non-reactive scattering of O^+ can be explained by a model in which the O^+ makes a collision with a free hydrogen or deuterium atom. That is, the collision is so impulsive that in large measure the effects of molecular binding can be ignored.

We have extended this impulse model to reactive collisions, and have compared its predictions with experiment. In this case, for the general reaction A(BC,C)AB, A hits B impulsively, B makes an impulsive elastic collision with C, and the molecule AB is formed if, as a result of these impulses, the energy of A relative to B is less than their binding energy. The molecule AC can also be formed from this sequence of collisions.

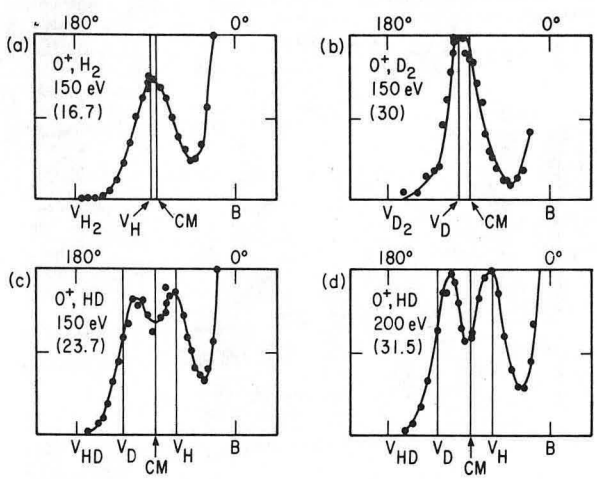

Fig. 1. Profiles of the intensity of O^+ scattered along the 0°-180° axis in the barycentric system of the atom and diatomic molecule. The label B locates the O^+ beam velocity; CM, the velocity of the center-of-mass; V_{H_2}, the velocity of O^+ scattered elastically from H_2; V_H, the velocity of O^+ scattered from a free H atom, and similarly for V_{D_2} and V_D. (a) 150 eV (lab) O^+ scattered from H_2. (b) 150 eV O^+ scattered from D_2. (c) 150 eV O^+ scattered from HD. (d) 200 eV O^+ scattered from HD. (XBL 737-6493)

We have made Monte Carlo calculations of the angular distribution of reaction products predicted by this sequential impulse model. Figure 2 shows a comparison of one of these calculated angular distributions with experimental data. For the reaction $O^+(HD,D)OH^+$, product formation can occur by two sequences. In the first case, O^+ hits H, H hits D, and O^+ and H combine to form OH^+. As shown in Fig. 2, this sequence is responsible for most of the small angle reactive scattering. In the second type of sequence, O^+ hits D, D hits H, and O^+ and H combine. This sequence is responsible for essentially all of the large angle scattering. The sum of the two processes is in reasonable agreement with the experimental distribution of products. The deviations between experiment and theory can be rationalized in terms of the very simple hard sphere potential surface used in the calculation. Thus the sequential impulse model provides a reasonably accurate description of the reaction dynamics at these hyperthermal energies.

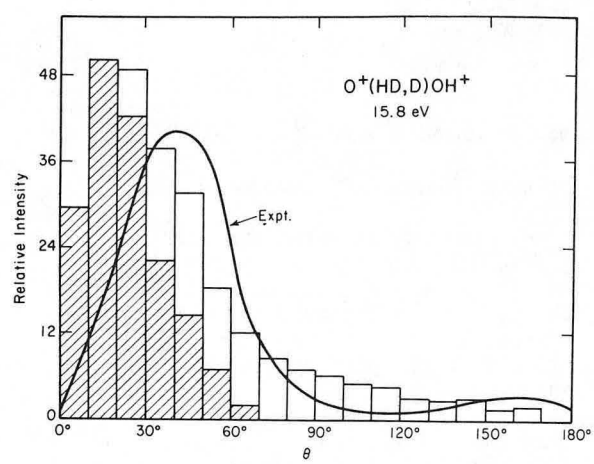

Fig. 2. Experimental and calculated angular distributions for the $O^+(HD,D)OH^+$ reaction at 15.8 eV initial relative energy. The histogram gives the results of a complete 3-dimensional sequential impulse model calculation. The shaded bars represent reaction with the atom first struck by the projectile, and the open bars represent the contribution from reaction with the second or trailing atom. (XBL 735-6132A)

*Abstracted from a paper to appear in J. Chem. Phys. (LBL-1886).

2. ANALYTICAL TREATMENT OF THE SEQUENTIAL IMPULSE MODEL FOR CHEMICAL REACTION

Bruce H. Mahan

We have developed an analytical treatment which allows one to predict the energy and angular distribution of reaction products using the sequential impulse model for chemical reactions. The treatment makes it clear how the relative masses of the H and D atoms in such reactions as $O^+(HD,D)OH^+$, $O^+(HD,H)OD^+$ control the angular and energy distributions of the isotopic products. It also makes clear the fact that the spectator stripping process which is observed so frequently in high-energy reactions is most likely to occur when a reactant diatomic molecule is oriented perpendicularly to the initial reactive velocity vector. In addition, it shows that stabilization by forward recoil of reaction products after high relative energy collisions will only be observed for exoergic reactions in which the exoergicity is released as product repulsion. In general, the model shows that the most obvious features of high-energy reactions can be deduced from the most rudimentary features of the potential energy surfaces.

3. DYNAMICS OF THE C^+-H_2 REACTION*

Bruce H. Mahan and Thompson M. Sloane

We have investigated the reaction $C^+(H_2,H)CH^+$ and its isotopic variants at relative energies ranging from 2 to 14 eV. The results have proved to be an important test of our ability to use the electronic properties of reactants, products, and intermediates to predict reaction dynamics. A representative product velocity vector distribution is shown in Fig. 1. The distribution is nearly symmetric about the ±90° axis in the barycentric system, which indicates that there is a strong attractive interaction between all three atoms in the collision complex before the products separate. As the initial relative energy is increased, the symmetry of the distribution about ±90° diminishes. At relative energies of 5 eV and above, the distributions are distinctly peaked at 0°, the direction of the primary C^+ beam.

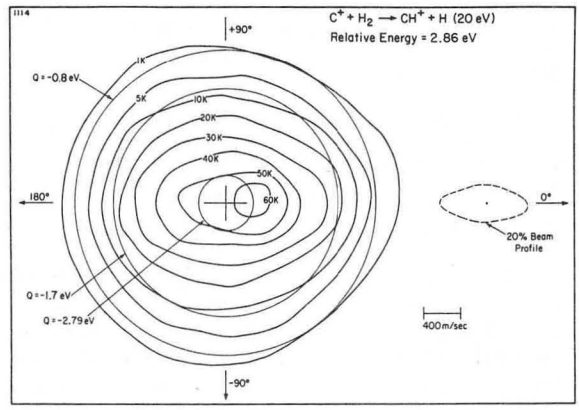

Fig. 1. A contour map of the intensity of CH^+ as a function of barycentric scattering angle and speed obtained from collisions with an initial relative energy of 2.86 eV. Note the symmetry of most of the intensity contours about the ±90° axis. (XBL 739-1810)

This general behavior indicates that the potential energy surface for the reaction has a "well" or depression which is accessible to reactants and products. Figure 2 is an electronic state correlation diagram which was constructed by using only experimental facts and ab initio calculations which pertain to reactants, products, and the symmetric intermediate CH_2^+. The major

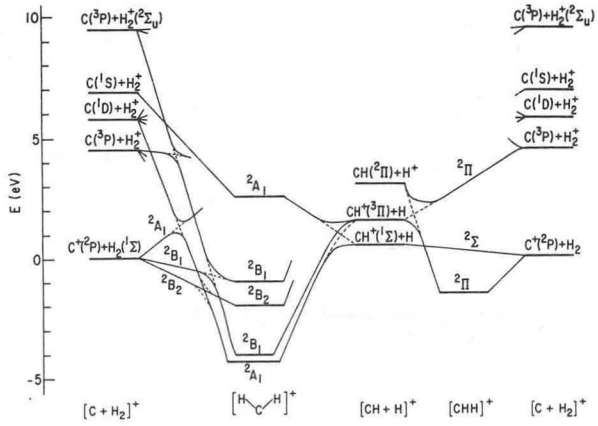

Fig. 2. A correlation diagram for the electronic states of the CH_2^+ system in its linear and isosceles-triangle conformations. At the left, C^+ approaches H_2 along the perpendicular bisector of the bond. At the right, C^+ approaches H_2 collinearly. Reactant, intermediate, and product electronic states are correlated using the considerations of electronic symmetry and molecular orbital configurations. (XBL 737-6443)

qualitative features of this diagram have since been verified by the ab initio self-consistent field and configuration interaction calculations performed by Schaefer and co-workers.[1] The correlation diagram shows that the potential energy well which corresponds to symmetric CH_2^+ can be reached from the reactants by collisions in which the C^+ approaches H_2 approximately along the perpendicular bisector of the H_2 bond. After strong interaction of all three atoms, the product CH^+ can be formed either in its ground electronic state $^1\Sigma$, or the low-lying $^3\pi$ state. Reaction via a path which involves nearly collinear CH H^+ is also possible, and would lead at the higher relative energies to product velocity vector distributions which are asymmetric about the ±90° line. Thus the technique of predicting reaction dynamics qualitatively from correlation diagrams based only on known properties of reactants, products, and intermediates is highly successful in this case, and very promising in general.

---

*Abstracted from a paper to appear in J. Chem. Phys. (LBL-1869).

1. D. H. Liskow, C. F. Bender and H. F. Schaefer, private communication.

4. LARGE ANGLE INELASTIC SCATTERING OF Na^+ BY D_2*

William L. Dimpfl and Bruce H. Mahan

We have measured the inelasticity of the large angle scattering of Na^+ by D_2, HD, and H_2 in the initial relative energy range 0.7 - 16.9 eV. Interpretation of the experimental data and analysis of the mechanics of these collisions using both simple models and exact trajectory calculations shows that perpendicular (C_{2v}) rather than collinear conformations of the Na^+-D_2 system produce the most intense inelastic scattering. Figure 1 shows exact trajectories for collinear Na^+-D_2 collisions calculated assuming an exponential repulsion between

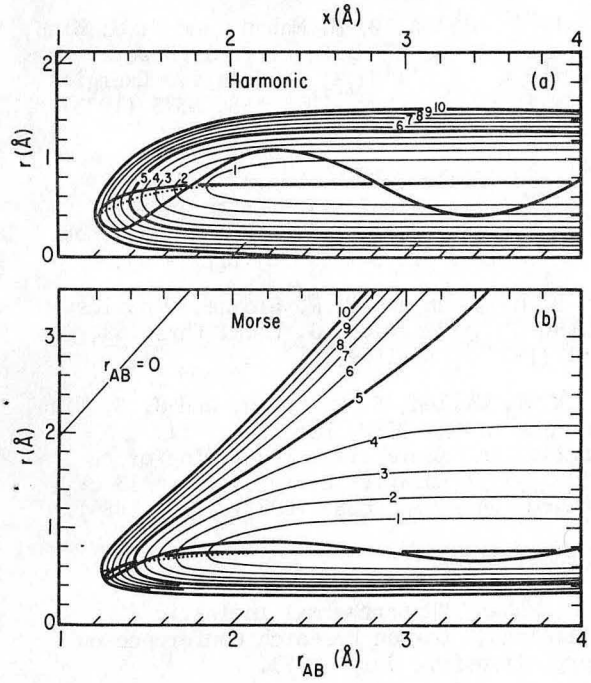

Fig. 1. Exact trajectories for the collinear collisions of Na^+ with D_2 at 10 eV initial relative energy. The potential energy contours are labeled in eV. The ordinate gives the oscillator internuclear separation, while the abscissa gives the separation of Na^+ from the nearest deuterium atom (r_{AB}), or the distance between Na^+ and the D_2 center-of-mass (x). (XBL 7311-5582)

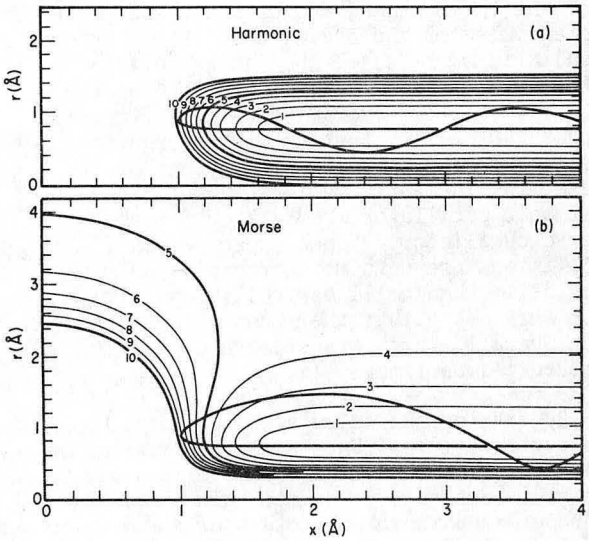

Fig. 2. Exact trajectories for the collisions of Na^+ with D_2 in the C_{2v} conformation at an initial relative energy of 10 eV. The ordinate is the D_2 internuclear separation, and the abscissa is the distance of Na^+ from the D_2 center-of-mass. The potential energy contours are labeled in eV. Note that in the Morse oscillator case, the initial phase of the collision induces an expansion of the oscillator which is not reversed until the collision partners are well separated. In the harmonic case this contraction occurs sooner, and some of the energy transiently in vibration is transferred back to translation. (XBL 7311-5583)

Na^+ and the D atoms, and harmonic and Morse potentials for the oscillator. For the more realistic Morse case, the inelasticity $\Delta E = 0.17$ eV, only a small fraction of the initial relative energy of 10 eV. Figure 2 shows that this situation is reversed for collisions in the C_{2v} conformation. In this case, the inelasticity is 1.6 eV for the harmonic oscillator, and 2.7 eV for the Morse oscillator. Since these perpendicular collisions are both more probable and more inelastic than collinear collisions, it is not surprising that their contribution to the overall energy transfer rate is of greatest importance.

By fitting the calculated inelastic energy spectrum of Na^+ to the experimental data at several initial relative energies, we have been able to deduce values for the strength and range parameters of an exponential repulsive potential for the Na^+-D_2 system.

*Abstracted from a paper submitted to J. Chem. Phys. (LBL-2530).

5. DYNAMICS OF THE N^+-H_2 REACTION AT LOW ENERGIES

James A. Fair and Bruce H. Mahan

We have completed construction of an apparatus which allows us to determine the velocity vector distributions of the ionic products of ion-molecule reactions carried out with projectile ion energies between 5 and 20 eV in the laboratory system. This apparatus thus allows us to extend the range of our collision dynamics experiments to significantly lower energies than has been previously possible in our laboratory.

The initial experiments with this apparatus have been on the reaction $N^+(H_2,H)NH^+$. The electronic state correlation diagram for this system shows that there are three potential energy surfaces available to the ground state reactants. One of these surfaces leads via a conical intersection to symmetric NH_2^+ in its $^3B_1$ ground electronic state. This state of NH_2^+ lies 6 eV below the reactants and products, so one would expect to observe the symmetric scattering pattern for NH^+ which is associated with strongly interacting collision complex with weak interactions between NH^+ and the freed H atom. At relative energies below 1 eV, symmetric scattering patterns are observed which indicate that at low relative energies, the system enters the deep potential energy well which corresponds to symmetric NH_2^+. Attempts are now being made to interpret these results in terms of the nature of conically intersecting potential energy surfaces.

6. RESEARCH PLANS FOR CALENDAR YEAR 1974

Bruce H. Mahan

We will continue to develop our analytical treatment of the sequential impulse model of chemical reactions in order to be able to apply it to systems with increasingly realistic potential energy surfaces. Our program of relating reaction dynamics to the electronic structure of reactant and products will continue as we complete investigations of the $N^+(H_2,H)NH^+$ reaction, and undertake studies of the $F^+(H_2,H)HF^+$ and $Cl^+(H_2,H)HCl^+$ reactions. We are also developing a method of obtaining the absorption spectra of polyatomic gaseous ions which, if successful, should greatly expand our understanding of the electronic properties and geometric structure of gaseous ions.

7. 1973 PUBLICATIONS AND REPORTS

Bruce H. Mahan and Associates

Journals

1. K. T. Gillen, B. H. Mahan, and J. S. Winn, Dynamics of the O^+-H_2 Reaction I. Reactive Scattering of $O^+(^4S_{3/2})$ at Relative Energies below 15 eV, J. Chem. Phys. 58, 5373 (1973) (LBL-1429).

2. K. T. Gillen, B. H. Mahan, and J. S. Winn, Impulsive Inelastic Scattering of $O^+(^4S)$ by Isotopic Hydrogen Molecules, Chem. Phys. Letters 22, 344 (1973) (LBL-1850).

3. B. H. Mahan and T. M. Sloane, Dynamics of the C^+-H_2 Reaction, J. Chem. Phys. 59, 5661 (1973) (LBL-1869).

4. K. T. Gillen, B. H. Mahan, and J. S. Winn, Dynamics of the O^+-H_2 Reaction. II: Reactive and Nonreactive Scattering of $O^+(^4S_{3/2})$ at Relative Energies Above 13 eV, J. Chem. Phys. 59, 6380 (1973) (LBL-1886).

Paper presented

B. H. Mahan, "Hyperthermal Inelastic Collisions," Gordon Research Conference on Energy Transfer, July 1973.

LBL reports

1. John S. Winn, A Beam Study of Ne^+ and $O^+(^4S_{3/2})$ Scattering by Molecular Hydrogen Isotopes and Helium (Ph.D. thesis), LBL-1820, June 1973.

2. William Lawrence Dimpfl, The Dynamics of Nonreactive Inelastic Ion-Molecule Collisions (Ph.D. thesis), LBL-1873, Aug. 1973.

3. K. T. Gillen, B. H. Mahan, and J. S. Winn, Dynamics of the O^+-H_2 Reaction. II: Reactive and Nonreactive Scattering of $O^+(^4S_{3/2})$ at Relative Energies Above 13 eV, J. Chem. Phys., in press (LBL-1886, Sept. 1973).

William H. Miller, Principal Investigator

1. IMPROVED CLASSICAL PATH APPROXIMATION FOR THE BOLTZMANN DENSITY MATRIX*

William H. Miller

A semiclassical approximation for the Boltzmann density matrix has been developed which is easily applicable and includes a large fraction of quantum effects non-perturbatively. The equilibrium density $\rho(\underset{\sim}{q}_1)$, for example,

$$\rho(\underset{\sim}{q}_1) \equiv \langle \underset{\sim}{q}_1 | e^{-\beta H} | \underset{\sim}{q}_1 \rangle \quad ,$$

is given within this model by

$$\rho(\underset{\sim}{q}_1) = h^{-N} \int d\underset{\sim}{p}_1 \exp[-\frac{2}{\hbar} \int_0^{(1/2)\hbar\beta} d\tau \, H(\tau)], \quad (1)$$

where

$$H(\tau) = H[\underset{\sim}{p}(\tau), \underset{\sim}{q}(\tau)]$$

is the Hamiltonian for the system of N degree of freedom:

$$H(\underset{\sim}{p}, \underset{\sim}{q}) = \sum_{i=1}^{N} p_i^2/2m_i + V(\underset{\sim}{q}) \quad ;$$

the "trajectory" $\underset{\sim}{q}(\tau)$, $\underset{\sim}{p}(\tau) \equiv \underset{\sim}{q}'(\tau)/m$ is determined by the classical-like equations of motion (note the sign change)

$$m_i \ddot{q}_i(\tau) = + \frac{\partial V(\underset{\sim}{q})}{\partial q_i} \quad ,$$

with intial conditions

$$\underset{\sim}{q}(0) = \underset{\sim}{q}_1$$
$$\dot{q}_i(0) = p_i/m_i \quad .$$

In the high-temperature limit ($\beta \to \infty$) it is easy to see that Eq. (1) becomes the standard classical expression

$$\rho(\underset{\sim}{q}_1) = h^{-N} \int d\underset{\sim}{p}_1 \exp[-\beta H(\underset{\sim}{p}_1, \underset{\sim}{q}_1)] \quad .$$

If Eq. (1) is expanded in powers of $\hbar$, one can show that the first quantum correction is given exactly correctly by Eq. (1); in applications, of course, one would not wish to make such an expansion, however, since the classical path approximation contains a large fraction of the quantum effects to infinite order in $\hbar$.

---

*Abstracted from J. Chem. Phys. 58, 1664 (1973).

2. POTENTIAL CURVES AND INELASTIC CROSS SECTIONS FOR LOW-ENERGY COLLISIONS OF O^+ AND He*

Stuart D. Augustin, William H. Miller, Peter K. Pearson, and Henry F. Schaefer

Potential curves corresponding to all the valence states of HeO^+ have been calculated by configuration interaction and are shown in Fig. 1. The principal inelastic process in low-energy collisions of ground state He and O^+ is seen to be

$$He + O^+(^4S) \to He + O^+(^2D) \quad , \qquad (1)$$

the transition arising from a spin-orbit interaction of the lowest $^4\Sigma$ and $^2\Pi$ states of HeO^+. Other observations that one can make from Fig. 1 are that (1) the ^2D state of O^+ will be readily quenched by collisions with He, but not the ^2P state; (2) low-energy collisions of He^+ with ground state oxygen atoms will lead to charge transfer exclusively into the ^2P state of O^+:

$$He^+ + O(^3P) \to He + O^+(^2P) \quad ;$$

(3) the ^1D state of O should be readily de-activated by He^+:

$$He^+ + O(^1D) \to He^+ + O(^3P) \quad ;$$

and (4) the ^1S state of O should be quenched by He^+ only via charge transfer into the ^4P state of O^+ (of the valence-excited configuration $2s2p^4$):

$$He^+ + O(^1S) \to He + O^+(^4P) \quad .$$

The spin-orbit interaction causing the transition in Eq. (1) was determined and the cross section calculated semiclassically; this is shown in Fig. 2.

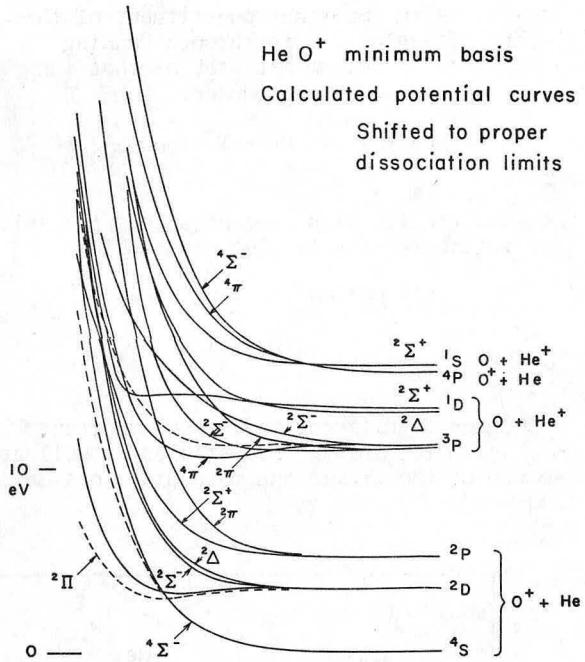

Fig. 1. Potential curves arising from the valence states of He and O^+, and He^+ and O, shifted vertically to match the known atomic energy levels at infinite separation. (XBL 7210-4234)

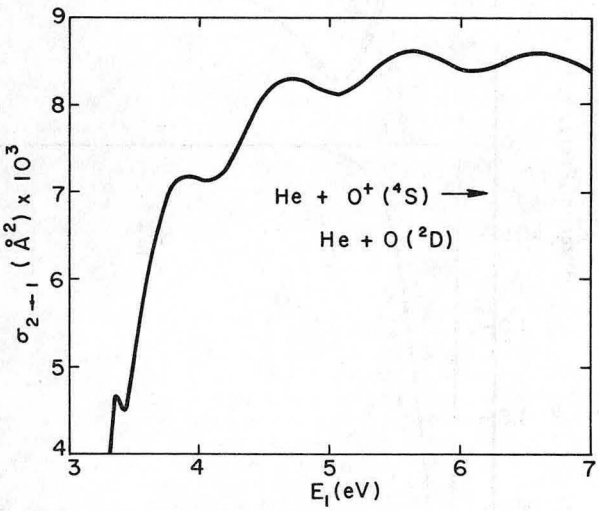

Fig. 2. The inelastic cross section for He + $O^+(^4S) \rightarrow$ He + $O^+(^2D)$, as a function of initial collision energy. (XBL 7210-4233)

*Abstracted from J. Chem. Phys. 58, 2845 (1973).

3. PARTIAL AVERAGING IN CLASSICAL S-MATRIX THEORY: VIBRATIONAL EXCITATION OF H_2 BY He*

William H. Miller and Andrew W. Raczkowski

Within the framework of a general semiclassical theory[1] that combines exact classical dynamics with the quantum principle of superposition it is shown how a certain averaging procedure allows one to treat some degrees of freedom in a completely classical sense while others are quantized semiclassically. This enormously simplifies the application of the theory to three-dimensional collision systems and also has an interesting formal structure: the quantum-like degrees of freedom are quantized semiclassically via use of double-ended boundary conditions, while the unquantized classical-like degrees of freedom enter only through a phase space average over their initial coordinates and momenta. Many of the aspects of the theory can thus be carried out in the same manner as standard classical trajectory calculations.

In practice, only the vibrational degrees of freedom need be quantized semiclassically, there typically being enough rotational states involved for their distribution to be treated completely classically. Figure 1 shows our preliminary results for vibrational excitation of H_2 by helium:

$$He + H_2(n_1=0,\ j_1=0) \rightarrow He + H_2(n_2=1,\ \text{all } j_2),$$

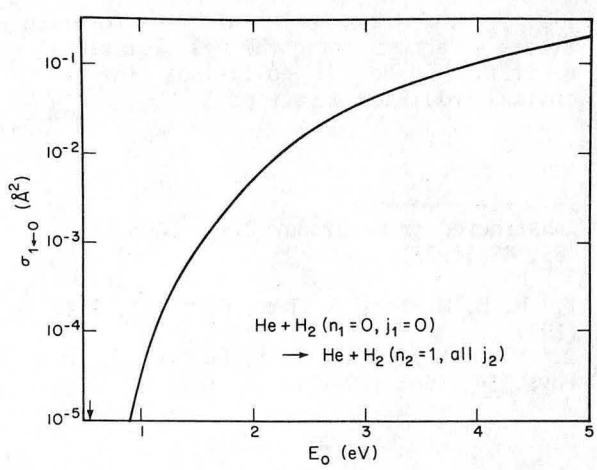

Fig. 1. The cross section for excitation of H_2 (by collision with He) from its ground state ($n_1=j_1=0$) to its first excited vibrational state ($n_2=1$), summed over all final rotational states, as a function of initial collision energy. (XBL 7312-7113)

where n and j denote the vibrational and rotational state of H_2. Over this entire energy region the vibrational excitation is "classically forbidden" so that complex-valued classical trajectories[2] are required to describe it. Figure 2 shows the distribution of final rotational states for the transition at a collision energy of 3 eV; although $j_2=0$ is the most probable final rotational state, it is seen that there is considerable rotational excitation which accompanies the 0→1 vibrational transition.

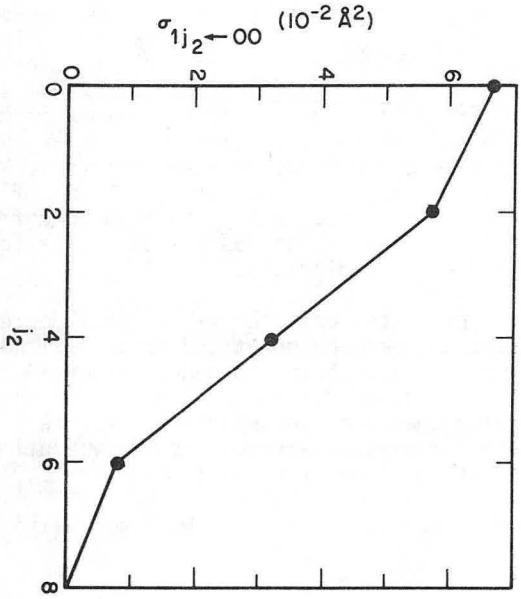

Fig. 2. The distribution of final rotation states j_2 accompanying the 0→1 vibrational excitation in He + H_2 collisions, for an initial collision energy of 3 eV.
(XBL 7312-7114)

*Abstracted from Faraday Disc. Chem. Soc. 55, 45 (1973).

1. W. H. Miller, J. Chem. Phys. 53, 1949 (1970).
2. W. H. Miller and T. F. George, J. Chem. Phys. 50, 5668 (1972).

4. PENNING AND ASSOCIATIVE IONIZATION OF TRIPLET METASTABLE HELIUM ATOMS†

Barbara J. Garrison, William H. Miller, and Henry F. Schaefer

The triplet metastable state of helium, $1s2s^3S$, is an important constituent of the helium afterglow; it is through Penning ionization by helium metastables that ions of other species are produced.

$$He^* + X \rightarrow He + X^+ + e^- .$$

At sufficiently high concentrations the self-destruction of the triplet metastable--

$$He^* + He^* \rightarrow He + He^+ + e^-$$
$$\rightarrow He_2^+ + e^-$$

--becomes significant and is an important mechanism for loss of metastables as well as source of the atomic and molecular ions He^+ and He_2^+.

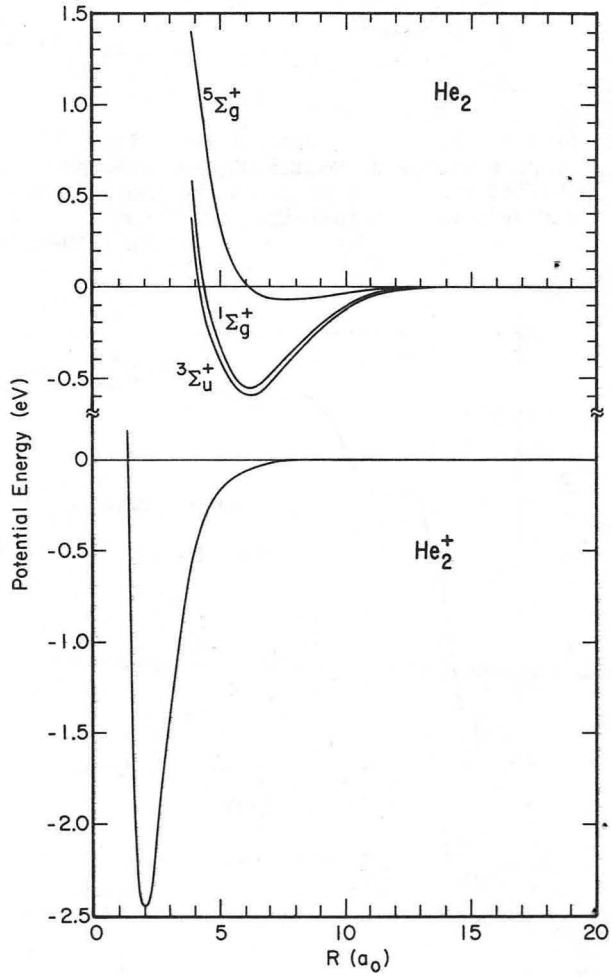

Fig. 1. Potential energy curves for the ground state of He_2^+ and the states of He_2 which arise from two $1s2s^3S$ atomic states.
(XBL 735-6092)

Potential energy curves for the $^1\Sigma_g^+$, $^3\Sigma_u^+$, and $^5\Sigma_g^+$ states which arise from two triplet metastable helium atoms have been calculated by a large configuration interaction expansion and are shown in Fig. 1. From the potential curves for the $^1\Sigma_g^+$ and $^3\Sigma_u^+$ autoionizing states, cross sections for Penning and associative ionization have been calculated; the results are shown in Fig. 2.

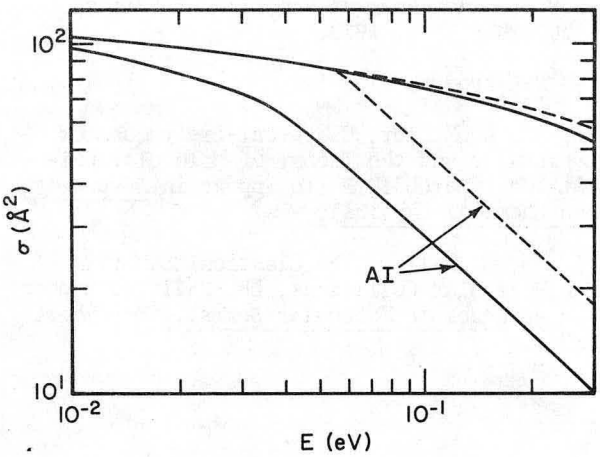

Fig. 2. The total ionization cross section (top curves) for the collision of two triplet metastable helium atoms, and the component of which leads to He_2^+ (lower curves labeled AI), as a function of the relative collision energy. The dashed curves are the results given by the orbiting model. (XBL 735-6081)

In this low-energy region the orbiting model is adequate for determining the total ionization cross section but not the partitioning between associated and dissociated product ions.
(All work partially funded by NSF.)

---

†Abstracted from J. Chem. Phys. 59, 3193 (1973).

5. RESEARCH PLANS FOR CALENDAR YEAR 1974

William H. Miller

One area for which our semiclassical collision theory makes a particularly significant contribution is the description of vibrational excitation on three-dimensional collision systems. Vibrational transitions are often too weak for a completely classical treatment to be meaningful, but the large number of rotational states which exist precludes an accurate quantum mechanical calculation. The situation is thus ideal for the partial averaging approach (see item No. 3), and we plan to pursue its application to at least a few different physical systems.

Classical S-matrix theory also makes it possible to study--without introducing any dynamical approximations--tunneling in chemical reactions with activation barriers. Since completely classical calculations are usually adequate for reactions without activation barriers, the inability to treat reactions with activation barriers is the principal gap in the theory of thermal energy kinetics. In light of these dynamically exact calculations it should also be possible to develop simple models which contain the essential features of the exact description.

Another large class of collision phenomena that we are actively engaged in involve electronic transitions in molecular collisions. As a prototype of the fine-structure transitions in F atoms which can take place in the reaction

$$F + H_2 \rightarrow FH + H ,$$

we are looking at fine-structure transitions in F caused by collisions with rare gas atoms, e.g.,

$$F(^2P_{1/2}) + Xe \rightarrow F(^2P_{3/2}) + Xe \quad .$$

Semiclassical scattering theory provides an excellent description of these processes.

Preliminary work has also begun on unimolecular reactions with the idea of exploring the relation between statistical and dynamical theories of these processes.

6. 1973 PUBLICATIONS AND REPORTS

William H. Miller and Associates

Journals

1. J. D. Doll, T. F. George, and W. H. Miller, Complex-Valued Classical Trajectories for Reactive Tunneling in Three-Dimensional Collisions of H and H_2, J. Chem. Phys. 58, 1343 (1973) (LBL-1153).

2. W. H. Miller, Improved Classical Path Approximation for the Boltzmann Density Matrix, J. Chem. Phys. 58, 1664 (1973) (LBL-1122).

3. S. A. Augustin, W. H. Miller, P. K. Pearson, and H. F. Schaefer, Potential Curves and Inelastic Cross Sections for Low Energy Collisions of O^+ and He, J. Chem. Phys. 58, 2845 (1973)(LBL-1187).

4. W. H. Miller and A. W. Raczkowski, Partial Averaging in Classical S-Matrix Theory; Vibrational Excitation of H_2 by He, Faraday Disc. Chem. Soc. 55, 45 (1973) (LBL-1427).

5. B. J. Garrison, W. H. Miller, and H. F. Schaefer, Penning and Associative Ionization of Triplet Metastable Helium Atoms, J. Chem. Phys. 59, 3193 (1973) (LBL-1825).

Chapters in books

1. T. F. George and W. H. Miller, Classically Forbidden Collision Processes, in Energy, Structure, and Reactivity, edited by D. W. Smith and W. B. McRae (Wiley, New York, 1973), p. 76 (LBL-2273).

2. W. H. Miller, Semiclassical Methods in Reactive and Non-Reactive Collisions, in The Physics of Electronic and Atomic Collisions (invited papers of the VIIIth International Conference on the Physics of Electronic and Atomic Collisions, Belgrade), 1973 (LBL-1839).

Papers presented

1. W. H. Miller, The Classical S-Matrix for Molecular Collisions, Symposium on Topics in Inelastic and Reactive Molecular Collisions, Weizmann Institute of Science, Rehovot, August 21, 1973.

2. W. H. Miller, lecturer on Semiclassical Scattering Theory, German Summer School on the Theory of Atomic and Molecular Collisions, Gars am Inn, Federal Republic of Germany, September 2-15, 1973.

LBL reports

1. W. H. Miller, Classical-Limit Quantum Mechanics and the Theory of Molecular Collisions, March 1973 (to appear in Advances in Chemical Physics).

2. W. H. Miller, The Classical S-Matrix in Molecular Collisions, LBL-2521 (to appear in Advances in Molecular Beams). December, 1973.

Rollie J. Myers, Principal Investigator

1. MOLECULAR FIELD EFFECTS IN ELECTRON PARAMAGNETIC RESONANCE SPECTROSCOPY

Michael R. St. John and Rollie J. Myers

The molecular field model has been very successful in explaining the bulk magnetic properties of many solids. In our work we have applied it to the situation of an ion substituted into a host lattice. In this way we have been able to determine values for the electron exchange interaction between the host and substituted ions.

One host lattice has been the tetragonal form of $NiSeO_4 \cdot 6H_2O$, and we have substituted Cu^{2+}, Co^{2+}, and Mn^{2+} into a few of the sites occupied by $Ni(H_2O)_6{}^{2+}$. At 1.3°K the EPR spectra of the substituted ions are shifted by the interactions with the surrounding Ni^{2+}. The molecular field model allows us to account for most of this shift by exchange interaction with the four nearest neighbor Ni^{2+}. We assume an isotropic exchange interaction of the form

$$H(\text{exch.}) = -2J\bar{S}(Ni)\cdot\bar{S}(X) .$$

The field shifts can be measured in terms of altered g values. The corrected g values are expected to be close to those in the diamagnetic $ZnSeO_4 \cdot 6H_2O$. Table I shows the effect of the corrections and the J value obtained for each ion.

One can see that as the substituted ion has more unfilled t_{2g} orbitals the net exchange interaction with Ni^{2+} decreases. For Mn^{2+} one has three unfilled t_{2g} orbitals which exactly cancels the two unfilled e_g orbitals. In the host lattice all of these interactions occur through water hydrates.

Experiments have also been done in other hosts. In $Ni(BrO_3)_2 \cdot 6H_2O$ the zero-field splittings of the $Ni(H_2O)_6{}^{2+}$ are small and its molecular field would be expected to have large fluctuations even at 1.3°K. No spectra can be observed for Cu^{2+} doped into this lattice from 1.3 to 300°K. For $Co(BrO_3)_2 \cdot 6H_2O$ the very short spin-lattice relaxation times expected for $Co(H_2O)_6{}^{2+}$ at higher temperatures could lead to a narrowing of the line width of a substituted ion. At room temperature a spectrum can be observed for Cu^{2+} in this lattice, but at 77°K it is broadened away. This is in agreement with the expected effect of temperature on the host Co^{2+} spin-lattice relaxation.

2. ELECTRON SPIN RELAXATION FOR $Cu(NH_3)_6{}^{2+}$ IN LIQUID AMMONIA

Richard C. Wilson and Rollie J. Myers

A very careful line width study has been made[1] for $Cu(H_2O)_6{}^{2+}$ in aqueous solution. Despite unresolved hyperfine splittings from Cu, we were able to make accurate line width measurements for each hyperfine component over a wide range of temperatures.

Table I. Molecular field results.

Ion	$g_{\parallel}$ values			$g_{\perp}$ values			Exchange
	Para.[a]	Corr.[b]	Dia.[c]	Para.[a]	Corr.[b]	Dia.[c]	($J\text{-}cm^{-1}$)
Cu^{2+}	2.901	2.431	2.430	2.482	2.091	2.097	0.083
Co^{2+}	6.46	6.02	5.99	3.36	3.18	3.26	0.055
Mn^{2+}	-	-	2.002	2.003	-	2.007	0.00

(a) In $NiSeO_4 \cdot 6H_2O$ or $NiSO_4 \cdot 6H_2O$.

(b) Corrected for molecular field.

(c) In $ZnSeO_4 \cdot 6H_2O$.

However, these data are only approximately fit by the tumbling complex theory developed by Kivelson.[2]

An important variable in line width theory is the viscosity of the solvent. Liquid ammonia is much less viscous than water, so that its viscosity near its freezing point is close to water at its boiling point. For this reason we have made a line width study of Cu^{2+} in liquid ammonia where the principal species is $Cu(NH_3)_6^{2+}$.

We have conducted experiments on isotopically pure (99.62%) ^{63}Cu in liquid ammonia from room temperature down to the freezing point (-77.7°C). The data was digitized and a least squares fit of four Lorentz lines to the data yielded the spectral parameters and the line widths of the hyperfine lines. Spectra were also taken of a frozen glass composed of equal parts of ammonia and tetrahydrofuran. The values of the principal values of the g and A tensors obtained from the glass spectrum were $g_{\parallel}=2.23$, $g_{\perp}=2.04$, $A_{\parallel}=170\times10^{-4}$ cm^{-1}, and $A_{\perp}=5\times10^{-4}$ cm^{-1}.

A qualitative comparison of the water and of the ammonia line widths shows that the high-temperature broadening mechanism which is only partly developed in water is fully developed in ammonia. This broadening is shown in Fig. 1, and it becomes a linear function of temperature over viscosity. This is in agreement with spin-rotation interaction.[3] In water solutions most of the line width is due to a combination of

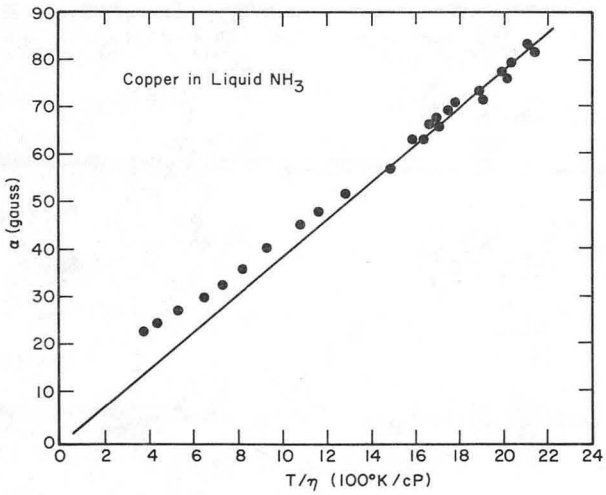

Fig. 1. Shows how the broadening in ammonia approaches a linear function of temperature/viscosity. (XBL 741-5451)

at least two terms. The high-temperature term is explained by the ammonia data, but the second term cannot be explained by the usual[2] theory. The most likely mechanism involves a dynamic Jahn-Teller distortion with a correlation time smaller than that of tumbling. Since an accurate theory has not yet been developed for this mechanism, we shall combine the water and ammonia results to establish the important parameters.

---

1. J. J. Chang (Ph.D. thesis) UCRL-19691.
2. R. Wilson and D. Kivelson, J. Chem. Phys. 44, 154 (1966).
3. R. Atkins and D. Kivelson, J. Chem. Phys. 44, 169 (1966).

3. ELECTRON SPIN RELAXATION FOR $Ni(H_2O)_6^{2+}$ IN SOLUTION

Thomas M. Hynes and Rollie J. Myers

Our work on proton spin relaxation in water solutions of Ni^{2+} has been extended to include measurements at 220 MHz. When these high-field measurements are combined with last year's work at 100 and 60 MHz, we have a broad set of data taken over wide ranges of field and temperature. In acidified solutions the principal mechanism for proton spin relaxation in these solutions is due to the spin-lattice relaxation of the $Ni(H_2O)_6^{2+}$. In this way we have been able to measure the very short electron spin relaxation time of Ni^{2+} in aqueous solution. This relaxation is so fast that no electron spin absorption can be directly measured.

The general theory of spin relaxation predicts that spin-lattice relaxation times must pass through a minimum when the Larmor frequency becomes nearly equal to the inverse of the correlation time of the relaxation, or when

$$\omega \approx 1/\tau_c \ .$$

This is a very general relation which has been found to apply to the previous spin systems which have been studied. For $Ni(H_2O)_6^{2+}$ in solution we find that there is no minimum value in its spin-lattice relaxation, and so this general relation seems to be violated.

This system has the extreme condition in that the electron spin-lattice relaxation time is close to the inverse of the Larmor

frequency when the correlation time is also this small. This condition seems to fall outside of the assumptions of the usual theory, but it is not clear that it should allow the prediction of a minimum in the spin-lattice relaxation time to disappear. Another special circumstance for $Ni(H_2O)_6^{2+}$ is that the principal mechanism for electron spin-lattice relaxation involves thermal modulation of the zero-field splitting.[1] This modulation may not follow the simple exponential decay associated with random thermal motions such as that found for rotational diffusion. It seems likely that either the failure of perturbation theory (strong interactions) or of the usual random fluctuation theory is responsible for the observed absence of a minimum in the spin-lattice relaxation time of $Ni(H_2O)_6^{2+}$.

1. N. Bloembergen and L. O. Morgan, J. Chem. Phys. 34, 842 (1961).

4. ELECTRON-ELECTRON DOUBLE RESONANCE FOR TWO RADICALS IN SOLUTION

Joyce T. Yarnell and Rollie J. Myers

In a double resonance experiment a signal is stored in one set of energy levels and its transmission to a second set is analyzed. The first electron-electron double resonance experiments[1] used a single radical species and analyzed the transfer of signal from one set of nuclear hyperfine levels to another. At low concentrations this transfer was purely intramolecular, and at high concentrations it became dominated by intermolecular exchange interaction between molecules.

We have built an electron-electron double resonance apparatus which has been previously described.[2] Two free radicals are placed in a solution and the frequencies of a bimodal cavity and the magnetic field are adjusted so that high microwave power is absorbed by one radical while the spectrum of the other is being observed. Any signal transferred from one radical to the other must be due to interactions between the two in solution. This interaction can either be due to intermolecular dipole-dipole interaction or to electron-electron exchange. For two identical species the latter is presumed to dominate, but for two different species either could be important. One advantage of the double resonance technique is that the sign of the spectrum change can be used to differentiate between the two interactions.

In Fig. 1 we show a double resonance result. The dotted spectrum is a reference and the solid spectrum shows the effect of 2.5 watts of power at the proper frequency to be absorbed by one radical while the spectrum of the other is being observed. The radical absorbing the high power is a nitroxide radical and the radical whose signal is decreased is called Galvinoxyl free radical. Since power absorbed by one radical caused a decrease in the signal of the other, the primary interaction between the two is electron-electron exchange.

In the near future we would like to examine the concentration dependence of this effect to establish the relative importance of dipole-dipole and exchange interaction in greater detail.

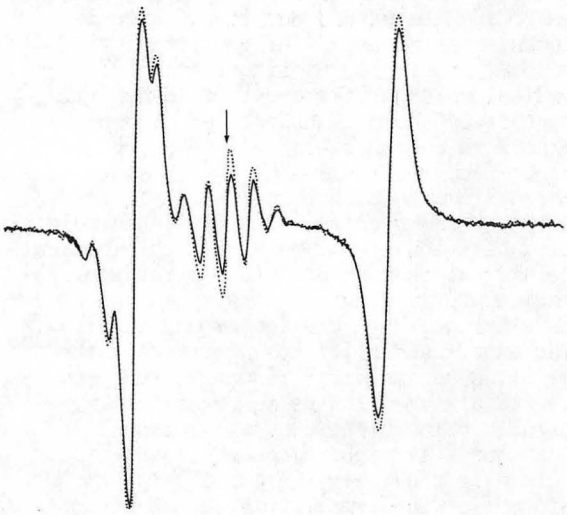

Fig. 1. A double resonance result. Near the arrow in the spectrum there is a large percentage decrease in signal over the dotted reference spectrum. The small percentage decrease shown for the large signals is due to thermal effects caused by the 2.5 watts of additional microwave power used during the solid spectrum. Double resonance can only occur over a narrow region of the sweeping magnetic field, and it is selected by the fixed difference in the two microwave frequencies.

(XBL 741-5450)

1. J. S. Hyde, J. C. W. Chien, and J. H. Freed, J. Chem. Phys. 48, 4211 (1968).
2. J. T. Yarnell and R. J. Myers, IMRD Annual Report for 1971, LBL-425, April 1972.

5. ELECTRON PARAMAGNETIC RESONANCE SPECTRA OF RADICAL ANIONS IN LIQUID AMMONIA

James H. Hammons and Rollie J. Myers

The special properties of liquid ammonia[1] make it a unique solvent for a number of chemical systems. These properties led us a few years ago[2] to develop a system for the production of anion-radicals in liquid ammonia directly in the cavity of an electron paramagnetic resonance spectrometer. At that time our primary attention was drawn to the radical anions of substituted 1,3-butadiene and pyridine.

A preliminary investigation was also made on cyclooctatetraene (COT). We found that it was easily reduced in ammonia and that, unlike other solvents, the dianion had little stability. A number of substituted COT compounds were available to us[3] and so we decided to extend our liquid ammonia techniques to a study of their radical anions. A simple substitution on COT radical anion breaks the twofold orbital degeneracy which is associated with nine electrons in the π-orbitals of a regular eight-membered ring. The ground state of the system can either correspond to one with low odd electron density at the point of substition or to one with high electron density at that point. As a first approximation, the π-electron density is expected to alternate high and low around the ring. The hyperfine splittings observed in the electron paramagnetic resonance spectrum should always allow us to quantitatively establish the electron distribution. In some cases it might also be possible to determine the energy of the first excited state from the temperature dependence of the hyperfine splittings.

We have investigated COT substituted with: F, CH_3, CN, OCH_3, cyclopropyl, and with four symmetrical CH_3 groups. As expected, the CN and CH_3 substitutions resulted in ground states with low and high, respectively, electron densities at the point of substitution. A very careful temperature study was made on several radicals using our accurate least squares fitting method to try to establish the excited-state energy. The data from these experiments are still being reduced and we should be able to determine small deviations from the expected alternation around the ring.

1. W. L. Jolly and C. J. Hallada, UCRL-11254.
2. D. H. Levy and R. J. Myers, J. Chem. Phys. 41, 1062 (1964).
3. Supplied by Prof. A. Streitwieser.

6. RESEARCH PLANS FOR CALENDAR YEAR 1974

Rollie J. Myers

The molecular field model will continue to be investigated. Since Mn^{2+} in $NiSeO_4 \cdot 6H_2O$ has been shown to have so little exchange interaction we will attempt to utilize an ion such as V^{2+} which only has half-filled t_{2g} orbitals. In this way it should be possible to map out the exchange interactions between both the e_g and e_g orbitals and the e_g and t_{2g} orbitals in this lattice. Experiments will also be done on interacting pairs of ions. From the interaction parameters of a pair of ions it should be possible to predict the magnetic properties of a bulk sample made up of a regular lattice of interacting ions.

Our work on electron spin relaxation for Cu^{2+} in both water and liquid ammonia will be continued. Since it seems likely that a dynamic Jahn-Teller interaction is an important mechanism in both of these solvents, special attention will be paid to experiments which will enable us to determine the rate of Jahn-Teller inversion. Some further work may also be done on spin-lattice relaxation for $Ti(H_2O)_6^{3+}$. Our previous work has established the importance of Orbach relaxation for this species, and it is a particularly interesting case for this type of electron spin relaxation.

The electron-electron double resonance data will be analyzed so that the diffusional theory for molecules in solution can be reconciled with the magnitude of the observed double resonance signal. It should be possible to place a lower limit on the size of the exchange interaction between two unlike radicals in solution.

A program will be started on clusters of interacting ions. A number of compounds have been prepared which contain sets of magnetically interacting ions. In some cases these sets should appear to exhibit what is called superparamagnetism. Work will be done on the small clusters formed in Fe^{3+} solutions undergoing hydrolysis. The relation between these clusters and the iron storage protein, ferritin, will be investigated.

7. 1973 PUBLICATION

Rollie J. Myers and Associates

Book

Rollie J. Myers, Molecular Magnetism and Magnetic Resonance Spectroscopy (Prentice-Hall, Inc., Englewood Cliffs, N.J., 1973), 244 pp.

Kenneth S. Pitzer, Principal Investigator

1. SOLUTIONS OF ELECTROLYTES

Kenneth S. Pitzer, Guillermo D. Mayorga, and Janice J. Kim

The general objective of this program is the prediction of the thermodynamic properties of mixed electrolytes with relatively high accuracy from a minimum number of readily measured parameters. The equations were selected in the light of modern statistical theory in a manner such that each parameter has general physical meaning.

The first paper on this work dealt with the selection of the equations and with tests of their effectiveness for pure solutes and mixtures. In the past year the data on all pure aqueous electrolytes at room temperature were critically reviewed and the constants evaluated by least squares. The results for 227 electrolytes with one or both ions univalent were presented in paper II.[1] The equations so determined fit the data substantially within experimental accuracy up to ionic strength of approximately 6 M in most cases. In a few cases the maximum concentration for full accuracy had to be set lower, and in other cases the data extend only to a lower concentration.

The anomalous behavior of 2-2 electrolytes is discussed in paper III[2] together with the advantages and disadvantages of treatments assuming association into ion pairs and higher polymers. It is shown that, for thermodynamic purposes, there are many advantages in avoiding the assumption of association, and that by adding one more term to the equations for other types of solutes, one can obtain satisfactory agreement for 2-2 electrolytes. Parameters are evaluated for the solutes which have been measured and certain special problems are discussed concerning the accuracy of different calculations.

The principal effort in the last few months has been directed toward mixed electrolytes. The available data have been evaluated. We find that it is possible to predict the properties of dilute solutions of mixed electrolytes with good accuracy from the parameters for the pure electrolytes. In most cases mixing terms were found not to be exactly zero (i.e., Bronsted's principle does not hold exactly), but their effect at 1 M is only a few percent in either osmotic or activity coefficient. At higher concentration the effect of mixing terms is proportionately greater. The mixing parameters measure the difference between the short-range interaction of unlike ions of the same sign from the appropriate average of this interaction for like ions. We are studying these results in the hope of drawing theoretical conclusions and developing means for estimating mixing parameters in cases where no measurements exist.

---

1. K. S. Pitzer and G. D. Mayorga, J. Phys. Chem. 77, 2300 (1973).
2. K. S. Pitzer and G. D. Mayorga, LBL-2282, Oct. 1973.

2. NUCLEAR SPIN SPECIES EFFECTS IN THE HEAT CAPACITY OF CH_4

Gerald J. Vogt and Kenneth S. Pitzer

The interconversion of nuclear spin species in CH_4 for $T < 15°K$ will lead to a non-lattice contribution to the heat capacity, if the rate of interconversion is sufficiently rapid. The rate of interconversion can be experimentally increased by doping a CH_4 lattice with a paramagnetic conversion catalyst such as O_2. Recent NMR measurements show that the rate of interconversion increases approximately in proportion to the O_2 concentration ($\leq$ 1 mole %) of the sample.

Measurements of the heat capacity of pure CH_4 (O_2 free) for $T < 30°K$ are being made in search for a possible spin species contribution. Soon, the experiments will begin a new phase by measuring the heat capacity of O_2-doped CH_4 in O_2 concentrations from 0.1 to 1 mole %. Hopefully, the series of experiments will shed light on the extent of interconversion in pure CH_4 as well as the effects of O_2 doping.

3. ANOMALOUS INTERNAL MOTIONS IN MOLECULES

Lawrence S. Bernstein and Kenneth S. Pitzer

Certain molecules have, in addition to several normal vibrations of small amplitude, one or more modes of motion with small restoring force and large amplitude. Internal rotations about single bonds fall into this category but are now well understood. In addition there are other large-amplitude motions which seem anomalous in molecular structure determinations.

A general treatment of large amplitude, multidimensional motion has been developed and applied to the following classes of molecules: MX_3, MX_5, MX_6, MX_7, four-membered rings, and five-membered rings. The theory predicts both the form of the potential governing the motion and a quantitative estimation of the potential from a knowledge of several experimentally observed parameters. These parameters are the force constants for the normal mode involved, the geometry of the molecule in the potential minimum, and the separation of the ground electronic state from the particular excited electronic states which are coupled via the inversion coordinates. The availability of these molecular parameters for most molecules lends a large measure of practicality to this approach, since it removes the need for detailed spectroscopic measurement of a large number of inversion levels.

As a test the theory was applied to a well-studied system--NH_3. Energy levels were calculated from the derived potential by a basis set expansion. The results were close to those of a five-parameter potential, fit to fourteen energy levels. Other known systems were also tested and in all cases close quantitative agreement with the empirical potential was obtained.

This method has been applied to some unusual molecules, the most conspicuous being XeF_6. Theory predicts a potential for three coordinates in XeF_6 which may be transformed to the equivalent of a vibrating diatomic molecule undergoing a slightly hindered rotation. This almost free two-dimensional pseudorotation introconverts XeF_6 through many different configurations, a situation which parallels the first documented pseudorotator-cyclopentane. The potential is being refined to yield quantitative agreement with the experimental entropy and the electron diffraction radial distribution curve. Furthermore, the potential accounts for unusual features found in the infrared and Raman experiments and is also in accord with the results of electric field deflection experiments.

4. RESEARCH PLANS FOR CALENDAR YEAR 1974

Kenneth S. Pitzer

a. Solutions of Electrolytes

The work on the osmotic and activity coefficients of mixed electrolytes at room temperature will be completed. Then we will direct our efforts toward the changes of properties with temperature and pressure which are, of course, related to thermal and volumetric properties, respectively. It is expected that some of this work directed particularly toward the high-temperature and high-pressure area will contribute to and be assisted by the geothermal project at LBL.

b. Nuclear Spin Species of Methane

The heat capacity of solid methane below 15°K shows anomalous properties presumably associated with conversion of nuclear spin species. The heat capacity measurements will continue for pure methane and for methane with controlled amounts of spin conversion catalysts such as oxygen. This should clarify the situation for pure methane, as well as providing information on the catalytic properties.

c. Anomalous Internal Motions in Molecules

The theoretical work on the anomalous internal motion of XeF_6 should be completed. Somewhat similar anomalies are shown by IF_7, ReF_7, VF_5, and possibly certain other pentafluorides, and one or more of these molecules will be studied by appropriate modifications of our present methods.

d. Quantum Chemistry of Heavy Atoms

We expect to initiate theoretical studies of the energy levels and other properties of ions and molecules containing very heavy atoms. Methods now established for molecules with light atoms must be modified to deal with relativistic effects and with the large number of inner shell electrons. Several alternative approaches to these problems will be studied before choosing a plan for detailed calculations.

5. 1973 PUBLICATIONS AND REPORTS

Kenneth S. Pitzer and Associates

Journals

1. K. S. Pitzer, Thermodynamics of Electrolytes. I. Theoretical Basis and General Equations, J. Phys. Chem. 77, 268 (1973)(LBL-846).

2. K. S. Pitzer and G. D. Mayorga, Thermodynamics of Electrolytes. II. Activity and Osmotic Coefficients for Strong Electrolytes with One or Both Ions Univalent, J. Phys. Chem. 77, 2300 (1973)(LBL-1434).

LBL report

1. K. S. Pitzer and G. D. Mayorga, Thermodynamics of Electrolytes. III. Activity and Osmotic Coefficients for 2-2 Electrolytes, LBL-2282, Oct. 1973 (submitted to J. Solution Chemistry).

E. NUCLEAR SCIENCE

Donald R. Olander, Principal Investigator

1. ISOTOPE EXCHANGE OF WATER VAPOR ON PYROLYTIC GRAPHITE

Rajarama T. Acharya, Alan Z. Ullman, and Donald R. Olander

The molecular beam apparatus[1] was modified to facilitate isotope exchange studies with H_2O and D_2O on pyrolytic graphite. This modification consists of a simple "doser" fabricated from a 1/16-in.-o.d. tubing and positioned in the target chamber so as to bathe the target with a continuous flux of D_2O molecules. A modulated molecular beam of H_2O is generated in the usual manner. A further modification was the installation of a low-frequency chopper, consisting of a beam flag attached to a rotary vacuum feed-through operated by a rotary solenoid, in the target chamber. The low-frequency chopper is used for modulation frequencies in the range of 0.01 to 1 Hz.

Since the normal lock-in detection technique has a lower modulation frequency limit of 10 Hz, pulse counting and wave form analysis is used in the low-frequency range. The output from the mass spectrometer is processed by a charge-sensitive pre-amplifier. The pulses are then shaped and amplified by a main amplifier. A lower level discriminator suppresses the rf pickup from the mass spectrometer power supply. A pulse divider is used to bring the pulse rate within range of the multi-scaler (i.e., a multichannel analyzer operated in the multiscaler mode). The wave form from the multiscaler is processed to provide amplitude and phase lags of the product signal from the reaction.

Isotope exchange studies with modulated beam of H_2O and a continuous flux of D_2O were conducted in the temperature range of 300 to 1800°K. The frequency range was extended to about 10,000 Hz by analysis of the higher harmonics in the beam. The "reaction product" in this study was HDO. The results can be explained by a diffusional process followed by a desorption step. The same mechanism was found to govern the reaction of O_2 with the prism plane of pyrolytic graphite. In the isotope exchange reaction, however, the same mechanism occurs on both crystallographic planes.

---

1. D. R. Olander, R. H. Jones, W. J. Siekhaus, and J. A. Schwarz, J. Vac. Sci. Tech. 9, 1429 (1972).
2. D. R. Olander, W. J. Siekhaus, J. A. Schwarz, and R. H. Jones, J. Chem. Phys. 57, 421 (1972).

2. THE OXIDATION OF AMMONIA BY O_2 ON POLYCRYSTALLINE PLATINUM BY MODULATED MOLECULAR BEAM MASS SPECTROMETRY

Alan Z. Ullman and Donald R. Olander

The modulated molecular beam apparatus is being used to study the oxidation of NH_3 on Pt. In commercial application, this reaction is catalyzed by platinum wire gauze, but here we use a wafer of polycrystalline metal. The ammonia is introduced as a modulated molecular beam. The oxygen may either be mixed with the ammonia or introduced separately as an unmodulated beam from a doser (see 1 above).

Preliminary tests with the latter method show competition for adsorption sites between the NH_3 and O_2 which lead to the odd result of negative apparent reaction probabilities for the production of the products NO and H_2O when the reactant NH_3 is in large excess. This phenomenon, when coupled with the high average reaction probability, leads to a situation in which the modulated reactant NH_3 exhibits a reaction phase lag (instead of leading the product emission signal, as is usually the case) while the products NO and H_2O show phase leads of 180° at low frequency. In effect, the off-on nature of the modulated NH_3 beam effects a chemical titration of adsorbed oxygen, and the results show that the maximum oxygen coverage on the Pt surface is approximately one monolayer. Thus, oxygen adsorption is not restricted to a few specialized reactive sites but can occur on the entire surface.

3. THE THERMAL ACCOMMODATION COEFFICIENTS OF HELIUM AND XENON ON UO_2 AND STAINLESS STEEL*

Donald R. Olander, Alan Z. Ullman and Rajarama T. Acharya

The thermal accommodation coefficients of helium and xenon on UO_2 and stainless steel are of practical importance in the prediction of the temperature distribution in nuclear fuel elements. In the fuel-clad gap, the mean free path of the gas molecules is

comparable to the dimension of the gas film, so it is necessary to account for the discrete nature of the heat transfer process from the gas to the fuel and the cladding. Knowledge of the thermal accommodation coefficients of the gas filling the gap (a mixture of helium and xenon) and the surfaces bounding the gap (the UO_2 fuel and the stainless steel cladding) is needed in the heat transport analysis.

This parameter has been measured by use of the modulated molecular beam phase shift technique which has been applied previously to other gas-solid systems.[1] Briefly, the gas temperature following interaction of the gas with the hot solid is determined by the change in the transit phase lag of the modulated beam. The transit phase lag is interpreted in terms of the equivalent Maxwellian temperature of the reflected gas molecules. Measurements were made for an incident gas temperature of 300°K and solid temperatures ranging from 500 to 1200°K. Two different combinations of incidence and reflection angles were investigated.

The results show that the thermal accommodation coefficients on both UO_2 and stainless steel are about 0.2, while for xenon the values are 0.5-0.6. These values are approximately an order of magnitude larger than the thermal accommodation coefficients currently utilized in codes which compute heat transfer in the fuel-clad gap, and suggest that application of gap conductance calculations underestimates the resistance of this process by a significant amount.

---

*Summary of a paper submitted to J. Nucl. Mater.

1. D. Olander et al., Surf. Sci. 33, 445 (1972).

4. DIFFUSION OF LANTHANUM IN MOLTEN URANIUM*

R. Yang and Donald R. Olander

The measurement of the diffusion coefficient of lanthanum in molten uranium has been completed. In order to obtain the lanthanum penetration profile in the uranium phase while diffusion was in progress, the diffusion zone was scanned by a scintillation γ-ray detector while the system was in the furnace. Due to the low solubility of lanthanum in uranium, accurate diffusion profiles could only be obtained by measuring the activity far from the interface. The large statistical errors in the count rates at distances far from the interface render such data unreliable. This is believed to be the principal reason for the inaccurate diffusivities obtained in previous experiments (see 1969 and 1972 Annual Reports).

In order to obtain high count rates at positions far from the interface, a slagging process was employed. A piece of alumina was inserted in the bottom of the crucible to act as a sink for the diffused lanthanum. The La-U interface was separated from the alumina plug by about 5 mm of molten uranium. The diffusion coefficient could be determined by measuring the cumulative count rate at the uranium-alumina interface as a function of time. A value of $D = (1.5\pm0.2)\times10^{-5}$ cm^2/sec at 1250°C was determined in this manner. This value is within the range of diffusivities expected in liquid metal systems, and suggests that there is nothing abnormal in the uranium-lanthanum system. Consequently, the project has been terminated.

---

*Summary of LBL-2553.

5. OXYGEN REDISTRIBUTION IN CERAMIC NUCLEAR FUELS*

Donald R. Olander

The analytical treatment of temperature gradient migration of oxygen in hyperstoichiometric urania summarized in last year's Annual Report has been extended to hypostoichiometric mixed oxide $[(U,Pu)O_{2-x}]$ which is to be the fuel for the first generation of liquid metal fast breeder reactors. In these ceramics, the oxygen potential is so low that the equilibrium pressures of H_2O and CO_2 (which are the oxygen carriers) are very low, and other mechanisms of oxygen transport along the temperature gradient may compete with the gas phase transport by the oxygen-bearing gases. In particular, the steady state distribution of the oxygen-to-metal ratio along the temperature gradient may be controlled by flow of H_2O or CO_2 in gas-filled cracks balanced by solid diffusion of oxygen ions in the fuel. The influence of solid state diffusion on redistribution depends upon the diffusion coefficients, densities, and flow areas of the solid and gaseous phases. With H_2O as the carrier gas, oxygen redistribution is practically eliminated with the crack-width-to-solid ratio of 10^{-5} but the effect of solid state diffusion is negligible when the solid contains > 1% cracks.

Transport by CO_2 follows the same general behavior as H_2O except that the maximum pressure of CO (or CO_2) is dictated by the requirement that the carbon activity cannot exceed unity. Otherwise, the carbon is precipitated according to the reaction: $CO = C + 1/2\ O_2$. This assertion assumes that the chemical state of the solid and gaseous phases in the fuel is governed by equilibrium thermodynamics. In actuality, however, the rate of reactions such as the one which leads to carbon deposition are quite slow, and the carbon potential of the gas may exceed that of pure graphite without loss of gas phase carbon. If this is so, CO_2 would still function as an effective oxygen redistributor in cracked, hypostoichiometric, mixed-oxide fuel.

In any case, solid state diffusion acts to reduce oxygen gradients established by other processes (which may be gas phase transport or true thermal diffusion of oxygen in the solid) but cannot by itself cause oxygen redistribution. Molecular diffusion in the solid performs an "enrichment limiting" function similar to that of back diffusion in isotope separation by the gas centrifuge or in thermal diffusion columns.

*Summary of an article published in J. Nucl. Mater. 47, 113 (1973).

6. THE CONSERVATION EQUATIONS GOVERNING POROSITY AND ACTINIDE REDISTRIBUTION IN MIXED OXIDE FUELS*

Donald R. Olander

It has often been stated that the movement of the as-fabricated porosity in a mixed oxide fuel due to the temperature gradient is responsible for actinide redistribution. A calculation has been made to assess the accuracy of this assertion. A temperature gradient is established in a nuclear fuel element as a consequence of the need to remove fission heat. As a result of the temperature gradient, pores originally uniformly distributed throughout the fuel move towards the centerline and form a central void. Just how or if these pores transport plutonium along with them is an important question, because plutonium relocation in the fuel affects the allowable power rating of the element. It has been claimed that plutonium redistribution is accomplished by a type of vapor phase zone refining process involving the moving pores. However, correct treatment of the conservation equations for the moving pores and the plutonium in the solid does not support this view. Migration of closed pores cannot contribute to actinide redistribution provided that:

(1) The density of the heavy metal oxides in the vapor contained in the pores is very much smaller than the solid density. If the vapor density were comparable in magnitude to the solid density (as is the case in true zone refining where the moving second phase is a liquid, but not for the rarified vapor in a pore), then the moving phase would have sufficient capacity to store one component and sweep it along the temperature gradient.

(2) Solid state diffusion of plutonium in the fuel must be negligible. If this condition is not met, the pores can "push" plutonium ahead of them and so accomplish redistribution (see item 8 of this report for detailed discussion of this effect).

*Abstract of paper published in J. Nucl. Mater. 47, 251 (1973).

7. THE KINETICS OF ACTINIDE REDISTRIBUTION BY VAPOR MIGRATION IN MIXED OXIDE FUELS (I). BY CRACKS*

Donald R. Olander

The kinetics of vapor migration-driven restructuring and actinide redistribution along continuous cracks was studied analytically. The fissured fuel was modeled by a network of rectangular cracks with the temperature gradient along the major axis. Redistribution of fuel constituents was considered to occur by molecular diffusion in the gas filling the cracks. Hyperstoichiometric U/Pu oxide was treated so that only a single diffusing species (UO_3) needed to be considered, at least in the early stages of the process. The dependence of the kinetics upon oxygen-to-metal ratio, temperature gradient, and crack dimensions was investigated for fuel containing 20% plutonium.

*Abstract of paper in J. Nucl. Mater. 49, 21 (1973).

8. THE KINETICS OF ACTINIDE REDISTRIBUTION BY VAPOR MIGRATION IN MIXED OXIDE FUELS (II). BY PORES*

Donald R. Olander

The migration velocity of a closed lenticular pore in hyperstoichiometric mixed oxide fuel has been calculated, and the U/Pu ratio of the solid near the moving pore has been determined. Pore migration in mixed oxides differs from the analogous process in pure stoichiometric urania in that the composition as well as the temperature of the two faces of the pore are different. It was found that pore migration is not as effective a mechanism of actinide redistribution as vapor transport along cracks. The velocity of the pores in $(U_{0.8}Pu_{0.2})O_{2+x}$ is ~ 3 1/2 times faster than that in pure UO_2.

*Abstract of paper in J. Nucl. Mater. 49, 35 (1973).

9. THE SHAPE OF THE DOPPLER-BROADENED SPECTRAL LINES PRODUCED BY LIGHT-ATOM BOMBARDMENT OF METALS*

Donald R. Olander, C. Kerkdijk, and C. Smits

A model for predicting the shapes of Doppler-broadened spectral lines due to de-excitation by photon emission of excited neutral atoms backscattered from solids is presented. The distribution of backscattered particles is calculated on the basis of single Rutherford collisions within the solid accompanied by energy loss due to electronic stopping during passage of the particle through the solid. The effect of the energy dependence of the stopping power, radiationless de-excitation of the escaping neutral atom, and the probability of the particle leaving the surface in the desired excited state are incorporated into the calculation. The broadening of the spectral line is determined by combining the Doppler-shift formula with the energy- and angular distribution of the backscattered particles.

*Abstract of article submitted to Rad. Effects. Work performed at the FOM Institute of Atomic and Molecular Physics, Amsterdam, Holland.

10. RESEARCH PLANS FOR CALENDAR YEAR 1974

Donald R. Olander

Investigation of the reaction $H_2O + C \rightarrow CO + H_2$ will be completed and a mechanistic model of the reaction proposed.

Ammonia oxidation of Pt will be completed and a reaction model proposed.

The reaction of graphite with hydrogen be investigated in the molecular beam apparatus. A high-temperature hydrogen atom furnace is under construction.

The F_2-UO_2 reaction, utilizing the newly constructed molecular beam system, will be investigated.

The gas phase radiolysis of oxygen by accelerator protons will be completed.

A thermal gradient furnace is being constructed to study the migration of metallic inclusions in ceramic oxide nuclear fuel materials.

11. 1973 PUBLICATIONS AND REPORTS

Donald R. Olander and Associates

1. R. T. Acharya and D. R. Olander, The Rate of Oxidation of the Basal and Prismatic Surfaces of Pyrolytic Graphite in the Transition Regime between Chemical and Diffusional Control, Carbon 11, 7 (1973) (LBL-488).

2. D. R. Olander, Oxygen Redistribution in $(U,Pu)O_{2-x}$, J. Nucl. Mater. 47, 113 (1973) (LBL-1469).

3. D. R. Olander, The Conservation Equations Governing Porosity and Actinide Redistribution in Mixed Oxide Fuels, J. Nucl. Mater. 47, 251 (1973) (LBL-1823).

4. D. R. Olander, The Kinetics of Actinide Redistribution by Vapor Migration in Mixed Oxide Fuels (I. By Cracks), J. Nucl. Mater. 49, 21 (1973) (LBL-1131).

5. D. R. Olander, ibid (II. By Pores), J. Nucl. Mater. 49, 35 (1973) (LBL-1131).

Papers presented

1. R. T. Acharya, "Study of the Reaction of Pyrolytic Graphite with Water by Modulated Molecular Beam Mass Spectrometry," 33rd Conf. on Physical Electronics, March 26-28, 1973, Berkeley.

2. D. R. Olander, "Surface Chemical Reactions by Modulated Molecular Beam Mass Spectrometry," at the FOM Institute of Atomic and Molecular Physics, Amsterdam, Nov. 8, 1972 and at the Technische Hogescholl Twente (Holland), April 11, 1973.

3. D. R. Olander, "Technical Basis of the Gas Centrifuge," CEA, Saclay (Paris), June 7, 1973.

4. D. R. Olander, "Oxygen and Plutonium Redistribution Kinetics in Oxide Fuels for Fast Reactors," CEA, Fontenany-aux-Roses (Paris), June 8, 1973.

5. D. R. Olander, "Plutonium Redistribution in Oxide Fuels," Argonne National Laboratory, Aug. 2, 1973.

LBL reports

1. Jack Hovingh, Diffusion of Lanthanum in Molten Uranium (M. S. thesis), LBL-1130, Feb. 1973.

2. Han-Chung Tsai, The Viscosity of Cesium Metal to Its Critical Temperature (Ph.D. thesis), LBL-1413, July 1973.

3. H. C. Tsai and D. R. Olander, The Viscosity of Liquid Cesium up to 1600°C, LBL-2201, Aug. 1973.

II. Metallurgy

A. CRYSTAL IMPERFECTIONS

Jack Washburn, Principal Investigator

1. TRANSMISSION ELECTRON MICROSCOPE INVESTIGATION OF THE GROWTH OF COPPER PRECIPITATE COLONIES IN SILICON

Erik Nes* and Jack Washburn

The growth of copper precipitate colonies in high-purity dislocation-free silicon single crystals has been examined by transmission electron microscopy. The colonies, being coplanar arrangements of copper-silicide particles on either {110} or {100} planes, nucleate and grow during rapid cooling from higher temperatures. The kinetics of the colony growth process has been analyzed in terms of a model based on repeated nucleation on a climbing dislocation. The possibility of having the growing copper-silicide particles dragged by the dislocations has been discussed, and a mechanism based on a particle dragging/dislocation climb effect has been suggested in order to explain the development of dendritic dislocation dipole branches.

Climb of the dislocation is caused by the chemical climb force due to the local vacancy subsaturation near a growing precipitate. Except for this dragging effect, the sequence between consecutive nucleations may still follow the pattern schematically illustrated in Fig. 1.

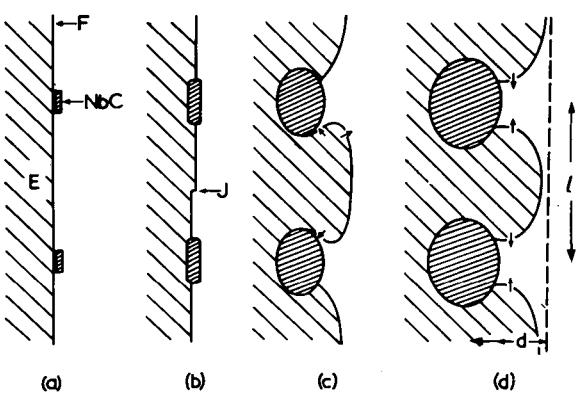

Fig. 1. Stages in the repeated nucleation process on a climbing edge dislocation. (XBL 732-5774)

*Present address: University of Oslo, Institute of Physics, Blindern, Oslo 3 Norway.

2. DETERMINATION OF LOOP TYPE IN As^+ IMPLANTED SILICON

Wei Kuo Wu

A simple method for determining loop type in foils near [111] orientation has been described and it has been shown to give the same results as previously used more cumbersome methods by applying it to phosphorous and arsenic implanted silicon.

The advantages of this method over others are:

(a) Only small angle tilting is necessary to know the sense of the Kikuchi pattern near ⟨111⟩. No high-angle tilting or dark field top-bottom determinations are needed.

(b) Only plus $\vec{g}$ and minus $\vec{g}$ bright field photographs are required.

This method is particularly useful in ion implantation studies with orientation near ⟨111⟩, because silicon usually gives very clear Kikuchi patterns. With this method, small prismatic loops in As^+ implanted silicon have been shown to be of interstitial type.

3. MEMORY SWITCHING EFFECTS IN As-Te-I CHALCOGENIDE GLASS

Robert Jecmen

The switching process from the memory state to the high resistance state seems to be governed by a Joule heating and subsequent melting of the crystalline filamentary path. Upon the cessation of the switching pulse, the filamentary region is quenched into a Te-rich glass of high resistivity. The switching process is a sensitive function of the heat conduction properties of the surrounding region.

The switching process from the memory state to the high resistance state is characterized by a visual disappearance of the memory state filament. Figure 1a shows the memory state filamentary path connecting the two vapor-deposited metal electrodes on the surface of the glass sample. The formation current magnitude was 0.8 mA, and the pulse rise, hold, and fall times were 5, 20, and 5 msec, respectively. In Fig. 1b, the memory filament is seen to disappear after a switching pulse I_s = 2.0 mA had been applied.

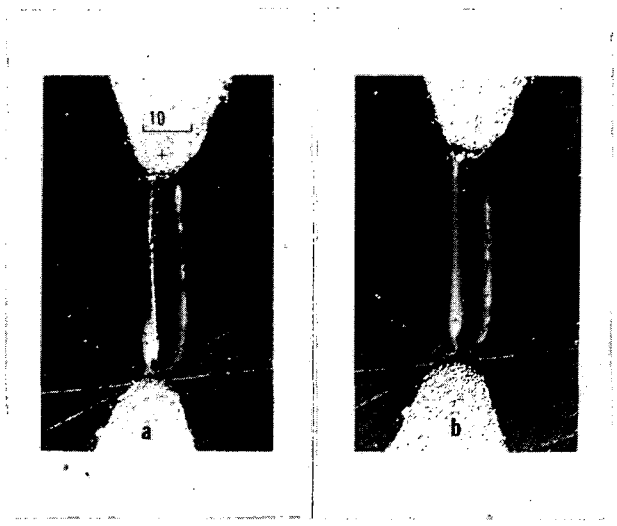

Fig. 1(a) Completed memory state filament. (b) Loss of filament upon switching to the high resistance state. (XBB 735-3366)

4. COMPUTER SIMULATION OF FRANK LOOP CONTRAST IN FIELD ION IMAGES

Kaj Gunnar Stolt

The contrast due to small Frank dislocation loops in field ion tips was analyzed by computer simulation. The simulation of the image was based on the shell model, and the displacement field of the dislocation loops was computed using the exact displacement equation for a closed dislocation loop in an isotropically elastic continuum (Burgers' formula). A simple method for taking the effect of surface relaxation on the displacement field into account was introduced. The method consists of superposing the displacement field of an image loop located in the mirror position of the real loop relative to the surface. Simulated field evaporation sequences were produced by either increasing the radius of the simulated tip while moving its center of curvature into the tip along its axis or by simply shrinking the simulated surface concentrically. The following conclusions were drawn from this investigation:

1) Frank loops will cause image contrast not only when they intersect the tip surface but when they are wholly inside the tip as well.

2) Frank loops of vacancy and interstitial type cause qualitatively different contrast, recognizable on inspection, and rather independent of loop plane and position.

3) Taking surface relaxation into account only enhances all analyzed contrast effects but does not alter them qualitatively.

4) Analysis of lattice defects by ion microscopy should be based on extensive and finely stepped evaporation sequences and absolutely not on single micrographs. This applies both to the characterization of the nature of a defect and to the determination of its size.

5) Determining the size of a Frank loop from its image contrast is very difficult, even using an evaporation sequence, since the contrast is caused by the strain field of the loop which is larger than the loop.

6) Comparison with experimental observations indicated the plausibility of the simulated contrast.

5. ON THE ANNEALING OF STACKING FAULT TETRAHEDRA AND FRANK DISLOCATION LOOPS IN SILVER

Thorvald Astrup and Jack Washburn

Direct observation of quenched-in stacking-fault tetrahedra and Frank dislocation loops in 99.999+% silver during annealing was made by hot stage transmission electron microscopy.

The defects produced by quenching from a few degrees below the melting point had a range of edge sizes L up to 2000 Å for the SFT and from 650 to 1350 Å for the triangular loops. The smaller SFT, L=600 Å, were found either to shrink or to completely anneal out above 600°C. One large SFT, L=2000 Å, was observed to collapse into a loop at 300°C. Shrinkage of loops taking place from one corner was detected.

The size ranges of faulted defects in gold and silver have been studied along with the different energy barriers involved in the collapse and/or shrinkage of these defects. It seems to be fairly well established that the annealing out of the faulted defects in gold does not pose any problem. For silver, however, the case is a little more complicated.

It is proposed that the ledge mechanisms are probable mechanisms for shrinkage of SFT, and in the case of collapse, nucleation of a Shockley loop near the corner instead of in the middle of the face might be energetically feasible. Escaig's suggestions regarding shrinkage of loops from one corner seem to be within reasonable ranges energetically.

All the calculations involve dislocation

configurations of core dimensions which along with assumption of isotropic elasticity and uncertainties on the value of the stacking fault energy make all attempts to pinpoint exact mechanisms of shrinkage and collapse questionable.

6. ON THE NATURE OF THE LONG-TERM DEGRADATION OF "CADMIUM SULFIDE" SOLAR CELLS

Terry M. Peterson and Jack Washburn

The spectral response of the Cu_xS/CdS (x=2, 1.95) heterojunction is calculated using a simple model, and a comparison with published data is made. This comparison suggests that there is a degradation of the djurleite cell (x=1.95) besides that due to the fact that djurleite has a smaller optical absorption constant than chalcocite. It is shown that the dislocation array necessary to accommodate the lattice mismatch between the djurleite and the cadmium sulfide could be a contributing factor in this degradation.

7. ELECTRON MICROSCOPE STUDIES OF MICRO-EROSION IN MgO SINGLE CRYSTALS

Jagdish Narayan and Jack Washburn

The plastic damage introduced in MgO single crystals by bombardment with Al_2O_3 microspheres (0.3, 10, 20 and 27 μm diameter) has been studied using optical, transmission, and scanning electron microscopy. Most of the damage is in the form of dislocation dipoles (two closely spaced dislocations of opposite sign) which lie on {110} slip planes. The dislocation density increases with the increase in the energy of the impinging particles. Using stereo-microscopy the damage has been shown to be uniformly distributed in thin foils. Studies done on indentations produced by a sharp pin show a very high density of single dislocations.

8. RESEARCH PLANS FOR CALENDAR YEAR 1974

Jack Washburn

1. Electron microscope studies of ion-implanted silicon: Effects of annealing treatments and ion-implantation dose on defects in the implanted layer will continue to be investigated for phosphorous, arsenic, and boron-implanted silicon. Habit planes of interstitial loops will be determined and correlated with the stresses present during nucleation and growth.

2. Field ion microscopy will be applied to a study of the effect of surface layer atoms on work function. Ni_4W in the ordered state permits surface layers consisting entirely of Ni atoms or of Ni + W to be exposed by field evaporation in certain regions of the field ion microscope tips. Work function measurements will be compared for the two kinds of surfaces.

3. Void growth is a serious problem for the inner wall of a fusion reactor, for electric power generation. It is known that preferential capture of interstitials at dislocations is the root cause of void growth. Radiation damage produced by electron bombardment of copper and copper aluminum alloys in the 650-kV electron microscope will be used in a continuing study of dislocation climb phenomena. In particular, the effect of stacking-fault energy on climb due to capture of interstitial atoms produced by electron irradiation will be investigated. To make these experiments practical it is planned to modify the column of the high-voltage microscope to permit use of side entry stages.

4. The possibility of producing a low-cost photovoltaic cell based on a sputtered thin film of ZnS will continue to be investigated along with a continuing study of the mechanism of operation of the cuprous sulphide/cadmium sulfide heterojunction solar cell.

5. The shape memory effect in NiTi is of potential use in a new kind of heat engine for operation at small ΔT. Electron microscope work will be undertaken to clarify the mechanism of the shape memory effect.

6. The production of silicon solar cells at low enough cost to permit their widespread use for direct conversion of solar energy to electric power probably requires the use of silicon of lower purity and in poly-crystalline thin film form. A cooperative program will be undertaken with Professor Gabor Somorjai to investigate the properties of various kinds of grain boundaries in silicon films.

7. Efficient collection of solar heat for heating and cooling of buildings and for preheating water to produce steam for electric power plants requires a spectrally selective surface of long life and low cost. Various methods of producing thin layers of copper

oxide on reflective metal surfaces are being investigated.

9. 1973 PUBLICATIONS AND REPORTS

Jack Washburn and Associates

Journals

1. J. Narayan and J. Washburn, Electron Microscopic Studies of Micro-Erosion in Brittle Solids, Wear 23, 128 (1973)(LBL-899).

2. J. Narayan and J. Washburn, Self Diffusion in Magnesium Oxide, Acta Met. 21, 533 (1973) (LBL-473).

3. J. Narayan, On the Interaction of Prismatic and Glissile Dislocations, J. Appl. Phys. 44 (6), 2449 (1973)(LBL-1405).

4. E. Nes and J. Washburn, Transmission Electron Microscope Investigation of the Growth of Copper Precipitate Colonies in Silicon, J. Appl. Phys. 44 (8), 3682 (1973) (LBL-1459).

5. J. Narayan, Prismatic Dislocation Loops on Impurity Precipitates in Magnesium Oxide Single Crystals, J. Appl. Phys. 44 (8), 3436 (1973)(LBL-1843).

6. J. Narayan, The Characterization of the Damage Introduced During Micro-Erosion of MgO Single Crystals, Wear 25, 99 (1973) (LBL-887).

7. J. Narayan, Subgrain Boundaries in MgO, J. Am. Ceramic Society, December, 1973 issue (LBL-828).

LBL reports

1. W-K. Wu, Determination of Loop Type in As^+ Implanted Silicon (M.S. thesis), LBL-1415, Feb. 1973.

2. J. Narayan, Transmission Electron Microscopic Studies of Prismatic Slip in Magnesium Oxide, LBL-1406, Jan. 1973.

3. W-K. Wu, L-J. Chen, J. Washburn, and G. Thomas, On Indexing of Diffracting Planes Using the Kikuchi Pattern, LBL-1811, Aug. 1973.

4. Robert M. Jecman, Memory Switching Effects in As-Te-I Chalcogenide Glass (M. S. thesis), LBL-1817, July 1973.

5. K. Seshan, Contribution of Radiation Damage to the Study of Basic Atomic Motion in Solids, LBL-1450, Feb. 1973.

6. W-K. Wu and J. Washburn, Identification of Interstitial vs. Vancancy Type Dislocation Loops in Ion Implanted Silicon, LBL-1812, Sept. 1973.

7. K. G. Stolt, Computer Simulation of Frank Loop Contrast in Field Ion Images, Ph.D. thesis, LBL-2200, Sept. 1973.

8. H. A. E.-F. Mohamed, Mechanism of Pressure Welding (M.S. thesis), LBL-2510, Dec. 1973.

9. W-K. Wu and J. Washburn, On Determination of the Burger Vectors and Loop Planes of Rod-Like Defects in Boron Implanted Silicon, LBL-2287, Nov. 1973.

B. THEORETICAL METALLURGY

John W. Morris, Jr., Principal Investigator

Introduction. The overall objective of this research program is to advance the theory of alloy design. The problem of designing an engineering alloy may be subdivided into four parts: (1) estimation of the thermodynamic properties of an alloy of given composition; (2) prediction of the microstructure resulting from a specified treatment of an alloy of given thermodynamic and kinetic properties; (3) prediction of the engineering properties of an alloy of given microstructure; (4) synthesis of this information in the selection of alloy composition and processing. Given the synthetic character of alloy design, its study seems best conducted in a program which maintains active research in each of the relevant problem areas.

1. THERMODYNAMICS

a. Phase Stability of Metals and Alloys*

Charles W. Krause and John W. Morris, Jr.

Despite its central importance in the science of metallurgy, the problem of predicting the preferred structure of a metal alloy remains unsolved. Moreover, the complexity of the problem is such that a viable theory of the crystal structure of alloys is unlikely to emerge for some time. In the interim the metallurgist will be forced to make do with a mixture of rough approximations and semiempirical rules, and the development of approximate techniques in alloy theory will continue to be important.

The pseudopotential theory of simple metals has yielded several models which promise to be useful in the prediction of structure. The simplest and most general of these follows from Harrison's development of Cohen's real space formulation of the pseudopotential theory. If a pseudopotential model of a simple metal is developed to second order in perturbation theory, that part of the cohesive energy which depends on the structure may be treated as if the atoms interacted in pairs according to a central, two-body potential. This two-body potential has an asymptotic form which is independent of the precise pseudopotential assumed, and which exhibits the Friedel oscillations. Under suitable assumptions one may make a rough estimate of the relative energies of candidate structures at 0°K by simply summing the energy of two-atom interactions according to the asymptotic, or Friedel, potential. This approach has been taken in several studies of the structure of simple metals and alloys and has been followed here, where we supplement prior work with new computations to explore the results of a simple structural model based on the two-body Friedel potential.

While the approximations involved in a structural model based on the Friedel potential are drastic, the model has several attractive features. It leads to equations which are easy to use and which incorporate aspects of the more fundamental theory while avoiding the recalcitrant problem of choosing proper pseudopotentials. Moreover, the model yields a prediction of alloy structure which is based on the electron-atom ratio, in the spirit of the Hume-Rothery and Engel-Brewer correlations, and which is in general agreement with known structural tendencies in simple metals and alloys.

The central equations of the structural model used here are derived as follows.

Employing the real space formulation of the pseudopotential theory of a simple metal, the cohesive energy per atom may be developed in the perturbation series

$$E = E_o + E_1 + E_2 + \ldots \qquad (1a.1)$$

whose successive terms involve perturbations of increasing order. The zeroth and first-order terms in this expansion depend on the volume per atom (Ω), but are independent of structure. The second-order term, E_2, is the first to show the influence of structure. It can be cast in the form

$$E_2 = \frac{1}{2N} \sum_{i,j}{}' V(r_{ij}) \ , \qquad (1a.2)$$

where N is the number of atoms, r_{ij} is the distance between the ith and j^{th} atom cores, and the prime on the summation indicates that terms having i=j are to be omitted. The function $V(r_{ij})$ appearing in the summation acts as a two-body potential in a restricted sense: it governs the change of energy in a relative displacement of atoms i and j which leaves the atomic volume, and hence E_o and E_1, constant. If we fix the atomic volume and neglect higher order terms in the perturbation expansion, the relative

energy of a given structure is measured by E_2; that structure which minimizes E_2 will be preferred at 0°K.

Computation of the structural energy, E_2, requires a specific expression for the effective interatomic potential, V(r). This potential is sensitive to the details of the pseudopotential used. However, irrespective of the pseudopotential, V(r) has the asymptotic form

$$V(r) \rightarrow V_o \cos(2k_F r)/(2k_F r)^3 \qquad (1a.3)$$

when $(k_F r)$ is large, where k_F is the Fermi wave number. The parameter V_o depends on fundamental quantities in a rather complicated way, but for our purposes it is sufficient to note that V_o is independent of structure. We may hence define a dimensionless two-body potential

$$v(r) = V(r)/V_o .$$

which becomes the Friedel potential

$$v(r) = \cos(2k_F r)/(2k_F r)^3 \qquad (1a.4)$$

when $k_F r$ is large. If we now uniformly approximate V(r) by its asymptotic form, the structural energy, E_2, may be rewritten in a dimensionless form which is independent of the pseudopotential:

$$\varepsilon = E_2/V_o = \frac{1}{2N} \sum_{i,j}' \cos(2k_F r_{ij})/(2k_F r_{ij})^3 \qquad (1a.5)$$

In fact, the dimensionless energy, $\varepsilon = \varepsilon(Z)$, is a function of structure and electron-atom ratio (Z) only; since the separation distances (r_{ij}) in a given structure scale as $\Omega^{1/3}$, where Ω is atomic volume, and since the Fermi wave number, k_F, is $k_F = (3\pi^2 Z/\Omega)^{1/3}$, the set of values of the quantity $(k_F r_{ij})$ in a given structure, and hence the dimensionless energy of the structure, is determined by Z.

Equation (1a.5) may be summed exactly for given structure, using a technique proposed by Shaw. Results for the common metal structures are shown in Fig. 1, where we have plotted the dimensionless energies of the hcp and bcc structures relative to that of the fcc structure as a function of electron-atom ratio Z. The result shows intriguing agreement with the phase stabilities of simple metals. At Z=1 the hcp structure is preferred, as in the simplest monovalent metals, Na and Li. At Z=2 the bcc and hcp structures are almost degenerate; both are observed. At Z=3 the fcc structure is preferred.

If only close-packed structures are considered, an approximate value for Eq. (1a.5) may be obtained in a very simple way. Blandin, Friedel, and Saada showed how Eq. (1a.5) may be approximately rewritten as a sum over close-packed planes of an interplanar potential which depends on whether the planes are in equivalent (i.e., A-A) or inequivalent (A-B or A-C) stacking positions. Hodges and Weire suggested a technique for performing the summation for close-packed structures. We modified this technique into a form allowing straightforward computation of the relative energies of arbitrary close-packed polytypes. In Fig. 2 we compare the dimensionless energies of the hcp and fcc structures to those of three simple close-packed polytypes: the double hexagonal (dhcp) structure, with stacking sequence ...hkhk...; the samarium (Sm) structure, with stacking sequence ...hhkhhk...; and a third structure, denoted A, which is two-thirds cubic in stacking, ...kkhkkh... . The polytypes intrude over a range of electron-atom ratio $1.24 < Z < 1.34$. This is the range of valence over which Blandin, Friedel, and Saada found that the fcc and hcp structures would be simultaneously unstable to faulting, and is a range in which polytypic structures are observed experimentally.

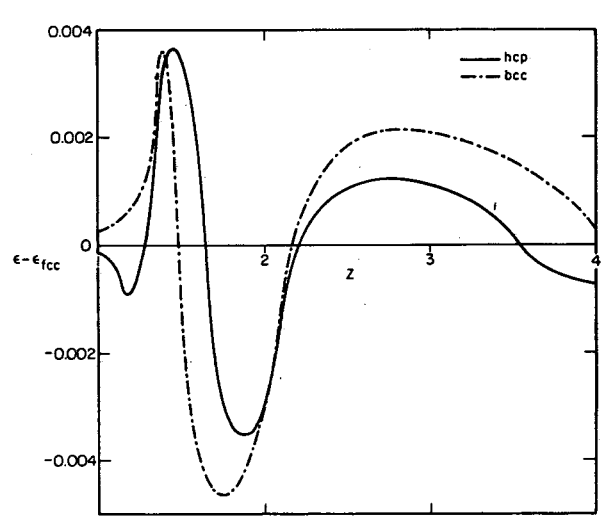

Fig. 1. Results for the dimensionless relative energies, $\varepsilon_{hcp}-\varepsilon_{fcc}$ and $\varepsilon_{hcp}-\varepsilon_{fcc}$, as determined by exact summation of the reduced Friedel potential as a function of Z. (XBL 738-1788)

As is apparent in Fig. 2, the energies of the close-packed structures are degenerate at $Z_c = 1.14$. This degeneracy is evident from the functional form of the interplanar interaction, and has led to an anticipation of anomalous faulting behavior near Z_c. As can be seen by comparing Figs. 1 and 2 the degeneracy is spurious; it is introduced with the approximation leading to the interplanar interaction.

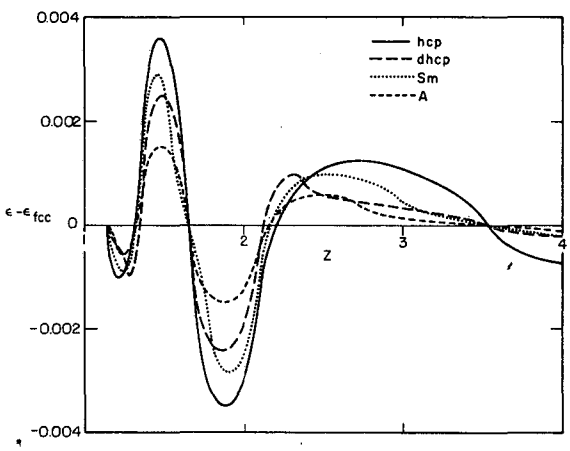

Fig. 2. Results for the dimensionless energies of the polytypic structure hcp, dhcp, Sm and A relative to the fcc structure as determined from the BFS interplanar interaction as a function of Z.
(XBL 735-6175)

A shortcoming of the simple Friedel potential is its unique association of preferred structure and electron-atom ratio. To study generalizations we considered a simple extension of the Friedel potential, obtained by adding a phase shift (2δ) in Eq. (1a.4) to obtain the modified potential

$$v(r) = \cos(2k_F r + 2\delta)/(2k_F r)^3 \quad . \quad (1a.6)$$

The inclusion of a phase shift in the potential is not arbitrary. It has been suggested as a device for accounting for some of the effects of d electrons, and Harrison has argued that a phase shift appears in the asymptotic form of the real space interaction in pseudopotential theory when nonnegligible third-order effects are included.

If the modified potential (1a.6) is substituted in the summation (1a.5) the relative energy of a structure becomes dependent on two parameters: the phase shift (δ) and the electron-atom ratio Z. Exact summation of Eq. (1a.5) then gives the results shown in Fig. 3, where we have plotted the domains of stability of the structures fcc, bcc, and hcp as functions of Z and 2δ. The phases appearing at reasonably small values of δ in this plot show interesting agreement with those empirically observed as a function of Z.

To study the stability of close-packed polytypes we recast the potential (1a.6) in the form of an interplanar interaction, and summed for relative structural energies. The resulting stability fields are shown in Fig. 4. Polytypic phases may be stabilized

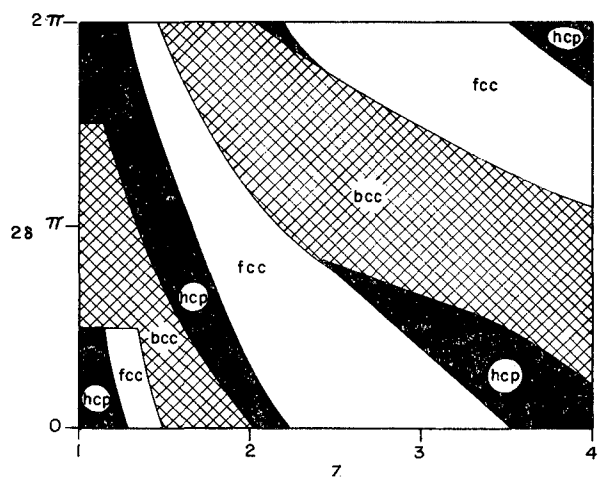

Fig. 3. Results from the determination of the most stable structure among fcc, hcp and bcc from the exact summation of the Friedel potential as a function of Z and a phase factor, 2δ. (XBL 735-6178)

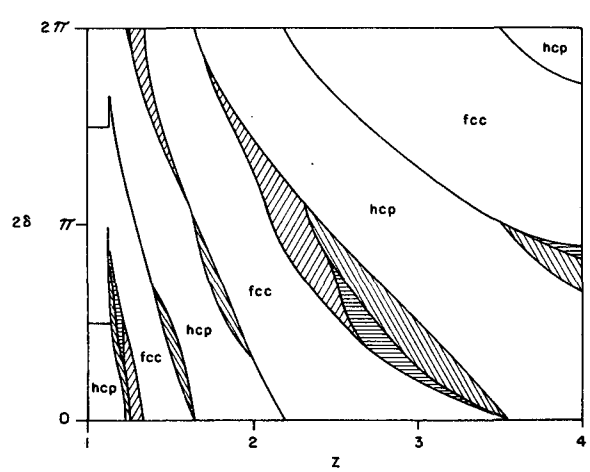

Fig. 4. Results from the determination of the most stable structure from among fcc, hcp, dhcp, Sm and A using the interplanar interaction as a function of Z and 2δ.
(XBL 735-6177)

by a small phase factor when $1.25 \leq Z \leq 1.60$ and when $3.0 \leq Z \leq 3.6$. These are the ranges of electron-atom ratio over which close-packed polytypes are commonly found.

*Abstracted from LBL-2214.

b. Diffusion

Faysal Hamzeh and John W. Morris, Jr.

Most problems of diffusion in simple metals and binary alloys at constant temperature and pressure may be solved in a straightforward way through use of Fick's equations, whose utility is well established experimentally. However, the theoretical treatment of diffusion in multicomponent systems or in more complex situations requires the use of relations in nonequilibrium thermodynamics whose correct forms are not firmly established. Since theoretical treatment of transformations in engineering alloys requires an understanding of diffusion in multicomponent systems in the presence of strain or temperature gradients, new research in the theory of diffusion is needed. We began research on this problem during the past year. The first problem considered was the optimal choice of fluxes and forces for describing diffusion in a multicomponent system.

It is generally assumed that if a system is reasonably close to equilibrium its regression to equilibrium can be described by a set of linear phenomenological equations of the form

$$\underset{\sim}{J}^{\alpha} = \sum_{\beta} \underset{\sim}{L}^{\alpha\beta} \cdot \underset{\sim}{x}^{\beta} , \qquad (1b.1)$$

where $\underset{\sim}{J}^{\alpha}$ is the flux of the αth thermodynamic quantity (heat or mass) measured in a specified reference frame, $\underset{\sim}{x}^{\beta}$ is a thermodynamic force appropriate to the βth quantity, and the $\underset{\sim}{L}^{\alpha\beta}$ are tensor coefficients which measure the coupling between the αth flux and β^{th} force. It is then convenient to assume that the coefficients $\underset{\sim}{L}^{\alpha\beta}$ are symmetric, in the dual sense that $\underset{\sim}{L}^{\alpha\beta} = \tilde{L}^{\alpha\beta}$ and that $\underset{\sim}{L}^{\alpha\beta} = \underset{\sim}{L}^{\beta\alpha}$. These symmetry constraints are known as the Onsager relations and are generally referred to a theorem by Onsager on the regression of fluctuations from equilibrium.

The Onsager symmetry relations have been strongly objected to in theoretical work by Coleman and Truesdell. They point out in particular that the relations are meaningless in the absence of a specific prescription for choosing the fluxes and forces in Eq. (1b.1); if the Onsager relations hold with one choice of the $\underset{\sim}{J}^{\alpha}$ and $\underset{\sim}{x}^{\beta}$, a simple redefinition of the $\underset{\sim}{x}^{\beta}$ will lead to a new set of equations of the form (1b.1) in which they do not hold.

In the course of an investigation of the symmetry constraints on the coefficients $\underset{\sim}{L}^{\alpha\beta}$ we found that it is possible to establish clear rules for the choice of fluxes and forces leading to symmetric coefficients if there in fact is a valid symmetry principle of the Onsager type. Treating the limiting case, suggested by Truesdell, in which the species exchange momentum in pairs at a rate proportional to the difference in their average velocities, it follows that the symmetry relations can be established if the fluxes $\underset{\sim}{J}^{\alpha}$ are measured with respect to an average velocity of the components making up the solutions (e.g., the barycentric velocity, the mean molar velocity, the mean volume velocity, or the velocity of one component). Each choice of reference velocity yields a preferred form for the diffusion force in which the symmetry relations hold. Since the limiting case considered is a valid limiting case for important physical processes (e.g., a dilute gas of dilute molecules or diffusion of dilute species through a solvent matrix) the results hold in general if the Onsager relations do.

2. CORRELATION OF MICROSTRUCTURE TO PROCESSING

a. TTT Curves of Idealized Alloys

John E. Sanchez and John W. Morris, Jr.

Alloy processing usually depends on the control of solid state reactions to achieve a desired microstructure. The processing times and conditions are chosen to control both the extent of transformation and the morphological features of the change of phase, since these two factors together determine the ultimate microstructure. In engineering practice, the choice of processing conditions is empirical; there are now virtually no solved problems on the evolution of microstructure during processing.

However, work principally by Cahn showed some years ago that under suitable assumptions it is possible to model many features of the transformation behavior of an idealized alloy on thermal processing. The idealizations involved treating the alloy as a thermodynamically simple, isotropic, pseudo-one-component material having a geometrically simple initial grain structure. Average

kinetics of the transformation may be computed for selected values of the thermodynamic properties of the alloy, and yield time-temperature-transformation curves, the nature of the nuclei dominating transformation, and information on average properties of the microstructure as a function of transformation time.

In our current work we are employing this model to survey isothermal transformation behavior as temperature, grain size, and thermodynamic properties are varied over a realistic range. The extension of the model to treat transformation on continuous heating or cooling is straightforward.

b. Computer Simulation of Transformation Behavior

Kenton L. Hanson and John W. Morris, Jr.

One of the most important features of alloy microstructure is its heterogeneity. Grains in real alloys are not regular in size or shape, nor are second phases distributed uniformly. This heterogeneity may have critical consequences for the mechanics of the alloy. It is, however, difficult to account for in an analytic model of transformation behavior, even in the most simple systems. Non-uniformities in microstructure can, however, be studied through direct computer simulation of the phase transformation. We hence began work on computer simulation of phase transformations in simple systems to obtain direct evidence on characteristics of microstructure and to provide guidance for theoretical work.

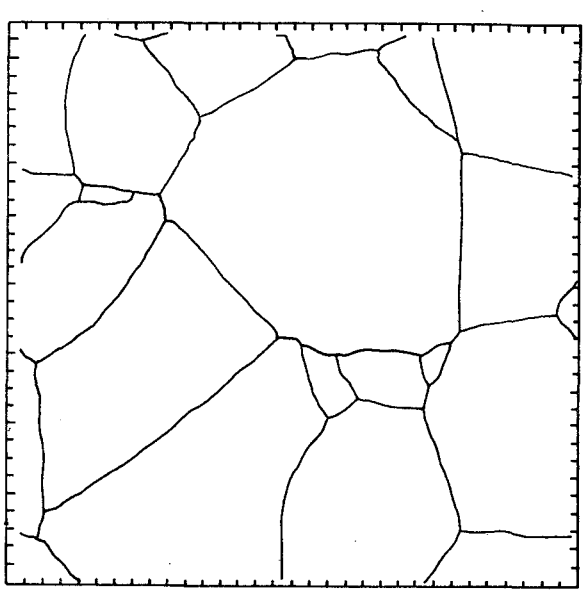

Fig. 1. Example of computer simulated microstructure assuming homogeneous nucleation and isotropic growth.
(XBL 741-5480)

Our initial code treats a material in which it is assumed that grains grow isotropically from distributed nuclei, which may be distributed randomly or on pre-selected heterogenous sites, and form at a rate given by a selected nucleation function. Both the nucleation and growth rate may be taken as functions of processing conditions. The code treats transformation in a cube with periodic boundary conditions, and yields microstructures obtained by slicing the cube along an arbitrary plane. An example of results obtained with a low, homogeneous nucleation rate is shown in Fig. 1. The code may then compute arbitrary topological properties of the microstructure.

3. CORRELATION OF MECHANICAL PROPERTIES TO MICROSTRUCTURE

a. Plastic Deformation of Idealized Crystals*

Kenton L. Hanson, Dale H. Klahn and John W. Morris, Jr.

Despite more than thirty years of research in the dislocation theory of plasticity, the number of solved problems remains small. This lack of solved problems is a serious barrier to alloy design, since a sound theory of plasticity is needed to estimate the effect of possible microstructural changes on the mechanical properties of engineering alloys. We have hence been conducting research on the plastic deformation of idealized crystals.

Our work has focused on what appears to be the simplest realistic problem in the dislocation theory of plasticity: the deformation of a crystal through the planar glide of non-interacting dislocations. The dislocations are idealized as flexible, extensible strings of constant tension. The crystal is assumed to contain microstructural features which are idealized as randomly distributed point barriers to dislocation glide. The deformation rate of the crystal is to be determined as a function of the applied stress, the temperature, and the nature and density of point barriers. This problem may be reduced to the problem of computing the velocity of thermally-activated glide of a dislocation through a field of immobile point obstacles, again as a function of applied stress, temperature, and the nature and density of the obstacles.

The problem may be described as follows (Fig. 1). Consider a crystal plane which is the glide plane of a dislocation. Let it contain a random distribution of points which act as obstacles to dislocation glide. Let an initially straight dislocation be introduced at one edge of the plane, and let this dislocation glide into the plane under the action of a resolved shear stress. The dislocation glides freely across the empty initial area of the plane. It may also mechanically pass some of the point obstacles, either by cutting through them or folding around them to close on itself. This glide continues until the dislocation finds itself in a configuration in which it is pinned along its whole length by obstacles which it cannot pass mechanically. Such a configuration is illustrated in Fig. 1. If the dislocation is confined to the glide plane and the stress is held constant, the dislocation remains pinned in this stable configuration until thermal activation carries it past at least one of the pinning obstacles. It then glides until a second mechanically stable configuration is reached and the process of thermal activation must be repeated. The problem is to compute the expected value of the velocity of dislocation glide through repeated thermal activation as a function of the applied stress, the temperature, and the nature and density of the point obstacles.

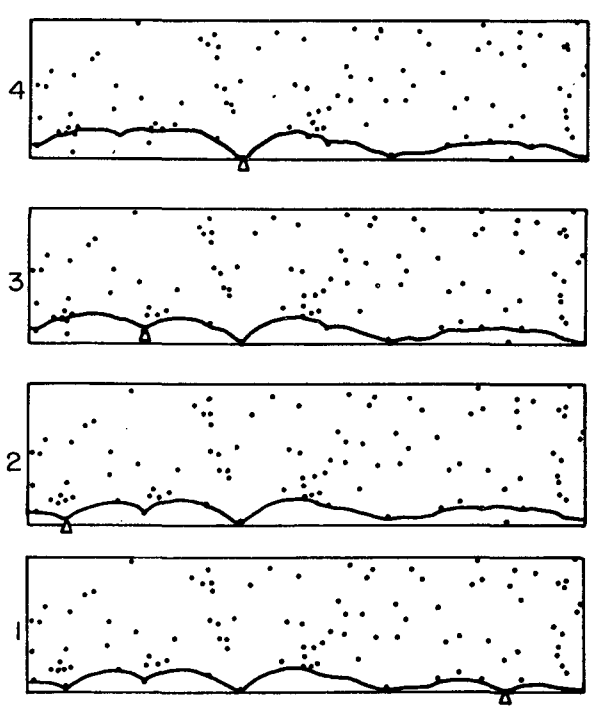

Fig. 1. Sequence of four possible configurations as a dislocation glides into a random array of point obstacles. The activation site is indicated by the symbol (Δ).
(XBL 732-5722)

The assumptions and basic equations used may be set in a simple dimensionless form. The glide plane of the dislocation is taken to be a square containing a random distribution of point obstacles, whose density is characterized by the area (a) per point or by the characteristic length $l_s = (a)^{1/2}$. The total area of the square array may be written in dimensionless form as the number of points contained: $A^* = A/a = n$. A dislocation in this plane is modelled as a flexible, extensible string of constant line tension, Γ, and Burgers vector, $\underset{\sim}{b}$, of magnitude b, taken to lie in the glide plane. The resolved shear stress τ impelling glide of this dislocation may be written in dimensionless form

$$\tau^* = \tau l_s b/2\Gamma \qquad (3a.1)$$

Let the dislocation, under the applied stress τ^*, encounter a configuration of point obstacles denoted by (i). Between two adjacent obstacles the dislocation will take the form of a circular arc of dimensionless radius R^* $(=1/2\tau^*)$. If the distance between any two adjacent obstacles along (i) exceeds $2R^*$ or if the dislocation line anywhere intersects itself then the configuration (i) is transparent to the dislocation and will be mechanically bypassed. If (i) is not transparent its mechanical stability is governed by the strength of the dislocation-obstacle interaction.

The obstacles are taken to be identical, circularly symmetric barriers to the dislocation which may be treated as point obstacles. At the $k^{\underline{th}}$ point obstacle along i the dislocation line forms the asymptotic angle ψ_i^k $(0 \leq \psi_i^k \leq \pi)$. The force, F_i^k, which the dislocation exerts on the $k^{\underline{th}}$ obstacle may be written in dimensionless form

$$\beta_i^k = F_i^k/2\Gamma = \cos\,(\psi_i^k/2)\ , \qquad (3a.2)$$

where $0 \leq \beta_i^k \leq 1$. The dislocation-obstacle interaction is given by a force-displacement relation, $\beta(x/d)$, the effective dimensionless point force on the dislocation as it sweeps through the obstacle, with d the effective range of the interaction $(d \ll l_s)$. The force β_c measures the mechanical strength of the obstacle. A non-transparent line configuration of obstacles forms a mechanically stable barrier to the glide of a

dislocation under stress τ^* if $\beta_i^k < \beta_c$ for all obstacles k on i. If the ith line configuration is mechanically stable, and if we neglect the possibility of thermally activated bow-out between adjacent obstacles, the dislocation remains pinned in this configuration until one obstacle is passed through thermal activation. If the function $\beta(x/d)$ is monotonically increasing between the values β_i^k and β_c (we assume it is), the activation energy may be written in dimensionless form:

$$g_i^k = u(\beta_c) - u(\beta_i^k) \ , \qquad (3a.3)$$

where $u(\beta)$ is the dimensionless area under both the force displacement curve and a horizontal line of height β.

Given these basic equations, the statistics of thermally activated glide are as follows: The stochastic probability for thermal activation past the (i, k) barrier in one attempt is

$$P_i^k = \exp\,(-\,\alpha g_i^k) \qquad (3a.4)$$

where g_i^k is given by Eq. (3a.3) and α is a dimensionless reciprocal temperature

$$\alpha = 2\Gamma d/kT \ . \qquad (3a.5)$$

Let the dislocation attempt the obstacles with mean frequency ν, taken to be the same for all obstacles. Then the expected residence time of the dislocation in the ith configuration is

$$\langle t^*_i \rangle = \Lambda_i^{-1} \ , \qquad (3a.6)$$

where Λ_i is the activation parameter

$$\Lambda_i = \sum_{k=1}^{N_i} P_i^k \ . \qquad (3a.7)$$

The expected residence time $\langle t^*_i \rangle$ is the mean time required for the dislocation to pass one obstacle in the ith configuration. We may also compute the probability $\eta(k,i)$ that the kth obstacle is the one passed. The result is

$$\eta(k,i) = P_i^k/\Lambda_i \ . \qquad (3a.8)$$

To compute the glide velocity of the dislocation at given stress and temperature we assume that glide is controlled by thermal activation in the sense that the time required for dislocation glide between successive stable obstacle configurations is negligible compared with the time required for thermal activation past these configurations. If there are r stable dislocation configurations along a particular glide path χ through the array, where χ is the sequence of obstacle configurations encountered, then the expected transit time of a dislocation along χ is

$$\langle t^* \rangle_\chi = \sum_{i=1}^{r} (\Lambda_i)^{-1} \ . \qquad (3a.9)$$

The dislocation may, of course, take any one of many available glide paths through the array. We can, however, show that the glide path is chosen through a sequence of Markov processes, and that the set of all possible elements of the glide path, the set of all mechanically stable obstacle configurations, forms an irreducible Markov chain. It follows from the ergodic property of such chains that the probability, u_χ, that the dislocation will follow the path χ is well defined. The expected transit time is then

$$\langle t^* \rangle = \sum_\chi u_\chi \langle t^* \rangle_\chi \ . \qquad (3a.10)$$

The velocity of glide is defined in a statistical sense only, but has the ergodic average

$$\langle v^* \rangle = n^{1/2}/\langle t^* \rangle \ , \qquad (3a.11)$$

where v^* is the dimensionless area swept out by the dislocation per unit time divided by its projected length, the edge length of the array.

The determination of the velocity of glide through a random array of point obstacles is complicated, since the available glide paths change with the applied stress, and the relative probabilities of these paths change with temperature. We have, however, identified approximations which are useful when either α is large (low temperature) or the applied stress τ^* is very close to the critical resolved shear stress τ^*_c for athermal glide through the array. Given either large α or $\tau^* \sim \tau^*_c$, the dislocation will tend to follow the "minimum angle" path χ_0 obtained under the constraint that the dislocation pass each configuration (i) by activating past the point k at which the angle ψ^k_i takes on its minimum value.

These results can be used to model steady-state deformation of an idealized crystal made up of parallel glide planes. The steady-state strain rate of such a crystal can be computed if characteristics of the mobile dislocation density are known, and if the dislocations are assumed independent of one another. Two limiting distributions of mobile dislocations lead to particularly simple equations. In the first we assume a constant density of non-interacting, mobile dislocations ergodically distributed through the whole crystal. In this case the average glide velocity ($\bar{v}^*$) is given by

$$\bar{v}^* = n^{1/2}/\bar{t}^* \quad , \qquad (3a.12)$$

where

$$\bar{t}^* = \frac{1}{S} \sum_{l=1}^{S} \langle t^* \rangle_l \qquad (3a.13)$$

is the average of the expected transit times in a crystal containing S glide planes. As a second limiting case, we assume a distribution of mobile, non-interacting dislocations which is uniform in the sense that the time average of the density of dislocations on each glide plane is the same. In this case the average glide velocity ($\tilde{v}^*$) is the simple average of the expected glide velocity on the planes composing the crystal:

$$\tilde{v}^* = \frac{1}{S} \sum_{l=1}^{S} \langle v^* \rangle_l = \frac{n^{1/2}}{S} \sum_{l=1}^{S} \langle t^* \rangle_l^{-1} \quad . \qquad (3a.14)$$

It should be apparent that if $\langle v^* \rangle$ varies from plane to plane these two dislocation distributions will yield different values for the overall average glide velocity. The velocity $\bar{v}^*$ is principally influenced by glide on those planes on which the transit time $\langle t^* \rangle$ is largest, or those on which glide is most difficult. The velocity $\tilde{v}^*$ is principally influenced by glide on those planes on which the expected velocity $\langle v^* \rangle$ is largest, or those on which glide is easiest. Moreover, if $\langle v^* \rangle$ varies from plane to plane, the two distributions will lead to qualitatively different types of crystal deformation. With an ergodic distribution of mobile dislocations all glide planes will be active and the overall deformation of the crystal will be evenly distributed among them. With a uniform distribution of mobile dislocations the deformation will be concentrated on a few well-defined planes, those on which glide is easiest.

Given the statistical relations governing thermally activated glide, the rate of deformation of an idealized crystal can be computed if the mechanical characteristics of the obstacle configurations encountered during glide are known, given the stress, temperature, and nature of the dislocation-obstacle interaction. To study these characteristics we have constructed and employed a computer code which directly simulates dislocation glide. The code is now in its third-generation form, and allows us to simulate glide through arrays of arbitrary size containing obstacles having an arbitrary distribution of properties at given values of stress and temperature. However, the bulk of research to date has focused on arrays of $\sim 10^3$ identical obstacles whose interaction with the dislocation is of a simple "step" form, giving dimensionless activation energy $g(\beta) = (\beta_c - \beta)$. We have studied in particular, (1) the critical resolved shear stress for athermal glide as a function of obstacle strength and the properties of the strength-determining configurations; (2) the characteristics of the configurations encountered during glide at finite temperature, with particular emphasis on the "minimum angle" path χ_0; (3) the velocity of glide as a function of temperature, (α), stress (τ^*), and obstacle strength (β_c); and (4) deformation of a crystal composed of a set of randomly chosen planes.

The strength-determining configurations in a random array of obstacles are of central importance, since they not only determine the critical resolved shear stress (τ^*_c) for athermal glide but also have a dominant influence on the velocity of thermally activated glide over a wide range of conditions. We first determined the strengths of these configurations in the following way. By fixing a stress (τ^*), arbitrarily setting β_c at 1.0, letting the dislocation move through the array along the minimum angle path χ_0, and measuring the maximum force (β_i) for each obstacle configuration encountered, we may determine the maximum force (β_1) which the dislocation exerts on the most stable obstacle configuration opposing glide at stress τ^*. This value (β_1) is the minimum value the obstacle strength (β_c) may have if the obstacle array is to be mechanically stable with respect to glide. Hence if $\beta_c = \beta_1$, $\tau^*_c = \tau^*$. Since it may be easily shown that β_1 is a monotonically increasing function of τ^* in a given array, a determination of β_1 as a function of τ^* is equivalent to a measure of τ^*_c as a function of β_c. The strength (β_1) is plotted as a function of the applied stress (τ^*) in Fig. 2. The bars indicate the range of values obtained in tests of several arrays.

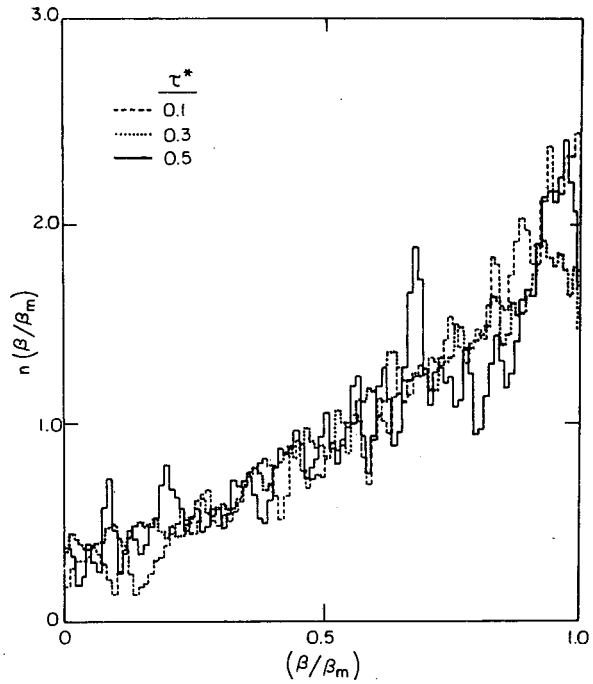

Fig. 2. The dependence of the strength (β_1) of the most stable configuration on the applied stress, τ^*. The solid bars show the range of values for four arrays. The dashed bars show the range of values for twenty arrays. The solid curve represents the data obtained by Foreman and Makin. The dashed curve is a plot of the Friedel relation. The insert shows normalized histograms of the β_1 values of 20 arrays at each of three stresses: $\tau^* = 0.1$, 0.3, and 0.5. (XBL 7310-5464)

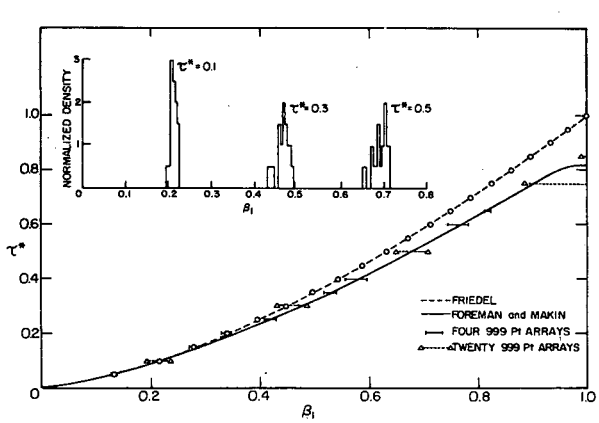

Fig. 3. Normalized histograms of the density of forces (measured as the ratio (β/β_m)) along stable configurations of strength $\beta_m \sim \beta_1$ at each of three stresses: $\tau^*=0.1(\beta_m=0.2339)$; $\tau^*=0.3(\beta_m=0.5080)$; and $\tau^*=0.5(\beta_m=0.7109)$. (XBL 7310-5461)

At low values of τ^* the "Friedel equation" (dashed curve) gives a good approximation. At higher values of τ^* not all arrays contain stable configurations. The limiting stress at which one-half the arrays become transparent is near 0.8. To indicate the nature of the scatter in data obtained at given stress, the insert in the figure shows normalized histograms of the β_1 values found in tests of the same arrays at three stress.

To study the distribution of forces along strong configurations we compiled and compared the $\{\beta_i^k\}$ for strong configurations in several arrays at given values of τ^*. The results are plotted in Fig. 3, which shows the normalized density of forces $(n(\beta/\beta_m))$ at $\tau^*=0.1$, 0.3, and 0.5. The slight drop in $n(\beta/\beta_m)$ is spurious; the configurations used in the compilations have a distribution of strengths. The normalized density functions nearly coincide. Contrary to a common

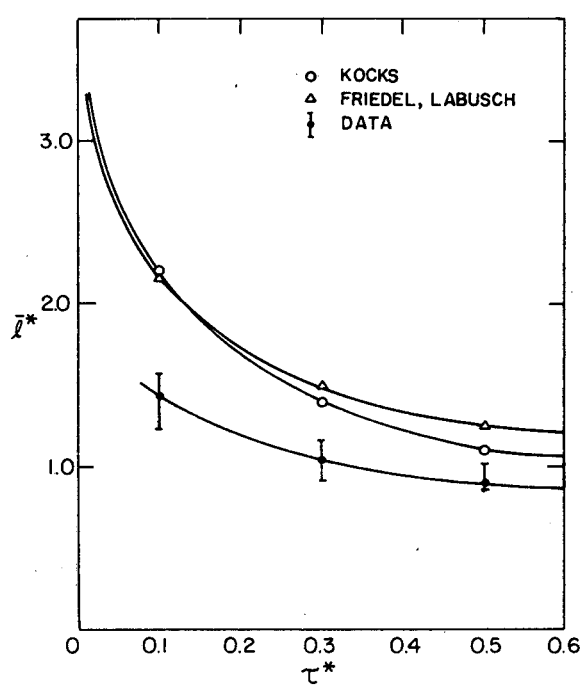

Fig. 4. The variation of the mean obstacle spacing ($\bar{I}^*$) in the strength-determining configurations with the applied stress (τ^*). The solid circles give the mean value obtained using configurations from 100 randomly chosen arrays at $\tau^* = 0.1$ and 0.3, and configurations from 20 random arrays at $\tau^* = 0.5$. The solid bars show the range of $\bar{I}^*$ for the strength-determining configurations in 20 arrays. The comparison curves plot the theoretical relations of Friedel, Labusch, and Kocks. (XBL 7310-5463)

speculation, there is no tendency for the distribution to become spiked at β_m as τ^* becomes small.

Figure 4 shows the trend with τ^* of the mean interobstacle segment length, $\bar{\ell}^*$, along the strong configurations. The plot also includes curves obtained from three estimates. Contrary to a frequent assumption, the data do not tend toward the Friedel-Labusch curve as τ^* becomes small; they rather diverge from it.

Our studies of the glide path χ focused on the minimum angle path, χ_o. We studied the distribution of strengths (β_i) of the configurations in χ_o and the distribution of forces ($\{\beta_i^k\}$) as a function of strength. The distribution of the β_i along χ_o was found as a function of τ^* by compiling the strengths of all lines encountered along the minimum angle path in 20 arrays each containing 10^3 points. Typical results are shown in Fig. 5, where we have plotted the density (per array) of configurations of strength β_i encountered along χ_o at stress $\tau^* = 0.1$, 0.3, and 0.5. The area under these curves gives the total number of non-transparent

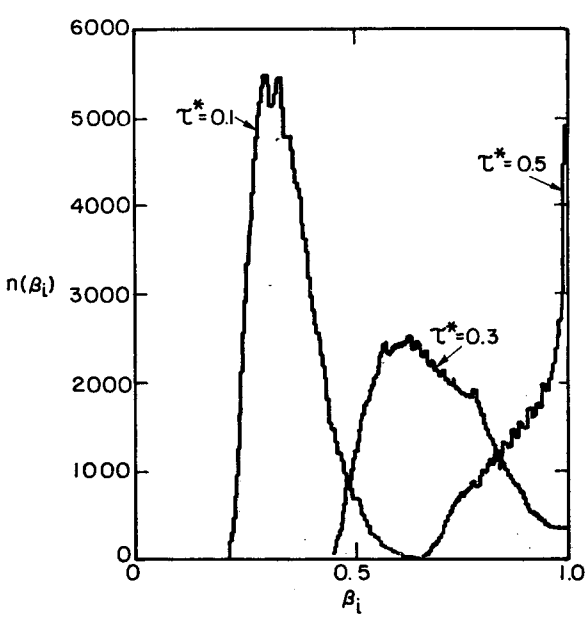

Fig. 5. Histograms showing the distribution of the strengths (β_i) of the configurations encountered along the minimum angle path (χ_o) at each of three stresses, $\tau^* = 0.1$, 0.3, and 0.5. The histograms were obtained by superimposing data from 20 random arrays. The area under the curves gives the mean number r of stable configurations on χ_o per array, and is r = 890 at $\tau^* = 0.1$, 750 at $\tau^* = 0.3$, and 470 at $\tau^* = 0.5$.
(XBL 7310-5457)

configurations (r per array) along χ_o at given stress, and is r = 890 at $\tau^* = 0.1$, r = 750 at $\tau^* = 0.3$, and r = 470 at $\tau^* = 0.5$. Given an obstacle strength, β_c, the expected number of mechanically stable configurations at τ^* is simply the area under the appropriate curve over the range $\beta \leq \beta_c$. The distribution of forces, $\{\beta_i^k\}$, along a configuration in χ_o is, to a reasonable approximation, determined by the strength, β_i. Excepting the first few configurations encountered as the dislocation moves into the array, the distribution of the β_i^k always approximates the strong-line distribution for $\beta \leq \beta_1$, and will also include one or a few $\beta > \beta_1$ scattered over the range $\beta_1 < \beta \leq \beta_i$. The third property of the path χ_o studied in this investigation was the spatial distribution of the strong obstacle configurations. The principal observation from this study is the tendency of the strong configurations to bunch so that they share many obstacle points in common.

As the temperature is raised from near zero the parameter α decreases and the path, χ, followed in glide becomes a stochastic sequence different from χ_o. It is difficult to characterize these finite temperature paths. However, one can make the general statement that a stochastic path χ will tend to contain fewer strong configurations than the minimum angle path χ_o, and hence will permit somewhat faster dislocation glide.

The expected velocity of glide was studied as a function of the parameters governing temperature (α), stress (τ_c), and obstacle strength (β_c). The principal observation from these studies was that, despite the fact that the path followed by the dislocation begins to deviate from χ_o at rather large values of α, an estimate of the glide velocity which assumes χ_o gives results in reasonable agreement with the simulation for α greater than about 50. If we assume the path χ_o and let α be large, the expected velocity of glide is given by the equation

$$\langle v^* \rangle = n^{1/2} \, [1-(Q-T_1)] \, \exp[-\alpha(\beta_c-\beta_1)] \quad , \tag{3a.15}$$

where Q and T_1 denote the series:

$$Q = \sum_{i=2}^{r_o} \exp[-\alpha(\beta_i-\beta_1)] \tag{3a.16}$$

and

$$T_1 = \sum_{k=2}^{N_1} \exp[-\alpha(\beta_1-\beta_1^k)] \quad , \tag{3a.17}$$

with r_0 the number of configurations in χ_0, β, the strength of the strongest configuration, and N_1 the number of obstacles in the strongest configuration. The series Q is the lead correction term giving the decrement in $\langle v^* \rangle$ due to the fact that the dislocation must activate past stable configurations in addition to the strongest along χ_0. The series T_1 is the lead correction term giving the increment to $\langle v^* \rangle$ from the possibility of thermal activation at a point other than the weakest in a stable configuration. The parameter T_1 specifically measures this effect for the strongest configuration (i=1).

Equation (3a.15) contains only known terms. The strength β_1 may be estimated for given τ^* from Fig. 2. The forces β_i in the series Q may be estimated from histograms as appear in Fig. 10. The distribution of forces β_1^k in the series T_1 may be estimated from histograms such as those in Fig. 3.

The effect of temperature, stress, and obstacle strength on $\langle v^* \rangle$ may be easily seen from Equation (3a.15). At large α, $\langle v^* \rangle$ obeys an Arrenhius equation with activation energy $(\beta_c-\beta_1)$. As α decreases $\langle v^* \rangle$ will deviate from the Arrenhius equation in a direction which depends on the relative magnitudes of Q and T_1. When τ^* is well below τ^*_c, Q dominates and the glide velocity falls below its asymptotic curve; when $\tau^* \sim \tau^*_c$, T_1 dominates and $\langle v^* \rangle$ lies above the asymptotic curve.

The deformation of a simple crystal is simulated by letting the crystal be made up of a set of independently chosen glide planes and assuming a distribution of non-interacting dislocations. The character of the results may be illustrated with a simple example. Let a hypothetical crystal contain four parallel glide planes, which we specify by randomly selecting four arrays of 10^3 points, and let the obstacles impeding glide through these planes have strength $\beta_c = 0.63$. The glide characteristics of these planes are shown in Fig. 6, where we have plotted the glide velocity $\langle v^* \rangle$ as a function of the thermal parameter, α, for each plane at each of the four stresses, $\tau^* = 0.1$, 0.2, 0.3 and 0.4. As shown in the figure, at $\tau^* = 0.1$ and 0.2 the velocity of glide is essentially the same in the four planes, while at $\tau^* = 0.3$ and $\tau^* = 0.4$ the velocities scatter by an amount which increases with α. The increasing spread in $\langle v^* \rangle$ as τ^* is raised is in large part attributable to the increasing spread in the β_1 values as τ^* is raised. At stresses of $\tau^* = 0.1$ and 0.2 the velocity v^* based on the ergodic distribution (e.g., V.9) is very nearly equal to the velocity $\tilde{v}^*$ based on the uniform distribution. However, at $\tau^* = 0.3$ and 0.4, $\tilde{v}^*$ is substantially less than $\bar{v}^*$. The two velocities are plotted in Fig. 6. The character of the crystal deformation obtained

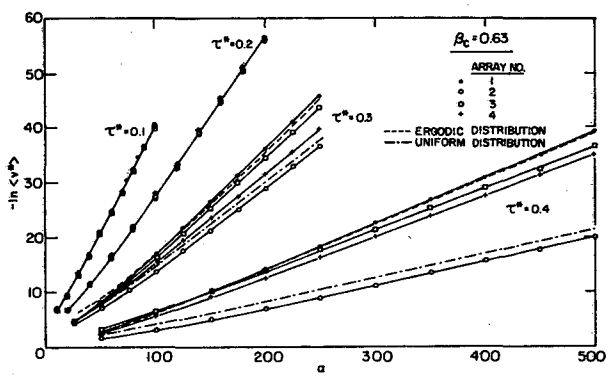

Fig. 6. Comparison of the velocity-temperature relations for four arrays of 999 obstacles having $\beta_c = 0.63$ at each of four stresses. Also included are the velocity-temperature curves for a crystal made up of these four arrays under each of two assumptions: an ergodic distribution of dislocations over the planes (----) and a uniform distribution of dislocations over the planes (-·-·). (XBL 7310-5467)

is illustrated in Fig. 7. Assume the hypothetical crystal contains a uniform distribution of dislocations, and, moreover, that the density of these dislocations is independent of temperature and stress. In this case the strain rate ($\dot{\gamma}$) of the crystal is simply proportional to the average glide velocity ($\tilde{v}^*$). Now imagine an experiment in which the crystal is strained by a fixed amount (for example, $\dot{\gamma} = 0.2$) at a given strain rate (for example, let $\ln v^* = -10$). As illustrated in Fig. 7, both the stress required to accomplish this deformation and the final appearance of the crystal depend markedly on the temperature at which the experiment is carried out. It is particularly interesting that at low temperature (large α) the deformation is concentrated on a unique slip plane. As temperature is raised (α decreased) the inhomogeneity disappears and dip becomes uniform. This behavior is qualitatively duplicated in the deformation of real crystals.

To complete the solution of the problem of glide through random arrays of point obstacles we require analytic solutions for the properties of obstacle configurations, to

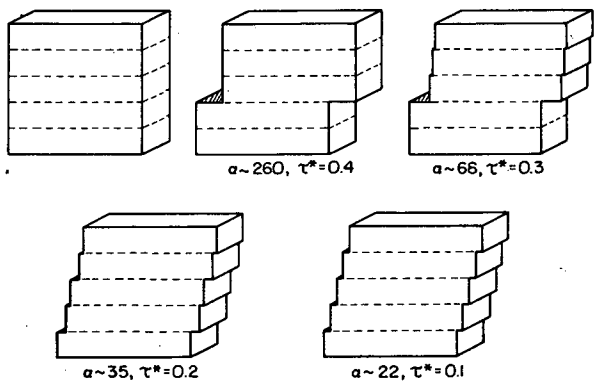

Fig. 7. Illustration of the deformation of a hypothetical crystal made up of the four glide planes whose properties are shown in Fig. 6. This figure shows the change in the appearance of the deformed crystal with temperature, assuming that the crystal contains a uniform distribution of dislocations of fixed density, and is given a total shear strain $\gamma = 0.2$ at a fixed strain rate such that $-\ln \tilde{v}^* = 10$. (XBL 7310-5468)

relieve our dependence on computer simulation. We have made progress in finding analytic approaches, and have recently obtained equations which allow us to estimate the properties of strength-determining configurations with reasonable accuracy.

*Abstracted from LBL-1166 and LBL-2276.

b. Solution Hardening*

Chol K. Syn and John W. Morris, Jr.

Much of the available theoretical work on solution hardening in metals is based on the assumption that the solute atoms may be treated as point barriers to dislocation glide. Similarly, the results of theoretical and computer simulation studies of the glide of dislocations through fields of point obstacles can only be applied to solution hardening to the extent that a point obstacle approximation can be sustained. It is, however, known that the interaction between a solute atom and a dislocation is of relatively long range, decreasing roughly with the inverse square of the separation distance between the atom and the dislocation. Since general criteria for the validity of point obstacle representations suggest that the range of interaction must be small (by some measure) compared to the separation of obstacle centers, the point obstacle approximation may only be useful in solution hardening theory when the solute concentration is very small.

Some indication of the applicability of the point obstacle approximation may be obtained from the solution of simple tractable models, such as the interaction of an idealized dislocation with square arrays of solute atoms which act as simple elastic strain centers in the glide plane. Previous solution of this problem have been used to argue that the point obstacle approximation is valid only in the limit of extreme dilution, $c \lesssim 10^{-5}$ (atom fraction). These results are, however, open to alternate interpretations; the extreme limiting conditions found may have resulted from the specific form of the point obstacle approximation used for comparison rather than from inherent shortcomings of the approximation itself. We have hence reinvestigated the problem.

A tractable problem is phrased under the following assumptions. The material is taken to be a linear elastic continuum containing a dislocation in edge orientation. The glide plane of this dislocation contains a square array of non-interacting solute atoms, modeled as elastic strain centers of magnitude determined by their size mismatch with the host lattice. The dislocation-solute interaction is assumed given by the elastic interaction between the dislocation and solute fields. This interaction is singular at the dislocation core; the singularity is artificially removed, using the Dorn-Stefansky modification of the Cottrell core correction. Taking the glide plane of the dislocation to lie midway between atom planes, we consider interaction only with solute atoms in planes immediately adjacent to the dislocation. The sign of the dislocation-solute interaction is reversed as an atom is displaced vertically through the glide plane of the dislocation. Hence the dislocation sees two distinct types of solute atoms. To partly account for this, the square array of barriers may be taken to consist of alternate attractive and repulsive strain centers.

Given these approximations, an edge dislocation of Burgers' vector b and line tension $\Gamma (\sim 3/4Gb^2$, where G is the shear modulus) will adopt an equilibrium configuration under resolved shear stress τ which is governed by the differential equation

$$\frac{d^2y/dx^2}{\{1+(dy/dx)^2\}^{3/2}} = -\frac{b}{\Gamma}(\tau+\tau_{yz}) , \qquad (3b.1)$$

where τ_{yz} is the resolved shear stress on the dislocation due to its interaction with solute atoms on the adjacent planes. If the glide plane is a close-packed plane in an fcc or hcp structure,

$$\tau_{yz} = \frac{6G\varepsilon r_o^3}{\sqrt{6}} \sum_{m,n=-\infty}^{\infty} (-1)^{m+n} \frac{(y-n\ell_s)\left\{1-e^{-\left(\frac{3}{b^2}\right)[(x-m\ell_s)^2+(y-n\ell_s)^2+b^2/6]}\right\}}{[(x-m\ell_s)^2+(y-n\ell_s)^2+b^2/6]^{5/2}} \qquad (3b.2)$$

for an array of alternate attractive and repulsive obstacles of separation ℓ_s, with r_o the radius of the solvent atom and ε the size mismatch parameter of the solute. Equation (3b.1) was solved numerically to obtain the dislocation configuration as a function of τ for given ℓ_s and ε, and to determine the stress (τ_y) at which the dislocation glides freely through the array of barriers as a function of ℓ_s for given ε=0.06. Computations were carried out for arrays of alternated attractive and repulsive barriers, for arrays of like repulsive barriers [in which case the factor $(-1)^{m+n}$ in Eq. (3b.2) becomes 1], and for arrays of like attractive barriers [$(-1)^{m+n}$ becomes -1]. Figure 1 shows the computed configurations of the dislocation at the instability point (τ_y) in the alternate array at five values of ℓ_s.

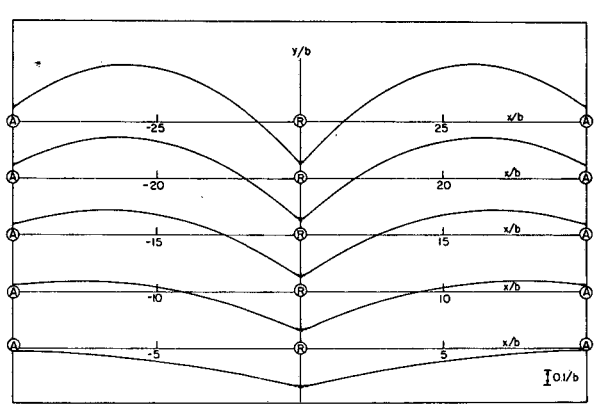

Fig. 1. Variation of equilibrium configurations of dislocation line at the flow stress level in alternating arrays with ℓ_s=10b to 50b, increasing by 10b. (XBL 739-1874)

To compare these results with those obtained from the point obstacle approximation we first found it necessary to phrase the point obstacle approximation in precise form. This was done using the Gibbs construction illustrated in Fig. 2. We enclose the obstacle in an imaginary circle (d) of small radius (d) appreciably greater than (d'), the distance over which the dislocation (L) is significantly perturbed by the obstacle. We then extrapolate the arms of L into D until they meet at a point

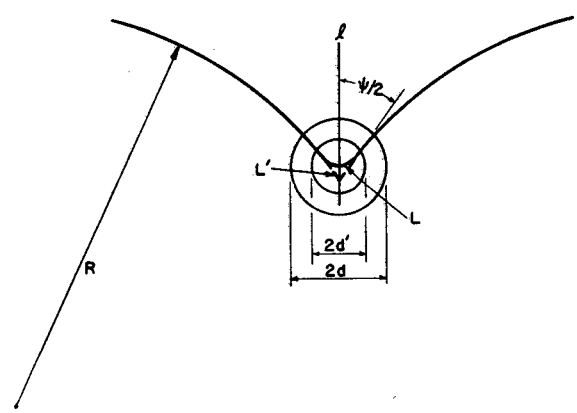

Fig. 2. A geometric construction used to define the point properties of an obstacle having a circularly symmetric interaction with a dislocation. (XBL 732-5723)

x, letting the extrapolated lines (L') represent the dislocation within D and letting the point of intersection represent the obstacle. By equating the energy of the hypothetical configuration (L') to that of the actual configuration (L) we obtain the energy (ω') of the dislocation-obstacle interaction in the point obstacle representation. By minimizing this energy we establish the conditions for equilibrium in the point obstacle representation

$$\tau b = \Gamma/R \qquad (3b.3)$$

everywhere on L', where R is the radius of curvature of the dislocation outside D, and

$$F = 2\Gamma \cos\psi/2 \qquad (3b.4)$$

at x, where F is the equivalent point force exerted by the obstacle and ψ is the asymptotic angle of the arms of the dislocation at x. A force-displacement curve for the dislocation-obstacle interaction is obtained by incrementing τ so that the dislocation moves through the obstacle at equilibrium.

Force-displacement diagrams for solute atoms in attractive and repulsive orientation were found from solution of Eq. (3b.1) for

arrays of like obstacles, after first confirming that the dislocation was perturbed only when very close ($\lesssim$ 1b) to the obstacle. The result for a repulsive obstacle is shown in Fig. 3. The maximum in the curve is related to the critical cutting angle (ψ_c) for the obstacle according to Eq. (3b.4). This maximum is displaced by $-\delta (\simeq 0.3\ b)$ toward the dislocation from the physical center of the obstacle, and effectively locates the equivalent point obstacle. The force-displacement curve for the attractive obstacle is nearly the mirror image of that for the repulsive obstacle. It is, however, slightly stronger (with a lower value of ψ_c) and is displaced by δ from the physical center of the obstacle.

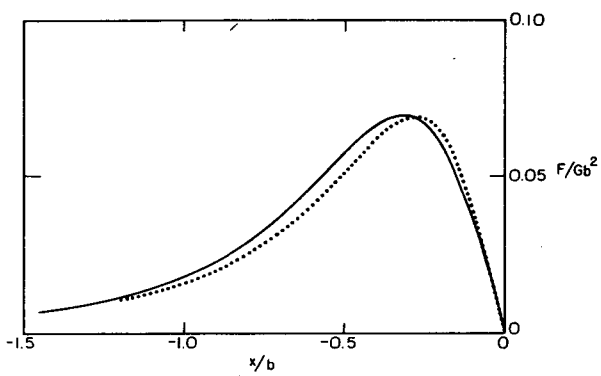

Fig. 3. The force-displacement relation for the interaction between a dislocation and a repulsive elastic barrier of size mismatch $\varepsilon = 0.06$. F is the force exerted by the dislocation on the obstacle at equilibrium as a function of distance from the physical center of the obstacle. The colid curve is computed from the point obstacle approximation. The dotted comparison curve assumes a rigid dislocation. (XBL 738-1655)

In the point obstacle approximation the flow stress for glide through a square array may be written in simple dimensionless form

$$\tau^*_y = \cos(\psi_c/2) , \qquad (3b.5)$$

where $\tau^*_y = \tau_c \ell_s b/2\Gamma$. The dimensionless flow stress is hence independent of the obstacle separation (ℓ_s). Figure 4 shows that τ^*_y is in fact independent of ℓ_s down to small ℓ_s (large solute concentration) in both the attractive and repulsive arrays; hence, the point obstacle approximation accurately represents the properties of these arrays of like obstacles.

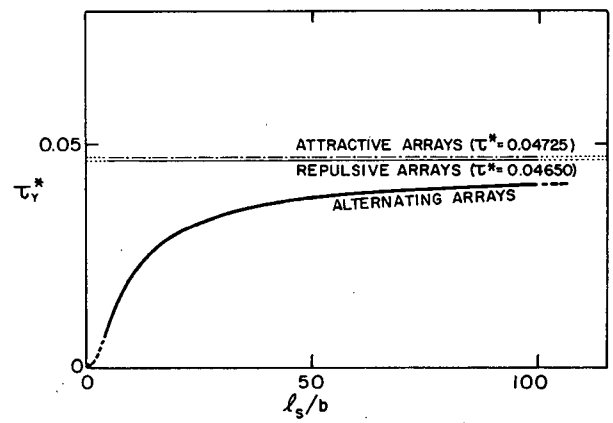

Fig. 4. Variations of the flow stresses τ_Y^* with ℓ_s/b. (XBL 739-1870)

The dimensionless flow stress, τ^*_y, in an array of alternating obstacles is strongly dependent on ℓ_s. However, this does not signify a major breakdown in the point obstacle approximation. Given the displacement of the equivalent point obstacle from the physical center fo the solute atom, and given that the displacement reverses sign for attractive and repulsive barriers, in the point obstacle representation of the alternate array the dislocation "sees" a zig-zag barrier of obstacles offset by $2\delta \sim 0.6$ rather than a linear barrier of equispaced obstacles. In this case Eq. (3b.5) must be modified to

$$\tau^*_y \sim \cos[\psi_c/2 - 2\delta/\ell_s] \quad . \qquad (3b.6)$$

This equation fits the flow stress curve for the alternate array down to values of ℓ_s corresponding to c near 0.01, a range of c which includes the whole range over which the assumptions underlying this analysis of solute hardening remain plausible.

We hence conclude that the point obstacle approximation can be applied to physically important cases of hardening by dilute solutes, a result supported by an analysis of experimental data.

A major assumption in our analysis of the point obstacle representation of the dislocation-solute interaction was the elastic isotropy of the lattice. To estimate the effect of anisotropy we analyzed the dislocation-solute interaction for an edge dislocation in the basal plane of an hexagonal lattice. We specifically treated the problem of Ag or Cd impurities in Zn. Contours of the dislocation-solute interaction for the

two impurities are shown in Fig. 5a & b, where it is assumed that the interaction is due to the anisotropic size effect only. The two impurities interact in rather different ways with the dislocation: Cd prefers a site immediately beneath the dislocation, while Ag prefers sites displaced slightly to either side of it.

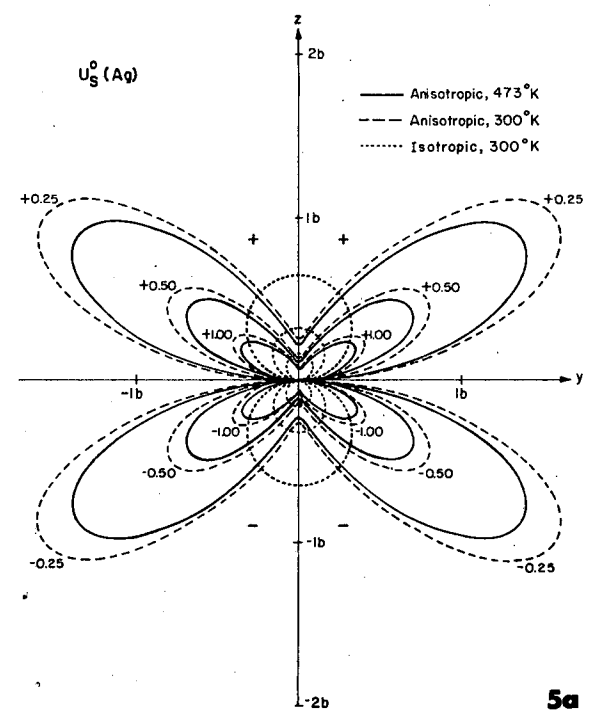

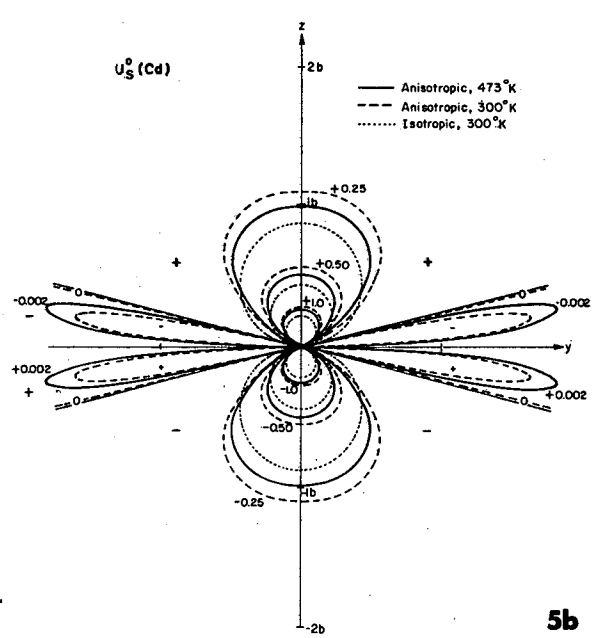

Fig. 5. (a) Anisotropic interaction energy contours for Ag and Cd.
(b) Anisotropic interaction energy contours for Ag solute atoms due to the "size" effect.
(XBL #'s 7310-5529, 5530 respectively)

The force-displacement relations for the two impurities, acting as attractive barriers, are shown in Fig. 6a & b and compared with relations computed assuming elastic isotropy. The most significant feature of these curves is the pronounced increase in the strength of the barrier when the anisotropic interaction is taken into account. The peak of the Cd interaction curve increases by more than a factor of 2; that of Ag rises by almost a factor of 10. These results indicate that the solute hardening effect may be much more pronounced

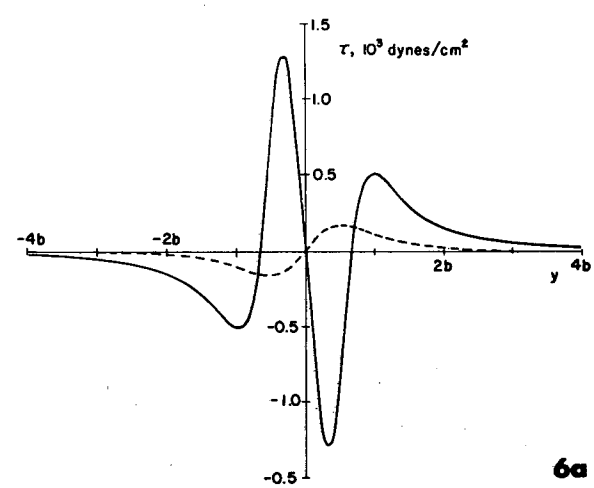

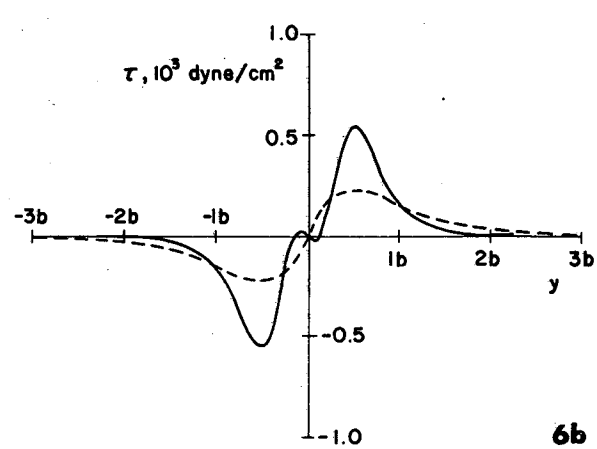

Fig. 6(a & b)Force displacement curves for interaction of an edge dislocation in the basal plane of Zn with (a) an Ag atom and (b) a Cd atom. The solid curves include anisotropy. The dotted curves assume isotropy.
(XBL #'s 7312-7147, 7148 respectively)

than is guessed from isotropic elasticity, a result which may help to explain anomalies in the experimental data on solution hardening.

*Abstracted from LBL-2270.

c. High-Temperature Creep*

Dionysios Grivas and John W. Morris, Jr.

A central problem in the study of high-temperature creep is the formulation of reliable constitutive equations to represent the creep data. While a precise constitutive equation cannot be written down until the mechanisms of creep are fully understood, the semi-empirical relations proposed by Dorn and his associates have been shown to represent the steady-state creep behavior of a number of important systems. The relevant work is summarized in a recent review by Bird, Mukherjee, and Dorn (UCRL-19056) who offer a general equation which we may write in the dimensionless form:

$$(\dot{\gamma}^*) = A(\tau^*)^n (d^*)^{-m} \exp(-\Delta H^*/RT) \qquad (3c.1)$$

The dimensionless shear strain rate ($\dot{\gamma}^*$) is given by ($\dot{\gamma}kT/D_0Gb$), where G is shear modulus and D_0 is a pre-exponential diffusivity; τ^* is the dimensionless stress (τ/G); d^* is the dimensionless grain diameter (d/b); ΔH^* is an apparent activation energy for creep; the symbols A, m, and n represent constants. Most of the suggested constitutive equations for high-temperature creep can be drawn from Eq. (3c.1) through proper choice of the constants A, m, and n.

Bird et al. support this equation with an extensive compilation of data on the steady-state creep of metals and simple alloys. They further conclude, on the basis of limited data, that the equation will also represent the steady-state creep of materials which exhibit superplasticity. They specifically suggest that as τ^* is decreased a superplastic material will pass through three distinct regions of steady-state creep behavior, in each of which a particular variant of the equation will be obeyed. (1) When τ^* is sufficiently large they predict a conventional steady-state creep controlled by a dislocation climb mechanism. They hence anticipate a stress exponent (n) in the range 4-7, an apparent activation energy (ΔH^*) near that for bulk diffusion, and a creep rate independent of grain size (m=0). (2) For smaller τ^* they suggests a region of well-defined "superplastic" creep. On semi-empirical grounds they anticipate n~2, ΔH^* near that for grain boundary diffusion, and an inverse-square grain size dependence (m=2). (3) For very small τ^* they predict a behavior dominated by the Coble mechanism of creep through grain boundary diffusion. They hence anticipate an exponent n=1, an activation energy ΔH^* equal to that for grain boundary diffusion, and an inverse-cube dependence on grain size (m=3).

Bird, Mukherjee, and Dorn support their interpretation of creep in superplastic materials by replotting the data of Avery and Backofen on a Pb-Sn eutectic alloy and the data of Ball and Hutchison on a Zn-Al eutectoid. They argue that both alloys show clear regions of "conventional" and "superplastic" creep, and find some evidence for Coble creep in Zn-Al at low stress. However, the data obtained in these two investigations are limited, and do not permit a full test of the proposed constitutive equations. Recently both Vaidya, Murty, and Dorn (LBL-459) and Misro and Mukherjee have reinvestigated the steady-state creep of Zn-Al eutectoid. Both sets of investigators claim verification of the Bird-Mukherjee-Dorn representation. There is, however, no comparable data for the Pb-Sn eutectic. While several investigators have studied the steady-state creep of this alloy, no single investigation contains enough information to evaluate all of the creep parameters. A superposition of data would be of dubious value, since the results of these investigations are inconsistent with one another.

We hence undertook an experimental investigation of the steady-state creep of superplastic Pb-Sn eutectoid. The investigation was conducted in two parts. First, we used an Instron machine to measure steady-state creep ratio over a range of τ^* from 2×10^{-5} to 2×10^{-3} at temperatures from 0°C-150°C for samples of grain size from 5-10 μm. Second, we used a constant-load creep machine to measure steady-state creep rates over a range of τ^* from 6×10^{-7} to 10^{-4} at temperatures from 98 to 170°C for samples of grain size from 2.8-7 μm.

The tests conducted at higher stress generally confirmed the expectations of Bird, Mukherjee, and Dorn. Logarithmic plots of measured steady-state strain rate as a function of applied stress divided naturally into two distinct regions: a high-stress region of "conventional" creep with slope n~7, and a lower-stress region of "superplastic" creep with slope n~2. These

regions of creep behavior are apparently associated with different dominant creep mechanisms. Samples tested in the conventional creep region showed significant primary creep, while samples tested in the superplastic region did not. Creep rates in the superplastic region depended on grain size, while creep rates in the conventional region did not. Hence, assuming that Eq. (3c.1) applies, the two distinct regions of creep behavior should be governed by different variants of the equation.

An analysis of the creep data showed that Eq. (3c.1) could be used to describe behavior in either region. The conventional creep data were fit to the equation with parameters $A=1.5\times10^{15}$, n=7.1, m=0, and $\Delta H^*=19.4$ kcal/mol. These values were in general agreement with those found in conventional creep of pure lead and pure tin (LBL-831). The value of ΔH^* is of the right order to be interpreted as an activation energy for bulk diffusion. The coalescence of the conventional creep data on a curve characterized by these parameters is illustrated in Fig. 1.

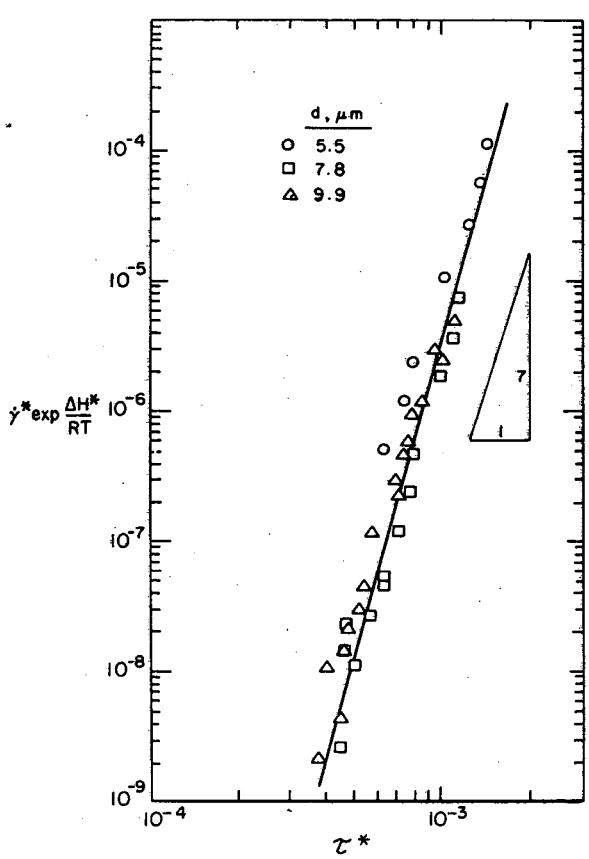

Fig. 1. Plot of $\dot{\gamma}^* \exp(\Delta H^*/RT)$ vs τ^* for the conventional creep region revealing no grain size dependence and a slope n = 7.1. (XBL 7211-7188)

Individual determination of the parameters characterizing superplastic creep gave A=900, n-2, m=1.8, and $\Delta H^*=11.5$ kcal/mol. These numbers are close to the anticipated values. The activation energy ΔH^* is of the right order to be interpreted as an activation energy for surface diffusion. The coalescence of the superplastic creep data on a curve determined by these values of the creep parameters is illustrated in Fig. 2.

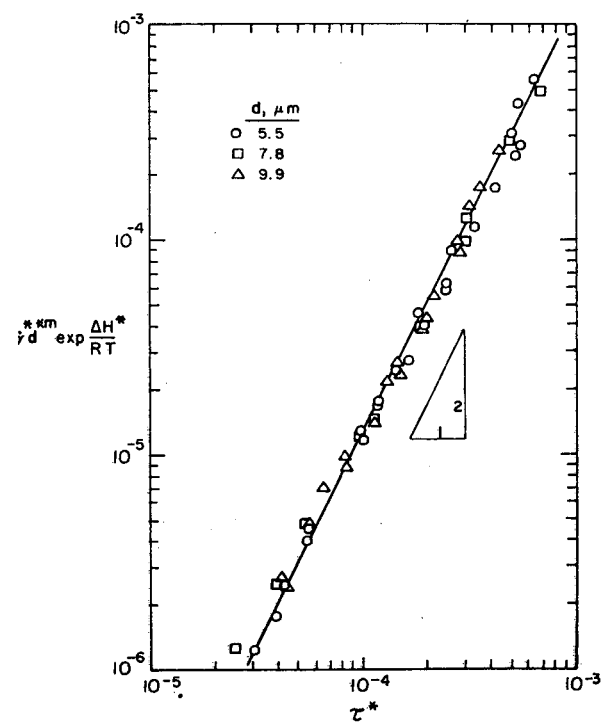

Fig. 2. Plot of the strain rate compensated for temperature and grain size vs τ^* for all superplastic data. (XBL 7311-6735)

While the Instron tests tended to support Bird et al., the lower stress tests revealed two surprising results. First, while we did observe a break in the creep curve indicating a change in mechanism at low stress, the low stress creep behavior was not of the Coble type. It was characterized by parameters $A=3.2\times10^{12}$, n=3, m=2.1, and $\Delta H^*=18.9$ kcal/mol. The coalescence of the creep data on a curve determined by these values of the creep parameters is illustrated in Fig. 3. The value of the activation energy and the concomitant observation of primary creep clearly point toward some bulk flow-mechanism in this low-stress region. The value of the stress exponent n=3 shows

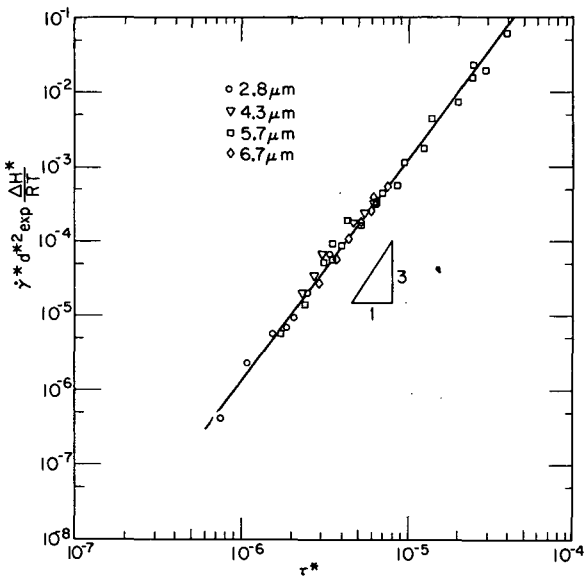

Fig. 3. A logarithmic plot of the strain rate compensated for temperature and grain size against τ*. (XBL 7312-6972)

that superplastivity is lost at low stress in this alloy. While we cannot definitively rule out a region of Coble creep at lower values of τ*, tests conducted at $\tau^* = 6.10^{-7}$ and d* = 2.8 μm, well within the range in which Coble creep is theoretically anticipated, failed to show any evidence for it.

Second, while tests conducted in the superplastic region in this series of experiments gave values of n, m, and ΔH* in good agreement with those obtained previously, the value of A was determined to be A=5000, more than an order of magnitude above the value (A=209) obtained in the earlier tests. This large increase in A is difficult to interpret. Given that the consistency of the two test techniques has been established previously, and that errors due to grain growth during testing would go in the opposite direction, the discrepency in A values seems attributable to some difference in the samples. We suspect a difference in microstructural state, since the samples for the two tests were prepared differently. If this is the case, Eq. (3c.1) is incomplete; the parameter A contains hidden variables which relate to the microstructural state. Such an interpretation may explain significant discrepencies between the results previously obtained by other investigators.

*Abstracted from LBL-2519 and LBL-2532.

4. ALLOY DESIGN*†

Sungho Jin, John W. Morris, Jr., and Victor F. Zackay

The specific objective of our principal alloy design activity is the identification of alloy compositions, microstructures, and processing techniques which may lead to new ferritic alloys combining high strength and toughness at very low temperatures. To accomplish this objective, initial alloy criteria were chosen to insure a beneficial combination of strength and ductility at low temperature. These may be summarized as follows:

(1) To ensure ductility the alloy must be structured so that internal stress concentrations are relieved before they lead to failure. This stress relief requires deformation of individual grains and reasonable accommodation of deformation at grain boundaries. Free deformation of the individual grains requires that these grains be provided with potentially mobile dislocations. The dislocations may come from a dense initial dislocation distribution or from a dense distribution of active dislocation sources. To insure the mobility of these dislocations, either the lattice concentration of free interstitials must be very low or the low temperature dislocation-interstitial interaction must be suppressed. The accommodation of deformation in adjacent grains is facilitated by fine grain size and requires that there be no significant brittle precipitation or film in the grain boundaries. Under appropriate conditions a ductile grain boundary phase may be beneficial.

(2) To achieve high strength consistent with ductility, available mobile dislocations must be efficiently pinned until the applied stress becomes large, in a way which does not sacrifice mobility once plastic deformation begins. One may devise solution-hardened, dislocation-hardened, or precipitation-hardened microstructures which will, at least in rough theory, function in this way. Our current emphasis is on precipitation-hardening techniques. Since the nature and distribution of precipitate phases may be specified through a proper choice of composition and processing and since the precipitate distribution remains roughly constant during deformation, the precipitation-hardening mechanism has an inherent controllability which makes it appealing in alloy design. The precipitates employed must, of course, form in the interior of the grains and must act without poisoning or embrittling the grain boundaries.

Given these criteria, the iron-nickel-titanium system is a natural candidate system from which to select initial compositions. The nickel-titanium couple in iron is known to be a chemically effective agent for reducing the free interstitial content and suppressing the embrittling effect of free interstitials. The phase diagram of the system contains a broad two-phase ferrite-austenite region at intermediate temperature, allowing use of a variety of processing and grain refining techniques. The ternary system also contains a series of Ni-Ti and Fe-Ti intermetallics which form preferentially in the ferrite phase and allow the use of precipitation hardening. Moreover, previous engineering experience has shown that high-nickel ferrites inherently possess good low-temperature properties.

Initial research on these alloys for cryogenic use was carried out by W. Horwood (LBL-1121), who studied the properties of a low-carbon Fe-12Ni-0.5Ti alloy. By treating forged alloys at temperatures near the two-phase ($\alpha+\gamma$) region he obtained fine-grained alloys which showed a promising combination of yield strength and Charpy impact toughness at liquid nitrogen temperature (77°K). However, despite early hopes, these alloys did not prove competitive in properties with available ferritic alloys, in particular the 9Ni cryogenic steel, at lower temperatures. Given the theoretical promise of these alloys we inaugurated new research with the specific objective of establishing superior cryogenic properties. The following alloy processing treatments were identified.

First, by dropping the titanium content from 0.5 to 0.25 weight percent, incorporating a cold working step into the processing sequence, and adding a low-temperature anneal at the end of the processing sequence, we obtained an alloy with an impact toughness exceeding the capacity of our test (225 ft. lb) at both 77 and 6°K, and with a yield strength competitive with the best available cryogenic alloys (140 ksi at 77°K; 185 ksi at 6°K). In choosing these modifications, the decrease in titanium content was motivated by the empirical results of exploratory tests. The cold-working step (~30% cold work) was added principally to enhance grain refinement during subsequent anneal; cold work also affects the dislocation substracture in ways we have not yet fully specified. The low-temperature anneal, at a temperature near 550°C, was added on the basis of exploratory work which showed that such an anneal causes a decomposition of the grain boundaries into a fine beaded structure, which, as transmission electron microscopy subsequently showed, consisted principally of equiaxed grains of retained austenite.

Second, we found through further work that the cold-working step in the alloy processing could be replaced by a thermal cycling treatment. Specifically, by periodically interrupting a 700°C anneal with an ice brine quench, and finishing processing with a final anneal at 550°C we were able to obtain an alloy having a yield strength of 185 ksi and an impact energy Of 205 ft lb at liquid helium temperature. The purpose of the

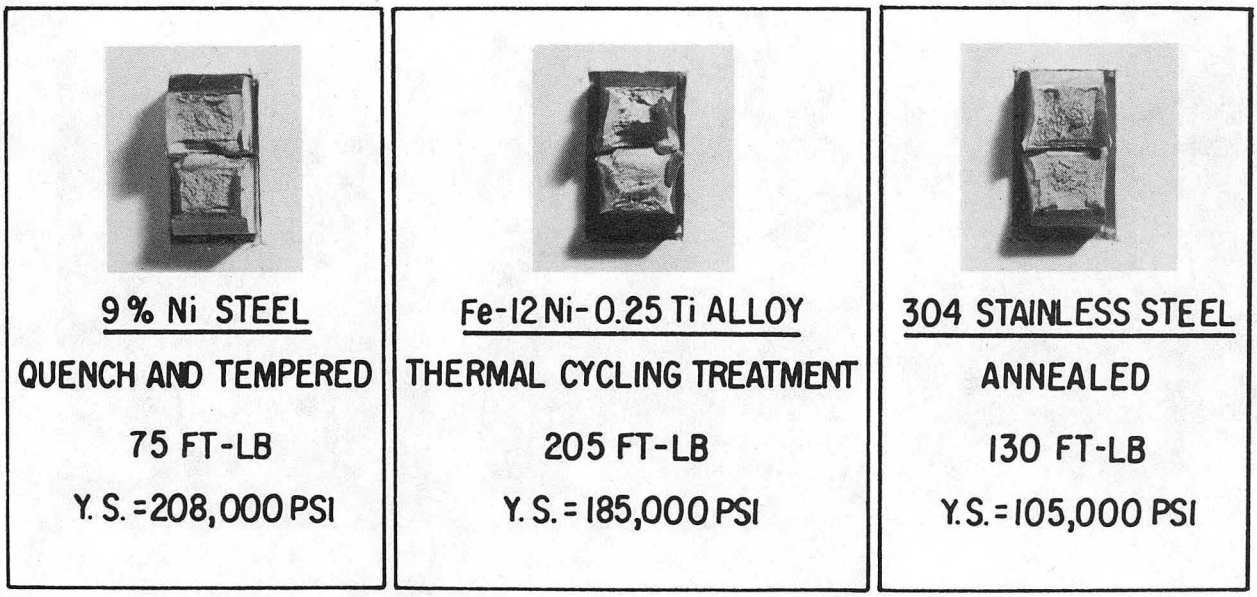

Fig. 1. Charpy specimens tested at 6°K. (XBB 732-1216)

thermal cycling treatment was grain refinement. Its effect on the substructure is not yet known. Figure 1 illustrates the results of Charpy impact tests, at 6°K, in which this alloy was compared with carefully processed 9Ni and 304 stainless steel.

Third, a combination of dilatometric and microstructural studies showed that the Fe-12Ni-0.25Ti alloy undergoes a shear reversion from the α to the γ phase on heating. This reversion occurs over a small temperature range near 700°C. Given the availability of alternate transformation paths, a thermal cycling about this shear reversion temperature should be a particularly efficient grain refinement technique. We found that six cycles of alternate anneals at 700 and 660°C lead to an alloy with an ultrafine grain structure of essentially equiaxed α phase, and that the 550°C final anneal decorated the grain boundaries of this structure with extremely fine grains, later found to be at least in part retained austenite (γ).

Tensile tests at 77 and 7°K showed that the engineering tensile properties of the ultrafine grained alloy were virtually identical to those previously obtained for this alloy, indicating that the tensile properties of the alloy are controlled by substructure more than grain structure. Charpy impact tests yielded good results (140 ft lb at 77°K, 134 ft lb at 6°K), though these results are less impressive than those obtained with other processing techniques. However, in fracture toughness test at 77°K, these alloys showed remarkable resistance to crack propagation. Using an ASTM standard "compact tension" fracture toughness specimens for tests at 77°K, the ultrafine grained alloy proved virtually immune to unstable crack growth, and subsequent fractography yielded no evidence of brittle or cleavage fracture in the sample. Figure 2 compares the load-displacement curves obtained at 77°K when 0.70-in. compact tension specimens of this alloy (labeled Treatment 4) were tested in comparison with the 9Ni steel and a sample given an alternate treatment. Figure 3

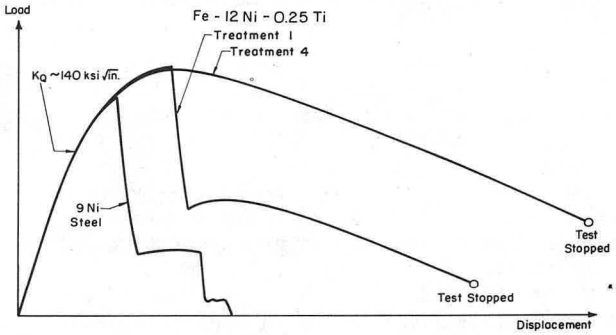

Fig. 2. Load-displacement curves obtained in fracture toughness tests comparing the 9-Nickel steel and two treatments of the Fe-12Ni-0.25Ti alloy at 77°K. (XBL 733-5855)

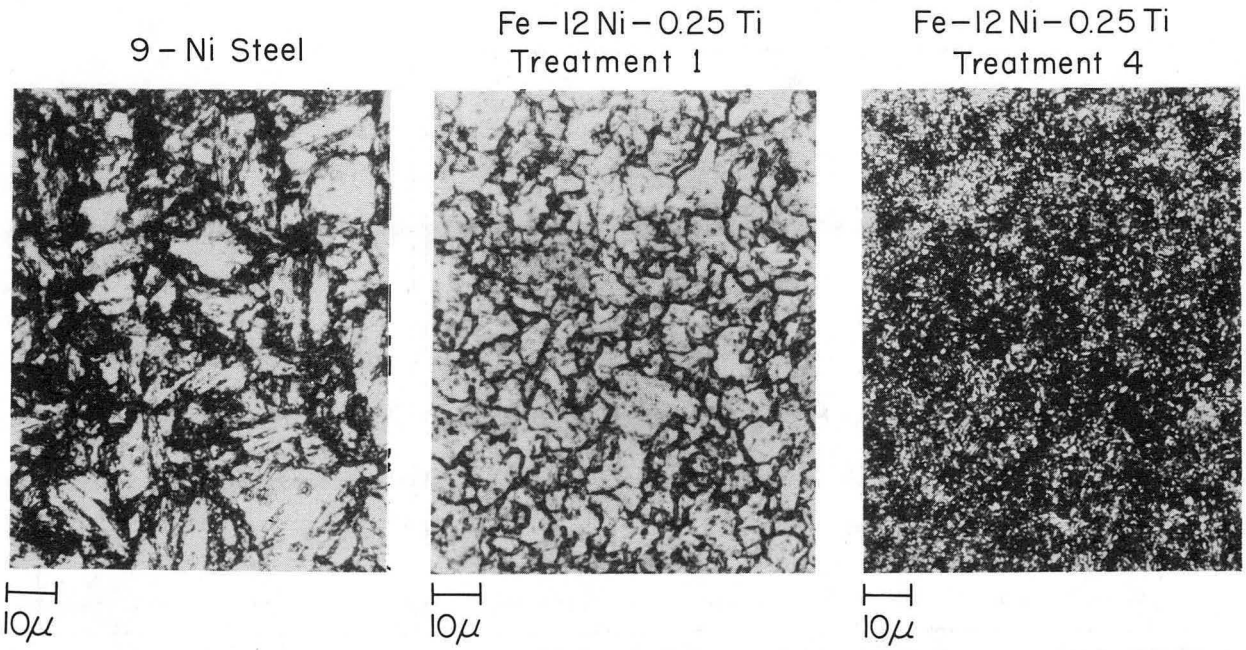

Fig. 3. Microstructures of alloys cited in Fig. 23. (XBB 737-4458)

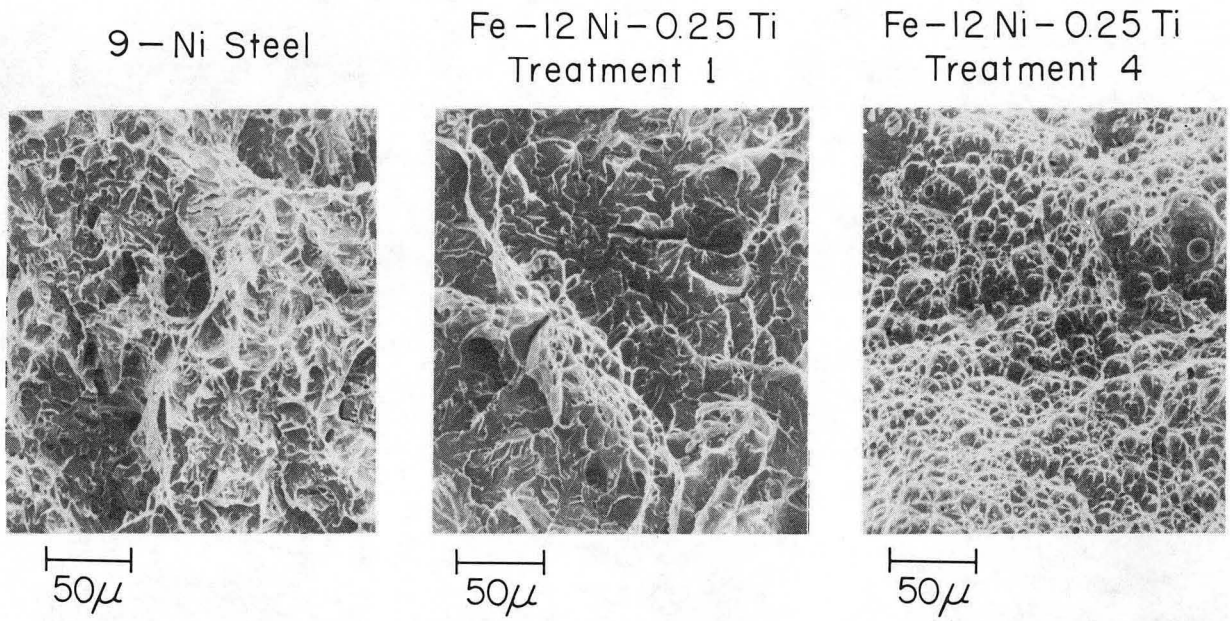

Fig. 4. Post-test fractographs of samples cited in Fig. 22. (XBB 737-4459)

compares the microstructures of the three alloys, and Fig. 4 compares scanning electron fractographs of the fracture surfaces.

Given the good low-temperature ductility of these ultrafine-grained alloys we began further research to improve their properties while simplifying the rather complex processing sequence initially used. Further dilatometric studies showed that at typical heating rates the shear reversion $\alpha \rightarrow \gamma$ initiates at a temperature slightly above 650°C, and is completed at a temperature slightly below 730°C. An anneal for ~ 2 hr at 650°C yields a fine lath-like mixture of α and γ which reverts entirely to α on cooling to room temperature. Subsequent alternate anneals at 730 and 650°C suffice to destroy the embrittling preferential orientation of intragranular laths. We therefore selected the processing sequence shown in Fig. 5, which consists of four anneals, alternately at 730 and 650°C. The successive steps are labelled 1A(730°C), 1B(650°C), 2A(730°C), and 2B(650°C). The evolution of the microstructure during this cycling is illustrated in Fig. 6. After final cycle 2B the bulk of the microstructure consists of a fine mixture of platelet grains ~1-4 μm long and a fraction of a micron in the short dimension. The preferential orientation of these platelets has been largely eliminated.

The available evidence indicates that the structure 2B is virtually 100% α phase at room temperature; we have been unable to detect γ. This conclusion was supported by

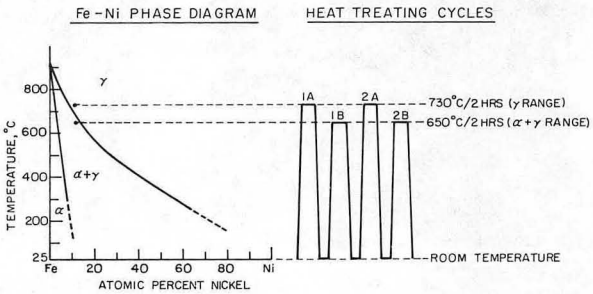

Fig. 5. The Fe-Ni equilibrium phase diagram with heat treating cycles. (XBL 739-1884)

the results of tests run for us by R. L. Miller of U.S. Steel, who employed advanced x-ray analysis techniques, which permit detection of as little as 0.1% retained γ.

We have explored the effect of adding additional 730°C/650°C cycles. These do give an apparent additional refinement of the larger grains remaining in the microstructure, but the effect is small and has no obvious influence on cryogenic mechanical properties.

The change in cryogenic mechanical properties on cycling is documented in Table I and in Fig. 7.

The results of tensile tests are shown in Table I. The yield strength at 77°K is in the range 140-150 ksi and is rather insensitive to microstructure. The samples

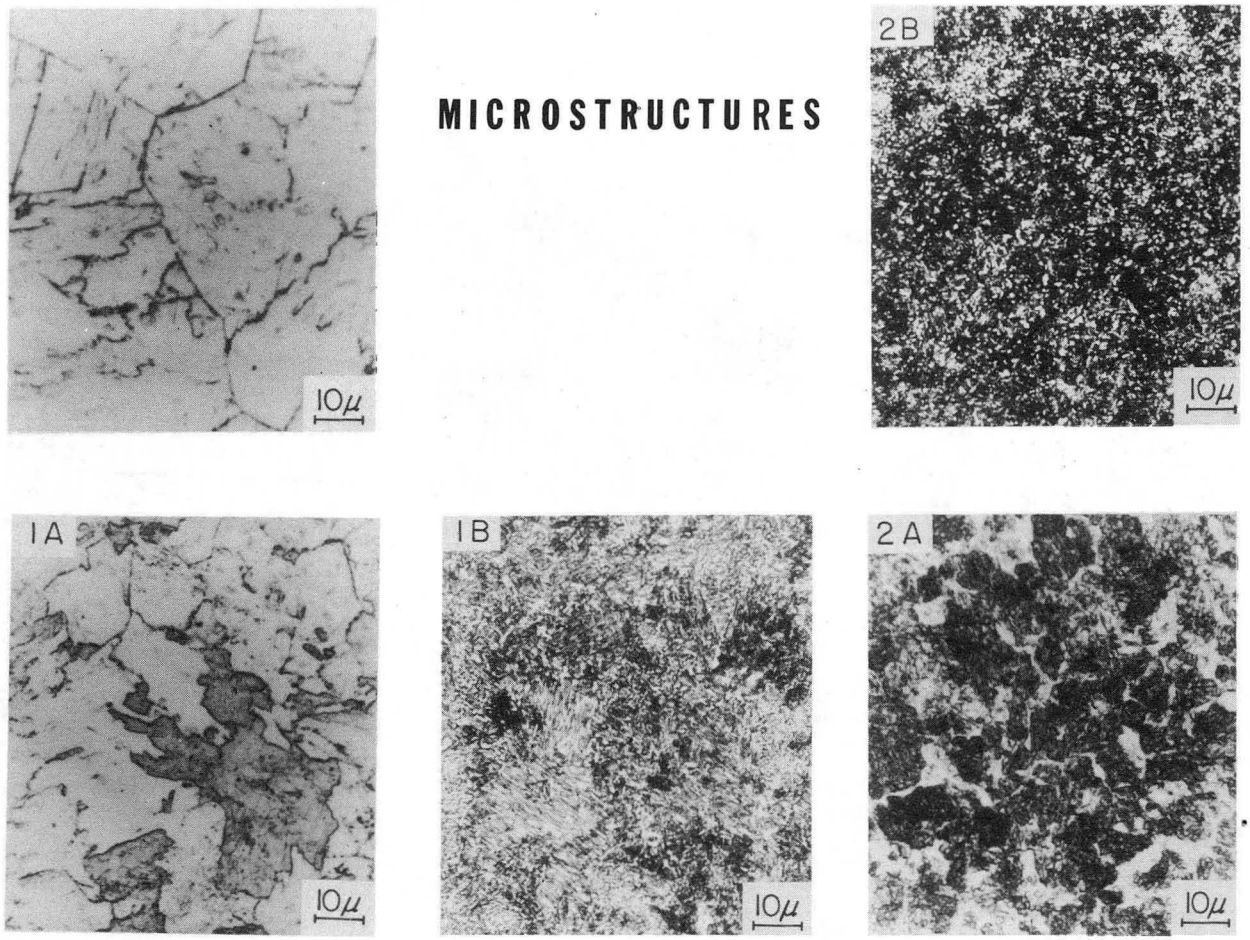

Fig. 6. Evolution of microstructure during thermal cycling. (XBB 739-5684)

Table I. Results of the tensile tests at 77°K

Specimen	Yield strength ksi (newton/m^2)	Tensile strength ksi (newton/m^2)	Elong. %	R. A. %
1A	134 (9.25×10^8)	142 (9.80×10^8)	31.1	73.8
1B	145 (10.09×10^8)	151 (10.42×10^8)	24.8	70.5
2A	141 (9.73×10^8)	150 (10.35×10^8)	29.3	72.9
2B	149 (10.28×10^8)	154 (10.63×10^8)	26.8	72.1

treated to stages 1B and 2B have slightly higher yield strength and lower tensile ductility than those at states 1A and 2A. These minor effects appear to be due to the precipitation of Ni_3Ti in the α phase at 650°C. Electron microscopic studies indicate that the extent of this precipitation is small.

Fracture toughness tests were conducted at 77°K on an MTS machine equipped with a liquid nitrogen cryostat. Compact tension (WOL) specimens of 0.70 in. (1.78 cm) thickness were used. Two specimens were tested at each stage of the thermal cycling treatment.

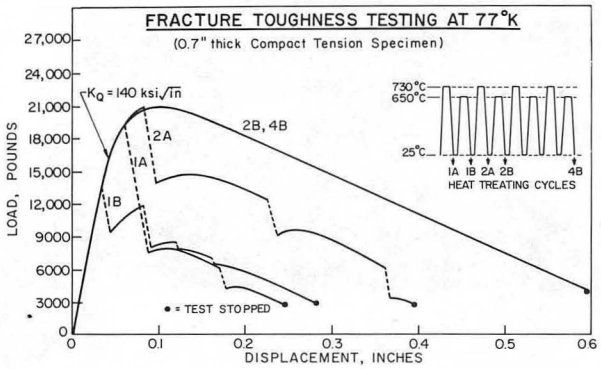

Fig. 7. Load-crack opening displacement curves in fracture toughness testing at 77°K. (XBL 739-1854)

The results of these tests are shown in Fig. 7. With the possible exception of sample 1B, these specimens were well away from plane strain conditions; a value of $K_Q \sim 140$ ksi $\sqrt{in.}$ was computed from the load-crack opening displacement (COD) curve. At stages 1A, 1B, and 2A the alloy exhibited unstable crack propagation as marked by the dotted lines in the load-COD curves. However the fine-grained alloy 2B seemed immune to unstable crack propagation. The specimen was fully plastic, and the preinduced crack grew slowly in a stable manner until the test was stopped. The post-test fracture toughness specimens are compared with one another in Fig. 8. The brittleness of specimens 1A and 1B, the repeated crack arrest in specimen 2A, and the ductility of specimen 2B are visually apparent. The fracture surfaces were examined by scanning electron microscopy. Figure 9 shows scanning electron fractographs taken slightly ahead of the pre-induced fatigue crack along the center line of the sample. Specimens processed to stages 1A and 1B propagated fracture in a quasi-cleavage mode. At stage 2A the fracture mode was a mixture of quasi-cleavage and ductile rupture. Fully grain refined specimens (2B) showed ductile dimple rupture over the whole fracture surface.

Given the success of this grain refining process in imparting cryogenic toughness,

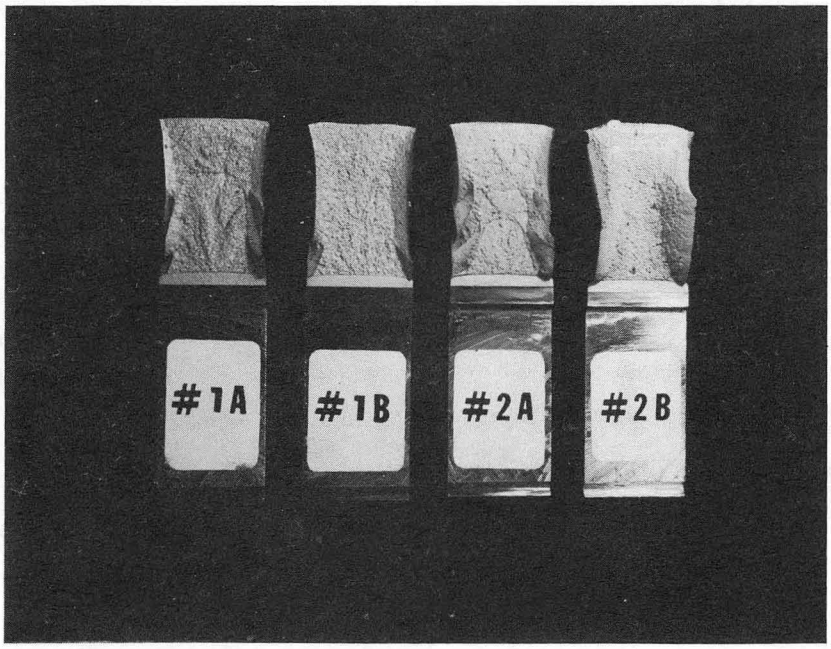

Fig. 8. Post-test fracture toughness specimens. (XBB 739-5644)

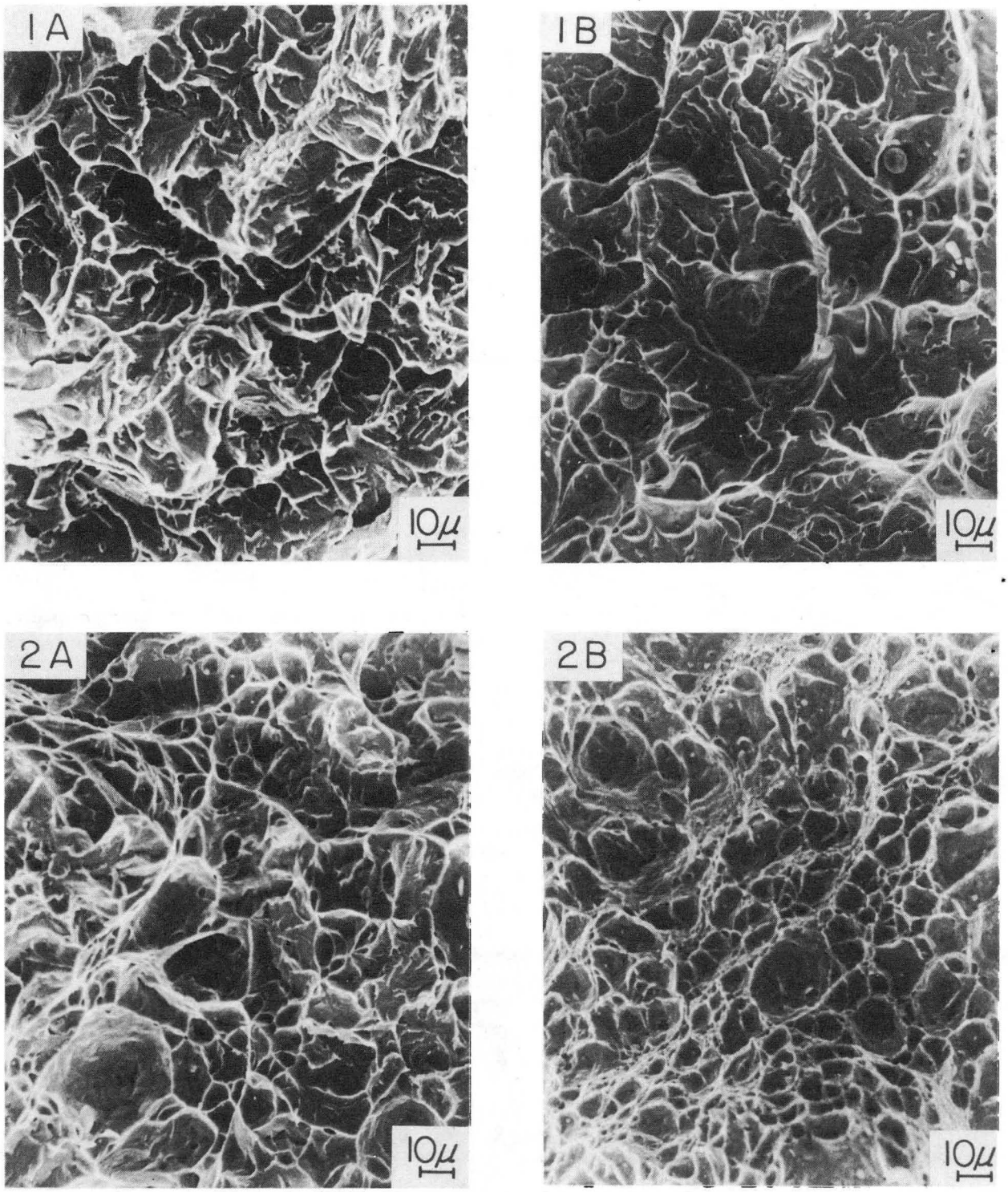

(XBB 739-5678)

Fig. 9. Scanning electron microscope fractographs of the specimens shown in Fig. 29.

we have attempted to modify it for alloys of higher titanium content to yield tough alloys of higher strength. A grain-refined Fe-12Ni-0.5Ti alloy has been made which has yield strength above 150 ksi at 77°K and shows fully plastic behavior in fracture toughness tests at 77°K using 0.7-in. WOL specimens. The alloy exhibits a value $K_Q > 150$ ksi $\sqrt{in}$. By increasing the Ti content to 1.0 wt.% we have obtained alloys having $\sigma_y > 160$ ksi with $K_Q > 160$ ksi $\sqrt{in}$. at 77°K. To obtain appreciably greater strengths in tough cryogenic alloys we require techniques which permit significant age hardening without serious loss of ductility. Research on this problem is in progress.

---

*This research is also supported by the Office of Naval Research.

†Abstracted from LBL-1483, LBL-1484, and LBL-2539.

5. RESEARCH PLANS FOR CALENDAR YEAR 1974

John W. Morris, Jr.

Our research objectives during 1974 include the following:

(1) We plan to explore the vibrational properties of idealized structures whose structural energies are determined by the Friedel potential. It is hoped that this investigation will lead to useful generalizations on the elastic properties and vibrational stabilities of simple structures.

(2) We plan to continue the studies on the theory of diffusion in multicomponent systems begun this year. Our initial goal remains a clear theoretical statement of the optimal choice of fluxes and forces for the treatment of diffusion in multi-component alloys.

(3) We plan to complete the investigation of TTT curves in simple one-component systems. Having done so, we hope to join the theory and computer simulation to be able to generate microstructures through arbitrary thermal processing. We also plan to expand the theoretical studies to treat more realistic systems.

(4) We hope to complete an analytic solution of the problem of dislocation glide through point obstacles. Having done so, we plan to attack the next level of sophistication of the problem, in which the obstacles are allowed to have an arbitrary distribution of mechanical properties. We also plan to initiate study on deformation through the simultaneous glide of interacting dislocations.

(5) We plan to use the results of our research on thermally activated dislocation glide to phase more realistic models of solution hardening. We hope to obtain theories of solution hardening which can be directly tested against experimental data.

(6) We plan to continue research on the design of tough ferritic alloys for cryogenic use. This research will take four paths: (1) application of our previous results in the design of low-Ni cryogenic alloys; (2) the design of tough alloys at strength levels to 200 ksi at 77°K, (3) the development of simplified grain refinement processes for Fe-Ni alloys; (4) research emphasizing transmission electron microscopy to sort out the evolution of microstructure during the processing of Fe-Ni-Ti alloys.

6. 1973 PUBLICATIONS AND REPORTS

J. W. Morris, Jr. and Associates

Journals

1. K. E. Amin, K. L. Murty and J. E. Dorn, Parametrization of Low-Temperature Deformation Characteristics in Single Crystals of Molybdenum, J. Appl. Phys. 44 (2) 615 (1973) (LBL-407 Rev.)

2. F. A. Mohamed, K. L. Murty, and J. W. Morris, Jr., Harper-Dorn Creep in Al, Pb, and Sn, Metallurgical Transactions, 4, 935 (1973)(LBL-831).

3. J. W. Morris, Jr. and P. L. de Bruyn, The Two-Phase Interface in a Simple One-Component Fluid, J. Colloid and Interface Science, 43, (1), 17 (1973)(LBL-454).

4. J. W. Morris, Jr. and D. H. Klahn, Statistics of the Thermally Activated Glide of a Dislocation Through a Random Array of Point Obstacles, J. Appl. Phys. 44 (11), 4882 (1973)(LBL-1166).

5. D. Klahn, D. Austin, A. Mukherjee and J. E. Dorn, "The Importance of Geometric Statistics to Dislocation Motion," Advances in Applied Probability, Supplement (2), W. L. Nicholson, ed., The Applied Probability Trust, Sheffield, England (1973), LBL-130.

6. M. L. Vaidya, K. L. Murty and J. E. Dorn, "High Temperature Deformation Mechanisms in Superplastic Zn-22Al Eutectoid," Acta Met., 21, 1616 (1973), LBL-459.

LBL reports

1. S. Jin, W. A. Horwood, J. W. Morris, Jr. and V. F. Zackay, A Simple Method for Charpy Impact Testing below 6°K, LBL-1483, March 1973 (Advances in Cryogenic Engineering, in press).

2. S. Jin, J. W. Morris, Jr. and V. F. Zackay, An Iron-Nickel-Titanium Alloy with Outstanding Toughness at Cryogenic Temperature, LBL-1484 Rev., July 1973. (Advances in Cryogenic Engineering, in press)

3. C. W. Krause and J. W. Morris, Jr., On the Relative Energies of Simple Metallic Structures, LBL-2214, Sept. 1973 (to be published in Acta Met.)

4. J. W. Morris, Jr. and C. K. Syn, The Point-Obstacle Representation of the Dislocation-Obstacle Interaction, LBL-2211, Sept. 1973 (to be published in J. Appl. Phys.)

5. J. W. Morris, Jr. and D. H. Klahn, Thermally Activated Dislocation Glide Through a Random Array of Point Obstacles: Numerical Simulation, LBL-2276, October 1973. (to be published in J. Appl. Phys.)

6. V. F. Zackay, E. R. Parker, J. W. Morris, Jr., and G. Thomas, "The Application of Materials Science to the Design of Engineering Alloys," LBL-2261, Oct. 1973 (to be published in Materials Science and Engineering).

7. Chol K. Syn, The Role of Dislocation Interaction with Solute Atoms in the Strengthening of Metals, Ph.D. thesis, LBL-2270, November 1973.

8. F. M. Hamzeh, On the Destruction of Magnetic Surfaces in Totoidal Systems, LBL-1448, Nov. 1973. (Submitted to Nuclear Fusion)

9. C. W. Krause and J. W. Morris, Jr., "A Correlation between Electronegativity and Electron Density," LBL-2523, Nov. 1973 (submitted to J. Phys. F: Metal Phys.).

10. I. F. Charo, Corrosion Fatigue Properties of Surgical Implant Materials, M. S. thesis, LBL-2207, Dec. 1973.

11. D. Grivas, K. L. Murty, and J. W. Morris, Jr., "Steady State Creep of a Superplastic Lead-Tin Eutectic Alloy," LBL-2519, Dec. 1973 (submitted to Metallurgical Transactions)

12. S. Jin, J. W. Morris, Jr., and V. F. Zackay, "Grain Refinement Through Thermal Cycling in an Fe-Ni-Ti Cryogenic Alloy," LBL-2539, Dec. 1973 (submitted to Metallurgical Transactions)

13. D. Grivas and J. W. Morris, Jr., "Steady State Creep of a Superplastic Lead-Tin Eutectic Alloy at Low Stress," LBL-2532, Dec. 1973 (submitted to Metallurgical Transactions).

Presentations

1. D. H. Klahn and J. W. Morris, Jr., "Statistics of Thermally Activated Glide," TMS Spring Meeting, Philadelphia, May 1973.

2. C. W. Krause and J. W. Morris, Jr., "Faulting and Phase Stability in Ideally Close-Packed Structures," TMS Spring Meeting, Philadelphia, May 1973.

3. S. Jin, W. A. Horwood, J. W. Morris, Jr., and V. F. Zackay, "A Ferritic Alloy Combining Strength and Toughness at Cryogenic Temperatures," TMS Spring Meeting, Philadelphia, May, 1973.

4. S. Jin, W. A. Horwood, J. W. Morris, Jr., and V. F. Zackay, "A Simple Method for Charpy Impact Testing at 6°K," Cryogenic Engineering Conference, Atlanta, Aug. 1973.

5. S. Jin, J. W. Morris, Jr., and V. F. Zackay, "An Iron-Nickel-Titanium Alloy with Outstanding Toughness at Cryogenic Temperature," Cryogenic Engineering Conference, Atlanta, Aug. 1973.

6. J. W. Morris, Jr., "Fe-Ni-Ti Cryogenic Steel," Naval Research Laboratory, Aug. 1973.

7. K. L. Hanson and J. W. Morris, Jr., "Stable Looping in Dislocation Glide," TMS/ASM Fall Meeting, Chicago, Oct. 1973.

8. C. K. Syn and J. W. Morris, Jr., "Point Obstacle Representations of the Dislocation-Solute Atom Interaction," TMS/ASM Fall Meeting, Chicago, Oct. 1973.

9. S. Jin. J. W. Morris, Jr., and V. F. Zackay, "Grain Refinement through Thermal Cycling in Fe-Ni-Ti Alloys," TMS-ASM Fall Meeting, Chicago, Oct. 1973.

C. MICROSTRUCTURE, PROPERTIES AND ALLOY DESIGN

Gareth Thomas, Principal Investigator

Synopses of Research Programs on Structure, Properties, and Design of Materials. The following is a summary of our major research programs and emphases.

Overall Objectives

To understand the factors that control the properties, especially strength and toughness, of materials (metallic and non-metallic). This involves studies of the effects of composition and processing on microstructure and properties, and includes basic studies of phase transformations and alloy strengthening. From fundamental principles, it is then possible to design microstructures in materials for particular applications. Special attention is paid to economic factors such as simplicity of composition and processing.

Since commercial alloys are always heat treated to undergo some kind of phase transformation, it is essential that we understand the mechanisms of transformations, the microstructures that result, and their influence on properties. Nucleation and growth reactions are generally not too satisfactory because of heterogeneities due to heterogeneous nucleation (e.g., at boundaries, dislocations, etc). Thus, our emphasis is on homogeneous reactions (spinodals, ordering) and martensitic reactions.

Synopses of Programs

Structural steels and duplex austenitic-martensitic alloys. This program is concerned with controlling economically the structure and mechanical properties of steels by compositional variables. The martensitic transformation is the most efficient way of producing uniformly densely dislocated structures. Such structures provide high strength and toughness often without tempering, provided transformation twinning is avoided. This means controlling composition. Bainitic transformations appear to be beneficial when compared to strong but brittle high carbon steels and considerable emphasis is now being placed on steels to produce 100% lower bainite by continuous cooling. New methods of strengthening include dispersion hardening of martensite, e.g., by ausaging, or prior spinodal reactions so as to simulate the benefits of processes such as ausforming, but without complex thermal-mechanical treatments. Mechanisms of martensite transformations in mestastable austenites are being studied using single crystals.

Homogeneous phase transformations. Since these reactions give uniform microstructures, they have great potential for controlling both mechanical and physical properties. The spinodal systems currently under investigation are Cu-Ni-Fe and Cu-Mn-Al. Applications are directed to control of properties through control of structure and design to produce double transformations so as to increase strengthening. The program includes studies of interphase interfaces and the problem of the grain boundary precipitation reaction, which causes serious deterioration in toughness, during aging.

Fundamental studies of short range order (sro) are being done in Ni base and other alloys, in order to characterize the physical nature of sro and mechanisms of the transformation. Ordering and spinodal decomposition in ceramic alloys are also under investigation, e.g., lithium spinels. Phase transitions in ceramic systems can now be more easily studied by electron microscopy with the perfection of ion thinning and the availability of our 650 kV high-voltage instrument. Also the acquisition of the new Phillips EM 301 100 kV instrument permits us to obtain lattice images. Applications of this technique to ordering systems are now in progress.

1. DESIGN OF EXPERIMENTAL STRONG, TOUGH, ECONOMICAL STRUCTURAL STEELS*

Gareth Thomas

The overall aim of this research program, which was started in 1963, is the development of strong, tough, structural steels utilizing martensitic and bainitic transformations as economically as possible. Thus we are concerned with alloys having simplicity of composition and heat treatment, and in which careful attention is paid to control of purity and processing. Alloys are designed so as to ensure for martensitic treatments that there is sufficient hardenability so that no prior decomposition of austenite occurs. The objectives are to design from first principles, desirable microstructures in steels which provide desirable mechanical properties (strength and toughness). Thus the experimental techniques involve detailed metallographic analyses of series of high-purity experimental

alloys of iron, carbon, and one or two substitutional alloying elements such as Cr, Mo, Mn, Ni, Co, etc. The microstructures are correlated with the tensile properties and fracture toughness values.[1-9]

Desirable microstructures from the point of view of good fracture resistance are: dislocated martensitic/bainitic lath ferrites, autotempered martensite, interlath films of retained austenite, tempered martensite free from interlath carbides, and lower bainite. These structures are classified in Table I and representative micrographs are shown in Figs. 1-3.

It should be emphasized that the identification of retained austenite at interlath boundaries requires painstaking electron diffraction and dark field analysis[8] as shown in Fig. 4.

One of the novel results of the work to date has been the attainment of high strength and high toughness (as measured by K_{IC}) in experimental ternary alloys (Table II) in the as-quenched untempered condition.

It is suggested that in order to obtain high strength and toughness, the following basic rules for controlling microstructure apply (assuming high-purity starting materials, and vacuum melting).

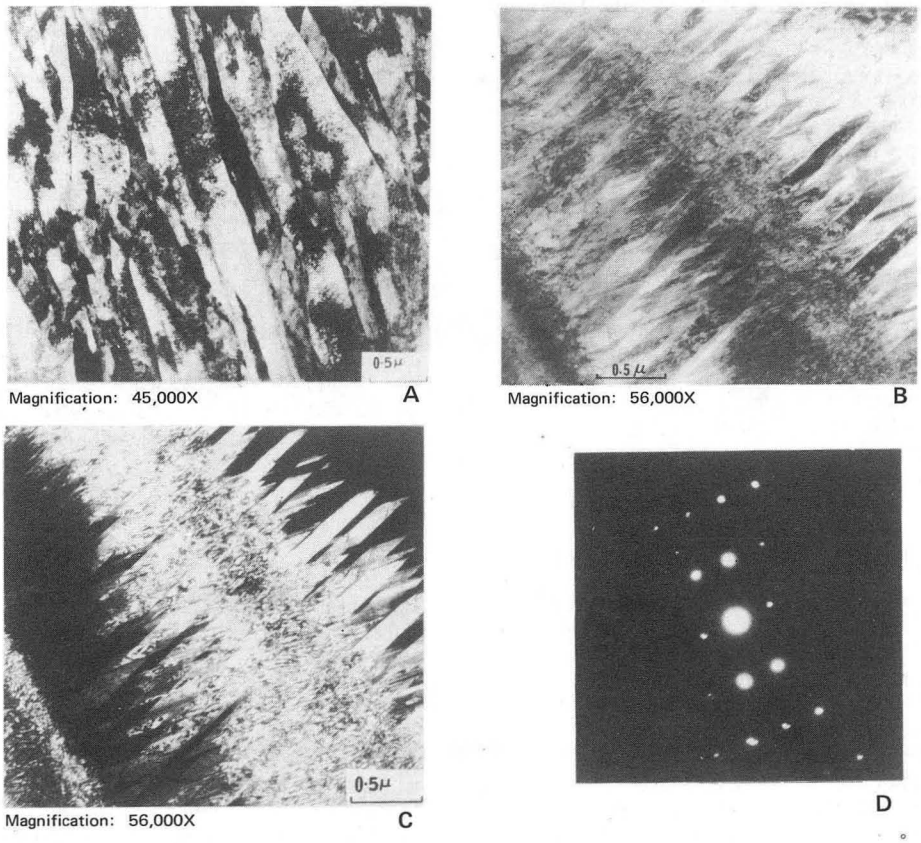

Fig. 1 A) Bright field image of as-quenched martensite in Fe-25Ni-10Co steel. The dislocated lath structure is typical of low carbon martensites and yields high toughness with moderate to high tensile strength. B) The bright field image of a twinned martensite plate in Fe-28.5Ni-10Co steel. C) A related dark field image of twin reflection. The corresponding selected area diffraction pattern is shown in D), and indicates the dark field image is formed by superimposed twin and matrix reflections. The complexity of the substructure, with matrix dislocations and multiple twinning, is revealed by this technique. Twinned martensite normally occurs when carbon content exceeds approximately 0.3% or in general when the total solute content increases. Except for cobalt, increasing the solute content also lowers the M_s temperature. The presence of a high twin density in a martensitic structural steel has been found to be associated with low fracture toughness and high yield strength. (XBB 729-4502)

TEMPERED TWINNED MARTENSITE

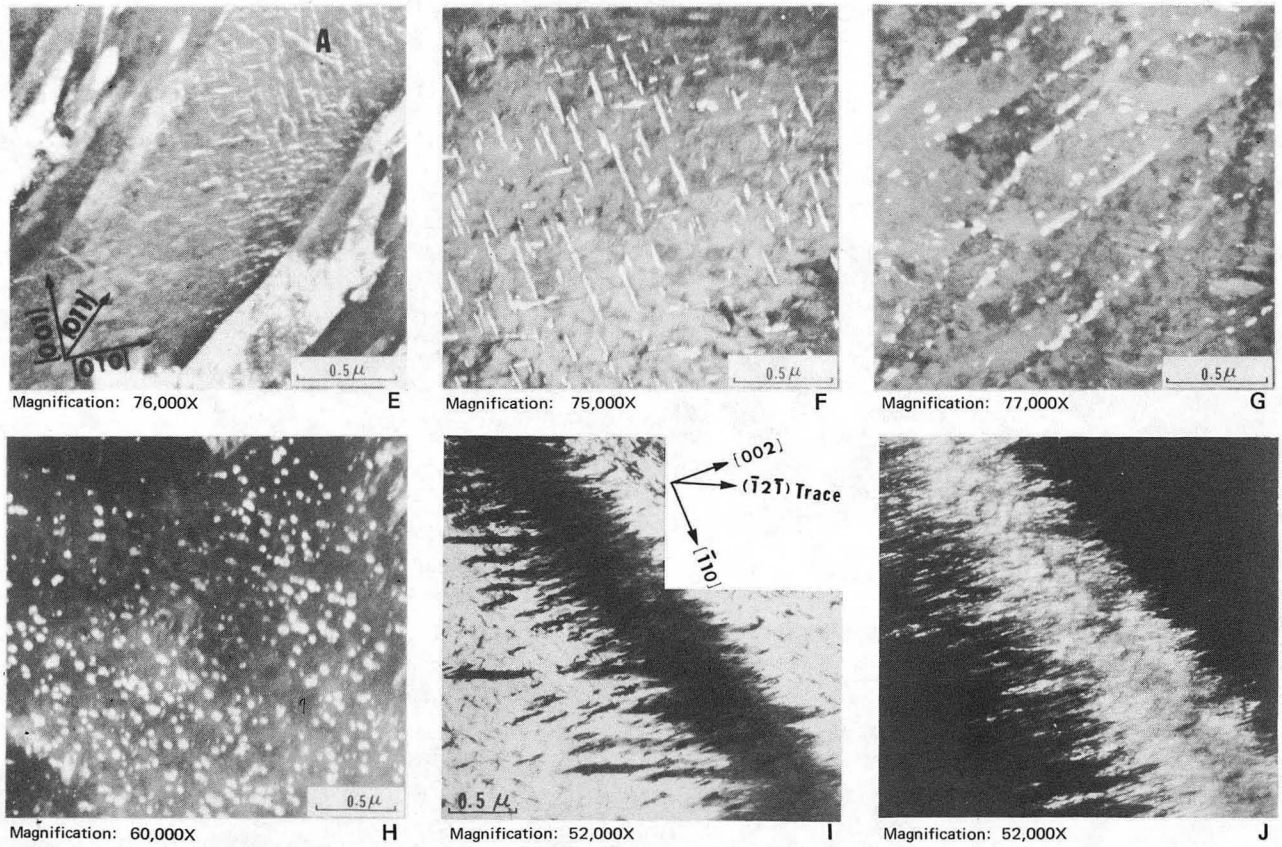

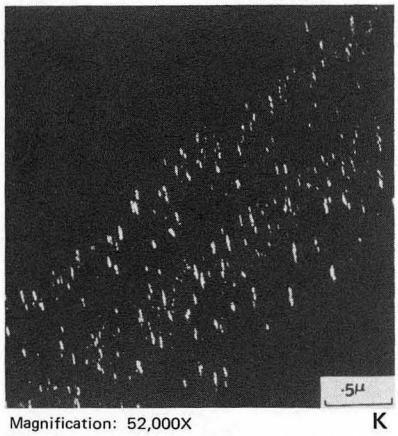

Fig. 2. Dark field imaging is an essential technique for determining the distribution and orientation of carbide precipitates in tempered martensites. (E) is a dark field image of a carbide reflection in Fe-9Ni-4Co-0.45C steel tempered at 500°F for 4 hrs, showing the precipitation of epsilon carbide on {100} martensite planes. The initial formation of Fe_3C on {110} martensite planes is seen at A. Epsilon carbide will precipitate only at low tempering temperatures and dissolves upon formation of Fe_3C at higher temperatures. (F) illustrates the dark field image of a Widmanstatten pattern of Fe_3C in Fe-4Cr-5.3Co-0.35C tempered at 400°F for 4 hours. This precipitate substructure is found in almost all dislocated martensites tempered at low temperatures, as well as in as-quenched martensites which undergo autotempering due to their high M_s temperatures. The formation of a Widmanstatten pattern of Fe_3C is accompanied by "normal" tempering behavior, viz., an increase in fracture toughness and a decrease in yield strength. At higher tempering temperatures, carbides may precipitate along martensite lath boundaries, causing a marked decrease in toughness. (G) shows a dark field image of interlath carbides in the same alloy as in (F) tempered at 800°F for 4 hours. At very high tempering temperatures, the carbides spheroidize, producing an increase in toughness and a further reduction in yield strength. A dark field image of spheroidized carbides is shown in (H), which is the same steel as in (F) tempered at 1000°F for 4 hours. When twinned martensites are tempered the carbides precipitate along the twin boundaries. The twin boundary carbides have been associated with a decrease in fracture toughness in structural steels. (I) is a bright field image of a twinned martensite plate in Fe-27Ni-10Co-0.1C steel, where the twin density is highest at the midrib. The steel was tempered at 200°C for 1 hour, and a Widmanstatten pattern of Fe_3C is seen outside the twinned area. (J) shows a dark field image of the twins, and (K) is a dark field image of the unidirectional carbides on the twin boundaries. Note that the particular Fe_3C reflection used in (K) illuminates only the twin boundary carbides

(Fig. 2 cont.)

and not the Widmanstatten pattern outside the twinned area. This points out the need for imaging several different carbide reflections in order to determine completely the precipitate morphology. These examples illustrate that the tempering behavior depends on the initial martensitic substructure, which can vary within each plate as well as from plate (or lath) to plate. (XBB 729-4504 & XBB 729-4505)

ISOTHERMAL TRANSFORMATIONS

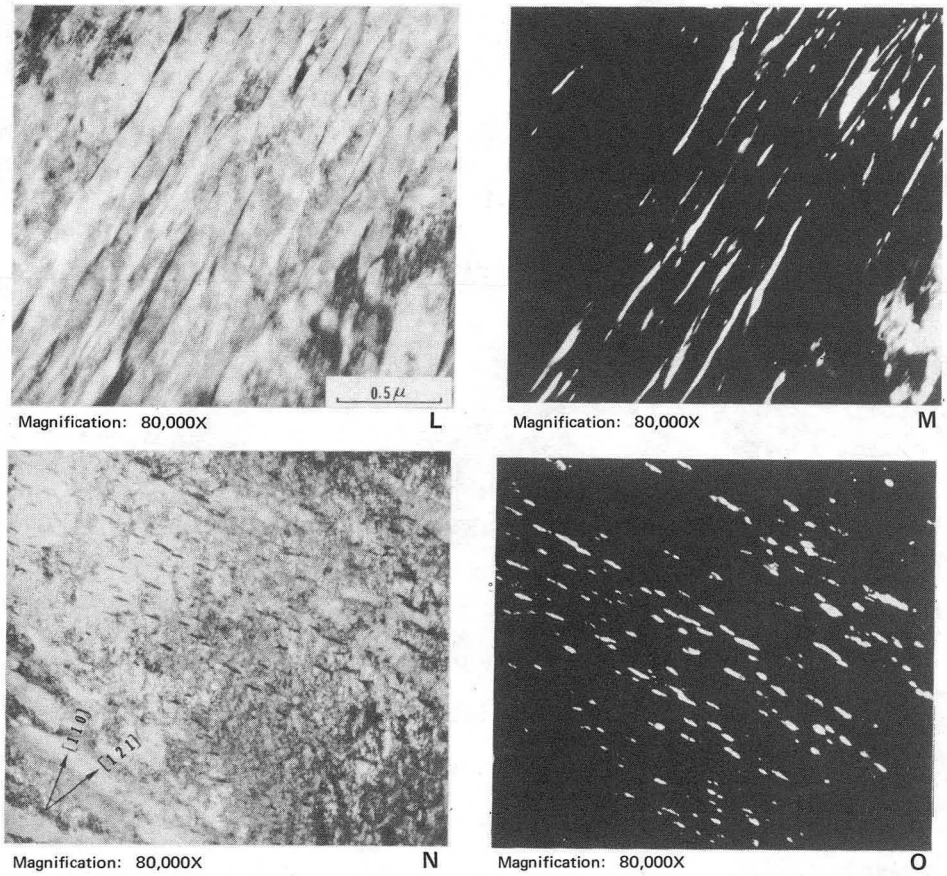

Fig. 3. (L) is the bright field image of upper bainite in Fe-4Cr-0.34C steel, and (M) is the dark field image of a carbide reflection, showing the characteristic elongated carbides between the bainitic ferrite laths. Upper bainite, which is formed at high isothermal transformation temperatures, normally has a low fracture toughness. Note the similarity of the carbide morphology in (M) with that shown in 2(G), a tempered martensite which is likewise embrittled by interlath carbides. At lower transformation temperatures the Fe_3C precipitates unidirectionally within the bainite laths. This is seen in (N), the bright field image of lower bainite in Fe-4Cr-5.3Co-0.35C steel. The dark field image in (O) reverses the contrast of the carbides. Normally the carbides in lower bainite form at an angle of 55° to 65° to the long direction of the bainite laths. The carbide morphology of lower bainite in (L) and (M) is similar to that of dislocated martensite tempered at low temperatures, as seen in (2E,F). Both structures also exhibit high toughness values. It is thus seen that by comparing upper bainite with tempered martensite having interlath carbides, and lower bainite with tempered martensite having Widmanstatten carbides, there is a strong correlation between microstructure and mechanical properties. In steels having a twinned martensitic substructure and poor toughness, it may be preferable to utilize isothermal transformations to produce dislocated lower bainite having a higher toughness due to the similarity of its structure with that of tempered dislocated martensite. (XBB 729-4503)

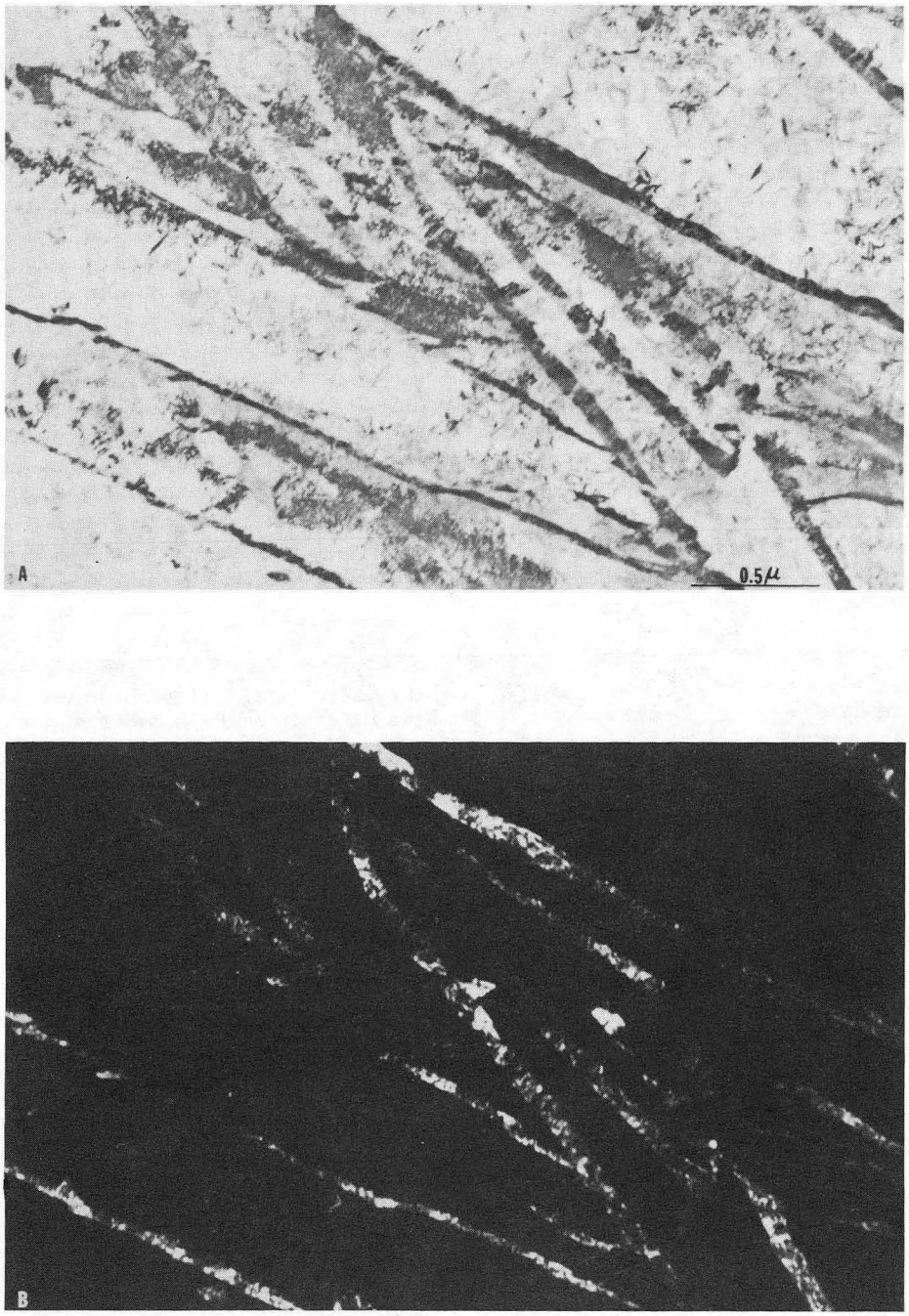

Fig. 4. Bright field image (a) of as-quenched alloy 0817, showing retained austenite films surrounding each martensite lath. The lath boundary films are illuminated in the dark field image (b) by using an FCC diffraction spot from the retained austenite. (XBB 7211-5624)

a. As-quenched Martensites

Austenitize at 1100°C or higher to take all carbides into solution; avoid transformation twinning by controlling carbon and keep M_s above about 300°C. This determines total alloy content permissable. For dislocated martensites the strength will mainly depend on carbon content: to avoid twinning %C $\leqslant$ 0.4%. Ternary alloying additions provide desired properties, e.g., hardenability, in order to prevent prior austenite decomposition to upper bainite, examples Fe-4Cr-0.35C, and Fe-2Mo-0.4C and correspond to steels with $M_s \approx 320°C$. Some autotempering during the cooling below M_s may be beneficial to toughness provided no interlath carbides nucleate. Also the presence of interlath retained austenite is beneficial for high toughness.

b. Tempered Martensites

Toughness drops when interlath carbides precipitate; these may be delayed from forming by allowing fine films of retained austenite to remain around the martensite laths (low additions of Ni, Mn, or Co may facilitate this).

c. Bainites

Upper bainite should be avoided at all cost. Lower bainite is similar to tempered martensite but does not usually contain interlath carbides. This structure is desirable for high toughness, and thus lower bainite could give attractive properties in high carbon steels (C > 0.4%). This can be achieved economically if 100% lower bainite can be formed on continuous cooling from the austenitizing temperature. Research along these lines is now in progress.

Table I. Summary of microstructures of martensitic and bainite steels.[a]

Constituent	Notes	Structure
Martensite (as-quenched)	$C \leqslant 0.4$ $M_s \geqslant 300°C$	Dislocated laths; if autotempered Widmanstatten {110} cementite.
	$C \geqslant 0.4$ $M_s \leqslant 200°C$	{112} and {110} (high C) twinned plates; carbides on twins.
Tempered martensite	Dislocated martensite	Epsilon carbide with {100} habit precipitates initially and is replaced by three variants of {110} Widmanstatten cementite as the tempering temperature is increased. Alloy carbides can form at higher temperatures, or longer tempering times.
	Twinned martensite	Single carbide variants on twin boundaries; as above.
Lower bainite		Dislocated ferrite with single-variant Fe_3C oriented 55-65° to lath; no interlath carbides; so far some new evidence for twinned ferrite; epsilon carbide possible.
Upper bainite		Dislocated ferrite; interlath carbides. No unique transition temperature for lower to upper bainite transformation--depends on composition.

[a]Mixtures of all of these constituents are possible depending on composition and transformation kinetics.

Table II. Examples of room temperature mechanical properties of vacuum melted experimental steels.

A. Fe-Cr-C series (Ref. 8)

Alloy	Treatment	0.2% offset yield strength (psi)	UTS (psi)	% el.	Plane strain fracture toughness, K_{1c} (ksi-in$^{1/2}$)
4Cr-0.17C	As-quenched[a]	160,000	194,000	10	83
	Temp. 200°C, 1 h	166,000	195,000	9.5	92
	Temp. 400°C, 1 h	162,000	185,000	9.7	83
	Temp. 600°C, 1 h	91,000	106,000	15.0	*
4Cr-0.35C	As-quenched[a]	240,000	306,000	5	70
	Temp. 200°C, 1 h	218,000	275,000	7.5	92
	Temp. 400°C, 1 h	201,000	237,000	9.0	77
	Temp. 600°C, 1 h	126,000	149,000	17.0	*

*Not determinable--even 1 in. thick specimens gave invalid K_{1c} data due to very high toughness (note high elongations).

B. Fe-Mo-C series (Ref. 9)

3.85Mo-0.18C	As-quenched[a]	160,000	198,000	12.6	93
	Temp. 400°C, 1 h	153,000	183,000	14	89
	Temp. 600°C, 1 h[b]	193,000	205,000	8.5	46
2.2Mo-0.4C	As-quenched[a]	258,000	311,000	2.5	54
	Temp. 400°C, 1 h	197,000	230,000	5.8	94
	Temp. 600°C, 1 h	206,000	223,000	10.7	73

[a]100% martensite.

[b]Secondary hardening--precipitation of Mo_2C.

*LBL-1871 Iron & Steel Inst. 46, 451-461 (1973).

1. S. K. Das and G. Thomas, Structure and Mechanical Properties of Fe-Ni-Co-C Steels, Trans. ASM 62, 659 (1969).
2. D. H. Huang and G. Thomas, Structure and Mechanical Properties of Tempered Martensite and Lower Bainite in Fe-Ni-Mn-C Steels, Met. Trans. 2, 1587-1598 (1971).
3. G. Thomas, Electron Microscopy Investigations of Ferrous Martensites, Met. Trans. 2, 2373 (1971).
4. G. Thomas and S. K. Das, Multiple Transformation Twinning in Ferrous Martensites, J. Iron Steel Inst. 209, 801 (1971).
5. M. Raghavan and G. Thomas, Structure and Mechanical Properties of Fe-Cr-C-Co Steels, Met. Trans. 2, 3433-3439 (1971).
6. I-Lin Cheng and G. Thomas, The Enhancement of Strengthening Dislocated Martensite, Met. Trans. 3, 503-516 (1972).
7. D. H. Huang and G. Thomas, Author's Reply to the Discussion of: Structure and Mechanical Properties of Tempered Martensite and Lower Bainite in Fe-Ni-Mn-C Steels, Met. Trans. 3, No. 1, 343-346 (1972).

8. J. McMahon and G. Thomas, Development of Strong, Tough, Economical Fe-Cr-C Steels, Third Int. Conf. on Strength of Metals and Alloys, Microstructure and Design of Alloys, Cambridge, England, 1973, 1, pp. 180-184. See also J. McMahon, M.S. thesis, LBL-1181 (1972).
9. R. A. Clark and G. Thomas, Met. Trans., to be published; see R. A. Clark, M.S. thesis, LBL-1801 (1973).

2. THE STRESS-INDUCED MARTENSITE-AUSTENITE INTERFACE IN Fe-15Ni-15Cr SINGLE CRYSTALS*

Glen A. Stone† and Gareth Thomas

A single crystal stressed in the $[\bar{2}\bar{1}3]_\gamma$ direction at 185°K was transformed to 5% α martensite and 2% ε martensite by volume. The austenite slip system of maximum shear stress is the $(\bar{1}11)_\gamma$ $[01\bar{1}]_\gamma$. Figure 1 shows a two-surface study using the electron and optical microscopes. The α martensite is confined between ε martensite plates with the $(0001)_\varepsilon \parallel (\bar{1}11)_\gamma$. The size of the acicular martensite crystals is controlled by the spacing of the ε martensite plates. These ε martensite plates are seen in Fig. 1A as dark vertical bands. The axes of the acicular crystals lie in the $(\bar{1}11)_\gamma$ plane. The ε martensite habit plane is defined as the plane perpendicular to the $(\bar{1}11)_\gamma$ containing the vector defining the crystal axis.

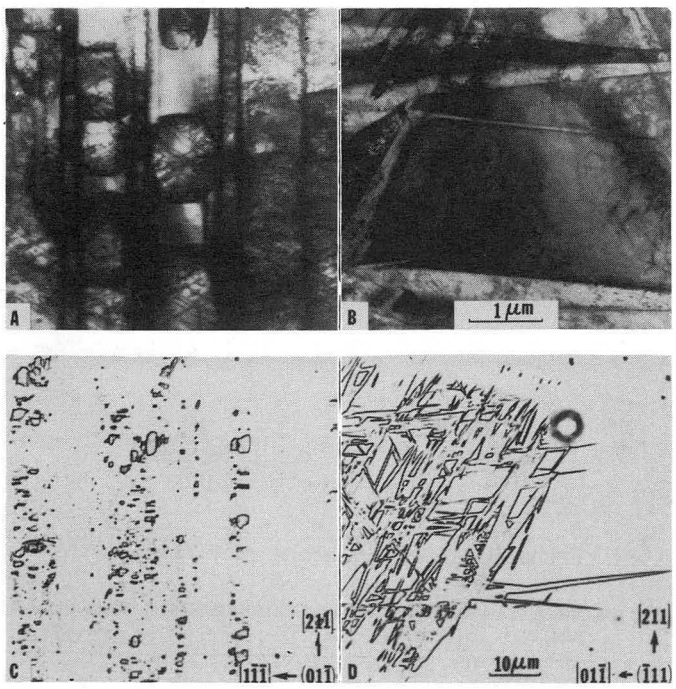

Fig. 1. Two-surface study of the $(01\bar{1})_\gamma$ and $(\bar{1}11)_\alpha$ planes using the electron microscope, A and B, and optical microscope, C and D. (XBB 732-586)

Measurements of the acicular crystal axis were made from optical micrographs, using the trace of an ε plate on the $(11\bar{1})_\gamma$ plane cutting the $(\bar{1}11)_\gamma$ in the $[101]_\gamma$ direction as a crystallographic reference. The results that follow are in the form of unit vectors and represent the average of no less than six independent measurements. The experimental error is estimated to be ±0.25°. Typical variation in the axis of α martensite crystals with seemingly the same crystallographic direction was ±1°. This variation is real and not due to experimental error. Results of the martensite crystal axis and the habit plane normal are given below:

Martensite Crystal Axis

0.63433004	-0.12805297	0.76238300
0.74554175	0.08445573	0.66108602
0.10843235	0.75505982	-0.64662748
0.07606209	-0.66600086	0.74206295

Habit Plane Normal

0.51409345	0.80639265	-0.29229920
0.33291765	0.81211692	-0.47919927
0.80926454	0.31072710	0.49853744
0.81294602	0.47234471	0.34060131

The physical nature of the interface is being revealed in some detail working with $(01\bar{1})_\gamma$ foils. Figure 2A is a bright field micrograph showing a α martensite crystal cutting the surface with its axis a few degrees out of the plane of the foil. Figure 2B is a dark field of the same area using a $(01\bar{1}1)_\varepsilon$ reflection. Fine lines light up in the interface defining a sheath surrounding the α martensite. Figure 2C is the $(200)_\gamma$ reflection that lights up the sheath as well, indicating the α martensite crystal is surrounded by alternate regions of faulted austenite and dislocated austenite. Figure 2D is the diffraction pattern from the same area and clearly shows this alloy obeys the Kurdjumov-Sachs orientation relationship. Specifically in this diffraction pattern the $(01\bar{1})_\gamma \parallel (\bar{1}11)_\gamma \parallel (\bar{2}110)_\varepsilon$ and $[\bar{1}11]_\gamma \parallel [110]_\alpha \parallel [0001]_\varepsilon$.

Efforts to image interface dislocations have been unsuccessful to date. It appears clear that the interface between the phases in this alloy is a composite of dislocated austenite and faulted austenite giving rise

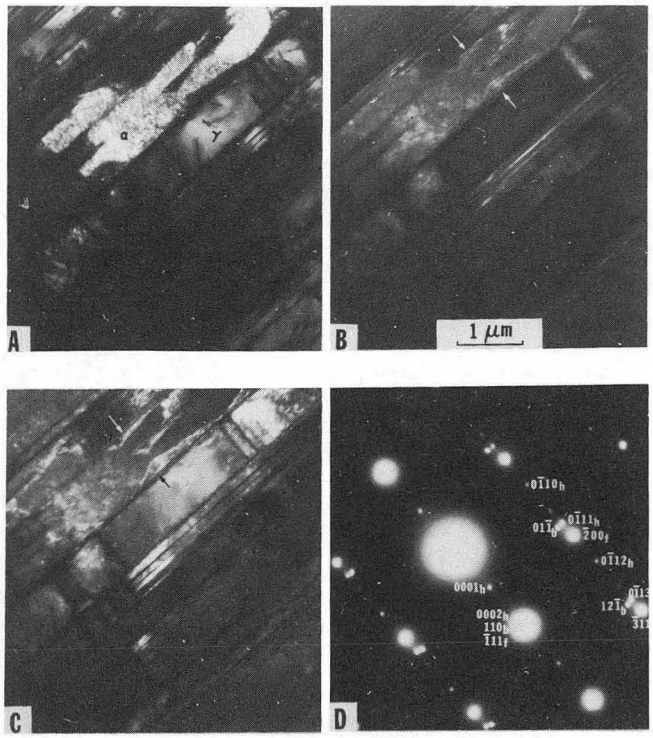

Fig. 2. Structure of the martensite interface. Bright field image A, $(01\bar{1}1)\varepsilon$ reflection B, $(200)\gamma$ reflection C, and diffraction pattern D. (XBB 734-2477)

to hcp reflections. Also the $(110)\alpha$ surface of the crystal is in contact with and parallel to the $(0001)\varepsilon$ plane. The large very thin ε plates appear to control the size of the acicular α crystals and forces the long axis of the crystals to remain parallel to the austenite slip plane which is the $(\bar{1}11)\gamma$ in this example.

*LBL-1499, Proc. 31st EMSA Congress 1973, p. 110 (Claitors Publishers, Ba. Rouge)

†Now at South Dakota School of Mines.

3. ON STRUCTURAL INTERPRETATION OF SHORT RANGE ORDER*

Santos K. Das† and G. Thomas

The various structural models of short range order in alloys are briefly reviewed. The success and limitations of structural models in interpreting diffuse scattering data are discussed. Particular emphasis is given to the systems for which the diffuse short range ordered maxima in the X-ray and electron diffraction patterns are non-coincident with the position of the super-lattice reflections. The recent electron diffraction results on these systems suggest microdomains with different superstructures are present in the short range ordered state. The justification for such multiple microdomain configurations is discussed in the light of some recent theoretical developments.

Although evidence has been obtained for microdomains in specimens quenched from above the critical temperature T_c, so far no convincing direct evidence has been obtained for the existence of domains above T_c. This is due to difficulties of excessive thermal diffuse scattering and possibly small degree of order in restricting contrast in the images.

Current work emphasizes high-resolution lattice imaging techniques as is discussed in the following abstract.

*Invited paper presented at International Symposium on Order-Disorder Transformations in Alloys, Tübingen, W. Germany, Sept. 3-6, 1973. To be published by Deutsche Gesellschaft für Metallk (LBL-2285).

†Now at Physics Division, Argonne National Laboratory.

4. LATTICE IMAGING OF ORDERED ALLOYS

Robert Sinclair,* Klaus E. Schneider,** and Gareth Thomas

The determination of the structural nature of short range order in alloys has been hampered by ambiguities in the interpretation of diffuse scattering in diffraction patterns and high-resolution dark field images in the electron microscope. Since modern electron microscopes are capable of 2 Å resolution, the formation of a direct lattice image (lattice fringes) has been applied to this problem. Fringe images were also computed by using many beam dynamical theory to facilitate interpretation of the experimental data. The appearance of the lattice fringe images compares favorably with theory and was found to be critically dependent on a number of factors, such as the reflections used to form the image, the proximity of the specimen orientation to the exact Bragg condition, the specimen thickness, and--for the case of ordered domains in a disordered matrix--the position of the domain within the foil.

Copper-gold alloys near the compositions Cu_3Au and CuAu were chosen as model systems. Images of the superlattice planes (e.g., {100} for Cu_3Au, {110} for CuAu) clearly show the structure at antiphase boundaries (as in Fig. 1). In partially ordered alloys, regions of order appear with the periodicity of the superlattice planes, whilst the disordered matrix shows the fundamental periodicity of the lattice (Fig. 2).

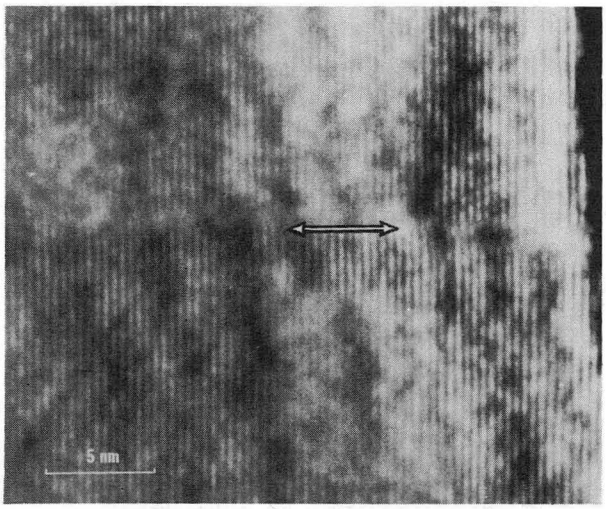

Fig. 1. Lattice image of the {100} planes in ordered Cu_3Au. The out-of-step nature of the antiphase boundary (arrowed) is revealed in the image. (XBB 741-285)

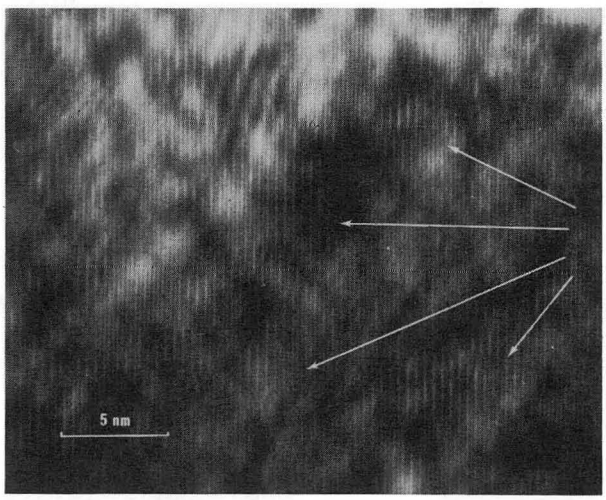

Fig. 2. Lattice image of partially ordered Cu_3Au. The fringe periodicity in the disordered matrix corresponds to the {200} d-spacing of the alloy. The ordered domains, approximately 2.5 mm in diameter, are manifested in the image by alternately wider and narrower white fringes and thus possess the periodicity of the superlattice. (XBB 741-286)

*Supported by NSF.
**Deutsche Forschung., Fellowship

5. THE METASTABLE PHASE Ni_2Mo AND THE INITIAL STAGES OF ORDERING IN Ni-Mo ALLOYS*

Santos K. Das† and Gareth Thomas

The initial stages of ordering in Ni_3Mo and Ni_4Mo have been investigated by transmission electron microscopy and diffraction. The development of long-range order in Ni_3Mo is associated with decomposition into the two metastable phases Ni_2Mo and Ni_4Mo, which are eventually replaced by the equilibrium Ni_3Mo at a later stage of ordering. Evidence for the presence of the metastable Ni_2Mo phase was also found during the early stages of ordering of Ni_4Mo. Examples of identification are shown in the image and diffraction pattern of Fig. 1. The presence of the metastable phase Ni_2Mo

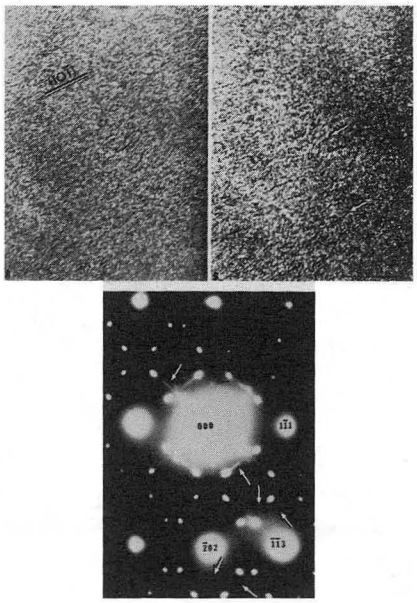

Fig. 1. Micrographs of Ni_4Mo sample after aging for 8 h at 650°: (A) bright field micrograph, (B) dark field micrograph of Ni_4Mo superlattice spot marked b in the [121] diffraction pattern shown in (C), which corresponds to the area in Fig. 1(A). In (C) the foil has been tilted from that in (A) to obtain a symmetrical diffraction pattern. The single large black-white arrows in (C) point to weak Ni_2Mo superlattice reflections, and the small double arrows are double diffraction spots from Ni_4Mo. (XBB 738-4981)

at Ni_4Mo composition and that of Ni_2Mo and Ni_4Mo at Ni_3Mo composition can be explained in terms of the recent thermodynamic calculations of the ground states of ordered binary alloys by Cahn and his co-workers. Figure 2 shows an example of the good agreement between theory and our results.

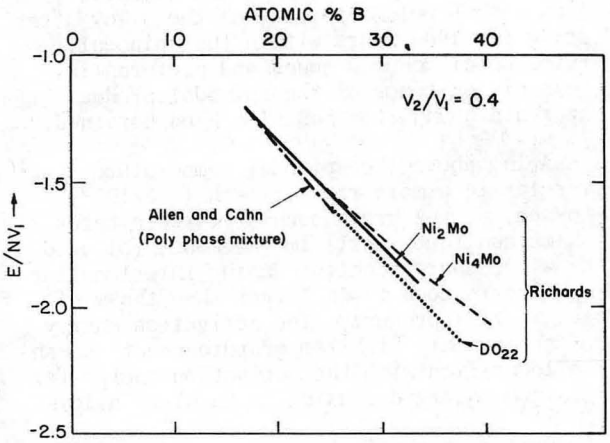

Fig. 2. The theoretical curves for energy of mixing versus composition for DO_{22}, Ni_4Mo, and Ni_2Mo structures calculated using $V_2/V_1 = 0.4$. (XBL 717-7037A)

*LBL-1868; Physica Status Solidi, in press 1973.

†Now at Physics Division, Argonne National Laboratory.

6. LOSS OF COHERENCY IN SPINODALLY DECOMPOSED Cu-Ni-Fe ALLOYS*

Ronald J. Livak† and Gareth Thomas

Coarsening of the spinodal microstructure in copper-nickel-iron alloys has been studied in detail using transmission electron microscopy. Loss of coherency in this lamellar microstructure occurs by the capture of slip dislocations and subsequent multiplication at the interphase interfaces. Based on the observations, it is proposed that the multiplication process providing the misfit-accommodating dislocation loops proceeds by the spiraling of the captured dislocations around the platelets by climb, similarly to the formation of helical dislocations. Because the Burgers vector of the captured dislocation is inclined at 45° to the {100} interface, diffusion-controlled rotation of the initial {100} coherent interface toward the {110} plane containing $\bar{b}$ occurs in order to lower the interfacial energy. This rotation of the semi-coherent interfaces results in a change of the initial platelet morphology to a microstructure containing rod-shaped and more equiaxed particles.

*Abstract of LBL-1842; Acta Met., in press.

†Now at Precision Founders Inc., San Leandro, Calif.

7. RESEARCH IN PROGRESS

a. Bainitic Transformation in Steels*

Der-Hung Huang

Epsilon carbide has been identified in the isothermally transformed bainitic structure of a Si steel by thin-foil transmission electron microscopy and diffraction. The crystallographic relationship between epsilon carbide and bainitic ferrite was found to follow the Jack orientation relationship:

$$(0001)_\varepsilon \parallel (011)_\alpha$$

$$(10\bar{1}0)_\varepsilon \parallel (2\bar{1}1)_\alpha$$

$$(\bar{1}2\bar{1}0)_\varepsilon \parallel (11\bar{1})_\alpha \ .$$

The calculated lattice misfit between epsilon carbide and ferrite further substantiated the fact that the Jack orientation relationship is preferable to the Pitsch-Schrader relationship in bainitic transformation products. The results support the model that supersaturated ferrite is formed initially in lower bainite where epsilon carbide precipitated rapidly and is subsequently replaced by cementite upon further transformation.

The cementite observed in the bainitic ferrite was in the shape of platelets which were formed on a specific ferrite plane. In many cases the Isaichev orientation relationship was found between the cementite and the ferrite.

Evidence has also been obtained which proves the existence of internal twinning in bainite. The fact that the observed twins, whether accommodation or transformation, persisted after isothermal holding suggests that the observed unidirectional precipitation of carbides cannot be attributed to carbides forming on the transformation twins.

Substructural investigations of a number of steels containing various alloying elements (e.g., Mn, Si, Ni, Co, Cr, etc.) show that there is no sharp transition temperature for a lower to an upper bainitic microstructure. It appears that there is a continuous change in the microstructure as the transformation temperature is raised. That is, at lower temperatures internal carbides are seen only inside the laths (typical of lower bainite), and at higher temperatures internal carbides are seen only in between the laths (typical of upper bainite), whereas in the intermediate temperature range both types of carbides are observed. This temperature range is very much composition dependent, and at similar transformation temperatures completely different microstructures were observed in different steels.

*Ph.D. thesis in preparation.

b. Precipitation Upon Nitriding Fe-0.3%Ti Alloy

D. H. Kirkwood* and Gareth Thomas

Nitriding increases the hardness of Fe-Ti alloys to 1300 VPN and has been shown to be associated with precipitation of fine coherent platelets on {100} having a very large lattice misfit. It is concluded that precipitates have the TiN structure.

*Sheffield University, United Kingdom

c. New Programs on Steels

Gareth Thomas and Asscoiates

1) Effects of boron on structure and properties of martensitic steels; Y. L. Chen, Ph.D. thesis initiated 1973/74.

2) Attempts to increase toughness in Fe/Cr/C steels:
- a) by bainitic transformations; R. L. Miller, M.S. thesis
- b) by nickel, J. Koo, M.S. thesis
- c) by variations of processing; B. Rao, M.S. thesis.

d. Phase Transformations

1. Grain Boundary Precipitation in Spinodally Decomposed Cu-Ni-Fe Alloys*

Ron Gronsky

The intergranular fracture of relatively ductile Cu-Ni-Fe alloys that have undergone spinodal decomposition has prompted this investigation into the nature of the cellular precipitation reaction originating from grain boundaries. Analysis by optical and transmission electron microscopy reveals that the cellular constituent grows at a rate of ~2 to 4×10^{-9} cm/sec and occupies less than 3 volume percent of the alloy after aging for 1000 hours within the spinodal. Evidence of denuded zones and preferential loss of coherency of the spinodal product at grain boundaries has also been obtained.

Aging above the spinodal temperature results in a more rapid growth (~ 6×10^{-9} cm/sec) of the grain boundary precipitates which continues until impingement, followed by a secondary reaction having interlamellar spacings 4 to 6 times larger than those of the initial product. The activation energy of the primary high-temperature reaction can be identified with the activation energy for grain boundary diffusion in Cu-Ni-Fe alloys.

Present emphasis has been placed on quantative TEM analysis to better establish the orientation relationships and morphological details of the grain boundary constituent, particularly the highly dislocated precipitate interfaces and the nature of the cell boundaries.

*M.S. thesis in progress.

2. Structure and Properties of Spinodal Cu-Mn-Al Alloys*

Fereshteh H. Mirmirani

Structure and mechanical properties have been studied in the Cu-Mn-Al alloy, which is in the center of the miscibility gap in this system. The results indicate that the alloys undergo order → spinodal → precipitation reaction sequences upon aging. Because of the extensive brittleness of these alloys, tensile mechanical properties could not be measured, and so hardness was used as an indication of the variation in strength with aging.

Vicker's hardnesses for as-quenched and aged specimens were measured and correlated to differences in lattice parameter, wavelength, and microstructure of the decomposed phases.

*M.S. thesis in progress.

8. RESEARCH PLANS FOR CALENDAR YEAR 1974

Gareth Thomas

a. Alloy Design

The basic metallographic characteristics suitable for obtaining strong, tough structural martensitic steels are now well understood. The current program includes research on the effects of alloying and heat treatment so as to obtain a fundamental understanding of the possible benefits resulting from retaining interlath austenite crystals. Specifically, attention is being focused on our highly promising Fe/4Cr/0.35C experimental steel. We will also be concentrating on bainitic steels in the Fe/Cr/C series, bearing in mind the relatively low cost of Cr compared to other substitutional alloying elements.

We are also continuing to study the role of other interstitial solutes on the structure and properties of low-alloy steels, In particular, nitrogen and boron are under investigation. Potential applications of these projects are towards economic improvements in properties of structural steels.

b. Phase Transformations

i) Ordered Alloys

Fundamental studies of phase transformations are essential to the overall alloy design programs in addition to the intrinsic scientific interest of such programs. Emphasis is being continued on understanding the nature of short range order (possible applications are in high-temperature alloys and reactor vessel alloys). This is being done by high-resolution lattice imaging techniques in the electron microscope and by the special high-voltage E.M. techniques of critical voltage. Systems under investigation include Cu-Au, Ni-Mo, Ni-W, Au-V, etc.

ii) Spinodal Alloys

The spinodal transformation is attractive because it gives rise to uniform microstructures. Unfortunately many systems are embrittled as a result of competing precipitation reactions at grain boundaries. A fundamental study is being made of this problem in Cu-Ni-Fe. We are also continuing our studies of the Cu-Mn-Al system, which is very complex but is interesting because one of the phases is ferromagnetic (Cu_2MnAl) and it may be possible to control the dispersion of the ferromagnetic phase, and hence the physical properties, of the alloys.

D. HIGH VOLTAGE ELECTRON MICROSCOPY

Gareth Thomas, Principal Investigator

1. CURRENT RESEARCH PROGRAMS

Gareth Thomas

This paper abstracts briefly some of the research programs currently being carried out using the 650 kV Hitachi electron microscope. Many of the programs are interdisciplinary in nature and involve projects in biology,[1] natural sciences, and engineering, and a recent summary was given at the Erice School.[2] In the present paper some examples of current work on contrast, resolution, and applications in ceramics and minerals will be outlined.

One of the main advantages of HVEM for crystals is increased penetration and resolution.[3] Except for light elements, the penetration does not improve much beyond 1 MeV; e.g., Si, 9-14μ from 1-2.5 MeV, but no gain was detected for stainless steel. Thus apart from studies of knock-on radiation damage and organic (biological) materials, 1 MeV appears to be optimum for penetration in inorganic materials.

a. Resolution and Contrast

Lih-Juann Chen*

We have shown earlier the advantages of bright field and dark field techniques utilizing high-order systematic reflections for improving resolution; e.g., Refs. 4 and 5. Further work using 13 beam systematic computations and experimental observations on several systems has provided some new results at 650 kV, as shown by the corresponding Figs. 1a-d. Figures 1c,d resolve partials of about 75 Å spacing of the pure edge components of a shear loop ($\vec{b}$=a/2[011]) in B-doped Si. This spacing is identical to that reported for 100 kV weak beam analysis by Ray and Cockayne[6] for pure Si. Thus the stacking fault energy in the B-doped specimen is also ~55 ergs/cm^2. The experimental result, Fig. 1c, shows higher contrast of the weak beam images at high voltage (compare to calculation of Fig. 1a).

For resolving closely spaced dipoles the best conditions for imaging have been shown by calculation (9 beam systematic) and experiment to be near 2g (outside contrast) in bright field or the corresponding weak beam d.f. in -1g. These conditions provide maximum image separation, best contrast, and only slightly wider images than if n>2.

Bell[7] first showed that bright field images in 2$\bar{g}$ of stacking faults were contrasty or not depending on the sign of the phase change $\alpha=2\pi\bar{g}_1\cdot\bar{R}$ at the boundary (g_1 is the first order of the systematic set). Subsequently, many more calculations and images have been examined for faults in Si which showed this effect depends on thickness (bright fields, Fig. 2) and w. However, the dark field image in g when 2g

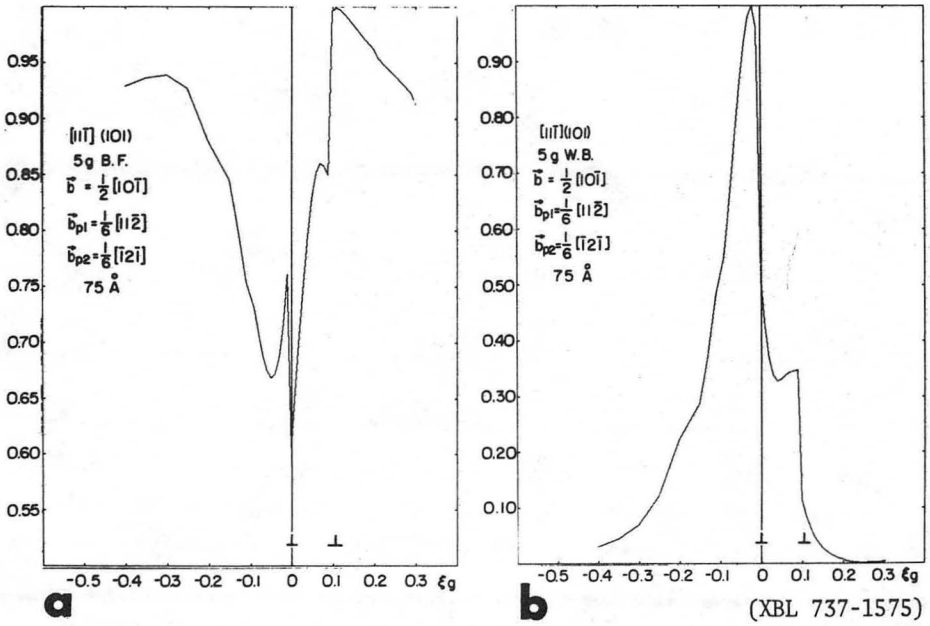

(XBL 737-1575)

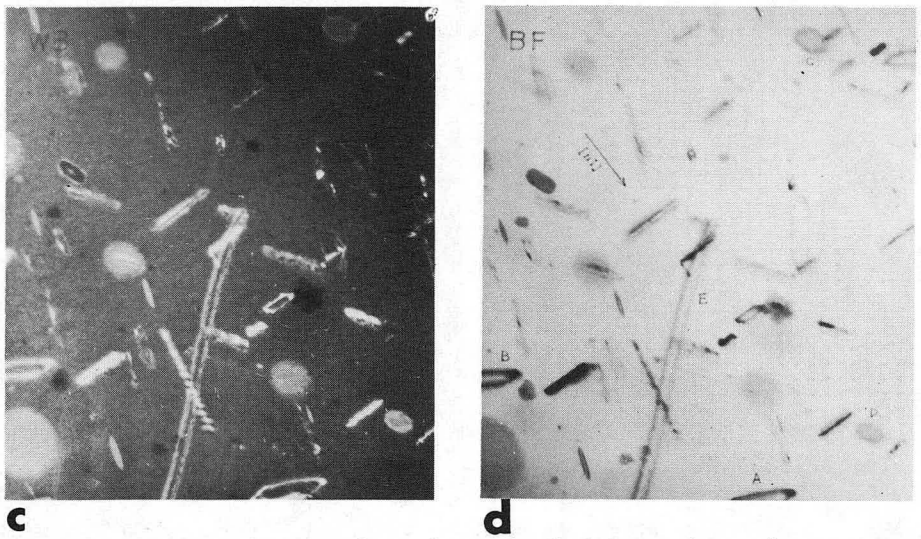

Fig. 1a,b -- Resolution of partials; depth 2.5ξg t=6ξg ξg/ξg=0.06.
1c,d -- Corresponding example. (XBL 737-1575) & (XBB 737-4581)

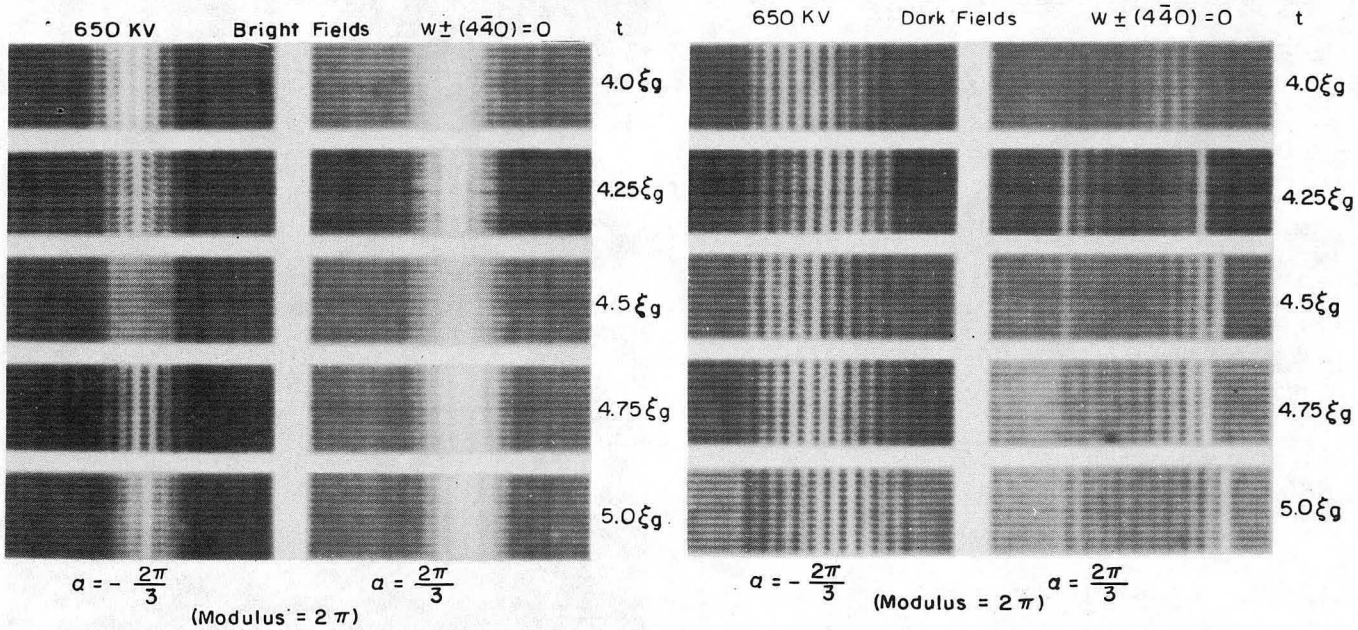

Fig. 2. Computer-simulated images of stacking faults in silicon. (XBB 737-4385A)

is satisfied (or slightly negative but not positive) is directly indicative of the sign of α independently of thickness (Figs. 2 and 3) being of better contrast when $\alpha = -2\pi/3$ (modulus 2π). Thus, this image gives a rapid method for determining whether faults are intrinsic or extrinsic, especially for loops etc. within the foil.

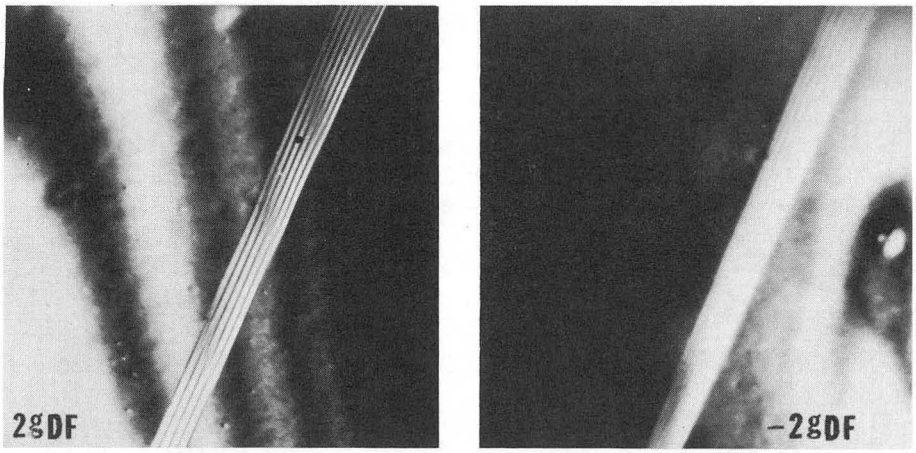

Fig. 3. Determination of the sign of α from a dark-field of g, when $W_{2g} = 0$. (XBB 737-4666)

*Ph.D. thesis, in progress.

b. Ceramics (Lithium Ferrite)

Omer O. Van der Biest*

Above 750°C lithium ferrite ($LiFe_5O_8$) has an inverted spinel-structure, i.e., with Fe^{3+} on tetrahedrally coordinated sites and a 3:1 mixture of Fe^{3+} and Li^+ on the octahedral sites. The latter take on an ordered arrangement below 750°C. The ordered structure contains antiphase boundaries (APB), with a displacement-vector of 1/2 ⟨110⟩ ; an example is shown in Fig. 4. The fringes are due to a small-angle boundary. Figure 5 shows an example of {110} cation faults. Applications of contrast criteria showed that the faults can be characterized by a displacement vector $\bar{R}$=1/4 ⟨110⟩ , with $\bar{R}$ always perpendicular to the fault plane. These faults are thus growth faults. As 1/4 ⟨110⟩ is a lattice vector for the oxygen sublattice, the displacement affects only the cations. For spinel reflections, the faults have all the properties of π faults.

Figures 6a, b, c show contrast conditions for APBs (a), {101} faults (b), and 1/4[101] partials (c). Weak π contrast occurs in 6(b) due to the influence of the superlattice reflections in the systematic set. This effect can cause difficulties in contrast identification at high voltages. Figure 6(c) shows the further advantage of high-resolution imaging[4] in ng (n=6) in which the two partials bounding the (101) fault are well resolved. Examples of {111} faulting

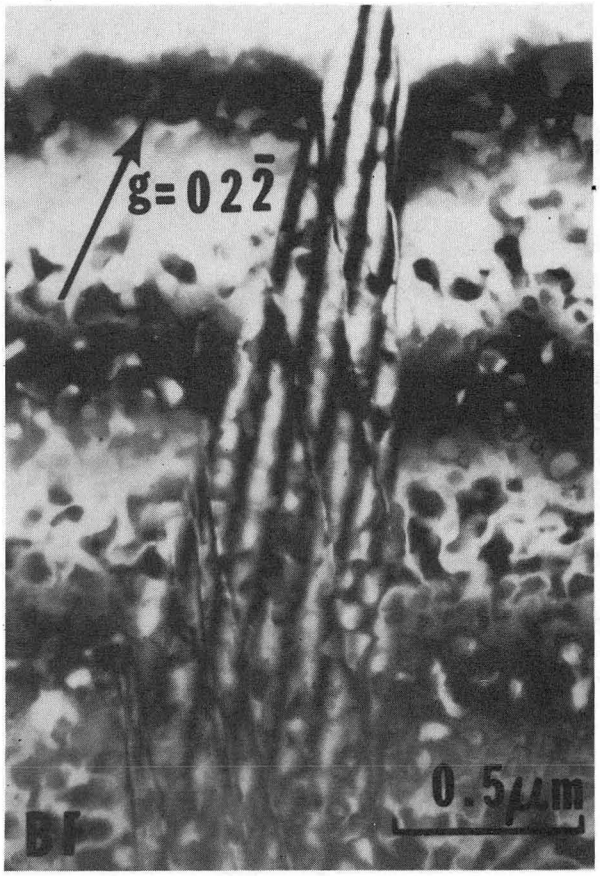

Fig. 4. $LiFe_5O_8$ quenched from 950°C, aged 16 min. 650°C [111] foil; bright field image 650 kV. (XBB 737-4644, left)

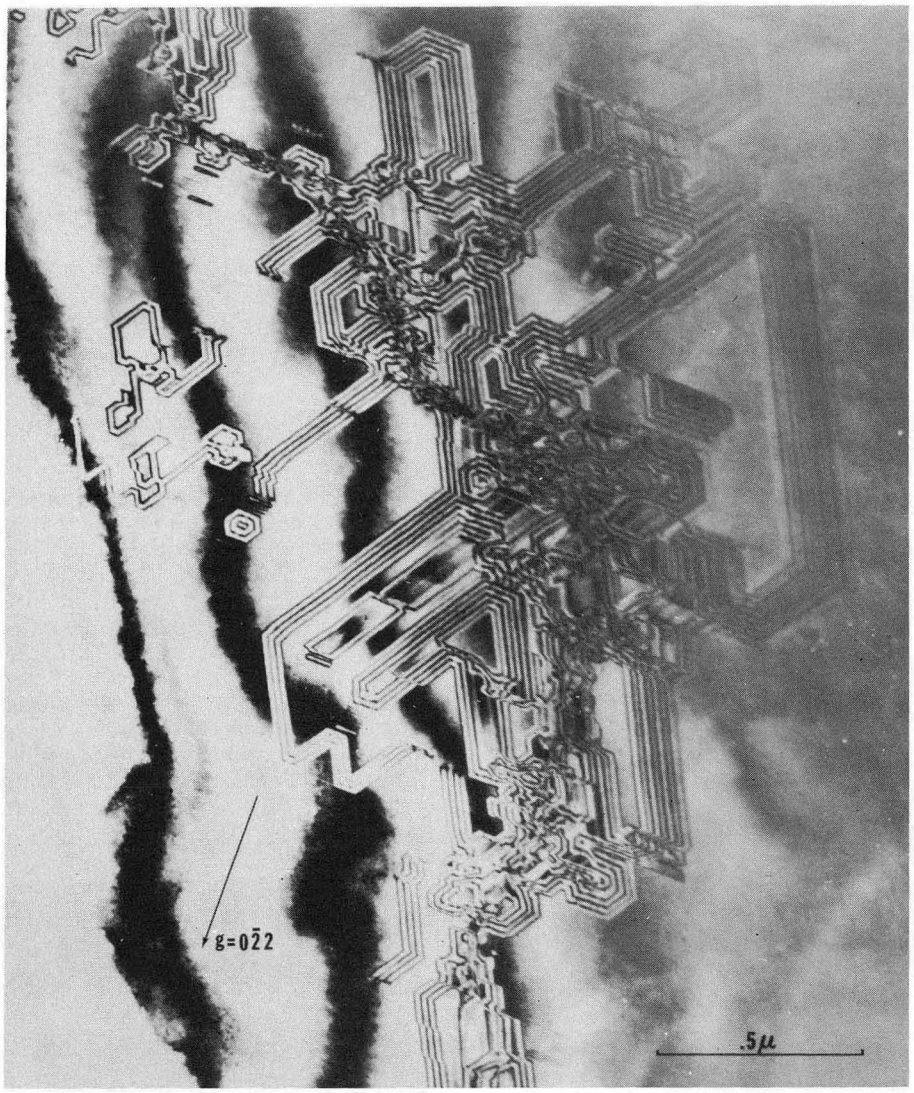

Fig. 5. Disordered $LiFe_5O_8$ showing {110} cation faults. (XBB 734-2443)

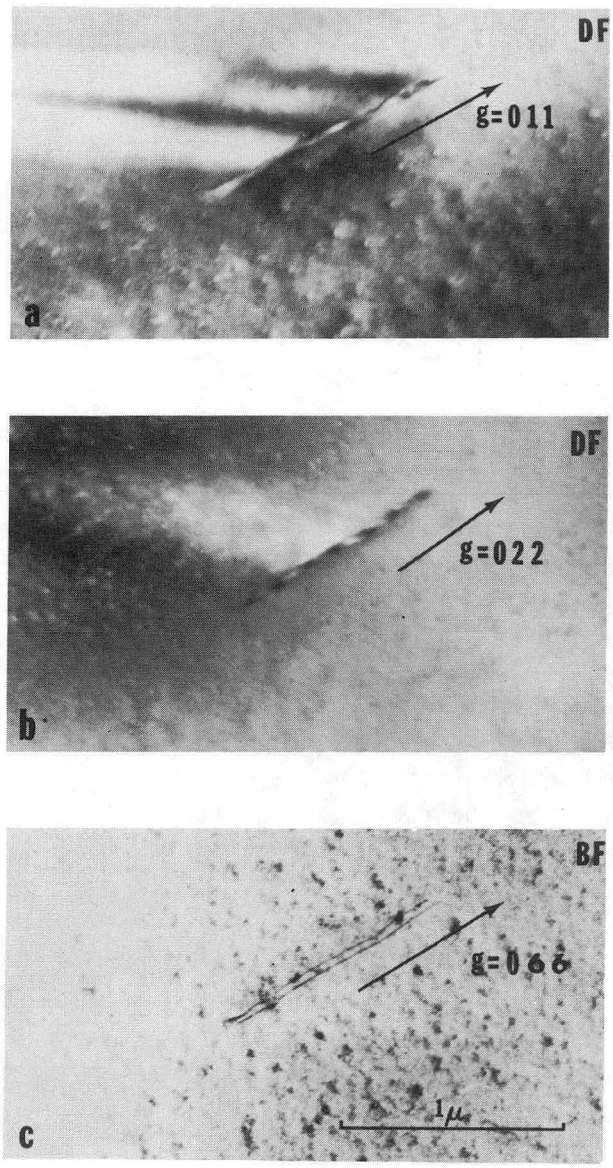

Fig. 6. Contrast examples showing defects in fully ordered $LiFe_5O_8$: (a) 011 superlattice reflection (b) 0.022 spinel reflection cation fault visible (c) 066 spinel reflection-partials resolved. (XBB 734-2815)

associated with a/6 ⟨111⟩ displacements have also been resolved.

*Ph.D. thesis, in progress.

c. Minerals[8]

W. F. Muller,* H. R. Wenk and Gareth Thomas

Several investigations of transformations and deformation of minerals (e.g., enstatite and feldspars) have been carried out. Here we summarize the main conclusions concerning the ordered structures of anorthites (Ref. 9). Two different types of APBs have been resolved: viz., type b APBs (b reflections h+k odd, ℓ odd) and type c APBs (c reflections h+k even, ℓ odd). Examples are shown in Fig. 7. The displacement vector of b-APBs was determined as 1/2[110]; i.e., the formation of b-APBs is connected with Si-Al ordering. The antiphase vector of c-APBs was found to be 1/2[111].

Mineralogy-Processing. Because of the increasing concern over sources of raw materials, considerable interest exists in searching for metal-producing ores on the ocean floors; e.g., the Pacific Ocean bed is estimated to contain at least 10^{11} tons of manganese nodules, containing Ni, Fe, Cu, etc. (e.g., Mero[10]).

Because of the higher resolution in diffraction and greater penetration, the high voltage electron microscope is useful not only in mineral identification of particles which are too small for X-ray analysis, but also for characterizing particle morphology (important in extractive metallurgy). Details of the present research program will be published elsewhere;[11] but

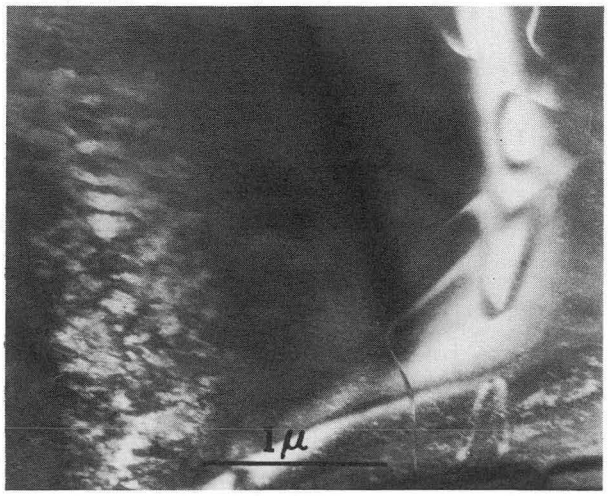

Fig. 7. Simultaneous dark field images of b reflection (right side) $g=21\bar{3}$ and c reflection (left side) $g = 20\bar{3}$ showing the coexistence of both b and c domains in linear breccia 15459. (XBB 732-865)

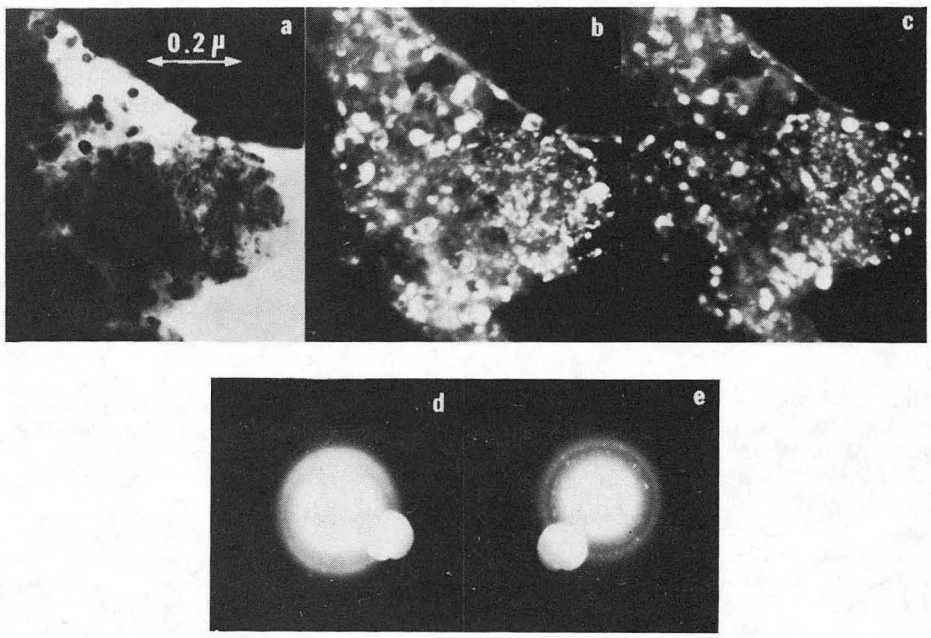

Fig. 8. (a) Bright field and (b), (c) dark field images of Mn nodule showing 100-540 Å particles of $Fe(OH)_3$ identified from rings indicated by doubly exposed image of objective aperture superimposed, nodule from 1270 meters. (XBB 733-2367)

one of the main conclusions was that ferric hydroxide is the main iron mineral in the nodules examined. Figure 8 shows an example of particles in the range 100-450 Å. Identification is carried out with the aid of computer programs, which are also used in environmental research; e.g., analysis of asbestos fibers which are too thick (~2μ) for identification at 100 kV (e.g., Thomas[12]).

*Now at Inst. für Kristall., Frankfurt, Germany

d. Radiation Damage in Organic Solids[1]

David G. Howitt*

Examination of microstructure of organic (including biological) materials in the electron microscope is limited by radiation damage. It appears that the damage rate decreases with increasing voltage. Experiments are being carried out using linacs and the 650 kV E.M. to determine the radiation sensitivity over a range of temperature and voltages. The mechanism of damage is also under investigation using high-resolution techniques.

*M.S. thesis; sponsored by N.I.H.

1. Joint Program with R. M. Glaeser of Donner Laboratory.
2. G. Thomas, in Electron Microscopy in Materials Science--New Developments and Prospectives, Edited by U. Valdré (Commission of European Communities, 1973), in press.
3. G. Thomas and J.-C. Lacaze, J. Microscopy, 97, 301 (1973).
4. W. L. Bell and G. Thomas, Electron Microscopy and Structure of Materials, edited by G. Thomas (Univ. of Calif. Press, Berkeley, 1971), p. 23.
5. M. J. Goringe, E. A. Hewat and C. J. Humphries, Fifth Europ. Electron Mic. Congress (Inst. of Phys., London, 1972), p. 538.
6. I.L.F. Ray and D. J. H. Cockayne, Phil. Mag. 22, 853 (1970).
7. W. L. Bell, Proc. 7th Int. Elec. Mic. Congress; Soc. Fran. de Mic. Electr. Paris, 1970, p. 81.
8. Cooperative program with H. R. Wenk, Geology Dept.
9. W. F. Müller, H. R. Wenk, W. L. Bell, and G. Thomas, Contr. Mineral. & Petrol. 40,63 (1973); LBL-1457.
10. J. L. Mero, Mineral Resources of the Sea (Elsevier, Amsterdam, 1965).
11. M. von Heimendahl, G. Hubred, D. W. Fuerstenau, and G. Thomas, (submitted to Deep Sea Research); LBL-1496 (1973).

12. G. Thomas, Proc. 28th EMSA Congress (Claitors Publishers, Baton Rouge, La., 1970), p. 2.

2. RESEARCH PLANS FOR CALENDAR YEAR 1974

Gareth Thomas

Electron Microscopy

i) Contrast

We will continue to back up the applications of electron diffraction microscopy with basic analyses of contrast phenomena especially for high resolution lattice imaging research, and high-voltage E.M. studies of minerals and ceramics. This approach is essential for quantitative, accurate interpretation of data. (Supported also by N.S.F. funding.)

ii) Radiation Damage

The basic program on stability of organic crystals to electron irradiation will be continued. Attempts will be made to study mechanisms of damage by using high-resolution techniques. The problems involved in measuring electron current density will be evaluated by comparison of Faraday cage and Li drifted detector techniques on specimens such as valine and adenosine. (Joint project with R. M. Glaeser of Donner Laboratory; supported also by N.I.H. funding.)

iii) Ceramic Systems

Little work has been done on microstructure-property relations in ceramics utilizing high-resolution microscopy. The current program involves a study of the lithium ferrites (ferrimagnetic) identifying ordering reactions and defect chemistry and takes advantage of the existence of our 650 kV microscope. We will search for a system which undergoes spinodal transformations again in an attempt to control the microstructure and properties.

3. 1973 PUBLICATIONS AND REPORTS

Gareth Thomas and Associates

Journals

1. R. D. Garwood and G. Thomas, The Tempering of Martensite in an Fe-1.5 pct N Alloy, Met. Trans. 4, 225 (1973)(LBL-470).

2. M. Bouchard, W. L. Worthington, D. J. Jurica, and P. R. Swann, A High-Angle Tilting Stage for the 650 kV Hitachi Electron Microscope, Rev. Sci. Instr. 44(4), 511 (1973)(LBL-1145).

3. W. F. Müller, H. R. Wenk, W. L. Bell, and G. Thomas, Analysis of the Displacement Vectors of Antiphase Domain Boundaries in Anorthites ($CaAl_2Si_2O_8$), Contr. Mineral. and Petrol. 40, 63 (1973)(LBL-1457).

4. S. K. Das, P. R. Okamoto, P. M. J. Fisher, and G. Thomas, Short Range Order in Ni-Mo, Au-Cr, Au-V and Au-Mn Alloys, Acta Met. 21, 913 (1973)(LBL-441).

5. G. A. Stone and G. Thomas, The Stress Induced Martensite-Austenite Interface in Fe-15Ni-15Cr Single Crystals, in 31st Ann. Proc. Electron Microscopy Soc. Amer., New Orleans, La., 1973, pp. 110-111. Edited by C. J. Arceneaux. (LBL-1499).

6. W. F. Muller and H. R. Wenk, Changes in the Domain Structure of Anorthites Induced by Heating, N. Jb. Miner. Mh., Jg. H. 1, 17 (1973)(LBL-1882).

7. P. R. Swann, G. Thomas, and N. J. Tighe, In situ Observations of the Nitriding of Tantalum, J. Microscopy 97, 249 (1973) (LBL-1196).

8. R. Sinclair, High Resolution TEM, Industrial Research, Oct. 1973, p. 62, LBL-2219.

9. G. Thomas and J.-C. Lacaze, Transmission Electron Microscopy at 2.5 MeV, J. Microscopy 97, 301 (1973)(LBL-1119).

10. S. K. Das and G. Thomas, The Metastable Phase Ni_2Mo and the Initial Stages of Ordering in Ni-Mo Alloys, Physica Status Solidi 20 [2], (1973)(LBL-1868).

11. G. Thomas, Role of Electron Microscopy in Design of Strong, Tough, Economical Structural Steels, Iron and Steel International 46, 451 (1973)(LBL-1871).

12. G. Thomas, Current and Future Trends of High Voltage Transmission Electron Microscopy, invited paper, Proc. EMSA Congress, 1973 (Claitors Publishers, Baton Rouge, La., 1973), p.2 (LBL-1802).

13. G. Thomas, Nonequilibrium Defects in Metals, in Science of Materials Used in Advanced Technology, edited by E. R. Parker and U. Colombo (Wiley, New York, 1973),

Chap. 2, p. 13 (UCRL-19696).

14. G. Thomas, Modern Metallographic Techniques, ibid., Chap. 3, p. 35 (UCRL-19697).

15. G. Thomas, Nonequilibrium Microstructures, ibid., Chap. 4, p. 71 (UCRL-19698).

16. J. McMahon and G. Thomas, Development of Economical, Tough, Ultra-High-Strength Fe-Cr-C Steels, in The Microstructure and Design of Alloys, Cambridge, England, August 20-25, 1973, Vol. 1, p. 180.

LBL reports

1. V. F. Zackay, E. R. Parker, J. W. Morris, Jr. and G. Thomas, The Application of Materials Science to the Design of Engineering Alloys, LBL-2261, Oct. 1973.

2. W. Wu, L. J. Chen, J. Washburn and G. Thomas, On Indexing of Diffracting Planes Using the Kikuchi Pattern, LBL-1811, Aug. 1973.

3. R. J. Livak and G. Thomas, Loss of Coherency in Spinodally Decomposed Cu-Ni-Fe Alloys, LBL-1842, July 1973.

4. G. Thomas, Some Applications of High Voltage Electron Microscopy to Inorganic Materials, presented as an invited paper for 3rd Intl. Conf. on HVEM at Oxford, U. K., August 27-30, 1973, LBL-1899, Aug. 1973.

5. S. K. Das and G. Thomas, On Structural Interpretation of Short Range Order, invited paper for Order-Disorder Conference, Tubingen, Germany, LBL-2285, Sept. 1973.

6. G. Thomas, Some Applications at Berkeley and Possible Future Trends, of High Voltage Transmission Electron Microscopy, Electron Microscopy: Physical Aspects, (in press, John Wiley & Sons, Inc.) LBL-2274,

7. G. Thomas, Introduction to Transmission Electron Microscopy, Electron Microscopy in Materials Science: New Developments and Perspectives, (in press, Commission of European Communities) LBL-1471, April 1973.

8. G. Thomas, Introduction to Contrast Analysis, Electron Microscopy in Materials Science: New Developments and Perspectives, (in press, Commission of European Communities) LBL-1472, April 1973.

9. G. Thomas, Some Applications of Transmission Electron Microscopy in Materials Science and Engineering, Electron Microscopy in Materials Science: New Developments and Perspectives, (in press, Commission of European Communities) LBL-1473, April 1973.

10. Glen Stone and G. Thomas, Deformation Induced Alpha and Epsilon Martensites in Fe-Ni-Cr Single Crystals, LBL-1853, July 1973.

11. M. von Heimendahl, G. Hubred, D. W. Fuerstenau and G. Thomas, A Transmission Electron Microscope Study of Deep-Sea Manganese Nodules, LBL-1496, Oct. 1973.

12. Robert A. Clark, Structure and Properties of Fe-Mo-C Steels, M. S. thesis, LBL-1801, June 1973.

13. L. J. Chen and L. M. Falicov, Pseudopotential Calculations of the Stacking Fault Energy in Silicon, LBL-1864, July 1973.

14. Marcel Bouchard and G. Thomas, Modulated Structures and Coarsening in Ordered $(Cu\text{-}Mn)_3Al$ Alloys, LBL-2294, Nov. 1973.

15. M. Bouchard and G. Thomas, Modulated Structures in $(Cu\text{-}Mn)_3Al$ Alloys II. Formation of an $L1_0$ Phase within the Cu_3Al-Side Phase, LBL-2295, Nov. 1973.

16. M. Bouchard and G. Thomas, Modulated Structures in Ordered $(Cu\text{-}Mn)_3Al$ Alloys, III. Formation of the γ Phase, LBL-2296, Nov.1973.

E. ALLOY DESIGN

Victor F. Zackay and Earl R. Parker, Principal Investigators

Introduction. In recent years we have shown that microstructure of alloys has considerable influence on their mechanical properties. An understanding and application of theories that relate microstructure to mechanical properties can obviate much empiricism in alloy development. The design of new alloys or obtaining considerable, rather than nominal, improvements in the properties of existing alloys, then largely involves achieving microstructural control through variations in chemical composition and heat treatment.

Microstructural influences on mechanical properties depend to a large extent on the specific mechanical property that is under consideration. For example, microstructural changes that affect fracture toughness do not influence fatigue crack growth resistance in the same way, as some of our investigations have indicated. In addition, elements of structure that are considered desirable for good cryogenic mechanical properties may not be the ones that benefit elevated temperature or room temperature properties. Therefore, it is essential that both the applicable temperature range and the relevant property be given due consideration when microstructural control is utilized in alloy development.

The main objectives of our research program have been a study of microstructural and compositional features that influence mechanical properties of alloys at cryogenic, room, and elevated temperatures, and application of the principles we have learned from our own studies and of the information available in the literature to develop new and improved alloys. Examples of present efforts directed toward our goals include the following:

1) Studies of the relationship between composition and heat treatment, microstructure, strength, toughness, and fatigue crack growth at temperatures as low as -196°C in interstitial-free Fe-Ni-Ti alloys.

2) Study of those compositional and microstructural features that control room temperature strength, fracture toughness, and fatigue crack growth properties of low and medium alloy high yield strength steels.

3) Investigation of the relation between microstructure, elevated temperature deformation behavior, and elevated temperature rupture and creep strengths of non-carbon-containing, Laves phase strengthened ferritic alloys.

4) Development and use of a rapid magnetometric technique to determine the time-temperature-transformation (TTT) curves for austenite decomposition in several low- and medium-alloy steels. Studies of the effect of alloying elements on bainitic hardenability.

1. DESIGN OF INTERSTITIAL-FREE CRYOGENIC ALLOYS

Michael J. Yokota and Go Sasaki

a. Introduction

The mechanical behavior of metals at cryogenic temperatures is of great scientific and technological importance. A detailed discussion of the philosophy behind the design of iron-base interstitial-free alloys for cryogenic applications was presented in the IMRD Annual Report for 1972. Last year we reported on the superior toughness exhibited by one bcc iron alloy containing 12% Ni and 0.5% Ti. The high Charpy impact energy values of well over 100 ft lb, at temperatures down to that of liquid nitrogen (-196°C), were achieved by a simple heat treatment in the lower temperature range of the γ phase field. The best evidence available at that time indicated that grain size reduction was of primary importance in improving toughness in the Fe-Ni-Ti system.

During this past year attention was focused on determining the role played by grain size on toughness, and on characterizing various processing methods which could be used to achieve efficient grain refinement. In addition, the study was expanded to include alloys with nickel contents from 8 to 16%.

b. Improvement in Impact Toughness from Simple Reheating

Figure 1, curve A, shows the improvement in impact toughness at -196°C of specimens initially austenitized at 900°C and reheated at 50°C/min to temperatures spanning both the equilibrium $\alpha+\gamma$, and the γ phase fields (600 to 800°C). Although modest improvement in toughness was observed when specimens

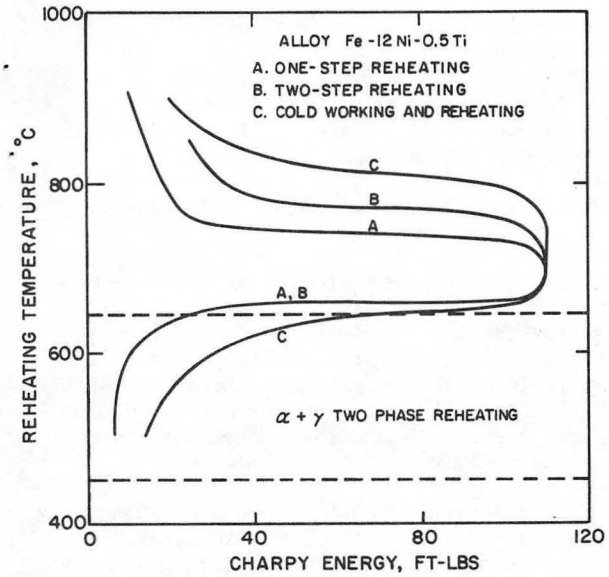

Fig. 1. Plots of Charpy V-notch impact energy at -196°C vs. reheating temperature for alloy Fe-12Ni-0.5Ti. The heat treatments were as indicated. (XBL 741-5482)

were heated into the two-phase α+γ phase field, it is only when they were heat treated to higher temperatures (in the single-phase γ field) that appreciable impact toughness resulted. The microstructure of specimens exhibiting good toughness showed a single-phase grain-refined structure. But, heat treating at temperatures well within the γ phase field again resulted in poor toughness. Microstructural examination of the latter specimens showed a single-phase structure, but with coarse grain size. Examination of the changes which occurred in the microstructure and in the impact toughness during heating at 700°C (in the middle of the high-toughness region) confirmed the view that appreciable toughness resulted only when the α→γ transformation was essentially completed with a corresponding refinement occurring in the grain structure. Electron microscope examination showed that new grains formed at prior austenite and lath colony boundaries via dissolution of the α+γ duplex structure which had formed earlier during heating.

c. Improvement in Impact Toughness from Two-Step Reheating

Reheating to temperatures much above the austenite finish temperature as previously mentioned produced progressively larger austenite grains and a drop in the impact toughness. The α to γ transformation during heating and holding at these higher temperatures occurred with little or no formation of α+γ duplex structure. In order to test the possible link between the α+γ duplex structure and the grain refining process, specimens were initially given an intermediate treatment at 650°C for several hours before heat treating at the higher 750 and 800°C temperatures which had previously produced poor impact toughness. Reheating via the additional 650°C treatment was found to produce finer grain sizes and a corresponding extension of the high toughness reheating range from 725 to 775°C, as indicated by curve B in Fig. 1. A similar improvement of grain refining was accomplished by an essentially equivalent process of a slower heat-up through the α+γ phase region. An examination of the dilatometric response and the resulting microstructures suggested that the presence of the α+γ duplex structure provided a larger number of γ nucleation sites for the formation of new γ grains and also retarded γ grain growth through the presence of α at the new grain boundaries.

d. Improvement in Impact Toughness from Cold Working Prior to Reheating

The α→γ transformation, during 700°C reheating, occurred preferentially at the prior austenite and lath colony boundaries. These initially transformed areas in effect dominated the final average grain size achieved upon completion of the α→γ transformation. It was reasoned that by cold working, the uniqueness of these prior austenite boundaries as high-energy sites for γ nucleation would be lessened somewhat, and nucleation of new γ grains could occur more uniformly throughout the prior austenite grain. This, in fact, appeared to be the case. A cold working treatment prior to reheating produced a finer grain size at all reheating temperatures and resulted in an extension of the high-toughness temperature range to 800°C, curve C of Fig. 1.

The above results showed that considerable improvement in the impact toughness of an Fe-12%Ni-0.5%Ti alloy was achieved by reheating to the lower end of the γ phase field. A much refined austenite grain size resulted during reheating and, when the alloy was cooled to room temperature the γ phase completely transformed back to the α (bcc) structure. The simple one-step reheating treatment produced a Charpy energy absorption peak with a 50°C wide reheating temperature range. When a thermal or mechanical treatment preceded the reheating step, this optimum reheating temperature

range was extended to nearly 100°C. The extension of the reheating temperature range resulted from the higher degree of grain refinement and/or grain boundary stabilization achieved by introducing the prior thermal or mechanical treatments.

The relationship between the refined austenite grain size and the resulting impact toughness is illustrated by Fig. 2, in which the impact energy at -196°G is plotted versus the grain size for the several grain refining treatments described above. Such a plot shows that whatever the method used to refine the grain size, an austenite grain size less than 15μ was needed for impact toughness exceeding 100 ft lb at -196°C. This 15 μm grain size can be considered a critical grain diameter for ductile behavior at -196°C of the Fe-12%Ni-0.5%Ti alloy investigated in this study.

Likewise, similar relationships existed for iron alloys containing 8 and 16%Ni and 0.5%Ti. For the 8%Ni alloy the critical grain size for ductile behavior at liquid nitrogen temperatures was somewhere below 5 μm. For the 16%Ni alloy the critical grain size was 30 μm.

From such data it was possible to determine a relationship between the nickel content

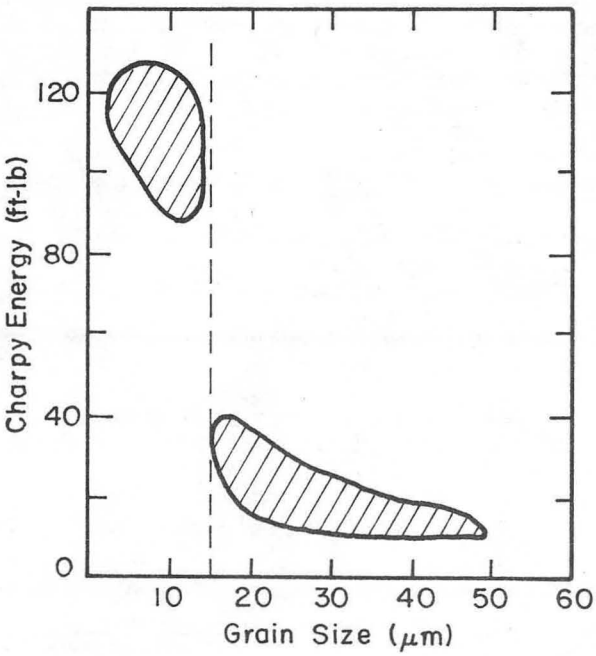

Fig. 2. Plot showing the effect of grain size on Charpy V-notch impact energy, at -196°C, in Fe-12Ni-0.5Ti alloy.
(XBL 7311-5599)

of the alloy and the critical grain diameter for ductile behavior at -196°C. From an alloy design point of view it is then necessary to compare the cost of heat treatment to achieve finer and finer grain sizes, and thereby produce increasingly higher toughness in alloys, with the cost of nickel additions which also produce similar toughness but with larger grain sizes.

Completion of such studies as described above should ultimately allow us to design an alloy for a given service temperature by optimization of the strength-toughness properties while minimizing the economic liabilities such as the number and complexity of heat treatments and the number and amounts of alloy additions.

This research which has been, to a large extent, supported by the U.S. Atomic Energy Commission has in recent months, received additional financial support from the National Aeronautics and Space Administration's Lewis Research Center, Cleveland, Ohio.

2. INFLUENCE OF MICROSTRUCTURE ON FATIGUE CRACK PROPAGATION IN A CRYOGENIC ALLOY

Henri Sirot

Fatigue crack growth rates at room temperature, -78°C, and -196°C were determined for a Fe-8%Ni-0.15%Ti-0.1%Al alloy in which microstructural variations were achieved through variations in heat treatment.

The alloy after an initial austenitizing treatment at 900°C was reheated to 750°C in the γ phase field region. Two different microstructures were obtained by changing the manner in which the alloy was cooled from 750°C. An ice brine quench from 750°C resulted in the formation of massive α' martensite (lath type). When the alloy was furnace cooled to 565°C (following the 750°C treatment), held at 565°C, and then furnace cooled to room temperature, a mixed microstructure consisting of both equiaxed α and massive α' was obtained.

Fatigue crack growth rates were measured at room temperature, -78°C, and -196°C for specimens with both the heat treatments described above. Fatigue tests were conducted on standard WOL type specimens. Cyclic loading with a P_{max}/P_{min} ratio of 10 (leading to a K_{max}/K_{min} ratio of 10) and at a frequency of 5 cycles per second was used in all tests. At room temperature, crack growth rates were determined from periodic measurements of crack length using

a telescope, and also from measurements of fatigue striation spacings using the scanning electron microscope. The two measurements were in good agreement. In cryogenic tests crack growth rates were obtained only from striation spacings.

Preliminary results indicated that there were little differences in crack growth rates between specimens with the massive martensite structure and specimens with the mixed microstructure; however, additional evidence is needed to draw definite conclusions. There was a threshold ΔK ($\Delta K = K_{max} - K_{min}$) below which crack propagation was extremely slow. The reasons for the existence of a threshold, and the influence of microstructure on the threshold are currently under investigation.

3. MICROSTRUCTURAL VARIABLES AND FRACTURE TOUGHNESS OF HIGH STRENGTH C-Mo AND C-Mo-Ni STEELS

Thomas Tom

The influence of microstructure on room temperature plane strain fracture toughness was investigated in several high strength C-Mo and C-Mo-Ni steels. The steels were austenitized at temperatures ranging from 870 to 1200°C, following which they were ice-brine quenched and refrigerated in liquid nitrogen. The influence of tempering on toughness was studied in steels tempered for 1 hour at temperatures up to 600°C. The results of room temperature tensile tests, plane strain fracture toughness tests (using compact tension specimens), and microstructural studies are briefly discussed below.

a. As-quenched Steels

The effect of austenitizing temperature on the room temperature plane strain fracture toughness, yield strength, and ultimate strength of as-quenched 0.30C-5Mo and 0.41C-5Mo steels is shown in Fig. 1. Both steels exhibited good fracture toughness for austenitizing temperatures above about 980°C, with about a 100% increase resulting in the fracture toughness of 0.30C-5Mo steel for increase in austenitizing temperature from 870 to 1200°C. Three factors were possibly responsible for the increased toughness resulting from austenitizing at high temperatures: 1) increase in prior austenite grain size, 2) minimization or elimination of undissolved carbides, and 3) increase in the degree of autotempering resulting from a raised M_s temperature. Several other C-Mo and C-Mo-Ni steels were

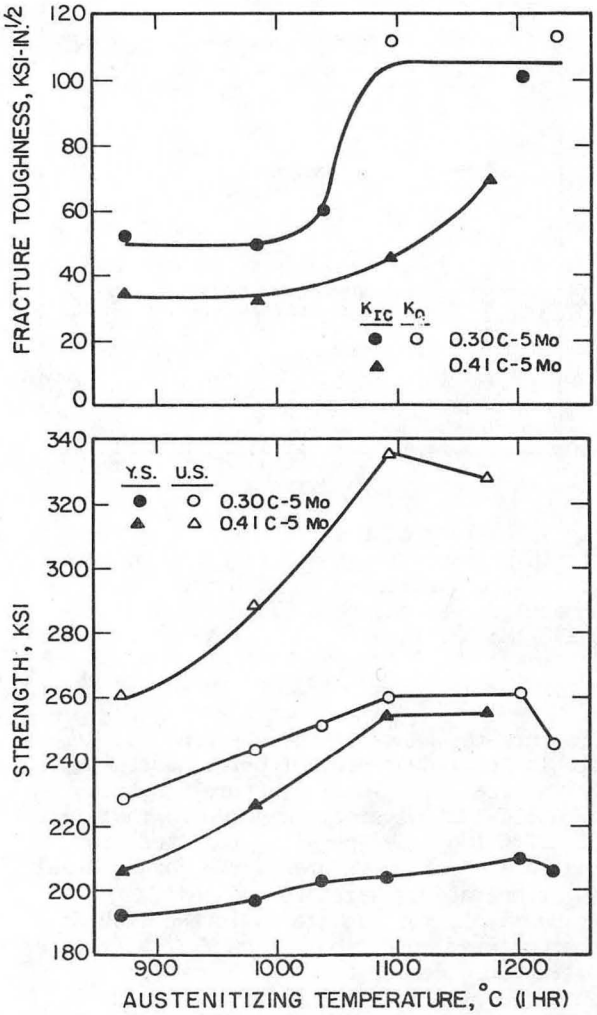

Fig. 1. Plots showing the influence of austenitizing temperature on room temperature fracture toughness (K_{IC} or K_Q), yield strength (Y.S.) and ultimate strength (U.S.) of 0.30C-5Mo and 0.41C-5Mo steels.
(XBL 737-6460A)

subsequently prepared in order to isolate the above variables and determine the individual effect of each on fracture toughness.

In Fig. 2 are shown plots of room temperature plane strain fracture toughness vs. grain size for as-quenched 0.34C-1Mo and 0.35C-1Mo-3Ni steels, austenitized at 870 and 1200°C, resulting in austenite grain sizes with ASTM numbers of 6 and 1 respectively. In both steels complete dissolution of carbides was obtained at 870°C as well as 1200°C. It was evident that in the absence of undissolved carbides,

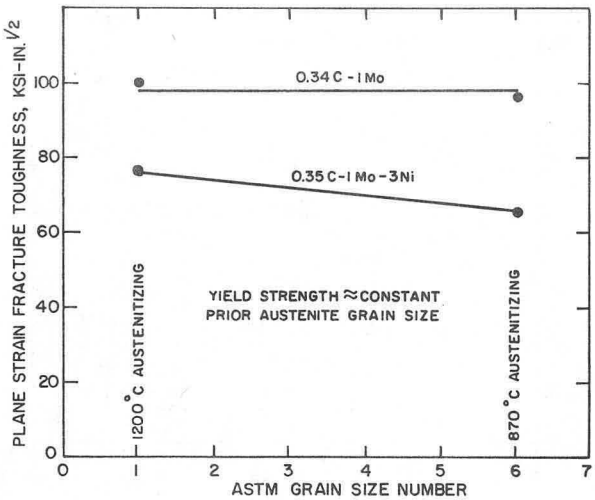

Fig. 2. Plots of room temperature plane strain fracture toughness vs prior austenite grain size (indicated by ASTM grain size number) for as-quenched 0.34C-1Mo and 0.35C-1Mo-3Ni steels. (XBL 737-6468A)

fracture toughness of the as-quenched steels was independent of prior austenite grain size. The lower fracture toughness of 0.35C-1Mo-3Ni steel compared to that of 0.34C-1Mo steel possibly resulted from the lower M_s temperature of the former steel (M_s temperatures were 390 and 464°C respectively for the steels in the 1200°C austenitized condition). Low M_s temperatures often cause decrease in the degree of autotempering of martensite, and in some cases cause internal twinning in martensite.

In order to determine the effect of undissolved carbides on fracture toughness, the results of microstructural examination and the toughness data of 0.30C-5Mo and 0.32C-2Mo steels were compared. Transmission electron microscopy, using carbon replicas extracted from specimens of as-quenched steels, indicated that austenitizing treatments at 870°C resulted in undissolved carbides of approximate diameter 0.05 microns in 0.32C-2Mo steel, and carbides of diameter 1-3 microns in 0.30C-5Mo steel. Plane strain fracture toughness to yield strength (0.2% offset) ratios of 0.27 and 0.42 respectively were obtained for as-quenched 0.30C-5Mo and 0.32C-2Mo steels (both steels austenitized at 870°C prior to testing). In addition, the plane strain fracture toughness of as-quenched 0.32-2Mo steel for the 870°C austenitizing treatment was comparable to that of as-quenched 0.30C-5Mo steel for the 1200°C austenitizing treatment. From these results it was concluded that undissolved carbides of diameter 1-3 microns caused a decrease in plane strain fracture toughness, but carbides of diameter smaller than 0.05 microns did not affect toughness.

b. Tempered Steels

Decreases in room temperature yield strength and increases in fracture toughness were observed when several 1Mo and 2Mo steels of the present investigation were tempered at increasing temperatures up to 600°C. The behavior is illustrated in Fig. 3 for

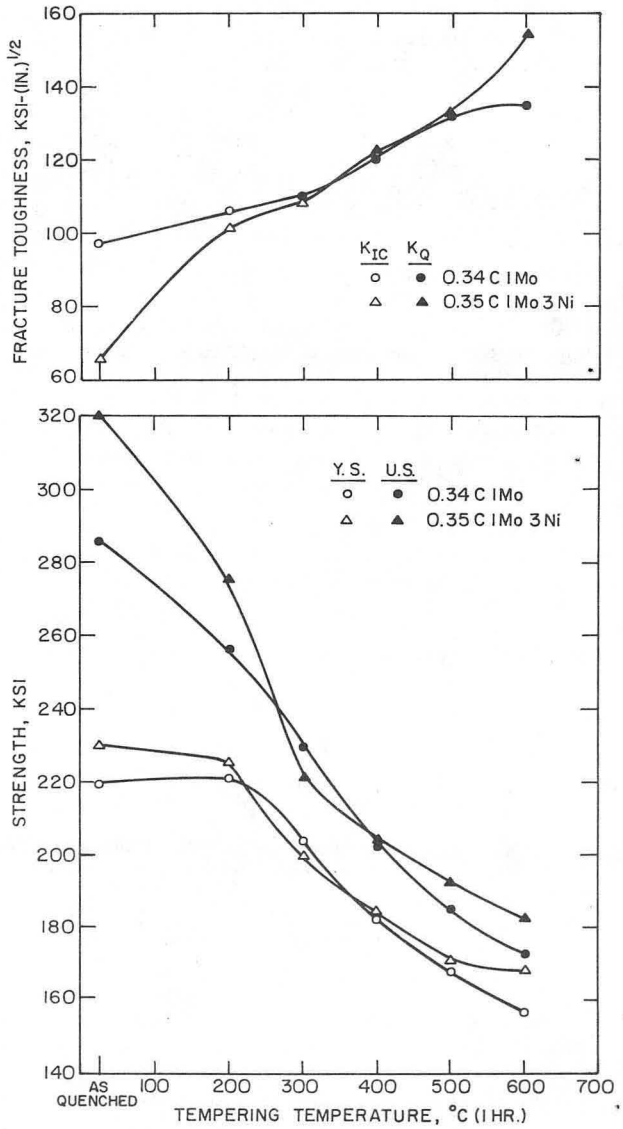

Fig. 3. Plots showing variation, with tempering temperature, of room temperature yield strength, ultimate strength, and fracture toughness for C-Mo and C-Mo-Ni steels. (XBL 737-6464)

0.34C-1Mo and 0.35C-1Mo-3Ni steels which were austenitized at 870°C prior to tempering at several different temperatures and testing at room temperature.

4. INFLUENCE OF HEAT TREATMENT ON THE FATIGUE CRACK GROWTH RATES IN A SECONDARY HARDENING STEEL

Ronald M. Horn

Investigations were continued on the relationship between microstructure and fatigue crack growth rates in a 0.3C-5Mo secondary hardening steel. The main objective of the study was to see whether the microstructural features that influenced plane strain fracture toughness influenced fatigue crack growth rates in the same way. Microstructural changes were accomplished by varying austenitizing and tempering treatments. An earlier study[1] had shown that both parameters influenced plane strain fracture toughness. In the present study, fatigue tests were carried out in moist air, simulating normal engineering conditions.

Austenitizing at 1200°C resulted in a complete dissolution of carbides. Because of the secondary hardening nature of this steel, tempering treatments following austenitization and an ice-brine quench led to drastic changes in microstructure. Figure 1 shows a plot of room temperature fatigue crack growth properties and plane strain fracture toughness vs. tempering temperaure. The number of cycles for crack growth of 1 in. at a given constant ΔK level was used as a measure of fatigue crack growth resistance. The as-quenched material had both good fracture toughness and good fatigue crack growth properties while tempering at 300°C led to a deterioration of fracture toughness, but not of fatigue crack growth resistance. Tempering at 600°C led to deterioration of both fracture toughness and fatigue crack growth resistance.

Scanning electron fractographs of the fatigue fracture surface of the as-quenched steel are shown in Fig. 2. While areas of

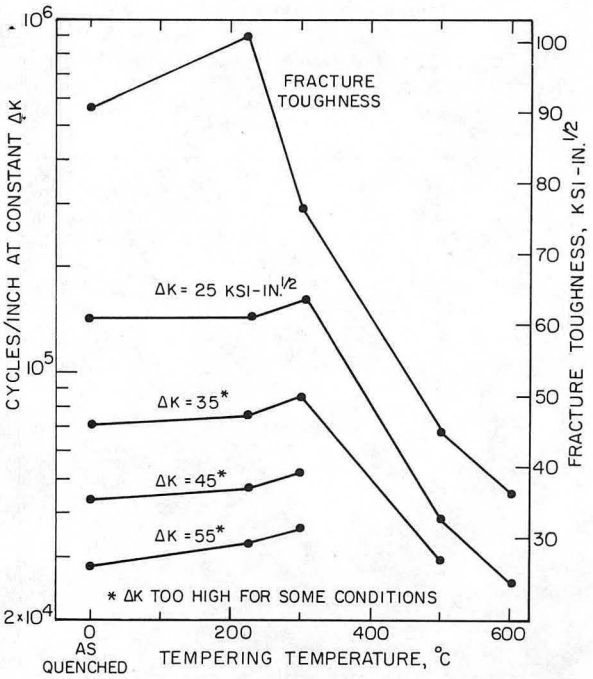

Fig. 1. Comparison of room temperature fatigue crack growth properties and plane strain fracture toughness of 0.3C-5Mo steel for the different tempering treatments after austenitization at 1200°C. The number of cycles for crack growth of 1 in. at a constant stress intensity range was used as a measure of crack growth resistance. (XBL 739-1860)

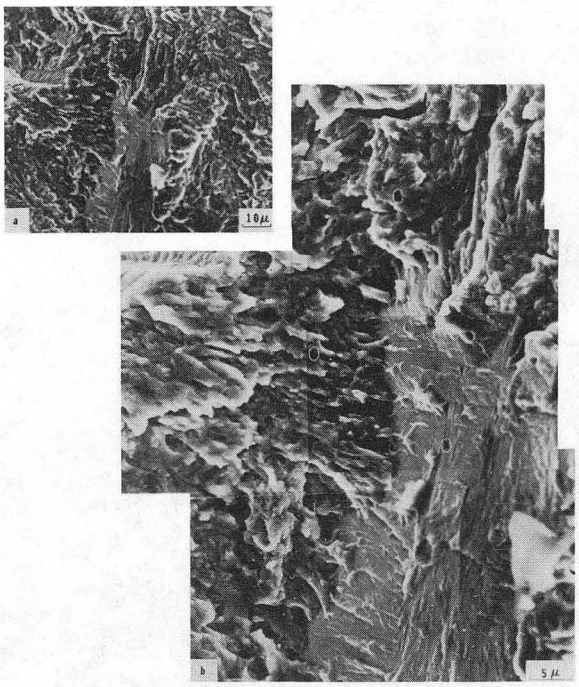

Fig. 2. Scanning electron fractographs of fatigue fracture region in 1200°C austenitized as-quenched 0.3C-5Mo steel. (a) Overall appearance of surface for ΔK=35 ksi-in.$^{1/2}$. (b) Composite enlargement showing quasi-cleavage at A, fatigue cracking through bulk microstructure at B, and local striations at C. (XBB 739-5579)

quasi-cleavage were observed at A in Fig. 2, the diffuse striations (as shown at C) were typical of all tempering treatments up to 300°C. The good fracture toughness of the as-quenched steel was attributed to the autotempered martensite free of extensive lath boundary precipitates.[1] This microstructure also led to good fatigue crack growth resistance.

The deterioration of fracture toughness on tempering at 300°C, was attributed to the growth of lath boundary precipitates during tempering. The presence of an easy crack path of lath boundary cementite did not, however, affect the fatigue crack growth rates. Fatigue properties, requiring plastic deformation, were insensitive to the microstructural changes that caused deterioration of plane strain fracture toughness.

With tempering in the 500-600°C range alloy carbides formed, leading to increased strength. This led to a further decrease in fracture toughness. The fatigue crack growth properties also worsened. Figure 3 shows a scanning electron fractograph of the fatigue surface of a specimen tempered at 600°C and tested at ΔK = 21 ksi-in.$^{1/2}$. The appearance of a second failure mode, intergranular failure, as noted in Fig. 3, accounted for the deterioration of fatigue crack growth resistance.

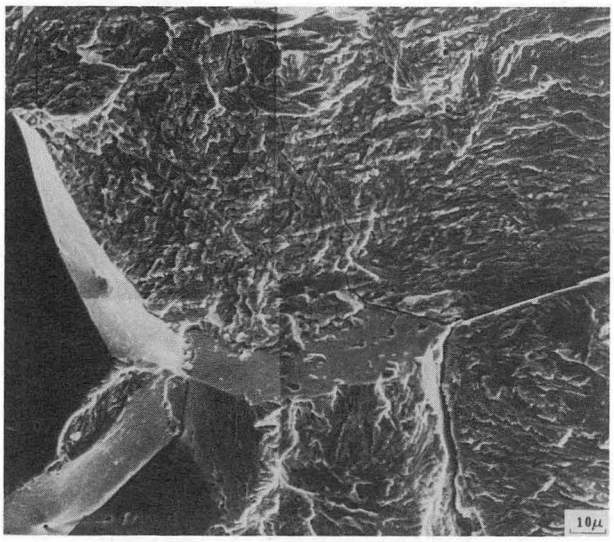

Fig. 3. Composite SEM fractograph showing fatigue fracture surface of 1200°C austenitized, 600°C tempered 0.3C-5Mo steel. Intergranular mode of failure was evident in fatigue area. ΔK=21 ksi-in.$^{1/2}$. (XBB 759-5583)

Austenitizing at 870°C led to a microstructure considerably different from the microstructure resulting from austenitizing at 1200°C. Alloy carbides were not completely dissolved at the lower austenitizing temperature and this resulted in lower strength and lower plane strain fracture toughness. Tempering led to little changes in mechanical properties. Figure 4 compares the fatigue crack growth properties of as-quenched 0.3C-5Mo steel for the 870 and 1200°C austenitizing temperatures. The 870°C austenitizing treatment led to much-improved fatigue properties. The improvement could be attributed to ferrite retained during austenitization. Although many undissolved carbide particles were present, leading to lower fracture toughness, the fatigue crack properties were controlled by other microstructural features.

Research in progress is aimed at investigating, in the 0.3C-5Mo steel, the possible interaction of microstructure, fatigue crack growth, and environment. The microstructure was varied by changing both the austenitizing and tempering temperatures.

This research was supported jointly by the U.S. Atomic Energy Commission and the Army Materials and Mechanics Research Center, Watertown, Massachusetts.

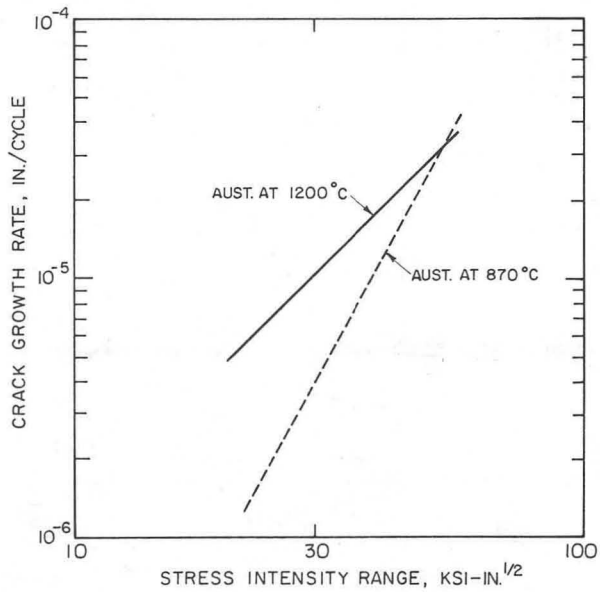

Fig. 4. Comparison of fatigue crack growth rates vs. stress intensity range for as-quenched 0.3C-5Mo steel. (XBL 7311-6732)

1. R. D. Goolsby (Ph.D. thesis), LBL-405, Nov. 1971.

0.34C-1Mo and 0.35C-1Mo-3Ni steels which were austenitized at 870°C prior to tempering at several different temperatures and testing at room temperature.

4. INFLUENCE OF HEAT TREATMENT ON THE FATIGUE CRACK GROWTH RATES IN A SECONDARY HARDENING STEEL

Ronald M. Horn

Investigations were continued on the relationship between microstructure and fatigue crack growth rates in a 0.3C-5Mo secondary hardening steel. The main objective of the study was to see whether the microstructural features that influenced plane strain fracture toughness influenced fatigue crack growth rates in the same way. Microstructural changes were accomplished by varying austenitizing and tempering treatments. An earlier study[1] had shown that both parameters influenced plane strain fracture toughness. In the present study, fatigue tests were carried out in moist air, simulating normal engineering conditions.

Austenitizing at 1200°C resulted in a complete dissolution of carbides. Because of the secondary hardening nature of this steel, tempering treatments following austenitization and an ice-brine quench led to drastic changes in microstructure. Figure 1 shows a plot of room temperature fatigue crack growth properties and plane strain fracture toughness vs. tempering temperaure. The number of cycles for crack growth of 1 in. at a given constant ΔK level was used as a measure of fatigue crack growth resistance. The as-quenched material had both good fracture toughness and good fatigue crack growth properties while tempering at 300°C led to a deterioration of fracture toughness, but not of fatigue crack growth resistance. Tempering at 600°C led to deterioration of both fracture toughness and fatigue crack growth resistance.

Scanning electron fractographs of the fatigue fracture surface of the as-quenched steel are shown in Fig. 2. While areas of

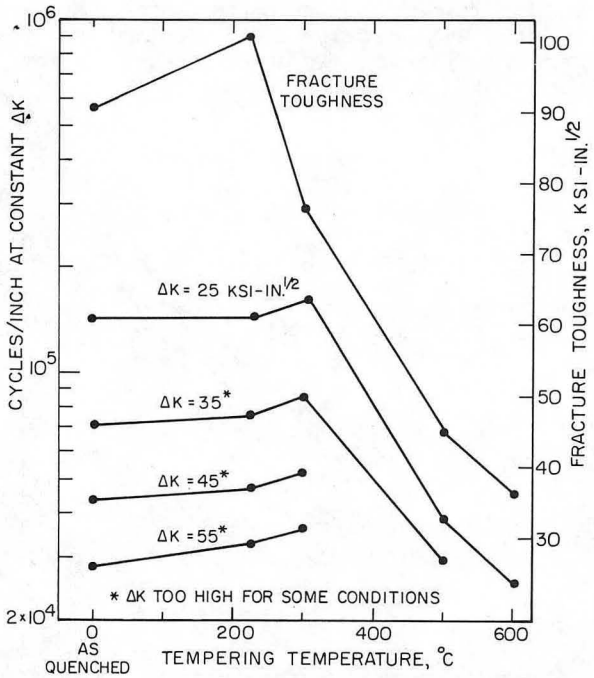

Fig. 1. Comparison of room temperature fatigue crack growth properties and plane strain fracture toughness of 0.3C-5Mo steel for the different tempering treatments after austenitization at 1200°C. The number of cycles for crack growth of 1 in. at a constant stress intensity range was used as a measure of crack growth resistance. (XBL 739-1860)

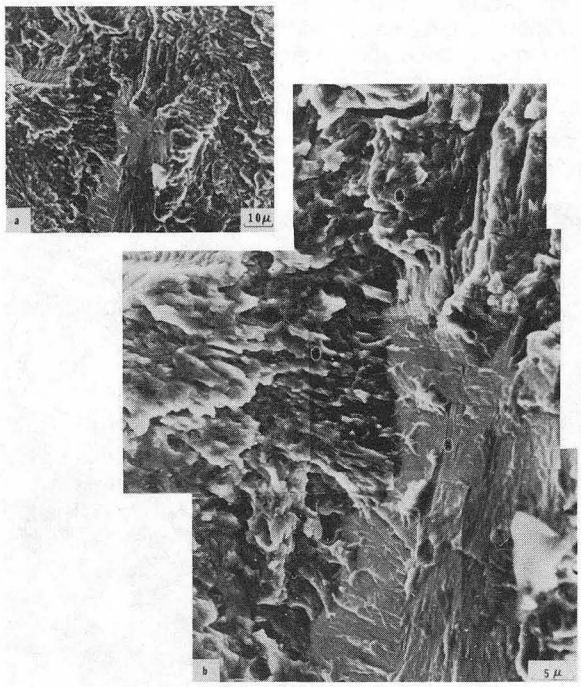

Fig. 2. Scanning electron fractographs of fatigue fracture region in 1200°C austenitized as-quenched 0.3C-5Mo steel. (a) Overall appearance of surface for ΔK=35 ksi-in.$^{1/2}$. (b) Composite enlargement showing quasi-cleavage at A, fatigue cracking through bulk microstructure at B, and local striations at C. (XBB 739-5579)

quasi-cleavage were observed at A in Fig. 2, the diffuse striations (as shown at C) were typical of all tempering treatments up to 300°C. The good fracture toughness of the as-quenched steel was attributed to the autotempered martensite free of extensive lath boundary precipitates.[1] This microstructure also led to good fatigue crack growth resistance.

The deterioration of fracture toughness on tempering at 300°C, was attributed to the growth of lath boundary precipitates during tempering. The presence of an easy crack path of lath boundary cementite did not, however, affect the fatigue crack growth rates. Fatigue properties, requiring plastic deformation, were insensitive to the microstructural changes that caused deterioration of plane strain fracture toughness.

With tempering in the 500-600°C range alloy carbides formed, leading to increased strength. This led to a further decrease in fracture toughness. The fatigue crack growth properties also worsened. Figure 3 shows a scanning electron fractograph of the fatigue surface of a specimen tempered at 600°C and tested at ΔK = 21 ksi-in.$^{1/2}$. The appearance of a second failure mode, intergranular failure, as noted in Fig. 3, accounted for the deterioration of fatigue crack growth resistance.

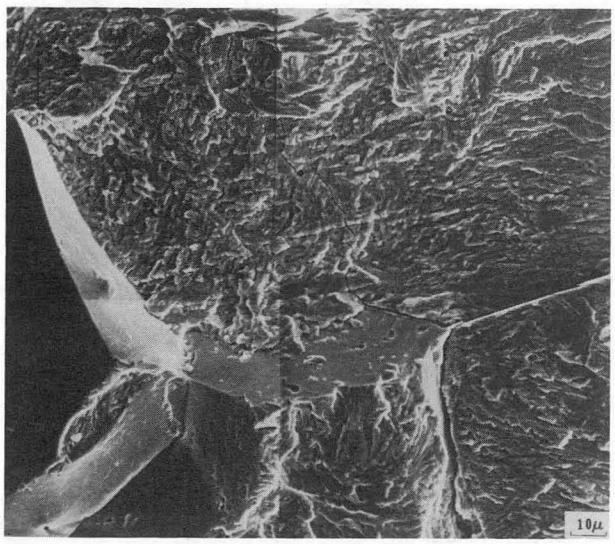

Fig. 3. Composite SEM fractograph showing fatigue fracture surface of 1200°C austenitized, 600°C tempered 0.3C-5Mo steel. Intergranular mode of failure was evident in fatigue area. ΔK=21 ksi-in.$^{1/2}$. (XBB 759-5583)

Austenitizing at 870°C led to a microstructure considerably different from the microstructure resulting from austenitizing at 1200°C. Alloy carbides were not completely dissolved at the lower austenitizing temperature and this resulted in lower strength and lower plane strain fracture toughness. Tempering led to little changes in mechanical properties. Figure 4 compares the fatigue crack growth properties of as-quenched 0.3C-5Mo steel for the 870 and 1200°C austenitizing temperatures. The 870°C austenitizing treatment led to much-improved fatigue properties. The improvement could be attributed to ferrite retained during austenitization. Although many undissolved carbide particles were present, leading to lower fracture toughness, the fatigue crack properties were controlled by other microstructural features.

Research in progress is aimed at investigating, in the 0.3C-5Mo steel, the possible interaction of microstructure, fatigue crack growth, and environment. The microstructure was varied by changing both the austenitizing and tempering temperatures.

This research was supported jointly by the U.S. Atomic Energy Commission and the Army Materials and Mechanics Research Center, Watertown, Massachusetts.

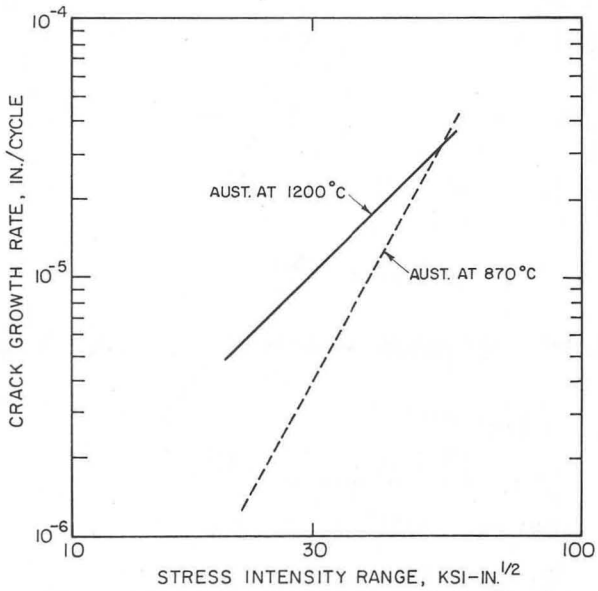

Fig. 4. Comparison of fatigue crack growth rates vs. stress intensity range for as-quenched 0.3C-5Mo steel. (XBL 7311-6732)

1. R. D. Goolsby (Ph.D. thesis), LBL-405, Nov. 1971.

5. STRUCTURE AND ELEVATED TEMPERATURE PROPERTIES OF NON-CARBON-CONTAINING FERRITIC ALLOYS STRENGTHENED BY A LAVES PHASE

Dilip Bhandarkar and Manjeshwar S. Bhat

Recent studies on the use of intermetallic compounds, rather than carbides, for obtaining elevated temperature strength in bcc iron resulted in the development of non-carbon-containing Fe-Ta-Cr and Fe-Ta-Cr-Mo alloys which derived their creep resistance from a uniform dispersion of almost spherical particles of the Fe-Ta Laves phase (referred to as Fe_2Ta hereafter).[1] The heat treatments pertaining to these alloys are described elsewhere.[1,2] Preliminary results of stress rupture tests at 1000°F(538°C) and 1100°F(593°C) indicated that the alloy Ta7Cr of atomic composition Fe-1 at.%Ta-7 at.%Cr and the alloy Ta7CrMo of atomic composition Fe-1 at.%Ta-7 at.%Cr-0.5 at.%Mo had higher rupture strengths than types 403 and 410 stainless steels, but lower rupture strengths than 0.3C-1Cr-1Mo-0.25V steel, Greek Ascoloy, and AISI type 422 stainless steel. The results of more extensive structural studies and mechanical testing are described below.

a. Creep and Stress Rupture Properties

The 1000-hour rupture stress (a measure of rupture strength), and stress for a creep rate of 1×10^{-4} %/h (a measure of creep strength) were estimated for alloys Ta7Cr and Ta7CrMo. The results at 1100°F(593°C) are compared in Table I with those reported in the literature for several common ferritic steels. The spheroidizing heat treatments[1] used for Ta7Cr and Ta7CrMo were, respectively, 10 min at 1100°C, and 3 cycles between 22 and 1100°C with a 15 min hold at 1100°C during each cycle. It was concluded that the rupture strength of alloy Ta7Cr was higher than the rupture strengths of ferritic steels containing 5 to 12 wt.%Cr and strengthened by dispersions of chromium and molybdenum carbides but lower than the rupture strength of ferritic steels containing significant amounts of vanadium and tungsten. The rupture and creep strengths of alloy Ta7CrMo were even superior to those of alloy Ta7Cr. Among the steels cited above, only the 422 stainless steel had a creep strength higher than that of alloy Ta7CrMo (3 cycle heat treatment). Additional studies revealed that when the alloy Ta7CrMo was given a 2 hour treatment at 1100°C (instead of the 3 cycle treatment), the 1000-hour rupture stress at 1100°F(593°C) was raised and approached that of (in fact, it was slightly higher than that of) Greek Ascoloy. The creep strength at 1100°F(593°C) for the 2 hour treatment was higher than that of 422 stainless steel.

b. Structural Investigations of Creep and Fracture in Alloy Ta7Cr

Transmission electron microscopic examination of substructure of crept specimens of alloy Ta7Cr indicated that the initial structure (before creep), which consisted of a lath-like substructure with dislocation tangles, subgrains, and a high unpinned dislocation density, underwent partial recovery during creep at 1100°F(593°C) and 1200°F(649°C). A regular subgrain structure with dislocation pile-ups and jogs was observed in crept specimens. Laves phase particles prevented total recovery by pinning individual dislocations and subgrain boundaries. A typical structure of a specimen which was crept at 1200°F(649°C) and 11,000 psi is shown in Fig. 1, where particle pinning of subgrain boundaries, dislocation pile-up (at A), and pinned dislocation segments (at B) are observed. Structural observations, measured apparent activation energy for creep, and the estimated stress sensitivity of steady state creep rate suggested that more than one parallel and independent process was involved in the creep of alloy Ta7Cr.

Fracture surface examination, by scanning electron microscopy, of specimens broken in stress rupture tests indicated that fracture was initiated by void formation at interfaces between Laves phase particles and the matrix. This resulted in a dimpled

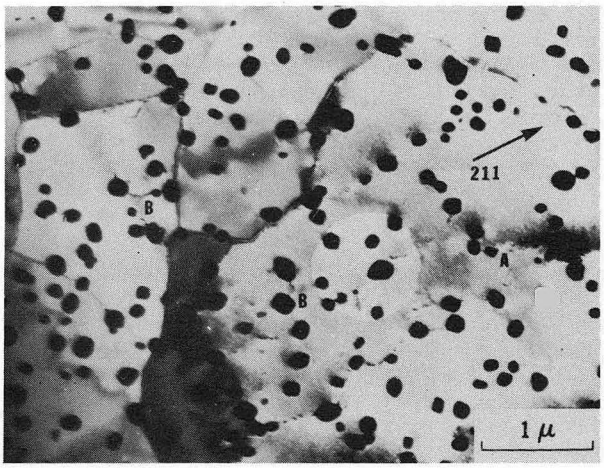

Fig. 1. Transmission electron micrograph of a thin foil specimen of alloy Ta7Cr (spheroidized for 10 min at 1100°C), tested in creep at 1200°F(649°C) and 11,000 psi. Bright field micrograph with $\bar{g}$=[211]. (XBB 738-5038, top)

appearance of fracture surfaces. Void formation sometimes occurred at grain boundaries during long time tests at 1100°F (593°C), but no intergranular fracture was observed. However, at 1200°F(649°C), extensive grain boundary void formation resulted in mixed intergranular and transgranular fractures.

c. Phase Transformation Characteristics of Alloy Ta7CrMo and Their Influence on Microstructure

Preliminary studies of the microstructure of alloy Ta7CrMo heat treated at 1100°C in the (γ + Fe_2Ta) phase field following solution treating and quenching indicated that the transformation to γ was slow and time dependent at 1100°C. This feature contrasted with the behavior of Ta7Cr alloy which exhibited a complete $\alpha \rightarrow \gamma$ transformation in 10 min at 1100°C. Subsequently, more detailed studies were conducted of the transformation behavior of alloy Ta7CrMo, both by cooling the alloy from the solution treating temperature to each of several temperatures in the (γ+Fe_2Ta) phase field (reaction on cooling), and by quenching the alloy to room temperature and then heating it to several temperatures in the (γ+Fe_2Ta) phase field (reaction on heating). The alloy specimens were held for increasing time intervals at each temperature and ice-brine quenched. The microstructure was then examined by optical metallography in order to determine the time at each temperature for the start and completion of the $\alpha \rightarrow \gamma$ transformation. (The formation of γ phase during hold was easily detected since on brine quench from the holding temperature, γ transformed to α by a massive type of reaction resulting in irregular grain boundaries in the transformation product.) The γ formation reaction both on heating and cooling exhibited C-curve kinetics. In Fig. 2 the C-curves are plotted for both the heating (solid curves) and the cooling (broken curves) reactions.

Typical micrographs illustrating the microstructure of partially transformed specimens are shown in Fig. 3 for both the heating and cooling reactions. The micrograph in Fig. 3(a) was obtained from a specimen cooled to 1020°C from the solution treating temperature and held for 10 min prior to quenching to room temperature. A characteristic lamellar γ+Fe_2Ta structure that is observed in several alloys that undergo a eutectoid reaction formed during holding at 1020°C. On subsequent quenching γ transformed to α while the fraction untransformed at 1060°C remained as such. The kinetics of the cooling reaction at

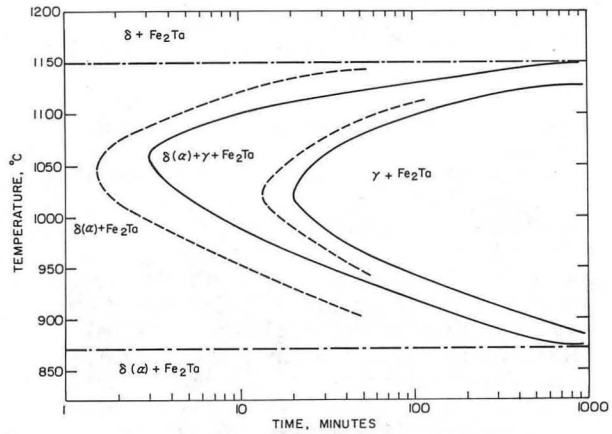

Fig. 2. Time-temperature-transformation curves for the heating (solid curves) and cooling (broken curves) reactions of alloy Ta7CrMo. (XBL 741-5483)

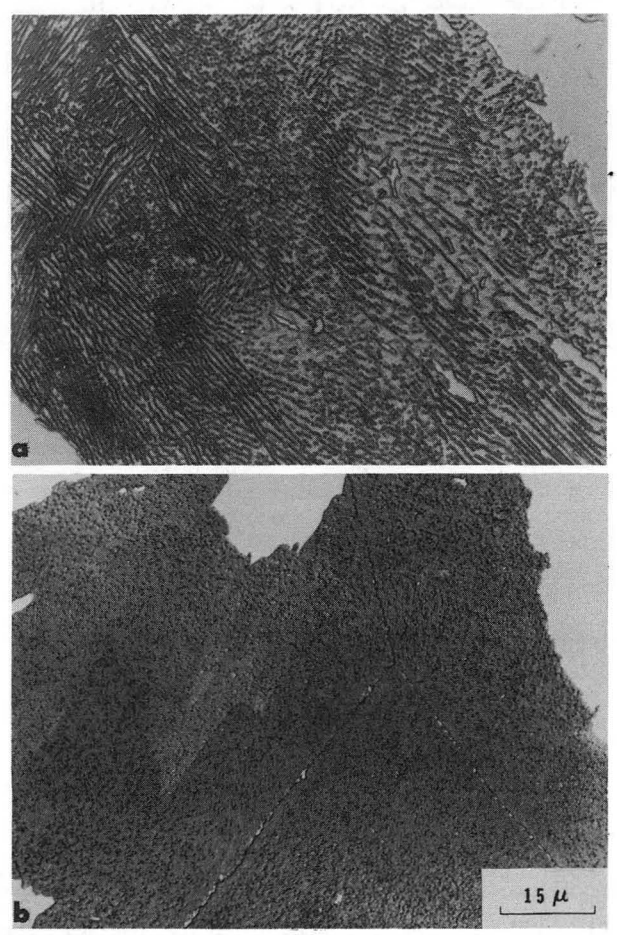

Fig. 3. Microstructures of alloy Ta7CrMo partially transformed by holding at 1020°C for (a) 10 min in the cooling reaction, and (b) 15 min in the heating reaction. (XBB-741-230)

Table I. Creep and rupture strengths of ferritic alloys at 1100°F (593°C).

Alloy	1000-hour rupture stress (psi)	Stress for a creep rate of 1×10^{-4} %/h (psi)
Alloy Ta7Cr	16,000	9,400
Alloy Ta7CrMo(3 cycle heat treatment)	21,600	15,000
0.3C-1Cr-1Mo-0.25V steel	36,900	--[a]
0.15C-9Cr-1Mo steel	14,100	6,300
0.15C-7Cr-0.5Mo steel	13,300	4,000
403 and 410 stainless steels	14,300	4,000
Greek Ascoloy	27,500	--[a]
422 stainless steel	33,800	19,000

[a]Creep strength decreases with increasing time at temperature.

several temperatures and the microstructures that resulted were similar in nature to those involved in the pearlite reaction in steels. A typical microstructure that resulted from the heating reaction is illustrated in Fig. 3(b) which shows the optical micrograph of a specimen heated to 1020°C (following solution treating and quenching to room temperature) and held for 15 min. The Laves phase formed as almost spherical particles in this case. The C-curve kinetics of the heating reaction were explained on the basis of thermodynamics, nucleation theory, and diffusion.

It was concluded that in alloy Ta7CrMo it was possible to control the heat treating time and temperature, and produce a variety of microstructures with the Laves phase in both spherical and lamellar morphologies. It is well known that creep properties of alloys containing a second phase dispersion are strongly influenced by particle size, morphology, and volume fraction of the second phase. It is proposed to investigate the influence of these and other variables on the creep properties of alloy Ta7CrMo.

1. V. F. Zackay, E. R. Parker, and D. Bhandarkar, Proc. John E. Dorn Mem. Symp. on Rate Processes in Plastic Deformation, Cleveland, Ohio, Oct. 1972. Also LBL-1174, Oct. 1972.
2. M. D. Bhandarkar (D. Eng. thesis), LBL-1858, Sept. 1973

6. INVESTIGATION OF BAINITIC HARDENABILITY IN STEELS BY THE USE OF A RAPID MAGNETOMETRIC TECHNIQUE

B. Naga Prakash Babu

A rapid magnetic permeability method was developed to conduct a systematic study of the influence of alloying elements and austenitizing temperature on the shape and position of time-temperature-transformation (TTT) curves of several low and medium alloy steels. The accuracy and reliability of the method were established by plotting the bainitic and martensitic transformation regions of the TTT diagram of commercial AISI 4340 steel austenitized at 870°C. The experimentally determined TTT diagram, shown in Fig. 1, was very similar, both in shape and position, to the diagram that has been reported in the literature.[1]

From Fig. 1 it is evident that when thick sections of commercial AISI 4340 steel are austenitized at 870°C and oil quenched, appreciable amounts of upper bainite can result in the microstructure of the steel. Upper bainite, even when present in small amounts in martensitic and lower bainitic steels, is a detrimental microstructural feature with regard to fracture toughness. In AISI 4340 steel, bainitic hardenability was considerably improved when austenitizing temperature was raised from 870 to 1200°C. The TTT diagram of the steel austenitized

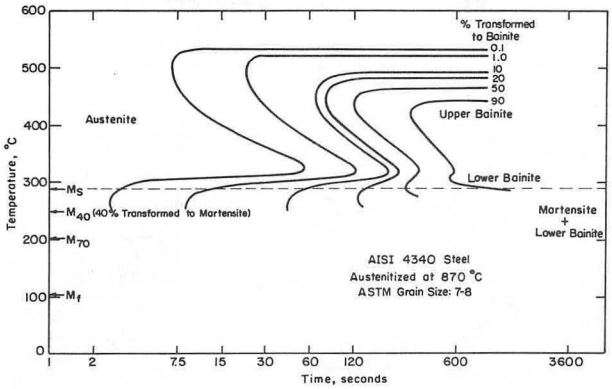

Fig. 1. The TTT curve of commercial AISI 4340 steel austenitized at 870°C.
(XBL 7311-6666)

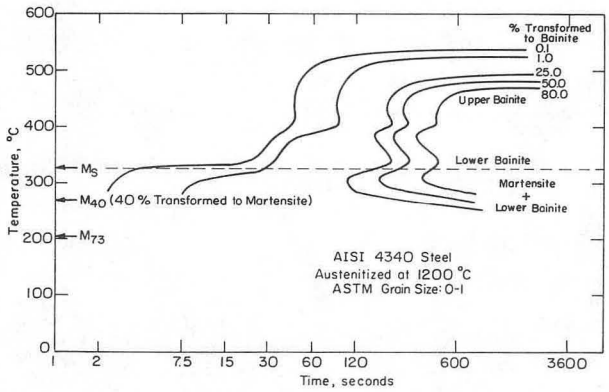

Fig. 2. The TTT curve of commercial AISI 4340 steel austenitized at 1200°C.
(XBL 741-5484)

at 1200°C is shown in Fig. 2. It was evident that in the steel austenitized at 1200°C the upper bainitic reaction was shifted to longer times without significantly affecting the lower bainitic reaction. Also evident were separate C curves for the two variants of bainite. The M_s temperature was raised by 25°C as a result of austenitizing at 1200°C.

It was believed that improvements in bainitic hardenability, similar to those achieved by the use of high austenitizing temperatures, could also be achieved by alloying additions. An objective of the present study was to determine quantitatively the relative influences of the common alloying elements such as Ni, Cr, Mn, Mo, and Si on bainitic hardenability. The composition of commercial AISI 4340 steel was chosen as the base composition. Systematic variations in composition were achieved by appropriate alloying additions, and the influence of these systematic additions was examined by experimentally determining the TTT curves for the several steels.

The results indicated that the alloying elements Ni, Cr, Mn, Mo, and Si improved the bainitic hardenability by moving the bainite C-curve to longer times. In general, for the same total alloying addition, the addition of two elements was more effective than the addition of a single element. This is illustrated in Fig. 3. where the TTT curves of two steels with compositions AISI 4340 + 2%Ni and AISI 4340 + 1%Ni + 1%Cr are compared. In addition, the results of this study showed that the combined addition of Cr and Mo was more effective in increasing the bainitic hardenability than the combined addition of Ni and Mo.

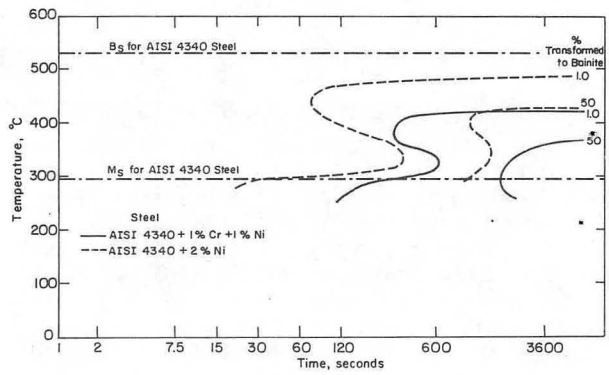

Fig. 3. The TTT curves of steels with compositions AISI 4340 + 1%Ni + 1%Cr (solid curves) and AISI 4340 + 2%Ni (broken curves). Both steels were austenitized at 900°C. (XBL 741-5485)

The addition of alloying elements Ni, Cr, Mn, Mo, and Si also lowered the B_s (the temperature above which no bainite forms on isothermal holding) and the B_f (the temperature below which fully bainitic structures are obtained). The B_s temperature of AISI 4340 was lowered by 25°C per wt.% addition of either Ni or Mn, by 55°C per wt.% addition of Cr, and by 100°C per wt.% addition of Mo. In combined additions, the effect of alloying elements in lowering the B_s temperature was nearly cumulative.

In the non-silicon modified 4340 steels, after the transformation within the B_s-B_f range, all or most of the remaining austenite transformed when the steel was

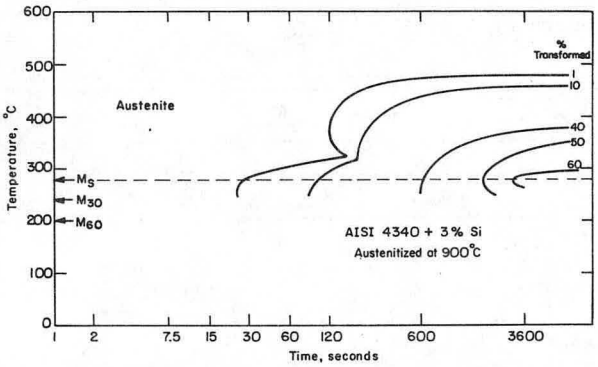

Fig. 4. TTT curves of AISI 4340 steel modified by addition of 3% Si.
(XBL 741-5486)

cooled to room temperature. However, in Si modified 4340 steels, the untransformed austenite was retained at room temperature. The TTT diagram for 3%Si modified 4340 is shown in Fig. 4. In this steel as much as 40% austenite was retained as part of the bainitic structure. The mechanical properties of steel with the above microstructure have not been studied. There is reason to believe that the retained austenite may enhance toughness by blunting cracks.

---

1. Isothermal Transformation Diagrams, United States Steel, 1963.

7. AN ISOTHERMAL STUDY OF BAINITIC AND MARTENSITIC TRANSFORMATIONS IN SOME LOW ALLOY STEELS

Clyde E. Ericsson

Some low alloy steels have good pearlitic hardenability without good bainitic hardenability. In these steels, significant amounts of proeutectoid ferrite, upper bainite, and lower bainite may form on quenching from the austenitizing temperature. Even small amounts of proeutectoid ferrite and upper bainite have been shown to have detrimental effects on fracture toughness, while lower bainite and tempered martensite are considered comparable to each other in their effectiveness in enhancing fracture toughness. The objective of the present investigation was to establish both the bainitic and the pearlitic hardenabilities of several commercial low alloy steels, namely, AISI 4130, AISI 4140, D6AC, and AMS 6416 (300-M). The TTT curves of these steels were determined by a rapid magnetometric (MPM) technique used in conjunction with computer-aided data processing and analysis. All steels were austenitized at 880°C prior to isothermal holding at several temperatures. In addition, the steels AISI 4130 and AMS 6416 (300-M) were also studied in the 1200°C austenitized condition.

The TTT diagram of AISI 4130 (austenitized at 880°C), as determined by the magnetometric technique, is shown in Fig. 1. It is evident that the upper and lower bainitic hardenabilities are in good agreement with those reported in the literature for the steel.[1] Similar good agreement was observed between the TTT curves determined in the present investigation and the curves reported in the literature for AISI 4140 and D6AC steels.[1,2] The TTT diagram of the present investigation for AMS 6416 (300-M) steel differed slightly from the diagram reported by other investigators[3] in two respects. First, the time for the nucleation of the bainite transformation

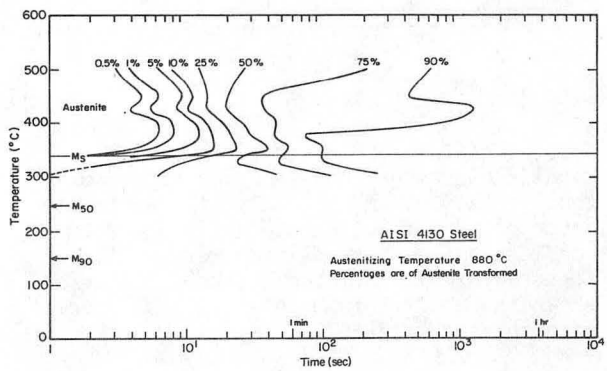

Fig. 1. The TTT diagram of AISI 4130 steel (austenitized at 880°C). (XBL 7311-6654)

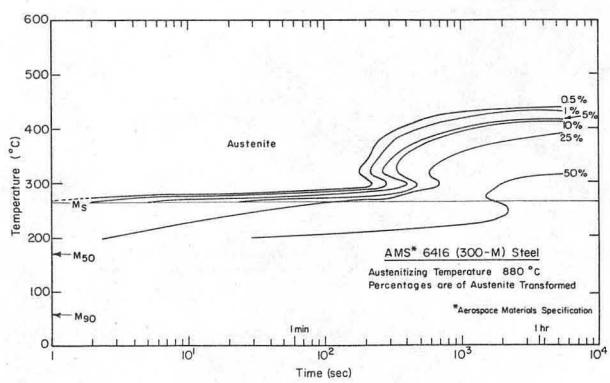

Fig. 2. The TTT diagram of AMS 6416 (300-M) steel (austenized at 880°C) (XBL 7311-6663)

Table I. Martensite range temperatures of steels.

Material	M_s		M_{50}		M_{90}	
	MPM values	Published values	MPM values	Published values	MPM values	Published values
AISI 4140						
Aust. at 880°C	295	340	200	300	90	270
D6AC						
Aust. at 880°C	290	290	170	--	50	--
AISI 4130						
Aust. at 880°C	340	360	250	320	150	300
Aust. at 1200°C	350	--	250	--	150	--
AMS 6416 (300-M)						
Aust. at 880°C	270	300	170	--	60	--
Aust. at 1200°C	290	--	190	--	60	--

(0.5% transformation) was an order of magnitude greater than the time reported in the literature, and secondly, the austenite decomposition reaction did not proceed to completion above the M_s temperature. These features are illustrated by the TTT diagram shown in Fig. 2 for AMS 6416 (300-M) steel (austenitized at 880°C).

The TTT curve of AISI 4130 steel austenitized at 1200°C is shown in Fig. 3.

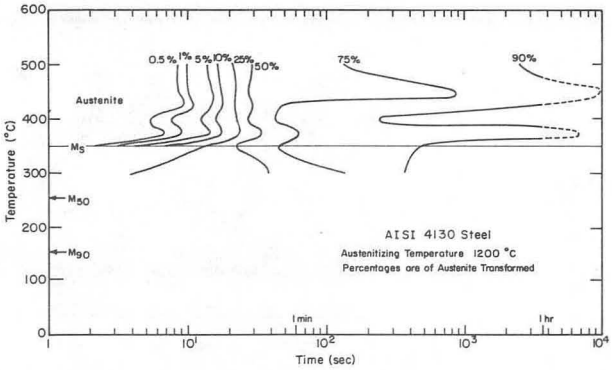

Fig. 3. The TTT diagram of AISI 4130 steel (austenitized at 1200°C). (XBL 7311-6651)

It was evident from a comparison of Figs. 1 and 3 that austenitizing at the higher temperature resulted in an increase in the time required for nucleation of upper bainite while the lower bainite transformation was virtually unaffected.

The M_s, M_{50}, and M_{90} temperatures determined in the present investigation for several steels are listed in Table I. Also listed in the table are the M_s, M_{50}, and M_{90} temperatures reported in the literature for the same steels. In general, the temperatures determined in the present study were higher than those reported in the literature.[1-3] In addition, all four steels exhibited an acceleration of austenite decomposition just above the M_s.

1. Isothermal Transformation Diagrams, United States Steel, 1963.
2. T. J. Koppenaal, Met. Trans. 1, 3371 (1970).
3. Isothermal Transformation Diagrams of Nickel Alloy Steels, International Nickel Company, Inc., 1965.

8. RESEARCH PLANS FOR CALENDAR YEAR 1974

Victor F. Zackay and Earl R. Parker

Further studies of the relationship between microstructure, fracture toughness, and fatigue crack growth of high-yield-strength steels are planned for the coming year. In particular, the effect of environment on fatigue crack growth will be investigated in several quenched and tempered steels. Also planned are additional studies on the effect of alloying elements on bainitic hardenability of low and medium alloy steels. The research on elevated temperature properties of ferritic alloys will include the effect of adding alloying elements such as tungsten to Fe-Ta-Cr alloys. Studies on optimization of microstructure and creep properties will be continued in Fe-Ta-Cr-Mo alloys.

Additional investigations of phase transformations and resulting microstructures in Fe-Ni-Ti alloys will be aimed at attaining further improvements in toughness at cryogenic temperatures. The influence of grain refining, and nickel and manganese contents on toughness will be investigated in iron-base alloys containing titanium. New projects will be initiated on using a linear elastic fracture mechanics approach to predict and prevent crack initiation in welded medium strength steels, and on the use of a magnetic technique for rapid determinations of continuous cooling curves for decomposition of austenite in steels. The theory and background of both these new projects have already been studied.

9. 1973 PUBLICATIONS AND REPORTS

Victor F. Zackay, Earl R. Parker, and Associates

Journals and books

1. E. R. Parker and V. F. Zackay, Enhancement of Fracture Toughness in High Strength Steel by Microstructural Control, Engr. Fract. Mech. 5, 147 (1973)(LBL-832).

2. R. A. McCoy and W. W. Gerberich, Hydrogen Embrittlement Studies of a TRIP Steel, Met. Trans. 4, 539 (1973)(LBL-439).

3. V. F. Zackay, E. R. Parker, and W. E. Wood, Influence of Some Microstructural Features on the Fracture Toughness of High Strength Steels, in Microstructure and Design of Alloys (Institute of Metals, London, 1973), p. 175 (LBL-1833).

4. V. F. Zackay, Enhancement of the Impact Properties of a BCC Cryogenic Alloy by Compositional and Microstructural Control, ibid., p. 591.

5. R. H. Jones, Predicting the Stress-Strain Behavior of Polycrystalline α-Iron Containing Hard Spherical Particles, Met. Trans. 4, 2799 (1973)(LBL-179 Rev.).

6. E. R. Parker, Ultra-High Strength Steels, in The Science of Materials Used in Advanced Technology, edited by E. R. Parker and U. Colombo (Wiley, New York, 1973), p. 355.

Papers presented

1. R. M. Horn, V. F. Zackay, and E. R. Parker, "Influence of Heat Treatment on the Fatigue Crack Growth Rates of a Secondary Hardening Steel," Materials Engineering Congress, Chicago, Illinois, Oct. 1973 (LBL-2239).

2. G. Y. Lai, W. E. Wood, R. A. Clark, V. F. Zackay, and E. R. Parker, "The Effect of Austenitizing Temperature on the Amount of Retained Austenite in AISI Type 4340 Steel," Materials Engineering Congress, Chicago, Illinois, Oct. 1973 (LBL-2250).

3. S. Jin, J. W. Morris, Jr., and V. F. Zackay, "Grain Refinement Through Thermal Cycling in an Fe-Ni-Ti Cryogenic Alloy," Materials Engineering Congress, Chicago, Illinois, Oct. 1973 (LBL-2539).

LBL reports

1. W. W. Gerberich and W. E. Wood, The Mechanical Nature of Stress-Corrosion Cracking in Al-Zn-Mg Alloys, LBL-418, Jan. 1973.

2. S. Jin, W. A. Horwood, J. W. Morris, Jr., and V. F. Zackay, A Simple Method for Charpy Impact Testing below 6°K, LBL-1483, March 1973 (Advances in Cryogenic Engineering, in press).

3. H. E. Adkins, Jr., Structure and Properties of TRIP Steels Processed by Deformation and Thermal Cycling, LBL-1491, April 1973.

4. W. E. Wood, E. R. Parker, and V. F. Zackay, An Investigation of Metallurgical Factors Which Affect the Fracture Toughness of Ultra High Strength Steels (D. Eng. thesis of W. E. Wood), LBL-1474, May 1973.

5. S. Jin, J. W. Morris, Jr., and V. F. Zackay, An Iron-Nickel-Titanium Alloy

with Outstanding Toughness at Cryogenic Temperature, LBL-1484 Rev., July 1973 (Advances in Cryogenic Engineering, in press).

6. Go Sasaki, Low Temperature Toughness of BCC Fe-Ni-Ti Alloys (D. Eng. thesis), LBL-1493, July 1973.

7. T. Tom, Microstructural Variables and Fracture Toughness of High Strength Mo and Mo-Ni Steels (D. Eng. thesis), LBL-1856, Sept. 1973.

8. M. D. Bhandarkar, Structure and Elevated Temperature Properties of Ferritic Alloys Strengthened by Intermetallic Compounds (D. Eng. thesis), LBL-1858, Sept. 1973.

9. E. Plaza-Meyer and M. W. Perra, Nuclear Magnetic Resonance Study of Precipitation Aluminum - 4% Copper, LBL-1883, Sept. 1973.

10. G. Y. Lai, W. E. Wood, E. R. Parker, and V. F. Zackay, Influence of Microstructural Features on Fracture Toughness of an Ultra-High Strength Steel, LBL-2236, Oct. 1973.

11. V. F. Zackay, E. R. Parker, J. W. Morris, Jr., and G. Thomas, The Application of Materials Science to the Design of Engineering Alloys, LBL-2261, Oct. 1973.

12. M. J. Yokota, G. Sasaki, W. A. Horwood, V. F. Zackay, and E. R. Parker, Developing High Impact Toughness in Fe-8 to 16%Ni-0.5%Ti Alloys at Liquid Nitrogen Temperatures, LBL-2278, Oct. 1973.

13. E. R. Parker and V. F. Zackay, Materials Science of Modern Steels, LBL-2286, Oct. 1973.

14. B. N. P. Babu, D. Ott, E. R. Parker, and V. F. Zackay, A Rapid Magnetometric Technique to Plot Isothermal Transformation Diagrams, LBL-2502, Oct. 1973.

15. W. E. Wood and W. W. Gerberich, The Mechanical Nature of Stress-Corrosion Cracking in Al-Zn-Mg Alloys: I. Evaluation of the Ductile Rupture Contribution, LBL-2229, Nov. 1973.

16. W. W. Gerberich and W. E. Wood, The Mechanical Nature of Stress-Corrosion Cracking in Al-Zn-Mg Alloys: II. Electrochemical-Mechanical Model, LBL-2230, Nov. 1973.

17. C. E. Ericsson, An Isothermal Study of Bainitic and Martensitic Transformations in Some Low Alloy Steels Using a New Magnetic Permeability Technique (M. S. thesis), LBL-2279, Dec. 1973.

18. A. Baghdasarian and S. F. Ravitz, Corrosion Resistance of TRIP Steels, LBL-2506, Dec. 1973.

F. HIGH FIELD SUPERCONDUCTIVITY

Milton R. Pickus, Principal Investigator

Introduction. In the years following 1960, when the first of the high-field superconducting compounds was discovered, progress in understanding their general phenomenology has been much more rapid than the development of appropriate materials for technological applications, most of which for this reason remain in the conceptual stage.

There are three fundamental and interrelated aspects to be considered in the development of suitable materials:

1) The intrinsic superconducting parameters of candidate compounds.

2) The need for special concepts and procedures to obtain these compounds in usable form, since all of the superior candidates are extremely brittle.

3) The fact that a usable form is one that is capable of incorporation into a conductor design that is compatible with the constraints imposed by the phenomenology of high-field superconductivity.* Perhaps the most basic of these constraints is that required to satisfy the conditions for adiabatic stability. This requirement implies a composite containing many fine superconducting filaments. The implication of additional constraints will be considered in another part of this report.

Since compounds with excellent superconducting properties are already available, it is with the latter two aspects relating to materials design and processing that this program is concerned.

*The subject of appropriate conductor design has been treated extensively by the Superconducting Applications Group of the Rutherford Laboratory (e.g., J. Phys. D: Appl. Phys., 1970, vol. 3, pp. 1517-1585).

1. PRESENT STATUS OF IMRD POWDER ROLLED SUPERCONDUCTING TAPE

Kanithi Hemachalam

A new method was devised for preventing a loss of tin during the cold rolling of a composite niobium-tin tape that met the two desired criteria of effectiveness and ease of execution. It involved carrying out the tin infiltration of the porous niobium tape under conditions that hardened the tin by a dispersion of intermediate phases of the niobium-tin system. This required simply an increase in infiltrating temperature from 650 to 850°C. Whereas at the previously used temperature of 650°C, it is thermodynamically possible to have niobium, Nb_3Sn, Nb_6Sn_5, $NbSn_2$ and tin all present in the infiltrated tape, the reaction kinetics for the short immersion times employed (~ one minute) are such that virtually none of the intermediate phases actually form. At 850°C, however, there is a marked change in reaction kinetics. Figures 1(a) and 1(b) show the corresponding microstructures. The changes in volume fraction of Nb_3Sn in tapes processed with different thermo-mechanical histories are

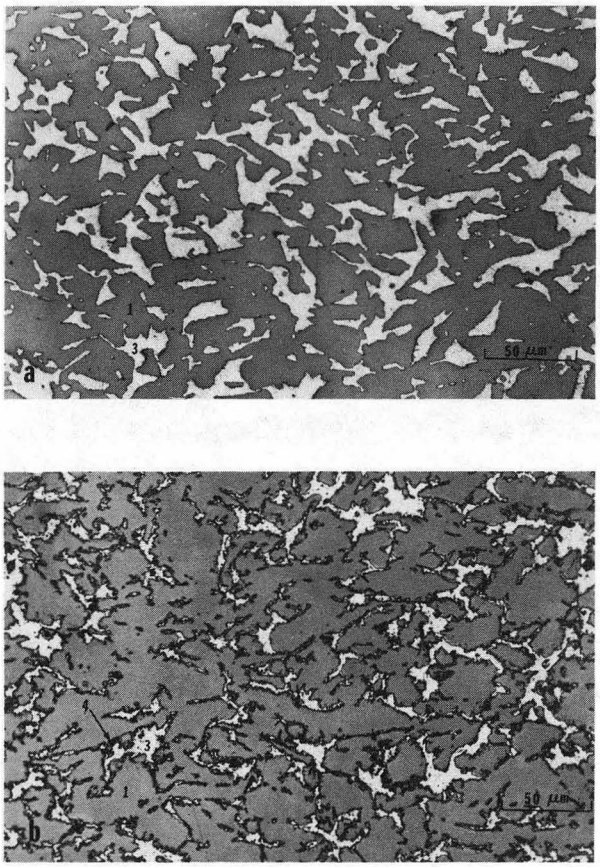

Fig. 1. Porous niobium tape infiltrated with tin. a) Infiltrated at 650°C, b) infiltrated at 850°C. Phase designations: niobium, 1; tin, 3; Nb_6Sn_5, 4. (XBB 737-4131)

shown in Fig. 2, in which (a), (b), and (c) correspond to volume fractions of 30, 40, and 50%, respectively. The current carrying capacity of these tapes at 4.2°K in pulsed magnetic fields up to 160 kG is shown in Fig. 3. The (a), (b), and (c) designations of the curves correspond with the photomicrographs of Fig. 2. Curve (d) shows the effect of doping the niobium powder with 1.5% of zirconium on a tape which contained an Nb_3Sn volume fraction of 37%. Curve (d') shows the shift in (d) corresponding to an increase in volume fraction to 50% which we are now able to achieve.

The morphological control and superconducting properties have been optimized to a sufficient degree that no further work on the powder rolled tape is presently contemplated. Rather, it will serve as a point of departure in exploring new directions.

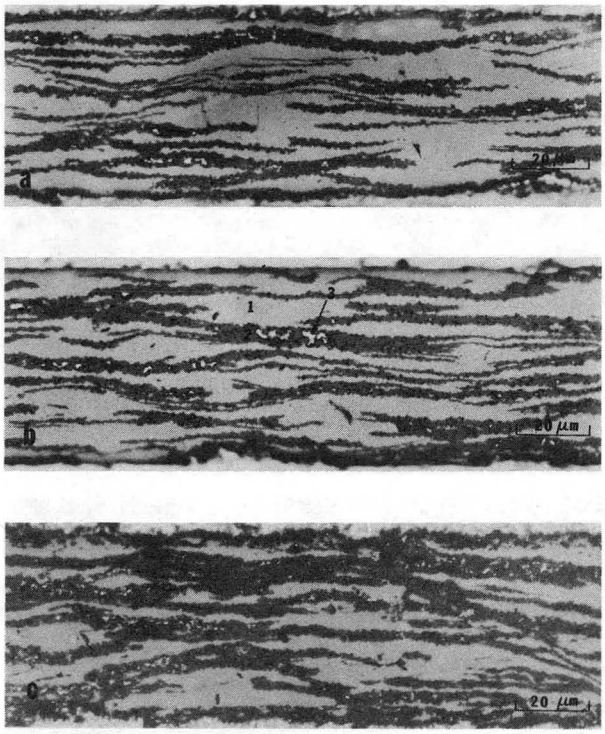

Fig. 2. Thermo-mechanically processed tape. a) Infiltrated at 650°C, rolled at room temperature, and reacted at 970°C; Nb_3Sn volume fraction is 30%. b) Infiltrated at 650°C, rolled at -72°C, and reacted at 970°C; Nb_3Sn volume fraction is 40%. c) Infiltrated at 850°C, rolled at room temperature, and reacted at 970°C; Nb_3Sn volume fraction is 50%. Phase designations: niobium, 1; Nb_3Sn, 2; unreacted tin, 3.

(XBB 737-4132)

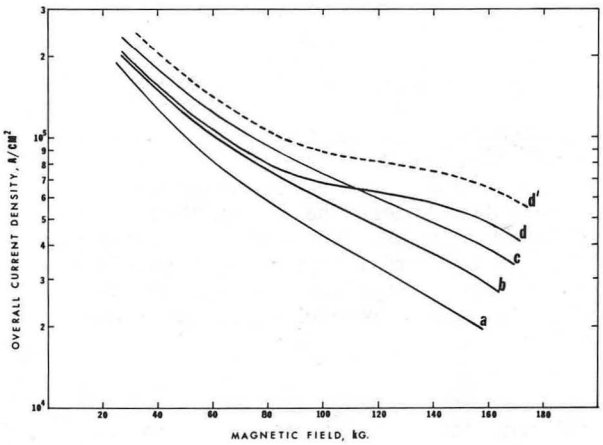

Fig. 3. Pulsed field dependence of current carrying capacity. Curves (a), (b), and (c) correspond to the photomicrographs of Fig. 2. Curve (d) shows the effect of doping with zirconium for a tape with an Nb_3Sn volume fraction of 37%; curve (d') represents curve (d) normalized to an Nb_3Sn volume fraction of 50%. (XBL 7311-6727)

2. RESEARCH PLANS FOR CALENDAR YEAR 1974

Milton R. Pickus

A critical evaluation of IMRD's superconducting tape has been made from the standpoint of the constraints imposed by the theoretically predicted and experimentally verified phenomenology of high-field superconductivity. In combination, these phenomenological constraints determine the essential features of a practical multipurpose superconductor.

The basic element should be a composite, approximately 10 mils in diameter, containing many fine (~ 5 micron diameter) superconducting filaments arrayed in a non-superconducting matrix. Several of these elements should be twisted together to form a strand. An appropriate number of these strands--to provide the required current carrying capacity--should be woven together in a fully transposed configuration.

When the extreme brittleness of the superior high-field superconducting compounds is considered in the context of these features, it becomes clear that the key requirement is the design of a material for the basic element. The design and means for producing such a material comprise the objective of the planned program.

IMRD tape has a number of desirable

features associated with its filamentary morphology. However, the deformation process employed results in an unfavorable aspect ratio between the thickness and width of the filaments. The thickness is of the correct order of magnitude, but the width corresponds to the original average pore size and is too great by a factor of approximately 4. Even this width must be considered critically: The interconnections between filaments, a characteristic deriving from the original capillary system of pores, could result in an effective width equal to the entire width of the tape.

It is planned therefore to produce the material in the form of a wire. A successful effort in this direction would retain the good features of the tape and provide a material for the basic element of a practical superconductor that could be given the form of either a round or a flat cable. Several methodologies providing axial symmetry will be investigated. Among them are pressureless sintering and isostatic compaction. Preliminary results with pressureless sintering already show promise. Additionally, a newly conceived approach will be explored.

3. 1973 PUBLICATIONS AND REPORTS

Milton R. Pickus and Associates

LBL report

1. M. R. Pickus, K. Hemachalam, and B. N. P. Babu, Superconducting Properties of a Powder Rolled Composite Tape Containing Nb_3Sn Filaments, LBL-1838 preprint. (To appear in Materials Science and Engineering, Vol. 14, No. 3, pp. 265-270.)

G. POWDER METALLURGY

Milton R. Pickus, Principal Investigator

Introduction. Powder metallurgy provides a number of advantages compared with other material-forming processes. Perhaps the one most commonly used is that based simply on economics. Contrasted with machining, for example, in the production of simple gears, powder metallurgy is advantageous in two important respects: a sharp reduction in labor and machine costs per part, and no waste corresponding to the generation of chips during machining, which can be as much as 50% of the starting material. Where optimum mechanical properties are required, however, there is a major problem due to residual porosity. Part of this program is addressed to the investigation of mechanisms for pore elimination.

Additionally there are certain unique capabilities of this process that are of particular value in materials design. Of these, two may be mentioned that are especially germane to another part of the program. One is the combining of normally incompatible components, such as metals and non-metals, while retaining the desired properties of each. The second is the ability to produce materials with a controlled porosity, which may be used directly as in the case of filters and metering devices or indirectly as a porous framework to be infiltrated with lower melting point materials, as we are doing in our work on superconducting materials and as we propose to do in our research on low-friction composites.

1. SUMMARY OF ACTIVITIES IN 1973

Milton R. Pickus, John J. Holthuis, and John A. Jacobsen

Formal research in this program commenced in October 1973 with two graduate students participating. John R. Klein has begun a basic study of the conditions required for the elimination of residual porosity, and Federico J. Reinel has started on the design of low-friction composites of the type needed in advanced technologies. In preparation for this program, substantial progress was made in the design, contruction, and acquisition of needed equipment, and in developing special procedures for evaluating powder metallurgy materials. The construction of a versatile isostatic press with a 2" diameter bore and a capacity of 130,000 psi has just been completed by IMRD personnel. Also ready is a pure, dry hydrogen sintering facility to complement our vacuum sintering capability.

Residual porosity in powder metallurgy materials complicates their metallography and density determination. Successful procedures for both have been worked out utilizing a newly constructed vacuum impregnating facility.

To provide a reference base for a study of the influence of alloying elements on the sintered microstructures of ferrous systems, the response to different modes of compaction and sintering was investigated for three different types of unalloyed iron powders: carbonyl, atomized and sponge. Additionally, to assist in a study of the iron-carbon system, diffusion couples on a macroscopic scale were prepared and studied.

2. RESEARCH PLANS FOR CALENDAR YEAR 1974

Milton R. Pickus

In regard to the basic study of the conditions required for consolidation of powders with a minimum of residual porosity, using only the two-step sequence of compaction and sintering, a selection of approaches that are consistent with contemporary theories of sintering has been made. These include liquid phase sintering and two variations of solid state sintering considered likely to impede grain growth: the presence of a dispersion of fine particles of a stable phase, or small amounts of certain solutes.

This part of the program will commence with a study of liquid phase sintering applied first to the iron-carbon system and then to other systems such as iron-boron, iron-silicon, iron-cerium, and iron-titanium. Initially, the effectiveness of various densification mechanisms will be evaluated by means of metallography and mercury porosimetry.

The second part of the program will be concerned with the development of materials that provide a special combination of properties: low coefficient of friction, stability at temperatures to and above 1200°F, and resistance to corrosion and erosion caused by the flow of hot gases. Materials with these properties are needed for improved energy conversion systems as well as many other applications. As an

example, there is an immediate need in respect to the internal combustion engine. In order to diminish air pollution by automobile emission gases, the use of lead-free gasoline has been attempted. A direct consequence was a ten- to twenty-fold increase in the wear rate of the exhaust valve seats. This causes not only malfunction of the engine, but has the contrary effect of actually increasing the amount of noxious gases released.

The knowledge and experience gained from our work on superconducting materials involving the infiltration of porous metallic frameworks will be applied to the design of materials for this type of service. Materials to be investigated include those suitable for the porous framework and stable solid lubricants to be infiltrated into the interconnected pore structure. Solid lubricants such as molybdenum disulfide have too limited a range of temperature stability. New materials must be found. Exploratory work by NASA on solid lubricants for use as surface coatings has indicated one new promising group of candidate materials that will be investigated: these are the lanthanide and alkali fluorides.

Test equipment will be developed to screen and evaluate the composites that are prepared.

3. 1973 PUBLICATIONS

Milton R. Pickus and Associates

Journal

1. Translated by J. Holthuis with assistance by L. Brewer: G. V. Samsonov and V. I. Yakovlev, The Influence of Additions of Transition Metals on the Sintering Behavior of Tungsten, Zeitschrift fur Metallkunde 62, 622-626 (1971).

2. M. R. Pickus, V. F. Zackay, E. R. Parker and J. T. Holthuis, A Powder Rolled Superconducting Composite with Controlled Morphology, International Journal of Powder Metallurgy 9, 3 (1973).

H. ADVANCED MATERIALS

Robert H. Bragg, Principal Investigator

1. K-EMISSION SPECTRA OF GLASSY CARBON--ADVANCED MATERIALS

Ram R. Saxena and Robert H. Bragg

The K-emission spectra of glassy carbon (GC) heat treated at 1000, 1800 and 2800°C were measured along with those from a (111) face of diamond and the "c" face of pyrolytic graphite (PG) using a lead octadeconate crystal (2d = 100.5 Å) as an analyzer. The results shown in Figs. 1 and 2 and summarized in Table I clearly show that the GC spectrum lies intermediate between that of diamond (sp^3 bonding) and PG (essentially sp^2 bonding) and moves toward that of PG with increasing heat treatment temperature. These results strongly support the model of GC proposed by Noda and Inagaki[1] and Kakinoki[2] that there is a mixture of sp^3 and sp^2 bonds in bulk GC. While a quantitative determination of the relative proportions of each component has not been made, the precision of these data justify the conclusion that there are significant differences between the bonding in GC and graphite.

A more accurate and detailed investigation of the emission spectrum of GC is not contemplated at this time because these K-emission data, coupled with the results reported in Ref. 3 below argue strongly in favor of diamond-like regions in GC.

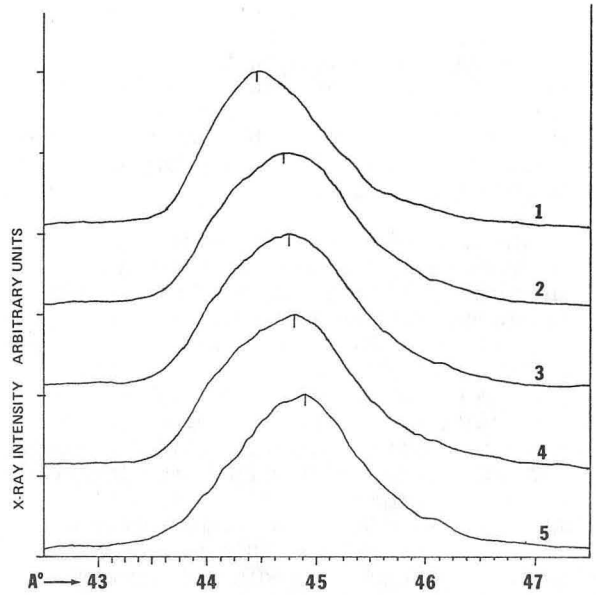

Fig. 1. Carbon K-emission band, peaks normalized.

1-Diamond

2-Glassy carbon (1000)

3-Glassy carbon (1800)

4-Glassy carbon (2800)

5-Pyrolytic graphite. (XBL 735-6196)

Table I. Comparison of K-emission band parameters for various forms of carbon.

Material	Peak position (Å)	Halfwidth (Å)	Halfwidth (eV)	Index of asymmetry	Shift in peak position from PG, Δ(eV)
PG	44.90	1.375	(8.8)	0.75	0
GC(2700)	44.80	1.5	(9.6)	0.75	0.64
GC(1800)	44.75	1.5	(9.6)	0.95	0.96
GC(1000)	44.70	1.5	(9.6)	1.00	1.28
Diamond	44.45	1.28	(8.0)	1.35	2.90
Diamond[a]	44.52	--	(8.1)	1.25	2.10

[a]Ref. 3.

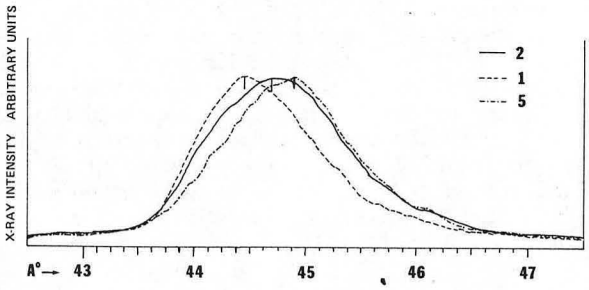

Fig. 2. Diamond, glassy carbon, and pyrolytic graphite K-emission bands superimposed on each other. (XBL 735-6211)

1. T. Noda and M. Inagaki, Bull. Chem. Soc. Japan 37, 1534 (1964).
2. J. Kakinoki, Acta Cryst. 18 578 (1963).
3. J. E. Holliday, J. Appl. Phys. 38, 4720 (1967).

2. VOID STRUCTURE OF GLASSY CARBON

Madan M. Biswal and Robert H. Bragg

Small-angle scattering measurements were made from GC heat treated at 1000, 2000, 2500, and 2800°C. At 1000°C heat treatments up to 8 hours produced no changes in void size within experimental error, but as shown in Fig. 1, changes were observed at 2000 and 2500°C. The data of D^3 versus time is linear at each temperature and indicate an activation energy of 1.9 eV. This is small compared to the activation energy for self diffusion, 7.8±0.3 eV, in graphite but close to 2.2 eV estimated from layer plane ordering. There is ample evidence that at these temperatures the close-lying lattice defects are the first to be annealed. Thus it is expected that prolonged anneals at the higher temperatures will reveal a second activation energy, i.e., a second mechanism of structural change. From what is known from work on graphitizing carbons it is expected that ultimately self-diffusion will be the dominant mechanism. There have been no direct determinations of the activation energy for self-diffusion in GC, but it should be the same as that for graphite.

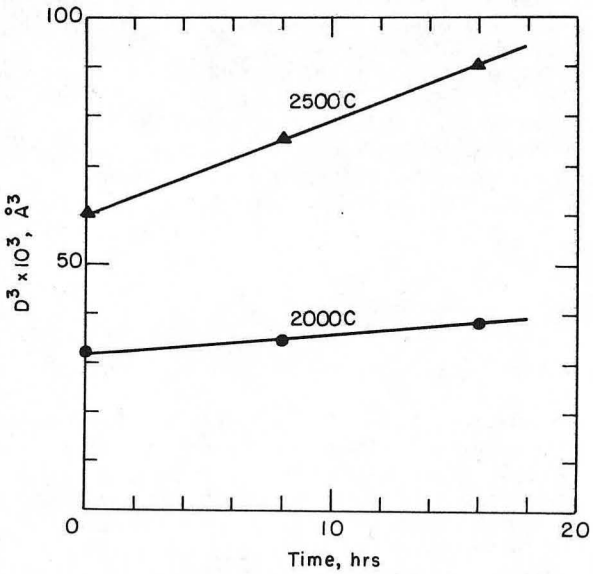

Fig. 1. Void radius versus time for glassy carbon. (XBL 741-5518)

3. CHARGE TRANSPORT IN GLASSY CARBON

Ram R. Saxena and Robert H. Bragg

Initial measurements of the conductivity of specimens of GC have been made. As shown in Fig. 1 the conductivity at low temperatures obeys a $T^{-1/4}$ law, suggesting a hopping mechanism (Fig. 2) analogous to Mott's prediction for amorphous semiconductors. At high temperatures the data follow a T^{-1} law with a band gap of 1.3 meV. From the observed crystallite widths of 120 Å and the total number of localized states, approximately one state per crystallite is indicated. The interpretation in terms of

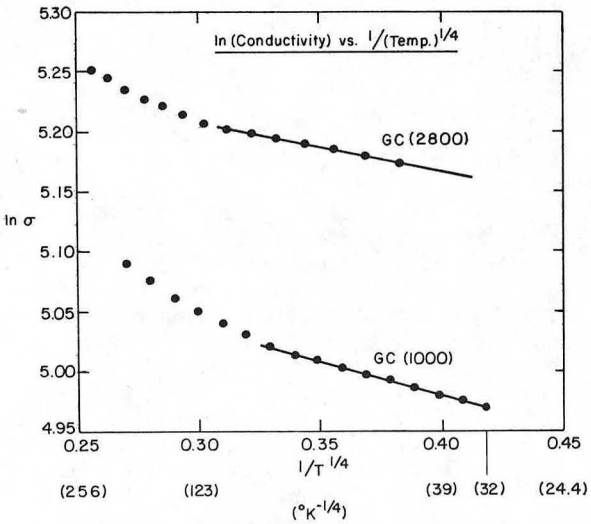

Fig. 1. Conductivity of glassy carbon showing a $T^{-1/4}$ dependence at low temperatures. (XBL 741-5519)

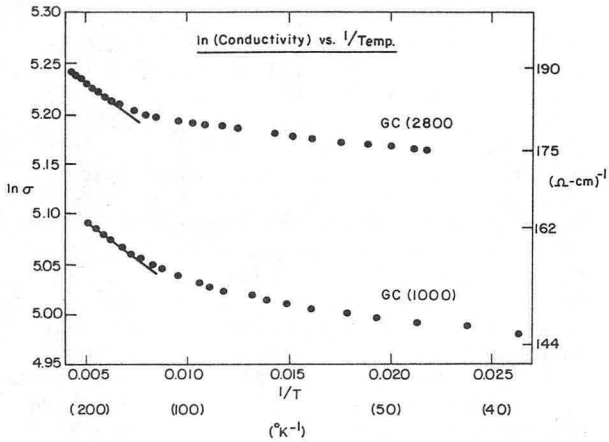

Fig. 2. Conductivity of glassy carbon showing a T^{-1} dependence at high temperatures. (XBL 741-5520)

an amorphous semiconductor at first glance seems inconsistent with the evidence from high-resolution electron micrographs that GC consists of highly interwound ribbons of graphite-like layers of carbon atoms. However, it is probable that a sufficiently large component of diamond-like bonds between the ribbons can account for the observed semiconducting behavior. Evidence for this is given in section 1.

4. ELECTRONIC PROPERTIES OF UNIDIRECTIONALLY SOLIDIFIED EUTECTICS

Louis J. Salmon, Kwaku Danso, and Robert H. Bragg

The parameter affecting the growth of large volumes of the Cu-Al_2Cu eutectic having a well aligned lamellar microstructure was studied. While the purpose of this work is to study electronic properties, for which large individual specimens are not required, it is necessary to prepare an adequate supply of standard reference material. It was found that with the furnace and crucible used, temperature gradients greater than 50°C/cm could not be obtained, much smaller than the maximum reported by Ankra in LBL-1182, in which gradients up to 206°C/cm were obtained. The difference is due either to crucible size or efficiency of chilling. Current work is concentrated on the latter, and results to date indicate a satisfactory solution will be found. Alloys of the Al-Si eutectic have been prepared from high-purity Al and Si for initial solidification experiments. While it might be expected from the phase diagram that the matrix phase (Al with Si in solid solution) would be the continuous phase, the opposite has been reported by Day.[1] Thus it is expected that the electronic properties of the grown composite will reflect the presence of interconnected rods of Si heavily doped with Al. Part of this work was the M.S. thesis of Louis J. Salmon.

---

1. M. G. Day, "The Solidification of Metals," 1S1 P110, The Iron and Steel Institute, London, 1967.

5. SMALL-ANGLE SCATTERING BY PYROLYTIC GRAPHITE

Madan M. Biswal, Faysel Hamzeh, and Robert H. Bragg

The theory derived for oriented ellipsoids of revolution was applied to data obtained earlier (UCRL-20517) from specimens cut from pyrolytic graphite (PG). They were cut in three orthogonal orientations so that any deviation from a statistically spherical void shape would be reflected in the intensity vs. angle data. A complete analysis of the data using the theory derived from oriented ellipsoids of revolution (LBL-1176) showed that a very detailed determination of void size, shape, and concentration is possible. For the particular material investigated, voids approximated oblate ellipsoids of revolution having axes 2a, 2a, 2b of 21b, 21b, and 108 Å respectively with the b axis normal to the deposition plane. The most stringent test of the theory was obtained from an absolute determination of the total void volume, which was found to be 3.1% compared to 3.5% obtained from pycnometric measurements, well within experimental error. This work has been concluded.

6. OTHER WORK IN PROGRESS

Robert H. Bragg

Some details of the reports on theoretical and experimental work on oriented ellipsoids of revolution were found to require revision and are now being prepared for publication. A search for stress relief by fine grinding of GC has produced no indication of the expected decrease in X-ray line widths for material which passes a 300 mesh sieve. This is coarse compared to the crystallite sizes

estimated from massive material, and the experiments are being extended to material ground in a vibratory ball mill which is capable of producing a sub-micron grain size.

7. RESEARCH PLANS FOR CALENDAR YEAR 1974

Robert H. Bragg

Work on the heat treatments and measurements of structure and electronic properties will continue. Since the low-temperature apparatus is now operational there are no serious experimental difficulties to be overcome in this area. There still remain the problems of obtaining kinetic data expeditiously, and also extending the upper limit of heat treatment temperatures to 3000°C. Modification in the design of the hot-zone heating element may solve the latter problem but not the former. It is expected that most of the data required for detailed analysis will be obtained in calendar year 1974. The work on the Al-$CuAl_2$ eutectic will be accelerated, and it is planned to complete a study of the dependence of conductivity on interlamellar spacing and aging at various temperatures during this year. Work on determining the growth parameters of the Al-Si eutectic will be initiated. It is expected that a Guest Scientist, Dr. Stephan Justi, who has done extensive work on the Na modified Al-Si eutectic, will join the group in March 1974.

8. 1973 PUBLICATONS AND REPORTS

Robert H. Bragg and Associates

LBL reports

1. Ram R. Saxena and Robert H. Bragg, K-Emission Spectra of Glassy Carbon, LBL-1860, July 1973.

2. Louis J. Salmon, Experimental Techniques for Growing Unidirectionally Solidified Oriented Eutectics, LBL-1834, June 1973.

3. F. M. Hamzeh and R. H. Bragg, Small Angle Scattering of X-rays from Groups of Randomly Oriented Ellipsoids of Revolution of Low Concentration, LBL-1874, Aug. 1973.

4. Madan M. Biswal, Faysel M. Hamzeh and Robert H. Bragg, Small Angle Scattering by Oriented Voids in Pyrolytic Graphite, LBL-812, Dec. 1973.

0 0 0 4 9 0 7 3 7 6

III. Ceramic Science

A. HIGH TEMPERATURE REACTIONS

Alan W. Searcy, Principal Investigator

1. THE VARIATION WITH TEMPERATURE OF THE CONGRUENT VAPORIZATION COMPOSITION OF GALLIUM SESQUISULFIDE (Ga_2S_3)

James A. Roberts, Jr., and Alan W. Searcy

In studies of congruently vaporizing solids, the fact that the composition for congruent vaporization may change with temperature is generally ignored. In most instances the composition changes are small and their neglect probably has no influence, to within experimental accuracy, on the quantities being determined, such as the heat of vaporization and total vapor pressure. However reasonable this supposition may be, it seems desirable to make an explicit test for at least a few solids of relatively narrow composition limits.

In this study such a test has been made for gallium sesquisulfide, which is known to vaporize congruently to yield $Ga_2S(g)$ + $S_2(g)$.[1] It proved possible not only to observe changes in composition for congruent vaporization but also to measure the effect of the composition variation on the partial pressure of each vapor species.

Ion intensity, time, temperature data were used to calculate the congruent vaporization composition as a function of temperature between 1050° and 1370°K (Fig. 1). The congruent composition remains fairly constant at 60.16 at.% S from 1050° to 1190°K. From 1190° to 1230°K the composition gradually changes to 60.11 at.% S. At 1230±5°K the congruent composition discontinuously jumps to 59.79 at.% S. Between 1230° and 1295°K the composition changes linearly to 59.68 at.% S, then discontinuously jumps to 57.6 at.% S. The composition changes between 1295° and 1370°K to 57.3 at.% S. The discontinuities in the congruent composition vs. temperature curves found at 1230±5°K and 1295±5°K indicate phase transitions. The 1230° transition had not previously been reported.

Intensity versus time data obtained when samples moved to new compositions after a temperature change were used to derive plots of partial pressures versus composition at several different constant temperatures for the two major species, $S_2(g)$ and $Ga_2S(g)$. A surprising result is that when the temperature is lowered to 1230°K so that the miscibility gap between phases is traversed, the $Ga_2S(g)$ partial pressure increases above

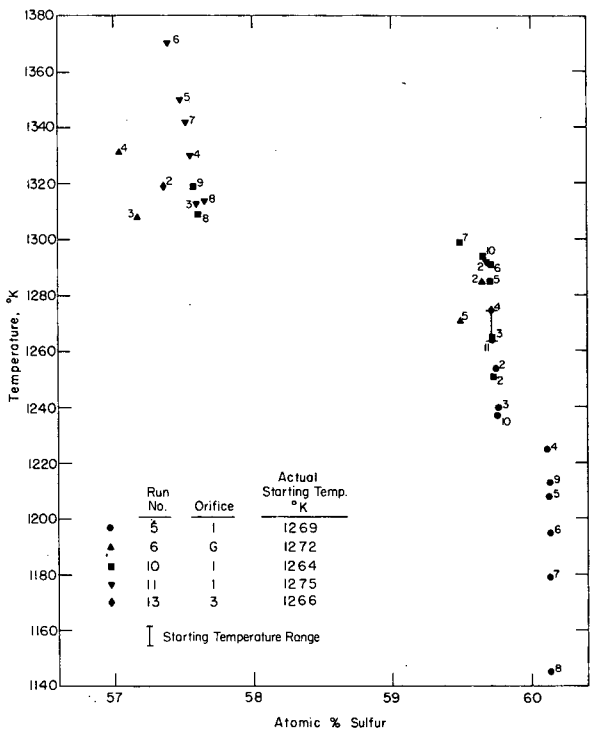

Fig. 1. Congruent vaporization composition vs. temperature for samples passing through the 1295°K transition. Run 10 is included for ease in comparing the composition scales. (XBL 7311-6701)

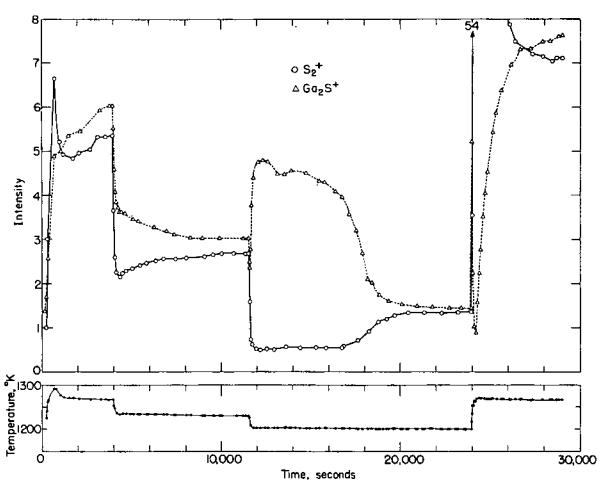

Fig. 2. Ion intensity (Ga_2S^+ and S_2^+) vs. time. The intensities are corrected only for isotopic abundance. (XBL 7311-6698)

its pressure at the higher temperature. This behavior is apparent from the original intensity versus time data (Fig. 2), so there can be no question that the effect is real. An explanation can be found by reference to schematic equilibrium free energy diagrams.

The second law heat of vaporization for the stoichiometric reaction $Ga_2S_3(S) = Ga_2S(g) + S_2(g)$ should not be significantly affected by the variations observed. For the temperature range 1286° to 1050°K, the heat of the dissociative sublimation to $Ga_2S(g)$ and $S_2(g)$ is 157.3±0.5 kcal/mol of Ga_2S_3.

---

1. O. M. Uy, D. W. Muenow, P. J. Ficalora, and J. L. Margrave, Trans. Far. Soc. 64, 2998 (1968).

2. KINETICS OF DISSOCIATIVE VAPORIZATION REACTIONS*

David J. Meschi and Alan W. Searcy

Experimental data for vaporization and condensation of crystalline solids are in good agreement with the Terrace-Ledge-Kink (TLK) model proposed by Kossel and Stranski.[1] However, most workers in this field tend to concentrate on the mechanics and dynamics of ledge formation and movement[2] and devote relatively little attention to the significance of experimentally determined apparent activation enthalpies and entropies. Comparison of the experimentally determined temperature dependence of the evaporation coefficient to that predicted by different theoretical models has not been fully exploited.

In this work, transition state theory for sequential chemical reactions is applied to the TLK model for the vaporization of solids and more specifically to compounds which vaporize according to the reaction

$$2AB = 2A(g) + B_2(g)$$

The variation of vaporization rate with temperature depends on the difference in enthalpy between the activated complex of the rate-determining step and the enthalpy of the bulk solid, and can thus be used as a guide in ascertaining which of the sequential steps is rate determining. This is illustrated with respect to the above vaporization reaction by comparing the case in which kink-pair nucleation is rate determining with that in which desorption is rate limiting.

For a temperature range in which two successive steps both are rate determining, the plot of the logarithm of an "apparent" equilibrium constant K* versus the inverse of the temperature will usually show a curvature. Experimental evidence of this effect in the vaporization of ice[3] and sodium chloride[4] is cited.

Extensive work has been done on the vaporization of II-VI compounds, and the data are consistent with a model in which a single step, probably either dissociation into the adsorption layer from thermally activated catalytic sites or desorption, is rate limiting. This is somewhat at variance with the interpretation of Hirth, Munir, and Seacrist[5] who propose a model based on surface morphologies in which two successive steps are both considered to be partly rate limiting.

---

*Accepted for publication in High Temp. Sci.

1. W. Kossel, Nach. Ges. Wiss. Göttingen 135 (1927); I. N. Stranski, Z. Physik. Chemie 136, 259 (1928).
2. J. P. Hirth and G. M. Pound, Prog. Met. Phys. 11 (1963).
3. J. G. Davy and G. A. Somorjai, J. Chem. Phys. 55, 3624 (1971).
4. C. T. Ewing and K. H. Stern, J. Phys. Chem. 77, 1442 (1973).
5. Z. A. Munir, L. S. Seacrist, and J. P. Hirth, Surface Sci. 28, 357 (1971); Z. A. Munir and J. P. Hirth, J. Appl. Phys. 41, 2697 (1970); and L. S. Seacrist and Z. A. Munir, High Temp. Sci. 3, 340 (1971).

3. THERMODYNAMICS OF DECOMPOSITION OF STRONTIUM SULFATE AND BARIUM SULFATE

Lloyd Manabu Fuke, Pirooz Mohazzabi, and Alan W. Searcy

The equilibrium dissociation pressure of strontium sulfate was measured, for the first time, by the torsion-effusion method in the temperature range 1370° to 1540°K. The total pressure for the reaction

$$SrSO_4(s) = SrO(s) + SO_2(g) + \frac{1}{2} O_2(g)$$

can be represented as

$$\log P = -(1.405\pm0.009) \times \frac{10^4}{T} + (7.167\pm0.065),$$

where the indicated errors are standard deviations from least-squares analysis. The Second Law Method yielded for the enthalpy of vaporization (ΔH_V^o) 127.4 kcal/g-atom and for the entropy of vaporization (ΔS_V^o) 58.5 eu. No dependency of vapor pressure upon the orifice area was observed.

Barium sulfate, in contrast, showed a dependence of apparent vapor pressures on orifice area. The total vapor pressure for the reaction $BaSO_4(s) = BsO(s) + SO_2(g) + 1/2\ O_2$ at 1420° to 1540°K is given by extrapolation to zero orifice area as

$$\log P = -\ (2.042 \pm 0.028) \times \frac{10^4}{T} + (9.058 \pm 0.189).$$

The second law heat and enthalpy of the reaction are 140.1 kcal and 60.2 eu.

4. MAGNETIC MOMENT OF THE Se_2 MOLECULE

David J. Meschi, Alfred Büchler, J. T. Hougen*, and Alan W. Searcy

The magnetic moment of the Se_2 molecule has previously been measured in this laboratory by means of a molecular beam technique[1] and found to be less than the one-tenth of a Bohr magneton which was taken as the detection limit for the apparatus then used. This low magnetic moment for a molecule with two unpaired electrons was attributed to a large splitting between the lower, non-paramagnetic 0^+ component of the ground state and the higher, paramagnetic 1 component. Barrow, Burton, and Callomon have since measured this splitting and found it to be 366.6 cm^{-1} (Ref. 2), which is too small to explain the low magnetic moment if Se_2 has coupling like that of O_2 and S_2.

It appears probable that the low magnetic moment is caused by a change in the type of coupling between the spin and the molecular rotation from that found in O_2 and S_2. These lighter members of the chalcogenide family in their diatomic form display Hunds case (b) coupling, but it is expected that as the molecular weight increases there will be a shift towards Hunds case (c).[3]

The sensitivity of the original apparatus has been improved by about a factor of 10, so that it appeared possible to obtain significant data even at the low coupling with the field to be expected for case (c). Calculations for Hunds case (c) have apparently not been made. Accordingly, we undertook a dual program of redetermination of the deflection of Se_2 molecules from a beam by the inhomogeneous magnetic field and of calculation of the predicted magnetic moment or its equivalent Zeeman effect for Se_2.

The method used to calculate the moment was that outlined by Hougen,[4] using as basis functions those applicable to Hund's case (a) coupling, and using Barrow's value for the splitting between states.

From the first-order terms, the following magnetic moments were derived:

$$\mu_H = \frac{2B}{\lambda}\ M_J\mu_B, \text{ for the } 0^+ \text{ state}$$

and

$$\mu_H = \frac{1}{J(J+1)}\ M_J\mu_B\ ,$$

$$\mu_H = 2\ [\frac{1}{J(J+1)} - \frac{B}{\lambda}]\ M_J\mu_B$$

for the two components of the 1 state. Here λ is the splitting constant, equal to half the splitting between the states, B is the rotational constant for Se_2, μ_B is the Bohr magneton, J is the total angular momentum quantum number, and M_J its projection in the direction of the magnetic field.

At 1000°K the modal value of J is approximately 60, and the three formulae give moments of the order of 0.01 to 0.06 Bohr magnetons for $|M_J|$ equal to J.

The second-order terms also result in appreciable magnetic moments for a field of 5000 gauss, ranging from 0.01 to 0.03 Bohr magnetons for the maximum M_J.

These moments appear marginally large enough to make possible meaningful experiments with the improved apparatus. But the low signal-to-noise ratio has necessitated a large number of measurements, so the data can be treated statistically. We are at present working out a method of using a computer to analyze the data in order either to extract a value for the mean magnetic moment or place a better upper limit on that value. This analysis should be complete within the next few months.

---

*National Bureau of Standards.

1. D. J. Meschi and A. W. Searcy, J. Chem. Phys. 51, 5134 (1969).
2. R. F. Barrow, W. G. Burton, and J. H. Calloman, Trans. Faraday Soc. 66, 2685 (1970).
3. R. F. Barrow, G. G. Chandler, and C. B. Meyer, Phil. Trans. Roy. Soc. (London) A260, 395 (1966).

4. J. T. Hougen, The Calculation of Rotational Energy Levels and Rotational Line Intensities in Diatomic Molecules, N.B.S. Monograph 115 (National Bureau of Standards, Washington, D. C., 1970).

5. THE KINETICS OF DECOMPOSITION OF BARIUM CARBONATE

Tushar Basu and Alan W. Searcy

The equilibrium vapor pressure of barium carbonate and the vacuum decomposition kinetics of the (001) face of its single crystal were studied by use of torsion-effusion and torsion-Langmuir techniques respectively. The equilibrium pressures showed a strong dependence on effusion orifice area. The apparent activation enthalpy of decomposition for the reaction

$$BaCO_{3(s)} = BaO_{(s)} + CO_{2(g)}$$

was found to be 54.0 kcal, which is less than the enthalpy of the equilibrium reaction, 60.25 kcal. The apparent entropy for the reaction was 12.8 eu. This entropy is also less than the entropy of the equilibrium reaction, 35.05 eu, in the temperature range studied.

The rate of the free surface decomposition reaction was constant, within the experimental scatter in the data, during the period of the measurements so the effusion of product gases through the porous product layer is not rate limiting. The ratio of the free surface decomposition pressure to the equilibrium decomposition pressure decreased in the temperature range of study from 1.9×10^{-4} at 1200°K to 2.4×10^{-4} at 1100°K.

These results constitute the third measurement made of the ratio of the pressure of vapor in a free surface decomposition reaction to the equilibrium decomposition pressure. The rate of dissociation of one of the three substances ($CaCO_3$) increases more rapidly with temperature than does the equilibrium dissociation pressure, the rate of dissociation of $BaSO_4$ increases with temperature in direct proportion to the equilibrium pressure, and the rate of dissociation of $BaCO_3$ increases more slowly with temperature than does the equilibrium pressure. These three substances thus illustrate the same three systematically different classes of kinetic behavior that were identified for congruent vaporization reactions.[1] The barium carbonate study is of particular interest in that it appears to be the first to demonstrate that the rate of a decomposition reaction may have a lower temperature dependence than does the equilibrium vapor pressure.

1. Alan W. Searcy in Chemical and Mechanical Behavior of Inorganic Materials, ed. A. W. Searcy, D. V. Ragone, and U. Colombo (Wiley-Interscience, New York, 1970) Chap. 6.

6. RESEARCH PLANS FOR CALENDAR YEAR 1974

Alan W. Searcy

Theoretical studies of the thermodynamics of solutions and of surfaces and interfaces will be continued.

We expect to attempt for a second solid, probably In_2S_3, a mass spectrometer study of the variation in composition for congruent vaporization and of the variation in partial pressures with small changes in composition of the kind completed in the 1973 fiscal year with Ga_2S_3. Studies of this type provide data on the variation of partial molar thermodynamic quantities in highly non-ideal solutions of kinds that have been little investigated and, in consequence, may provide useful tests of solution theories.

We will complete for publication a theoretical paper that extends transition state theory for vaporization kinetics to endothermic decomposition reactions. The paper will predict the kinetics of decomposition reactions both when equilibrium is maintained at the interface between the reactant and solid reaction product and when equilibrium is not maintained at the solid-solid interface. It also will predict the influence of a porous product layer on the reaction kinetics. Theoretical work on the kinetics of vaporization and decomposition reactions will be continued with probable major emphasis on the role of surface diffusion.

Paramagnetism of transition metal ions in condensed phases has been extensively studied, but little or no direct information on paramagnetism in gas molecules has been available. Preliminary deflection experiments with an inhomogeneous magnetic field acting on a beam of FeF_2 gas show an appreciable magnetic moment, consistent with Hunds coupling case (b). Similar measurements

will be made for NiF_2 gas with an improved apparatus, and additional measurements are planned for FeF_2 and CoF_2 in order to ascertain trends in paramagnetism with d oribital occupancy.

To clarify the role of porous product layers as effusion barriers in decomposition reactions, a mass spectrometer study of the effect of porous lids on the apparent partial pressures of sodium chloride monomers and dimers has been initiated. A particular porous alumina lid passes a beam in which the dimer/monomer ratio is reduced about a factor of 100 below the ratio for the saturated vapor. The porous-lid technique will be tested as a method to replace the cumbersome double-oven technique for determining mass spectrometer fragmentation patterns and will then be used to study effusion and surface diffusion transport of high-temperature vapors through porous bodies.

We hope to resume at the University of Genova, in collaboration with Dario Beruto of that institution, a study of the influence of carbon dioxide pressures on the rate of calcite decomposition. The study should yield both the activation enthalpy for the decomposition reaction to the metastable oxide and the enthalpy of formation of that oxide from stable calcium oxide.

We shall be involved through a consortium agreement in two research projects funded by NASA at NASA-Ames Research Center:

(1) Gases evolved during the pyrolysis and burning of fabrics designed for use in aircraft, such as Durette, a chlorinated aromatic polyamide, have been shown to be toxic. The gas mixtures will be analyzed by gas chromatography and mass spectrometry with the ultimate purpose of identifying the toxic component.

(2) Certain dry chemicals such as sodium bicarbonate act as flame extinguishants. Flames containing amounts of dry chemical just below the extinction dosage will be sampled by means of a time-of-flight mass spectrometer. It is hoped the data obtained will help to establish the mechanism of flame extinction by dry chemicals.

We will attempt to identify a substance which is available as single crystals and which decomposes to a porous solid product and two or more gas species each of which is at pressures that can be measured with a mass spectrometer. A study of the kinetics of decomposition of such a substance would complement our study of vaporization through porous lids and provide a new kind of experimental information bearing on the influence of porous product layers on the kinetics of decomposition reactions.

7. 1973 PUBLICATIONS AND REPORTS

Alan W. Searcy and Associates

Journals

*1. Z. A. Munir, D. J. Meschi, and G. M. Pound,† The Partial Pressures of Hg gas and Se_m gases in Equilibrium with Crystalline Mercury Selenide, J. Crystal Growth 15, 263 (1972) (not previously listed).

2. H. B. Skinner and A. W. Searcy, Mass Spectrometric Studies of Gaseous Oxides of Rhenium, J. Phys. Chem. 77, 1578 (1973) (LBL-1139).

3. D. H. Feather and A. Büchler, Gaseous Thallium (I) Metaborate and Thallium (I) Aluminum Fluoride, J. Phys. Chem. 77, 1599 (1973) (LBL-1482).

4. R. T. Coyle and A. W. Searcy, The Anomalous Vaporization Behavior of Magnesium Nitride, High Temp. Sci. 5, 335 (1973) (LBL-1498).

LBL reports

1. A. W. Searcy, A. Büchler, and D. Beruto, The Relationship Between Forward and Reverse Reaction Rates Under Non-equilibrium Conditions, LBL-1460, Jan. 1973.

2. R. T. Coyle and A. W. Searcy, The Anomalous Vaporization Behavior of Magnesium Nitride, LBL-1498, April 1973.

3. L. M. Fuke, Vaporization Studies of Strontium Sulfate (M.S. thesis), LBL1832, June 1973.

4. D. Meschi and A. W. Searcy, The Kinetics of Dissociative Vaporization Reactions, LBL-1853, July 1973.

5. A. W. Searcy and D. Beruto, Transition State Theory for Vaporization and Condensation, LBL-2215, Nov. 1973.

*Work done with UC-Davis and General Electric.

†Stanford University

B. MICROSTRUCTURE AND MECHANICAL BEHAVIOR OF CERAMIC MATERIALS: GLASS AND CERAMIC-METAL SYSTEMS

Joseph A. Pask, Principal Investigator

A continuing overall objective of the research program is to contribute to the development of a fundamental understanding of the factors involved in obtaining ceramic materials with controlled character (which includes microstructure), and of the relationship of character to mechanical behavior at room and high temperatures. This objective involves studies on the kinetics and mechanisms of solid state reactions and distribution of phases which in general play a part in the development of microstructure. It also involves studies on the mechanisms responsible for the mechanical behavior of single crystals, and on the application of such knowledge to the understanding of the behavior of polycrystalline ceramic materials.

The compositions under study--mullite, alumina, forsterite, spinel, magnesia--are basic materials of industrial ceramics and refractories, and sintering is the basic method for their manufacture. The fundamental approach in these studies in terms of physical chemistry, solid state chemistry, and dislocation theory also makes the work relevant in that the determined principles should be applicable to other polycrystalline metal and ceramic materials.

A second objective of this program is concerned with structural, thermodynamic, and electrochemical studies of glass-metal and ceramic-metal systems. It involves studies related to wetting, bonding, and the nature of the interfaces between dissimilar phases; to the thermodynamics and kinetics of chemical reactions at such interfaces; and to the kinetics and mechanisms of dissolution and diffusion in glasses. A basic understanding of the nature of interfaces and the mechanisms of reactions at interfaces is critical in all materials.

1. DIFFUSION AND PHASE RELATIONSHIP STUDIES IN THE SILICA-ALUMINA SYSTEM*

İlhan A. Aksay† and Joseph A. Pask

Sapphire-fused silica diffusion couples, which were annealed in the temperature range of 1678 to 2003°C and analyzed by electron beam microprobe, provided data on the stable phase equilibria of the SiO_2-Al_2O_3 system. Under stable equilibrium conditions, the intermediate compound of this system, mullite ($3Al_2O_3 \cdot 2SiO_2$) melts incongruently at 1828±10°C, and its solid solution field extends from 70.5 to 74.0 wt% Al_2O_3. The stable phase diagram is a composite of the two binary eutectic diagrams: silica-mullite in the absence of alumina and silica-alumina in the absence of mullite. Under metastable conditions, mullite melts congruently at 1890±10°C, and its solid solution field extends to ≈ 83 wt% Al_2O_3 (See Figs. 1 and 2).

The activation energy for diffusion in the aluminum silicate melts, above the softening temperature of fused silica, decreased from 211 kcal/mol for pure silica to 42 kcal/mol at 63.1 mol% Al_2O_3. This

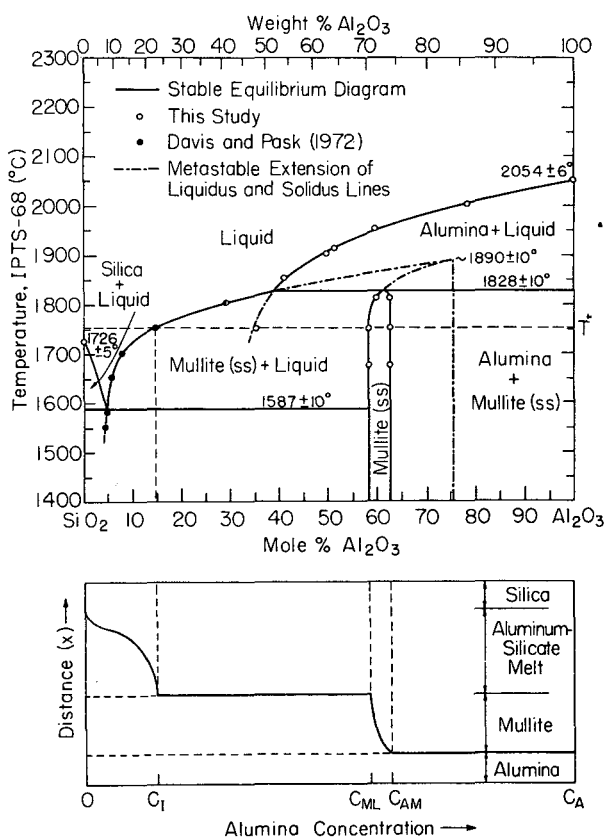

Fig. 1. The relationship between the concentration profile of a semi-infinite SiO_2-Al_2O_3 diffusion couple and the stable equilibrium phase diagram is shown at temperature T below the melting point of mullite. Metastable extensions of the silica-mullite system and the alumina liquidus are superimposed on the stable silica-alumina diagram. C_A corresponds to 100% Al_2O_3.
(XBL 736-6222)

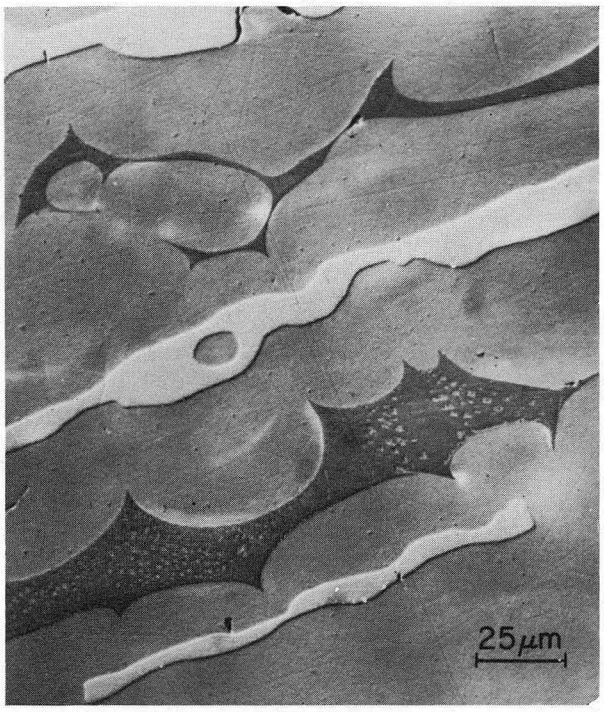

Fig. 2. Nomarski interference-contrast micrograph of a 71.8 wt% Al_2O_3 and 28.2 wt% SiO_2 mixture melted in a sealed Mo crucible at 1953°C for 460 min, cooled to 1753°C in 30 min, annealed at 1753°C for 29.4 days, and quenched from 1753°C (see Fig. 1). The light gray precipitates are alumina that are completely enveloped with a layer of mullite (gray). The glassy inclusions (dark gray) between the mullite layers also contain fine precipitates of mullite formed during cooling. It is important to note that the overall specimen composition corresponds to that of stoichiometric mullite; and the formation of alumina within a melt of this composition can only be explained by the incongruent growth of mullite. However, when the same specimen is heat treated again within the above-mentioned temperature intervals but with rapid cooling from 1953 to 1753°C, the microstructure shows no alumina precipitates and could easily be misinterpreted as being indicative of the congruency of mullite.
(XBB 7210-5188)

substantial change in activation energy for diffusion is attributed to the gradual increase in the ratio of AlO_6/AlO_4 groups with increasing alumina content and thus the formation of non-bridging oxygens. Below the softening point, the activation energy for diffusion in fused silica increases to 338 kcal/mol due to the tightening of the network structure. At 45 mol% Al_2O_3 content, the continuous network structure of fused silica is broken down to form discrete anionic groups. High activation energies in fused silica and high-silica melts are attributed to the rupture of M-O bonds of tetrahedrally coordinated silicon and aluminum. Diffusion in high alumina liquids, on the other hand, is by mutual rotation of anionic groups involving only Coulombic interaction and thus requires a lower activation energy. The structural model for the SiO_2-Al_2O_3 melts is further supported by the viscosity and density data.

An activation energy of 168±7 kcal/mol was determined for diffusion in mullite.

---

*Abstracted from LBL-1835 and partially from LBL-1403.

†Present address: Xerox Corp., Wilson Research Center, Webster, N.Y.

2. PERMEATION OF SILICATES IN MAGNESIA AND FORSTERITE COMPACTS*

Abbaraju P. Raju,† İlhan A. Aksay,‡ and Joseph A. Pask

$CaO(K_2O)$-MgO-SiO_2 liquids permeated into magnesia and forsterite compacts at elevated temperatures when continuous or "open" channels were available at the liquid-solid interface. Rearrangement of grain shapes occurred. Solid solution formation at the liquid-forsterite interface resulted in closing off the open channels. Sessile drop and permeation experiments provided information used to interpret microstructure development.

---

*Abstracted from Bull. Am. Ceram. Soc. 52 [2], 166-169 (1973).

†Present address: Bharat Electronics, Ltd., Bangalore, India.

‡Present address: Xerox Corp., Wilson Research Center, Webster, N.Y.

3. PHASE DISTRIBUTION IN SOLID-LIQUID-VAPOR SYSTEMS*

İlhan A. Aksay,† Carl E. Hoge, and Joseph A. Pask

The development of microstructure in a solid-liquid vapor system is highly dependent

on the relative interfacial tensions of the phases involved. Under chemical non-equilibrium conditions, interfaces are in a state of continual change. During this transient stage, the classical Young's and the dihedral angle equations are only valid in terms of the dynamic interfacial tension values of the chemical non-equilibrium conditions. The thermodynamics of non-equilibrium conditions in a solid-liquid-vapor system are discussed. Spreading and subsequent pull-back phenomena, which are often observed in wetting studies, are successfully explained by the dynamic interfacial tension. Such phenomena play an important role in the initial particle arrangement and solution-precipitation stages of liquid phase sintering. Sessile drop experiments and permeation studies of liquids into porous compacts provide a means in understanding the nature of phase distribution in the presence of chemical non-equilibrium conditions.

*Abstracted from LBL-2205.

†Present address: Xerox Corp., Wilson Research Center, Webster, N.Y.

4. THERMODYNAMICS OF WETTING*

İlhan A. Aksay,† Carl E. Hoge, and Joseph A. Pask

The thermodynamics of a solid-liquid-vapor system both under chemical equilibrium and non-equilibrium conditions, based on the model of Gibbs, is discussed. Under chemical equilibrium conditions, the degree of wetting or non-wetting of a flat and non-deformable solid by the liquid is defined by Young's equation in terms of the static interfacial tensions. Under chemical non-equilibrium conditions, mass transfer across an interface results in a transient decrease in the corresponding specific interfacial free energy and the interfacial tension by an amount equal to the free energy of the effective chemical reaction per area at that interface. When the reaction is between the solid and the liquid, this transient lowering of the interfacial tension can cause the liquid drop to spread on the solid substrate if the interfacial tension reduction is large enough and if the diffusion rates of the reacting components, and thus the growth rate of the reaction product, are slow enough relative to the flow rate of the liquid.

*Abstracted from LBL-1870.

†Present address: Xerox Corp., Wilson Research Center, Webster, N.Y.

5. THERMODYNAMICS OF SOLID STATE SINTERING*

Carl E. Hoge and Joseph A. Pask

A thermodynamic analysis of solid state sintering of a single phase isotropic material of uniform particle size indicates that the ratio of the solid/solid and solid/vapor interfacial energies (γ_{SS}/γ_{SV}) is critical; in order to realize theoretical density the ratio must be smaller for less dense packings of unfired compacts. Another critical requirement is that pores must remain on grain boundaries during sintering. Pores on planar grain boundaries are effectively pinned. Curved grain boundaries can break away from pores when they achieve critical curvatures; this feature is essentially independent of γ_{SS}/γ_{SV} or the corresponding dihedral angle in the normal range of values. Non-uniform particle or grain size distribution thus must be avoided since they lead to grain boundary curvatures.

*Abstracted from LBL-1495.

6. KINETICS OF INTERMEDIATE AND FINAL STAGES OF SOLID STATE SINTERING

Boon Wong and Joseph A. Pask

Adequate understanding of the sintering process of oxide ceramics is most critical in the control of their densification and microstructure development. The existing diffusion models for the later stages of sintering polycrystalline refractories have a deficiency in that they do not take into account the grain growth that normally occurs during the process.[1-3]

Recently, Skorokhod[4] has developed a viscous flow model for sintering porous viscous solids. Using this model and assumed geometries at several later stages of sintering, associated with Nabarro-Herring type creep models, kinetic equations have been derived for pressureless sintering of a polycrystalline refractory for several conditions.

Experimental sintering studies to verify

the derived relationships are in progress. MgO, and CaO doped MgO powders are being used; it is expected that CaO will prevent discontinuous grain growth. Compacts are being made by cold pressing and sintering in controlled atmospheres.

1. R. L. Coble, J. Appl. Phys. 32, 787 (1961).
2. R. L. Coble, J. Appl. Phys. 32, 793 (1961).
3. P. J. Jorgensen, J. Am. Ceram. Soc. 48, 207 (1965).
4. V. V. Skorokhod, Poroshkovaja Metallurgiya, No. 12 (72), 18-21, (Dec. 1968).

7. KINETICS AND THERMODYNAMICS OF LIQUID PHASE SINTERING

Carl E. Hoge and Joseph A. Pask

The basic driving force in sintering is the reduction in free energy associated with the decrease in interfacial area. At any instance during the sintering process, the differential of the free energy of the system, at constant temperature, pressure, and mole fraction, may be expressed as

$$\delta G_{syst_{(T,P,n_i)}} = \sum_j \gamma_j \, \delta A_j \quad , \qquad (1)$$

where

γ_j = interfacial energy of the jth interface,

δA_j = differential area of the jth interface,

j = number of interfaces.

As long as δG_{syst} is negative, sintering is thermodynamically favored. When δG_{syst} becomes equal to zero, sintering ceases, since the system has attained a minimum free energy configuration. Sintering is usually associated with densification by means of bulk diffusion, grain boundary diffusion, or viscous flow mechanisms. However, surface diffusion and vaporization-condensation, which lead to changes in surface topography but not to densification, also contribute to the sintering process.

Sintering of powder compacts is generally separated into two classifications; solid phase sintering which is characterized by solid-solid and solid-vapor interfaces, and liquid phase sintering which additionally has solid-liquid and liquid-vapor interfaces. In order to fully characterize a sintering compact, one must have a thorough knowledge of interfacial phenomena, diffusion mechanisms, capillary forces, defect-internal surface interactions, geometric factors, and reaction kinetics. Although progress has been made in specific areas, no universal sintering theory is available at the present time. The purpose of this work is to improve the understanding of liquid phase sintering phenomena by investigating thermodynamic and kinetic relationships based on specific idealized geometric models.

Generally, idealized models are formulated to simulate a sintering compact. Relationships are derived for the ideal case and then extended to real compacts. Since no one model can accurately simulate the complete sintering process, several models are needed. When one model becomes inoperative, a "stage" of sintering is said to be completed. A different model must then be applied to the succeeding stage.

Idealized two-sphere models have been formulated to describe the kinetics of various stages and configurations of liquid phase sintering systems. Using numerical integration techniques, the dependency of densification on time and particle size has been derived.

Additionally, thermodynamic analyses have been performed for liquid phase sintering of idealized three-dimensional models. Results indicate that critical ratios of

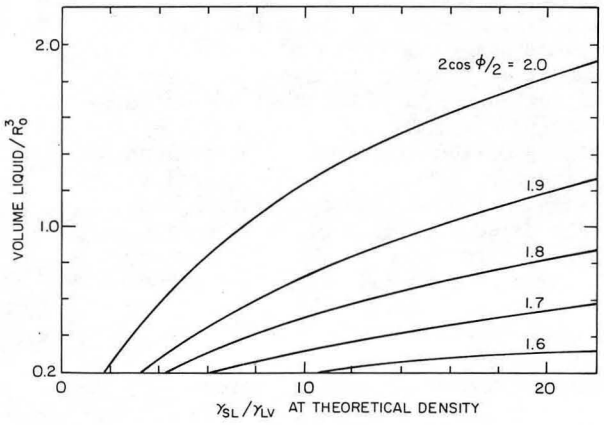

Fig. 1. Combinations of volume fraction of liquid phase and ratio of solid-liquid to liquid-vapor interfacial energies to the left of any particular curve for dihedral angle yield theoretical densities based on the sintering model; combinations which fall to the right lead to endpoint densities less than theoretical. (XBL 7310-1962)

interfacial energies exist. Above such ratios, endpoint densities less than theoretical are thermodynamically predicted as illustrated in Fig. 1. Figure 1 is a plot of volume fraction liquid phase versus the ratio of the solid-liquid and the liquid-vapor interfacial energies at several dihedral angles formed between two grains and the liquid.

Experiments are being performed to relate dihedral angles of real sintering compacts to endpoint densities in order to verify the dependency of the degree of densification on the free energy of a sintering system.

8. POLYCRYSTALLINE SPINEL FROM POWDERS PREPARED BY FREEZE DRYING TECHNIQUE

Chi-Shine Tao and Joseph A. Pask

The nature of the starting powder is extremely critical in realizing microstructures that are uniform and homogeneous on both macroscopic and microscopic scales, especially if the powder is a compound of several oxides. The powders should be of uniform submicron size and free of aggregates. The use of the freeze drying technique is a possible method of obtaining such powders. Work has continued on the preparation of stoichiometric spinel ($MgAl_2O_4$) powders by calcining freeze dried powders formed from an aqueous solution prepared from magnesium sulphate hydrate and aluminum sulphate hydrate in proper proportions.

Work was done to understand the relationship between the size and morphology of the calcined spinel powder and the freeze dried powder. The freeze dried powder forms a framework because of the loss of the large amount of water in the solution. The fineness of the framework is determined by the freezing rate of the aqueous solution as seen in Fig. 1. On calcination, the freeze dried particles break down into sizes equivalent to the web of the framework; the calcined powders are thus pseudomorphic after the framework of the freeze dried powder.

One of the difficulties, however, is that large aggregates of strong structure frequently form in the calcined spinel powder. Upon green pressing of such powders, regions of different green density are formed which result in heterogeneous sintered microstructures. Factors leading to the formation of large aggregates were identified as remelting during drying, melting upon calcination, and partial sintering during calcination. Processing studies were

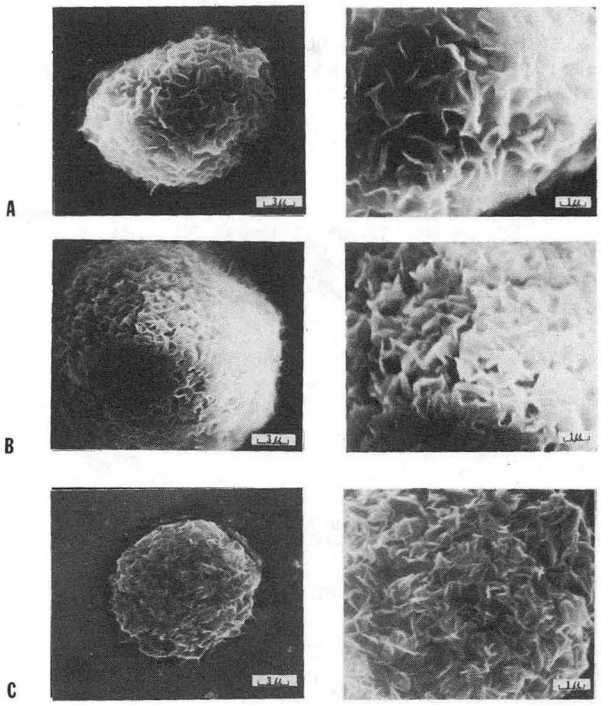

Fig. 1. SEM micrographs of three freeze dried powders at two magnifications: (A) frozen in freon-12 at -28°C, (B) frozen in hexane at -40°C, and (C) frozen in heptane at -60°C. (XBB 7310-6098)

undertaken to optimize drying and calcining conditions in order to reduce aggregation in the prepared spinel powders. Use of such powders resulted in more homogeneous sintered microstructures.

Anion impurities are a major factor that must be considered in the realization of full densification of spinel compacts. For sulfate-derived oxides, a minor residue of sulfate usually stays in the structure up to an elevated temperature. This residue, although small in quantity, will be present as entrapped gas in the final stage of sintering and prevent full densification. Thermodynamic calculations indicate that the sulfate can be reduced by hydrogen at low temperatures. Such experiments will be performed.

9. EFFECT OF FABRICATION ON POLYCRYSTALLINE MgO MICROSTRUCTURE

Truett B. Sweeting and Joseph A. Pask

The objective of this study is to determine

the effect of hot pressing and annealing environments on the character or microstructure of polycrystalline MgO. A parallel objective is to correlate the resulting microstructures with their stress-strain behavior at elevated temperatures.

A series of experimental hot pressings in vacuum with graphite dies have been made in order to analyze the types of reactions which occur during the hot pressing and annealing stages. These reactions are significant to this study since any entrapped reaction product in the bulk, or more likely, on the grain boundaries, can affect the mechanical properties of the specimen. There was evidence of reaction, as shown by the appearance of the samples. The appearance, as characterized by the color and uniformity of the normally white MgO, varied after hot pressing depending on the source of MgO powder and the nature of the forming conditions. The particular variables found to be significant were the temperature at which pressure was applied, and the final temperature reached during the run. The subsequent annealing treatment of these pieces also resulted in differences in appearance for different compacts. Further work is being done to define the exact conditions under which the reactions occur, and then to determine the actual reactions and their products.

A set of specimens for stress-strain analysis is in the process of preparation. A difficulty that has been encountered is powder agglomeration which is resulting in microstructure inhomogenieties.

10. IMPACT FRACTURE OF BRITTLE TRANSPARENT MATERIALS

William E. Snowden and Joseph A. Pask

Study of fracture initiation in brittle transparent materials subjected to transient stresses has continued. Principal objectives of the work are to determine the relation between pulse characteristics and crack growth, and to correlate observed material behavior with predictions arising from a two-dimensional finite-difference computer program HEMP. The experimental system consists of a Schlieren optics system, high-speed cameras, and a magnetic hammer system for generating pulses of varying amplitude and duration on impact.

During the past year an intensive investigation of the motion of various flyer plates, particularly flyers made of aluminum, was completed by using high speed photography. Streaking camera records were used to obtain complete time-displacement-velocity histories for each shot. Flyer planarity was examined using a high-speed framing camera. Optimum initial spacing between flyer and target was established from an examination of the records of more than 50 shots, and was found to be approximately 3 mm. At that displacement, flyer velocity was within 15% of its maximum value for each shot, and the flyer was still planar relative to its thickness across the projected area of impact.

Flyer velocities at 3 mm displacement for aluminum flyers ranged from 0.022 mm/μsec to 0.279 mm/μsec. For impacts on glass having an acoustic impedance close to that of aluminum, the corresponding range in impact pressure is approximately 2-25 kbars. Flyer velocity was found to be reproducible to within 5% for constant fire conditions, assuring reasonable reproducibility of impact pressure. In addition, projected impact times were reproducible to within 2.0 sec, facilitating synchronization of the impact event and subsequent initiation of fracture with high-speed cameras.

Significant differences between measured flyer velocities and values arising from theoretical analyses were attributed to difficulties in estimating magnetic field strength. Using oscilloscope traces of current vs. time, however, it was possible to predict flyer velocity to within 15% of the experimental values. Velocities determined in this manner are useful in providing a check on flyer velocity during fracture experiments.

An estimate of the capabilities of the magnetic hammer system was made by considering the energy available for flyer acceleration and that required to melt the flyer. A maximum pressure of ~ 55 kbars was estimated for impacts on glass.

At present, problems related to precracking thick glass plates are being investigated, and attempts to examine pulse characteristics in impacted plates using carbon gauges have been started. Computer studies to determine the limitations of one- and two-dimensional stress field approximations are also in progress.

11. CREEP OF LITHIUM FLUORIDE SINGLE CRYSTALS AT ELEVATED TEMPERATURES*

Donald R. Cropper† and Joseph A. Pask

The creep deformation of lithium fluoride

single crystals was studied in compression over the temperature range 650-750°C (0.8-0.9 T_m). Extended primary creep was observed for crystals deformed with the compression axis in ⟨100⟩ orientation; strains of 0.20 or more were required for the establishment of steady-state conditions. Crystals with compression axes in the ⟨111⟩ direction reached steady state quickly, at strains of 0.05 or less. The steady-state strain rate was found to be proportional to the stress raised to the power n, where n ranged from 3.1 for ⟨111⟩ crystals to 4.0 for ⟨100⟩ crystals. The activation energy for creep was determined to be 53±7 kcal/mol over the temperature range considered, regardless of crystal orientation or impurity content up to 300 ppm total impurities; this compares favorably with the activation energy for lattice diffusion of the fluorine ion in LiF. Well-developed substructures were observed in the deformed crystals, the subgrain diameter varying inversely with the applied stress. These results suggest that the creep deformation of lithium fluoride single crystals may be similar to that for metals and is probably dependent upon the dislocation climb process.

---

*Abstracted from Phil. Mag. 27, 1105-1124 (May 1973).

†Present address: The Head Royce Schools, 4315 Lincoln Ave., Oakland, Calif. 94602.

12. TIME-DEPENDENCE OF MECHANICAL BEHAVIOR OF MgO SINGLE CRYSTALS

Chung P. Dokko and Joseph A. Pask

An investigation has been undertaken to determine whether conventional stress-strain behavior can be correlated with creep behavior, using MgO single crystals as the test material. The specimens, both in ⟨100⟩ and ⟨111⟩ orientations, were deformed at high temperatures (±1/2 T_m) at various strain rates and crept at a number of stress levels.

Gradual yielding was observed at low strain rates, compared with sharper yielding at higher strain rates. When the 0.1% offset yield stresses are plotted against strain rates (log-log), the slope appears to be close to that of a plot of stress vs. steady state creep rate. This relationship suggests a possibility that the deformation mechanisms are the same, whether dislocation motion takes place in the annealed condition or in the presence of substructures. The yield stress, however, becomes rather insensitive to strain rates in the range where sharp yielding is exhibited. These observations were made for both orientations.

On the other hand, stress-strain curves upon instantaneous increase in the strain rate during a test showed a different response. In ⟨100⟩ crystals, there is little change in flow stress although the strain-hardening rate increases considerably. In contrast, the ⟨111⟩ crystals show a noticeable increase in flow stress, followed by rapid decay in the strain-hardening rate. It was also found that steady state creep was far more readily achieved in the latter orientation.

If it is assumed that the dislocation structure remains the same immediately prior to and immediately after the strain-rate change, then the change in strain-hardening rates should define the dynamic recovery rate that occurs during deformation. This concept is being evaluated.

The steady-state creep rate shows a stress dependence of ~4.5 and ~3 for ⟨100⟩ and ⟨111⟩ crystals, respectively. A similar result was reported by Cropper in the case of LiF (see No. 11). However, it is also possible to represent the creep rate of ⟨100⟩ by two exponents, 3 and 6, for lower and higher stress ranges, respectively. The exponent of 3, which is lower than values predicted by accepted creep theories, warrants further study.

Another means of looking at short-time (stress-strain) and long-time (creep) behavior on the same basis is the concept of internal and effective stresses which has gained much attention recently. The internal stress represents structural contribution, or the resistance to dislocation motion. Hence, the difference between applied (σ) and internal (σ_i) stress, which has been termed effective stress (σ_e) in the literature, should be independent of structure for a given strain rate. This, however, needs to be established before it is applied to both steady and non-steady state conditions for which the structures are different. This aspect is currently being examined. The different transient behavior between ⟨100⟩ and ⟨111⟩ crystals will be examined from this viewpoint.

13. INTERFACIAL REACTIONS AND WETTING BEHAVIOR OF GLASS-IRON SYSTEMS*

Carl E. Hoge, John J. Brennan† and Joseph A. Pask

The $Na_2Fe_xSi_2O_{5+x}$ and $Na_{2-2x}Fe_xSi_2O_5$ glasses reacted with substrate iron at 1000°C by evolving Na vapor according to Eq. (1):

$$Fe + Na_2O(glass) = FeO(glass) + 2Na, \quad (1)$$

when the ambient P_{Na} was low and the $\alpha(FeO)_{gl}/\alpha(Na_2O)_{gl}$ ratio at the glass-metal interface was relatively small. This reaction occurs more readily as the O/Si ratio of the glass increases. Continued reaction results in initial precipitation of SiO_2, fayalite (F_2S), or FeO, depending on the value of the O/Si ratio in the glass.

Maintenance of a low P_{Na} at the interface requires the removal of reduced Na by diffusion and by bubble nucleation when the Na vapor pressure exceeds the total ambient pressure. The time of Na migration by diffusion depends on the length of the diffusion path, i.e., the thickness of the glass, and the P_{Na} of the ambient atmosphere. A lower atmospheric P_{O_2} results in a higher metal surface energy (γ_{SV}) and a lower α(FeO) at the metal interface, both of which are favorable for reaction to occur at the interface; under these conditions the sessile drop forms smaller contact angles and may spread, resulting in thinner glass layers.

Armco iron is less reactive than Marz iron because of its higher iron oxide content. The α(FeO) at the interface thus remains high for a longer time because it takes longer for α(FeO) in the interfacial zone to equilibrate with the lower α(FeO) in the bulk glass.

Quantitative analyses of the glass-metal reactions discussed are complicated by side reactions, i.e., loss of Na_2O at the glass/vapor interface at low ambient P_{Na} and P_{O_2}, possible decomposition of FeO at low P_{O_2}, and reaction of any Fe^{3+} present with the substrate Fe.

Any reactions involving the iron substrate increase the Fe^{2+}, or FeO, content of the glass at the interface. This composition change is desirable for attaining or maintaining interfacial compositions approaching saturation with iron oxide, i.e. a high $\alpha(FeO)_{int}$, which is necessary for maximum chemical bonding at the glass/metal interface.

*Abstracted from J. Am. Ceram. Soc. 56 [2], 51-54 (1973).

†Present address: Research Laboratories, United Aircraft Corp., East Hartford, Conn. 06108.

14. EFFECT OF COMPOSITION ON GLASS-METAL INTERFACE REACTIONS AND ADHERENCE*

John J. Brennan† and Joseph A. Pask

Reduction-oxidation reactions and enhanced wetting or spreading of $Na_2Fe_xSi_2O_{5+x}$, $Na_2Co_xSi_2O_{5+x}$, and $Na_2Ni_xSi_2O_{5+x}$ glasses on substrates of Fe, Co, Ni, Ni-Fe, and Ni-Co were observed at 1000°C at low partial pressures of O_2 and Na as the O/Si ratio of the glass increased. When the substrate had a higher oxidation potential than the metal of one of the cations in the glass, e.g., CoO-containing glass on Fe, metallic precipitates formed by redox reactions under all conditions. A redox reaction based on reduction of the valence of a cation in the glass, e.g., Fe^{3+} to Fe^{2+}, also occurred. Adherence developed between substrates and glasses containing amounts of substrate oxide, either in the starting composition or formed by redox reactions, approaching saturation.

*Abstracted from J. Am. Ceram. Soc. 56, [2], 58-62 (1973).

†Present address: Research Laboratories, United Aircraft Corp., East Hartford, Conn. 06108.

15. METAL-GLASS INTERFACES

Glenn A. Holmquist and Joseph A. Pask

Studies on the mechanisms of the reactions that occur at glass-metal interfaces are continuing. Systems being investigated are platinum and gold with fused silica and silica containing small amounts of soda. Sessile drop experiments of molten gold on fused silica in air have shown the appearance of gas bubbles at the interface. The nature of the reaction mechanism is under study.

16. RESEARCH PLANS FOR CALENDAR YEAR 1974

Joseph A. Pask

a. Solid State Reactions

Studies on the silica-alumina system are continuing. Efforts to determine the existence and extent of the spinodal region will be made. Factors playing a role in the nucleation of α-Al_2O_3 and mullite on the high-Al_2O_3 side of the diagram will be investigated. The effect of additives on the solid solution range of and diffusion kinetics in mullite will also be determined.

b. Development of Microstructures

Studies of the factors that play a role in liquid phase sintering and in the development of microstructure are continuing. Experiments will be performed to relate dihedral angles of sintering compacts to degree of densification.

Theoretical equations representing intermediate and final stages of solid state sintering are being developed. Experimental supporting studies will be made using MgO powder and CaO-doped MgO powder compacts.

Freeze drying techniques are continuing to be utilized in the preparation of spinel powders for purposes of attaining polycrystalline compacts with controlled microstructure. Particular attention will be paid to the optimization of the process to prevent the formation of aggregates and to eliminate the inclusion of anion impurities.

c. Mechanical Behavior

An investigation of crack propagation in brittle transparent materials is continuing. Experiments will be made on precracked thick glass plates and transparent glass-ceramics.

Studies on the correlation of compressive stress-strain behavior with compression creep behavior are continuing. Single crystals of MgO in ⟨100⟩ and ⟨111⟩ orientations are being used at high temperatures.

The stress-strain behavior of polycrystalline MgO specimens with different characters or microstructures will be evaluated. Different fabrication techniques are being utilized in the preparation of the specimens.

d. Glass-Metal Interfaces

Effect of glass composition and experimental conditions on the mechanisms and kinetics of interfacial reactions and on wetting in gold-glass and platinum-glass systems will be studied. Studies will also be initiated on wetting and reactions in selected molten metal-ceramic systems.

17. 1973 PUBLICATIONS AND REPORTS

Joseph A. Pask and Associates

Journals and books

1. Equilibria and Kinetics in Modern Ceramic Processing, editor with S. Saito, Y. Kotera, S. Somiya, H. D. Batha, and R. Roy (U.S. - Japan Seminar Reports on the Basic Science of Ceramics, Berkeley, Calif.; Niagara Falls, N.Y.; and University Park, Penna.) 1972.

2. A. P. Raju, I. A. Aksay, and J. A. Pask, Permeation of Silicates in Magnesia and Forsterite Compacts, Am. Ceram. Soc. Bull. 52 [2], 166-169 (1973)(LBL-159 Rev.).

3. C. E. Hoge, J. J. Brennan, and J. A. Pask, Interfacial Reactions and Wetting Behavior of Glass-Iron Systems, J. Am. Ceram. Soc. 56 [2], 51-54 (1973)(LBL-480).

4. J. J. Brennan and J. A. Pask, Effect of Composition on Glass-Metal Interface Reactions and Adherence, J. Am. Ceram. Soc. 56 [2], 58-62 (1973)(LBL-481).

5. D. R. Cropper and J. A. Pask, Creep of Lithium Fluoride Single Crystals at Elevated Temperatures, Phil. Mag. 27 [5], 1105-1124 (1973)(LBL-1152).

6. T. Sugita and J. A. Pask, Changes of Preferred Orientation in Hot-Pressed Al_2O_3 during Creep, J. Am. Ceram. Soc. 56, [7], 403-404 (1973)(LBL-1147).

Invited talks and participation

1. "Glass-Metal Interfaces," Dept. of Ceramic Engineering, Ohio State University, Columbus, Ohio, Feb. 14, 1973.

2. "Glass-Metal Interfaces," Division of Ceramics, Dept. of Metallurgy, Massachusetts Institute of Technology, Cambridge, Mass., Feb. 23, 1973.

3. Chairman of Session, Symposium on

"Surfaces and Interfaces of Glass and Ceramics," at N.Y. State College at Alfred Univ., Aug. 27-29, 1973.

4. "Thermodynamics of Solid State Sintering," III, International Round Table Meeting on Sintering, Herceg Novi, Yugoslavia, Sept. 3-8, 1973.

LBL reports

1. İ. A. Aksay, Diffusion and Phase Relationship Studies in the Alumina-Silica System (Ph.D. thesis), LBL-1403, April 1973.

2. C. E. Hoge and J. A. Pask, Thermodynamics of Solid State Sintering, LBL-1495, March 1973.

3. İ. A. Aksay and J. A. Pask, The SiO_2-Al_2O_3 System: Stable and Metastable Equilibria at 1.0 atm, LBL-1835, June 1973.

4. İ. A. Aksay, C. E. Hoge, and J. A. Pask, Thermodynamics of Wetting, LBL-1870, July 1973.

5. İ. A. Aksay, C. E. Hoge, and J. A. Pask, Phase Distribution in Solid-Liquid-Vapor-Systems, LBL-2205, Aug. 1973.

C. RELATION OF MICROSTRUCTURE TO PROPERTIES IN CERAMICS

Richard M. Fulrath, Principal Investigator

Introduction. Unlike metals the mechanical, electrical, and magnetic properties of ceramic materials are essentially fixed during the process of forming dense polycrystalline shapes. The processing-property relationship is coupled through the microstructure developed in the processing techniques. For ceramics used in high-temperature structural applications the density and grain size are the primary parameters that control mechanical properties. In electrical and magnetic ceramics the density and grain size not only determine the mechanical properties but influence the electrical and magnetic properties. However, in these materials the dominant factor in developing electrical or magnetic properties is the defect structure.

Defects in ceramics can be developed through compositional control of the atomic species that make up the ceramic or by the equilibrium state developed during the high-temperature process (sintering or hot pressing) used to densify a powder compact.

This research effort is directed toward two primary areas. The first principal area involves developing a better grasp of the sintering process used to densify ceramic powder compacts. This encompasses sintering studies in materials where only crystalline solid phases are present and in systems where both liquid and crystalline solid phases coexist.

The second research area involves the processing of ferroelectric and ferromagnetic ceramics under conditions where controlled defect structures are produced. The properties of these materials are then related to the defect structure.

1. RELATION OF PROCESSING PARAMETERS TO THE PROPERTIES OF LITHIUM FERRITE*

Gautam Bandyopadhyay† and Richard M. Fulrath

Lithium ferrite spinel ($LiFe_5O_8$) has attracted considerable attention because of its square loop properties coupled with superior temperature stability. Its processing is difficult owing to the loss of lithium and oxygen during the sintering process. In this investigation, lithium ferrite and related compositions were studied to characterize the material loss behavior with heat treatment, and also to determine the influence of sintering parameters, stoichiometry, and selected dopants on the densification, microstructure, and electrical and magnetic properties of the sintered material.

a. Thermogravimetry of Spinel Ferrites

Extensive thermogravimetric work in air was done with compositions which varied widely from the excess lithia side (anion deficient) to the excess Fe_2O_3 region (cation deficient). These data are important because the material loss has a strong influence on the defect structure, which in turn influences the sinterability and most other properties of the sintered ferrite. It was noted that there was a strong tendency for the copositions to adjust themselves through weight loss (lithium or oxygen loss as the case may be), and move into the spinel single-phase region and then equilibrate with the atmospheric oxygen. The schematic representation for this compositional shift for the lithia-rich (point a) and Fe_2O_3-rich (point b) starting materials and their path of entry (shown by dotted lines with arrows) to the single-phase region is shown in Fig. 1.

The weight loss behavior of nickel ferrite and zinc ferrite compositions was also

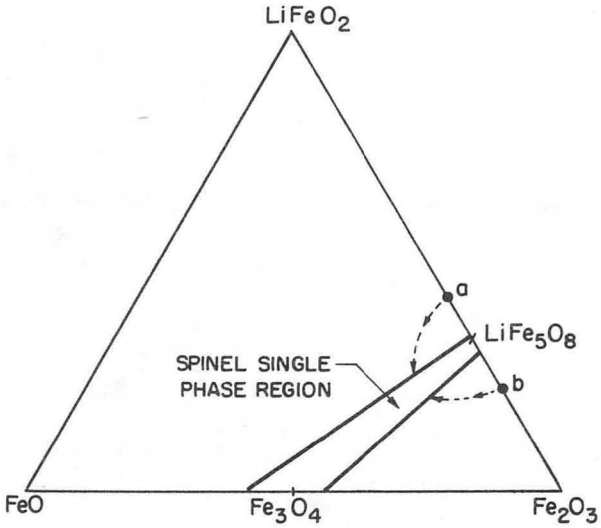

Fig. 1. Schematic representation of the path of entry of the two-phase starting compositions into the single-phase region.
(XBL 737-1594)

studied for comparison purposes. It was demonstrated that the cation-deficient inverse spinel compositions (e.g., Fe_2O_3 excess lithium ferrite or nickel ferrite) exhibit a different behavior than that exhibited by normal (zinc ferrite) or near-normal (magnesium ferrite) cation-deficient ferrites. The activation energy for the solid-oxygen equilibria in an inverse composition was found to be 32.75 kcal/mol, whereas the same for the near-normal magnesium ferrite composition was reported to be 22.8 kcal/mol.[1]

b. Lithium Ferrite--Processing and Properties

Polycrystalline compacts were sintered using a packing powder technique where the specimens were buried deep into a packing powder to control the lithium loss. A high-oxygen atmosphere was used to control the oxygen loss. The activation energy for the sintering process was found to be 143 kcal/mol. It was observed that the stoichiometry of the starting composition had a pronounced effect on most of the properties that were investigated. Anion-deficient compositions led to denser specimens with higher dc resistivity values and square B-H loops having low coercive forces. Discontinuous grain growth was favored in these compositions. Also, it was observed that the dc resistivity of these polycrystalline specimens was strongly dependent on the microstructure. It is postulated that the grain boundaries acted as the higher conducting path in these systems. The influence of the packing powder composition on the properties of sintered lithium ferrite was also investigated. The strongest influence was observed on the coercive force value.

c. Effect of Dopants

Lithium ferrite compacts doped with controlled amounts of NiO or $NiFe_2O_4$ were sintered using a stoichiometric packing powder under one atmosphere oxygen pressure. Both the dopants had only a slight effect on the densification. NiO favored discontinuous grain growth (Fig. 2), whereas $NiFe_2O_4$ suppressed it (Fig. 3). It has been postulated that NiO reacts with $LiFe_5O_8$ following the reaction

$$2NiO + LiFe_5O_8 = 2NiFe_2O_4 + LiFeO_2 ,$$

thereby forming $LiFeO_2$ in the specimen. This reaction was supported by the X-ray analysis and thermogravimetry of the reacted compositions. Experiments were also done relating dc resistivity and B-H loop parameters with the amount of dopants, and the results were discussed in terms of compositional defect and microstructure.

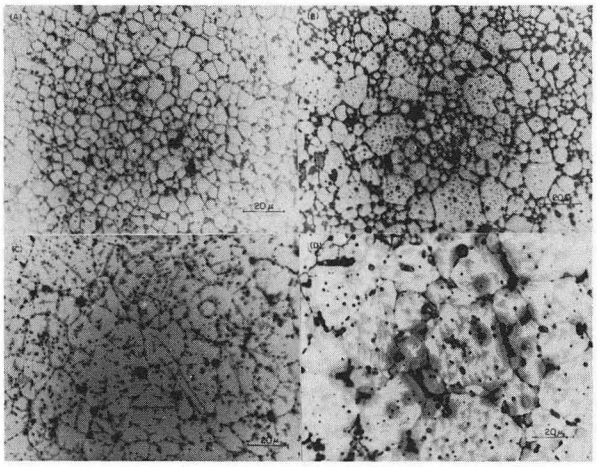

Fig. 2. Influence of NiO dopant on the microstructure of the specimens sintered at 1150°C for 2h in 1 atm O_2 and using stoichiometric packing powder. (A) 1 mol% NiO, (B) 3 mol% NiO, (C) 5 mol% NiO, (D) 10 mol% NiO. (XBB 739-5468)

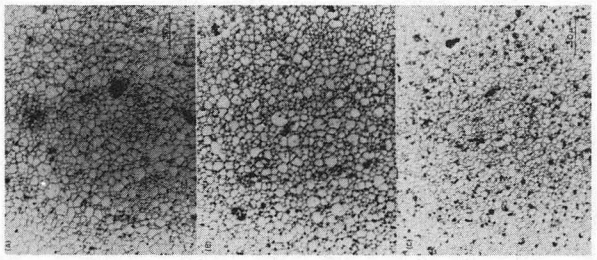

Fig. 3. Influence of $NiFe_2O_4$ dopant on the microstructure of the specimens sintered at 1150°C for 2 h in 1 atm O_2 and using stoichiometric packing powder. (A) 1 mol% $NiFe_2O_4$, (B) 10 mol% $NiFe_2O_4$, (C) 20 mol% $NiFe_2O_4$. (XBB 739-5467)

---

*Abstracted from G. Bandyopadhyay, Relation of Processing Parameters to the Properties of Lithium Ferrite (Ph.D. thesis), LBL-2263, Oct. 1973.

†Present address: Argonne National Lab., Materials Science Dept., Argonne, Ill. 60439.

1. P. Reinjnen, Reactivity of Solids, edited by G. M. Schwab ed., (Elsevier, Amsterdam, 1965), pp. 562-571.

2. A LIQUID PHASE DENSIFICATION TECHNIQUE FOR THE LEAD ZIRCONATE TITANATE SYSTEM

John W. Sherohman and Richard M. Fulrath

Because of the ferroelectric nature of the lead zirconate titanate (PZT) system, it has been utilized for many years in the fabrication of piezoelectric devices. Recently, electro-optic device applications have also been realized in the system, since lanthanum-modified lead zirconate titanate (PLZT) has the ability to behave as an electrically controlled light scatterer or retarder.

The densification of the PZT ceramics has been achieved by both hot pressing and normal sintering techniques; yet, both processing schemes require many hours at relatively high temperatures. Consequently, difficulties exist in maintaining controlled stoichiometry due to a high vapor pressure of lead oxide (PbO) in the system and obtaining densities higher than 95% in the case of unmodified PZT. Since sintering with applied pressure (hot pressing) or in the presence of a liquid phase (liquid phase sintering) can lead to enhanced densification, the purpose of this study is to employ a combination of these methods to investigate a unique liquid phase densification technique that will develop a highly dense, unmodified single phase PZT ceramic with fixed stoichiometry.

The procedure for this technique is essentially a two-step process. The first step makes use of a low-temperature liquid phase that can optimize, with the aid of applied pressure, the rearrangement process on melting of the liquid. The second step involves a subsequent heat treatment without applied pressure to allow liquid phase sintering to occur. During this heat treatment, a fixed PbO atmosphere is established that permits the liquid to be removed in a controlled manner.

The liquid phase is a lead oxyflouride ($PbO \cdot PbF_2$) that has a melting temperature of approximately 500°C. Various weight percent of the liquid phase composition is mixed with a $PZ_{.5}T_{.5}$ powder made from both a mixed oxide[1] and chemically prepared[2] preparation. The mixed material is cold pressed and placed in a stainless steel hot press die assembly as shown in Fig. 1. A stainless steel insert is used to provide movement of the zirconia sand into the free volume and give a better transfer of force to the sample. A typical comparison of displacement versus time at 600°C for the mixed oxides and chemically prepared materials is shown in Fig. 2. Original pressings were performed in both O_2 and in air and it was observed that a black coloration existed in the center of the samples. X-ray analysis of the center region indicated that metallic lead had formed. From preliminary results it is assumed that this is a pressure-induced reaction in the $PbO \cdot PbF_2$ liquid. In any case, pressing in helium gives a uniform

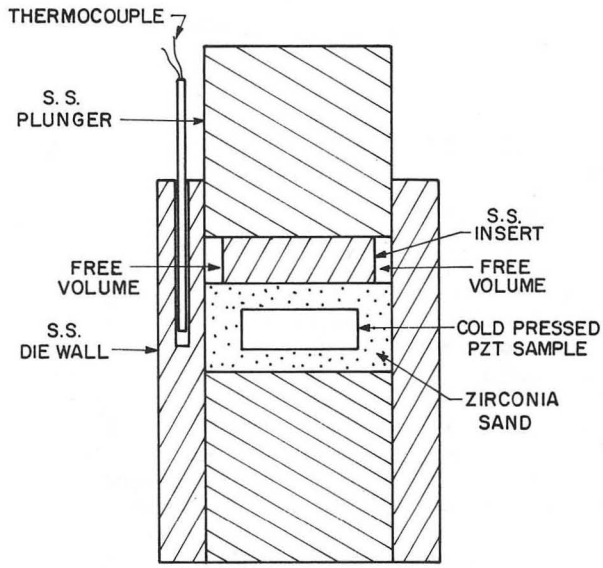

Fig. 1. Stainless steel hot press die assembly. (XBL 7310-5499)

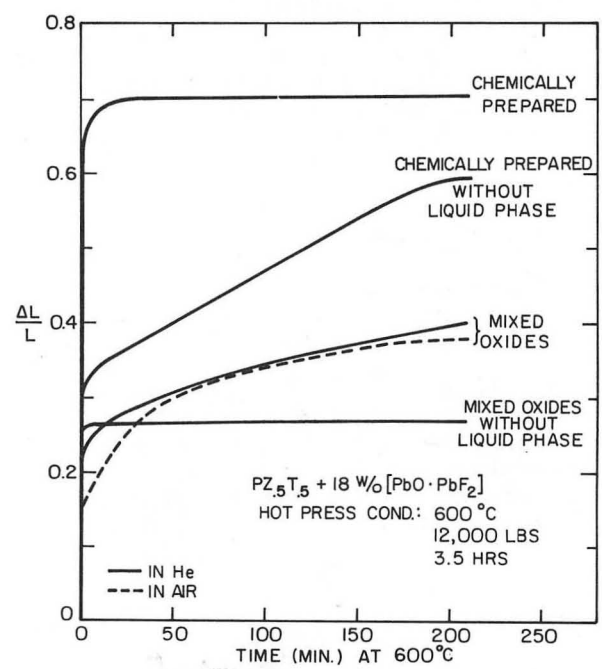

Fig. 2. Displacement versus time for $PZ_{.5}T_{.5}$ made from both a mixed oxide and chemically prepared preparation. (XBL 7310-5498)

blackness throughout the sample and also a greater displacement as shown in Fig. 2; hence, all hot pressings were performed in helium.

To determine the amount of liquid remaining after the first step in the process, the removal of the liquid phase from the pressed samples was monitored using thermogravimetric analysis (TGA). By removing the liquid quickly in an attempt to prevent liquid phase sintering from occurring, the measured density after the TGA indicated the optimum liquid content for hot pressing. Both the amount of liquid remaining and the resulting densities after TGA are shown in Fig. 3. For the chemically prepared $PZ_{.5}T_{.5}$, it is observed that a density as high as 98% is obtained for an initial 18 wt% liquid phase addition; an initial 22 wt% liquid phase gives a density of 82% for $PZ_{.5}T_{.5}$ made from mixed oxides.

The second step in the process involves removing the liquid phase in a controlled manner by a subsequent heat treatment within a fixed PbO atmosphere. A study using three different packing powder compositions was performed on the mixed oxides prepared $PZ_{.5}T_{.5}$ sample of optimum liquid content as determined in the first step of the process. The packing powder compositions were chosen to establish atmospheres of various PbO activities that would allow the sample to attempt to equilibrate by losing PbO, but still maintain the sample in its single-phase region. A "control experiment" packing powder ($PZ_{.5}T_{.5}$ + P) of the same PbO activity as that of the sample was used to prevent PbO loss but allow only the PbF_2 portion of the liquid to evaporate. The results of the study are shown in Fig. 4. It was observed that

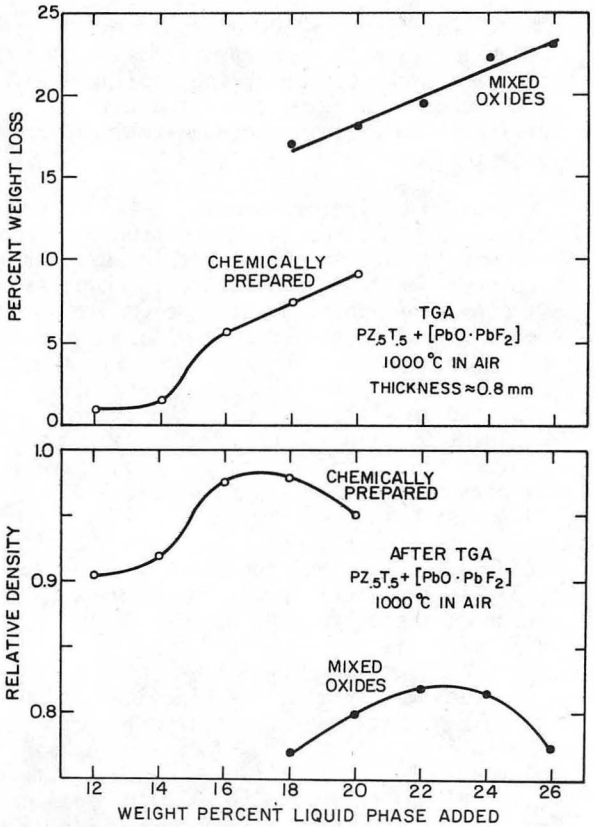

Fig. 3. Amount of liquid phase remaining in samples after hot pressing as determined by thermogravimetry, and a comparison of the resultant densities. (XBL 7310-5495)

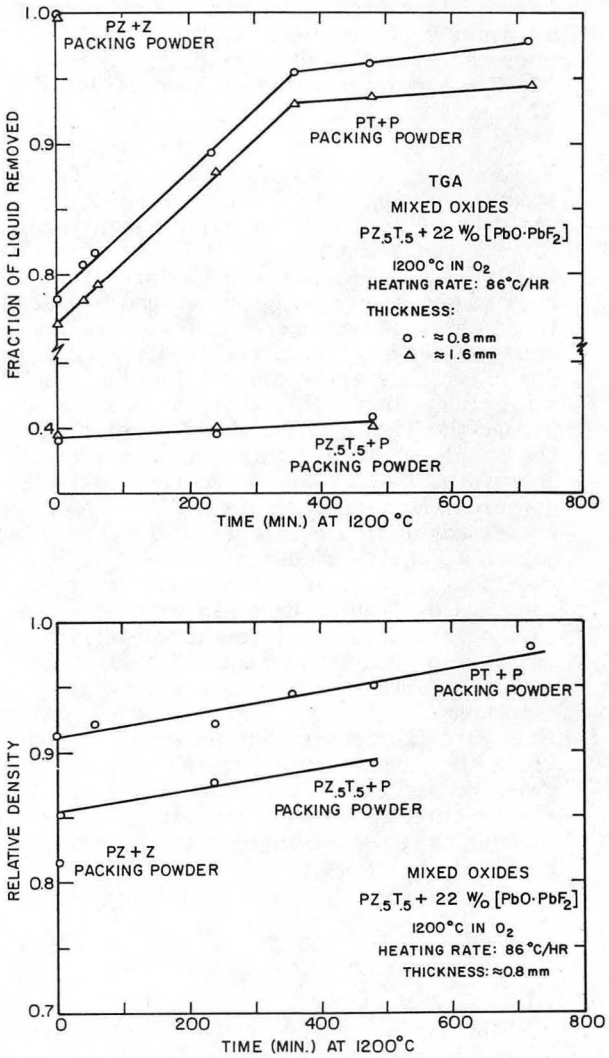

Fig. 4. Removal of the liquid phase from the sample by various packing powder compositions, and a comparison in density after liquid removal. (XBL 7310-5497)

for two samples of different thickness the rate of removal of the PbO portion of the liquid is dependent on the lead oxide activity established by the packing powder compositions. In the case of the lead zirconate plus excess zirconia (PZ + Z) where the PbO activity difference from the sample is large, all the liquid was removed before reaching temperature. Comparison of the density with that in Fig. 3 indicates very little liquid phase sintering had occurred. For the lead titanate plus excess lead oxide (PT + P) packing powder where the PbO activity difference is small, it is seen that the rate of PbO loss is thickness independent until a density of approximately 94% is reached. Above this value a closed-pore situation develops and the loss of PbO becomes thickness dependent. With respect to density, there tends to be a steady increase with the mixed oxides prepared $PZ_{.5}T_{.5}$ sample reaching as high as 98% in 12 hours.

From the information of Fig. 4, a further study involving the PZ + Z packing powder would be of interest for various heating rates: since the rate of PbO loss from the sample is dependent on the PbO activity created by the packing powder and appears to be thickness independent for densities below 94%, the large activity difference for PZ + Z may allow control liquid phase sintering. Increasing the heating rate will permit the liquid phase to be present in the sample at temperature for longer times. Therefore, a study of the density for different heating rates in a PZ + Z packing powder may indicate an optimum rate to obtain a density of 94% after removal of the liquid. In this way a high density is acquired by liquid phase sintering that is thickness independent; further densification can be achieved by a normal sintering mechanism without entering a region of thickness dependency. From the data obtained thus far, it appears that by using methods known to enhance sintering, this liquid phase densification technique for the PZT system provides an easy two-step process to develop a dense single-phase material of fixed stoichiometry.

---

1. The mixing of PbO, ZrO_2, and TiO_2 powders in the correct amounts to give $Pb(Zr_{.5}Ti_{.5})O_3$ after calcination.
2. The mixing of PbO powder and solutions of $Zr(OBu)_4$ and $Ti(OBu)_4$ in isopropyl alcohol and water to form a precipitate than can form $Pb(Zr_{.5}Ti_{.5})O_3$ upon heating.

3. LIQUID PHASE SINTERING IN SELECTED SYSTEMS

Leo Froschauer*

Liquid phase sintering of powdered compacts, i.e., sintering where part of the sample is in the liquid state, is a processing technique that is common to a variety of materials including metal systems (Fe-Cu), cermets (WC-Co), and ceramic porcelains. In many of the more refractory systems such as the carbides and borides it is only through liquid phase sintering that the desired density of a powder compact can be achieved.

The technology of liquid phase sintering is much further developed than the theoretical understanding of the process. This is essentially due to two reasons:

1) The existence of at least three phases at the sintering temperature increases the number of process parameters, especially surface energies, solubilities, and volume fraction of phases.

2) Changing surface energies and solubilities with temperature changes the texture of the sample during cooling and thus makes room temperature examination difficult to explain the high-temperature behavior.

Thus investigators nearly always determine densification rates and microstructures and attempt to explain the results by using the known properties of the system. Comparison of sintering kinetics with the results of model calculations leads to a formulation of three possible stages of densification: 1) rearrangement of the solid particles assisted by viscous flow of the liquid, 2) solution of solid material at solid-solid contact points and reprecipitation aided by diffusion in the liquid phase, and 3) densification of a rigid solid skeleton by diffusional processes in the solid. The wetting behavior and the solubility of the solid in the liquid phase should decide which of these stages should occur in different systems.

It is by comparing the kinetics with model calculations that different micro events in the sintering process have been assumed. The fast initial and often time-proportional shrinkage is usually explained as viscous flow with a rearrangement of particles even if there is no experimental evidence. With the hot stage of the scanning electron microscope there is now a tool available to observe the change of microstructure during this stage. Visual evidence

can clarify which of the assumed mechanisms are actually responsible for densification.

Three systems have been chosen for study of liquid phase sintering based on different characteristics at high temperatures.

1) A system with the solid soluble in the liquid phase and incomplete wetting of the solid by the liquid (Fe-Co).

2) A system with no solubility of the solid in the liquid and incomplete wetting of the solid by the liquid (W-Cu).

3) A system with the solid soluble in the liquid and complete wetting of the solid by the liquid (WC-Co).

Other parameters (amount of liquid phase, particle size of the components, green density) can be varied in each system. For all three systems previous investigators have assumed extensive rearrangement in the first stage of densification.

The first qualitative examination of sintering of these systems in the scanning electron microscope hot stage showed that in the WC-Co and W-Cu systems extensive rearrangement occurs when the liquid phase first appears. In the Fe-Cu system no viscous flow was observed with up to 40 volume percent liquid phase. This is probably due to the formation of a rigid Fe skeleton during the heating. The nonwetting liquid cannot penetrate the Fe-Fe contact areas and thus the skeleton exists throughout the sintering process. In the W-Cu system the diffusion of W is too slow to form a skeleton during heating. Figures 1 and 2 show samples of loose powders of iron and tungsten with 40 volume percent copper before and after melting the copper. The difference in behavior is apparent. A detailed investigation in these systems is now under way. Figure 3 shows an example of the densification of Fe combined with different liquid phase volumes. Figure 4 gives the

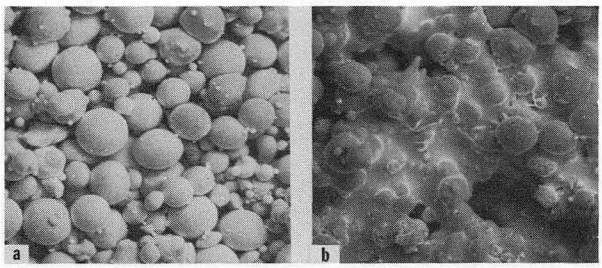

Fig. 1. The same area of view of a loose powder mixture of 60% Fe and 40% Cu before (a) and after (b) liquid phase formation. (XBB 742-811)

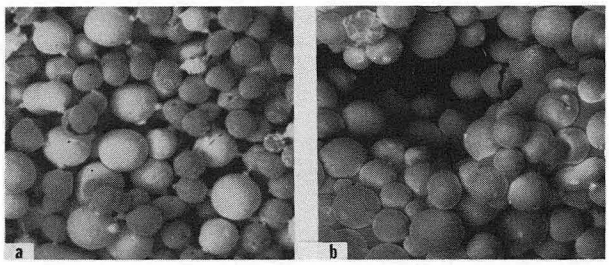

Fig. 2. The same area in a sample of 60% W and 40% Cu before (a) and after (b) liquid phase formation. (XBB 742-812)

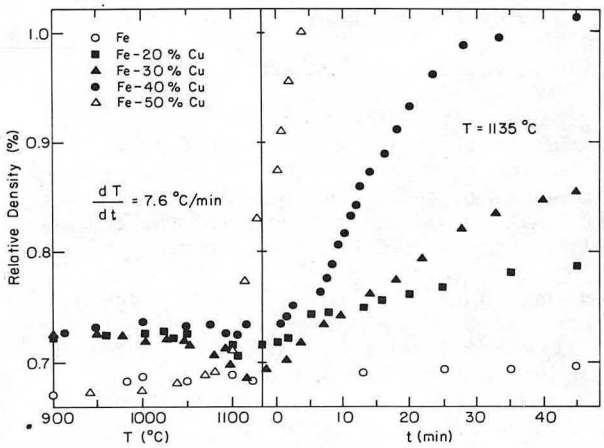

Fig. 3. Densification of Fe-Cu powder compacts with varying amounts of a Cu-rich liquid. (XBL 7312-6798)

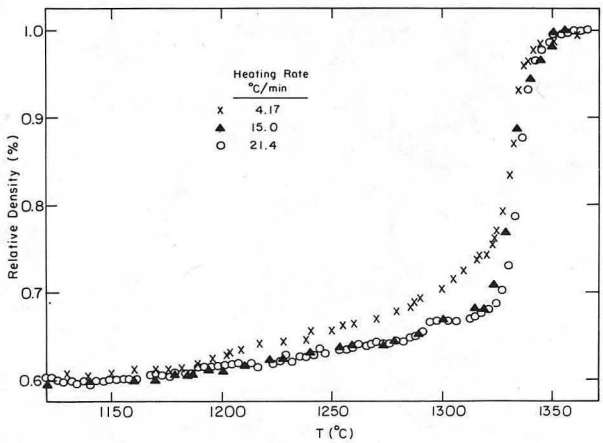

Fig. 4. Densification of WC-10% Co as a function of the heating rate of hot stage in the scanning electron microscope. (XBL 7312-6797)

densification characteristics of WC-10% Co under three different heating rates.

The importance of the scanning electron microscope hot stage facility is readily apparent in these studies.

*Dr. Froschauer is supported on a Post Doctoral Fellowship from the Deutsche Forschungsgemeinschaft.

4. SOLID STATE SINTERING STUDIES

David N. K. Wang and Richard M. Fulrath

The densification of ceramic powder compacts without the aid of liquid phases is an important processing step in the production of refractory ceramic materials. The first quantitative studies of the densification process (solid state sintering) of Al_2O_3 were started in 1972 and have been continued in 1973. The work to date has concentrated on the sintering characteristics of Al_2O_3 + 0.1 wt% MgO. Powder compacts made by cold pressing submicron Al_2O_3 particles doped with MgO and containing binders and lubricants are first heated in air to 900°C for one hour to remove the organic materials. These compacts containing 60% porosity are heated in the hot stage of the scanning electron microscope under programmed heating rates to various temperatures to determine the sintering characteristics. The linear shrinkage of the compact is determined by placing W microsphere markers on the sample's surface and recording on 16 mm film the marker's movement continuously during the sintering run. Using this technique, the sintering of Al_2O_3 has been continuously monitered from a green compact density of 40% to nearly 100% theoretical density.

Figure 1 shows the results of two sintering runs where the samples were heated at a rate of 4°C/min to isothermal temperatures of 1350 and 1385°C. After reaching the indicated temperature the temperature was held constant to observe the isothermal sintering behavior. In both cases every datum point is the average of nine individual shrinkage measurements. The statistical scatter in the measurements indicates that sample W-7 was inhomogenous in its shrinkage, with different areas of the sample densifying more than others. Overlaying a magnified picture of the final marker positions on the picture of the original positions points this out dramatically. Sample W-5 showed homogenous shrinkage with little scatter in the data.

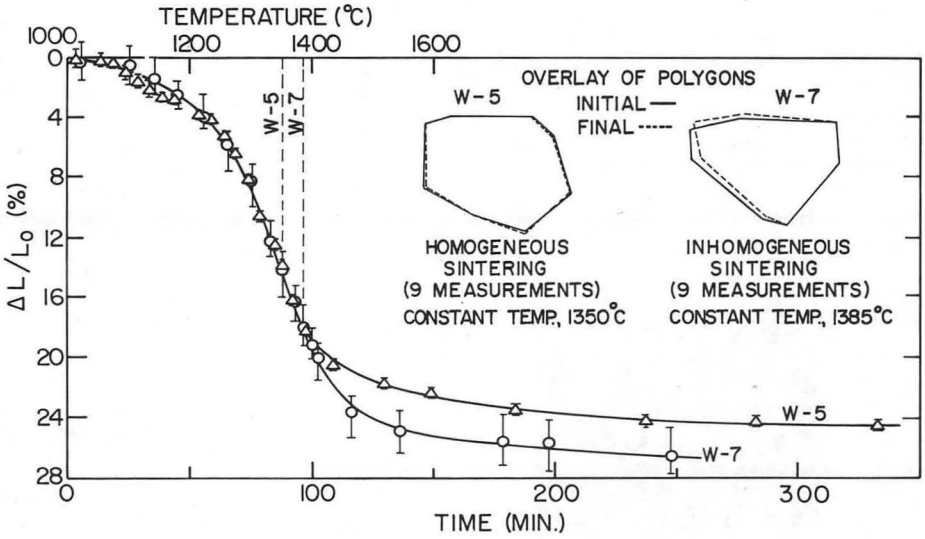

Fig. 1. Linear shrinkage of Al_2O_3 compacts heated at 4°C/min to the indicated temperature and then held at that temperature for the indicated time. (XBL 742-5585)

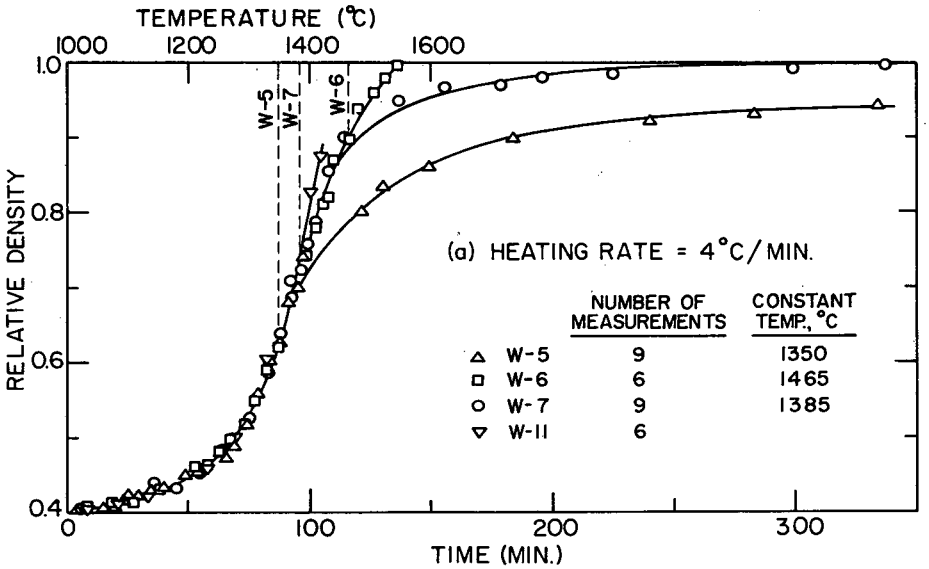

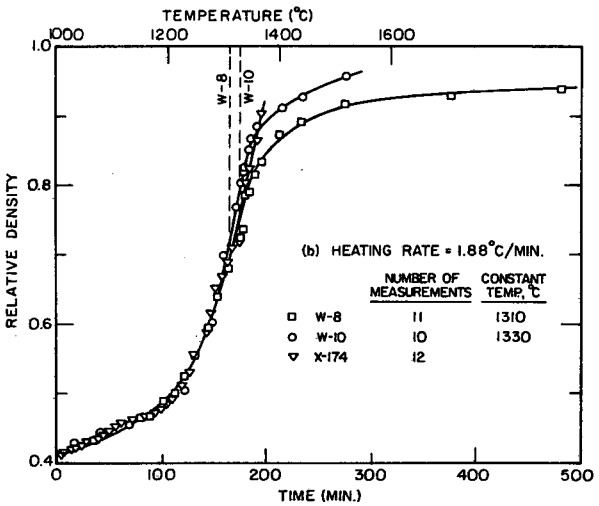

Fig. 2. The relative density changes determined from linear shrinkage data as a function of the heating rate and isothermal holding temperature.

(XBL 742-5586 & 5587)

Figure 2 shows the change in relative density as calculated from linear shrinkage data for various heating rates and isothermal temperature holds. As indicated, a higher density is obtained at a given temperature, the slower the heating rate.

Figure 3 gives the densification rates calculated from the data in Fig. 2. The most interesting observation is that no matter what the heating rate the densification rate is the same at a given temperature below approximately 1375°C, even though the actual density of the specimen may be quite different. For example, at 1330°C a sample heated 4°C/min has achieved a density of 58% TD (theoretical density) while a sample heated at 1.88°C/min at the same temperature has a density of 76% TD, and yet each have the same densification rate. This shows that the densification rate below a given critical temperature is not a function of porosity or heating rates but a function of temperature only. This observation and the exponential shape of the densification rate curve are in agreement with the Coble intermediate stage sintering model; however, these data are extended beyond the Coble model and show that on holding at an isothermal temperature below the critical temperature the densification rate decreases with time, which is not predicted by the model.

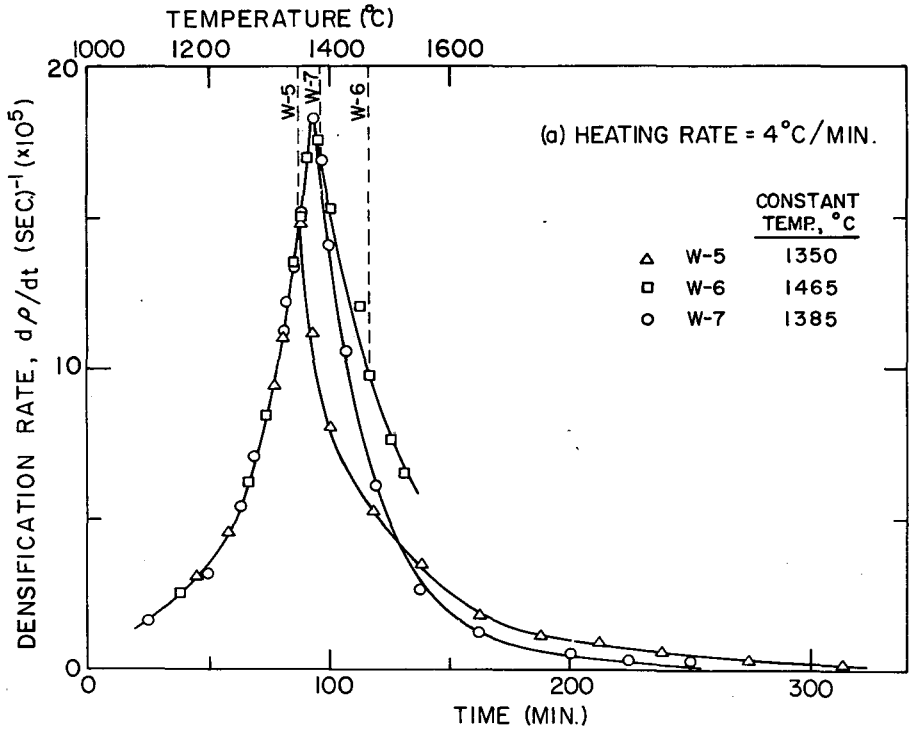

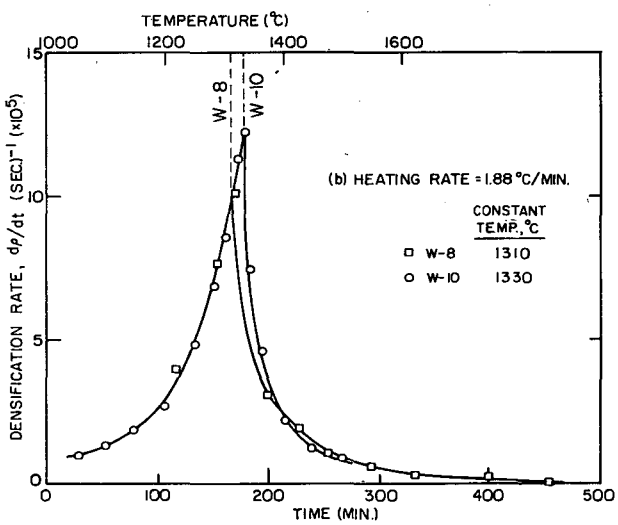

Fig. 3. Densification rate as a function of temperature and time at temperature for the data in Fig. 2. (XBL 742-5588 & 5589)

Figure 4 is a plot of the temperature-compensated densification rate against 1/T, from which an activation energy of 50.3 kcal/mol is calculated for the sintering process below the critical temperature of 1375°C. This value is close to the 57.6 kcal/mol activation energy experimentally determined for oxygen grain boundary diffusion and much lower than activation energy for sintering calculated by previous investigators.

New modifications made in the hot stage of the scanning electron microscope in 1973 have allowed its use to be extended to 1750°C.

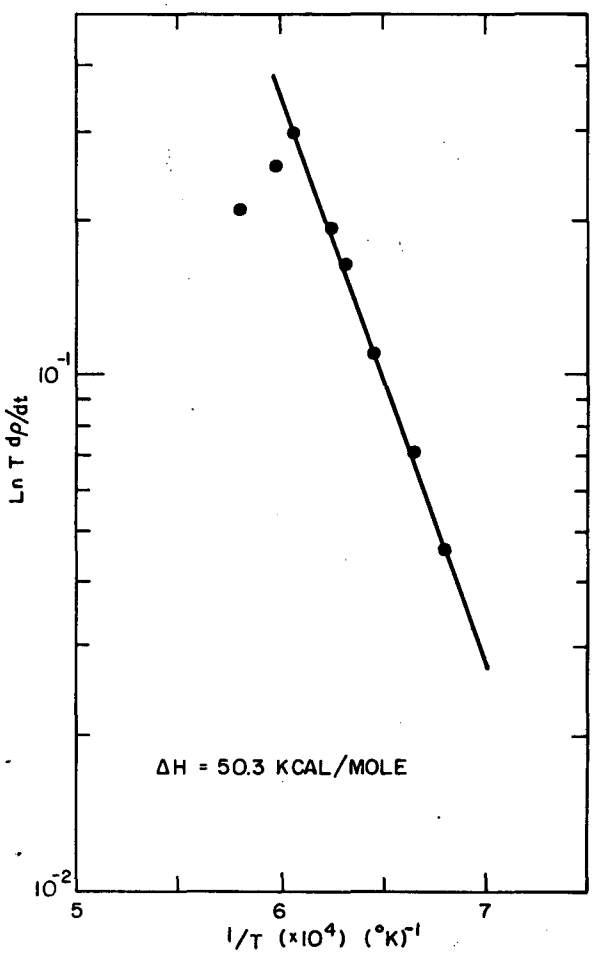

Fig. 4. Temperature-compensated densification as a function of 1/T for the sintering of submicron MgO-doped Al_2O_3. (XBL 742-5590)

5. PERMEATION OF HELIUM IN POLYCRYSTALLINE Al_2O_3

Jiunn-Jye Dih and Richard M. Fulrath

Previous work in this laboratory determined that He would permeate through 94 wt% and 99.5 wt% commercial alumina bodies at temperatures between 1000 and 1500°C in measurable quantities. The activation energy for permeation of approximately 15 kcal/mol agreed with that predicted for He permeation through a glass phase. A glass phase was identified in the lower-purity alumina, but no continuous glass phase could be identified in the higher-purity material. The question of whether He grain boundary permeation would exist in a very-high-purity Al_2O_3 and the possibility of determining more information on the nature of the grain boundary through permeation studies resulted in initiating a research effort in this area in early 1972.

The major problem in permeation studies is to form specimens with analytically determined geometries and suitable area-to-thickness ratios to allow measurable quantities of the permeating gas to flow through the specimen. During 1972 alumina shapes of the required geometry were obtained and by a hot pressing technique a few permeation specimens were fabricated. These specimens were vacuum tight to He at room temperature, but on thermal cycling they developed microcracks at alumina-alumina joins which allowed He flow. During 1973 a number of alumina-alumina joining techniques to give He-tight seals at temperatures to 1500°C were attempted without success. These processes included active metal seals, direct alumina-alumina joining by hot pressing and sintering, and an experimental high-temperature mixed oxide liquid phase join suggested by an industrial laboratory. None of these processes could produce satisfactory specimens. Therefore, in late 1973 a review of the cost and lack of success in fabricating specimens resulted in dropping this research effort.

6. RESEARCH PLANS FOR CALENDAR YEAR 1974

Richard M. Fulrath

Sintering studies both liquid phase sintering and solid state sintering will be emphasized. The systems Fe-Cu, W-Cu, and WC-Co will be used for liquid phase sintering studies, and the solid state sintering studies will concentrate on Al_2O_3 and UO_2. The primary objective of these two studies is to obtain the complete densification kinetics from the initial compact density to nearly theoretical density. These data will assist in developing a better theory to guide the sintering of powder metal products and refractories.

Studies in the defect structure and the processing parameters that control it in electronic and magnetic ceramics will be continued. Primary emphasis will be on the intrinsic and extrinsic defect structures in lead zirconate titanate and their influence on piezoelectric and ferroelectric properties. Electrical resistivity will be used to determine semiconductor characteristics and charge carriers.

Fracture in brittle matrix composites

will be investigated to determine the applicability of either the "work to fracture" or the Griffith criteria for the strengthening mechanism.

7. 1973 PUBLICATIONS AND REPORTS

Richard M. Fulrath and Associates

Journals

1. J. S. Reed and R. M. Fulrath, Characterization and Sintering Behavior of Ba and Sr Ferrites, J. Am. Ceram. Soc. 56 [4], 207 (1973)(LBL-815).

2. J. S. Masaryk and R. M. Fulrath, Characterization of the Short Time in Gaseous Diffusion Analysis, J. Am. Ceram. Soc. 56 [6], 342 (1973)(LBL-1454).

3. J. S. Masaryk and R. M. Fulrath, Diffusivity of Helium in Fused Silica, J. Chem. Phys. 59 [3], 1198 (1973)(LBL-847 Rev.).

4. R. L. Holman and R. M. Fulrath, Intrinsic Non-Stoichiometry in the Lead Zirconate-Lead Titanate System Determined by Knudsen Effusion, J. Appl. Phys. 44, (1973)(LBL-1462).

5. R. M. Fulrath, Let's Test the Model, Office of Research Services Highlights, College of Engineering, University of California, Berkeley, April 1973 (LBL-1806).

LBL reports

1. R. L. Holman and R. M. Fulrath, Solution Kinetics of La and Sc Ions in $PbTi_{.5}Zr_{.5}O_{.3}$, LBL-1455, Jan. 1973.

2. Joseph S. Masaryk, Diffusion of Gases in Glass (Ph.D. thesis), LBL-1818, May 1973.

3. G. Bandyopadhyay and R. M. Fulrath, Processing Parameters and the Properties of Lithium Ferrite Spinel, LBL-1875, July 1973.

4. G. Bandyopadhyay and R. M. Fulrath, Thermogravimetry of Spinel Ferrites, LBL-2204, Aug. 1973.

5. G. Bandyopadhyay and R. M. Fulrath, Influence of NiO and $NiFe_2O_4$ Dopants on the Processing and Properties of Lithium Ferrite Spinel, LBL-2255, Oct. 1973.

6. G. Bandyopadhyay, A. M. Lacy, and R. M. Fulrath, Densification and Grain Growth in Doped Lithium Ferrite Spinel, LBL-2245, Sept. 1973.

7. Gautam Bandyopadhyay, Relation of Processing Parameters to the Properties of Lithium Ferrite (Ph.D. thesis), LBL-2263, Nov. 1973.

0 0 0 ~ 4 0 0 7 3 8 9

IV. Solid State Physics

A. THEORETICAL SOLID STATE PHYSICS

Marvin L. Cohen, Principal Investigator

Introduction. New refinements in the pseudopotential method have led to extremely accurate band structures in well-studied materials and new results for complex and amorphous materials. Theoretical schemes have been developed to take advantage of lattice symmetry in complex calculations, making significant reductions in computer calculations possible. Bonding and superconducting properties of a variety of materials have been analyzed. (All work jointly funded with NSF.)

1. SEMICONDUCTORS AND INSULATORS*

Marvin L. Cohen

We have continued our calculations on the electronic structure of semiconductors with emphasis on studies related to electronic band structure and charge density distributions. Narrow gap semiconductors were explored in some detail. These materials are particularly interesting from the device point of view as they are used as generators and detectors of infrared radiation. Our work in this area was related to HgTe-CdTe alloys, IV-VI compounds like PbTe, and InSb. The electronic properties of the narrow gap materials are very rich in unusual physical phenomena. Band edges invert, temperature coefficients of the gaps can be positive or negative, the Fermi surfaces are complex, and some of these materials are superconducting. We have done detailed studies in all of these areas and have fortunately explained many of the observed phenomena, using one-electron theory.

Ultraviolet and X-ray photoemission (UPS and XPS) studies of semiconductors have yielded a great deal of detailed information about the valence electron structure of a large number of crystals. These studies have shown that the standard pseudopotential band structure calculations which involve the use of optical data don't necessarily give the correct density of states for the valence bands. We have augmented the usual approach with a non-local scheme. As a preliminary and more or less simple step we have used an effective mass to obtain the corrections at least to first order. This scheme was very successful and paved the way for a more sophisticated approach using a non-local d-well potential. This latter approach has resulted in ultra-accurate band structures for Ge and GaAs and we are presently extending this work to look at other crystals. The above band structures are probably the most accurate band structures ever calculated for any material. For example, in GaAs, the largest discrepancy between theory and Schottky barrier electroreflectance measurements is 0.08 eV. The non-local schemes have helped us to interpret photoemission and reflectivity spectra. Structures which were previously unidentified or misinterpreted have been identified in terms of electronic transitions between band states.

Complex materials like ternary and layer compounds have been explored successfully, indicating the flexibility of the pseudopotential method. Charge density studies have been particularly useful in these cases. This approach was also used to study materials in different crystal structures.

A model potential scheme was developed to attempt to understand the trends in the Group IV materials (C, Si, Ge. Sn, Pb). This approach involves only two parameters and it illustrated many of the features found in going from C to Pb. The simplicity of the scheme allowed a detailed variation of the electronic structure and it has lead to a systematic picture of the trends in bonding and electronic structure for this important group of elements.

A study of the dependence of the energy gaps and band edges on pressure was done. The calculated results were in good agreement with experiment, but a complete theory is yet to be developed.

*Journals 1, 2, 4, 5, 7, 8, 10, 11, 13, 15 and reports 1, 5, 6, 7, 8, 10, 13, 14, 15, 16.

2. AMORPHOUS MATERIALS*

Marvin L. Cohen

We have had a great deal of success in explorations of the amorphous state of Ge and Si using complex polytypes of these materials. The modifications considered are FC-2 (face-centered cubic with two atoms per cell), 2H-4 (hexagonal with four atoms per cell), BC-8 (body-centered cubic with eight atoms per cell), and ST-12 (simple tetragonal with twelve atoms per cell). The long-range order is preserved in our calculations and it is the changes in the short-

range order which were studied to discover the important features necessary to give the observed features in common with the amorphous materials. Very detailed studies of the band structure, density of states, and dielectric functions of the modifications were made. These studies were extended to explore amorphous III-V semiconductors. The importance of odd versus even number of rings of atoms in the Group IV materials was shown previously by our studies. In the III-V case it appears that it is not the rings which are of prime importance, but the existence chains of like or unlike atoms. The relevant feature is the presence of like or unlike bonds; e.g., for GaAs, Ga-Ga and As-As bonds versus GaAs bonds. Our calculations make prediction of the features in the density of states which can be measured to illustrate the existence of unlike bonds. At this point these bonds have not been unambiguously discovered. The polytype studies have also yielded an analysis of the observed reflectivity or dielectric function as a function of frequency in general terms. The frequency dependence of the joint density of states and dipole matrix elements can be explored separately using the results of the studies for the Si and Ge polytypes. The observed reflectivity for amorphous materials usually has a characteristic one-hump structure and this can be understood using the above analysis.

*Journals 6, 12, 15 and report 4.

3. NEW THEORETICAL METHODS FOR SOLID STATE STUDIES*

Marvin L. Cohen

We have discovered a set of "special points" in the Brillonin zone from which the average over the Brillonin zone of a periodic function of wavevector (e.g., energy, charge density, dipole matrix elements, etc.) can be determined in a simple and accurate way once the function at these points are specified. A specific scheme for increasing the number of points to obtain increased accuracy is also given. The general method and results for some specific lattice structures are given. The special point scheme can save a great deal of computer time for many solid state calculations.

We have applied the formalism connected with the special point scheme to the problem of generating Wannier functions. These functions are the real-analogs of the Bloch functions used for k-space calculations. The Wannier functions should be useful in a variety of calculations such as surface studies and studies of amorphous materials.

Analytic expressions for the charge density in Group IV materials were derived. These expressions are useful to study bonding, trends in electronic properties, and other aspects of the electronic properties of these elements.

*Journals 1, 7, 14 and reports 2, 8.

4. CRYSTAL STRUCTURE*

Marvin L. Cohen

Despite the vast progress made in solid state theory it is still not possible to make accurate predictions of crystal structure starting with atomic properties. Our studies in these directions have focused on semiconductors, with emphasis on the zincblende-rocksalt and zincblende-wurtzite transitions. We previously used charge density plots to show the bonding change which is related to the crystal structure change. We have discovered a relationship between the ionicity parameter and the splitting between the first two valence bands in zincblende crystals. This relationship allows a study of ionicity and hence structure through observations of the band gap. This gap can be observed in photoemission data. We have extended this latter study to show the relationship between the gap, the ionicity parameter, and the potential difference between the atoms.

Another study relating the pseudopotential directly to the bonding was done by studying NaCl and GaAs for both in the zincblende and rocksalt structures. This investigation revealed the features of the potential which caused the resultant structure. For example, it is the large core of Na which appears to be important in formation of NaCl in the rocksalt structure.

ZnS occurs in both the wurtzite (hexagonal) and zincblende (cubic) structures. Detailed charge density studies were made for both cases. These studies showed that for the wurtzite case the c/a ratio was intimately connected with the overall dipole moment. Hopefully charge density studies will lead to possible predictions of the c/a ratio.

*Journals 4, 7, 11 and reports 3, 11.

5. METALS, SUPERCONDUCTIVITY AND X-RAY SCATTERING*

Marvin L. Cohen

Our studies of metals include X-ray and charge density calculations for Al. This represents our first charge density calculation for a metal. It illustrates the free-electron nature with a slight build-up of charge along bonding directions. The X-ray form factors are in relatively good agreement with experiment; it is hoped that more detailed experiments or new types of experiments in this area will give more severe tests of the theory. The optical constants were also calculated.

Nb, NbC, NbN, and $NbSe_2$ were studied in detail. A non-local d-potential was used to allow a pseudopotential study of these materials. Since these materials are superconducting at relatively high temperatures (Nb, NbC-NbN) or with unusual superconducting properties ($NbSe_2$), part of the emphasis in these studies centered around the superconductivity features. For $NbSe_2$, charge density calculations indicate the bonding features of this material. The layer structure allows many interesting bonding properties.

For NbC and NbN charge density, band structure, density of states, and Fermi surface studies appear to give a good picture of the electronic structure for these materials. Some speculations relating Fermi-surface and charge density properties to the superconductivity were made.

Superconductivity studies in addition to the above included a calculation relating superconducting transition temperatures to the softening of phonons in transition metal compounds. In addition, for the case of PbTe some experimental studies found some evidence for superconductivity at high temperatures (e.g., in the 22°K range). Our investigations indicate that the possibility that conventional mechanisms can cause such a high transition temperature are unlikely and the proposed non-conventional excitonic mechanism is also unlikely. Our preliminary investigations seem to indicate that the observations cannot be readily reconciled with existing theory and suggestions that further experimental tests be made to verify the earlier observations are made.

*Journals 3, 9 and reports 6, 9, 12.

6. RESEARCH PLANS FOR CALENDAR YEAR 1974

Marvin L. Cohen

We plan to explore XPS data on metals provided by Professor Shirley's group with the intention of examining the role of Mahan singularities in the spectra.

Detailed studies of chalcopyrite semiconductors (e.g., $ZnGeP_2$) will be made. Reflectivity, bonding, and XPS spectra will be analyzed. These materials are very nonlinear and may be technologically useful. Ultra-accurate band structures similar to those done for GaAs will be computed for other zincblende, diamond, and rocksalt semiconductors. In the latter case PbTe, which is a narrow-gap semiconductor, will be analyzed in great detail, particularly for energies and states near the band gap. The role of this material in infrared work makes these states particularly interesting.

Local field effects in the dielectric function will be explored. Calculations for Si will attempt to explain some current scattering measurements. Some general theory will be attempted to explore the relationship between local field effects and electron-phonon interactions.

Some work on Cs at varying pressures will be performed. Crystal structure transitions and the change in bonding will be studied with an attempt to understand both the one-electron and superconducting properties of this material.

An attempt to study AgBr will be made. The role of this type of crystal in the photographic process will be analyzed to some extent; i.e., the influence of the electronic band structure will be explored.

Some calculations on the superconducting proximity effect will be attempted. Measurements by Professor Clarke's group are serving as the motivation for this work.

We plan to continue our close association with Professor Shen's group and to perform theoretical calculations relevant to the measurements made by this group.

7. 1973 PUBLICATIONS AND REPORTS

Marvin L. Cohen and Associates

Journals

1. D. J. Chadi and M. L. Cohen, Electronic

Structure of $Hg_{1-x}CdTe$ Alloys and Charge Density Calculations Using Representative k-Points, Phys. Rev. B 7, 692 (1973)(LBL-1105).

2. C. Varea de Alvarez, J. P. Walter, R. W. Boyd, and M. L. Cohen, Calculated Band Structures, Optical Constants, and Electronic Charge Densities for InAs and InSb, J. Chem. Phys. Solids 34, 337 (1973)(LBL-482).

3. J. P. Walter, C. Y. Fong, and M. L. Cohen, Electronic Charge Density of Aluminum, Solid State Comm. 12, 303 (1973)(LBL-893).

*4. W. D. Grobman, D. E. Eastman, and M. L. Cohen, A Relationship Between Photoemission-Determined Valence Band Gaps in Semiconductors and Insulators and Ionicity Parameters, Phys. Letters 43A, 49 (1973).

5. M. L. Cohen, Electronic Charge Densities in Semiconductors, Science 179, 1189 (1973).

6. J. D. Joannopoulos and M. L. Cohen, Electronic Properties of Complex Crystalling and Amorphous Phases of Ge and Si. I. Density of States and Band Structure, Phys. Rev. B 7, 2644 (1973)(LBL-1169).

7. J. D. Joannopoulos and M. L. Cohen, Electronic Charge Densities for ZnS in the Wurtzite and Zincblende Structures, J. Physics C 6, 1572 (1973)(LBL-1193).

8. C. Varea de Alvarez and M. L. Cohen, Calculated Band Structure and Reflectivity Spectra of $ZnGeP_2$, Phys. Rev. Letters 30, 979 (1973)(LBL-1480).

9. C. Y. Fong and M. L. Cohen, Pseudopotential Calculation of the Electronic Structure of a Transition Metal-Niobium, Phys. Letters 44A, 375 (1973).

10. S. E. Kohn, P. Y. Yu, Y. Petroff, Y. R. Shen, Y. Tsang, and M. L. Cohen, Electronic Band Structure and Optical Properties of PbTe, PbSe, and PbS, Phys. Rev. B 8, 1477 (1973).

11. C. Varea de Alvarez and M. L. Cohen, Model Pseudopotential Calculations of the Electronic and Bonding Properties of Group-IV Elements, Phys. Rev. B 8, 1603 (1973)(LBL-1479).

12. J. D. Joannopoulos and M. L. Cohen, Electronic Properties of Complex Crystalline and Amorphous Phases of Ge and Si. II. Band Structure and Optical Properties, Phys. Rev. B 8, 2733 (1973)(LBL-1826).

13. J. Chelikowsky, D. J. Chadi and M. L. Cohen, Calculated Valence-Band Densities of States and Photoemission Spectra of Diamond and Zincblende semiconductor, Phys. Rev. B 8, 2786 (1973)(LBL-1827).

*14. D. J. Chadi and M. L. Cohen, Approximate Wannier Functions, Solid State Comm. 13, 1007 (1973).

15. J. D. Joannopoulos and M. L. Cohen, New Insight Into the Optical Properties of Amorphous Ge and Si, Solid State Comm. 13, 1115 (1973)(LBL-1828).

Published abstracts

1. C. Varea de Alvarez, M. L. Cohen, Y. Petroff, S. Kohn, and Y. R. Shen, Electronic Structure of $ZnGeP_2$. Bull. Am. Phys. Soc. 18, 351 (1973).

2. W. D. Grobman, D. E. Eastman, and M. L. Cohen, A Relationship Between Photoemission-Determined Valence-Band Gaps and Ionicity Parameters, Bull. Am. Phys. Soc. 18, 384 (1973).

Reports

1. C. Y. Fong and M. L. Cohen, Electronic Charge Densities for Two Layer Semiconductors--SnS_2 and $SnSe_2$,

*2. D. J. Chadi and M. L. Cohen, Special Points in the Brillouin Zone, (published 1/74)

*3. D. J. Chadi and W. D. Grobman and M. L. Cohen, Atomic Pseudopotentials and the Ionicity Parameter of Phillips and Van Vechten, (to be published Jan. 1974).

4. J. D. Joannopoulos and M. L. Cohen, Electronic Density of States of Amorphous III-V Semiconductors, LBL-2266, Oct. 1973.

5. J. R. Chelikowsky and M. L. Cohen, High Resolution Band Structure and the E_2 Peak in Ge, LBL-2267, Oct. 1973.

6. M. L. Cohen, Electronic Structure of Narrow Gap Semiconductors, Proceedings of the International Conference on Narrow Gap Semiconductors, Nice, France, Sept. 10-12, 1973 (LBL-2269, Sept. 1973).

7. C. Varea de Alvarez and M. L. Cohen, Pressure Coefficients for Band Gaps in Silicon, LBL-2268, Oct. 1973.

*8. D. J. Chadi and M. L. Cohen, Analytic Expression for Electronic Charge Density Distribution in Diamond Structure Crystals, Oct. 1973.

9. D. J. Chadi and M. L. Cohen, Electronic Band Structures and Charge Densities of NbC and NbN, LBL-2557, Nov. 1973.

10. J. R. Chelikowsky and M. L. Cohen, Electronic Structure of GaAs, LBL-2560, Dec. 1973.

11. Y. W. Tsang and M. L. Cohen, Pseudopotential Study of Bonding in the Zincblende and Rock Salt Structures, LBL-2558, Dec. 1973.

12. C. Y. Fong and M. L. Cohen, Band Structure and Charge Densities of 2H-$NbSe_2$, LBL-2254, Dec. 1973.

13. J. R. Chelikowsky and M. L. Cohen, Calculated Valence Band Density of States and Reflectivity for ZnSe, LBL-2555, Dec. 1973.

14. I. Ch. Schlüter and M. Schlüter, Electronic Structure and Optical Properties of PbI_2, LBL-2559, Dec. 1973.

15. Carmen Varea de Alvarez, Electronic Structure of Diamond, Zincblende and Chalcopyrite Semiconductors (Ph.D. thesis), LBL-1863, Sept. 1973.

16. C. Varea de Alvarez, M. L. Cohen, L. Ley, S. P. Kowalczyk, F. R. McFeely, D. A. Shirley and R. W. Grant, Electronic Density of States and Bonding in Chalcopyrite Type Semiconductors, LBL-2330, Dec. 1973.

---

*Not supported by IMRD funds.

B. FAR INFRARED PROPERTIES OF SOLIDS

Paul L. Richards, Principal Investigator

1. FAR INFRARED PHOTOCONDUCTIVITY OF ULTRAPURE GERMANIUM

Eugene E. Haller and Paul L. Richards

Ultrapure germanium is produced at LBL in substantial quantities for the construction of "germanium intrinsic detectors" of electromagnetic radiation and particles. A continuing problem in the production of this material is the identification of residual impurities at the level of a few parts in 10^{12}. Far infrared photoconductivity using the IMRD Fourier spectroscopy facility provides the most sensitive known method for identifying common acceptors such as B, Al, Ga, and In.

Isolated acceptor atoms produce a quasi-hydrogenic series of energy levels within the Ge energy gap. If the sample is maintained in the 10-15°K temperature range, a far infrared photon can promote a hole from the ground state to one of many empty excited states. There is a substantial probability that the hole will subsequently absorb a phonon and be excited to the valence band. Its presence in the valence band is observed as an increase in the electrical conductivity. Since the first two states involved in this process are sharp, the photoconductivity peaks are narrow ($\delta\nu < 0.1$ cm^{-1}). Since there are few thermally excited holes, the photo-excited holes cause a large change in the sample conductivity. Signals 100 times greater than noise have been observed for acceptor concentrations ~ 10^{10} cm^{-3}.

Because the ground state wave function samples the immediate vicinity of the impurity, the ground state energy varies with the atomic number. The excited state energies are much less sensitive to the acceptor species as long as it is neutral. The cluster of photoresponse lines looks the same for each acceptor, but the frequency at which the cluster occurs identifies the acceptor responsible. This is shown in Fig. 1 where the frequencies expected from B, Al, and Ga are compared with the spectrum observed for a sample containing these impurities.

Photoconductivity spectra have been measured on a large number of samples obtained from many different boules. These measurements have proved useful in identifying the impurities which limit the volume and the performance of "germanium intrinsic detectors." The sensitivity for shallow acceptors appears to be adequate to identify these impurities even at levels which are no longer important for detector performance.

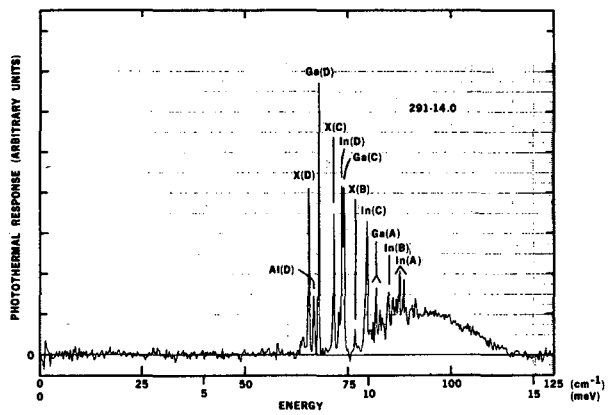

Fig. 1. Far infrared photoconductivity spectrum of ultrapure Ge containing B, Al, Ga, and X (unknown). The positions of the lines agree with lower-resolution results previously obtained for doped samples. Above 75 cm^{-1} there is a continuum spectrum associated with photo excitation into the valence band. (XBL 7310-1396)

During the course of these experiments, several new phenomena have been observed which will be investigated to determine their cause. These include two series of lines which correspond to unknown centers with ionization energies between those of B and Al, and those of In and Th.

Attempts will be made to develop noise-free contacts at low temperature so that these measurements can be extended to N-type material.

2. BALLOON-BASED MEASUREMENTS OF THE COSMIC BACKGROUND RADIATION

John C. Mather, Paul L. Richards, and David P. Woody

Big bang cosmology theory and measurements in the microwave and optical frequency region support the idea that the universe is filled with isotropic blackbody radiation with a characteristic temperature of 2.7°K. Accurate measurements of this radiation are not available for frequencies above the

peak of the blackbody spectrum (which occurs at ~6 cm^{-1} or $\lambda \approx 1.7$ mm).

A far infrared spectrometer has been developed that can be flown by balloon to an altitude of ~40 km to measure this radiation over the frequency range from ~3 to ~18 cm^{-1}. The principal features of the system are shown in Fig. 1. These include a cooled two-section horn antenna, a cooled polarizing Michelson interferometer used for Fourier spectroscopy, and a germanium bolometer detector. The bolometer is illuminated with immersion optics for improved sensitivity. Blackbody sources are used in flight to calibrate the spectrometer for absolute radiometry with an anticipated sensitivity of better than 0.02°K for a 1 sec observation of a Rayleigh-Jeans source.

LIQUID HELIUM COOLED
FAR INFRARED INTERFEROMETER

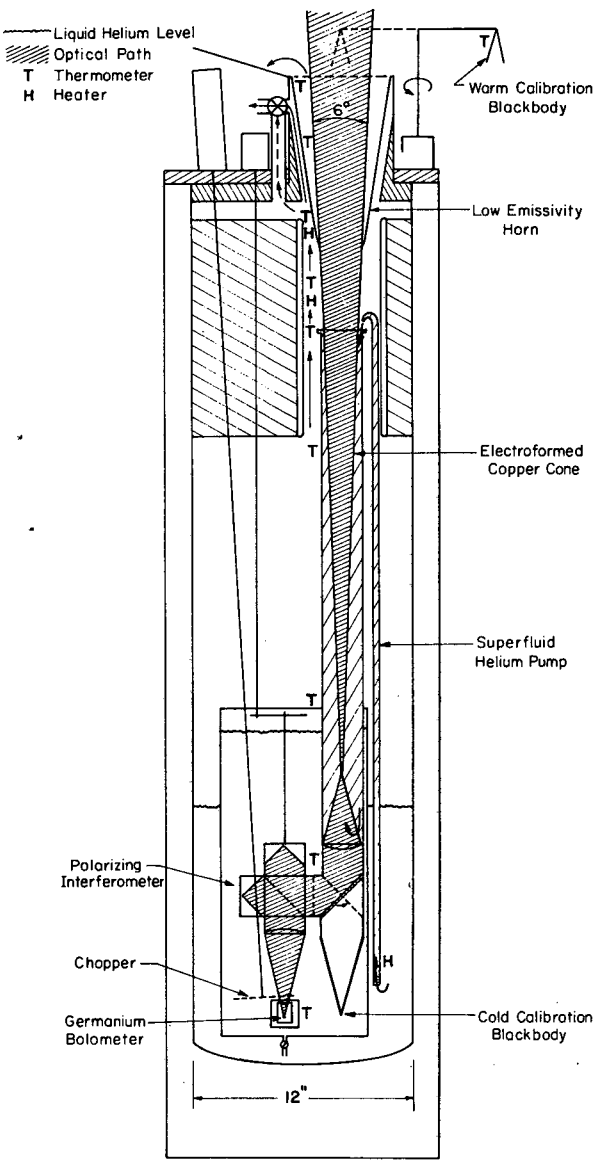

Fig. 1. Scale drawing of radiometer-spectrometer for measurements of the cosmic background radiation. The cryostat is ~1.5 m high and maintains the apparatus at minimum temperature for more than 10 hours.
(XBL 737-6388)

One critical feature of this measurement is the avoidance of signals from extraneous warm objects. Radiation from the apparatus is reduced by cooling to liquid helium temperature all portions of the optical system which contact the geometrical beam. The temperature of the warm horn at the top of the antenna (which contacts only diffraction side lobes) is varied in flight to check for residual emission. All windows in front of the antenna are removed for the measurement. The antenna has been designed for minimum side lobes at large angles to avoid observing signals from the earth or the balloon hardware. The measured antenna pattern is shown in Fig. 2.

The most important remaining sources of extraneous radiation are the line emissions from the residual atmosphere above 40 km. The important lines arise from water, ozone, and oxygen. Since the relative line strengths

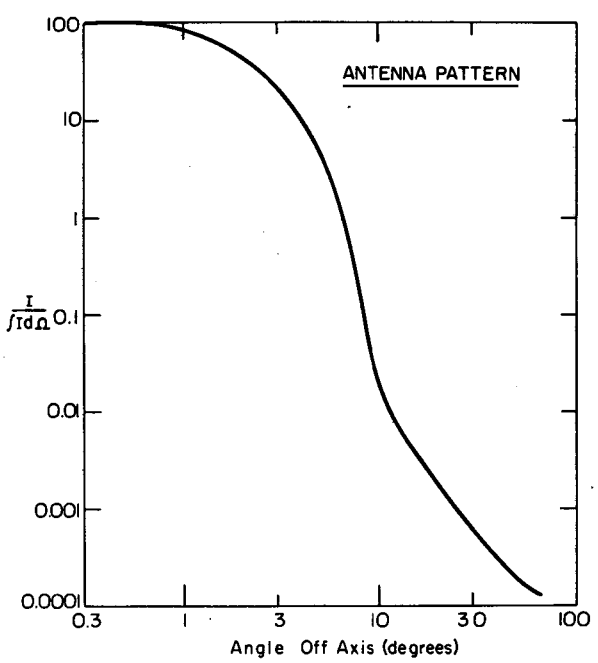

Fig. 2. Response of the radiometer to a point source as a function of the angle of the source from the axis of the antenna.
(XBL 741-5430)

and positions are accurately known, the observed spectra will be used to determine the amounts of the three gases present. Computer programs have been written to generate simulated atmospheric emission spectra, which will be subtracted from the observed spectral data to obtain the residual background radiation. An example of such a simulated atmospheric emission spectrum (plotted as an antenna temperature) is compared with a 2.7°K blackbody curve in Fig. 3.

The apparatus described here has been constructed and tested in space environment simulators (cold and vacuum) and interfaced to a balloon gondola developed by Professor K. Anderson's group at the Berkeley Space Sciences Laboratory. The first flight was launched from Palestine, Texas, on October 26, 1973. During the flight the payload temperature dropped to -60°C. This was considerably colder than the temperature of -20°C anticipated from the experience of others, and colder than our minimum design temperature

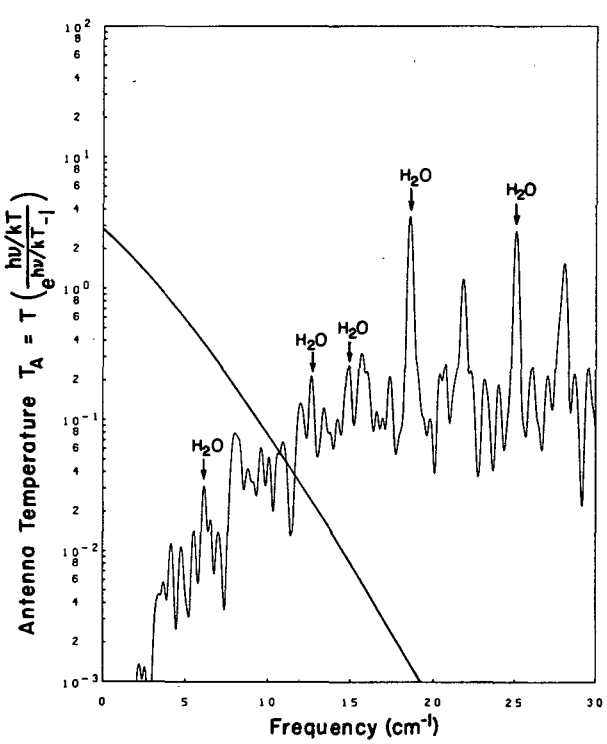

Fig. 3. The antenna temperature of a 2.7°K blackbody compared with that of an estimate of the residual atmospheric antenna temperature above 40 km. Antenna temperature is defined as the temperature of a Rayleigh-Jeans source with unit emissivity which gives the same emitted power as the actual source. The frequency range of this measurement is from ~3 to ~18 cm^{-1}. (XBL 737-1577)

of -50°C. At this low temperature the mechanical drive to the interferometer lost power and stopped working. Consequently, although all other electrical and mechanical systems functioned well, very few spectral data were obtained. The payload was recovered undamaged near Anniston, Alabama.

Despite the absence of spectral data much of value was learned from the flight. The reason for the low temperature is now understood and can be corrected. Preliminary data analysis indicates that another flight with the same apparatus (with a working interferometer drive) will produce significant new information on the cosmic background radiation. A second flight is planned in early 1974, after minor modifications to the apparatus have been completed.

Another potential application of this apparatus is the study of the composition of the atmosphere. If the apparatus is modified to look horizontally and to measure spectra out to 100 cm^{-1}, the sensitivity to minor atmospheric constituents will be greatly increased. A rough estimate suggests that a detection limit of ~ 10^8 molecules/cm^3 can be achieved in a 1 sec observation for a gas with an electric dipole moment of 1 debye. (Partially funded by NASA)

3. SURFACE MAGNETIC RESONANCE IN MnF_2

Robert B. Bailey, Paul L. Richards, and William E. Tennant

The far infrared transmission spectrum of a single crystal of the classic antiferromagnet MnF_2 is well known to show a single low-frequency mode, the antiferromagnetic resonance (AFMR) at 8.7 cm^{-1}. In the course of studying magnetic resonance modes in disordered antiferromagnets, the far infrared spectra of MnF_2 powders were measured. The results in Fig. 1 show either one or two extra modes (marked SM) in addition to the AFMR. The strengths of these SM depend on the size of the powder particles.

Detailed analysis of the data shows that these extra modes cannot be reasonably attributed to impurities, to strain, or to magnetostatic modes. The most likely explanation is that they arise from the sample surface. We believe these modes to be the first observation of a magnetic surface mode.

The surface mode identification is most convincing for the SM at 8.3 cm^{-1} whose strength is observed to vary in proportion

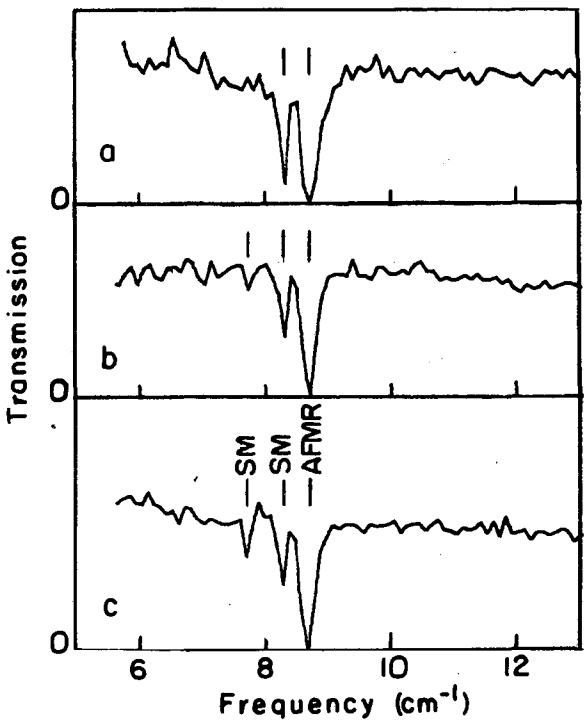

Fig. 1. Far infrared transmission spectra of powder samples of MnF_2. The powder particle size increases in going from curve a to curve c. These spectra show SM at 7.7 and 8.3 cm^{-1} in addition to the well-known AFMR at 8.7 cm^{-1}. (XBL 738-1610)

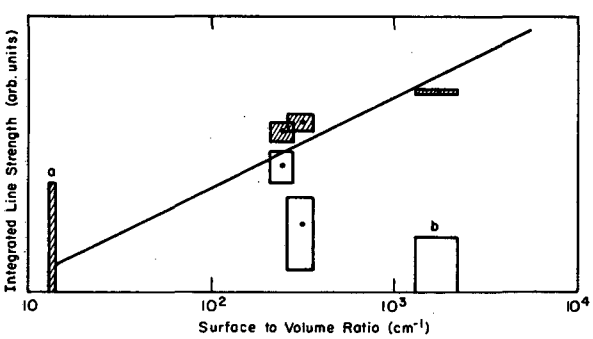

Fig. 2. A log-log plot of the integrated line strengths of the SM at 7.7 cm^{-1} (open squares) and the SM at 8.3 cm^{-1} (shaded squares), plotted as a function of the sample surface area normalized to the volume (which was the same for all samples). The shaded squares fit a line with slope 1/2 which is the expected result for saturated unresolved Lorentzian lines whose actual strength is proportional to surface area. (XBL 738-1611)

to the surface area of the powder. Its splitting in a magnetic field is the same as that for a bulk mode, as would be expected if the surface spins have the same alignment as the bulk spins. The mode at 7.7 cm^{-1} is strongest for intermediate particle sizes and was not strong enough to observe the magnetic field splitting. The data for the dependence of the strength of both modes on sample surface area are shown in Fig. 2.

The theory of antiferromagnetic surface modes predicts that a sharp resonance frequency is associated with a single crystallographic plane. The surface of our powder particles is expected to be dominated by the (110) cleavage planes of MnF_2. Preliminary calculations for this plane, done in collaboration with Dr. T. Wolfram of the Rockwell Science Center, give frequencies in the neighborhood of 8 cm^{-1}, but predict mode strengths ~200 times smaller than the observed modes.

Microwave apparatus is being constructed to search for these resonances on single crystals of MnF_2 with large cleaved 110 surfaces. Higher sensitivity and resolution should be available from the microwave spectrometer than from the infrared technique.

4. FAR INFRARED NONLINEAR SPECTROSCOPY IN $LiNbO_3$

James Morris, Kei-hsiung Yang, Paul L. Richards, and Y. R. Shen

A system for generating continuously tunable far infrared radiation by beating two dye lasers in $LiNbO_3$ was described in the annual report last year. The power generated at a number of frequencies using forward collinear phase matching has been measured and the values of the nonlinear coefficient $\chi^{(2)}$ shown in Fig. 1 computed from them. The values of $\chi^{(2)}$ do not agree with the theoretical values derived from the published infrared and Raman data. However, good agreement was found, as shown in Fig. 1, when the infrared absorption was remeasured by observing the width of the phase matching curve. The new results for the infrared absorption coefficient of $LiNbO_3$ obtained in this way are shown in Fig. 2. They reveal considerable structure which is believed to arise from frequency-dependent phonon damping. The infrared absorption in the wings of the lowest optical phonon frequency depends on the lifetime of the phonon created. Since this lifetime is controlled by the decay into two or more phonons, the

singularities on the joint densities of states of the product phonons will cause structure on the infrared absorption. This novel method for measuring the frequency-dependent phonon damping competes favorably with the more conventional Raman technique.

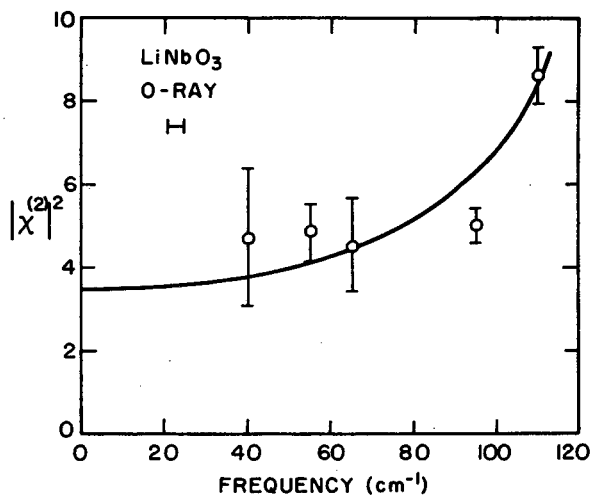

Fig. 1. Square of the nonlinear coefficient $\chi^{(2)}$ computed from the measured difference frequency power (points) compared with that computed from the Raman cross section and the infrared absorption coefficient (line). (XBL 736-6308)

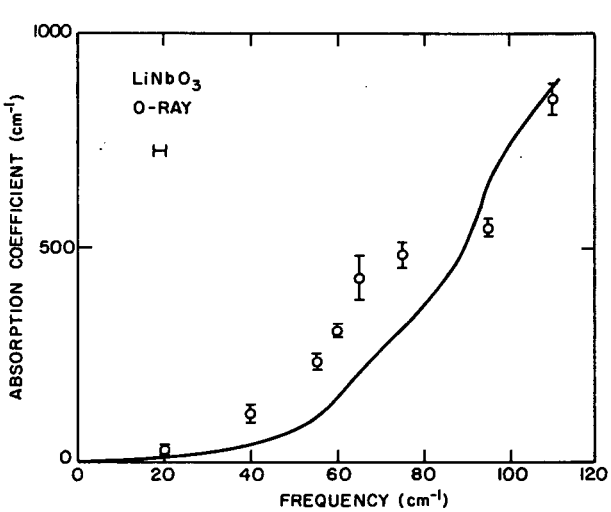

Fig. 2. Infrared absorption coefficient (points) measured from the effective coherence length for difference frequency generation, compared with directly measured infrared data (line) from the literature. (XBL 736-6307)

5. INSTRUMENTATION FOR FOURIER SPECTROSCOPY

Paul L. Richards

The IMRD Fourier spectroscopy facility includes a Michelson interferometer and two polarizing interferometers for far infrared spectroscopy in the frequency range from 2 to 450 cm^{-1}, with a maximum resolution of 0.05 cm^{-1}. These instruments are coupled on-line to a PDP-11 computer programmed for fast Fourier transforms and phase corrections.

A new rapid scan Michelson interferometer has been built to cover the frequency range from 400 to 10,000 cm^{-1} with a resolution of 1 cm^{-1}. This instrument was first operated with an HgCdTe photoconductive detector which limited its range to the 700-4,000 cm^{-1} region. With this detector the rate of data acquisition was about 100 times faster than for a conventional chemical IR spectrometer with the same resolution. New programs and interfaces are being developed to process the data from this new interferometer.

6. FAR INFRARED SPECTRA OF Mn^{3+} IN Al_2O_3

Richard L. Aurbach and Paul L. Richards

Fourier transform spectroscopy has been used to measure the transmission of Mn-doped Al_2O_3 as a function of frequency, field, orientation, polarization, and temperature. Several resonances have been observed in the frequency range from 3 to 30 cm^{-1}. The splitting of these modes in a magnetic field parallel to the c-axis is shown in Fig. 1. The strengths of several modes increase with magnetic field, possibly indicating admixture of higher lying levels. In the $H \perp c$ orientation, the modes show strong polarization dependence. The temperature has been varied from 1.3 to 4.2°K in order to identify ground state transitions, and a level diagram for the infrared active modes has been assembled. These resonances are attributed to the Mn^{3+} ion, which is expected to show strong dynamic Jahn-Teller interactions. The samples for this study were provided by Dr. R. A. Forman of the National Bureau of Standards. A theoretical analysis of Mn^{3+} in Al_2O_3 is being carried out by Dr. C. Bates of Nottingham University concurrently with these measurements.

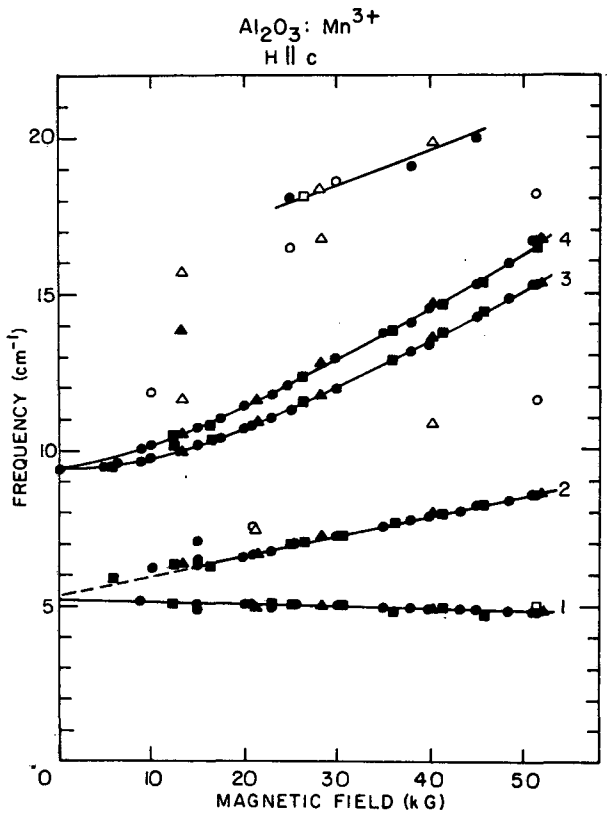

Fig. 1. Transmission minima observed in three samples of Al_2O_3:Mn^{3+} with magnetic field parallel to the c-axis.

(XBL 7312-7101)

7. SUPERCONDUCTING TUNNEL JUNCTION BOLOMETERS

John Clarke, Gary I. Hoffer, and Paul L. Richards

In most parts of the infrared spectrum the most sensitive available detector is the He temperature doped Ge bolometer. The minimum detectable power (NEP) varies with the bolometer area, but is well characterized by the figure of merit

$$D^* = \sqrt{\text{Area}}/\text{NEP} \approx 3 \times 10^{12} \text{ cm W}^{-1}\text{Hz}^{1/2}$$

for a good bolometer. We are investigating two new types of superconducting infrared bolometer. Both use evaporated film superconducting tunnel junctions as thermometers. In one, the temperature-dependent Josephson current in a Pb-CuAl-Pb superconductor-normal metal-superconductor junction is measured with a SQUID galvanometer. In the other, the temperature-dependent quasiparticle tunneling current in a Pb-Al_2O_3-Al superconductor-insulator-normal metal junction is measured with a conventional field-effect transistor amplifier. Either type of junction is deposited on a low-heat-capacity sapphire substrate covered on the reverse side with a thin Bi film to absorb infrared radiation. The best performance achieved thus far is for the SNS bolometer which is pictured in Fig. 1. It presently has an electrical

$$\text{NEP} \approx 5 \times 10^{-15} \text{ W}/\sqrt{\text{Hz}} \text{ and } D^* \approx 10^{14} \text{ cm W}^{-1}\text{Hz}^{1/2}.$$

Some improvement in these values is anticipated.

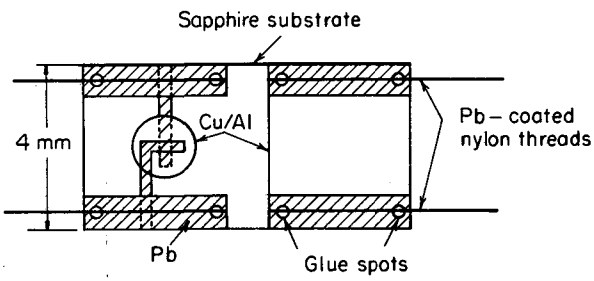

Fig. 1. Configuration of the superconductor-normal metal-superconductor junction bolometer.

(XBL 7112-4927A)

8. RESEARCH PLANS FOR CALENDAR YEAR 1974

Paul L. Richards

Measurements of the photoconductivity of ultrapure Ge will continue, both as a service to the LBL group producing material for "germanium intrinsic detectors" and in order to explore some of the new physical effects discovered. At least one balloon flight of the cosmic background apparatus is planned. A single successful flight should provide significant new data on this important problem. Exploration of the zero-field far infrared resonance modes in the iron group fluorides will continue on the (Fe, Co)F_2 and (Zn,Mn)F_2 systems, and Zeeman splittings of the modes already discovered in the (Fe,Mn)F_2 and (Co,Mn)F_2 systems will be measured. An attempt will be made to verify the hypothesis that the observed extra modes in powdered MnF_2 are the first observation of a surface magnon. Interface and software development will be continued so that data can be analyzed on-line from the new near infrared Fourier spectrometer. Far infrared studies of the dynamic Jahn-Teller effects on Cr^{2+} and Mn^{3+} will be

continued. The development of high sensitivity superconducting tunnel junction bolometers will be continued. In addition, more conventional superconducting bolometers operating at the resistive transition will be restudied. If sufficient progress is made, a project to study the far infrared absorptivity of metals based on these bolometers may be initiated. In addition, they may be used to improve the sensitivity of the cosmic background apparatus.

In addition to the above, a project to design and construct superconducting Josephson effect mm wave mixers and parametric amplifiers is funded by the Office of Naval Research.

9. 1973 PUBLICATIONS AND REPORTS

Paul L. Richards and Associates

Journals and conference proceedings

1. K. H. Yang, P. L. Richards, and Y. R. Shen, Coherent Phonon Generation by Optical Mixing in a One-Dimensional Superlattice, J. Appl. Phys. 44, 1417 (1973).

*2. P. L. Richards, F. Auracher, and T. Van Duzer, Millimeter and Submillimeter Wave Detection and Mixing with Superconducting Weak Links, Proc. IEEE 61, 36 (1973).

3. B. Enders, P. L. Richards, W. E. Tennant, and E. Catalano, Antiferromagnetic Resonance Modes in $(Co,Mn)F_2$ and $(Fe,Mn)F_2$, in Magnetism and Magnetic Materials 1972, edited by C. O. Graham, Jr., and J. J. Rhyne (AIP, New York, 1973), Sec. 7, p. 179.

4. P. L. Richards, W. E. Tennant, and E. Catalano, Antiferromagnetic Resonance in Alloys of the Iron-Group Fluorides, Bull. Am. Phys. Soc. (Ser. II) 18, 418 (1973).

5. K. H. Yang, J. Morris, P. L. Richards, and Y. R. Shen, Phase Matched Generation of Tunable Far Infrared Radiation by Mixing Two Dye Lasers, Bull. Am. Phys. Soc. (Ser. II) 18, 350 (1973).

†6. G. I. Rochlin, P. L. Richards, and F. Auracher, Quasiparticle Interference Current in Superconducting Weak Links, Bull. Am. Phys. Soc. (Ser.II) 18, 77 (1973).

LBL and other reports

‡1. P. L. Richards, Optical Analysis of Solar Energy Collection (1973 Materials Research Council Report).

‡2. P. L. Richards, Microwave Conductivity Measurements on Anisotropic Organic Crystals (1973 Materials Research Council Report).

3. John Clarke, G. I. Hoffer, and P. L. Richards, Superconducting Tunnel Junction Bolometers, in Proceedings of the International Conference on the Detection and Emission of Electromagnetic Radiation with Josephson Junctions, Perros-Guirec, France, 1973 (to be published); LBL-2222, Aug. 1973.

*4. Y. Taur, J. H. Claassen, and P. L. Richards, Conversion Gain and Noise in a Josephson Mixer, in Proceedings of the International Conference on the Detection and Emission of Electromagnetic Radiation with Josephson Junctions, Perros Guirec, France, 1973 (to be published).

5. R. L. Aurbach, P. L. Richards, and R. A. Forman, Far Infrared EPR of $Al_2O_3:Mn^{3+}$, LBL-2231 Abs., Oct. 1973.

6. K. H. Yang, J. R. Morris, P. L. Richards, and Y. R. Shen, Phase-Matched Far-Infrared Generation by Optical Mixing of Dye Laser Beams (to be published); LBL-2226, Sept. 1973.

7. William E. Tennant, Low-Temperature Studies: I. New Antiferromagnetic Resonance Effects in the Iron-Group Fluorides. II. Impedance Matching a Josephson-Effect Galvanometer by Means of a Superconducting Transformer (Ph.D. thesis), LBL-1844, Nov. 1973.

8. W. L. Hansen and E. E. Haller, A View of the Present Status and Future Prospects of High Purity Germanium, LBL-2435, Nov. 1973.

9. E. E. Haller and W. L. Hansen, Impurities in High-Purity Germanium as Determined by Fourier Transform Spectroscopy, LBL-2436, Nov. 1973.

---

*Sponsored by the ONR (Office of Naval Research).

†Partly sponsored by the ONR (Office of Naval Research).

‡Sponsored by ARPA (Advanced Research Projects Association).

C. SUPERCONDUCTIVITY

Gene I. Rochlin, Principal Investigator

1. PAIR-QUASIPARTICLE INTERFERENCE CURRENT IN SUPERCONDUCTING TUNNEL DEVICES

Gene I. Rochlin

Previous calculations of the effects of the phase-dependent pair-quasiparticle interference conductance, $G_1 \cos\phi$, on the I-V characteristics of superconducting Josephson-type devices have been extended to treat a wide range of values of G_1/G_0 between +1 and -1. The results have also been parametrized to treat the bias voltage dependence of the normal conductance G_0. Several effects are noted: for a given value of G_1, all I-V curves may be reduced to a single family with a universal scaling factor β_c which depends only on the junction's measurable $G_0(V)$ and capacitance; deviations of the I-V curve from the $\beta_c \to 0$ limit persist to very small values of β_c; stable solutions exist even for $|G_1/G_0| > 1$. The latter effect in particular is most astonishing, since it corresponds to a pendulum whose damping exceeds the driving force over part of the rotation. Theories which assumed that $|G_1/G_0| \leq 1$ was the physical limit requirement will have to be re-examined in this light.

The experimental observations on Sn-I-Sn unshunted thin-film oxide junctions only confirms that $G_1/G_0 \leq 0$, but we have not been able to determine the magnitude of this ratio from our data, which remains a puzzle.

2. TUNNEL JUNCTIONS WITH FLUOROCARBON BARRIERS

Michael D. Jack and Gene I. Rochlin

The electrical characteristics of In-I-In and In-I-Pb superconducting tunnel junctions have been studied in detail. Since In does not readily form pinhole-free oxide layers, a thin insulating dielectric was formed on freshly deposited In film by passing an electric discharge through an atmosphere of fluorocarbon gas. Junctions were then completed by depositing a thin counter electrode of In or Pb. The same process was used to prepare high-resistance junctions with Au as the base electrode; these were not, however, studied in detail.

In-I-In and In-I-Pb junctions were produced with resistances in the range 0.01 to 10^{10} ohms at liquid helium temperatures. Low-resistance junctions exhibited nonlinear electrical characteristics associated with good quality "oxide" superconducting junctions including (a) the dc Josephson effect, (b) quasiparticle tunneling characteristics, (c) phonon structure, and (d) inelastic tunneling phenomena. The magnitude of the Josephson current for In-I-In junctions agreed to within a few percent of the value predicted by strong-coupling theory. Current voltage (I-V) and first- and second-derivative curves for In-I-In and In-I-Pb were compared with curves for Al-I-In and Pb-I-Pb junctions. Discrepancies between the characteristics can be, for the most part, explained on the basis of existing theories of phonon-mediated superconductivity, using recent data from inelastic neutron scattering studies of In. Nonlinear structure at voltages below the phonon spectrum was observed and is most likely associated with Kohn singularities. At higher voltages, second-derivative curves exhibited resonances characteristic of CH and OH impurities in the barrier as well as a complex spectrum associated with the vibrational spectrum of the fluorocarbon dielectric. To better characterize this dielectric, a variety of surface analytic

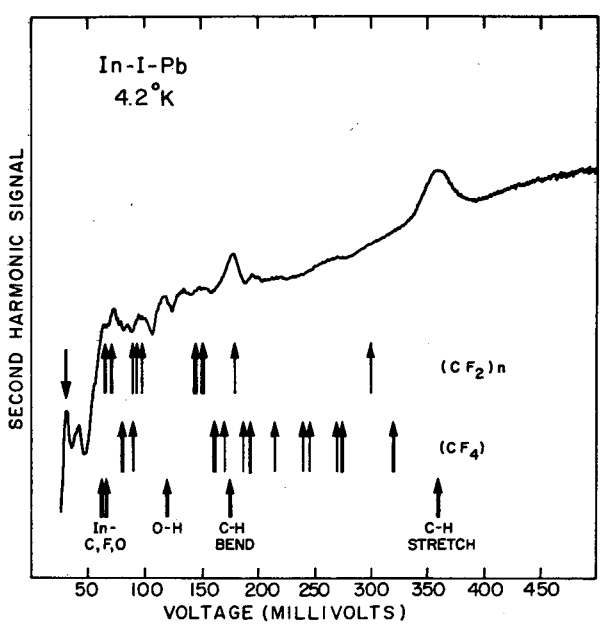

Fig. 1. "Tunneling spectrum" of an In-I-Pb junction at 4.2°K. The arrows represent prominent peaks in the infrared spectrum of $(CF_2)_n$, poly-tetrafluoroethylene, and (CF_4), tetrafluoromethane. (XBL 7212-7368)

techniques were used to determine the complex index of refraction, the chemical composition, and chemical homogeneity of the barrier. I-V curves for high-resistance junctions were used to determine the potential at the metal-insulator interface (see Fig. 1).

3. METAL OXIDE TUNNEL BARRIERS

Duncan E. McBride and Gene I. Rochlin

We have developed a method of characterizing the barrier in a metal-insulator-metal tunneling junction on the basis of experimental current-voltage curves and a simple theoretical model. We are able to determine unambiguously the barrier height ϕ and barrier thickness S by, first, measuring the quantity $S\phi^{3/2}$ from the slope of the Fowler-Nordheim plot. Then experimental data are compared with a family of current-voltage curves calculated for various pairs of S and ϕ with $S\phi^{3/2}$ fixed at the measured value, and the pair which gives the best fit is determined. This procedure has been tested on the best-understood tunneling barrier, that is grown thermally on an aluminum film, and is found to give a barrier height of about 2.6 eV, in good agreement with independent measurements. (See Fig. 1)

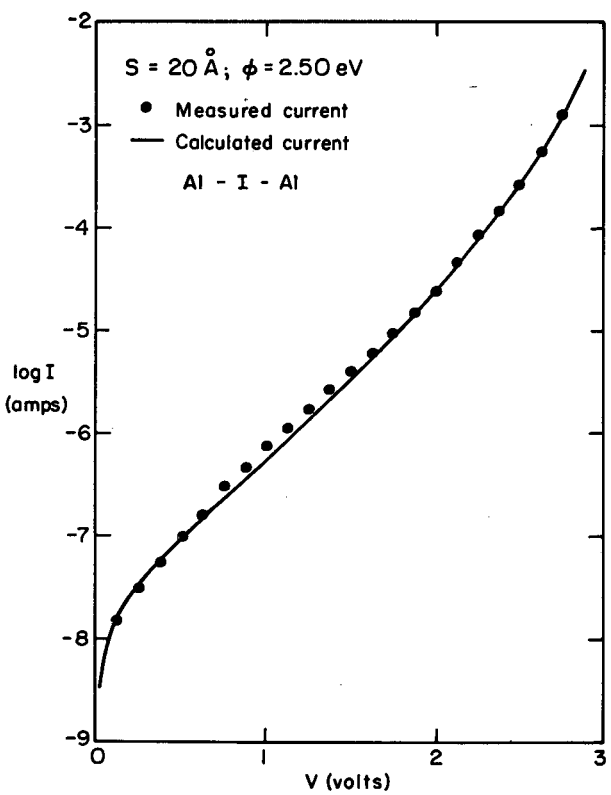

Fig. 1. The curve which gave the best fit for the particular junction with $S\phi^{3/2}$ = 79 A(eV)$^{3/2}$ is plotted on top of the experimental data. The agreement is excellent over five orders of magnitude of current. The slight hump in the data points near V = 1 volt is not understood.

(XBL 733-5843)

Our method also enables us to construct a qualitative description of the tunneling barrier which provides a context for the quantitative measurements. The barrier seems adequately described by a trapezoidal model, often with unequal sides but of nearly uniform height over the junction area. Although the barrier thickness is not uniform, the variation occurs on a microscopic scale in a well-prepared junction, and the magnitude of the variation is a small fraction of the mean thickness.

We have also used the method to measure parameters of barriers grown thermally on chromium, thin film vanadium, and bulk vanadium, and we obtain barrier heights of 0.6, 0.1, and 0.2 eV respectively. The technique is a convenient one for the analysis of data from an experiment, and the results it gives are unambiguous, consistent, and provide a sensitive measurement of the characteristics of the barrier.

4. RESEARCH PLANS FOR CALENDAR YEAR 1974

Gene I. Rochlin

The work on the pair-quasiparticle interference term will be completed.

5. 1973 PUBLICATIONS AND REPORTS

Gene I. Rochlin and Associates

Journals and books

1. G. I. Rochlin and P. K. Hansma, Inexpensive Model of a Josephson Weak Link, Am. J. Phys. 41, 878 (1973)(LBL-1185).

2. F. Auracher, P. L. Richards, and G. I. Rochlin, Observability of Quasiparticle-Pair Interference Current in Superconducting Weak Links, Phys. Rev. B 1, (1973)(LBL-1197 Rev.).

0 0 0 0 4 0 0 7 3 9 7

Papers presented

1. G. I. Rochlin, P. L. Richards and F. Auracher, "Quasiparticle Interference Current in Superconducting Weak Links," APS meeting, Now York, Jan. 1973.

2. D. E. McBride, G. I. Rochlin, and P. K. Hansma, "A New Method for Determining Tunnel Junction Parameters," APS meeting, San Diego, March 1973.

LBL reports

1. D. E. McBride, G. I. Rochlin, and P. K. Hansma, Characterization of Metal-Oxide Tunnel-Junction Barriers, LBL-1854, June 1973 submitted to J. Appl. Phys.

2. G. I. Rochlin, On Connecting the Microscopic and Macroscopic Theories of Type II Superconductivity, LBL-2202, Aug. 1973; submitted to Am. J. Phys.

3. Duncan E. McBride, Characterization of Metal-Oxide Tunneling Barriers (Ph. D. thesis), LBL-1855, Sept. 1973.

4. M. D. Jack, Properties of Tunnel Junctions with Fluorocarbon Dielectric Barriers, LBL-1805, Nov. 1973.

John Clarke, Principal Investigator

1. 1/f NOISE IN DIFFUSIVE SYSTEMS

John Clarke and Richard F. Voss

Noise limits the accuracy of most measurements. Understanding the physical mechanism of the noise and being able to give a quantitative estimate of its frequency spectrum is of primary importance in optimizing sensitive experiments. Although Johnson noise and shot noise are most frequently quoted as the limits to electrical sensitivity, most low-frequency experiments are, in fact, limited by 1/f noise, whose identifying characteristic is a spectrum varying as $1/f^{\gamma}$ where $0.7 \lesssim \gamma \lesssim 1.5$ over many decades.

By considering Brownian motion of particles in one, two, and three dimensions, we have been able to show theoretically that fluctuations in the number of particles in a given subvolume of a large reservoir have such a 1/f-like spectrum. Some theoretical calculations as well as sample spectra from a computer simulation are shown in Fig. 1. The theory applies to any quantity obeying a diffusion equation. It implies, for example, that the temperature of an object has 1/f-like fluctuations. Consequently, there are a large number of mechanisms through which 1/f noise may influence most systems. The diffusion mechanism also implies a characteristic length, $\lambda(f) \equiv (D/\pi f)^{1/2}$, which is a measure of the average spatial extent of a fluctuation at frequency f. Low-frequency fluctuations are correlated over large volumes.

We have observed these effects by shining a beam of light through a colloidal suspension. The frequency spectrum of the fluctuations in the intensity of the transmitted light is shown in Fig. 2 for two different samples. We have also been able to show that 1/f noise in metal films is caused by temperature fluctuations modulating a temperature-dependent resistivity. The amplitude of the noise in the films is in excellent agreement with our theory. We have also demonstrated experimentally that 1/f noise in thin films is correlated over distances on the order of the frequency-dependent correlation length, $\lambda(f)$.

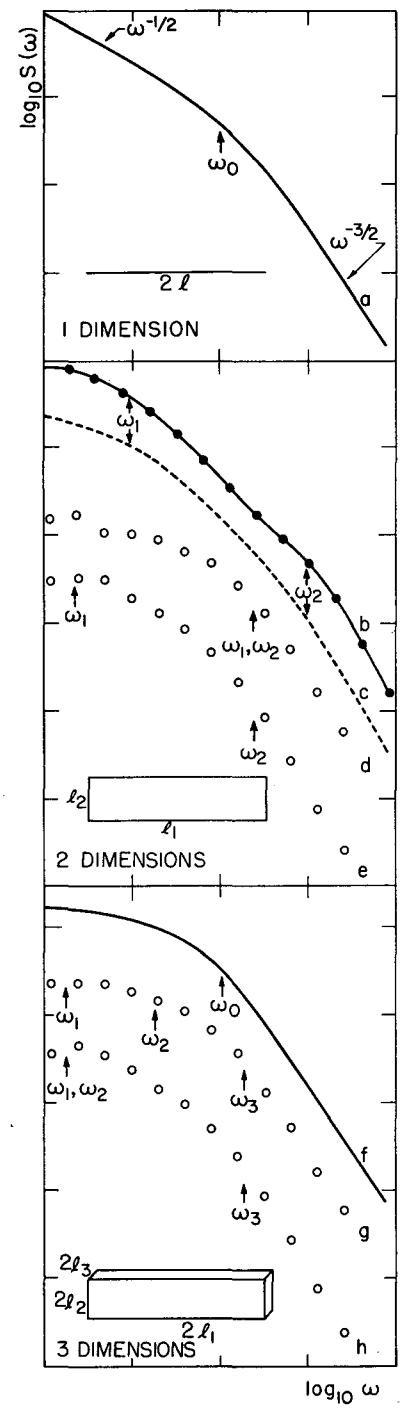

Fig. 1. Fluctuation spectra: (a), (b), (c), and (f) are calculations, while (d), (e), (g) and (h) are computer simulations. Each scale division represents one decade. (XBL 7312-6764)

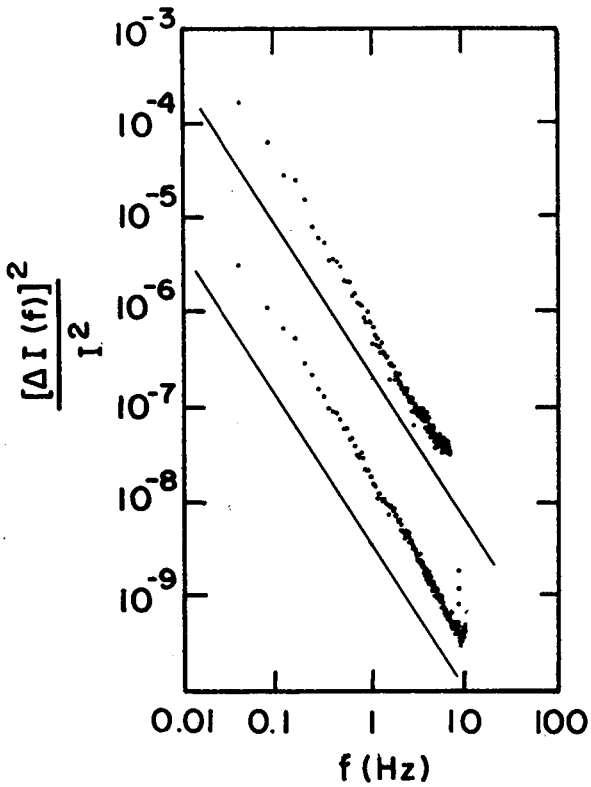

Fig. 2. Fluctuation spectra of light transmitted through two different colloidal suspensions. The calculated spectra are also shown. (XBL 7312-6763)

2. 1/f NOISE IN CRITICAL SYSTEMS

Gilbert Hawkins and John Clarke

Systems that are close to a critical point undergo large fluctuations in one or more of their thermodynamic properties. For example, the concentration fluctuations in a binary mixture are large near the critical point because of the divergence of the osmotic compressibility at the second-order phase transition. We have constructed an apparatus to measure the frequency spectrum of these fluctuations. A light beam is passed through a cell containing the mixture, and the spectrum of the fluctuations in the intensity of the transmitted beam is measured. Preliminary measurements indicate that the spectrum is 1/f-like. In addition, the amplitude of the noise is strongly temperature dependent. Both of these results are expected on theoretical grounds.

This system is of interest because the 1/f noise can be measured in an equilibrium system, unlike electrical noise in a resistor. The equations governing the dynamics of fluctuations in equilibrium binary mixtures are well understood, so that the system can be analyzed in detail theoretically. Furthermore, we expect to be able to deduce the behavior of the long-range correlation length which characterizes the spatial extent of the concentration fluctuations.

3. RELAXATION OF QUASIPARTICLE BRANCH IMBALANCE IN SUPERCONDUCTORS

John Clarke and James L. Paterson

Under appropriate conditions, a normal current can propagate in a superconductor. The flow of a normal current implies an imbalance of the quasiparticles above and below the Fermi level. The characteristic time, τ_Q, required for this imbalance to relax to equilibrium governs the dissipation generated by the normal current. Apart from the fundamental interest in the problem, this imbalance is important in various applications; for example, the dissipation that occurs when a normal current is converted to a supercurrent at the interface of a normal metal and a superconductor.

We have generated a branch imbalance by passing a current from a normal metal into a superconducting film via a tunnel junction. The imbalance creates a quasiparticle voltage V that is measured by means of a second junction grown on top of the superconductor, where

$$V = I\tau_Q/2e^2\Omega N(0)g_{NS}(0)$$

Here, I is the injection current, Ω the volume of the superconductor, N(0) the density of states at the Fermi surface (for one spin) in the superconductor, and $g_{NS}(0)$ the conductance of the second tunnel junction. Figure 1 shows $\zeta = (V/I)g_{NS}(0)\Omega$ versus reduced temperature for Sn. For Sn:3 wt.% In, only phonon processes are important. The solid curve is a fit using

$$\tau_Q^{ph} = 1.0\times10^{-10}\ \Delta(0)/\Delta(T)\ \text{sec}.$$

In the clean samples, elastic processes also contribute. The dashed lines are a fit to both inelastic and elastic scattering, with

$$\tau_Q^{el} = \frac{\tau_1}{\langle a^2\rangle_o}\left[1+\left(\frac{\hbar}{2\tau_1\Delta}\right)^2\right]\frac{k_BT^*}{\Delta}\left[1+\frac{k_BT^*}{\Delta}\right].$$

In this equation, τ_1 is the elastic scattering time, $\langle a^2 \rangle_o$ the mean square gap anisotropy, and T^* the mean quasiparticle temperature. At low temperatures, we obtain a good fit with $T^* = 2T_c$.

Preliminary results have been obtained for Pb. It appears that recombination may be the major process contribution to branch relaxation in this metal. Further investigation of this result is planned.

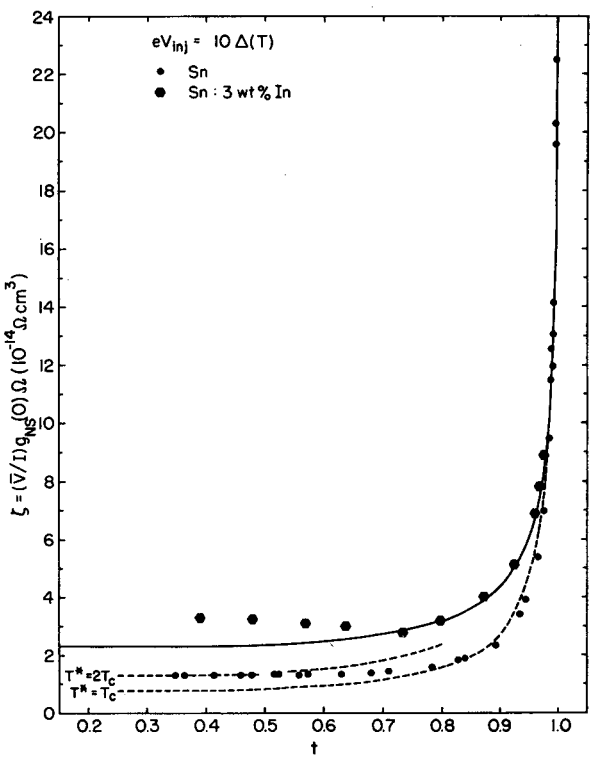

Fig. 1. ζ versus $t=T/T_c$ for Sn. Solid curve is for phonon processes only. Dashed curves include elastic processes which are important in clean Sn. (XBL 736-6355)

In Fig. 2, we summarize τ_Q, τ_R (the recombination time) and $t(T_c)$ (the time for injected quasiparticles to cool to T_c) for Sn and Pb.

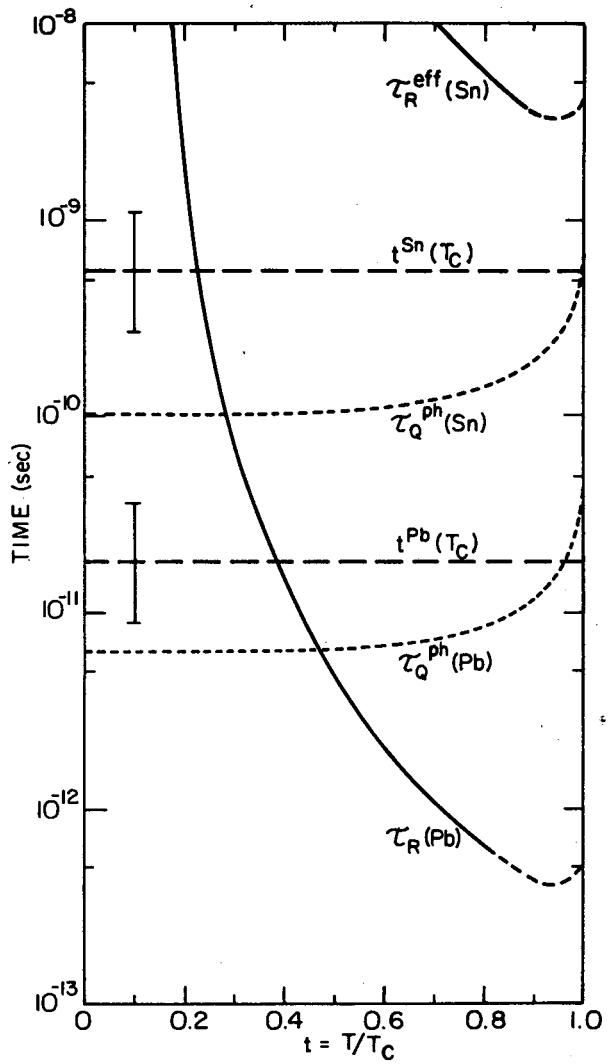

Fig. 2. τ_Q, τ_R, and $t(T_c)$ for Sn and Pb. (XBL 7311-5591)

4. ELECTRON FOCUSING IN BISMUTH: A NEW METHOD OF MEASURING THE DIAMETER OF A FERMI SURFACE

John Clarke and Louis Schwartzkopf

There are a number of techniques available for measuring various properties of the Fermi surface of a metal. However, none of these gives a very accurate determination of the diameter of the Fermi surface, except in certain special cases. We have developed a new method for measuring the diameter of any Fermi surface, using electron focusing, and applied it to bismuth.

Two interlocking superconducting combs are evaporated onto the surface of the crystal [Fig. 1(a)]. The resistance R(H) between the combs at liquid helium temperatures is measured as a function of a magnetic field parallel to the teeth of the combs. There is a resistance anomaly [Fig. 1(b)] whenever electrons are focused between teeth of different combs or of the same combs.

Single crystals were grown from 99.999+

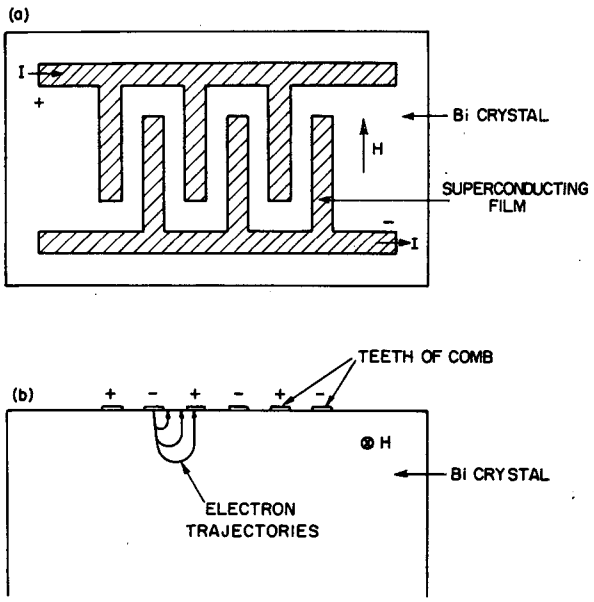

Fig. 1. Comb structure: (a) plan view; (b) side view, showing orbits. (XBL 738-1727)

pure bismuth, and spark-cut to the desired orientations. The surface was chemically polished, and any contamination removed in a glow discharge. The tin combs were evaporated onto the cleaned surface. Figure 2 shows the variation of R(H) with magnetic field for the binary plane. Measurements of R(H) have been obtained for the other principal crystal orientations. Some of the hole orbits have also been observed.

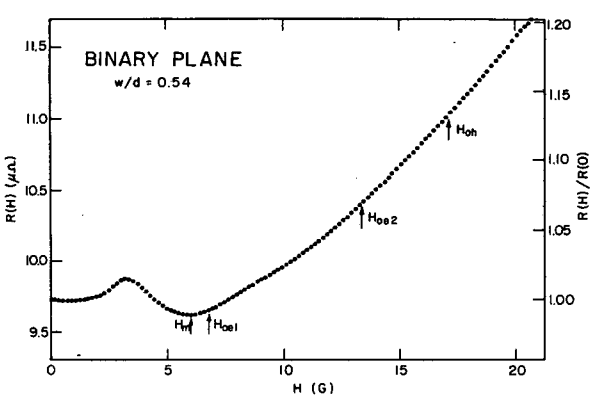

Fig. 2. R(H) versus H for the binary plane of bismuth. (XBL 736-6254)

At present, our overall accuracy is about ±4%. To within the various experimental errors, our values of the measured diameters are in good agreement with those in the literature. However, we feel that our accuracy could be readily improved to much better than 1%; this method would then be the most accurate available for measuring diameters.

5. DETERMINATION OF BCS PARAMETER N(O)V IN "NORMAL" METALS

John Clarke and Michael L. Rappaport

There are a large number of metals that do not become superconducting at the lowest achievable temperature ($\lesssim$ 1 mK). However, it is of interest to have estimates of the transition temperatures T_c of such metals, even though these temperatures are not presently attainable. These estimates can then be compared with theoretical predictions in order to test the reliability of the theory. Our experiment measures the parameter N(O)V [N(O) is the density of states at the Fermi surface for are spin, and V is the electron-electron interaction parameter], which is related to the Debye temperature θ_D and T_c by the relation $T_c = 1.14\ \theta_D \exp[-1/N(O)V]$.

The experiment involves the measurement of the resistance of SNS sandwiches down to very low temperatures in a dilution refrigerator. S is a superconductor, usually Pb or Sn, and N is the metal being studied. From the reduction in resistance as the temperature is lowered, one can deduce a value of N(O)V in the normal metal. So far, we have obtained data in which the normal metal is Ir, Rh, Cu, and Ag.

The transition temperature of Mg is of particular interest because theoretical predictions place it close to 1 mK. Because Mg oxidizes very rapidly, we have designed and built a new high-vacuum sputter-evaporation system to prepare samples. Sputter-etching is used to remove surface contamination from a rolled foil, and then Pb or Sn is evaporated onto the Mg without venting the chamber to air. We hope to obtain data on Mg in the near future.

Theoretical calculations of the temperature dependence of the resistance of SNS sandwiches are under way in collaboration with Professor Cohen's group.

6. SUPERCONDUCTING TUNNEL JUNCTION BOLOMETERS

John Clarke and Gary I. Hoffer

There is considerable need for improved bolometers in the submillimeter region. We have developed a new type of bolometer that consists of a superconductor-normal-metal (SNS) Josephson junction evaporated onto a sapphire substrate. The sapphire is suspended on lead-coated nylon treads inside a vacuum can (Fig. 1). The critical current, I_c, of the junction is a rapid function of temperature. Measurement of I_c with a SQUID enables small changes in the temperature of the substrate to be detected. Our best bolometer has an electrical NEP $\approx 5\times10^{-15}$ W/$\sqrt{\text{Hz}}$, and a detectivity $D^* \approx 10^{16}$ cm $\sqrt{\text{Hz}}$/W. The detectivity is a factor of 30 larger than that of the best bolometers currently available. The reverse side of the sapphire substrate is coated with a thin film of bismuth to absorb the far infrared radiation.

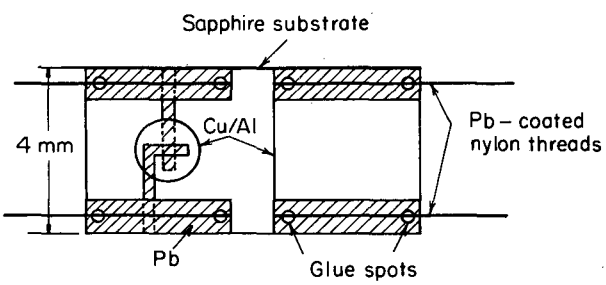

Fig. 1. Configuration of SNS bolometer. (XBL 7112-4927A)

We have also investigated the use at a superconductor-insulator-normal metal (SIN) quasiparticle tunnel junction as a bolometer element. The resistance of this junction at voltages below the superconducting energy gap is a rapid function of temperature. The sensitivity of this junction should be comparable to that of the SNS junction. However, we have found that only Al-AlO_x-Pb or Al-AlO_x-Sn junctions are of sufficiently high quality to be usable as bolometers. Unfortunately, these junctions deteriorate rapidly when stored at room temperature. Junctions with better storage properties, such as Nb-NbO_x-Cu have leakage currents that make them unusable as bolometer elements. We are therefore concentrating our effort on the SNS bolometer.

7. STABLE SENSITIVE SUPERCONDUCTING DEVICES

John Clarke, Thomas Y. Hsiang, and Myron Frommer

For a number of years, we have used ultrasensitive superconducting devices, SQUIDS, to measure tiny magnetic fields and voltages. We are now working to develop a highly reliable and stable device that can be used in an environment outside the laboratory.

We have designed, built, and tested a toroidal dc SQUID and its associated electronics. The SQUID has a resolution of 10^{-5} flux quanta/$\sqrt{\text{Hz}}$ at 100 Hz: this figure represents an order-of-magnitude improvement over the sensitivity of other SQUIDS. The noise spectrums is 1/f. The SQUID utilizes point contacts as Josephson junctions.

We are now developing a thin-film SQUID that we hope will be extremely stable and reliable. The device is made of Nb-NbO_x-Pb tunnel junctions. We have constructed a stainless steel ultra-high vacuum system in which we have mounted a Sputter Gun. The system has been used successfully to fabricate tunnel junctions that are of high quality, and that also appear to be very stable with respect to thermal cycling and room temperature storage. We hope soon to be able to test a tunnel junction SQUID. One advantage of tunnel junctions is that their critical current is independent of temperature below 4.2°K. We believe that this will make the devices relatively free from long-term drift, an important consideration in geophysical measurements, and other applications requiring long-term stability.

8. RESEARCH PLANS FOR CALENDAR YEAR 1974

John Clarke

We have developed a theory of 1/f noise that we believe is applicable to a large variety of systems. We plan to considerably expand our work on this project both theoretically and experimentally. The measurements of 1/f noise in metal films will be extended to semiconducting films. In this way we hope to be able to understand the mechanisms of 1/f noise in semiconductors, and to apply these ideas to semiconducting devices, such as diodes and transitors. The performance of these devices is severely limited by 1/f noise at low frequencies.

A program has been started to study 1/f noise at low temperatures. We will measure

the noise at the superconducting transition of thin films to test the validity of our theory at low temperatures. These results should enable us to predict the ultimate performance of superconducting bolometers. We plan also to examine the noise in semiconducting bolometers in order to determine their ultimate resolution. The low-frequency noise of Josephson junctions will be measured, and an attempt made to fit the results to the theory. The low-frequency noise and long-term drift of these devices is of great importance in certain applications, for example, geophysical measurements. We hope to be able to determine which types of junction have the best long-term stability.

The 1/f spectra of various critical fluids will be measured. We hope to be able to incorporate these fluctuations into our theory. It should also be possible to obtain information about the correlation lengths at or near the critical point from these results.

We now have a good understanding of pair-quasiparticle non-equilibrium processes in superconductors. We propose to study the possibility of using these processes in devices.

The measurements of the resistances of superconducting-normal metal superconducting sandwiches at very low temperatures will be continued. In particular, we plan to use Mg as the normal metal. These experiments should enable us to estimate the values of N(0)V and hence of the superconducting transition temperature in various metals that are not known superconductors.

We hope to improve the noise equivalent power of the Josephson junction bolometer to about 10^{-15} W/$\sqrt{\text{Hz}}$. The response of the bolometer in the millimeter and submillimeter range will be determined. The bolometer will be developed into a hardened device for astrophysical and other applications.

We will continue to develop highly reliable and stable Josephson junctions for use in SQUIDS. We hope to be able to use these SQUIDS for various measurements outside the laboratory, for example, the measurement of noise and drift in the Earth's magnetic field.

9. 1973 PUBLICATIONS AND REPORTS

John Clarke and Associates

Journals

1. J. Clarke, Low-Frequency Applications of Superconducting Quantum Interference Devices, Proc. IEEE 61, 8 (1973)(LBL-1112).

2. J. Clarke, La Cryoelectronique, La Recherche, No. 38, 845 (1973)(LBL-1810).

3. R. Dalven, Electron and Hale Effective Masses in Lead Polonide (PbPo), J. Phys. C6, 671 (1973).

4. R. Dalven, Electronic Structure of PbS, PbSe, and PbTe, in Solid State Physics, Vol. 28, edited by F. Seitz, D. Turnbull, and H. Ehrenrach (Academic Press, New York, 1973), pp. 179-224.

5. R. Dalven, Empirical Relation between Energy Gap and Lattice Constant in Cubic Semiconductors, Phys. Rev. B, 8, 6033 (1973) (LBL-2218).

Conferences

1. J. Clarke and L. Schwartzkopf, Electron Focusing in Bi: A New Method of Measuring the Caliper of a Fermi Surface, San Diego Meeting of the APS, March 19-22, 1973.

2. J. Clarke, G. I. Hoffer, and P. L. Richards, Superconducting Tunnel Junction Bolometers, International Conference on Detection and Emission of Electromagnetic Radiations with Josephson Junctions, Perros-Guinec, France, Sept. 3-5, 1973 (LBL-2222).

3. R. Dalven, Recent Studies of Lead Polonide (PbPo), Proc. Int. Conf. on Semimetals and Narrow Gap Semiconductors, Nice-Cardiff, 1973 (to be published)(LBL-2524).

LBL reports

1. John Clarke and James L. Paterson, Measurements of the Relaxation of Quasiparticle Branch Imbalance in Superconductors, LBL-2289, Nov. 1973.

2. J. Clarke, Josephson Junction Detectors, LBL-2283, Oct. 1973.

3. R. Dalven, Proposed Search for Superconductivity in the Semiconductor Site (to be published)(LBL-2525).

4. R. Dalven, Comments on the Probable Electronic Structure of the Group II Polonides (to be published)(LBL-2526).

5. R. Dalven, Proposed Measurement of the Knight Shift in Lead Polonide (PbPo), (to be published)(LBL-2527).

6. James L. Paterson, Pair-Quasiparticle Potential Differences in Current-Carrying Superconductors (Ph.D. thesis), LBL-1840, July 1973.

7. Richard F. Voss and John Clarke, Fluctuation Spectra for Systems Obeying a Diffusion Equation, LBL-2534, Dec. 1973.

8. John Clarke and Richard F. Voss, 1/f Noise from the Diffusion of Particles or Heat, LBL-2536, Dec. 1973.

D. EXPERIMENTAL SOLID STATE PHYSICS AND QUANTUM ELECTRONICS

Y. Ron Shen, Principal Investigator

1. TUNABLE FAR INFRARED GENERATION BY OPTICAL MIXING

James R. Morris, Patrick K. H. Yang, Paul L. Richards, and Y. Ron Shen

The generation of tunable far infrared (FIR) by optical mixing in nonlinear crystals has attracted much attention recently.[1-7] In this paper we report the generation of continuously tunable radiation from 20 to 190 cm^{-1} using a dual-frequency dye laser system. We observed FIR radiation in the 20 to 160 cm^{-1} frequency range with various phase matching schemes in $LiNbO_3$: forward collinear (FCPM), backward collinear (BCPM),[3,4] and non-collinear (NCPM). We have also investigated FCPM in ZnO, ZnS, CdS, and CdSe at selected frequencies as high as 190 cm^{-1}.

Figure 1 shows the basic experimental arrangement for FIR generation with FCPM and BCPM. This single dye cell system was rather simple and very convenient to use. We also used two separate dye lasers[8] pumped with a single ruby beam, especially for the NCPM[9] case. The single dye cell system was composed of a single dye cell pumped nearly longitudinally by a ruby laser, a Glan-Thomson prism[10] (GTP) to divide the cavity into two independent arms with orthogonally polarized beams, two echelle gratings to tune independently the frequencies of the two beams, and a single output mirror to insure spatial overlap of the two beams. Temporal overlap of the beams was obtained by equalizing the net gain in the two arms of the cavity. To achieve this, the pump beam was circularly polarized or linearly polarized at 45° with respect to the axes of the polarizer. Fine tuning of the relative gain of the two arms was obtained with a microscope slide in the cavity. With a 30-MW, 30-nsec ruby laser beam the dye laser (DTTC iodide in DMSO) output had a peak power of 600 kW and its two wavelengths could be tuned independently from 8100 to 8400 Å. The linear polarizations were pure to within 10%.

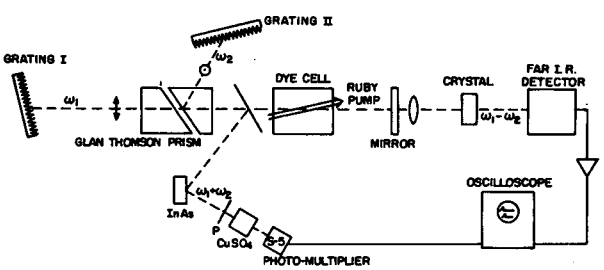

Fig. 1. One of the far infrared generation setups. The wavelength of the two beams can be independently varied from 8100 to 8400 Å using a single dye cell.

(XBL 735-6007)

The FIR output from the nonlinear crystal was detected by an n-type InSb (Putley) detector at 1.4°K for the 20-95 cm^{-1} range and a Ge:Ga detector at 4.2°K for the 95-200 cm^{-1} range. Our results on FCPM and NCPM in $LiNbO_3$ are shown in Fig. 2. The data agree well with the solid theoretical curves.

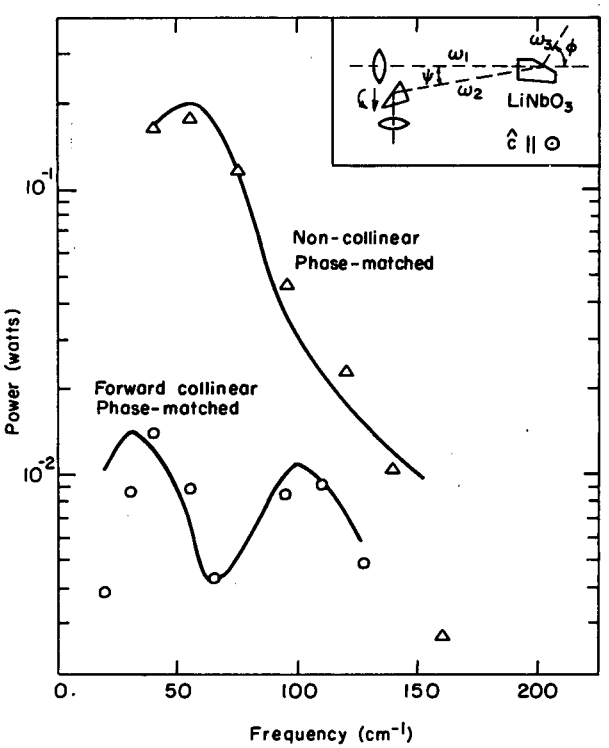

Fig. 2. Far-infrared power generated vs. frequency for two phase-matching conditions. The far infrared power is normalized by a sum frequency power. The solid curves are the theoretical calculations based on data of the far infrared absorption and the Raman cross section in $LiNbO_3$. The insert shows the experimental geometry for non-collinear phase-matching which was achieved by a coupled translation and rotation of the prism.

(XBL 738-1787)

We have also verified that the dual-frequency dye laser system, shown in Fig. 1, can be operated with a flashlamp-pumped Rhodamine 6G dye laser, although the dye laser output of our system was insufficient to generate detectable FIR in the mixing experiment. However, a flashlamp-pumped dye laser system of 100 kW peak power and 1 μsec pulsewidth would yield the same FIR signal for each pulse as our laser-pumped system with 600 kW peak power and 30 nsec pulsewidth. Because a repetition rate greater than 1 pulse/sec is possible with such a dye laser, the dual-frequency single dye cell scheme described here should make a very useful source for FIR spectroscopy. Compared with the other FIR generation experiments using CO_2 lasers,[2, 5-7] this system has the advantages of a large continuously tunable FIR range and the use of room-temperature mixing crystals.

2. OPTICAL-FIELD INDUCED ORDERING IN THE ISOTROPIC PHASE OF A NEMATIC LIQUID CRYSTAL

George K. L. Wong and Y. Ron Shen

The linear optical properties of liquid crystalline materials have been the subject of extensive investigation recently. The nonlinear optical properties of the same materials, however, have not yet received much attention. In this paper, we report the first measurements on the optical-field-induced refractive index for a nematic substance in its isotropic phase. Ordering in the molecular orientation induced by the optical field is essentially responsible for this nonlinear refractive index. Field-induced ordering in the isotropic phase of a nematic system has been previously observed with an applied dc electric or magnetic field, but the same effect obtained with an optical field has never been reported before. Using a Q-switched laser pulse, we have also been able to measure directly the relaxation time for the variation of the orientational order. The transient response of the order parameter is governed by the equation

$$\nu\partial Q_{\alpha\beta}/\partial t + AQ_{\alpha\beta} = f_{\alpha\beta}(t) \ ,$$

$$f_{\alpha\beta} = \Delta_\chi(3E_\alpha^* E_\beta - |E|^2\delta_{\alpha\beta})/9 \ , \qquad (1)$$

where ν is a viscosity coefficient. For an input laser pulse with a Gaussian pulse shape,

$$f_{\alpha\beta}(t) = C_{\alpha\beta}\exp(-b^2t^2) \ ,$$

we have

$$Q_{\alpha\beta}(t) = (C_{\alpha\beta}/b\nu)\exp(-t/\tau)\exp(1/4b^2\tau^2) \times \{1 + \mathrm{erf}[bt-(2b\tau)^{-1}]\} \qquad (2)$$

which varies as $\exp(-t/\tau)$ when $bt \gg 1$.

We can find $Q_{\alpha\beta}(t)$ by measuring the field-induced $\Delta_{\chi\alpha\beta}(t)$. Results were obtained for MBBA at various temperatures in the isotropic phase. In every case, we obtained a perfect exponential tail for $Q_{\alpha\alpha}(t)$ from which we calculated the relaxation time τ. In Fig. 1, we present the experimental data τ as a function of T. They agree very well with

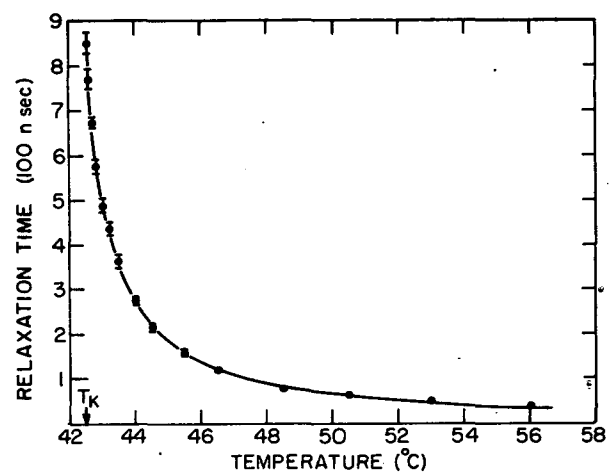

Fig. 1. Relaxation time τ of the order parameter as a function of temperature. The solid curve is the theoretical curve obtained for $\tau=\nu/a(T-T^*)$ with $T^*=314.7°K$ and $\nu=\nu_0\exp(2800°K/T)$. The dots are the experimental data points.

(XBL 7212-7358)

the theoretical expression $\tau=\nu/a(T-T^*)$ of de Gennes[1] if we assume $\nu=\nu_0\exp(W/T)$ with $W=2800°K$ as suggested by Stinson and Litster[2] and $T^*=314.7°K$. The clearing temperature of our material is $T_K=315.5°K$. The relaxation time varies from ~40 nsec at temperatures far above the phase transition to > 800 nsec near the transition. These results are in good agreement with those obtained from light scattering by Stinson and Litster.[2] However, we believe our measurements are more straightforward and accurate.

The optical Kerr constant of MBBA is unusually large. In comparison with CS_2, we found $B(MBBA)/B(CS_2) = 10$ at 326°K. Because of the large nonlinearity, a liquid

crystalline material can have potential applications in nonlinear optical devices.

1. P. G. de Gennes, Phys. Lett. 30A, 454 (1969), and Mol. Cryst. Liquid Cryst. 12, 193 (1971).
2. T. W. Stinson, III, and J. D. Litster, Phys. Rev. Lett. 25, 503 (1970).

3. EXPERIMENTAL STUDY OF TRANSIENT SELF-FOCUSING

George K. L. Wong and Y. Ron Shen

The liquid crystalline material MBBA in its isotropic phase has a large field-induced refractive index due to molecular reorientation. The orientational effect has a relaxation time which varies with temperature from ~40 to > 800 nsec. The system is therefore ideal for study of the transient self-focusing effect using Q-switched laser pulses which have pulsewidths in the range of 10 nsec. This is a problem which has been attracting a great deal of attention of research workers in nonlinear optics. There already exist a number of theoretical calculations on the subject.[1] However, no quantitative experimental results were available, since in ordinary liquids the orientational relaxation time is of the order of psec and it is difficult to obtain quantitative information from picosecond pulse measurements.

We have observed transient self-focusing in MBBA in the isotropic phase. We have studied the dynamics of the effect as a function of temperature and input power. The results are in semi-quantitative agreement with the theoretical calculations.[1] In this case, the phase modulation of light is relatively slow, and hence no appreciable spectral broadening can be detected. There is evidence that stimulated Raman and Brillouin scattering is initiated by self-focusing of light in the medium, but stimulated Raman and Brillouin scattering is not the mechanism to limit the diameter of the self-focused beam.

1. See, for example, F. Shimizu, IBM J. Res. and Develop. 17, 286 (1973).

4. LUMINESCENCE AT HIGH EXCITON DENSITIES IN CdSe

Eric Hanson, Arnold J. Schmidt, and Y. Ron Shen

High excitation of semiconductors has recently attracted much attention and has been studied in a large number of materials. We have investigated the photoluminescence spectrum of CdSe, on which a number of partially conflicting reports exist.[1-3]

The excitation source used was a flashlamp pumped dye laser, which was developed in our group. A peak intensity of 2 MW/cm^2 in a 1 μsec pulse could be obtained at the sample. All measurements were done at 4.2 or 1.8°K. The excitation frequency could be varied between 5800 and 6100 Å. The luminescence spectra were recorded via a double monochromator, a photomultiplier, and an oscilloscope. In addition to the well-known luminescence spectrum at low excitation levels, a broad intense new luminescence band appears with increased excitation power. Its intensity grows superlinearly with excitation and its position is shifted to longer wavelength correspondingly. The shift grows with power and is ~ 40 Å at 1 MV/cm^2, which is close to the damage threshold. The band is scarcely structural and has a width of ~ 20 Å. All parts of the luminescence spectrum show the same time dependence as the excitation pulse.

Very close to the damage threshold (~2 MV/cm^2) a narrow (<10 msec) inherent spike grows out of the otherwise smooth signal. Its position varies randomly from shot to shot, and its origin is not yet understood.

We also attempted to measure the decay time of the luminescence in various parts of the spectrum. For these investigations, the laser pulse was curtailed by a Pöckels cell with a fast risetime. The fall time of the pulse was better than 5 nsec. Some experiments were performed with a nsec excitation pulse. This pulse was obtained by switching a Pöckels cell between two crossed polarizers from 0 to 180° phase shift with a fast pulse and thereby slicing a 3-nsec pulse out of the center of the originally 1-μsec-long laser pulse. All parts of the luminescence spectrum, which according to various models are due to exciton-exciton collision, exciton molecules, and/or exciton molecule collisions, have decay times smaller than 5 nsec.

1. J. Bille, H. Liebing, and P. Mengel, Phys. Stat. Sol. 53, 353 (1972).
2. H. Saito, S. Shinoga, and E. Hanamura, Solid State Communications 12, 227 (1973).
3. H. Kuroda, S. Shionoya, and E. Hanamura, Solid State Communications 12, 533 (1973).

5. DISPERSION OF NONLINEAR OPTICAL SUSCEPTIBILITIES $\chi^{(2)}(2\omega)$ OF III-V SEMICONDUCTORS

Don Bethune, Arnold J. Schmidt, and Y. Ron Shen

Nonlinear optical susceptibilities have always been the most important subject in nonlinear optics. They are essential for the design of modern optical devices. Most of the theories and experiments on nonlinear susceptibilities deal with frequencies in the transparent region. Only a few of them cover a narrow region in the absorption band. No work has yet been reported on nonlinear susceptibilities over a wide frequency range.

We are presently making measurements on the nonlinear optical susceptibilities $\chi^{(2)}(2\omega)$ of GaAs, InAs, and InSb at 80 and 300°K using a flash-pumped dye laser. The fundamental frequency varies from 1.8 to 2.8 eV. Our results therefore complement those earlier results of Parsons and Chang[1] using a ruby-laser-pumped dye laser. In this region, either ω or 2ω appear in resonance with a number of known critical points. There is also possible enhancement of $\chi^{(2)}(2\omega)$ due to simultaneous resonances of w and 2ω with some critical points. We shall compare our experimental results with the theoretical calculations which are being carried out in cooperation with Prof. C. Y. Fong of U. C. Davis, using the pseudopotential method with the available band structures of these compounds.

1. F. G. Parsons and R. K. Chang, Optics Comm. 3, 173 (1971).

6. RESONANT RAMAN SCATTERING IN Cu_2O

Peter Y. Yu, Yves Petroff, and Y. Ron Shen

Resonant Raman scattering (RRS) close to free or bound excitons has been the subject of a number of reports, but the same effect involving a "forbidden" exciton has received little attention. We have found strong resonant enhancement in the 220-cm^{-1} Raman mode of Cu_2O at the Γ_{12}^--phonon-assisted absorption edge of the forbidden 1s yellow exciton. The results are shown in Fig. 1 together with a theoretical curve which yields good agreement with the experimental data. It shows that the 220-cm^{-1} mode is due to scattering of two Γ_{12}^- phonons and the resonant enhancement is strongly affected by the exciton lifetime. The latter effect has never been considered or observed before in RRS.

We have also observed sharp resonant enhancements in some other two-phonon Raman modes of Cu_2O around the n=2 to 6 peaks of the yellow exciton series. An example is

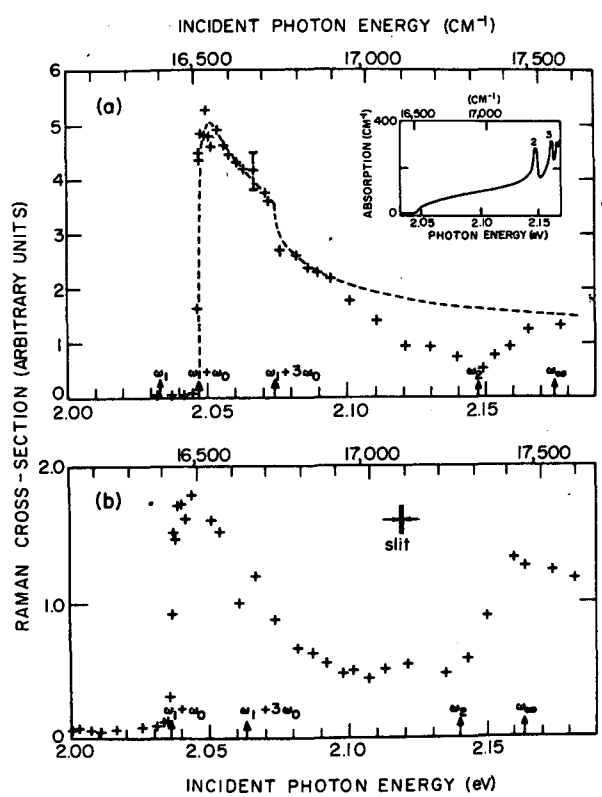

Fig. 1. Raman cross section of the 220-cm^{-1} line of Cu_2O at two different temperatures: (a) ~16°K and (b) ~80°K. [These temperatures represent those of the lattice obtained in (a) from the lineshape of the phonon-assisted free-exciton recombination spectra and in (b) from the position of the 1s yellow exciton in the luminescence.] Inset in (a), absorption spectra of Cu_2O at 4.2°K. Dashed curve in (a) is the theoretical curve.
(XBL 7210-7111)

shown in Fig. 2. We are able to explain the results quantitatively by a theory which allows for multiple resonances in the scattering process. The calculated curve is seen to be in good agreement with the experimental data in Fig. 2.

We have also measured the resonant enhancement of five one-phonon Raman modes of Cu_2O in the vicinity of the blue and indigo excitons. The experimental results show qualitative agreement with the theoretical predictions.

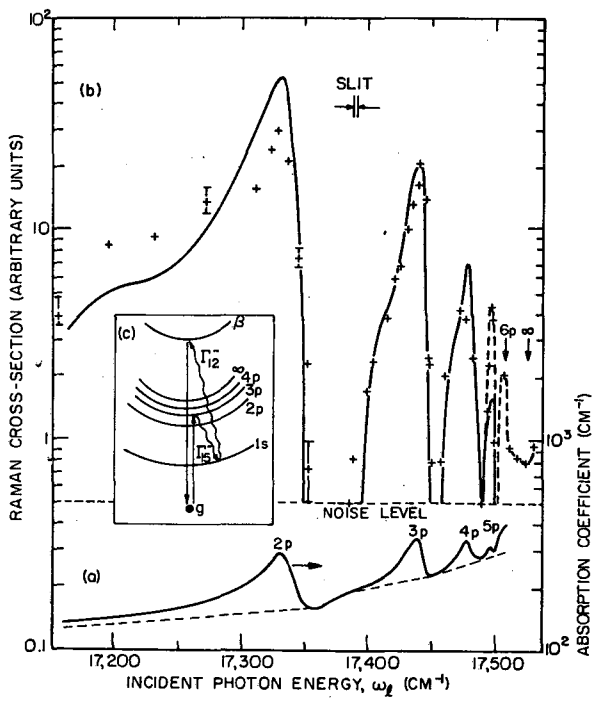

Fig. 2. (a) The absorption spectrum of Cu_2O measured at ~ 5°K. The dotted curve represents the background absorption due to phonon-assisted transitions. (b) The Raman cross section of the $\Gamma_{15}^{-(2)}$ (LO) + Γ_{12}^{-} (770 cm^{-1}) mode of Cu_2O obtained at ~ 10°K as a function of incident photon energies. The solid curve is the theoretical curve. (c) A schematic diagram of the dominant resonant Raman process at $\omega_\ell \sim \omega_{30}$. g stands for the ground state and β an allowed exciton. (XBL 7311-5575)

7. ABSORPTION, PHOTOLUMINESCENCE, AND RESONANT RAMAN SCATTERING IN BiI_3--THE NONEXISTENCE OF BIELECTRONS IN BiI_3

Yves Petroff, Peter Y. Yu and Y. Ron Shen

Recently Gross and coworkers[1] have reported observing a series of lines in the absorption and luminescence spectra of BiI_3. The frequencies of these lines seem to obey the equation

$$\nu_n = \nu_\infty + \frac{R}{n^2} = 15{,}978 + \frac{1995}{n^2}\ cm^{-1} \qquad (1)$$

with n = 3,4,5,6, and 7. This series converges towards the low-frequency side and therefore has the form of an "inverted" hydrogenic series. Gross et al. suggested that this series is due to the formation of "bielectrons" or "biholes" in the crystal. A bielectron (or bihole) is formed by two electrons (or holes) with a negative reduced mass and coupled to each other by Coulomb interaction to form a hydrogen-like bound state with energies given by an inverted hydrogenic series.

The question whether such bielectrons or biholes can exist or not is an interesting one. So far, there has been no direct experimental evidence of their existence. Although the bielectron model can account for the energy of certain absorption and luminescence lines observed by Gross et al., there are difficulties in reconciling this model with other optical properties of BiI_3. We have therefore repeated the experiments of Gross et al. and, in addition, we have measured the luminescence excitation spectrum and the resonance Raman scattering in BiI_3 using a cw tunable dye laser. The results on absorption and photoluminescence are shown in Fig. 1. We found that our results

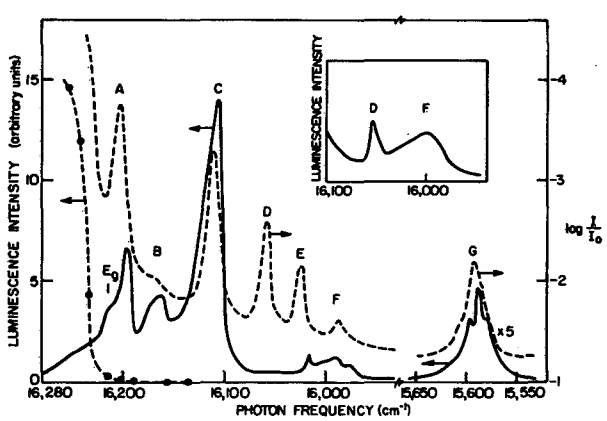

Fig. 1. Absorption, luminescence, and luminescence excitation spectra of BiI_3. Solid line is the luminescence spectrum of sample A at 4.2°K. Dotted line is the absorption spectrum of sample A at 1.8°K. The insert shows the luminescence of sample C in the region where it differs from sample A. ---- · ---- · --- is the luminescence excitation spectrum for peak C in sample C at 4.2°K. (XBL 738-1600)

cannot be explained by the bielectron model. We are led to conclude that the line spectra observed by Gross et al. in BiI_3 is probably due to impurities or defects, as suggested by Timofeev and Vashchenko.[2]

1. E. F. Gross, V. I. Perel, and R. I. Skekhmamet'ev, Zhetf Pis. Red. 13, 320 (1971); [English Translation: JETP Lett. 13, 229 (1971]; E. F. Gross, N. V. Starostin, and R. I. Skekhmamet'ev, Fizika Tverdogo Tela 13, 3393 (1971); [English Translation: Soviet Physics--Solid State 13, 2850 (1973)].
2. V. B. Timofeev and V. I. Vashchenko, Opt. Spektr. 24, 740 (1968); [English Translation: Opt. and Spect. 24, 396 (1968)].

8. RESONANT RAMAN SCATTERING IN CRYSTALLINE Se

Peter Y. Yu, Nabil Amer, Yves Petroff, and Y. Ron Shen

The optical spectra of trigonal Se at low temperatures show a strong polarization-dependent excitonic peak in the region around 2 eV.[1,2] We have measured the resonant Raman scattering (RRS) in trigonal Se at liquid helium temperatures between 1.9 and 2.2 eV using a cw tunable dye laser. The Raman active modes of symmetry A_1 (235 cm^{-1}) and E(147 cm^{-1}) were found to exhibit different resonance enhancements. The A_1 mode showed broad structures near the absorption edge while the E mode has a sharp resonance at 1.99 eV. The infrared active (Raman forbidden) A_2 mode (112 cm^{-1}) also showed sharp resonance due to the exciton labeled as a-exciton.[1] We are presently doing resonant Raman measurements on many other modes. They all seem to show interesting resonant enhancement behavior. We shall try to compare the RRS lineshapes with existing theories.

1. S. Tutihasi and I. Chern, Phys. Rev. 158, 623 (1967).
2. W. Henrian, in The Physics of Selenium and Tellurium, edited by W. C. Cooper (Pergamon Press, Oxford, 1969).

9. WAVELENGTH-MODULATION SPECTROSCOPY OF SOLIDS

Stanley Kohn, Yves Petroff, and Y. Ron Shen

We have used our wavelength-modulation spectrometer to study a number of solids. We discuss the various cases separately in the following.

a. PbS, PbSe, and PbTe

The narrow-gap IV-VI semiconductors have been the object of extensive research over the past few years. Particular emphasis has been placed on studies of band-edge properties and the fundamental gap, but few experiments have been done at higher energies. We have measured the wavelength-modulated reflectance of PbTe, PbSe, and PbS from 1.5 to 6 eV at temperatures ranging from 5 to 300°K. We have also made empirical pseudopotential calculations of the band structures, the $\varepsilon_2(\omega)$ spectra, and $(1/R)dR/d\omega$ for these compounds and compared with the experimental results. They confirm the critical-point assignment for the spectrum of PbTe made previously by Cohen and Tsang.[1]

1. M. L. Cohen and Y. W. Tsang, Proc. of the Conference on the Physics of Semimetals and Narrow Gap Semiconductors, 1970, edited by D. L. Carter and R. T. Bates (Pergamon Press, New York, 1971), p. 303.

b. GaSe, GaS, and Alloys

The interest in the properties of layer materials has grown considerably in the last few years. In particular the optical properties of GaSe have been widely investigated.

The first reflectivity spectra were reported by Bassani et al.[1] and Gasanova et al.[2]. More recently electroreflectance, electroabsorption, and thermoreflectance measurements have been reported. There is some disagreement about the position of the electronic transitions and also their assignment.

To help a new pseudopotential band structure calculation of GaSe, we have measured the wave-modulation spectra in the energy range 2 to 6 eV at 300,77, and 5°K, of GaSe, GaS, $GaSe_{0.8}S_{0.2}$, and $GaSe_{0.2}S_{0.8}$. A large number of new structures has been observed.

1. F. Bassani, D. L. Greenaway, and G. Fischer, in Proc. Intern. Conf. on the Physics of Semiconductors (1964), p. 51.

2. N. Gasanova and G. A. Akhundov, Opt. Spectry. 20 193 (1966).

c. SbSI and $ZnGeP_2$

We report here the study of the normal reflectivity spectra R and the corresponding derivative spectra (1/R)dR/dE of SbSI between 2 and 6 eV. The spectra show very strong anisotropy. We have also tried to use the change of the wavelength modulation spectrum to monitor the change in the band structure of SbSI due to the phase transition at 292°C ($D_{2h}^{16} \rightarrow C_{2v}^{9}$). Careful examination of the spectra at various temperatures around T_c shows no observable change. We report also the wavelength-modulated reflectivity spectra of the chalcopyrite crystal $ZnGeP_2$ at 5°K between 2 and 6 eV, for E ∥ C and E ⊥ C. The experimental results are compared with the theoretical band structure calculation by de Alvarez and Cohen.[1]

1. C. de Alvarez and M. L. Cohen, Phys. Rev. Lett. 30, 979 (1973).

d. Effect of Carrier Concentration on Reflectivity Spectra of Ge and InSb

We have measured at 5°K the derivative spectra (1/R)dR/dE around the E_1 and $E_1 + \Delta_1$ structures, of Ge and InSb with different impurity concentrations. In the more highly doped samples, the peaks are broadened and shifted slightly to lower frequencies. The change in the value of (1/RdR/dE is much larger than recently predicted by Seraphin and Aspnes, based on the surface field effect. Different possibilities for the effect are discussed. Wavelength modulation measurements on samples with an applied surface electric field have shown no difference.

10. RAYLEIGH-WING SCATTERING IN A LIQUID CRYSTALLINE MATERIAL

David Y. S. Lin, Nabil M. Amer, and Y. Ron Shen

Light scattering as a means to probe the various dynamic properties of liquid crystalline materials has become increasingly popular recently. While most of the published work deals with scattering from low-frequency thermal fluctuations, little effort goes into studies of high-frequency fluctuations. In particular, the depolarized Rayleigh-wing scattering has received practically no attention. This latter effect, which presumably arises from orientational fluctuations of individual molecules in media composed of anisotropic molecules, has, however, long been the subject of extensive investigation on ordinary liquids. We have done what we believe to be the first investigation of Rayleigh-wing scattering in liquid crystalline materials. We are particularly interested in the change of the Rayleigh-wing spectrum as the temperature varies near the isotropic-nematic phase transition. We found that, as in ordinary liquids, the spectrum can be decomposed into two Lorentzians, one having a half width of a few cm^{-1} and the other one order of magnitude broader. Both Lorentzians narrowed appreciably as the temperature was lowered, but there was a sudden increase in the linewidths at the isotropic-to-nematic transition. The results are interpreted with the usual model for orientation fluctuations of individual molecules, incorporated with the sudden change of the order parameter at the phase transition.

11. THEORETICAL PROBLEMS

Y. Ron Shen

a. Far Infrared Generation by Optical Mixing and Stimulated Raman Scattering via Spin-Flip Transitions in InSb

Far infrared generation by optical mixing and by stimulated scattering via spin-flip transitions is treated, using the general formalism of coherent excitations of

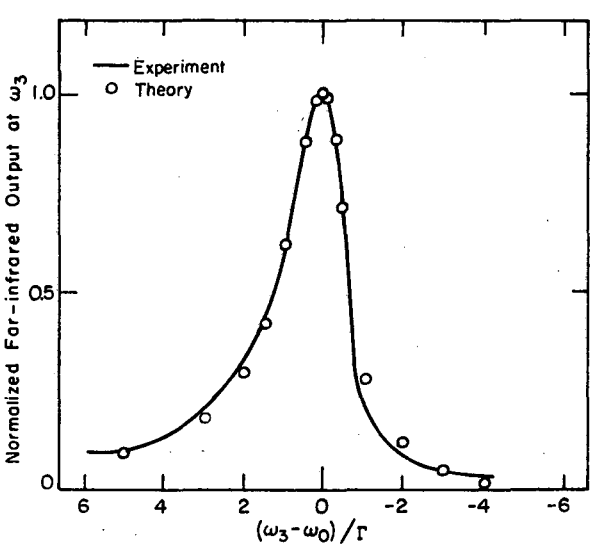

Fig. 1. Theoretical results (crosses) of normalized far infrared power output in optical mixing as a function of $(\omega_3 - \omega_0)/\Gamma$ in comparison with the experimental results (curve of Ref. 1). (XBL 7312-7167)

polaritons. Practical numerical examples for InSb are given. The result for the case of optical mixing agrees well with the experimental result of Nguyen and Bridges[1] (see Fig. 1). The calculation also suggests that the infrared output from a spin-flip Raman laser should be easily observable.

1. V. T. Nguyen and T. J. Bridges, Phys. Rev. Lett. 29, 359 (1972).

b. Distinction Between Resonant Raman Scattering and Hot Luminescence

With the advance of tunable lasers, resonance Raman scattering has become a subject of much investigation. There is, however, apparent confusion in the literature on the difference between resonance Raman scattering (RRS) and hot luminescence (HL). Recently, Klein[1] showed that in some cases the resonance Raman scattering efficiency could be written as the product of the absorption coefficient and the quantum yield for hot luminescence. He then concluded that RRS was often equivalent to HL. In the literature, usually either one or the other was used to interpret the observed resonant Raman data.[1-5] We have derived expressions for the cross-sections of RRS and HL using the density-matrix formalism which takes into account relaxation due to random processes more properly than the golden-rule approach. We show that RRS and HL are in fact two distinct physical processes, although they are simultaneously present in ordinary RRS experiments.

The physical differences between the two processes are quite obvious. RRS is a two-photon direct process, while HL is a two-step process. HL arises from radiative decay of the excess population pumped into the intermediate state by the exciting field, but RRS does not. The two processes have in general different lineshapes. If the exciting field is abruptly shut off, HL should have an exponential decay corresponding to the decay of the excess population in the intermediate state, aside from the usual induction decay. These differences can be seen more clearly in the following derivation.

1. M. V. Klein, Phys. Rev. B8, 919 (1973).

12. RESEARCH PLANS FOR CALENDAR YEAR 1974

Y. Ron Shen

We shall continue our research on resonant Raman scattering and luminescence in various types of semiconductors using the cw tunable dye laser. We shall try to set up a pulsed dye laser system for the resonant Raman work in order to cover a larger spectral range. We plan to investigate other nonlinear optical effects in liquid crystals and to measure the optical effects in a homologous series of liquid crystals. We shall start new experiments on high-intensity excitations in solids. We shall try to extend the range of wavelength-modulation spectroscopy into vacuum uv. We shall also continue the measurements of nonlinear optical susceptibilities in various crystals.

13. 1973 PUBLICATIONS AND REPORTS

Y. Ron Shen and Associates

Journals

1. R. Zucca and Y. R. Shen, Wide-Range Wavelength Modulation Spectrometer, Appl. Optics 12, 1293 (1973)(LBL-1184).

2. S. Kohn, Y. Petroff, P. Y. Yu, and Y. R. Shen, Wavelength Modulation Spectra of PbS, PbSe, PbTe, and SnSe, J. Nonmetals 1, 147 (1973)(LBL-456).

3. S. Kohn, Y. Petroff, and Y. R. Shen, Wavelength Modulation Spectra of GaSe, GaS, and Alloys, Surface Science 37, 205 (1973) (LBL-1407).

4. P. Y. Yu, Y. R. Shen, and Y. Petroff, Resonance Raman Scattering in Cu_2O at the Blue and Indigo Excitons, Solid State Communications 12, 973 (1973)(LBL-1441).

5. P. Y. Yu, Y. R. Shen, and Y. Petroff, Resonance Raman Scattering at the Forbidden Yellow Exciton in Cu_2O, Phys. Rev. Letters 30, 283 (1973)(LBL-1192).

6. Y. R. Shen, Optical Wavelength-Modulation Spectroscopy, Surface Science 37, 522 (1973) (LBL-1402).

7. Y. Petroff, S. Kohn, and Y. R. Shen, Optical Spectra of CsI, CsBr, $ZnGeP_2$, and SbSI, Surface Science 37, 540 (1973) (LBL-1409).

8. George K. L. Wong and Y. R. Shen, Optical-Field-Induced Ordering in the Isotropic Phase of a Nematic Liquid Crystal, Phys. Rev. Letters 30, 895 (1973)(LBL-1433).

9. S. E. Kohn, P. Y. Yu, Y Petroff, Y. R. Shen, Y. Tsang, and M. L. Cohen, Electronic Band Structure and Optical Properties of PbTe, PbSe, and PbS, Phys. Rev. B 8, 1477 (1973)(LBL-1132).

10. Y. Petroff, S. Kohn, and Y. R. Shen, Effect of Carrier Concentration on the Reflectivity Spectrum of Ge and InSb, Surface Science 37, 591 (1973)(LBL-1410).

11. K. H. Yang, P. L. Richards, and Y. R. Shen, Coherent Phonon Generation by Optical Mixing in a One-Dimensional Superlattice, J. Appl. Phys. 44, 1417 (1973)(LBL-1889).

12. N. M. Amer and Y. R. Shen, Low-Frequency Raman Mode in Smectic Liquid Crystals Near the Phase Transitions, Solid State Communications 12, 263 (1973)(LBL-1156).

13. Y. R. Shen, Theory of Far Infrared Generation by Optical Mixing and Stimulated Raman Scattering via Spin-Flip Transitions in InSb, Appl. Phys. Lett. 23, 516 (1973).

14. M. M. T. Loy and Y. R. Shen, Study of Self-Focusing and Small-Scale Filaments of Light in Nonlinear Media, IEEE J. Quantum Electron. QE-9, 409 (1973)(LBL-431).

15. K. H. Yang, J. Morris, P. L. Richards and Y. R. Shen, Phase-Matched Generation of Tunable Far Infrared Radiation by Mixing of Two Dye Lasers, Bull. Am. Phys. Soc. 18, 350 (1973)

16. C. Varea de Alvarez, M. L. Cohen, S. Kohn, Y. Petroff and Y. R. Shen, Electronic Structure of $ZnGeP_2$, Bull. Am. Phys. Soc. 18, 351 (1973),

17. P. Y. Yu, Y. Petroff and Y. R. Shen, Resonance Raman Scattering in Cu_2O at the Blue and Indigo Excitons, Bull. Am. Phys. Soc. 18, 411 (1973)(LBL-1446 Abs.).

18. Y. Petroff, P. Y. Yu, and Y. R. Shen, Optical Properties of BiI_3, Bull. Am. Phys. Soc. 18, 412 (1973)(LBL-1444 Abs.).

19. P. Y. Yu and Y. R. Shen, Free Carrier Effects on the Resonance Raman Scattering of InSb at the E_1 Transition, Bull. Am. Phys. Soc. 18, 413 (1973)(LBL-1442 Abs.).

20. P. Y. Yu and Y. R. Shen, Wave Vector Dependence in the Resonance Raman Scattering of InSb Near the E_1 Transition, Bull. Am. Phys. Soc. 18, 413 (1973)(LBL-1447 Abs.).

21. Y. Petroff, P. Y. Yu, and Y. R. Shen, Resonance Raman Scattering in BiI_3, Bull. Am. Phys. Soc. 18, 413 (1973)(LBL-1445 Abs.).

22. G. K. L. Wong and Y. R. Shen, Laser-Field-Induced Ordering in the Isotropic MBBA, Bull. Am. Phys. Soc. 18, 437 (1973) (LBL-1443 Abs.).

23. D. Bethune, A. J. Schmidt, and Y. R. Shen, Dispersion of Nonlinear Optical Susceptibility $\chi^{(2)}$ (2w) of III-V Semiconductors, Bull. Am. Phys. Soc. 18, 1577 (1973)(LBL-2271 Abs.).

24. G. K. L. Wong and Y. R. Shen, Transient Self-Focusing of Light in MBBA, Bull. Am. Phys. Soc. 18, 1588 (1973)(LBL-2262 Abs.).

25. P. Y. Yu, N. M. Amer, and Y. R. Shen, Resonant Raman Scattering in Selenium, Bull, Am. Phys. Soc. 18, 1589 (1973)(LBL-2272 Abs.).

26. K. H. Yang, J. R. Morris, P. L. Richards, and Y. R. Shen, Phase-Matched Far Infrared Generation by Optical Mixing of Dye Laser Beams, Appl. Phys. Lett. 23, 669 (1973) (LBL-2226).

LBL reports

1. Y. Petroff, P. Y. Yu, and Y. R. Shen, Absorption, Photoluminescence, and Resonance Raman Scattering in BiI_3, LBL-1890, Aug. 1973.

*2. Y. R. Shen, Distinction between Resonance Raman Scattering and Hot Luminescence, June 1973.

3. C. Y. Fong, Y. Petroff, S. Kohn, and Y. R. Shen, Wavelength-Modulation Spectra of SbSI and Its Electronic Structure, LBL-2225, Aug. 1973.

4. P. Y. Yu and Y. R. Shen, Multiple Resonance Effects in Raman Scattering, LBL-2290, Nov. 1973

*Work done while on Sabbatical leave at Laboratoire d' Optique Quantique, Univ. of Paris, 1972.

0 0 0 0 4 0 0 7 4 0 6

Appendices

0 0 0 0 4 0 0 7 4 0 7

IMRD STAFF FOR 1973

Principal Investigators	Postdoctoral Fellows and Other Scientists	Graduate Students
Neil Bartlett	C. Adams D. McKee *W. Roland *B. Zemva	K. Leary D. McKee T. Richardson
Robert Bragg		K. Ankra M. Biswal *Y. Chen K. Danso F. Hamzeh R. Mishra L. Salmon R. Saxena
Leo Brewer	*C. Chang *W. Duley *W. Smeltzer	G. Bullard J. Stiga
John Clarke	*R. Dalven M. Frommer *G. Hawkins J. Kruger	G. Hoffer T. Hsiang *M. Ketchen J. Paterson M. Rappaport L. Schwartzkopf R. Voss
Marvin Cohen	*G. Martinez *M. Schluter *J. Wang	*D. Chadi *J. Chelikowsky *J. Joannopolous *C. Varea de Alvarez
Robert Connick		W. Earl T. Rowland
Lee Donaghey	C. Wright	*T. Anderson R. Bissinger *P. Chen K. Geraghty C. Manke P. Mundkur R. Pong *S. Styer
Richard Fulrath	*L. Froschauer	G. Bandyopadhyay *T. Basu D. Biswas K. Crabtree J. Dih J. Masaryk J. Sherohman D. Wang

Principal Investigator	Postdoctoral Fellows and Other Scientists	Graduate Students
Charles Harris	H. Brenner *T. Gough A. Nishimura R. Schlupp *H. Schuch	W. Breiland J. Brock *A. Burns M. Fayer J. Koert *M. Lewellyn R. Panos R. Shelby *M. Tarrasch P. Wilday
Ronald Herm		R. Behrens B. Earl A. Freedman L. Gundel L. Loh T. Parr C. Sholeen
Ralph Hultgren		
Harold Johnston	S. Chang *D. Fielder E. Kamaratos D. Martin T. Paukert R. Watson G. Whitten	J. Birks P. Connell E. Franzblau J. Girman R. Graham D. Martin *B. Nordstrom G. Streit
William Jolly	J. Howdeshell M. Lazarus *T. Schaaf K. Strom	T. Briggs J. Illige W. Perry L. Pont J. Reed D. Yang
George Jura		T. Chen R. Glienna B. Jurado
Bruce Mahan	*K. Gillen T. Sloane	W. Dimpfl J. Fair W. Ruska P. Schubart R. Terkowitz J. Winn

Principal Investigators	Postdoctoral Fellows and Other Scientists	Graduate Students
William Miller	*W. Hunt *R. Preston *C. Sloane *O. Weres	S. Augustin B. Garrison S. Hornstein A. Raczkowski *P. Whitlock *G. Zahr
J. W. Morris, Jr.	*D. Klahn *Y. Ohtakara *C. Syn	I. Charo W. Gourdin D. Grivas F. Hamzeh K. Hanson H. Hwang S. Jin C. Krause J. Sanchez C. Syn S. Wen B. Whitaker
Rolf Muller	J. Mathieu	C. Brown C. Chew J. Cooper F. McLarnon M. Sand
Rollie Myers		T. Hynes D. Lindner M. St. John R. Wilson J. Yarnell
John Newman		P. Appel R. Homsy J. Miksis C. Mohr K. Nisancioglu
Donald Olander	A. Ullman	R. Acharya *V. Kruger A. Machiels *F. Nuh R. Yang
Earl Parker Victor Zackay Milton Pickus	M. Yokota	B. Babu B. Francis K. Hemachalam L. Miwa G. Shiflett T. Tom

Principal Investigators	Postdoctoral Fellows and Other Scientists	Graduate Students
Earl Parker	D. Bhandarkar	*H. Adkins
Victor Zackay	*S. Bush	B. Babu
	*J. Evans	D. Bhandarkar
	*G. Lai	M. Bhat
	*F. Ravitz	R. Clark
	M. Yokota	C. Ericsson
		B. Francis
		W. Garrison
		R. Horn
		S. Ivy
		G. Kohn
		*A. Llopis
		R. Lott
		H. Offer
		E. Plaza
		P. Ruf
		*J. Sanchez
		G. Sasaki
		E. Saur
		M. Schanfein
		H. Sirot
		L. Thompson
		T. Tom
		*J. Wert
		W. Wood
		J. Yuen
		P. Zajchowski
Joseph Pask	I. Aksay	I. Aksay
	R. Langston	P. Dokko
	*C. Marumo	C. Hoge
		G. Holmquist
		*S. Risbud
		W. Snowden
		T. Sweeting
		C. Tao
		B. Wong
Norman Phillips	*G. Brodale	S. Bader
	*E. Hornung	W. Fogle
		T. Hall
		*B. Krusor
		G. Schwartz
		M. Wun
Milton Pickus		K. Hemachalam
		J. Klein
		F. Reinel
Paul Richards	S. Buckner	R. Aurbach
	*J. Claassen	R. Bailey
		*J. Mather
		Y. Taur
		W. Tennant
		D. Woody
		K. Yang

Principal Investigators	Postdoctoral Fellows and Other Scientists	Graduate Students
Earl Parker Victor Zackay	D. Bhandarkar *S. Bush *J. Evans *G. Lai *F. Ravitz M. Yokota	*H. Adkins B. Babu D. Bhandarkar M. Bhat R. Clark C. Ericsson B. Francis W. Garrison R. Horn S. Ivy G. Kohn *A. Llopis R. Lott H. Offer E. Plaza P. Ruf *J. Sanchez G. Sasaki E. Saur M. Schanfein H. Sirot L. Thompson T. Tom *J. Wert W. Wood J. Yuen P. Zajchowski
Joseph Pask	I. Aksay R. Langston *C. Marumo	I. Aksay P. Dokko C. Hoge G. Holmquist *S. Risbud W. Snowden T. Sweeting C. Tao B. Wong
Norman Phillips	*G. Brodale *E. Hornung	S. Bader W. Fogle T. Hall *B. Krusor G. Schwartz M. Wun
Milton Pickus		K. Hemachalam J. Klein F. Reinel
Alexander Pines	J. Chang	E. Abramson *S. Allison *M. Hoza T. Shattuck
Kenneth Pitzer	*G. Mayorga L. Silvester	*L. Bernstein J. Kim *Y. Lee G. Vogt
Paul Richards	S. Buckner *J. Claassen	R. Aurbach R. Bailey *J. Mather Y. Taur W. Tennant D. Woody K. Yang

Principal Investigators	Postdoctoral Fellows and Other Scientists	Graduate Students
Gene Rochlin		M. Jack D. McBride
Alan Searcy	*D. Beruto A. Buchler *R. Coyle D. Meschi	T. Basu L. Fuke S. Lim P. Mohazzabi J. Roberts K. Shah
Y. Ron Shen	*A. Mysyrowicz A. Schmidt P. Yu	D. Bethune W. Garrison E. Hanson S. Kohn Y. Lin J. Morris J. Stokes K. Wong
Gabor Somorjai	K. Baron S. Brumbach *C. Chang M. Chesters *J. Deville *J. Doll D. Hagen *L. Kesmodel *M. Martin *W. Siekhaus T. Taylor *Y. Tsang	S. Bernasek D. Blakely *J. Crump L. Firment J. Gland *R. Johnson D. Kahn C. Megerle S. Overbury *P. Stair J. Wasilczyk
Gareth Thomas	*D. Kirkwood *K. Schneider *R. Sinclair *M. Von Heimendahl	L. Chen *Y. Chen R. Clark R. Gronsky R. Hall D. Howitt D. Huang J. Koo J. McMahon R. Miller F. Mirmirani B. Narasimha Rao M. Okada G. Stone O. Van der Biest
Charles Tobias	*T. Lengas L. Silvester	R. Acosta E. Carlson *O. Chacon U. Landau J. Riggs

Principal Investigators	Postdoctoral Fellows and Other Scientists	Graduate Students
Jack Washburn		S. Alavi
		T. Astrup
		R. Drosd
		T. Huo
		R. Jecmen
		T. Kosel
		J. Lira-Olivares
		H. Mohamed
		T. Peterson
		J. Roberts
		K. Seshan
		A. Srivastava
		K. Stolt
		W. Wu

*Participant Status

0 0 0 0 4 0 0 7 4 1 0

VISITING SCIENTISTS/SEMINAR SPEAKERS

Dr. Anthony Francis, Department of Chemistry, University of Illinois Chicago, Illinois

Professor Heinz Gerischer, Institute for Physical Chemistry, Munich, Germany

Professor Oskar Glemser, Director of the Institute for Inorganic Chemistry, University of Gottingen, Gottingen, Germany

Professor Paul Hagenmuller, Structural Inorganic Chemistry Laboratories, University of Bordeaux, Bordeaux, France

Professor Rudolph Hoppe, Director of the Inorganic Chemistry Institute, Justus Liebig University, Giessen, Germany

Dr. M. Jaksic, Instiute of Chemical Technology and Metallurgy, Belgrade, Yugoslavia

Dr. F. A. Kuznetsov, Deputy Director, Institute of Inorganic Chemistry, Siberian Division of the Academy of Sciences, U.S.S.R.

Dr. Rudiger Mews, Inorganic Chemistry Institute, University of Gottingen, Gottingen, Germany

Dr. Dieter Naumann, Institute fur Anorganische Chemie, Universitat of Dortmund, Dortmund, West Germany

Dr. Josik Portier, Structural Inorganic Chemistry Laboratories, University of Bordeaux, Bordeaux, France

Dr. Peter Robertson, Swiss Federal Institute of Technology, Zurich, Switzerland

Professor Peter Sartori, Inorganic Chemistry Institute, The University, Aachen, Germany

Professor Martin Schmeisser, Rector of the University of Dortmund, Dortmund, Germany

Professor Fritz Seel, Director of the Inorganic Chemistry Institute, The University of the Saarland, Saarbrucken, Germany

Dr. Friedrich O. Sladky, Institute for Inorganic Chemistry, University of Innsbruck, Innsbruck, Austria

Dr. Alain Tressaud, Structural Inorganic Chemistry Laboratories, University of Bordeaux, Bordeaux, France

Dr. Don Webster, Research Scientist, Lockheed, Palo Alto Research Laboratory, Palo Alto, California

DEGREES AWARDED IN 1973

Ph.D. Degrees

1. İlhan A. Aksay, Diffusion and Phase Relationship Studies in the Alumina-Silica System (LBL-1403, April).
2. Gautam Bandyopadhyay, Relation of Processing Parameters to the Properties of Lithium Ferrite (LBL-2263, Nov.).
3. William Lawrence Dimpfl, The Dynamics of Nonreactive Inelastic Ion-Molecule Collisions (LBL-1873, Aug.).
4. Boyd Lorel Earl, Photochemical Studies of Alkali Halide Vapors (LBL-1866, Aug.).
5. John Louis Gland, Low Energy Electron Diffraction and Work Function Studies of Adsorbed Organic Layers on the (100) and (111) Crystal Surface of Platinum, (LBL-1816, Sept.).
6. Donald D. Gibler, Perfluoro Cations of the Non-Metallic Elements (LBL-1157, April).
7. Michael David Jack, Properties of Tunnel Junctions with Fluorocarbon Dielectric Barriers, (LBL-1805, Nov.).
8. Daniel Roy Kahn, The Hydrogenolysis of Cyclopropane on Platinum Stepped Single Crystals at Atmospheric Pressure (LBL-1891, Sept.).
9. Douglas R. Martin, Kinetics of Fluorescence of Sulfur Dioxide (LBL-1199, March).
10. Joseph S. Masaryk, Diffusion of Gases in Glass (LBL-1818, May).
11. Duncan Eldridge McBride, Jr., Characterization of Metal Oxide Tunneling Barriers (LBL-1855, Sept.).
12. Douglas Edward McKee, Preparative and Structural Studies Involving Noble-Gas and Related Compounds (LBL-1814, May).
13. Charles Arthur Mims, Molecular Beam Chemistry of Alkaline Earth Atoms (LBL-1159, May).
14. Kemal Mustafa Nisancioglu, Current Distribution and Mass Transfer in Rotating Electrode Systems (LBL-1880, Sept.).
15. Per-Erik Nordal, Nuclear Double Resonance Study of KH_2PO_4 (LBL-117, May).
16. Rodney M. Panos, Phosphorescence Microwave Double Resonance Studies of the Lowest Excited Triplet State of p-Dichlorobenzene (LBL-1822, June).
17. James L. Paterson, Pair-Quasiparticle Potential Differences in Current-Carrying Superconductors (LBL-1840, July).
18. Jeffrey Andrew Stokes, Wavelength Modulation Spectroscopy of Some Semiconductors and Metals (LBL-1125, March).
19. Kaj Gunnar Stolt, Computer Simulation of Frank Loop Contrast in Field Ion Images (LBL-2200, Sept.).
20. Chol Kyl Syn, The Role of Dislocation Interaction with Solute Atoms in the Strengthening of Metals (LBL-2270, Nov.).
21. Frederick John Szalkowski, Auger Electron Spectroscopy Analysis of Vanadium and Vanadium Compound Surfaces (LBL-888, Oct.).
22. Han-Chung Tsai, The Viscosity of Cesium Metal to its Critical Temperature (LBL-1413, July).
23. Carmen Varea De Alvarez, Electronic Structure of Diamond, Zincblende and Chalcopyrite Semiconductors (LBL-1863, Sept.).
24. John S. Winn, A Beam Study of Ne^+ and $O^+(^4S_{3/2})$ Scattering by Molecular Hydrogen Isotopes and Helium (LBL-1820, June).

D.Eng. Degrees

1. Mangalore Dilip Bhandarkar, Structure and Elevated Temperature Properties of Ferritic Alloys Strengthened by Intermetallic Compounds (LBL-1858, Sept.).
2. Go Sasaki, Low-Temperature Toughness of BCC Fe-Ni-Ti Alloys (LBL-1493, July).
3. Thomas Tom, Microstructural Variables and Fracture Toughness of High Strength Mo and Mo-Ni Steels (LBL-1856, Sept.).
4. William Edwin Wood, An Investigation of Metallurgical Factors which Affect the Fracture Toughness of Ultra High Strength Steels (LBL-1474, May).

M.S. Degrees

1. Howard E. Adkins, Structure and Properties of TRIP Steels Processed by Deformation and Thermal Cycling (LBL-1491, April).
2. Charles Ray Brown, Interferometry of Solid Thin Films (LBL-2264, Dec.).
3. Israel Frederic Charo, Corrosion Fatigue Properties of Surgical Implant Materials (LBL-2207, Dec.).
4. Robert Allan Clark, Structure and Properties of Fe-Mo-C Steels (LBL-1801, June).
5. Clyde Ernest Ericsson, An Isothermal Study of Bainitic and Martensitic Transformations in Some Low Alloy Steels Using a New Magnetic Permeability Technique (LBL-2279, Dec.).
6. Lloyd Manabu Fuke, Vaporization Studies of Strontium Sulfate, (LBL-1832, June).
7. Ronald M. Horn, Influence of Heat Treatment on the Fatigue Crack Growth RAtes of a Secondary Hardening Steel (LBL-2292, Dec.).
8. Jack Hovingh, Diffusion of Lanthanum in Molten Uranium (LBL-1130, Feb.).
9. Robert M. Jecmen, Memory Switching Effects in As-Te-I Chalcogenide Glass (LBL-1817, July).
10. Roy Neal Lott, Evaluation of the End Quench Test as a Design Criterion (LBL-1476, June).
11. Hani Abo El-Fotoh Mohamed, Mechanism of Pressure Welding (LBL-2510, Dec.).
12. Leslie Oga Pont, X-Ray Photoelectron Spectroscopy of Some Nickel and Iron Compounds (LBL-1829, June).
13. Louis Jean Salmon, Experimental Techniques for Growing Unidirectionally Solidified Oriented Eutectics (LBL-1834, June).
14. John J. Wasilczyk, Measurement of Intensities of Low Energy Electron Diffraction Beams from Platinum Surfaces and From Absorbed Overlayers (LBL-1807, June).
15. Wei-Kuo Wu, Determination of Loop Type in As^+ Implanted Silicon (LBL-1415, Feb.).
16. Harry Hung-Kwan Yip, Mass Transfer Coefficient in Packed Bed at Low Reynolds Numbers (LBL-1831, June).

0 0 0 5 4 0 0 7 4 1 2

LEGAL NOTICE
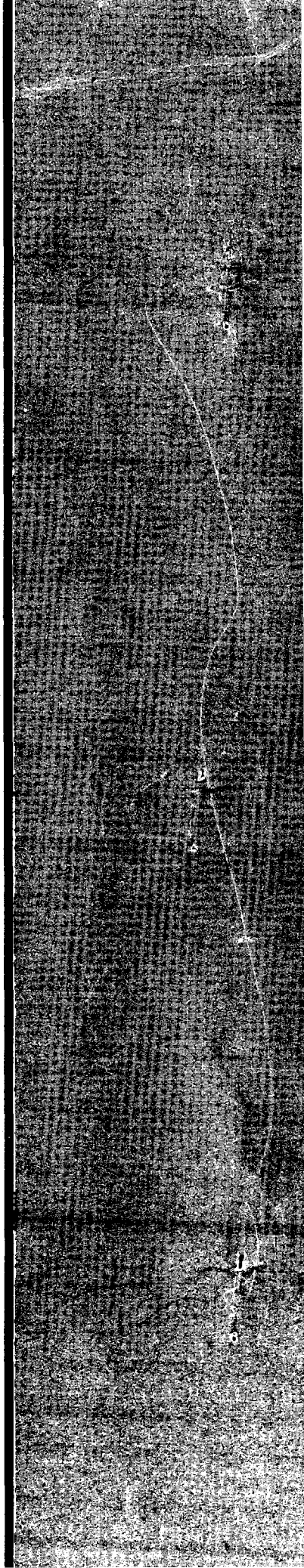
This report was prepared as an account of work sponsored by the United States Government. Neither the United States nor the United States Atomic Energy Commission, nor any of their employees, nor any of their contractors, subcontractors, or their employees, makes any warranty, express or implied, or assumes any legal liability or responsibility for the accuracy, completeness or usefulness of any information, apparatus, product or process disclosed, or represents that its use would not infringe privately owned rights.